IAHR 2017

37th IAHR WORLD CONGRESS

13-18 August, 2017
Kuala Lumpur, Malaysia

Supported by Spain Water and IWHR, China

INSTRUMENTATION AND EXPERIMENTAL METHODS

WHY MOVING-BOAT ADCP STREAMFLOW MEASUREMENT DOES NOT REQUIRE A STRAIGHT-LINE PATH?

HENING HUANG[(1)]

[(1)] Teledyne RD Instruments, 14020 Stowe Drive, Poway, CA, USA,
hhuang@teledyne.com

ABSTRACT

This paper presents a mathematical proof and field verification of the path-independence principle: the discharge measured by a moving-boat ADCP is independent from the path of the survey boat under the assumption that the flow is steady and homogeneous in streamwise direction. The field measurement was made on the Choa Praya River under a steady flow condition; it involves eight transects with a variety of boat's paths including straight, curved, and looped. The measured discharges from the eight transects are very consistent; the relative maximum residual discharge is only 2.03%; the relative uncertainty (Type A) associated with the mean of the transect discharges is only 0.93%.

Keywords: ADCP; discharge measurement; river and streams.

1 INTRODUCTION

An acoustic Doppler current profiler (ADCP) is commonly mounted on a survey boat or a small float to transverse a river or open channel when making streamflow measurements. This is usually referred to as the moving-boat ADCP method. During a transect from the start bank to the end bank, an ADCP mainly collects three kinds of data along the boat's track: (1) velocity relative to the ADCP, known as the water tracking velocity; (2) velocity relative to the river bottom, known as the bottom tracking velocity (which is the boat velocity if no moving bottom exists); and (3) water depth. The boat velocity is removed from the relative velocity to obtain the actual water velocity that is used in discharge calculation. Detailed discussion on the ADCP technology and moving-boat ADCP streamflow measurements can be found in (Simpson, 2001; Oberg et al., 2005; Mueller and Wagner, 2009).

An important feature of moving-boat ADCP streamflow measurements is that the measurement does not require a straight-line path of the survey boat. A survey boat can make an arbitrary path and the measured discharge will be the same or have no systematic error due to paths (however, the measurement will still have random or sampling errors). This feature is referred to as the path-independence principle. The path-independence principle is a "controversy" with respect to the traditional current meter method for streamflow measurements. The current meter method requires measurements be made on a straight-line that is approximately perpendicular to the main flow. A tag-line or cableway is often needed when using the current meter method. The path-independence principle has been demonstrated in field measurements. However, to the knowledge of the author, the mathematical proof of the principle cannot be found in the ADCP literature. Because of the lack of a mathematical proof, the path-independence principle is sometimes questioned by some ADCP users.

This paper presents a mathematical proof of the path-independence principle associated with the moving-boat ADCP method for streamflow measurements. The transect discharge data collected in a field measurement that consisted of eight transects with a variety of paths are presented as a verification of the path-independence principle.

2 THE PATH-INDEPENDENCE PRINCIPLE

In hydrology or water resources, discharge Q is defined as the volume of water flowing per unit time past an observation point on a river or stream. Mathematically, Q is the flux of a water velocity vector field through a surface area. Assume that the water flows in the direction parallel to the river banks and there is no water flowing into or out of the river in the vicinity of the observation point. The flow is constituted by a water velocity vector field if imagining that it was measured by velocity sensors placed everywhere in the water columns. We further assume that the velocity vector field is constant along the direction of the flow, i.e. the flow is steady and homogeneous in streamwise direction. In a moving-boat ADCP streamflow measurement, an imagined vertical sheet, i.e. a curved-sectional surface covering the river bottom to the water surface along the path of the survey boat, between the start point and end point (assume that edges are ignored), is the surface which the water velocity vectors go through. Figure 1 shows a sketch of plan view of a water velocity vector field and an arbitrary curved-sectional surface associated with a path of the survey boat.

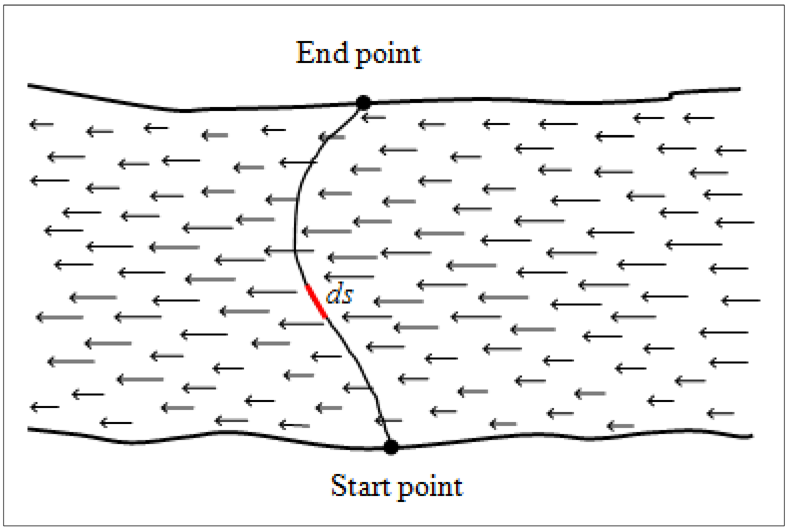

Figure 1. Sketch of plan view of a water velocity vector field and an arbitrary curved-sectional surface.

Let $\vec{u}$ denote the water velocity vector measured by a moving-boat ADCP along the boat's track; *S* denote an arbitrary curved-sectional surface associated with the boat's track, $\vec{\xi}$ the unit vector normal to *S* (pointing downstream) at a differential area *ds*. The river discharge *Q* can be determined by the so-called flux integral (Christensen and Herrick, 1982):

$$Q = \iint_S \vec{u} \bullet \vec{\xi}\ ds \qquad [1]$$

where $\vec{u} \bullet \vec{\xi}$ is the dot product of $\vec{u}$ and $\vec{\xi}$.

Figure 2 shows a sketch of plan view of the vectors $\vec{u}$ and $\vec{\xi}$ and the differential area *ds*. Figure 2 also shows the angle *θ* between the flow direction and $\vec{\xi}$, and the projected area *dA* of *ds* (*dA* is the differential area on the perpendicular cross-section that is a vertical flat surface). Note that *θ* is also the course direction if measured from the perpendicular cross-section. Recall that the traditional current meter streamflow measurement requires that the measurements are made on the perpendicular cross-section.

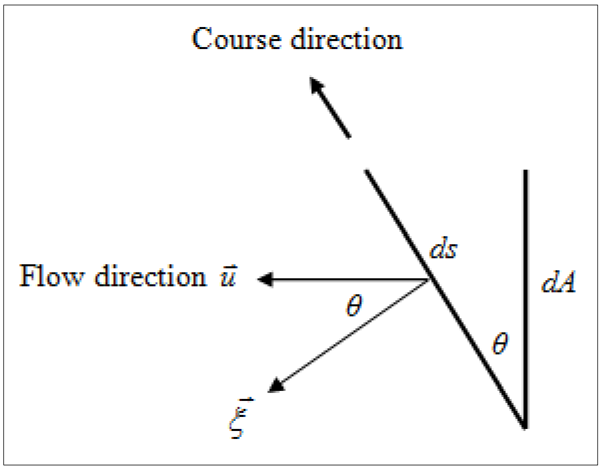

Figure 2. Sketch of plan view of the vectors and differential elements.

The dot product of $\vec{u}$ and $\vec{\xi}$ can be calculated as:

$$\vec{u} \bullet \vec{\xi} = |u| \cdot |\xi| \cos\theta = |u| \cos\theta \qquad [2]$$

Thus, the differential flux, denoted by *dQ*, is:

$$dQ = \vec{u} \bullet \vec{\xi}\, ds = |u| \cos\theta\, ds = |u|\, dA \qquad [3]$$

It can be seen from Figure 2 that, the velocity vector $\vec{u}$ can be divided into a tangential and a normal component with respect to the surface *S*. The dot product of $\vec{u}$ and $\vec{\xi}$ suggests that, only the normal component $|u|\cos\theta$ contributes to the differential flux. The physical meaning of this is that, the water can only flow in or out of the differential area *ds* when its flowing direction is normal to *ds*; if parallel to *ds*, the water flows neither in nor out. On the other hand, note from Eq. [3] that, the differential flux *dQ* is a product of the water speed $|u|$ and the differential area *dA* which is the differential area *ds* projected onto the perpendicular cross section. It is important to note that no matter whatever *θ* is, the flux integral is the same. That is:

$$Q = \iint_S \vec{u} \bullet \vec{\xi}\; ds = \iint_A |u|\; dA = VA \qquad [4]$$

where *A* is the perpendicular cross-sectional area, and *V* is the channel mean velocity. Note that *Q*=*VA* is the classical area-velocity formula for river discharge.

Eq. [4] suggests that the flux integral is independent from the angle *θ*, or the path of the survey boat, as long as the boat traverses from one bank to the other.

An interesting feature of the flux integral, Eq. [1], is that, if the surface *S* is a looped-sheet, *i.e.* the survey boat makes a closed path, the flux is zero:

$$Q = \iint_{closed\ path} \vec{u} \bullet \vec{\xi}\; ds \equiv 0 \qquad [5]$$

This is because the flux (*Q*), though is a scalar quantity, is given a positive sign if the water flows out of a surface, and a negative sign if the water flows into a surface. The water flows into and out of a closed path are cancelled, resulting in a zero flux. However, if the boat velocity is derived from a GPS, Eq. (5) may not work unless the ADCP is precisely aligned with the GPS and there is no compass error. A small misalignment angle or compass error may cause a significant directional bias error in the measured discharge.

The flux integral, Eq. [1], is rewritten as follows in the ADCP discharge calculation algorithm (TRDI, 2012):

$$Q = \int_0^T \left[\int_0^H \vec{u} \cdot dz \right] \bullet \vec{\xi}\, |V_b| \cdot dt = \int_0^T \int_0^H (\vec{u} \times \vec{V}_b) \bullet \vec{k} \cdot dz\, dt \qquad [6]$$

where *dz* is the differential depth, *dt* is the differential time, $\vec{V}_b$ is the boat velocity vector, $|V_b|$ is the boat speed, *z* is the vertical coordinate, *z*=0 is the river bottom and *z*=*H* is the water surface, $\vec{k}$ is the unit vector in the vertical direction, and *T* is the total transect time from the start point to the end point. In addition, note that $(\vec{u} \times \vec{V}_b) \bullet \vec{k}$, is the cross-product of water velocity and boat velocity and $ds = |V_b| \cdot dz \cdot dt$. Detailed discussions on the integral Eq. (6) can be found in Simpson and Oltmann (1993), RDI (1992) and TRDI (2012).

3 FIELD VERIFICATION

A moving-boat ADCP streamflow measurement was made at a site on the Choa Praya River, Thailand on November 1, 2013. The river was about 270m wide with the maximum depth about 16m; it was under a steady flow condition during the measurement. The measurement was made using a 600kHz RiverRay ADCP manufactured by Teledyne RD Instruments. The RiverRay ADCP is an intelligence discharge measurement system; it can automatically choose cell size, number of cells, and operation mode (*i.e.* broadband or pulse-coherent) in real-time based on the present water depth and velocity.

During the measurement, the survey team intentionally made different paths with the survey boat for each transect to verify the path-independence principle and to test the robustness of the moving-boat ADCP method. Figure 3 shows the eight different paths made, with the depth averaged velocity vectors on the boat's tracks. The first two transects were made with straight-line paths; the third transect with an arched path towards upstream; the fourth transect with an arched path towards downstream; the fifth transect with a S-shaped path; the sixth transect with a loop in the middle of the river; the seventh transect with two stops (the boat was drifting); and the eighth transect with a straight-line path and the fastest boat speed among all transects. Table 1 shows some descriptive statistics of the measured transect discharges.

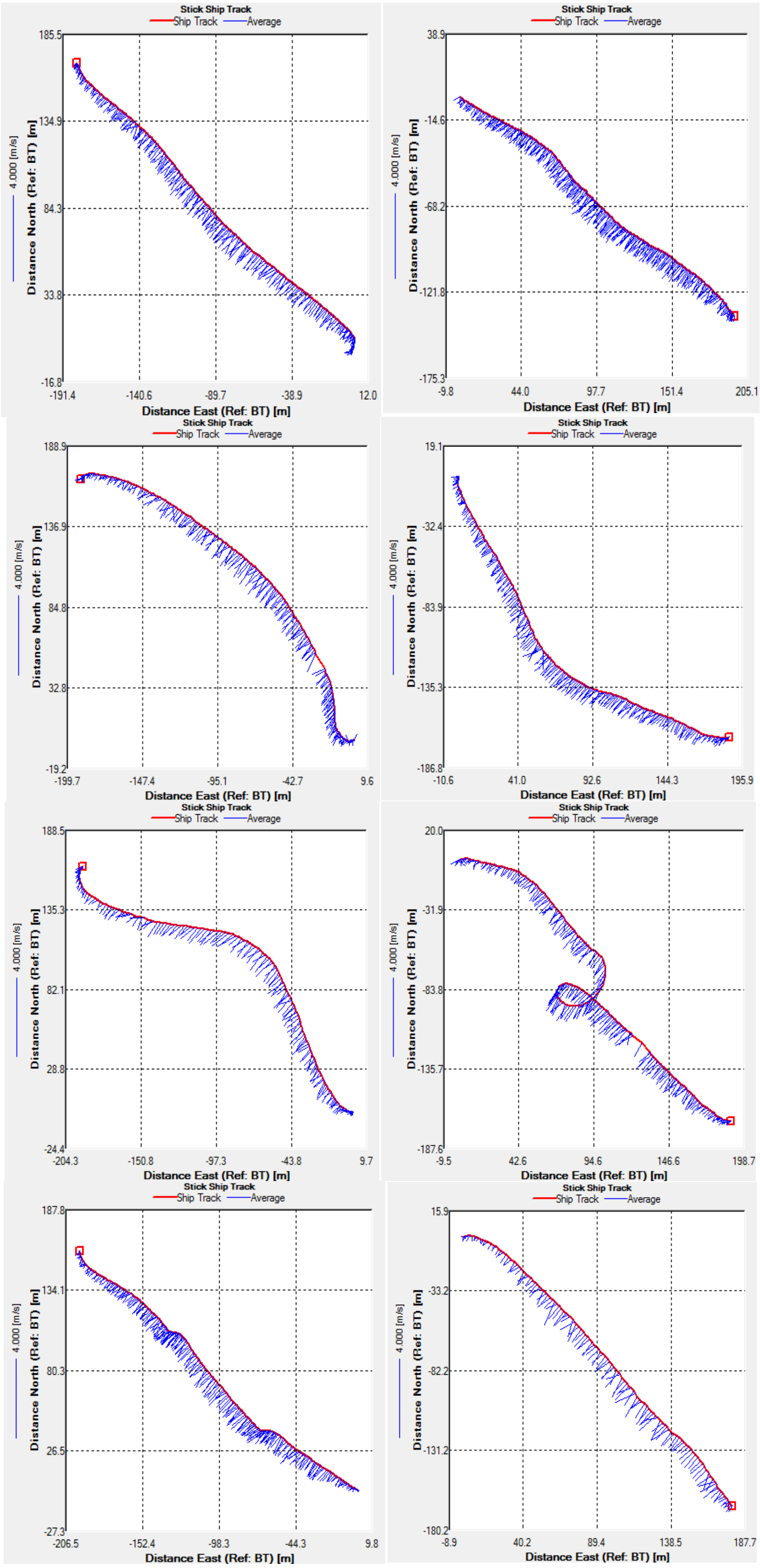

Figure 3. Eight different paths of the survey boat made during the Choa Praya River measurement (velocities are referenced to the bottom tracking).

Table 1. Discharge data collected on the Choa Praya River.

Transect	Number of ensembles	Start time	Duration (s)	Discharge (m^3/s)	$\Delta Q/\overline{Q}$ (%)	Boat's path
1	245	10:53:41	181	2140	-0.66	Straight-line
2	258	10:57:32	194	2155	0.05	Straight-line
3	228	11:02:00	175	2174	0.95	Arched upstream
4	224	11:05:10	166	2161	0.34	Arched downstream
5	185	11:08:53	135	2110	-2.03	S-shaped
6	237	11:11:16	183	2168	0.65	A loop in the middle
7	234	11:15:53	174	2126	-1.27	Straight-line with two stops
8	131	11:18:59	98	2196	1.96	Straight-line; fast boat speed
Mean $\overline{Q}$				2154	0	

It can be seen from Table 1 that the mean of the eight transect discharges, denoted by $\overline{Q}$, is 2154m^3/s. The relative residual discharge, defined as $\Delta Q/\overline{Q} = (Qi - \overline{Q})/\overline{Q}$, ranges from -2.03% to 1.96% (the relative maximum residual is 2.03%). The transect discharges from different paths agree well with each other. There is no significant bias associated with any particular transect. The variation in the transect discharges is attributed to random or sampling errors, which can be evaluated by the Type A uncertainty according to the "Guide to the Expression of Uncertainty in Measurement" (GUM) (JCGM 2008).

The Type A uncertainty, denoted by *U*, associated with the mean discharge $\overline{Q}$ can be calculated by a median-unbiased estimator of the *z*-based uncertainty at the 95% probability limit (Huang, 2015a; 2016):

$$U = 1.96\frac{C_{OE}\,s}{\sqrt{n}} \qquad [7]$$

where *s* = sample standard deviation of transect discharges, $s = \sqrt{\sum (Q_i - \overline{Q})^2 /(n-1)}$; *n*= number of transects; C_{OE} = estimator coefficient (Huang, 2015a):

$$C_{OE} = \left(1 - 0.0167\, e^{-0.9(n-2)}\right)^{-1}\left(1 - \frac{2}{9(n-1)}\right)^{-\frac{3}{2}} \qquad [8]$$

For the Choa Praya River discharge measurement, *n*=8, C_{OE} =1.05, and *s*=27.54m^3/s. Thus, *U*= 20.0m^3/s. The discharge measurement and uncertainty estimation results can then be expressed in the following format to comply with GUM (JCGM, 2008):

$$Q = \overline{Q} \pm U = 2154 \pm 20.0 \text{ (m}^3\text{/s)} \qquad [9]$$

Moreover, the relative uncertainty, denoted by *RU,* is estimated as:

$$RU = \frac{U}{\overline{Q}} = \frac{20.0}{2154} = 0.93\,\% \qquad [10]$$

Note that *RU*=0.93% is much smaller than 4.09%, the maximum permissible relative uncertainty (*MPRU*). The *MPRU*=4.09% is the uncertainty-based quality control criterion for moving-boat ADCP streamflow measurements; it was derived from the existing four transects relative maximum residual (*RMR*) ≤ 5% criterion (Huang, 2015b). It should be pointed out that the estimated Type A uncertainty only accounts for the random error sources encountered at the site. It does not include any contribution of bias error sources.

4 CONCLUSIONS

The path-independence principle associated with the moving-boat ADCP method for streamflow measurements is valid under the assumption that the flow is steady and homogeneous in streamwise direction. It is mathematically and experimentally demonstrated. In practice, however, a straight-line or nearly straight-line path perpendicular to the main flow direction is usually preferred because it results in the most appropriate representation of the perpendicular cross-sectional area. The perpendicular cross-sectional area would be distorted if a boat made a diagonal, curved, or irregular path.

ACKNOWLEDGEMENTS

The author would like to thank Siam Advantech Co., Ltd, Thailand, for their organizing the field test and collecting the discharge data on the Choa Praya River. The Royal Irrigation Department, Thailand, provided support and assistance with the survey boat, which is greatly appreciated. The author would also like to thank two anonymous reviewers for their helpful comments.

REFERENCES

Christensen, J.L. & Herrick, L.E. (1982). *Mississippi River Test: Volume 1,* Final Report DCP4400/300, prepared for the U.S. Geological Survey, AMETEK/Straza Division, El Cajon, California, under contract No. 14-08-0001-19003.

Huang, H. (2015a). Optimal Estimator for Uncertainty-Based Measurement Quality Control. *Accreditation and Quality Assurance,* 20(2), 97-106.

Huang, H. (2015b). Statistical Quality Control of Streamflow Measurements with Moving-Boat Acoustic Doppler Current Profilers. *Journal of Hydraulic Research,* 53(6), 820-827.

Huang H. (2016). Estimation of Type A Uncertainty of Moving-Boat ADCP Streamflow Measurements, *River Flow 2016, Proceedings of the Eighth International Conference on Fluvial Hydraulics,* eds. Constantinescu, G., Garcia, M. & Hanes, D., Taylor & Francis Group, London, 696-701.

Joint Committee for Guides in Metrology (JCGM). (2008). *Evaluation of Measurement Data - Guide to the Expression of Uncertainty in Measurement* (GUM 1995 with minor corrections), Sevres, France.

Mueller, D.S. & Wagner, C.R. (2009). *Measuring Discharge with Acoustic Doppler Current Profilers from a Moving Boat,* U.S. Geological Survey Techniques and Methods 3–A22, 72.

Oberg, K.A., Morlock, S.E. & Caldwell, W.S. (2005). Quality-Assurance Plan for *Discharge Measurements Using Acoustic Doppler Current Profilers*. Scientific Investigations Rep. 2005-5183, U.S. Geological Survey (USGS), Reston, VA, USA.

RD Instruments (RDI). (1992). *Transect Users' Manual* (for Broadband ADCPs), San Diego, California.

Simpson, M.R. (2001). *Discharge Measurements Using a Broad-Band Acoustic Doppler Current Profiler*. Open-File Rep. 01-1, U.S. Geological Survey (USGS), Reston, VA, USA.

Simpson, M.R. & Oltmann, R.N. (1993). *Discharge Measurement Using an Acoustic Doppler Current Profiler*, U.S. Geological Survey Water-Supply Paper 2395, 32.

Teledyne RD Instruments (TRDI). (2012). *WinRiver II User's Guide*, Poway, California.

A REVIEW ON CLIMATE CHANGE IN WEATHER STATIONS OF GUILAN PROVINCE USING MANN-KENDAL METHOD AND GIS

(1)JALAL BEHZADI

(1) Islamic Azad University, Lahijan Branch,
(1) Guilan, Lahijan, Islamic Azad University, the Faculty of Agriculture and Natural Resources,
drbehzadijalal@yahoo.com

ABSTRACT

Climate has always been changing during the lifetime of the earth, and has appeared in the form of the ice age, hurricanes, severe and sudden temperature changes, precipitation and other climatic elements, and has dramatically influenced the environment, and in some cases, has caused severe changes and even destructions. Some of the most important aspects of climate changes can be found in precipitation types of different regions in the world and especially Guilan, which is under the influence of strong ground change and greenhouse gas emissions. Also, agriculture division, industrial activities and unnecessary land conversions have a huge influence on climate change. Climate change is a result of abnormalities of meteorology parameters. Generally, the element of precipitation is somehow included in most theories about climate change. The present study aims to show precipitation abnormalities in Guilan which lead to climate change, and possible deviations of precipitation measurement based on annual, seasonal and monthly series check. The Mann-Kendal test is used to show likely deviations leading to climate change. The trend of precipitation changes in a long-term study using this method. Also, the beginning and end of these changes are studied in five stations as representatives of all the thirteen weather stations. Then, the areas which have experienced climate change identified using the GIS software along with the severity of the changes with an emphasis on drought. These results can be used in planning and identifying the effects of these changes on the environment.

Keywords: Climate change; Guilan; Mann-Kendal; GIS.

1 INTRODUCTION

In today's world, people, plants and animals are most dependent on climate. But unfortunately, dramatic global changes in climate have had their own consequences and compensating these changes is so difficult, and in some cases, even impossible. Some of the most important aspects of climate changes can found in precipitation types of different regions in the world, which is influenced by drastic land conversions and greenhouse gases. Climate change is with us. A decade ago, it was the guess. Now the future is unfolding before our eyes. Many businesses are cussing that climate change is real. Meanwhile, powerful forces, notably the polluting industries and fossil fuel sector, have deep vested interests in maintaining business-as-usual. The basic science is straightforward. Climate researchers showed that gases such as carbon dioxide, methane and others can trap heat in the Earth's atmosphere – a phenomenon known as the greenhouse effect. Human activities such as industry; transport, energy generation and deforestation all produce these greenhouse gases. The total concentration of these gases rose greatly since the start of the Industrial Revolution in Europe and the average global temperature also rose over that time period. As the atmosphere heats, scientists predict that this will have dangerous disruptive effects on the Earth's climate. While no single event we can prove the result of climate change, many climatic trends and events observed already are consistent with scientific predictions. The main source of scientific information on climate change is the Intergovernmental Panel on Climate Change (IPCC), which it adjusted in 1988 by the UN Environment Programmed and the World Meteorological Organization. The impacts of climate change are many and varied, as all life on earth and many of the planet's physical processes are heavily influenced by temperature. This contributes to rising seas but also (in the case of glaciers) increasing the risks of flooding in the short-term, and decreased river flow in the longer term. Climate change may also affect water supplies in other ways, such as altering the South Asian monsoon. Other impacts include changes distribute crop pests and species that spread vector-borne diseases such as malaria, as well as other impacts of human health. These show that the world has not been as warm as it is now for a millennium or more. In this study was, (Ebrahimi et al., 2014), for detecting trends than Mann-Kendal non-parametric test in the anzali site during a statistical period (1951-2005). The result showed the anzali site index of maximum temperature has negative trend ، minimum temperature has positive trend and Rainfall has non-trend.

1.1 The geographical location and climatic condition of the studied area

Guilan province is found in the north of Iran in 37.2774°N and 49.5890°E. The area of the province equals 13810.5 km2 and possesses the first rank of annual precipitation among other provinces based on the statistics of the Meteorological Organization of I.R. of Iran. Based on the statistics of the studied 30 years (1977-2015), the average annual precipitation has been 1070 millimeters. The average annual precipitation in the 30 years' period equals 1393 mm in Astara, 1745 mm in Anzali, 1491 mm in Lahijan, 1369 mm in Rasht, and 1220 mm in Saravan stations. The seasonal precipitation percentage is 15% in spring, 22% in summer, 39% in autumn, and 24% in winter. According to the first amount of rainfall stations of Guilan province with their coordinates interpolated even been identified. Then, in the second 2 showers are ranked based on the value of Erie's past.

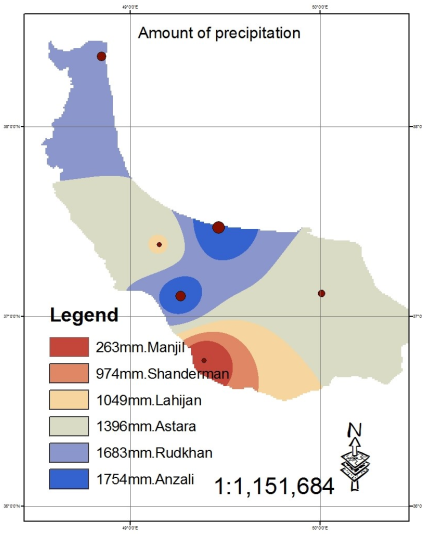

Figure 1. Guilan amount of precipitation stations.

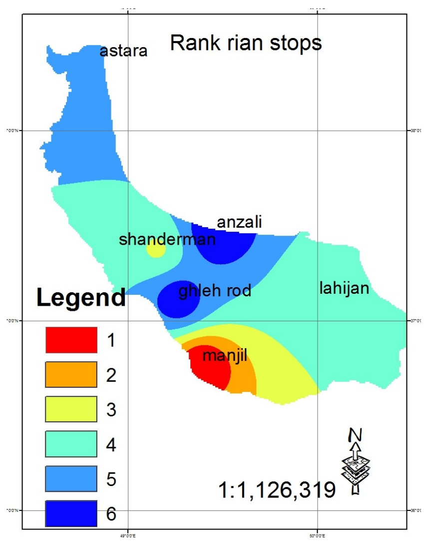

Figure 2. Rank rain stops Guilan.

2 PROJECT SITE

Since precipitation and the Mann-Kendal method are the basis of this work, respective formulas and data analyses are presented.

$$t = \frac{4p}{N.(N-1)} \quad [1]$$

$$p = \sum_{i=1}^{n} n_i \quad [2]$$

$$to = o \pm tg\sqrt{\frac{4N+10}{9N(N-1)}} \quad [3]$$

$$E = \frac{n_i(n_i-1)}{4} \quad [4]$$

$$V = \frac{n_i(n_i-)(2n_i+5)}{72} \quad [5]$$

$$U = \frac{\sum t_i - E}{\sqrt{V}} \quad [6]$$

$$E' = \frac{(N-n_i+1)(N-n_i)}{4} \quad [7]$$

$$V' = \frac{(N-n_i+1)(N-n_i)(2(N-n_i+1)+5)}{72} \quad [8]$$

$$U' = \frac{-\sum t'_i - E'}{\sqrt{V'}} \quad [9]$$

Because of the magnitude of work in all the stations, only five of them were picked out, and the resulting data table belonging to Anzali station is presented in the following section.

where:

t = Kendal statistics

p = sum of the values larger than nj which come after it.

In this equation, the following equation has been used to evaluate the significance of the statistics “t” and “to” critical statistics:

tg = the value of the standard variable Z compatible with the level of the test, which in the present study tg =1.96 with a possibility of 95%.

The Mann-Kendal test has also been used to determine the variation type and variation time.

The fifth column (ti) equals the values smaller than ni row which is before it and in the next column $\sum t_i$ which is the sum of “ti”s from the top to the respective row. The t'_i column includes the values smaller than ni which is after it and the $\sum t'_i$ column is the sum of all the “t'_i”s from the bottom to the respective row. In order to calculate the next columns which are E, V, U, E’, V’, and U’, the following equations are used respectively:

Then the values of U and U’ in each time series are present using a diagram. The collision of U and U’ curves inside the area of critical values write down the beginning of variations. When the collision of those two outside the area indicates the trend. In the present study, the critical value at the level of 5% equals 1.96. After drawing graphical diagrams of u and u’ which are presented in the shape of curves, the significance is only achieved when u and u’ curves cross each other. If these values cross each other inside the critical area of ±1.96, then no trend exists; and if they cross each other outside the critical area, this indicates a trend in the time series.

3 DATA COLLECTION PROGRAM

The annual Mann-Kendal test was developed and studied for the weather stations of the province with respect to the data in table 2 and the 30 years’ precipitation diagrams. Annual precipitation series were studied using the Mann-Kendal test in order to determine a number of precipitation time variations in the studied weather stations.

Anzali station: Time variations in Anzali station show one increasing oscillation outside the significance level and three decreasing oscillations. The first one occurred in 2001 when the annual precipitation was 1502 millimeters. The next ones were seen in 2015. In 2015, the amount of oscillation was equal to 405 millimeters less precipitation compared to the 30 years' average of 1776 mm and in 2006 this decrease was 300 mm.

Rasht station: Studying the Mann-Kendal diagram for Rasht reveals two decreasing and three increasing trends which are not oscillations in a significant level. Precipitation trend in the 30 years' statistical period indicates a direct line with zero regression coefficients. In other words, this station has experienced a more monotonous trend compared to the others.

Lahijan station: An increasing trend of precipitation can observe in Lahijan during the 30 years' period in the Mann-Kendal diagram. The diagram for this station indicates a decreasing oscillation out of significance level and an increasing oscillation in a period of time which is slightly out of the significance level. This time period belongs to 2013-2014. Precipitation in 2013 was 745 mm more than the total average. In 2014, precipitation was 95 mm more than the 30 years' average.

Table 1: Estimative statistics of climate change in Anzali station (Role model).

Year	Annual	Rank	ti	Sum ofti	ti`	Sum of ti`	E	V	U	E`	V`	U`
1986	1981.8	25	0	0	24	242	0	0	0.00	217.50	785.42	0.87
1987	2336.2	29	1	1	27	218	0.5	0.25	1.00	203.00	710.50	0.56
1988	1821.1	19	0	1	18	191	1.5	0.91	-0.53	189.00	640.50	0.08
1989	1566.8	9	0	1	8	173	3	2.1	-1.38	175.50	575.25	-0.10
1980	1705	13	1	2	11	165	5	4.1	-1.49	162.50	514.58	0.11
1991	1501.7	6	0	2	5	154	7.5	7.08	-2.07	150.00	458.33	0.19
1992	2662.1	30	6	8	23	149	10.5	11.08	-0.75	138.00	406.33	0.55
1993	1566.7	8	1	9	6	126	14	16.33	-1.24	126.50	358.42	-0.03
1994	1944	23	5	14	17	120	18	23	-0.83	115.50	314.42	0.25
1995	1787.4	16	3	17	11	103	22.5	31.25	-0.98	105.00	274.17	-0.12
1996	2098.4	28	8	25	19	92	27.5	41.25	-0.39	95.00	237.50	-0.19
1997	1760.4	14	4	29	9	73	33	53.17	-0.55	85.50	204.25	-0.87
1998	1701.9	12	3	32	8	64	39	67.17	-0.86	76.50	174.25	-0.95
1999	1817.8	18	7	39	10	56	45.5	83.42	-0.71	68.00	147.33	-0.99
2000	1593.3	10	3	42	6	46	52.5	102.08	-1.04	60.00	123.33	-1.26
2001	1237.8	1	0	42	0	40	60	123.33	-1.62	52.50	102.08	-1.24
2002	1785.2	15	8	50	6	40	68	147.33	-1.48	45.50	83.42	-0.60
2003	1805.4	17	10	60	6	34	76.5	174.25	-1.25	39.00	67.17	-0.62
2004	1560	7	2	62	4	28	85.5	204.25	-1.64	33.00	53.17	-0.68
2005	1367.6	2	1	63	0	24	95	237.5	-2.08	27.50	41.25	-0.55
2006	1473	5	2	65	2	24	105	274.17	-2.42	22.50	31.25	0.27
2007	1981.2	24	17	82	6	22	115.5	314.42	-1.89	18.00	23.00	0.83
2008	1921.6	22	16	98	5	16	126.5	358.42	-1.51	14.00	16.33	0.50
2009	1442.6	4	2	100	1	11	138	406.33	-1.88	10.50	11.08	0.15
2010	2009.8	27	21	121	5	10	150	458.33	-1.35	7.50	7.08	0.94
2011	1903.6	21	17	138	3	5	162.5	514.58	-1.08	5.00	4.10	0.00
2012	1424.8	3	2	140	0	2	175.5	575.25	-1.48	3.00	2.10	-0.69
2013	1847.6	20	18	158	1	2	189	640.5	-1.22	1.50	0.91	0.53
2014	1981.5	26	24	182	1	1	203	710.5	-0.79	0.50	0.25	1.00
2015	1605.1	11	10	192	0	0	217.5	785.42	-0.91	0.00	0.00	0.00

Rudkhan Castle station: Time variations in Rudkhan Castle station show two increasing and two decreasing oscillations out of the significance level. The increasing precipitation trend possesses a regression coefficient of 0.01. Decreasing and increasing oscillations are not significant.

Manjil station: This station has two increasing oscillations out of the significance level and two decreasing oscillations which were once out of the significance level in 2012 with a precipitation equal to 230 mm, which indicates a 35 mm decrease compared to the 30 years precipitation average. The precipitation trend wasa decreasing one with a regression coefficient of 0.1 and is consider as the most intense decreasing trend among all other stations.

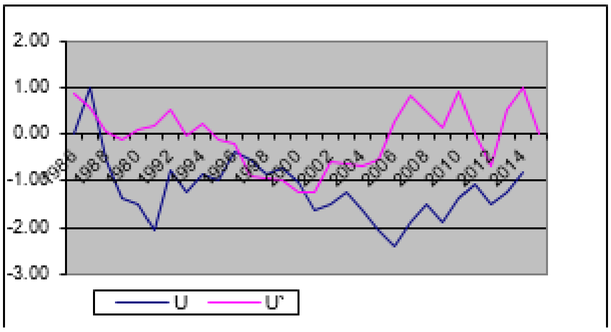

Figure 3. Climate change diagram for Anzali station.

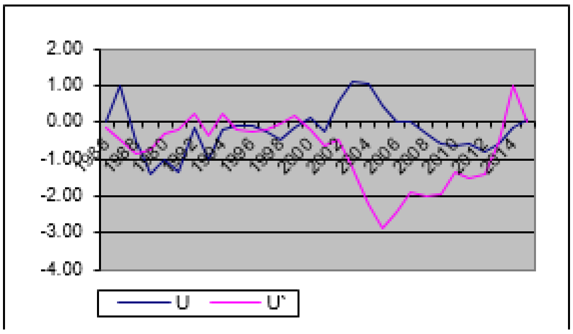

Figure 4. Climate change diagram for Rasht station.

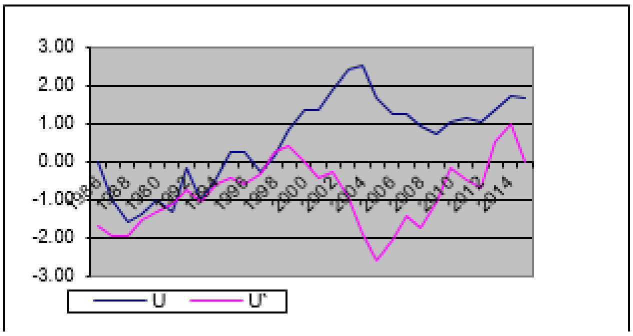

Figure 5. Climate change diagram for Lahijan station.

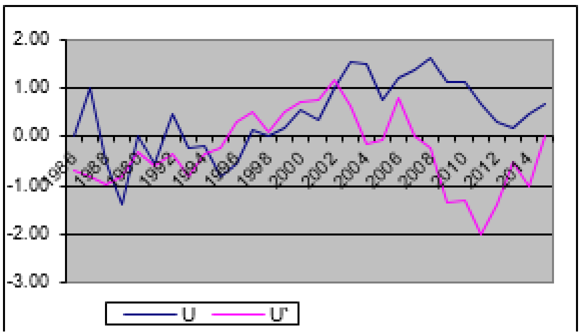

Figure 6. Climate change diagram for Rudkhan Castle station.

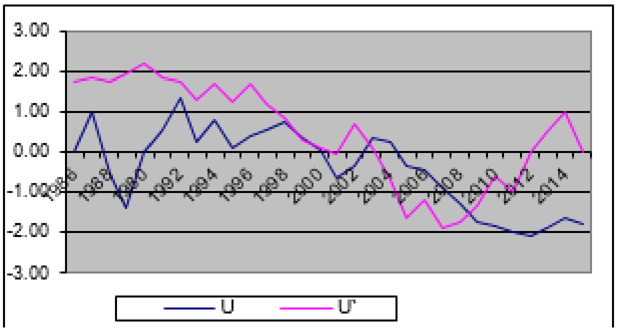

Figure 7. Climate change diagram for Manjil station.

By studying the Mann-Kendal diagram of the studied stations in the 30 years' statistical period it was found out that there was a precipitation decreasing trend in Anzali and Manjil stations from 1986 to 2015, and no increasing trend was observed in Lahijan, Rudkhan Castle, and Rasht stations. Then, in the second 2 showers are ranked based on the value of Erie's past. Anzali station achieved the highest intensity and number lahijan, stations and Rasht second, And Manjil is ranked third. The rest of the stations are not changes, and valuation was not. Valuation was based on three groups. Changes were interpolated through GIS. And the changes revealed the extent of Guilan. Many studies on climate change with the help of GIS is done. Pradeep (2014) conducted a study to evaluate the effects of climate change and its geohydrological non-seasonal crops in the watershed through the development of GIS in weather Informatics, Informatics land use, water and Informatics growing and Informatics Thumerer (2010) To assess the consequences of sea level rise along the East Coast English, depending arc of the GIS data used to determine coastal vulnerability to flooding.

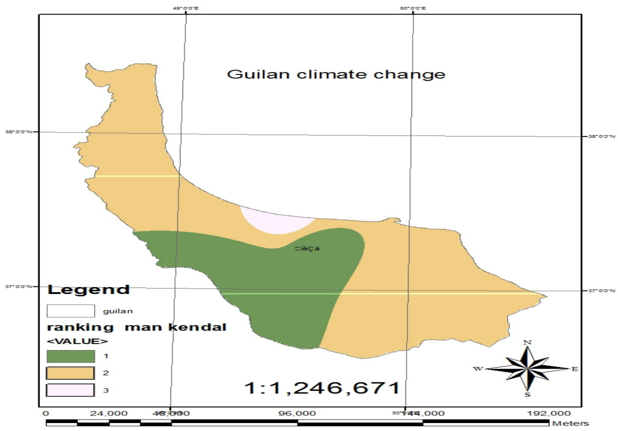

Figure 8. Climate change map Guilan.

4 CONCLUSIONS

Climate change are dynamic processes which its trend is find using different tools and methods in different places in the world. It is an ongoing process which has significant impacts on the lives of humans and the environment. There are many theories and hypotheses about climate change, from its causing factors to its impacts. What we know is that climate change is predominant on earth, but it may weaken or strengthen in various parts of the world which depend on the factors that caused it. In the 21st century and especially recent decades, climate change has become more intense. Scientists blame industrial activities, agricultural development, urbanization, etc. for this phenomenon. They also believe that by increasing inappropriate human activities, the crisis resulting from climate change will worsen in all parts of the world. Climate change has various impacts on nature and species. The consequences of climate change can be observed in variation in the amount of rainfall and wind direction, increase of natural disaster occurrences such as storms, whirlwinds and flood, increase of droughts, growth of desert areas, intensification of air pollution, increase of duration and intensity of precipitations, raising water levels in oceans and seas, decrease of snow supplies in mountains, and so on. On the other hand, the increase in consumption and demand for urban, suburban and regional waters lead to an intensification of the climate change phenomenon. Among some of the most important impacts of climate change on nature are their effects on plants, generally through the mutual action of temperature and carbon oxide raise. However, intense decrease and increase of climatic elements resulting from climate change studied in different regions along with its effects. For instance, the monthly average of climatic variables including temperature, radiation, and precipitation under the condition of double carbon dioxide in Tabriz predicted using GFDL and GISS General Circulation Methods. The results obtained from stimulation climatic conditions using general circulation methods were applied in long-term metrology statistics, and then the effects of such conditions on growth, performance and water requirements of sugar beet and potato evaluated using OSBOL stimulation model. Various climatic factors such as temperature, wind, humidity, evaporation, perspiration and precipitation also have a significant impact on the production performance of surface mines. Since the occurrence of these factors is random, it is difficult to control their undesirable outcomes. Most scientists believe the increasing amount of carbon dioxide in the atmosphere, which is a result of combustion of fossil fuels such as oil, gas, and coal, makes our planet so warm that is not explainable with natural changes. As Ronald says, the meteorology pattern analyzed in this study was the most complicated pattern studied to date in which some existing doubts from previous predictions that used simpler patterns addressed.

In the present study, five weather stations were picked and studied out of 13 weather stations of Guilan. Some tables developed based on the Mann-Kendal method. Also, a diagram obtained based on “U,U” which indicates rises and falls from the balance line, and it may beneath or above the significance line.

“U,U” collide in this rise and fall. This collision might be severe or weak depending on the distance to the significance line. When the lines cross the significance line, especially after collisions, climate change occurs, and the farther it is from the significance line it becomes more intense. In diagrams for Anzali, Rasht, Lahijan and Manjil, they crossed the significance line. In Anzali diagram, all the occurrences that crossed the significance line are in negative trend, or in other words, drought. It can observe in the diagram of Rasht that this city experienced two consecutive dry years by crossing the significance line twice. In Lahijan diagram, one line is above and the other is under the significance line. Manjil station, which holds the fourth rank, is inside the negative area below the significance line with a decreasing trend. And in Rudkhan Castle, almost there is no crossing of the line, or in other words no climate change. Although there are about five rises and falls in every station, none of them is higher than the significance level. The base in the present study is the trend below the balance line in the negative area, i.e. an emphasis on drought. The rainfall map of Guilan and rating it at the station was found; with maps of climate change on precipitation, stations are not compatible. Climate change means that precipitation in the province made changes; the changes will vary from point to point.

Station rankings determined based on the significance level in drought trend. The force of climate change in drought trend is observable in this ranking. Then the locations with climate change determined on the map using the GIS software and force of these changes was also pointed out along with their area. The results of this study are applicable in all the considerations of the environment, civil engineering, jungles, fishery, agriculture, hydrology, and so on. What we know is that areas with intense climate change give us the conditions needed to study the changing phenomena, and these phenomena can easily be studied with the correlation of climate.

REFERENCES

Canyon, D.V., Speare, R. & Burkle, F.M. (2016). Forecasted Impact of Climate Change on Infectious Disease and Health Security in Hawaii by 2050. *Journal Disaster Med Public Health Prep,*10(6) ,797-804.

Dhyani, S. & Thummarukuddy, M. (2016). Ecological Engineering for Disaster Risk Reduction and Climate Change Adaptation. *Journal Environ Sci Pollut. Res Int*, 23(19), 49-52.

Ebrahimi, H. & Kardavani, P. (2014). Recognitionthe Climate Change in International Anzali Wetlandusing Mann-Kendall Test. *Journal of Wetland Ecobiology*, 6(21),59-72.

Lin, N. & Emanuel, K. (2012). Physically Based Assessment of Hurricane Surge Threat Under Climate Change. *Nature Climate, Change advance online publication*, 2, 462-467.

Nadeau, C.P., Urban, M.C. & Bridle, J.R. (2016). Coarse Climate Change Projections for Species Living in a Fine-Scaled World. *Journal Glob Chang Biolvolume*, 23(1) ,12-24.

Pradeep, K.R. (2014). GIS Development to Monitor Climate Change and Its Geohydrological Consequences on Non-Monsoon Crop Pattern in Himalaya. *Computers & Geosciences Computers & Geosciences*, 70, 80–95.

Takahashi, L., Burnham, B., Terracina, M., Sopchak, C. & Selfa, A. (2015). Climate Change Perceptions of NY State Farmers: The Role of Risk Perceptions and Adaptive Capacity. *Journal Environ Manage*, 38(6), 946-957.

Thumerer, T., Jones, A.P. & Brown, D. (2010). A GIS Based Coastal Management System for Climate Change Associated Flood Risk Assessment on The East Coast of England. *International Journal of Geographical Information Science*,14(3), 265-281.

COMPARATIVE AND COMPLEMENTARY DISCHARGE MEASUREMENTS USING ADCP AND RADAR-TECHNOLOGY

FABIAN NETZEL[1], CHRISTOPH MUDERSBACH[2] & MARC SCHEIBEL[3]

[1,2] Bochum University of Applied Sciences, Bochum, Germany,
fabian.netzel@hs-bochum.de
[3] Wupperwaterboard (Wupperverband) – Water Management and Flood Protection, Wuppertal, Germany,
schei@wupperverband.de

ABSTRACT

Open channel discharge can be determined by using different types of measurement equipment. Common systems are the current meter and ultrasonic systems. In some fields, even acoustic Doppler current profiler (ADCP) and Radar-technology are becoming more popular. Especially for the non-contact Radar systems and ultrasonic systems located at the banks on both sides of the river, it is necessary to know the exact value and shape of the discharge section area and the velocity profile of the measurement site for determining the discharge. In a joint research project with the Wupperwaterboard (Wupperverband) and the Bochum University of Applied Sciences, the mentioned measurement systems have been comparatively and complementarily applied. By the use of different analyzing and fitting processes, corrected k-Values for the computation of the mean velocities out of the measured surface velocities have been derived and the cross-section for the conducted measurement has been revised. Hence, the deviation between the Radar-measurement and the comparative systems has been minimized and an optimization of a discharge measurement by combining different types of measurement systems has been achieved.

Keywords: Open channel discharge; Radar; ADCP; optimization.

1 INTRODUCTION

Discharge measurements provide the basis for a variety of tasks in water management processes. The generated hydrologic key figures, water level w and discharge Q, are used for different designing- and controlling plans as well as for further issues related to water management and infrastructure. These wide fields of application and the demand of quality for each measured value, result in preferably accurate measurement processes (Morgenschweis, 2010; ISO, 2007). In cooperation with the Wupperwaterboard several discharge measurement campaigns were carried out and compared to each other at different characteristic gauges for an optimization of the measurement processes and values. Preliminary studies showed significant deviations between the systems concerning the hydrometric variables water level w, discharge Q, mean velocity v_m and the discharge area A. Extended investigations considering the measured velocities and water levels at different verticals (resp. cross-sectional area) along the cross-section were performed to asses these deviations. The gained information led to a validation and – if required – adjustment of the extrapolation methods (k-value) for the Radar-measurement.

2 MEASUREMENT SITE AND DATA BASIS

The comparative measurement campaigns were carried out at characteristic gauges, which were chosen to transfer the obtained results to similar gauges with mainly analogical cross-section profiles and conditions. Subsequently are two of the chosen gauges described.

The first site, Hueckeswagen (SHUE), exhibits a partitioned trapezoidal cross-section profile. The riverbed is fixed by a rough concrete slab. Both riverbanks are paved with natural stones and show some light to thick growth of grass. The mean discharge amounts to 4.06 m³/s with a corresponding water level of 39.4 cm and a river width of 16.00 m.

For the second site, Hummelsheim (SHUM), only the riverbanks are partly equipped with bigger stones. There is a natural unpaved river bed. The mean discharge here amounts to 1.68 m³/s. The mean water level comes to 35.9 cm with a river width of about 10.00 m. Figure 1 shows both gauges.

Figure 1. Measurement sites gauge Hueckeswagen (left) and Hummelsheim (right).

Several measurements were carried out by the use of the current meter, ultrasonic systems with fastened transducers, tracer-, radar- and ADCP-Systems. Depending on the conditions at the measurement site, like water level, river width, etc. the systems were applied simultaneously or in quick succession.

The data basis for the following investigations was built up by the raw datasets out of the measurement systems, as well as the evaluated datasets out of the related software products for the two measurement campaigns. Enabling a comparison between the ADCP-measurements and the additional systems, the ADCP-Datasets were processed by the AGILA software tool referring to LAWA (1991). Here, a reference cross-section, perpendicular to the main current, is determined and the transects of the ADCP-data are projected onto it. Thus, the geometry and the current distribution is evaluated and can be compared (Adler and Nicodemus, 2012).

3 DETAILED COMPARISON OF THE MEASUREMENT SYSTEMS

The outcomes of the first systematic comparisons of the values A, Q, v_m and w, gave rise to a more detailed investigation of these parameters, especially the respective velocity distributions and cross-section areas.

During a discharge measurement, the Radar-system only detects the surface velocity v_o. A k-value is used to compute the mean velocity v_m out of the measured value respectively out of the surface velocity distribution. The parameters v_m, v_o and A were evaluated by the use of comparative measurements with the current meter and an ADCP-system. This was done with a view to reassess and possibly correct the used k-values and the utilized profiles for the discharge computation of the Radar-measurement.

3.1 Comparison between mean velocity and surface velocity

For the discharge determination by the use of the Radar-system, the whole discharge cross-section is divided into several smaller sections. The Radar-sensor is then centrally arranged for each section, sending constant radar waves towards the water surface. There, the signal gets reflected and becomes shifted into another frequency than emitted. By the use of the Doppler-effect and the computed frequency shift out of the received backscattered signal, the local surface velocity can be calculated for one section (Sommer GmbH, 2013).

The basic idea, using contactless Radar-measurements for discharge determination, is the reproduction of the velocity distribution of the discharge cross-section at the surface of a waterbody. Therefore, the mean velocity vm for the cross-section is evaluated by the use of the following equation:

$$v_{m,i} = v_{o,i} * k \quad [1]$$

where,

$v_{m,i}$ = mean velocity for each section
$v_{o,i}$ = measured surface velocity for each section
k = k-value

The required k-value can be taken as a predefined factor in the range of ±0.7 to ±0.9 or can be modelled by the use of the actual cross-section (Sommer GmbH, 2013).

By means of a rigorous comparison between the mean- and surface velocity out of simultaneously performed measurement datasets, the k-values are to be reviewed.

For that reason, the mean velocity vm,lot and surface velocity vo,lot for each vertical was computed out of the ADCP- and current meter dataset. Figure 2 und Figure 3 show the velocity distribution at the gauges SHUE and SHUM.

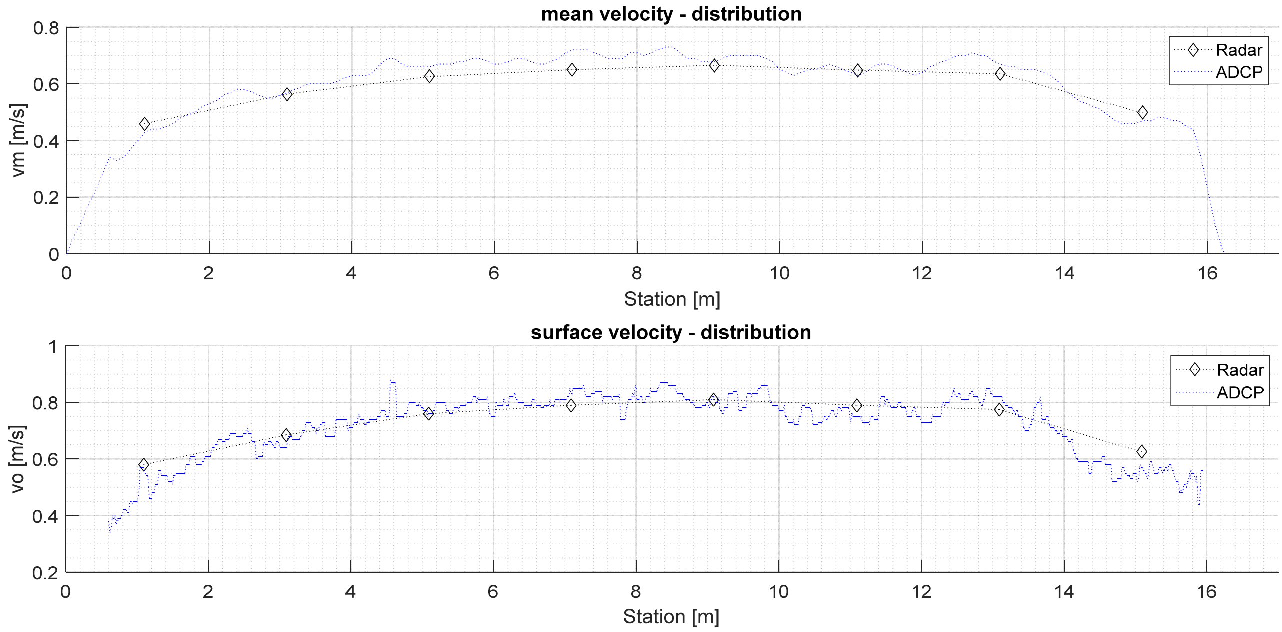

Figure 2. Velocities $v_{m,lot}$ and $v_{o,lot}$ for each vertical, gauge Hueckeswagen.

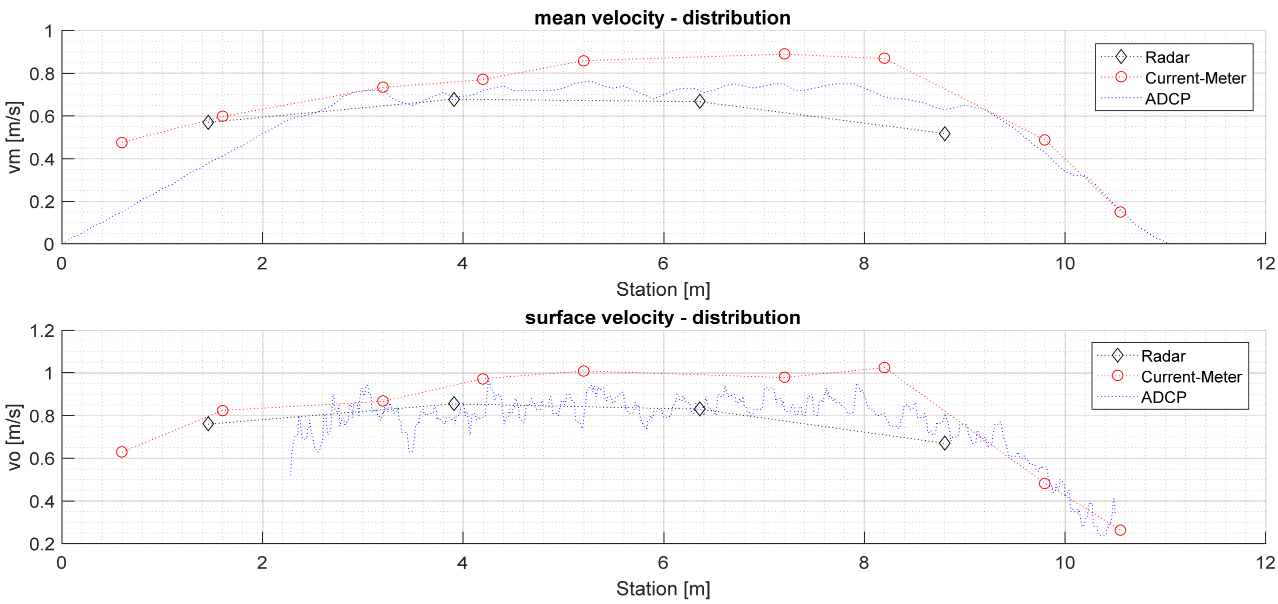

Figure 3. Velocities $v_{m,lot}$ and $v_{o,lot}$ for each vertical, gauge Hummelsheim.

The comparison of the vm,lot- and vo,lot distribution for the ADCP and Radar-measurement at the gauge SHUE (Figure 2) yields only minor changes. In the core area of the cross-section, the mean velocity characteristic out of the ADCP-data is a bit higher, referred to the Radar. On average, the values match very well. Concerning the surface velocity, only the left and right edges differ between the two measurement systems.

Comparing the values vm,lot and vo,lot at the second gauge SHUM (Figure 3), the deviations between the relative systems are much higher. Both in the core area and in the edges, the values show a considerable variance.

Continuing, a direct comparison of vo and vm to the Radar-measurement was executed. For every section of the Radar-measurement, the mean velocity and the surface velocity of the contained verticals was taken to an average value for the whole section (vm,section and vo,section). Afterwards these means were compared to the radar-values. Figure 4 till Figure 7 show the comparison and the percentagewise deviation for the two measurement campaigns.

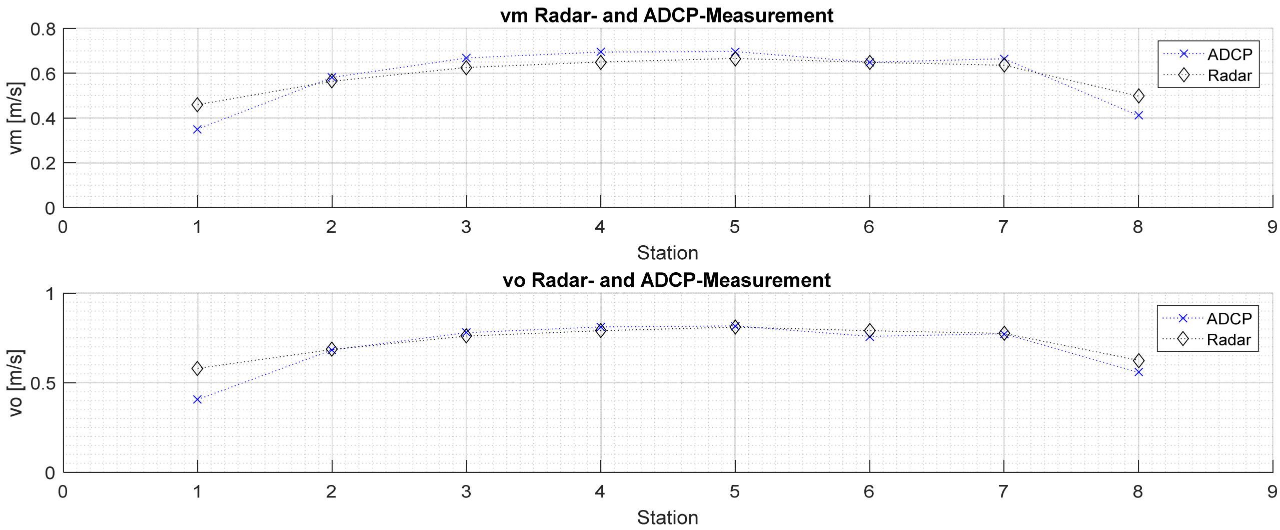

Figure 4. Velocities $v_{m,section}$ and $v_{o,section}$ for each Radar-station, gauge Hueckeswagen.

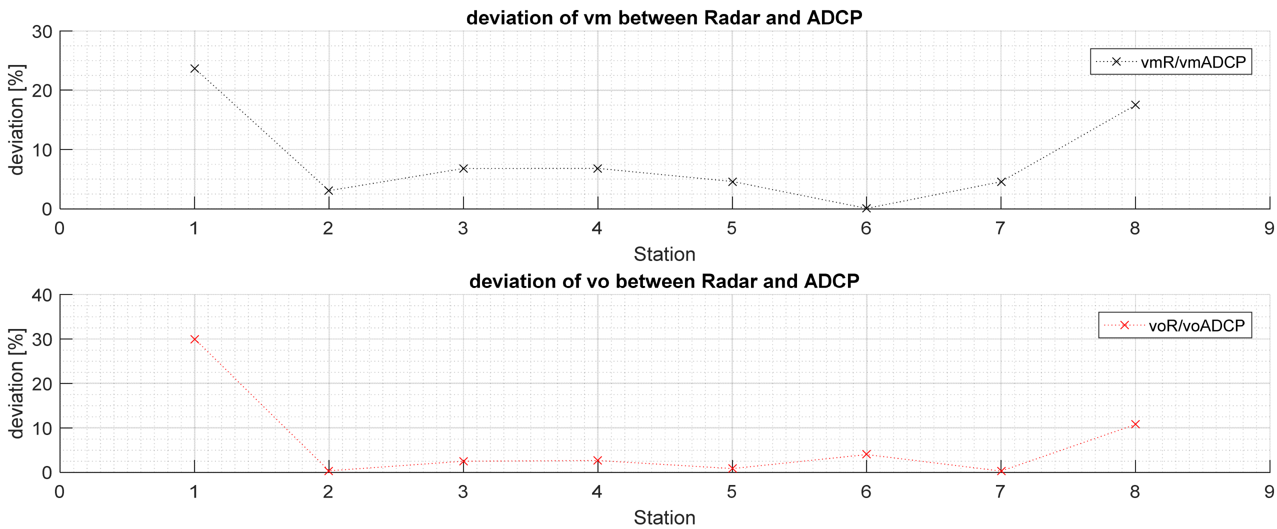

Figure 5 Deviation between $v_{m,section}$ and $v_{o,section}$ for each Radar-station, gauge Hueckeswagen.

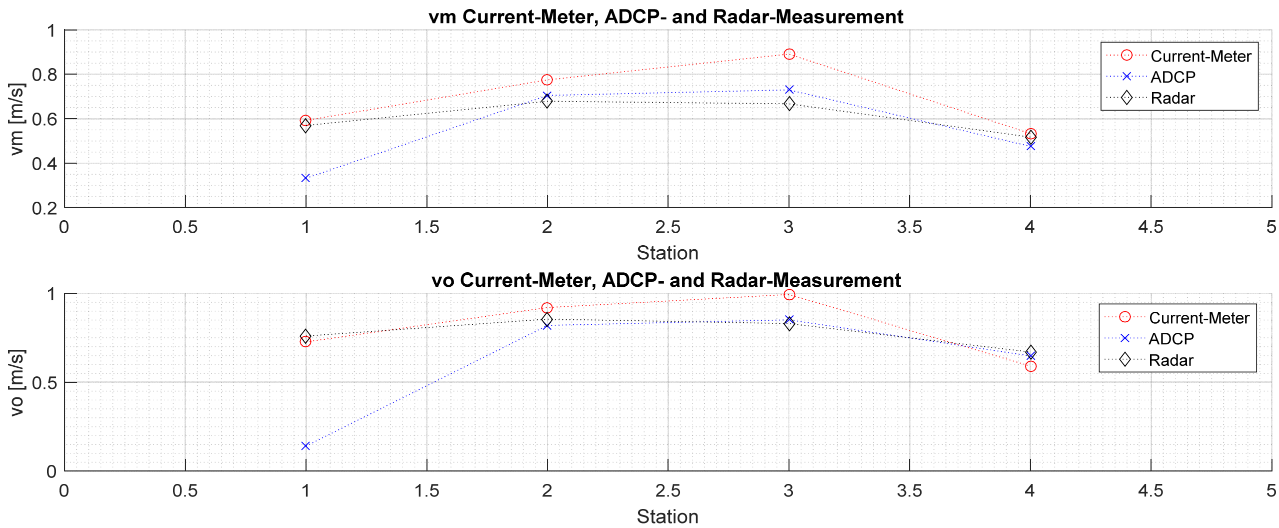

Figure 6. Velocities $v_{m,section}$ and $v_{o,section}$ for each Radar-station, gauge Hummelsheim.

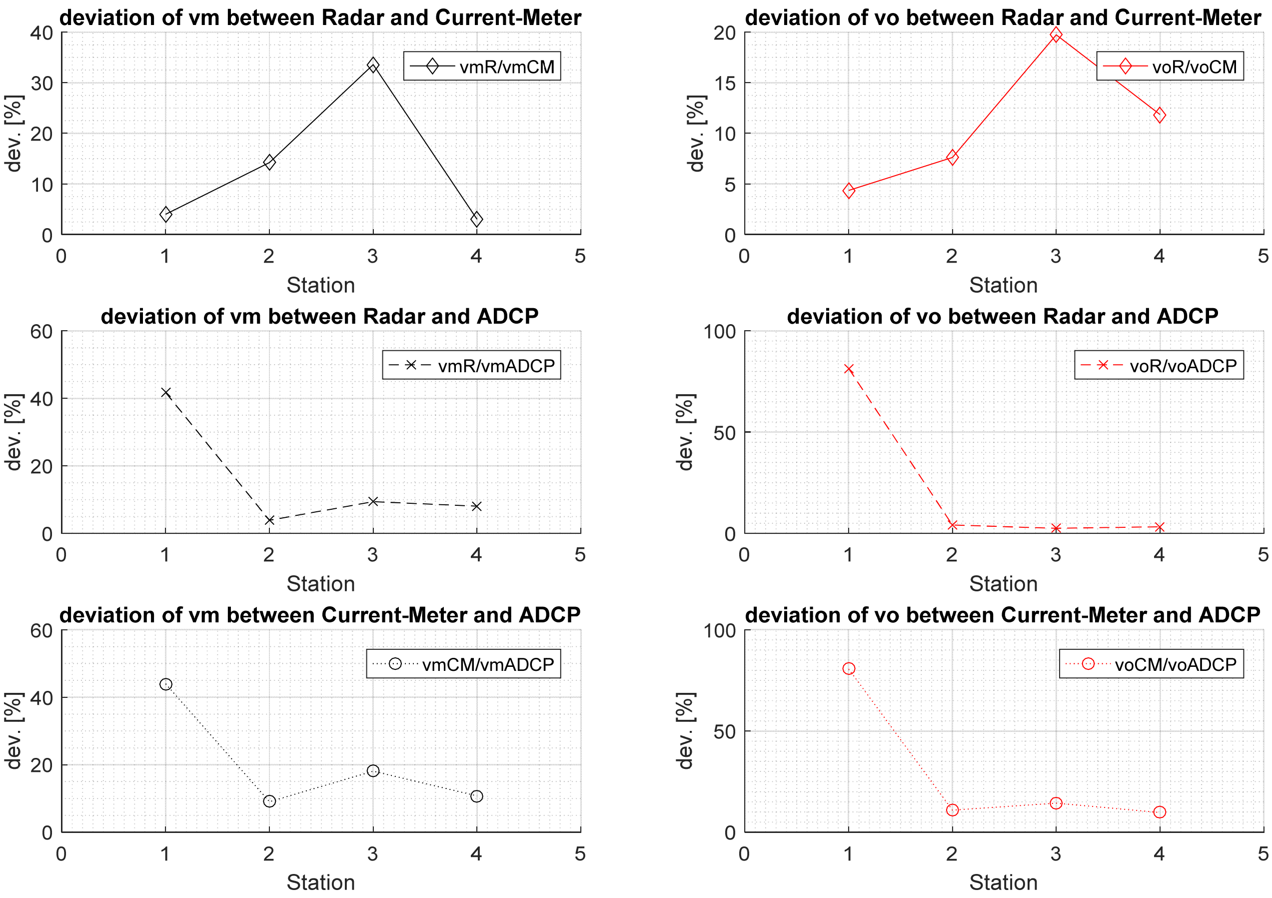

Figure 7. Deviation between $v_{m,section}$ and $v_{o,section}$ for each Radar-station, gauge Hummelsheim.

Just like the findings for the mean and surface velocity of each vertical, the average velocities for each Radar-section vm,section and vo,section at the gauge SHUE only contain small deviations (Figure 4, Figure 5). Again, for the left and right edges there are small but noticeable variations. With regard to a tentative k-value adjustment, the values should be slightly decreased in the edge area, and increased for the core area.

As distinguished from the gauge SHUE, the results of the comparisons for the values vm,section and vo,section at the second gauge SHUM reveal much taller variations. These variations exist especially in the core area. In the edge area, the current meter measurement and the radar measurement fit quiet well. However, the ADCP-data differs a lot (40-80%, Figure 7). At this point, further investigations are required since for the left edge, measured data could not be gathered by the ADCP-system due to insufficient water depth.

Thus, there are only recommendations for the k-value adjustment in the core area. Because the mean velocities out of the Radar-measurement are set too low, the k-values should be increased for these sections.

3.2 Comparison of the cross-sectional area

The comparisons done before the presented investigations already showed significant variations between the discharge cross-sections for the different measurement systems (e.g. gauge SHUM 6-15 %). Therefore, a particularly comparison of the discharge cross-section A, used for the Radar-measurements, was made in addition to the investigation of the mean velocities.

During a current meter measurement, the cross-section is described by the recorded water depths for each vertical. The more verticals, the more accurate the profile gets represented (Morgenschweis, 2010; Boiten, 2008; LAWA, 1991). By acoustic sampling of the waterbody during the transect from bank to bank, the ADCP-measurement however generates a very detailed representation of the measured profile. Figure 8 and Figure 9 show the particular discharge cross-sections of the compared measurement system for each gauge.

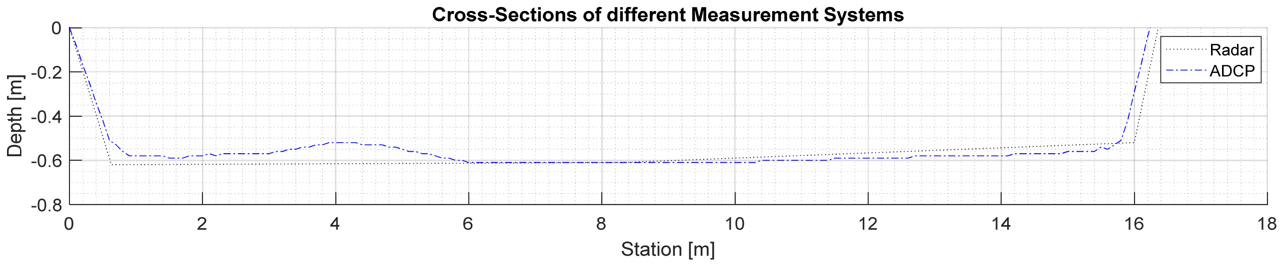

Figure 8. Cross-sections at gauge Hueckeswagen, obtained by using different methods of measurement.

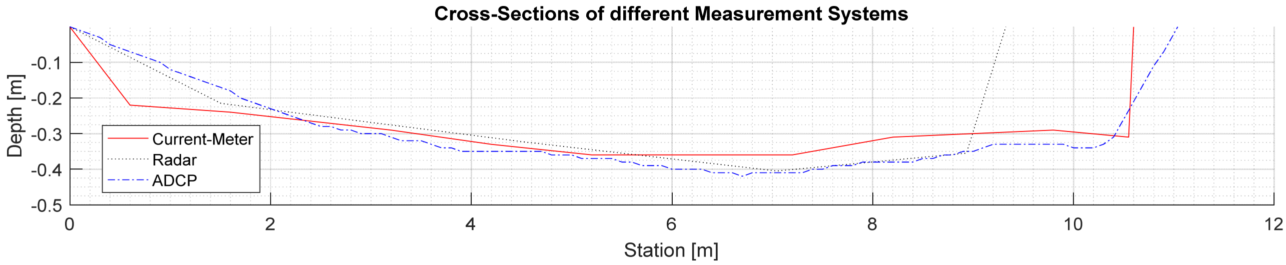

Figure 9. Cross-sections at gauge Hummelsheim, obtained by using different methods of measurement.

Regarding the analyses at gauge SHUM as well as the analyses at gauge SHUE, one can notice that the actual cross-section is only displayed approximately by the Radar-measurement. The measurement campaign at gauge SHUM, especially, shows tall variations between the present cross section and the one used for the Radar-measurement (Figure 9).

As a last step, the simultaneously recorded cross-sections (by ADCP or current meter) combined with the k-value adjustment were used for the discharge determination out of the Radar-data. Considering the measured surface velocities, the Radar-measurement was then evaluated again. For the gauge SHUE, the ADCP dataset was used to compute the discharge cross section for the Radar-measurement. Due to missing ADCP-data at the edges of the cross section at gauge SHUM, the discharge cross-section was thereby taken out of the current meter dataset.

3.3 k-value adjustment and evaluation

Taking into account the adapted cross-section and the velocity distributions ($v_{m,section}$ and $v_{o,section}$), the k-values were adjusted for each of the sectors of the Radar-Measurement. Therefore, the mean velocities of the ADCP-measurement were compared to the mean velocities of the Radar-Measurement for each Radar-Station. The k-values then were modified with the result that the differences between these two values were minimized. The original and modified k-values, cross-section areas and partial discharges prior to and after the adjustment are summarized in Table1.

Table 1. Original and modified k-values, subareas and partial discharges of the Radar-measurement at the gauge Hueckeswagen.

Section	**k-value *original***	**k-value *modified***	**subarea *original***	**subarea *modified***	**partial discharge *orinial***	**partial discharge *modified***
1	0.792	0.783	1.099	1.008	0.506	0.458
2	0.823	0.851	1.234	1.109	0.695	0.647
3	0.823	0.860	1.228	1.118	0.786	0.730
4	0.823	0.884	1.223	1.220	0.794	0.852
5	0.822	0.852	1.201	1.220	0.799	0.842
6	0.821	0.835	1.155	1.196	0.747	0.789
7	0.820	0.812	1.108	1.167	0.702	0.734
8	0.796	0.785	1.108	1.075	0.548	0.527
		TOTAL	9.356	9.111	5.575	5.578

After the Radar-measurement was evaluated once again, the key values A, Q, and v_m were compared to the comparatively conducted measurements. Table 2 shows the results of the variations between the Radar-system and the reference-values for the original and adjusted dataset.

Table 2. Variations between the Radar-measurement and the reference values before a k-value adjustment and including the k-value adjustment at the gauge Hueckeswagen.

	A	Q	v_M
without k-value adjustment	3 %	1 %	3 %
including k-value adjustment	0 %	0 %	0 %

The described adjustments, taking into account the customized cross-sections and velocity distributions, were also carried out for the second gauge SHUM. Table 3, again, encapsulates the k-values, cross-section areas and partial discharges prior to and after the adjustment.

Table 3. Original and modified k-values, subareas and partial discharges of the Radar-measurement at the gauge Hummelsheim.

Section	k-value *original*	k-value *modified*	subarea *original*	subarea *modified*	partial discharge *orinial*	partial discharge *modified*
1	0.750	0.878	0.521	0.573	0.295	0.383
2	0.794	0.937	0.862	0.776	0.559	0.622
3	0.835	0.972	1.062	0.878	0.708	0.707
4	0.722	0.883	1.201	0.915	0.623	0.541
		TOTAL	3.609	3.143	2.185	2.286

As already mentioned, the evaluated Radar-measurement was compared again to the other measurement systems regarding the values A, Q, and v_m. Table 4 displays the results of the comparison for the gauge SHUM.

Table 4. Variations between the Radar-measurement and the reference values before a k-value adjustment and including the k-value adjustment at the gauge Hummelsheim.

	A	Q	v_M
without k-value adjustment	15 %	10 %	21 %
including k-value adjustment	0 %	6 %	7 %

By looking at both Table 2 and Table 4, a significant reduction of the variations between the Radar-measurement and the conducted reference values can be noticed.

4 CONCLUSIONS

In the course of measurement campaigns at different gauges, comparative and complementary discharge measurements were conducted by use of the current meter, Radar- and ADCP-systems. Through preliminary comparisons the values A, Q and v_m were systematically evaluated for these systems and yielded significant variations. Subsequently, more detailed investigations of the respective values were conducted. In the present publication, these investigations were shown especially for the Radar-measurement.

By comparing both the mean velocities and the surface velocities for defined sections of the discharge cross-section, adjustments for the k-values of the Radar-measurement were made. Hence variations between the parameters vm and vo, as well as the total discharge were obviously diminished.

The investigations were carried out at two different gauges with characteristic local conditions. Evaluating the comparisons for the first measurement site (SHUE), with fixed riverbed and robust riverbanks, only little variations could be noticed between the Radar-measurement and the comparative ADCP-measurement. For the second gauge (SHUM), with unsteady cross-section profile, wide variances for the discharge cross-section and the different velocity distributions were ascertained.

It can be concluded, that a periodic review and correction of the cross-section is necessary for gauges with appropriate conditions. The corrections can be made for both contactless discharge-measurement systems like Radar and ultrasonic transducers, mounted in a cross-section. Furthermore, the conducted investigations emphasize the advantages of combining different discharge measurements. The associated possibilities of adjustment and corrections entail a significant increase of accuracy and quality for discharge measurements.

Giving an outlook, an evaluation of alternative possibilities for combining different measurement systems can be conducted and automatic adjustments for instance of cross-sections or k-values could be developed and applied.

REFERENCES

Adler, M. & Nicodemus, U. (2012). Benutzerhandbuch. AGILA 7. Programm zum Auswerten und Archivieren von ADCP-Messungen. *Bundesanstalt für Gewässerkunde*, Koblenz, Germany.

Boiten, W. (2008). Hydrometry. 3rd edition. *A Comprehensive Introduction to The Measurement of Flow in Open Channels*. CRC Press Balkema (Unesco-IHE Delft lecture note series), London, UK

ISO (2007). *Hydrometric Uncertainty Guidance (HUG),* ISO/TS 25377:2007, International Organisation of Standardization, Geneva, Switzerland.

LAWA (1991). Pegelvorschrift, Anlage D: Richtlinie für das Messen und Ermitteln von Abflüssen und Durchflüssen. *Länderarbeitsgemeinschaft Wasser (LAWA) und Bundesminister für Verkehr (BMV),* Hamburg und Bonn, Germany

Morgenschweis, G. (2010). Hydrometrie. Theorie und Praxis der Durchflussmessung in offenen Gerinnen. *Springer,* Berlin Heidelberg, Germany.

Sommer GmbH (2013). RP-30 Radar Profiler. Mobiles Abfluss-Messsystem. Benutzerhandbuch. Ausgabe Oktober 2013, Koblach, Austria.

Proceedings of the 37th IAHR World Congress
August 13 – 18, 2017, Kuala Lumpur, Malaysia

SCOURING AT THE INTERFACE BETWEEN FIXED AND MOBILE BED IN STEEP SLOPED CHANNELS

FABIAN FRANZINI[1], TZU YIN CHEN[2], HERVÉ CAPART[3] & SANDRA SOARES-FRAZAO[4]

[1,4] Institute of Mechanics, Materials and Civil Engineering, Université catholique de Louvain, 1348 Louvain-la-Neuve, Belgium,
fabian.franzini@uclouvain.be
[1] Fonds National de la Recherche Scientifique, 1000 Bruxelles, Belgium,
[2,3] Department of Civil Engineering and Hydrotech Research Institute, National Taiwan University, Taipei, Taiwan.

ABSTRACT

The intense scouring occurring at the interface between fixed and mobile bed can have a strong impact on the stability of structures and on the global morphological changes in rivers. Often, this transition is studied in flat or mild-slope channels. However, in order to better understand this phenomenon, it is important also to understand what can happen in steeper channels. The research presented here focuses on an experimental study of scouring at the interface between fixed-mobile beds in a steep channel with a 5% bed slope. The experiments are conducted in an 8m long flume featuring a 2m long fixed bed followed by a mobile bed portion. Results are captured using two types of cameras: a classical camera capturing 12 pictures per second and a high-speed camera capturing 500 pictures per second. The first one is used to capture the bed- and water-level evolution during the scouring process. The second one allowed the study of the movement of the individual sand particles. The flow is controlled by a fixed discharge upstream and a 0.30m high weir downstream. The experiments are run using four different constant discharges. All tests are repeated 3 to 5 times and showed good repeatability. The results highlighted four different stages in the scouring process as well as the links between the velocity field and the evolution of the bed morphology. The experimental results are then compared to numerical simulations using a one-dimensional finite-volume model.

Keywords: Erosion processes; flow-structure interactions; flow visualization and imaging; laboratory experiments; Particle Tracking Velocimetry (PTV).

1 INTRODUCTION

Local scouring due the interaction between flow and hydraulic structures is an important phenomenon to take into account when studying the stability of hydraulic structures built along rivers. Majority of researches focus on the study of the local scour around bridge abutments and piers (Melville et al. 2008; Richardson and Richardson 2008). However, the scouring occurring after the transition between a fixed and mobile bed can have a tremendous impact on the stability of the downstream structures.

During the Sinlaku Typhoon in 2008 in central Taiwan, the Houfeng Bridge, located on the Da-Chia River, collapsed due to an important scouring amplified by a transition between fixed and mobile bed (Hong et al. 2012). During this event, a pipeline, located 20 m upstream of the bridge and originally buried in the bed, became visible. The non-erodible protection around the pipe created a transition between this fixed bed and the mobile riverbed that generated a deep scour hole downstream. This scour hole weakened the foundations of the bridge pillars, leading to their destruction. These transitions between fixed and mobile bed are not only occurring around structures. Along the course of a river, portion of non-erodible bedrock in sand beds create a similar problem.

To simulate these transitions in rivers, the shallow-water equations complemented by the Exner equation for the bed evolution are used, often with a non-equilibrium sediment transport model (Daubert and Lebreton, 1967; Bell and Sutherland 1983; Wu and Wang 2008). To validate these models, well-documented test cases are needed. These test cases should include different flow regimes. However, majority of the researches currently focus on flat bed or mild slopes (Mohamed and McCorquodale 1992; Iervolino 2005; Savary 2007; Zech et al. 2009). The work presented here focuses on the experimental study of the transition between fixed and mobile bed in a steep-slope channel, with a slope of five percent. Data on the bed and water level evolution as well as on the velocity fields in the scour hole were collected.

The paper will be divided as follows. First, the experimental setup and the measurement techniques will be presented. Then, the results will be analyzed by isolating the different stages of the erosion process and comparing the experiment to a one-dimensional finite-volume model.

2 EXPERIMENTAL SETUP

The experiments were conducted in an 8m long and 0.25m wide flume with a slope of 5%. The 8m length was divided as follows, from upstream to downstream (see Figure 1): 2.6m of sand (mobile bed), 2m of wood (fixed bed), and 3.4m of sand (mobile bed). As the slope is steep, the length of the fixed-bad part, although limited, is sufficient to reach uniform flow conditions before reaching the mobile bed. The sand used has a mean diameter (d50) of 1.8mm and a specific weight (ρ) of 2615kg/m3. As the wooden part was much smoother than the sand bed, the resulting important discontinuity of the friction coefficient between the fixed and mobile bed would have influenced strongly the erosion process. Therefore, to ensure a better continuity of the friction factor, a layer of sand has been glued on the wood. Furthermore, the wooden part was not built as a rectangle but as a trapezoid, with angles of 60° at the base. Even though the channel is relatively narrow, the sidewalls impact on the flow can be neglected, as the depth is small and the sidewalls are made of glass and thus have a much lower friction coefficient.

The flow was controlled by a fixed discharge upstream and a 0.30m high weir downstream. The experiments were run using four different constant discharges (2, 6, 10 and 20 l/s). All tests were repeated three to five times to control repeatability.

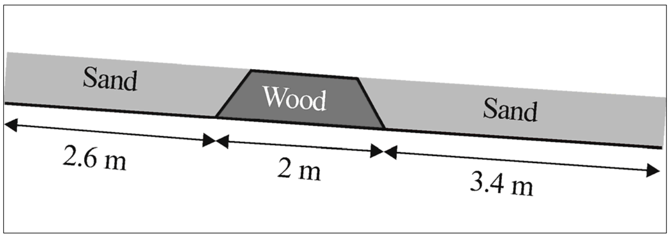

Figure 1. Experimental setup.

3 MEASUREMENT TECHNIQUE

Results were captured using two types of cameras: a classical camera capturing 12 pictures per second and a high-speed camera capturing 500 pictures per second. The first one was used to capture the bed and water level evolution during the scouring process. The second one allowed the study of the movement of the individual sand particles to evaluate the velocity field in the scour hole.

The treatment of the images was done as follows. First, the pictures were corrected by removing all the distortions due to the lenses of the camera (e.g. fish-eye effect). Then, the sediment particles positions were captured by detecting the brightness intensity peaks (Figure 2). These first two steps are used for both analyses: bed- and water-level evolution and velocity-field capture.

To detect the bed level, the picture is first divided into a rectangular mesh. For each element of the mesh, the density of points (the number of particles detected) is determined. Then, the bed level is defined as the highest particle in the highest mesh cell with a density higher than the threshold value (Figure 3). For the water level, the vertical gradient of brightness is calculated for every element of the mesh. Then, the water level is defined as the elevation with the largest gradient and located higher than the bed. The detected bed and water levels are represented in Figure 4.

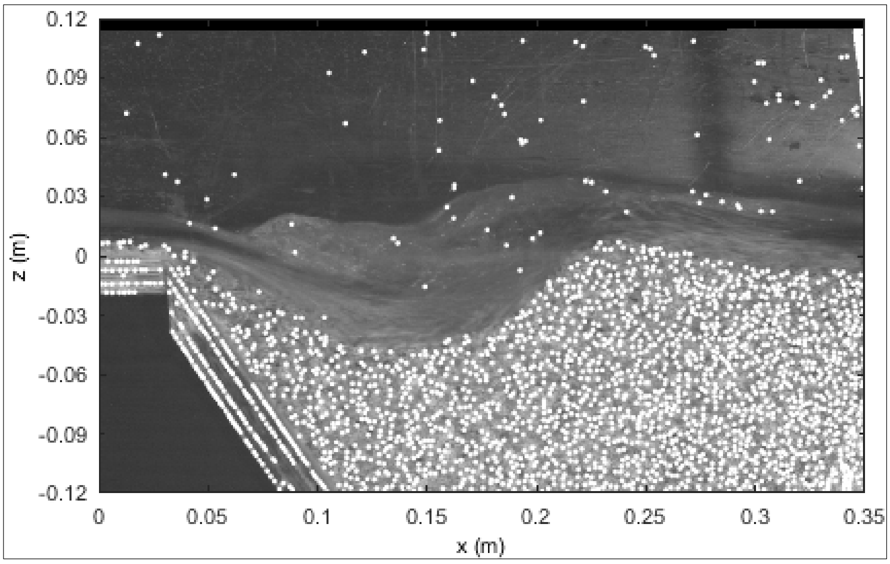

Figure 2. Particles capture.

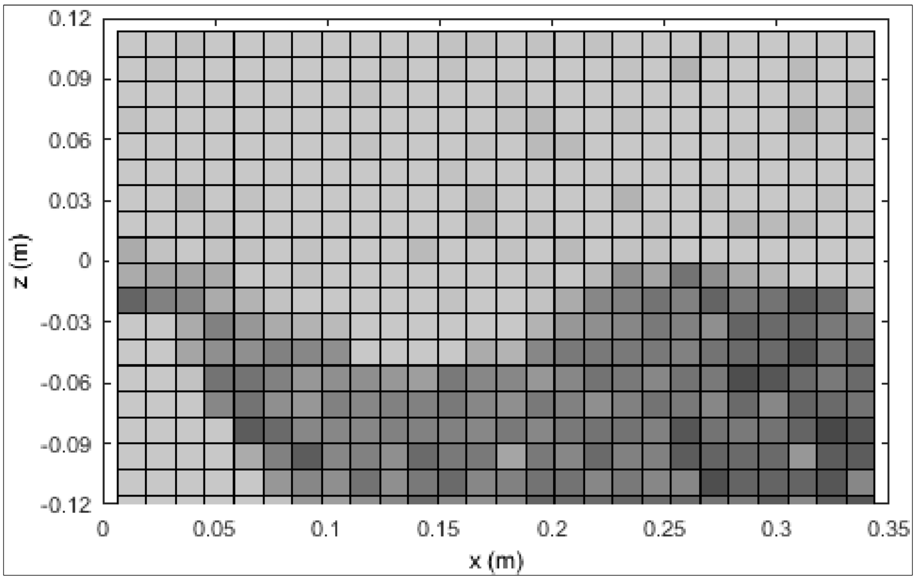

Figure 3. Density mesh to capture the bed level.

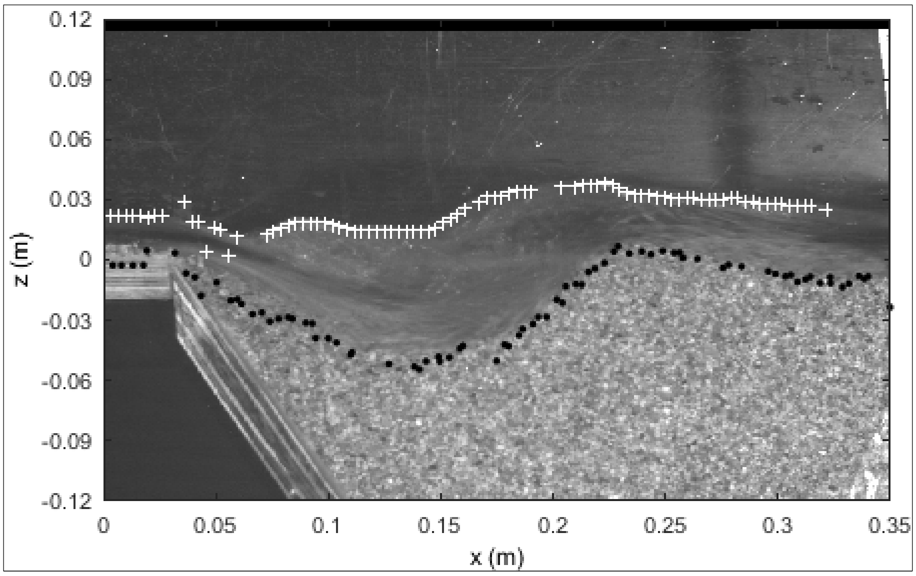

Figure 4. Bed level (black dots) and water level (white cross).

The velocity fields are determined using the Particle Tracking Velocimetry, also known as PTV. This method, unlike the Particle Image Velocimetry (PIV), tracks individual particles from one picture to the other. To track one particle, three methods are mainly used in the literature: nearest neighbor, pattern tracking and path tracking. The first method considers that the particle in the next frame is simply the particle nearest to the previous position. It is the simplest method of the three however, in rapid and dense flows, the results are not always accurate. The second method was developed by Capart et al. (2002), Instead of matching individual particles, group of particles, described by their Voronoi diagrams, are matched. The third and last method was first developed by Sethi and Jain (1987). It uses a sequence of pictures to find the trajectories of the particles and then correct the tracking by checking the coherence and the continuity of the calculated trajectories.

To check that the results are repeatable, the measured water and bed levels for three different tests at 10 l/s after 40s are compared (Figure 5). It can be observed that, even though there are small differences, a good repeatability is obtained.

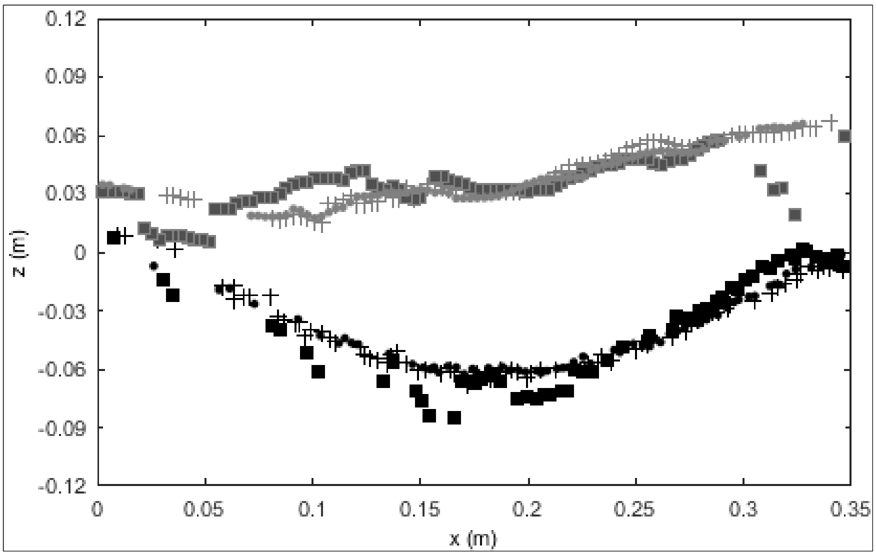

Figure 5. Repeatability: results obtained with three different tests at10 l/s.

4 EXPERIMENTAL RESULTS

When the fast supercritical flow reaches the mobile bed, the erosion process progressively starts, and a hydraulic jumps forms when the scour hole reaches a given depth. This jump rapidly evolves to a submerged jump with a complex velocity distribution and cyclic flow patterns. This process can be described by four distinct stages described below: (1) Attached flow, (2) Stationary hydraulic jump, (3) Surface jet and (4) Moving hydraulic jump.

During the first stage, the flow remains attached to the bed with low erosion and shallow depth. The flow field was not captured during this stage, as the water depth is too shallow to allow a correct measurement.

Rapidly, after the initial formation of the scour hole (in less than one second), a stationary jump is created just downstream of the transition (stage 2). This is the main stage of the erosion process, as it lasts uninterrupted for 100 s in average. This stage is also the main cause of the intense scouring. As observed in Figure 6, the water flows mainly along the bed with a recirculation (the jump) near the water surface. These high velocities, close to the bed, have a very strong erosion capacity.

When the scour hole becomes too deep, the main velocity vectors detach from the bed and become horizontal, and a recirculation zone appears at the bottom, close to the bed (Stage 3, Figure 7). The erosion is greatly reduced during this regime and the upstream slope becomes milder because, due to the recirculation at the bottom, the sand particles are transported upstream. In addition, the length of the scour hole is increased. After 2-3 s, when the upstream slope is sufficiently mild again, the flow reattaches to the bed and a new hydraulic jump is formed at the downstream end of the scour hole (Stage 4, Figure 8). The erosion process is similar to Stage 3, with a low erosion rate and sand particles close to the bed moving in the upstream direction. This jump then proceeds to move upstream where it becomes stationary, resulting in the situation of Stage 2 again (Figure 6) and the whole process, from Stage 2 to Stage 4, starts again in a cyclic way.

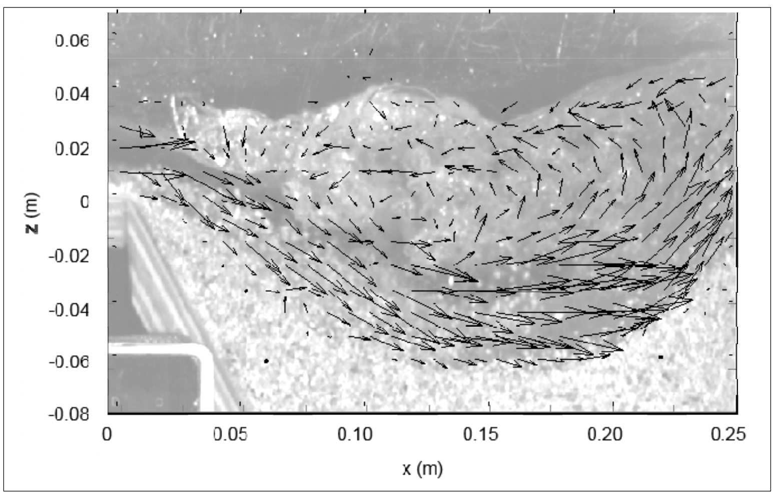

Figure 6. Velocity field during stage 2 of the erosion process.

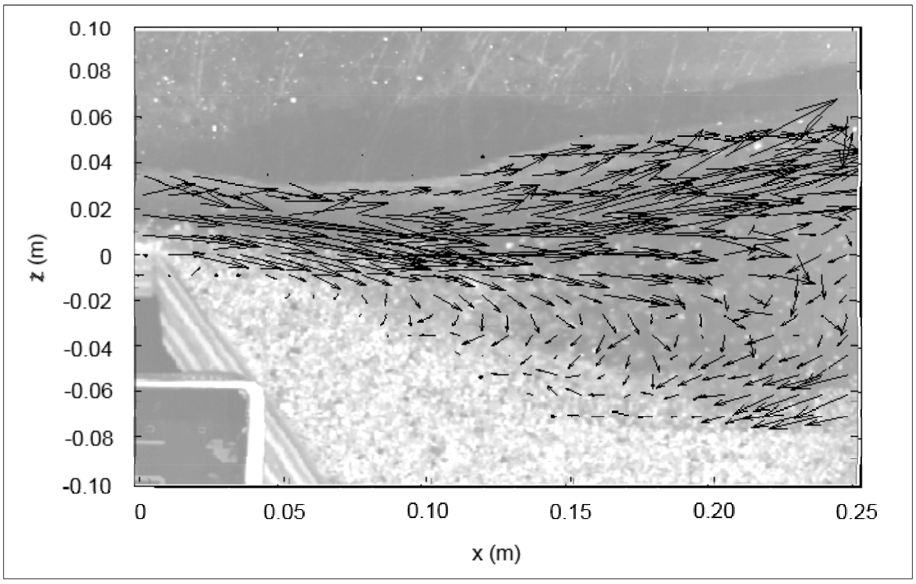

Figure 7. Velocity field during stage 3 of the erosion process.

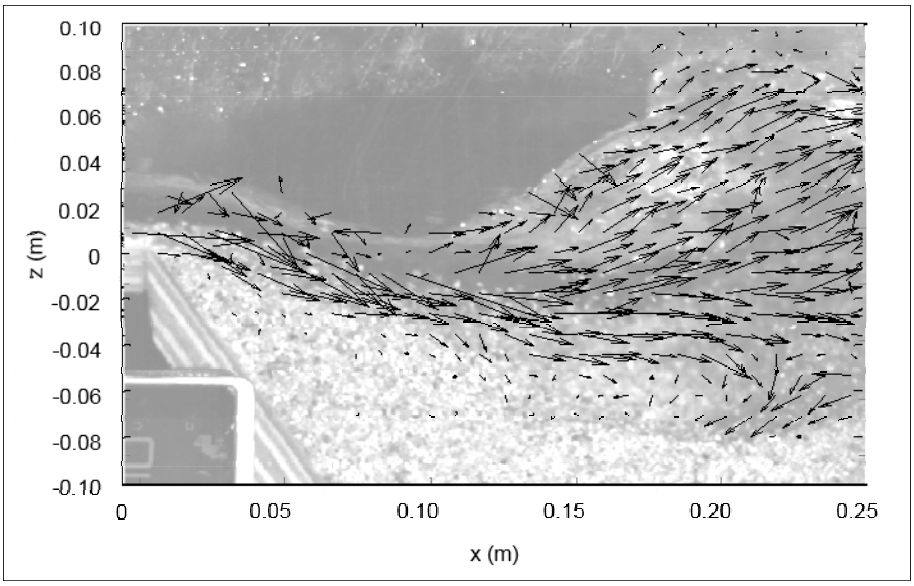

Figure 8. Velocity field during stage 4 of the erosion process.

The evolution of the scour geometry is summarized in Figure 9 to Figure 11 for the tests with 10 l/s. It can be observed that the shape of the scour hole is similar for each time step, the downstream and upstream slopes being constant (Figure 9) until the scour depth reached the fixed channel bed (t = 600 s). In addition, the maximum scour depth evolves linearly (Figure 10). The longitudinal position of the deepest point, illustrated in Figure 11, also evolves almost linearly, showing that the extent of the scour hole progressively increases. The influence of stage 3 and 4 on the deepening on the scour hole cannot be observe on Figure 10 because the deepest scour position reaches the end of the measurement frame before stage 3 appear.

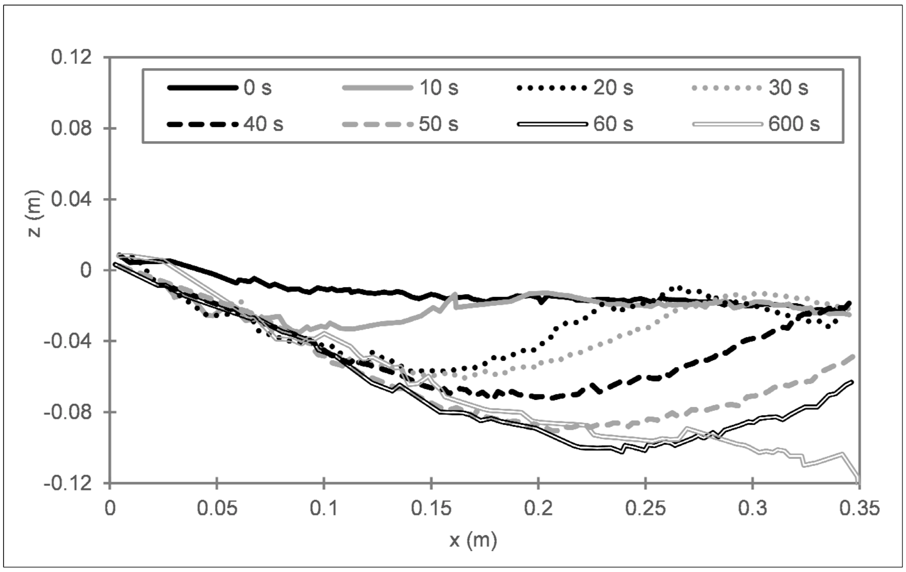

Figure 9. Evolution of the scour hole geometry with 10l/s.

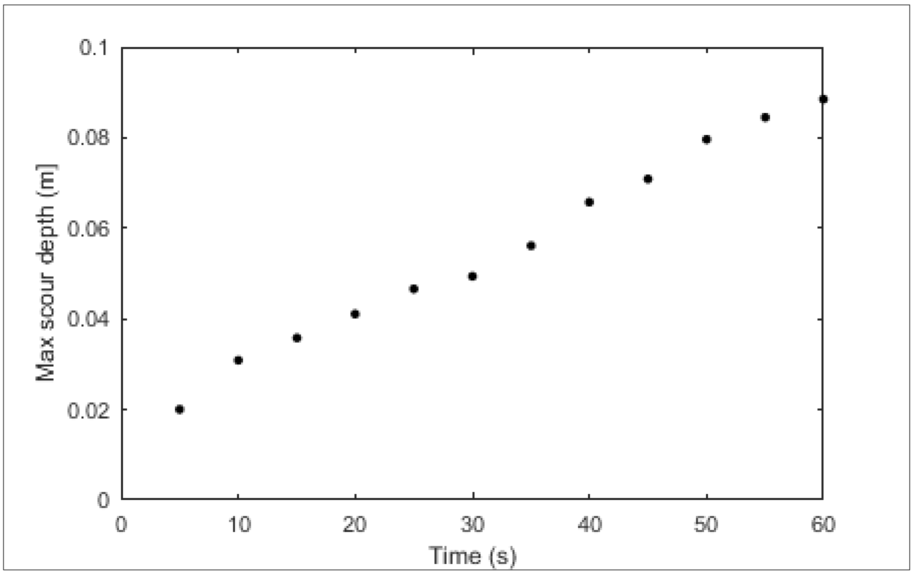

Figure 10. Evolution of the max scour depth for 10l/s.

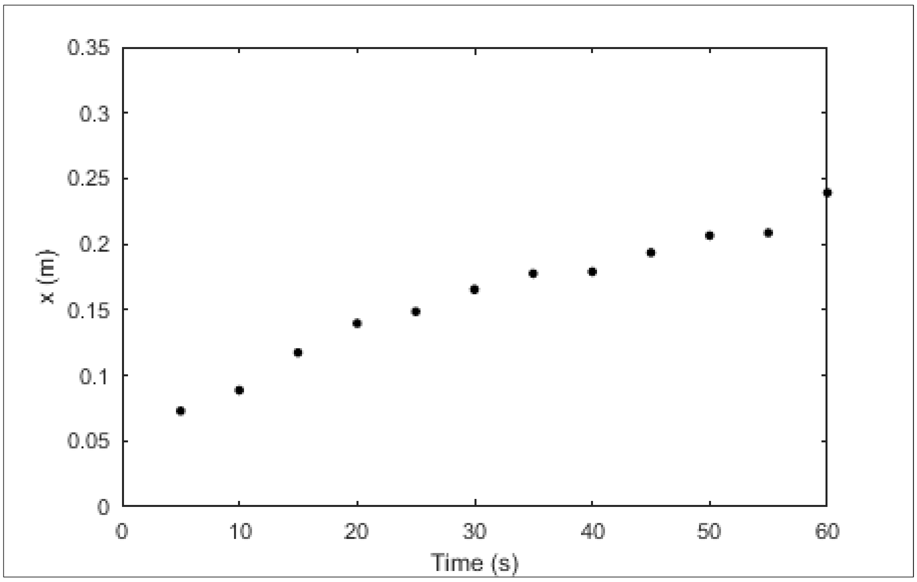

Figure 11. Evolution of the position of the bottom of the scour hole for 10l/s.

5 COMPARISON WITH NUMERICAL SIMULATIONS

A one-dimensional model based on the Saint-Venant equations and the Exner equation for the bed evolution is used to represent the flow. These equations are:

$$\frac{\partial A}{\partial t}+\frac{\partial Q}{\partial x}=0 \qquad [1]$$

$$\frac{\partial Q}{\partial t}+\frac{\partial}{\partial x}\left(\frac{Q^2}{A}+gI_1\right) = gA(S_0\text{-}S_f) \qquad [2]$$

$$\frac{\partial A_b}{\partial t}+\frac{\partial}{\partial x}\left(\frac{Q_s}{1-\varepsilon_0}\right)= 0 \qquad [3]$$

where Q is the discharge, A the wetted area, S_0 the bed slope, A_b the area of the sediment bed, Q_s the sediment transport rate and ε_0 the bed porosity. The integral gI_1 represents the hydrostatic pressure thrust.

The sediment transport rate is determined by the Meyer-Peter and Müller (1948) equation:

$$Q_s=8B\sqrt{g(s\text{-}1)d_{50}^3}\,\left(\frac{RS_f}{(s\text{-}1)d_{50}}-\theta_{cr}\right)^{1.5} \qquad [4]$$

where s is the specific gravity of the sediments, d_{50} the median bed sediment diameter, R the hydraulic radius (defined as $R = A/P$), and θ_{cr} the non-dimensional shear stress for initial sediment motion (here the value is set at 0.047). According to Garcia (2008), the sediment transport over the entire cross-section is obtained by multiplying the unit-width sediment transport by the width B of the channel at the level of the free surface. The sediment transport is always considered to be at capacity, equal to the value of [4], if sediments are available.

The system of equations [1] to [3] is written in vector form as

$$\frac{\partial \mathbf{U}}{\partial t}+\frac{\partial \mathbf{F}}{\partial x}+\mathbf{H}\frac{\partial \mathbf{U}}{\partial x}=\mathbf{S} \qquad [5]$$

with,

$$\mathbf{U}=\begin{bmatrix} A \\ Q \\ A_b \end{bmatrix} \qquad [6]$$

$$\mathbf{F}=\begin{bmatrix} Q \\ \frac{Q^2}{A}+gI_1 \\ \frac{Q_s}{1-\varepsilon_0} \end{bmatrix} \qquad [7]$$

$$\mathbf{S}=\begin{bmatrix} 0 \\ -gAS_f \\ 0 \end{bmatrix} \qquad [8]$$

$$\mathbf{H}=\begin{bmatrix} 0 & 0 & 0 \\ 0 & 0 & \frac{gA}{B} \\ 0 & 0 & 0 \end{bmatrix} \qquad [9]$$

The finite-volume scheme is then solved using a Roe solver with a lateralized treatment of the source terms (Franzini and Soares-Frazao submitted).

$$\mathbf{U}_i^{n+1}=\mathbf{U}_i^n+\frac{\Delta t}{\Delta x}\left(\mathbf{F}_{i-1/2}^{*R}-\mathbf{F}_{i+1/2}^{*L}\right) \qquad [10]$$

$$\mathbf{F}^{*L}_{i+1/2} = \mathbf{F}_i + \sum_{\lambda_m<0}^{m} \left((\lambda\alpha - \beta)\mathbf{e}\right)_{m,i+1/2} \qquad [11]$$

$$\mathbf{F}^{*R}_{i+1/2} = \mathbf{F}_{i+1} - \sum_{\lambda_m>0}^{m} ((\lambda\alpha - \beta)\mathbf{e})_{m,i+1/2} \qquad [12]$$

with the wave strength and the projection of the source terms defined as:

$$\boldsymbol{\alpha} = \mathbf{E}^{-1}\delta\mathbf{U} \qquad [13]$$

$$\boldsymbol{\beta} = \mathbf{E}^{-1}\mathbf{S} \qquad [14]$$

The matrix ***E*** is the matrix of the eigenvectors **e** and λ are the eigenvalues (wave celerities). The eroded area, A_b, is uniformly distributed along the section width.

Error! Reference source not found. show the numerical results and the experiments after 30s. It can be observed that, even though the model is able to capture the creation and deepening of the scour hole, the complete erosion occurs on the wooden part and the scour hole is much shorter than observed during the experiments. Similar results were presented by Zech et al. (2009) for a case of local scouring on a horizontal bed. The shorter scour hole occurs because the sediment transport is considered to be at capacity all the time. However, in the reality, some distance is required before the sediment transport rate reaches its full capacity. In addition, the model is unable to capture the vertical velocities, being cross-section averaged. Yet, in this experiment, the majority of the erosion is created by the 3D velocities, as illustrated in Figures 6, 7 and 8.

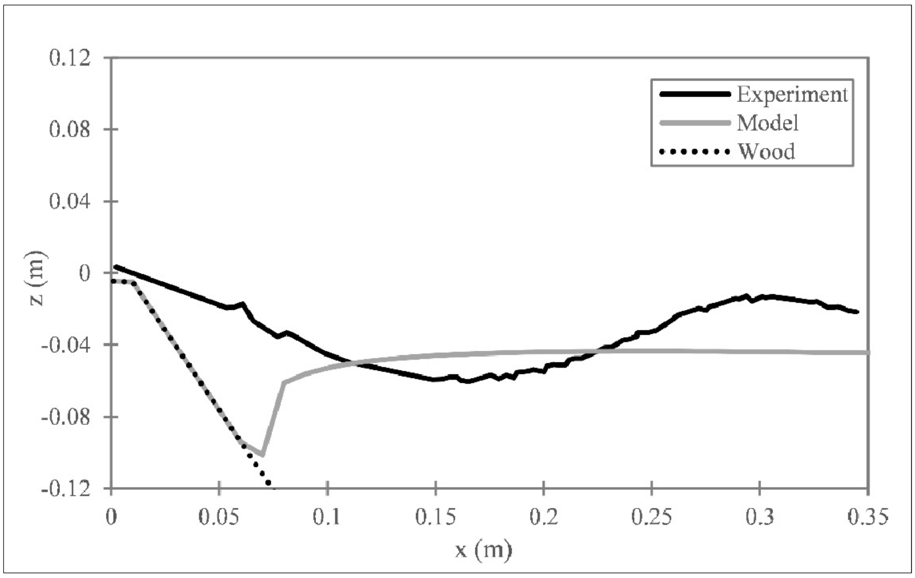

Figure 12. Comparison between the numerical model and the experiment for 10l/s after 30s.

6 CONCLUSIONS

Experiments of scouring at the transition between fixed and mobile in a steep-sloped channel have been presented. During the experiments, the evolution of the bed and water levels were filmed through a side window using a suitable digital video camera. It was shown that the scour hole progressively evolves during the whole erosion process keeping constant upstream and downstream slopes. The deepest point of the scour hole was tracked and it was observed that both the depth and the position of this point evolved linearly; the position being progressively pushed in the downstream direction.

A high-speed camera (500 fps) was used to capture the movement of the sand particles in the scour hole. This tracking achieved using PTV (path tracking) allowed to determine the velocity fields during the erosion process. Four different stages were observed during the experiments: (1) attached flow, (2) stationary hydraulic jump, (3) surface jet and (4) moving hydraulic jump. The first stage, the attached flow, only occurred during the first instants of the experiments as long as the erosion remained limited. The second and most important stage, both in terms of duration and erosion capabilities, presented a stationary hydraulic jump with the main flow field close to the bed surface. Then, the third and fourth stages were relatively short and the main flow field became horizontal before returning to the second stage, starting a new cycle of stages 2-3-4.

Finally, the experimental results were compared to a one-dimensional finite-volume model computing the sediment transport using the Meyer-Peter and Müller formula and considering equilibrium sediment transport. The comparison showed that the model was able to capture the creation and deepening of the scour hole. However, the length of the scour hole was not well predicted, the scour hole being too short and located too close to the transition between the fixed and mobile beds.

Future work will focus on an appropriate lag formulation for the sediment transport rate in order to better represent the progressive evolution of this transport rate towards the full transport capacity.

ACKNOWLEDGEMENTS

This work was supported by the Fonds National de la Recherche Scientifique, Belgium.

REFERENCES

Bell, R.G. & Sutherland, A.J. (1983) Nonequilibrium Bedload Transport by Steady Flows. *J. Hydraul. Eng.,* 109(3), 351–367.

Capart, H., Young, D.L. & Zech, Y. (2002). Voronoï Imaging Methods for the Measurement of Granular Flows. *Experiments in Fluids*, 32(1), 121-135.

Daubert, A. & Lebreton, J.C. (1967). Etude Expérimentale sur Modèle Mathématique de Quelques Aspects des Processus D'érosion des Lits Alluvionnaires, en Régime Permanent et Non-Permanent. *Proc. 12th IAHR Congress,* 3, 26-37, Rotterdam, The Netherlands.

García, M.H. (2008). *Sedimentation Engineering Processes, Measurements, Modeling and Practice*, García, M.H. (ed.), ASCE Manuals and Reports on Engineering Practice 110, ASCE, Reston VA, 21–163.

Hong, J.H., Chiew, Y.M., Lu, J.Y., Lai, J.S. & Lin, Y.B. (2012). Houfeng Bridge Failure in Taiwan. *Journal of Hydraulic Engineering,* 138(2), 186-198.

Iervolino, M. (2005). Transporto Solido di Fondo in Condizioni Non Stazionare: Modellazione Onodimensionale. *PhD thesis,* Università degli Studi di Napoli "Frederico II", Naples, Italy (in Italian).

Melville, B.W., Parola, A.C. & Coleman, S.E. (2008). *Sedimentation Engineering Processes, Measurements, Modeling and Practice*, García, M.H. (ed.), ASCE Manuals and Reports on Engineering Practice 110, ASCE, Reston VA, 543–577.

Meyer-Peter, E. & Müller, R. (1948). Formulas for Bed Load Transport. *Proc., 2nd Meeting*, IAHR, Stockholm, Sweden; 39–64.

Mohamed, M.S. & McCorquodale, J.A. (1992). Short-Term Local Scour. *Journal of Hydraulic Research*, 30(5), 685-699.

Richardson, J.R. & Richardson, E.V. (2008). *Sedimentation Engineering Processes, Measurements, Modeling and Practice*, García, M.H. (ed.), ASCE Manuals and Reports on Engineering Practice 110, ASCE, Reston VA, 505–542.

Savary, C. (2007). Transcritical Transient Flow Over Mobile Beds Boundary Conditions Treatment in a Two-Layer Shallow-Water Model. *PhD Thesis*, Université catholique de Louvain, Louvain-la-Neuve, Belgium.

Sethi, I.K. & Jain, R. (1987). Finding Trajectories of Feature Points in Monocular Image Sequence. *IEEE Transactions on Pattern Analysis and Machine Intelligence,* 9(1)*,* 56-73.

Wu, W. & Wang, S.S. (2008). One-Dimensional Modeling of Dam- Break Flow Over Movable Beds. *Journal of Hydraulic Research*, 133(1), 48–58.

Zech, Y., Soares-Frazão, S., Spinewine, B., Savary, C. & Goutière, L. (2009). Inertia Effects in Bed-Load Transport Models. *Canadian Journal of Civil Engineering*, 36(10), 1587-1597.

Proceedings of the 37th IAHR World Congress
August 13 – 18, 2017, Kuala Lumpur, Malaysia

SWING GATE GENERATED DAM-BREAK WAVES

NILS GOSEBERG[1], JACOB STOLLE[2], CAREN DERSCHUM[3] & IOAN NISTOR[4]

[1] Ludwig-Franzius-Institute for Hydraulic, Estuarine and Coastal Engineering, Leibniz Universität Hannover, Hannover, Germany,
contact@nilsgoseberg.de (corresponding author)
[2,4] Department of Civil Engineering, University of Ottawa, Ottawa, Canada,
jstol065@uottawa.ca, inistor@uottawa.ca
[3] Department of Architecture, Civil Engineering, and Environmental Science, Technische Universität Braunschweig, Braunschweig, Germany, c.derschum@tu-braunschweig.de

ABSTRACT

Bore-type flow is often associated with natural hazards such as dam- or dike-breaches, storm surges or on-land tsunami flow. In this paper, dam-break waves generated by a swing gate are investigated in an attempt to model such hazard in laboratory conditions. An analytical framework for the gate motion is presented. The motion of the swing gate is analyzed with respect to the parameters, which are counter weight and impoundment depth that influence the gate opening time. While the repeatability of the gate opening was proven to be very favorable, resulting free surface time-histories showed major influence of the gate opening velocity close to the gate. Further downstream, the surface time-histories returned to the theoretically prescribed Ritter solution for ideal dam-breaks.

Keywords: Dam-break; extreme flow conditions; swing gate; experimental hydraulics; opening time.

1 INTRODUCTION

Breaching of dams and dikes represents one of the major threats to human communities downstream of impoundment reservoirs or in flood-prone areas. Cautionary examples of dam failure are the collapse of Gleno Dam, Italy, induced by structural failure right after initial filling (Pilotti et al., 2011) and Tous Dam, Spain, as a result of overtopping (Alcrudo and Mulet, 2007). Aging infrastructure and climate-change related increases in flood intensity may further amplify the dam-related risks associated to the sudden release of large volumes of water. At the same time, interest in dam-break waves has increased as the resulting water profile is comparable to tsunami on-land flow (Chanson, 2009). Dam-breaks have historically been of interest (Dressler, 1954; Whitham, 1955) and the investigation of the breaching of dams (Wurbs, 1987), the resulting dam-break wave and bottom interactions were studied extensively in two or three dimensions (Fennema and H.-Chaudhry, 1987; Cao et al., 2004; Spinewine and Zech, 2007; Oertel and Bung, 2012). Analytically, the sudden removal of a dam impounding (also known as an 'ideal' or 'sudden' dam-break) a volume of water was first investigated by Ritter (1892), who described the spatial and temporal evolution of the wave downstream of the dam for a frictionless case with horizontal bottom and rectangular cross-section.

Laboratory-based investigations of dam-breaks and the resulting waves were predominantly conducted by using a rapid vertically lifting gate of planar shape. A pneumatically-driven vertical lift gate mounted to a tilting flume was used by Lauber (1997) and Lauber and Hager (1998) to advance the knowledge of dam-break waves examining the influence of bottom slope, channel contractions, and viscosity in the wave front. Most importantly, Lauber and Hager (1998) provided analytical formula readily available for application and for defining wave and velocity profiles. Their work also provided information on minimum removal time of vertically moving gates, which is based on a fixed location X=x⁄(k_0=10) downstream of the gate, with x being the flow-wise coordinate and h_0 the impoundment depth. The authors also provided a mechanistic description of the collapse process after sudden removal of a gate indicating that the bottom particles will propagate with nearly wave celerity. Thus, this will become a limiting condition for swing gate openings, where the radial gate velocity at the gate tip requires to be at least equal or greater than the wave celerity of the impounded water body.

Following the advances in understanding ideal dam-break conditions with dry and wet downstream conditions, bores generated by vertically-moving gates were utilized to study a number of problems related to natural hazards and building on the requirements for assuring fully ideal dam-breaks. Soares-Frazao and Zech (2007) studied the wave structure interaction between a dam-break wave and an isolated objected placed downstream of the impoundment; the authors noted that the opening time of the gate obtained during the experiments dropped below the time prescribed by previous research. The effect of an extreme hydrodynamic condition on an idealized city layout was investigated by Soares-Frazao and Zech (2008), experimentally and numerically. A comparison between experimental and numerical results indicates that truly ideal dam-breaks in simulations matched well with those results obtained through experimental work. A popular and educational extension to the dam-break solution of Ritter (1892) was later presented by Chanson (2009) who followed a conceptual approach of Whitham (1955) separating the flow into a region of ideal-fluid flow that follows behind a tip region that is mostly resistance-dominated; the approach allows to utilize Darcy-Weisbach friction to predict the influence of frictional losses in the tip region often observed with experimental research. A study by Feizi Khankandi et al. (2012) provided insight into the effect reservoirs with shapes deviating from straight channels have on the dam-break wave; more importantly, additional, yet difficult to achieve velocity measurements close to the dam-break location were reported. More recently, detailed dam-break experiments have been also used to validate three-dimensional Navier-Stokes equations code in the context of coastal engineering applications (Lara et al., 2012). All of the above addressed research assumes profound knowledge of the detailed opening process of the vertically-moving gate, where guidance was built over a number of significant scientific contributions. To the author's knowledge, similar insight into swing gate generated dam-break waves is currently absent, yet greatly needed as the number of facilities equipped with such type of dam-break generator is increasing.

The lower bounds for the opening velocity of a vertically-moving gate, initializing the dam-break, were provided by Lauber and Hager (1998). However, most of the vertically-moving dam-break gates were used in narrow flumes and the weights of the gate constructions were usually limited in order to minimize cost and effort in building the opening mechanisms. A recent cost review of the authors revealed that construction cost for vertically-moving gates increases exponentially with flume width, impoundment potential and constrained by the prescriptions made to minimize the opening time. As vertically moving gates become less economically feasible, in wider flumes or when greater length scales are of interest; more recently rapidly-swinging gate mechanisms have been used to initiate a dam break in wider flumes. Nistor et al. (2009) and Nouri et al. (2010) investigated the effects of an advancing bore impacting a free-standing, surface-piercing structure where the bore was found to resemble flows observed in the context of tsunami on-land flow. The advancing bore was generated by a top-hinged gate mounted in a fast-flow facility and the resulting wave front velocity was found to agree with findings from numerical modeling. In an attempt to provide benchmark data of boulder motion on a sloping beach, Nandasena et al. (2011) and Nandasena and Tanaka (2013) used a hinged gate with varying impoundment depth to generate surge-like flow conditions which the authors validated against known Froude and Reynolds numbers observed during tsunami and storm events. Although it was concluded that good agreement was obtained for those non-dimensional numbers, comparisons with classic analytical formula governing the ideal dam-break were omitted.

The hydrodynamics of the generated wave may, however, differ from those of an 'ideal' dam-break as the gate motion may interact with the collapsing water column in cases where the opening dynamics are too slow. To date, no specific investigation about dam-break waves generated by swing gates in terms of gate dynamics and hydrodynamics exists and guidance on the minimum opening velocities is missing. The objectives of the present study are a direct outcome of the above presented literature review and include the following:

I. Provide an analytical framework for the motion of swing gates when mechanically-driven.
II. Present experimental work and the analysis thereof with respect to opening velocities and resulting hydrodynamic parameter water surface elevation.
III. Provide a discussion on swing gate's usefulness and future research demand in that respect.

The paper is organized as follows: the section on "Analytical Framework" briefly outlines mathematical context in which the swing gate's motion can be described and how to obtain parameters such as instantaneous swing gate velocity and opening duration; the section on "Experimental Setup" details the dam-break flume at the University of Ottawa and the instrumentation used in the experiments; results are presented in the "Results" section; and finally, the "Discussion" and "Conclusions" sections place the current research in context of previous work and detail the potential next steps in examining swing gate motion further.

2 ANALYTICAL FRAMEWORK

The swing gate under investigation mechanically depicts a two-dimensional (2D) rigid body pivoting about one axis (Meriam and Kraige, 2012). For the present system, let θ be the angular position coordinate, $\omega = \dot{\theta}$ be the angular velocity, and $\alpha = \ddot{\theta}$ be the angular acceleration, where angular velocity and acceleration are first and second time derivatives of the angular position coordinate, respectively. For varying angular acceleration, as is the case for the swing gate, angular position coordinates are obtained by integrating the angular acceleration over time as shown in Eq. [1]:

$$\theta(t) = \iint_{t_0}^{t_{end}} \alpha \mathrm{d}t \qquad [1]$$

Reducing the general three-dimensional momentum equation about a fixed point O in space to the 2D-case yields the following momentum/torque balance:

$$\sum M = 0 = I_O\alpha + H_i \qquad [2]$$

where M depicts the momentum balance, $I_0 = I_{CM} + I_{CM-O}$ is the moment of inertia with respect to point O, I_{CM} is the moment of inertia of the pivoting object about the center of mass, I_{CM-O} depicts the additional moment of inertia as the object pivots about an axis different from the center of mass based on the *parallel axis theorem*, H_i collects all externally driving torques such as hydrodynamic forces and gravity forces, respectively. Figure 1 provides a systematic sketch of the present system as well as a photograph of the swing gate used at the University of Ottawa. Eq. [2] describes the driving external torques, given over time, and the total moment of inertia for the swing gate, and yields the angular acceleration. It is straightforward to note the moments of inertia as components of the entire swing gate; likewise, based on known gate geometry, acting forces and cantilevers are determined. Angular acceleration can be numerically integrated based on known boundary conditions, e.g. counter weight, swing gate mass, and impoundment depth. This approach allows predicting the overall opening time at predefined swing gate angular position coordinate where complete detachment between gate surface water interface is assumed.

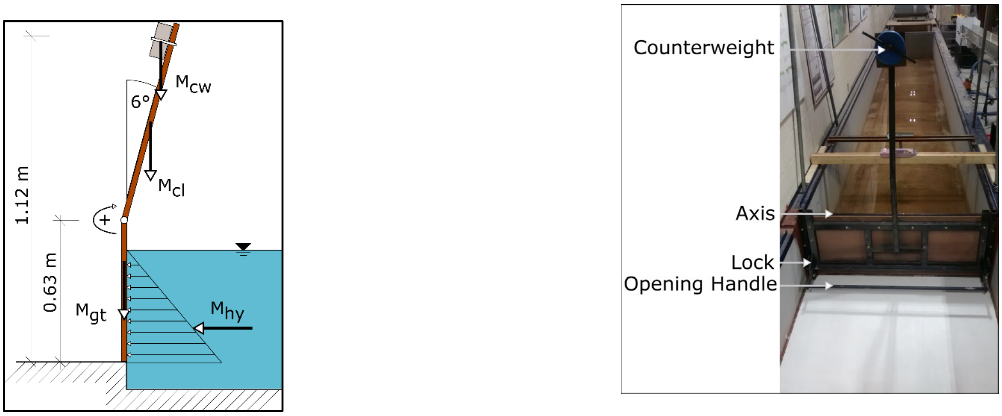

Figure 1. (a) Schematic sketch of the swing gate system with counter weight, axis and dimensions. Masses and forces are depicted by arrows and denoted are the mass of the gate (gt), of the cantilever (cl), the counterweight (cw), as well as the hydrostatic force (hy). (b) Photograph of the swing gate indicating the system elements and the release mechanism.

3 EXPERIMENTAL SETUP

3.1 University of Ottawa Dam-break Facility

The experiments reported herein were performed in the Hydraulics Laboratory of the Department of Civil Engineering University of Ottawa, Canada. The experiments were performed in a dam-break flume (DBF), 30 m long, 1.5 m wide, and 0.70 m deep (Figure 2). The reservoir to impound water was 21.55 m long kept behind a swinging gate, which was placed on a 0.20 m false floor. The false floor was covered with fixed layer of 0.001 m sand grains, which resulted in an experimentally-determined Darcy-Weisbach friction factor (f) of 0.014. The swing gate was manually opened to generate the dam-break wave; various counter weights were placed on the top of the gate to aid in the opening of the gate. The waves generated for a number of impoundment depths are compared to the analytical solution for dam-break waves in Section 0. The spatial origin of the experiment (0, 0) was considered to be the center of the flume at the upstream edge of gate. The y-axis was chosen positive in the flow direction, using a right-hand coordinate system, the positive x-direction was to the right and the positive z-direction pointed upwards.

3.2 Instrumentation

Figure 2 depicts the various instrumentation used in the DBF close to the swing gate installed in the flume. The sampling rate of all the instrumentation is presented in Table 1. One wave gauge (WG2) was placed inside the reservoir (RBR WG-50, capacitance-type) and located 0.01 m upstream of the swinging gate. WG2 was used as the reference gauge to determine the reference time for each experiment. The zero time of each experiment was considered to be at the time the water level began to drop at WG2. Two other wave gauges (WG1 and WG3) were placed at various positions on the false floor to measure the time-history of the water level as the dam-break wave propagated through the flume. Before the wave gauges were placed in the flume, they were calibrated ensuring R^2 values greater than 0.99.

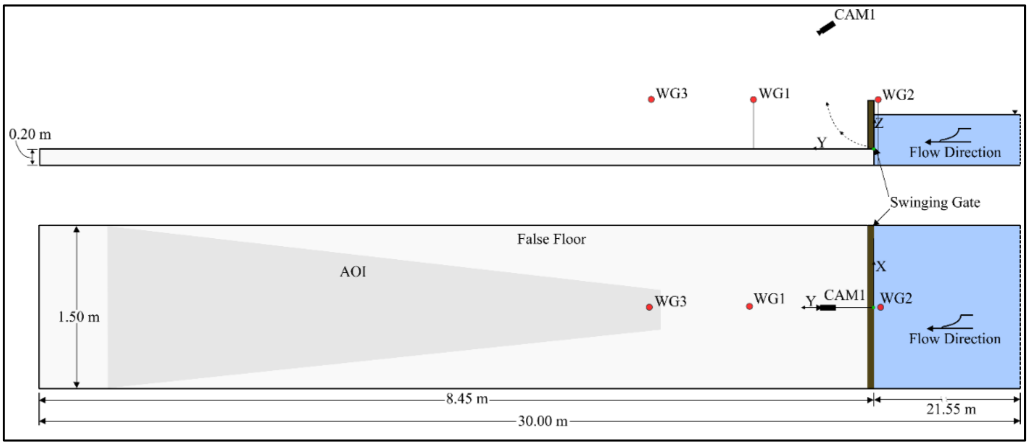

Figure 2. University of Ottawa Dam-break Flume (DBF). 30 m long x 1.5 m wide with a swinging gate. 0.70 m deep at the reservoir when an impoundment depth of 0.5 m was aimed at, 0.20 m false floor.

Table 1. Instrumentation used in the DBF.

Instrument	Model	Sampling Rate	Units
Wave Gauge	RBR WG-50 Capacitance	1200 Hz	WG1
(WG)	Akamina AWP-24	1200 Hz	WG2, WG3
Camera (CAM)	Basler AG pil900-32gc	25 Hz	CAM1
HIGH-CAM	GoPro Hero4 (1280 x 720)	60 fps	CAM2

A high-definition camera (CAM1) was mounted in the flume. CAM1 was mounted center-flume at a height of 2.95 m. The area of interest (AOI) of CAM1 extended the width of the flume from y = 3.00 m to y = 8.45 m. In addition, a GoPro Hero4 (CAM2) was directed towards an angular scale with its center matching with the swing gate axis' center. A needle was attached to the swing gate axis allowing to either semi-automatically or manually read off the time-history of the swing gate opening. A semi-automated algorithm was developed in MATLAB to extract time-histories of gate positions (in degree). The workflow for this algorithm comprises extraction of single frames of the video recorded by CAM2, image correction (distortion, rectification, cropping, warping, shown in Figure 3), image processing (background subtraction, thresholding, edge detection), and manual selection of center of swing axis as well as the end of the needle indicator. Trigonometric functions allowed to determine the time-history of the opening angle of the gate based on the coordinates obtained by the semi-automatic algorithm. Subsequent smoothing of the vectors with a moving-average technique and differentiation yielded the opening velocities. As a cross-check, selected experiments were also analysed using a manual technique where the average velocity of the gate was determined by utilizing the absolute time difference for the gate to pivot by 30° and little difference was found between the two approaches.

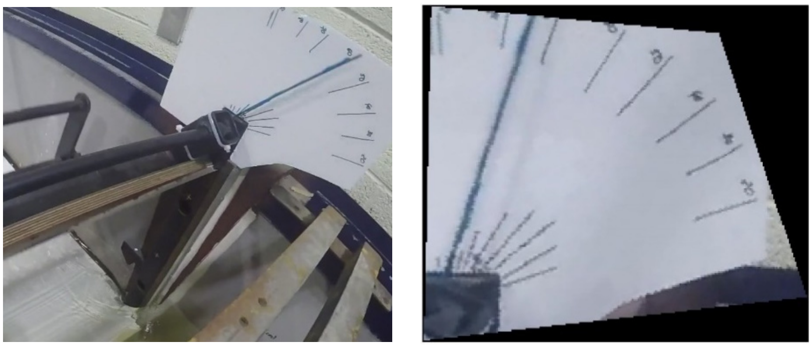

Figure 3. (a) Sample still image depicting the swing gate fully open, the needle attached and the angular scale, (b) Rectified image resulting from image processing techniques allowing to determine instantaneous angular positions of the gate during the opening process.

3.3 Experimental Protocol

The experiments presented in this paper are part of a larger experimental program as a result of a collaboration between the University of Ottawa (Canada), the University of Hannover (Germany), and Waseda University (Japan). The experiments used in this paper are shown in Table 2. For experiments of the category C01, five repetitions were accomplished in order to obtain information on the repeatability of the experiments. Each other experiment in the categories C02-C04 was then repeated only once as the primary aim was to investigate the gate dynamics. Between each experiment, excess water on the false floor was removed to the point that there was no pools of water. Due to time constraints, the false floor still had a thin layer of water on the surface before the beginning of each experiments. As shown in Figure 7, the water had little effect on the repeatability of the hydraulic boundary condition. However, the presence of the layer of water may be partially responsible for the steeper surge front that was observed during the wave propagation (St-Germain et al., 2013).

Table 2. Experimental Protocol for tests performed at the DBF in the University of Ottawa.

Category	Impoundment Depth [m]	Counter weight [kg]	Experimental Number [#]
C01	0.4	15 kg	1-5
C02	0.2	varying	23-26
C03	0.4	varying	19-22
C04	varying	15 kg	19,23,27-29,31

4 RESULTS

4.1 Time-histories of gate angles and opening velocity

Figure 4 and Figure 5 present time-histories of opening angles and tangential velocities of the swing gate as obtained by the methodology described in Section 0 for the categories C02 and C03. Opening angles were determined by a semi-automatic method. Time derivatives were computed from the opening angle time-history (the angular velocity v_a, Eq. [1]) and by converting the angular velocities yielded into linear velocities v_{lin} at the lower gate edge (Eq. [2]).

$$v_a = \Delta\alpha_i / \Delta t_i \quad [1]$$

$$v_{lin} = r \cdot v_a \quad [2]$$

Where $\Delta\alpha_i$ is the incremental angular velocity, Δt_i the incremental time step determined by the inverse of the frame rate of the camera CAM2. Opening angle time-histories are presented for two different impoundment depth, and firstly, counter weights are varied between 0.0 kg to 15 kg. The resulting opening angle time-history is a non-linear function over time, which agrees with the analytical model shown in section **Error! Reference source not found.**. While the gravity force exerted by the weight is constantly contributing to a force balance, its contribution is governed by the sine function which is determined by the cantilever between the weight and the gate axis.

Generally, it is found that the opening angles depend on the counter weight. The greater weight reduced the overall opening time, which the authors defined to be an angle of 30°, while 0° was the angle when the gate is closed. Overall opening times varied between 0.31 s and 0.43 s for the largest and smallest weight, respectively, for an impoundment depths of 0.2 m. Shorter overall opening times are found for the C03 category where those times are increased from 0.24 s to 0.33 s, for the largest and the smallest weight, respectively. Smaller overall opening times are a result of the additional force from the higher hydrostatic pressure at the instantaneous opening of the gate. As a result of the fluctuating measurements of the opening angle time-history, some fluctuation is introduced into the tangential velocities found at the lower edge of the gate for the investigated cases. Tangential velocities of up to 1.6 m/s and 1.8 m/s are measured for the two different impoundment depth and with the highest counter weights used. As outlined by Lauber and Hager (1998), the front velocity close to the bottom of the collapsing impoundment front face was close to the wave celerity of the impoundment; thus, it is $c = \sqrt{g \cdot h_0}$, leading to values of $c = 1.98\,m/s$ and $c = 1.40\,m/s$ for the impoundment depth h_0 of 0.4 m and 0.2 m, respectively. In the case of a swing gate, this observation and the theoretical consideration of ideal dam breaks suggest that the opening velocities obtained for the reported experiments may have been too slow to prevent interaction between the lower gate edge and the advancing wave front entirely. Further research deems necessary to rule out such interaction and to provide mature guidance as towards minimum opening velocities.

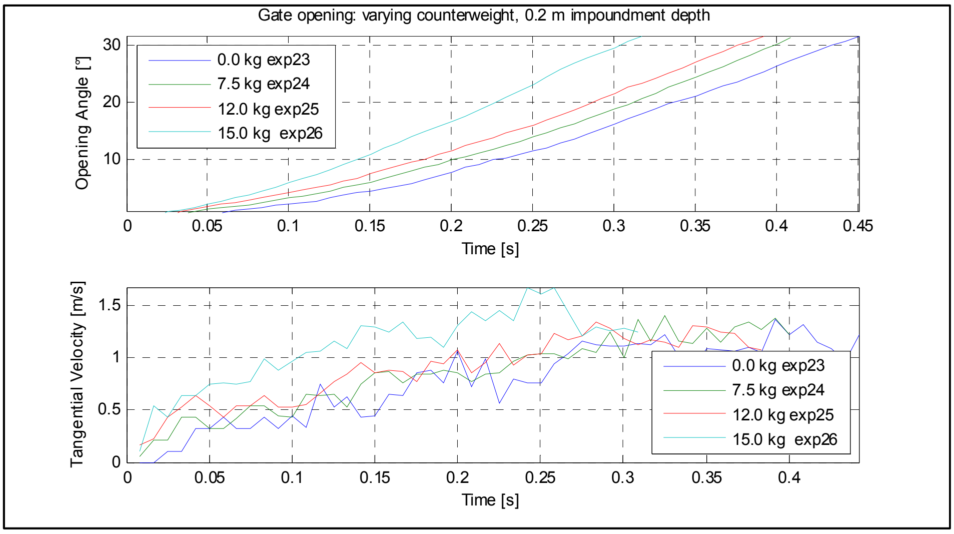

Figure 4. Time-history of (a) opening angles and (b) tangential velocities for a variation of counter weights at a fixed impoundment depth of 0.2 m. Times are referenced to the opening instance at which the gate opening is initialized.

Similarly, Figure 6 presents the dependency between the opening angle and tangential velocity time-histories and the time for case C04 where the counter weight was fixed at 15 kg while the impoundment depth was varied. Similar to the previous cases, a non-linear behavior is found for the opening angle time-history; yet, here the difference is simply a result of the time-dependent cantilever of the weight to the gate axis. Forces exerted on the swing gate by the integral of the hydrostatic water pressure act on the gate only for a very short instance at and closely after the gate mechanism is released. The hydrostatic forces, therefore, acts as an instantaneous impulse force at the time of gate release; for simplification, one can neglect any later energy transfer that may transfer energy while the gate started its motion. It is remarkable that time-histories of the opening angles for impoundment depth of 0.1 m and 0.2 m deviate quite significantly from the remaining three impoundment depth. A potential reason might be the small resulting hydrostatic force originating from the impoundment; secondly, dam-breaks in these experiments might have been slow enough to allow the gate-water interface to separate quickly enough to exclude any mutual influences.

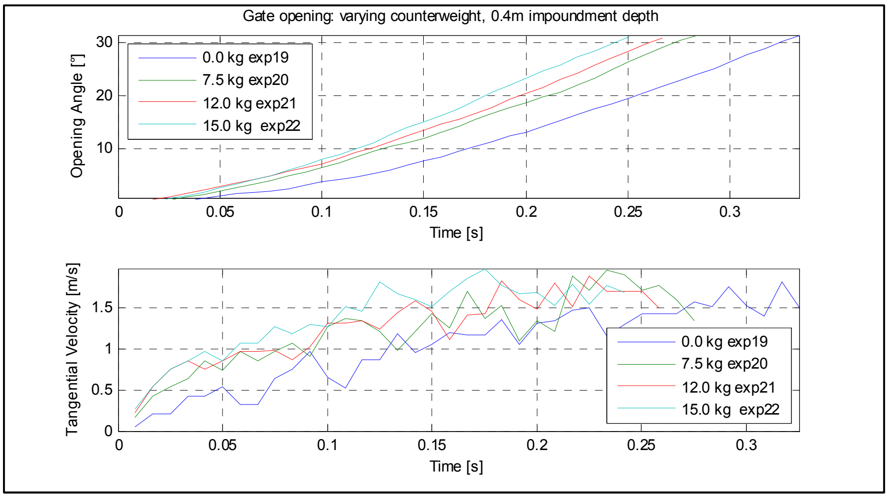

Figure 5. Time-history of (a) opening angles and (b) tangential velocities for a variation of counter weights at a fixed impoundment depth of 0.4 m. Times are referenced to the opening instance at which the gate opening is initialized.

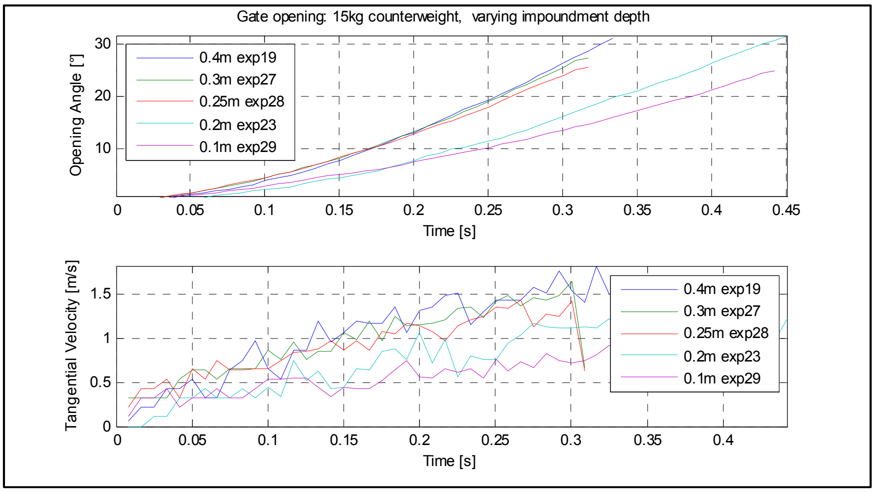

Figure 6. Time-history of (a) opening angles and (b) tangential velocities for a variation of impoundment depth and for a fixed counter weight of 15.0 kg. Times are referenced to the opening instance at which the gate opening is initialized.

4.2 Repeatability of the Opening Process

Figure 7 shows the comparison of the water depths in the flume to the Ritter solution for the three wave gauges: WG2 (a), WG3 (b), and WG1 (c). As it can be observed in Figure 7, the experimental results closely resemble the analytical solution. In the case of the experimental results, the wave arrived later than predicted by the analytical solution. The discrepancy is a result of the Ritter solution being calculated for a frictionless surface whereas the current experimental surface was rough due to the sand coating. The incoming wave front also has a steeper initial front, which was again a result of the bed roughness in the current experiments (Chanson, 2006). Additionally, as discussed in Section 0, the presence of a thin layer of water would have slowed and steepened the incoming wave front (St-Germain et al., 2013). Most importantly, Figure 7 shows that the wave profile was highly repeatable between the experiments. In addition to comparing experimental results at the dam-break position to the analytical model of Ritter (1892), results reported by Feizi Khankandi et al. (2012) were added for a long reservoir (green circles) and for a trapezoidal reservoir (red circles), respectively. Agreement between the experimental data from Feizi Khankandi et al. (2012) and the analytical solution show that the experimental data does not match the theory as closely as it could. It is noteworthy that the obtained experimental spatial surface elevation at the gate location and upstream does not entirely agree with previous research and analytical formula. Based on Ritter (1892), the water depth is fixed at $h = 4/9h_0$. While the downstream agreement is very good, a reason for the partial mismatch could be found in the fact that the gate is located to the end of the false floor. Hydraulically, the dam-break flow propagating upstream through the reservoir quickly extends towards the 20 cm deeper bottom, driven by the shear zone on the hypothetical bottom extending the false floor into the reservoir. Analogies from free-surface flow over a forward-facing step or over a bottom sill might apply in this case rather than the comparison with the classical Ritter solution. In addition, Martin (1990) reported that differences between experimental research and the Ritter solution exist, and further argues that reasons lie within the curvature of streamlines close to the dam-break position. Even larger curvature of streamlines, along with extensive losses at the edge of the false floor occur in the current configuration, which may eventually result in the deviation from the theoretical results. As further measurement inside the reservoir to elucidate reasons for the deviations were limited due to time constraints, further research is required to provide analytical solutions that fully apply to the specific flume geometry.

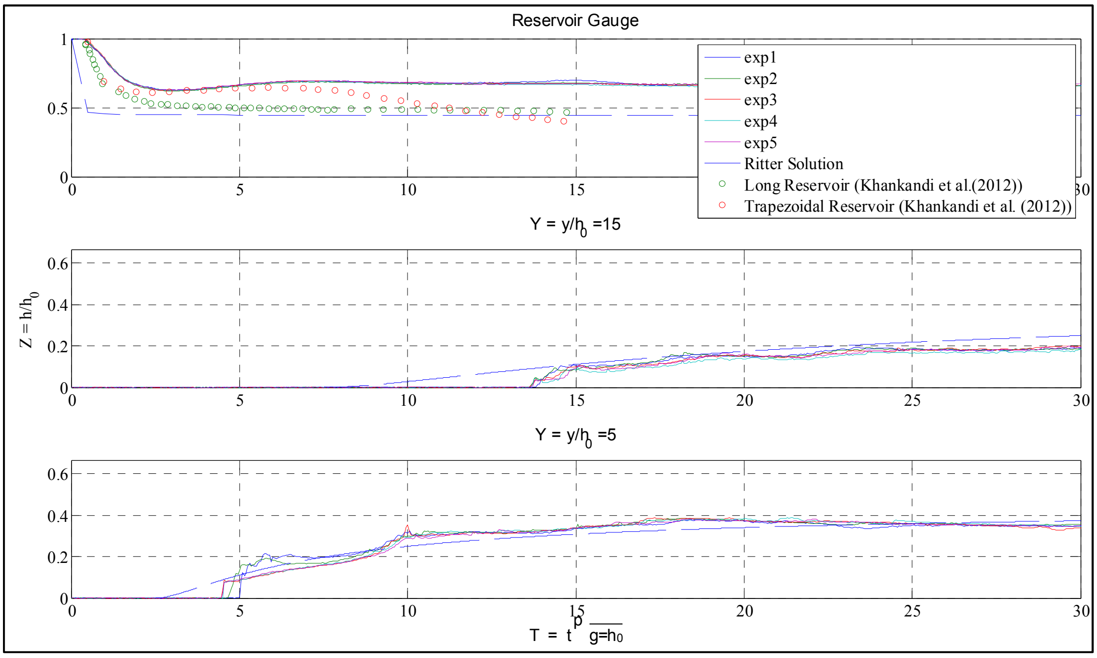

Figure 7. Dimensionless time-history of water levels from an initial impoundment depth of 0.40 m comparing the experimental results (solid line) to the Ritter (1892) solution (dashed line). (a) Reservoir Gauge (WG2); (b) Y = 5 (WG1); and (c) Y = 15 (WG3).

4.3 Influence of Counter Weight and Impoundment Depth

Based on the analytical framework presented in Section **Error! Reference source not found.**, the torque balance contributing to the instantaneous opening velocity is influenced by both, the counter weight and the impoundment depth. Figure 8 presents free-surface time-histories in dimensionless form for two locations downstream of the dam-break gate, comparing to the Ritter solution. The figures depict cases in category C03 where firstly a variation of the counter weights was tested. For the downstream location $Y = 3$, it becomes apparent that agreement between the theoretical and the experimental results are good; with decreasing counter weight, the agreement becomes less favorable. As a larger counter weight generally results in shorter opening time, it is conjectured that counter weights smaller than 15 kg led to opening times too long to allow for a proper detachment of the gate surface from the impounded water volume. While this conclusion holds for closer proximity to the dam-break gate, it can be observed that no differences between the tests are noticeable for a downstream location of $Y = 10$. Also, the comparison with the theoretical Ritter solution reveals an excellent agreement further down the flume.

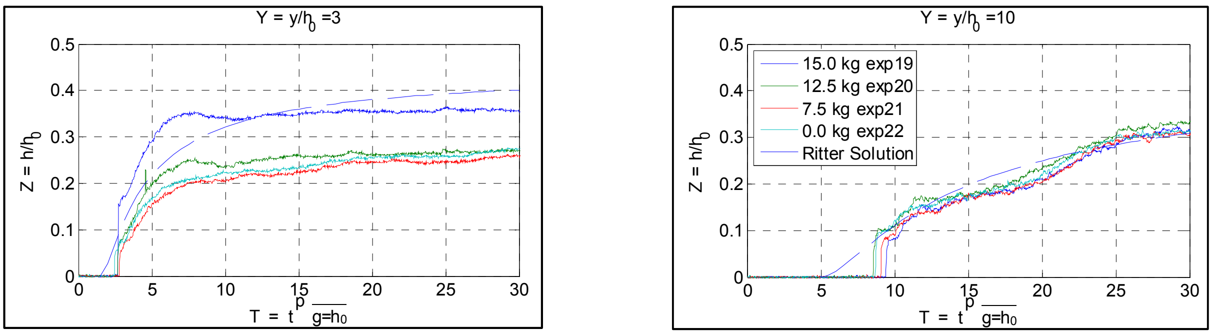

Figure 8. Dimensionless time-history of water levels for an impoundment depth of 0.4 m at two different distances from the gate and for four different counter weights attached to it. Experimental results are indicated by a solid line and the Ritter (1892) solution is a dashed line. (a) Downstream distance to gate Y=y/h0=3, and (b) Y=y/h0=10

While the deviation at the wave front is due to the roughness of the flume's false floor surface, time-histories of surface elevation follow closely the theoretically predicted values. As the wave front and its tip region is highly friction-dominated and governed by high turbulence, it can be assumed that the higher temporal surface gradients at the location closer to the gate resulted in excess turbulence, thus dissipation for this case was higher. The larger energy dissipation is therefore also believed to be the reason for the "self-correction" effect observed between $Y = 3$ and $Y = 10$.

Figure 9 provides information about the influence of varying impoundment depth, while also considering the contribution to the torque balance ascribed in Section **Error! Reference source not found.**, has on the temporal evolution of the free surface time-history downstream of the gate. Results of category C04 experiments were analyzed and it becomes evident that hydrostatic forces exerted by the impoundments when released by the gate have a smaller influence on the overall gate dynamics. Close to the gate, at location $Y = 3.43$, all of the time-histories are below the predicted theoretical water level. Deviations between theoretical and experimental values increase with decreasing impoundment depth, as would have been predicted based on the analytical framework. With decreasing impoundment depth, less torque was contributed to the opening dynamics, allowing less-than-ideal interaction between the collapsing impoundment front surface and the opening gate. While closer proximity water levels fall short of the predicted values, opposite was observed for the gauge position $Y = 10.0$ where larger values than predicted are found. Firstly, this is a surprising observation, and its explanation is difficult as the wage gauge WG2 directly at the gate recorded corrupted data in some of the experimental runs. It is thus speculated that a combination of viscosity effects (Lauber and Hager, 1998) and excess surface gradients accelerating the wave front in between to two locations are responsible for this behavior.

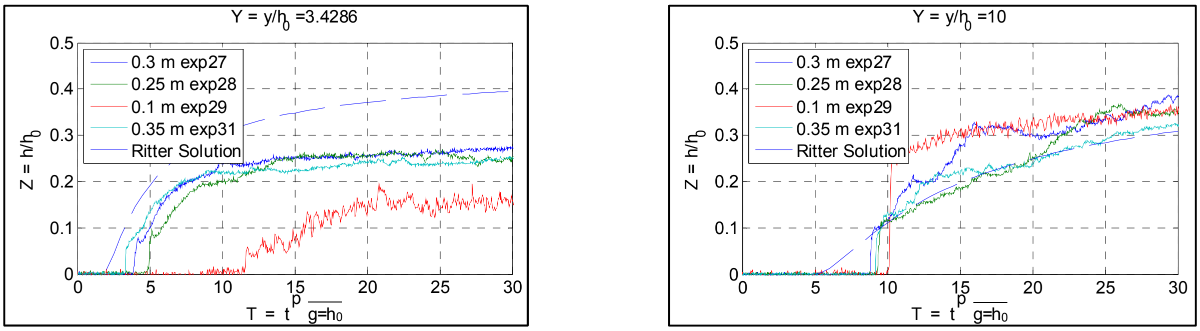

Figure 9. Dimensionless time-history of water levels for an impoundment depth of 0.4 m at two different distances from the gate and for four different impoundment depth stored behind. Experimental results are indicated by a solid line and the Ritter (1892) solution is a dashed line. (a) Downstream distance to gate Y=y/h0=3.43, and (b) Y=y/h0=10

DISCUSSION AND CONCLUSIONS

This paper presents the results of a study examining the dynamics of a swing gate releasing an impounded volume of water. This opening mechanism has not been studied before with respect to resulting opening velocities and how these will influence downstream dam-break characteristics. Although this study has revealed remarkable repeatability related to downstream surface elevation time-history, remaining inaccuracies probably originate from the release mechanism that posed challenges to the gate operator; particularly in cases where smaller impoundment depth or low counter weights were tested. Future studies may be required to look into release mechanisms that depend less on the operator's ability to release the impounded volume of water than was the case in this study. In addition, it is noted that the main difference between the dam-break solution of Ritter and the geometric constraints applying to this work was related to the forward-facing step over which the dam-break flow propagates. It cannot be ruled out that losses generated by flow separation and vortex evolution on the edge of the false floor contribute to the deviations found in this study.

Based on the recorded data and their analysis, the authors have drawn the following conclusions:

1) Swing gate dynamics is governed by a mechanistic momentum balance that allows for the prediction of opening time by numerical integration of angular acceleration.
2) Experimentally determined opening times are dependent on the two factors, impoundment depth and counter weight; opening times between 0.24 s and 0.43 s were found.
3) Longer opening times have an influence on downstream free surface time-history that particularly showed close to the swing gate. Further downstream, surface elevation time-history returned towards the theoretically described profile, revealing the flow's ability to adopt through turbulent dissipation and viscous effects.

ACKNOWLEDGEMENTS

The authors acknowledge the support of several funding organizations which supported this research program: the European Union, Research Executive Agency through a Marie Curie International Outgoing Fellowship within the 7th European Community Framework Programme, the Discovery Grant awarded by the Natural Science and Engineering Research Council (NSERC).

REFERENCES

Alcrudo, F.& Mulet, J. (2007). Description of the Tous Dam Break Case Study (Spain). *Journal of Hydraulic Research,* 45(sup1), 45–57.

Cao, Z., Pender, G., Wallis, S. & Carling, P. (2004). Computational Dam-break Hydraulics over Erodible Sediment Bed. *Journal of hydraulic engineering,* 130(7), 689–703.

Chanson, H. (2006). Tsunami Surges on Dry Coastal Plains: Application of Dam Break Wave Equations. *Coastal Engineering Journal,* 48(4), 355–370.

Chanson, H. (2009). Application of the Method of Characteristics to the Dam Break Wave Problem. *Journal of Hydraulic Research,* 47(1), 41–49.

Dressler, R.F. (1954). Comparison Of Theories And Experiments For The Hydraulic Dam-break Wave. *International Assocociation Science Hydrology* 3(38), 319–328.

Feizi Khankandi, A., Tahershamsi, A. & Soares-Frazao, S. (2012). Experimental Investigation Of Reservoir Geometry Effect On Dam-break Flow. *Journal of Hydraulic Research,* 50(4), 376–387.

Fennema, R.J. & H.-Chaudhry, M. (1987). Simulation Of One-dimensional Dam-break Flows. *Journal of Hydraulic Research*, 25(1), 41–51.

Lara, J.L., Jesus, Del, M. & Losada, I.J. (2012). Three-dimensional Interaction of Waves and Porous Coastal Structures. Part II: Experimental Validation. *Coastal Engineering* 64, 26–46.

Lauber, G. (1997). *Dambreak Wave Experiment in a Smooth Rectangular Channel [Experimente zur Talsperrenbruchwelle im glatten geneigten Rechteckkanal*]. *Mitteilungen* - Versuchsanstalt fur Wasserbau, Hydrologie und Glaziologie, ETH Zurich 152.

Lauber, G. & Hager, W.H. (1998). Experiments to Dambreak Wave: Horizontal Channel. *Journal of Hydraulic Research,* 36(3), 291–306.

Martin, H. (1990). *Plötzlich veränderliche instationäre Strömungen in offenen Gerinnen (Abruptly varied unsteady flows in open channels)*, Technische Hydromechanik 2. VEB Verlag für Bauwesen.

Meriam, J.L. & Kraige, L.G. (2012). *Engineering Mechanics - Dynamics, 7th ed*. John Wiley & Sohn, Inc.

Nandasena, N.A.K., Paris, R. & Tanaka, N. (2011). Reassessment Of Hydrodynamic Equations: Minimum Flow Velocity to Initiate Boulder Transport by High Energy Events (storms, Tsunamis). *Marine Geology,* 281(1), 70–84.

Nandasena, N.A.K. & Tanaka, N. (2013). Boulder Transport by High Energy: Numerical Model-fitting Experimental Observations. *Ocean Engineering,* 57, 163–179.

Nistor, I., Nouri, Y., Palermo, D. & Cornett, A. (2009). Experimental Investigation of the Impact of a Tsunami-induced Bore on Structures. *Proceedings of Coastal Engineering Conference*. 3324–3336.

Nouri, Y., Nistor, I., Palermo, D. & Cornett, A. (2010). Experimental Investigation of Tsunami Impact on Free Standing Structures. *Coastal Engineering Journal,* 52(1), 43–70.

Oertel, M. & Bung, D.B. (2012). Initial Stage of Two-dimensional Dam-break Waves: Laboratory Versus Vof. *Journal of Hydraulic Research,* 50(1), 89–97.

Pilotti, M., Maranzoni, A., Tomirotti, M. & Valerio, G. (2011). 1923 Gleno Dam Break: Case Study and Numerical Modeling. *Journal of Hydraulic Engineering,* 137(4), 480–492.

Ritter, A. (1892). Die Fortpflanzung der Wasserwellen. *Zeitschrift des Vereins deutscher Ingenieure,* 36(33), 947–954.

Soares-Frazao, S. & Zech, Y., 2007. Experimental Study of Dam-break Flow Against an Isolated Obstacle. *Journal of Hydraulic Research,* 45(sup1), 27–36.

Soares-Frazao, S. & Zech, Y. (2008). Dam-break Flow through an Idealised City. *Journal of Hydraulic Research,* 46(5), 648–658.

Spinewine, B. & Zech, Y. (2007). Small-scale Laboratory Dam-break Waves on Movable Beds. *Journal of Hydraulic Research,* 45(sup1), 73–86.

St-Germain, P., Nistor, I., Townsend, R. & Shibayama, T. (2013). Smoothed-Particle Hydrodynamics Numerical Modeling of Structures Impacted by Tsunami Bores. *Journal of Waterway, Port, Coastal, and Ocean Engineering,* 140(1), 66-81.

Whitham, G.B. (1955). The Effects of Hydraulic Resistance in the Dam-break Problem. *Proceedings of the Royal Society of London A: Mathematical, Physical and Engineering Sciences,* 227(1170), 399–407.

Wurbs, R.A. (1987). Dam-Breach Flood Wave Models. *Journal of Hydraulic Engineering,* 113, 29–46.

EXPERIMENTAL INVESTIGATION OF THE PERFORMANCE OF TILT CURRENT METERS IN WAVE-DOMINATED FLOWS

ASGER BENDIX HANSEN(1) & STEFAN CARSTENSEN(2)

(1,2) Fluid Mechanics, Coastal and Maritime Engineering, Department of Mechanical Engineering, Technical University of Denmark,
asbha@mek.dtu.dk ; scar@mek.dtu.dk

ABSTRACT

In recent years, tilt current meters (TCMs) have received renewed attention as they provide an inexpensive method for measuring currents in the coastal zone. However, previous studies focused mainly on current dominated flows or the current component of the flow. This study investigates the performance of tilt current meters in wave-dominated flows and capturing the wave orbital velocities. A series of laboratory experiments were performed in which tilt current meters were used to measure flow velocities in pure current, pure wave and combined wave-current flows. Both spherical and cylindrical TCMs were investigated in order to assess the effect of TCM shape on its performance. The measured TCM tilt is compared with the flow velocity measured by conventional methods. Furthermore, the ability of a TCM to measure wave orbital and wave-averaged velocities is discussed.

Keywords: Tilt current meter; observational techniques; surf zone; coastal hydrodynamics.

1 INTRODUCTION

The tilt current meter (TCM) is an old measurement technique, which uses the tilt of a tethered object as an indicator for measuring current speed in water. Although the technique had been replaced by more advanced and accurate methods such as acoustic Doppler velocimetry, it is now again receiving attention as it provides an inexpensive alternative to the costly acoustic techniques. Due to the availability of low cost accelerometers, magnetometers and microcontrollers, it is now possible to construct a TCM for a cost well below 100 USD. Since TCMs are also easy to deploy, they allow researchers to obtain velocity measurements with a larger spatial resolution than what would have been possible using acoustic instruments.

With this as the motivation, several studies have recently studied the performance of TCMs in different coastal flows (Figurski et. al., 2011; Lowell et. al., 2015; Marchant et. al., 2014; Radermacher et. al., 2015). The flows considered have mainly been tidal flows with current speeds smaller than 1 m/s. One exception is Figurski et al. (2011) who used a TCM to estimate wave conditions by looking at the standard deviation of the TCM tilt. Results from previous studies show that TCMs can deliver quite good accuracies (0.05m/s, Marchant et. al (2014) or 2% Lowell et. al. (2015)). These results encourage further development of the use of TCMs so that they might be applied to measure under a wider range of flow conditions.

We are interested in extending the use of TCMs so that they may also be used to measure velocities in and around the surf zone. The surf zone presents a very challenging environment with very large flow velocities, unsteady flow due to wave orbital motion and significant turbulence. In order to be able to measure such flows, it is necessary to develop a TCM with a measurement range much larger than the previous ones and which performs well even in unsteady flow.

This paper presents an experimental study of the behavior of spherical and cylindrical TCMs. The objective of this study is two-fold. First, we examine how varying the proportions of a cylindrical TCM affects the relationship between tilt angle and flow velocity in order to optimize the measurement range. Secondly, we examine how well a given TCM performs in unsteady flows with either pure wave motion or combined waves and currents.

2 MEASUREMENT PRINCIPLE

A TCM estimates the flow speed (U) from the measured tilt angle (θ). This requires the relationship between tilt angle and flow speed (here referred to as the response curve) is known. A theoretical response curve can be determined by considering the force balance in the angular direction (see Figure 1) between the in-line force (F_x) and the net buoyancy force (F_B) acting on the TCM.

$$tan\,\theta = \frac{F_x}{F_B} \qquad [1]$$

The net buoyancy force can be expressed as

$$F_B = g(\rho V - m) \quad [2]$$

where ρ denotes the density of the water, g the acceleration of gravity, V the volume and m the mass of the floatation body.

In steady current, the in-line force is solely due to drag. The drag force on a spherical TCM exposed to steady current is from a geometrical perspective insensitive to the tilt angle and can be expressed as

$$F_x = F_D = \frac{1}{2}\rho C_D A U^2 \quad [3]$$

Here, C_D is the drag coefficient and A is the frontal projection area of the floatation body.

Inserting the expressions for the forces ([2] and [3]) into equation [1] and solving for U gives

$$U = k\sqrt{tan\,\theta} \quad [4]$$

where k is a function of the TCM properties (essentially mass and diameter) as well as the drag coefficient

$$k = \sqrt{\frac{2g(\rho V - m)}{\rho\, C_D\, A}} \quad [5]$$

Hence, the shape of the response curve is the same for all spherical TCMs but the steepness will increase with increasing k. Although the theoretical response curve goes to infinity when the tilt angle approaches 90°, in practice a TCM will only give useful results up to a certain angle that then defines the measurement range of the TCM. Equations [4] and [5] thus show that the larger and lighter a TCM, the larger the measurement range.

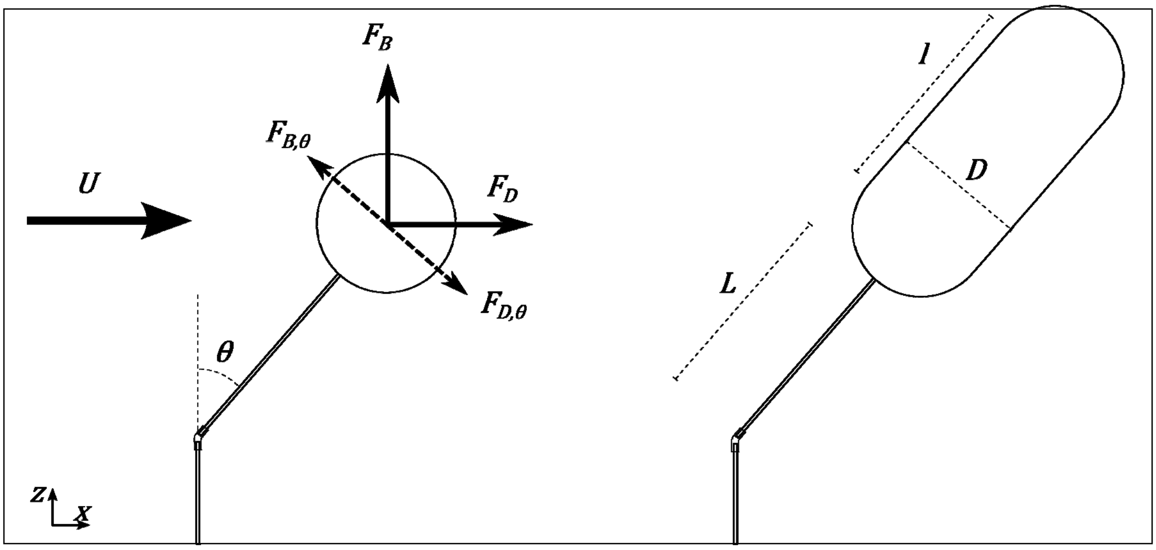

Figure 1. Definition sketch. Left: Spherical TCM with indication of current speed, tilt angle and forces on the floatation body. Subscript θ indicates projection onto the angular direction. Right: Cylindrical TCM with indication of tether length, cylinder length and diameter.

The drag coefficient will generally vary considerably with Reynolds number ($Re = DU/\nu$), but in the range $1{\cdot}10^3 < Re < 2{\cdot}10^5$, the drag coefficient for a smooth sphere assumes an approximately constant value between 0.4 and 0.5 (Schlichting and Gersten 2017). A gradual variation in the drag coefficient affect the tilt response but this can be accounted for and hence does not pose a problem for the flow measurement. However, an abrupt change in the drag coefficient as experienced for a stationary sphere at the drag crisis would result in a vertical step in the response curve. This discontinuity will cause a range of velocities to give the same tilt angle and hence be undistinguishable by the TCM. When designing a TCM, it is therefore important to ensure that the drag crisis occurs outside of the desired measurement range.

In an unsteady flow the relationship between flow speed and tilt angle becomes considerably more complicated since inertia forces can potentially be of importance, the TCM itself is moving and the natural frequency of the TCM may coincide with frequencies in the flow causing resonance. The combined drag and inertia forces are described by the Morison equation (Sumer and Fredsøe, 2006) and depend on both the flow velocity and acceleration relative to the TCM. The relative importance of the drag force and inertia forces can be described by the Keulegan-Carpenter number

$$KC = \frac{U_m T}{D} \qquad [6]$$

where U_m is the maximum wave orbital velocity, T is the wave period and D is the diameter of the body. The drag force becomes increasingly important and the inertia forces less so as KC is increased. For example, a fixed cylinder may be considered drag-dominated for KC numbers larger than 20-30 (Sumer and Fredsøe, 2006). This suggests that inertia may be neglected as long as the TCM is sufficiently small.

The natural frequency of the TCM may be calculated by considering the TCM as an oscillator damped by viscous friction and inertia forces (Sumer and Fredsøe, 2006). Hence, the natural frequency is given as

$$f_n = \frac{1}{2\pi}\sqrt{\frac{g(\rho V - m)}{L(m + m')}} \qquad [7]$$

where L is the tether length, $m' = C_m \rho V$ is the hydrodynamic mass of the TCM and C_m (= ½ for a sphere, hence ½ ≤ C_m < 1 for $l \geq 0$ in an ideal fluid) is the hydrodynamic mass coefficient. If the TCM is exposed to wave motion with frequencies close to its resonant frequency it may resonate which could result in a frequency dependent response. To avoid this, the TCM should be chosen to have a resonant frequency that is significantly larger than the frequencies of the waves.

When choosing a TCM for measuring currents and wave orbital motion in the surf zone, one is faced with a number of challenges: (1) The measurement range should be relatively high, reaching several meters per second; (2) The KC numbers should be large; (3) The drag coefficient should not experience abrupt change and (4) The natural frequency should be considerably higher than the wave frequency.

One way of increasing the achievable measurement range of a TCM is to make it cylindrical. In this case, the angle of attack of the flow on the floatation body changes with the tilt angle. An analytical expression for the tilt response of a cylindrical can be obtained by applying the cross flow principle (Sumer and Fredsøe, 2006) according to which the drag force in the angular direction should be calculated by only considering the component of the flow which is orthogonal to the cylinder. This gives the expression

$$F_{D,\theta} = \frac{1}{2}\rho C_D (\cos\theta\, U)^2 A \qquad [8]$$

For the cylindrical TCM, the theoretical expression for the response curve then becomes

$$U = k\sqrt{\frac{\tan\theta}{\cos\theta}} \qquad [9]$$

where k is given by the same expression as for the sphere but with the volume and frontal projection area relevant to the cylinder. It is important to note that A is the frontal projection of the floatation body when the TCM is in the vertical position. Due to the factor $\cos\theta$ in the denominator of equation [9], the response curve for a cylinder becomes considerably steeper than for a sphere with the same value of k thus giving a larger measuring range. The drag coefficient, however, will be different for the cylinder. For Reynolds numbers in the range $1 \cdot 10^3$ to $3 \cdot 10^5$ an infinitely long smooth cylinder has a drag coefficient between 1.0 and 1.3 (Schlichting and Gersten, 2017). This suggests that the drag coefficient increases and causes a reduced impact of the change in geometry.

3 EXPERIMENTAL SETUP

The experiments were carried out in the hydraulic laboratory at the Technical University of Denmark (DTU) in a 3m wide, 1m deep and 35m long current flume. The flume was equipped with a carriage mounted on rails, which run along the length of the flume. The TCMs were mounted on a streamlined frame that was attached to the carriage. For low velocities (less than 1.4m/s), constant currents were simulated by towing the TCMs through still water. Higher velocities were simulated by generating a current in the flume and then towing the TCMs against the current. By utilizing both the movement of the carriage as well as the flow in the flume, it was possible to test the TCMs in current speeds up to approximately 2m/s. The duration of each of the steady current tests was 20 seconds or more depending on towing speed.

The TCMs consisted of a hollow plastic floatation body attached to the end of a tether made from a carbon fiber tube (2mm outer diameter). The tether was attached to an instrument box through a joint made from silicone tube. Tilt angle and direction were measured with a 3-axis accelerometer placed inside the floatation body and logged at the highest frequency possible (approximately 20Hz). The flow velocity relative to the TCM was measured using a combination of an Armfield H33 propeller velocimeter mounted on the carriage and a laser distance meter, which recorded the position of the carriage at a frequency of 25Hz.

A total of 1 spherical and 12 "cylindrical" TCMs were tested in the experiments (see Table). The floatation bodies of the cylindrical TCMs were circular cylinders with semispherical endings (see Figure 1). The properties of the cylindrical TCMs were varied by varying the tether length and the cylinder length. Three tether lengths (L) and four cylinder lengths (l) were tested. The spherical TCM was included mainly as a reference since it can be viewed as a cylinder with l = 0.

Tilt angles were determined by comparing the instantaneous acceleration vector to the acceleration vector measured when the TCM was at rest in the vertical position. Comparing the vertical acceleration vectors between consecutive tests showed changes in direction of a few degrees in the direction of the flow in the preceding test. This is interpreted as a symptom of some stiffness in the joint.

Table 1. Properties of the tested TCMs. The optimal cylindrical TCM has been highlighted. $m^* = m/\rho V$ denotes the dimensionless mass of the floatation body. The small difference in diameter, and hence KC numbers, between the sphere and cylindrical TCMs has no practical significance for the measurement range.

Type	L [mm]	l [mm]	D [mm]	V [cm^3]	A [cm^3]	m [g]	k	m^*	f_n [s^{-1}]
Sphere	15	0	30	14	7	5	0.44	0.35	1.11
Cylinder	50	25	32	37	16	22	0.38	0.60	1.30
Cylinder	100	25	32	37	16	22	0.37	0.60	0.94
Cylinder	150	25	32	37	16	22	0.36	0.60	0.77
Cylinder	50	50	32	57	24	28	0.43	0.49	1.42
Cylinder	100	50	32	57	24	28	0.42	0.49	1.06
Cylinder	150	50	32	57	24	28	0.41	0.49	0.88
Cylinder	50	100	32	98	40	41	0.46	0.42	1.38
Cylinder	100	100	32	98	40	41	0.45	0.42	1.10
Cylinder	150	100	32	98	40	41	0.44	0.42	0.93
Cylinder	50	150	32	138	56	53	0.47	0.39	1.28
Cylinder	100	150	32	138	56	53	0.46	0.39	1.05
Cylinder	150	150	32	138	56	53	0.46	0.39	0.92

4 RESULTS

4.1 Steady current

The spherical TCM was first tested in steady current to document the presented measurement principle and serve as a reference when comparing to the different cylindrical TCMs. The measured tilt response is shown in Figure 2 (left panel). The right panel shows the apparent drag coefficient calculated using equation [4]. The apparent drag coefficient of approximately 1 that was observed for tilt angles between 10 and 60 degrees was larger than the value of approximately 0.5 (normally found for a fixed smooth sphere). This agrees well with observations made by Williamson and Govardhan (1997) who found a 100% increase in drag coefficient due to vortex-induced oscillations of the sphere. In the present case, the drop in apparent drag coefficient observed at very small tilt angles was found to coincide with a reduction of the amplitude of the vortex induced oscillations. Despite this, there was a good agreement between the theoretical expression ([4]) with C_D = 1 and the measured tilt response for tilt angles up to 60°.

For larger velocities, the tilt angle continued to increase approximately linearly. Quite remarkably, this steady increase continued up to tilt angles larger than 100° corresponding to the TCM pointing slightly downwards. This behavior cannot be explained by the analytical framework presented above. However, the present results suggested that the measurement range of spherical TCMs effectively extended up to tilt angles of 100°.

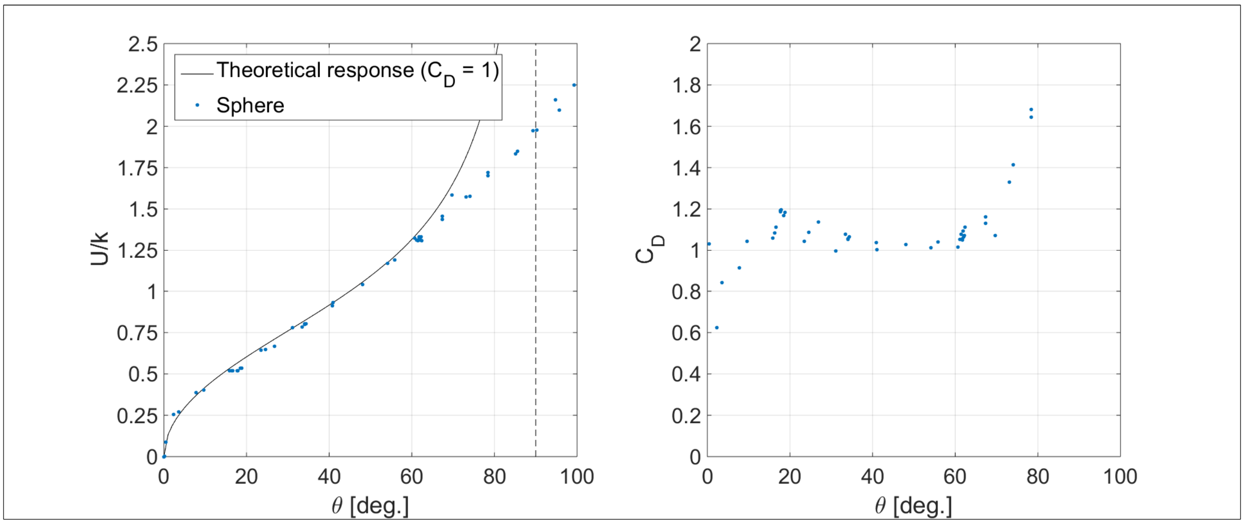

Figure 2. Results from the experiments with the spherical TCM in steady current. Left: Tilt response shown together with theoretical response curve ([4]) for C_D = 1. Right: Apparent drag coefficients.

Figure 3 shows the measured tilt responses for the tested cylindrical TCMs. Each panel shows TCMs with the same cylinder length but with different tether lengths. Included in each panel is also the theoretical response curve ([9]) corresponding to C_D = 1.5. This facilitates easy comparison between panels. The results show that the tether length has little to no effect on the tilt response. Only panel a (l = 2.5cm) shows some effect of the tether length namely that increasing the tether length results in a flattening of the response curve (increased drag coefficient).

Comparing the four panels (a to d) in Figure 3 shows the effect of extending the length of the cylinder. The shortest cylinder with l = 2.5cm (panel a) has a tilt response similar to that of the spherical TCM in the sense that it is relatively flat for tilt angles larger than 60°. As the cylinder length increases, the general tendency is for the response curve to become steeper for tilt angles larger than 60° and flatter for tilt angles smaller than 60°. The behavior for tilt angles less than 60° could be expected since the drag coefficient for a cylinder is larger than for a sphere.

At very large tilt angles, some of the cylinders showed a “drop-off” where the tilt response suddenly increased dramatically. This suggests a sudden increase in the apparent drag coefficient similar to what was seen for the spherical TCM at tilt angles larger than 60°. Although this is not necessarily a problem for the velocity measurement, it does suggest that one should be cautious if using the TCM to measure in this velocity range.

The shape of the response curve of the long cylinders is undesirable as it gave a very high accuracy for a small range of velocities but a very poor accuracy in the rest of the measurement range. In fact, Lowell et al. (2015) who used a very long cylindrical TCM reported that for tilt angles larger than 70° they were unable to detect changes in the current speed. Thus, there is a clear trade-off when selecting the cylinder length; spheres or very short cylinders give rather small measurement ranges while long cylinders give larger uncertainties. Of the cylinders tested in this study, the one with L = 10cm and l = 5cm is considered to be the optimal as it provided the largest measurement range while still giving a nicely shaped tilt response. The theoretical response curve was not a perfect match to the measured response curve. However, improved accuracy of the TCM was obtained by fitting a curve to the measured data and using this to estimate flow velocities based on measured tilt angle. This is utilized in the following.

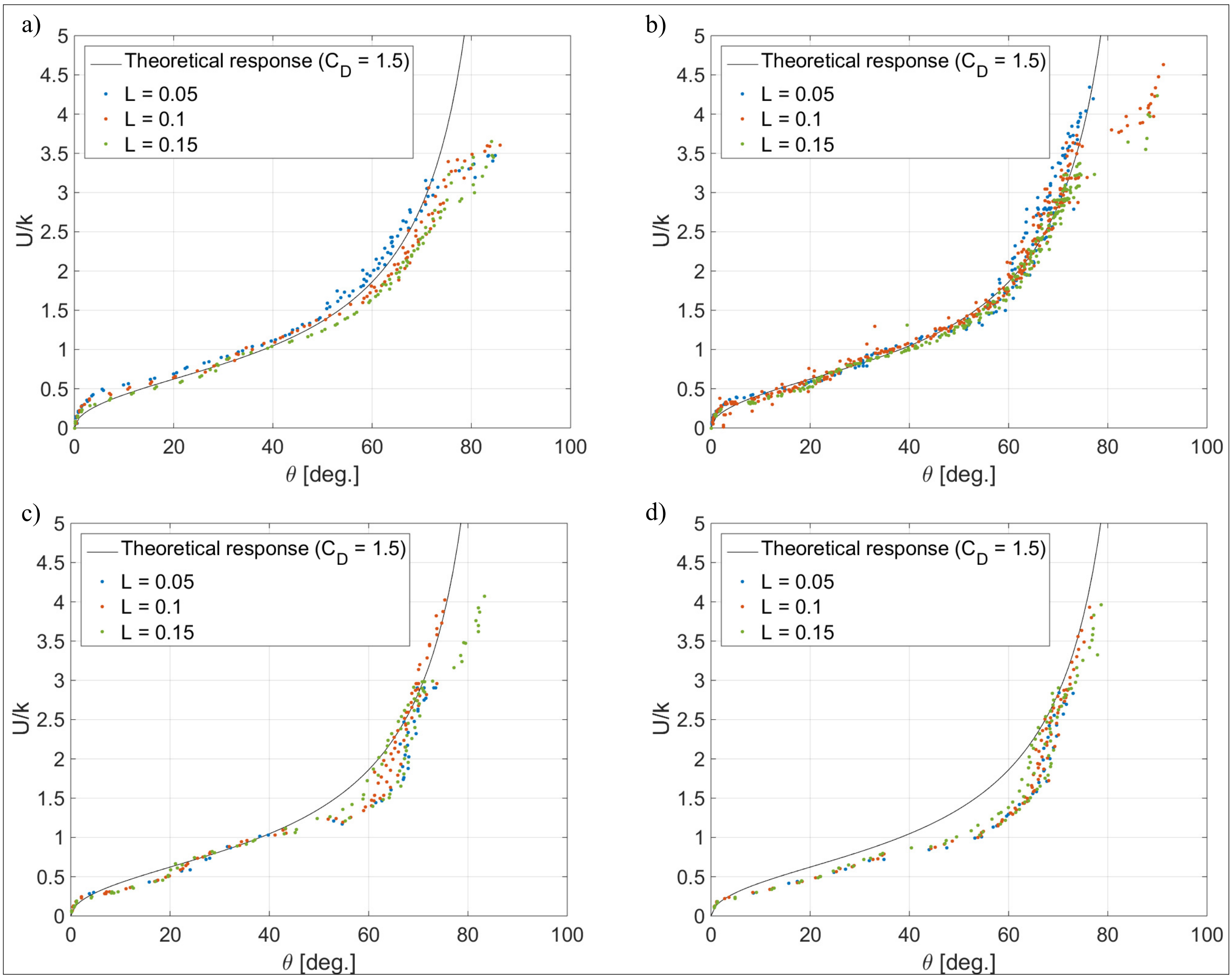

Figure 3. Results of tests with cylindrical TCMs exposed to steady current. Left: Tilt response including analytical response curve ([9]) for C_D = 1.5. a) l = 25mm, b) l = 50mm, c) l = 100mm, d) l = 150mm.

Figure 4 shows the tilt response of the optimal cylindrical TCM together with that of the spherical TCM. The figure shows that choosing this cylindrical TCM instead of a sphere gives a general steepening of the response curve but the main benefit occurs above 60°. It should be noted that whereas the spherical TCM was very lightweight in its construction, the cylindrical TCM was heavier and could potentially be optimized. The potentially achievable measurement range of a 32mm cylindrical TCM with l = 50mm is also shown in Figure 4.

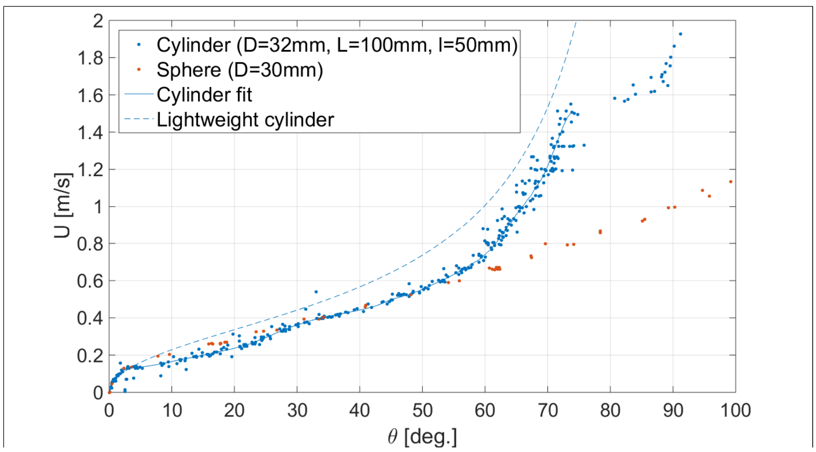

Figure 4. Comparison of observed tilt responses for the spherical and the optimal cylindrical TCM. The dashed line indicates the expected response curve of the optimal cylinder if it were constructed as lightweight as the sphere.

4.2 Pure waves

The optimal cylindrical TCM was tested in a range of different wave conditions with periods ranging from 1.7 to 30 seconds. KC numbers ranged from around 30 to 300. The TCM has a natural frequency of approximately 1.06s^{-1}, which is larger than the largest wave frequency (0.6s^{-1}). Therefore, resonance is not expected to be an issue.

Figure 5 shows corresponding values of tilt angle and maximum orbital velocity (crosses). The figure shows that there is good agreement between the tilt response found in pure waves and the one found in pure current.

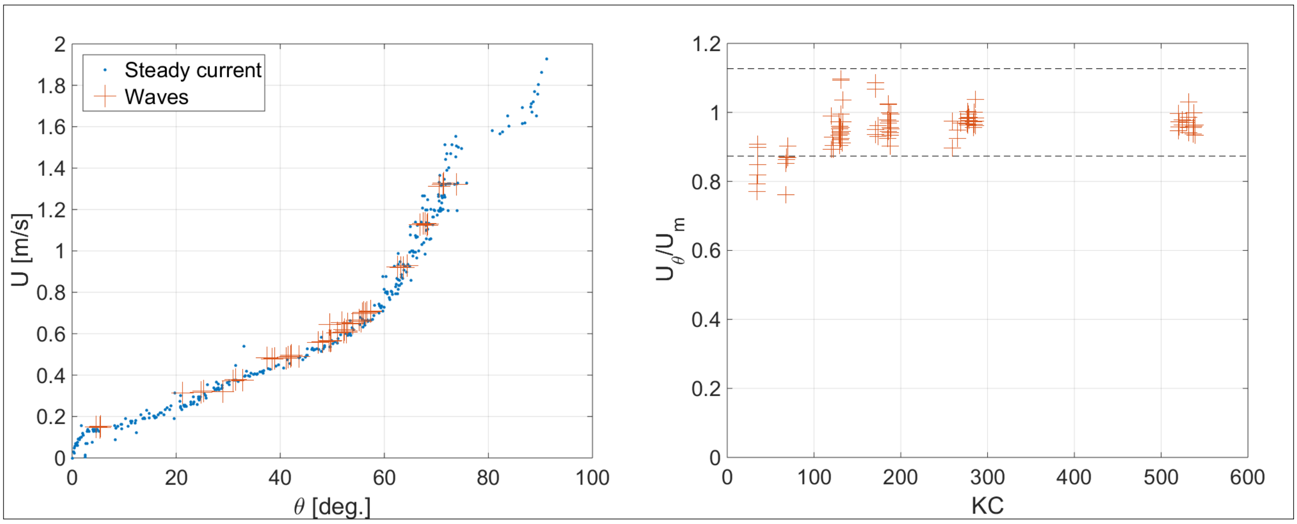

Figure 5. Results from the tests with the optimal cylindrical TCM (L=100mm and l=50mm) in pure wave motion. Left: Tilt response plotted together with tilt response found for current tests. Right: Ratio of velocity predicted by the TCM and the actual velocity plotted against KC number. Dashed lines indicate the standard deviation in pure current ($KC = \infty$).

A closer examination of the TCM behavior in waves was done by considering the ratio $U_{m,c}/U_m$, where $U_{m,c}$ is the amplitude of the orbital velocity estimated by applying the steady current response curve to the measured tilt angles. It should be noted that this ratio is directly related to the ratio of the drag coefficient in steady current ($C_{D,c}$) and in waves ($C_{D,w}$). Combining equations [5] and [9] gives the relationship as

$$\frac{C_{D,w}}{C_{D,c}} = \left(\frac{U_{m,\theta}}{U_m}\right)^2 \qquad [10]$$

The comparison in Figure 5 (right panel) shows that the predicted amplitude of the orbital velocity agreed very well with the actual one for KC numbers larger than 100. For KC number smaller than 100, the TCM tended to underestimate the velocities slightly. With increasing KC number, the unsteady flow became increasingly drag-dominated approaching the steady current case, hence the result is as expected. However, it is important to note that this experimental setup does not reproduce the horizontal pressure gradients present in real wave motion that give rise to the Froude-Krylow force (Sumer and Fredsøe, 2006).

4.3 Combined waves and current

The TCM performance in combined waves and currents was tested by running a steady current in the flume while moving the carriage in a sinusoidal motion. Two current speeds of 15cm/s and 46cm/s were tested. Each of these was combined with a test series of wave conditions which approximately corresponded to those considered for the pure wave case.

In the same way as was done for the pure waves tests, the performance of the TCM was evaluated by considering the velocities close to the peaks of the wave orbital motion. However, in the case of combined waves and current, it was found necessary to consider the forestroke of the wave (current and wave flow in the same direction) separately from the backstroke (current and wave flow in opposite directions) since TCM performance was different for the two. For the forestroke, it was found that the steady current response curve gave a good estimate of the peak velocities (Figure 6). During the backstroke, however, the TCM tended to underestimate the magnitude of the peak orbital velocity.

The observed behavior has yet to be explained. Possible reasons are that this is the result of the flow regime; stiffness in the joint as noted in the section on the experimental setup or the relative turbulence level affecting the apparent drag. In the surf zone, current and waves are often at an angle to each other. Furthermore, the turbulence levels in the surf zone may affect the apparent drag coefficient. Hence, it is concluded that the logical next step is to carry out a field validation rather than exploring the discrepancy in the laboratory. The discrepancy may not present an issue in the field as this situation may not be present. The TCM for a field validation in the surf zone should be chosen to have a measurement range that covers the expected orbital flow velocities. Then both the orbital velocities and the wave-averaged velocities can be measured provided the above-mentioned issue is absent or has been resolved. In the surf zone, one may experience large cross-shore orbital flow velocities and small longshore currents. In this case, it may be important to choose the smallest possible measurement range in order to ensure adequate measurement accuracy for the longshore current. This is due to the shape of the response curve at small tilt angles and hence small flow velocities.

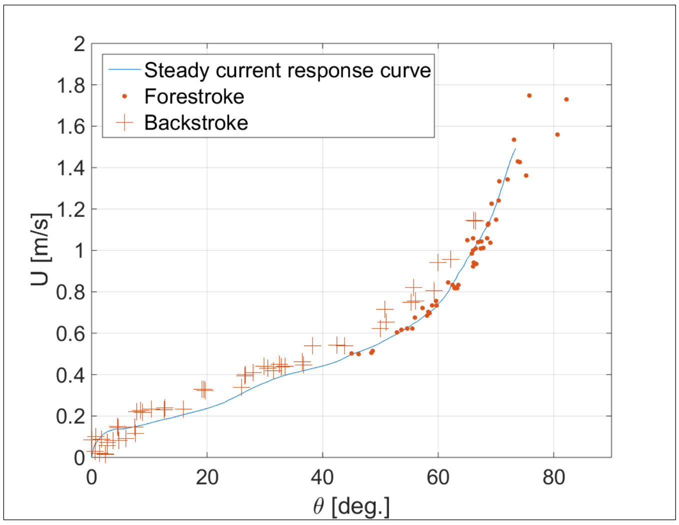

Figure 6. Tilt response observed in the wave-current tests with the optimal cylindrical TCM.

5 CONCLUSIONS

The behavior of spherical and cylindrical TCMs was investigated with the objective of finding a TCM suitable for use in the surf zone. The main requirement for a TCM is measurement range of several meters per second and also able to capture the unsteady flow of the wave orbital motion.

A large measurement range could be achieved by increasing the size of the TCM. However, the size of the floatation body should be kept small to give large KC numbers in ensuring a drag-dominated unsteady flow. Additionally, it is desirable to have a relatively constant apparent drag coefficient and necessary to have relatively high natural frequency.

The benefit of a cylindrical floatation compared to spherical floatation body was demonstrated. The results showed that a short cylinder gave a considerable increase in the measuring range without increasing diameter. For long cylinders, the response curve became very flat for tilt angles smaller than 60° while for larger angles the response curve became so steep that it would give very large uncertainties in the velocity estimate. The effect of tether length was investigated, but it was found to be negligible for the present cases. Out of the 12 TCMs considered in the present study, the one with tether length 10cm (L/D = 3.1) and cylinder length 5cm (l/D = 1.6) was found to be preferable.

This cylindrical TCM had a response curve in waves similar to the one in steady current. The noticeable discrepancies were found, as expected, for small KC values (KC < 100). The response curve in combined waves and current was similar to the steady current response curve, when the current and wave was in the same direction; however this response curve tended to underestimate the flow speed when the current and waves were in opposite directions.

Overall, the present findings show that it is possible to choose a TCM so that it is able to capture both mean current and orbital flow velocities as experience in the surf zone.

The present study, however, only considered unidirectional flow whereas the current is expected to often be almost orthogonal to the wave motion in the surf zone. The turbulence levels in the in the surf zone could be an issue as well as the apparent drag coefficient may change. Such conditions are hard to establish in the laboratory. Therefore, the next step shall be to carry out a field validation of the described TCM.

REFERENCES

Figurski, J.D., Malone, D., Lacy, J.R. & Denny, M. (2011). An Inexpensive Instrument for Measuring Wave Exposure and Water Velocity. *Limnology and Oceanography Methods*. 9, 204–214.

Lowell, N.S., Walsh, D.R. & Pohlman, J.W. (2015). A Comparison of Tilt Current Meters and an Acoustic Doppler Current Meter in Vineyard Sound, Massachusetts. *IEEE/OES Eleventh Current, Waves and Turbulence Measurement*. 1-7

Marchant, R., Stevens, T., Choukroun, S., Coombes, G., Santarossa, M., Whinney, J. & Ridd, P. (2014). A Buoyant Tethered Sphere for Marine Current Estimation. *Journal of Oceanic Engineering*, 39(1), 2-9.

Radermacher, M., Thackeray, Z., De Schipper, M., Gordon, L., Chrystal, C., Leuci, R. & Reniers, A. (2015). Tilt Current Meter Array: Field Validation. *E-proceedings of the 36th IAHR World Congress*, 1-9.

Schlichting, H. & Gersten. K. (2017). *Boundary-Layer Theory*. Springer.

Sumer, B.M. & Fredsøe, J. (2006). *Hydrodynamics Around Cylindrical Structures*. Advanced Series on Ocean Engineering, 26, World Scientific

Williamson, C.H.K. & Govardhan, R. (1997). Dynamics and Forcing of a Tethered Sphere in a Fluid Flow. *Journal of Fluids and Structures.* 11(3), 293–305

UNSTEADY TURBULENT VELOCITY PROFILING USING AN ARRAY OF TWO VECTRINO II PROFILERS IN TIDAL BORES AND OPEN CHANNEL FLOWS

XINQIAN LENG [(1)] & HUBERT CHANSON [(2)]

[(1,2)] The University of Queensland, School of Civil Engineering, Brisbane QLD 4072, Australia,
xinqian.leng@uqconnect.edu.au; h.chanson@uq.edu.au

ABSTRACT

The propagation of positive surges in rivers and open channels is a highly unsteady turbulent process, with intensive sediment scouring and mixing. Despite its ecological and engineering significance, systematic physical studies of the unsteady turbulent characteristics of tidal bores remain limited. The present investigation performs ensemble-averaged velocity measurements using an array of two Vectrino II Profilers to investigate the vertical and transverse variability of the instantaneous velocity field during the propagation of breaking bores in open channel flows. Results highlight satisfactory performances of Vectrino II Profilers in highly unsteady turbulent open channel flows. Rapid longitudinal deceleration, transient recirculation and large velocity fluctuations in all directions are observed with the bore passage. The vertical velocity increased then decreased with the sharp free-surface rise. The transverse velocity data highlighted drastic transverse motions of bores and existence of large vortical structures in the flow. Overall, the results suggest that the propagation of tidal bore is a highly unsteady turbulent process, and a three-dimensional phenomenon. The process is associated with large fluctuations in all velocity components, as well as formation of large vortical structures and intense turbulent mixing in the wake of the surge.

Keywords: Open channel flow; turbulence; velocity profiling; unsteady flows.

1 INTRODUCTION

A sudden rise of water depth in open channel flows induced by the rapid closure of a downstream regulation gate is called a positive surge. In nature, a positive surge could occur during spring tide period in a funnel-shaped estuary with large tidal range and low freshwater level. This phenomenon is also called a compression wave or a tidal bore. Figure 1 illustrates the breaking tidal bore in the Qiantang River (China). To date, there are estimated to be over 400 rivers and estuaries where tidal bores were found, including all continents except for Antarctica (Chanson, 2011). The propagation of a tidal bore is an unsteady turbulent process, with intense shear and mixing underneath. The strength and shape of a bore is characterized by its Froude number Fr_1 defined as:

$$Fr_1 = \frac{V_1 + U}{\sqrt{g \times d_1}} \qquad [1]$$

where V_1 is the initial flow velocity positive downstream, U is the bore celerity positive upstream, g is the gravitational acceleration (equals to 9.80 m/s^2 as in Brisbane, Australia), d_1 is the initial water depth. When $Fr_1 < 1$, a tidal bore cannot form. When $1 < Fr_1 <$ 1.3-1.4, the bore is undular, characterized by a smooth free-surface rise and a train of secondary quasi-periodic waves (Treske, 1994; Koch and Chanson, 2008; Leng and Chanson, 2017a; 2017b). When $Fr_1 >$ 1.5-1.6, the bore is fully breaking, with a turbulent breaking roller and energetic white water splashes (Hornung et al., 1995; Leng and Chanson, 2017a; 2017b).

Herein, new experiments were conducted to study the unsteady turbulent characteristics of breaking bores in a systematic manner under controlled flow conditions. The experimental channel was a relactively large rectangular tilting flume. The breaking bores were generated by rapidly and fully closing a downstream Tainter gate and propagated upstream. An array of two Nortek™ Vectrino II Profilers were mounted side-by-side at mid-channel for velocity measurements. The two Profilers were equipped respectively with a fixed down-looking probe and a flexible probe mounted in a side-looking fashion. The present physical study aims to: (1) validate the performances of two Vectrino II Profilers when conducting velocity measurements simultaneously in an array under highly unsteady turbulent flow conditions; and (2) study the vertical and transverse distributions of the three-dimensional velocity characteristics associated with propagations of breaking bores.

Figure 1. Photographs of tidal bores in natural rivers: breaking bore in Qiantang River, Jiuxi, China (20/09/2016) – Bore propagation from left to right.

2 EXPERIMENTAL FACILITY AND INSTRUMENTATIONS

2.1 Experimental flume and instrumentations setup

The flume was 19 m long and 0.7 m wide rectangular prismatic, with glass sidewalls, a smooth PVC invert and an adjustable bed slope. Water was supplied by an upstream water tank through a smooth convergent intake into the test section. The discharge was measured by a magneto flow meter with an accuracy of 10^{-5} m^3/s. The measured discharge was frequently checked against the brink depth d_b at the end of flume. A fast-closing Tainter gate was located near the downstream end at x = 18.1 m, where x was measured from the upstream end. The gate closure time was within 0.2 s, so that no effect would be caused by the closing mechanism on the bore properties. Figure 2a shows a sketch of the flume with all experimental apertures and instrument mountings.

During the steady flow period before the gate closure, the water depths were measured using point gauges with an accuracy of 0.001 m. In unsteady flows, water depths were recorded using a series of acoustic displacement meters (ADMs) (Fig. 2b). A Microsonic™ Mic+35/IU/TC unit was located at x = 18.17 m immediately downstream of the Tainter gate. Further nine Microsonic™ Mic+25/IU/TC units were spaced along the channel from x = 17.81 m to 1.96 m. All ADMs were calibrated against point gauge measurements and the sensors were sampled at 100 Hz on the channel centerline.

The velocity measurements were performed using an array of two Nortek™ acoustic Doppler velocimeter Vectrino II Profilers. The fixed-head Profilers (Hardware ID VNO 1366, firmware ID 1950, referred to as Profiler 1) was validated and used previously by Leng and Chanson (2017a,b). Herein, it was used to measure velocity at the same time as a validating reference of the newly introduced Profiler, called Profiler 2. The Profiler 2 (Hardware ID VNO 1436, firmware ID 1950) was equipped with a flexible head, mounted in a side-looking fashion. Both Profilers used coherent Doppler processing technology, and had a three-dimensional head, which is able to record velocity in the longitudinal, transverse and vertical directions. Both Profilers were configured to quasi-simultaneously sample the velocity at 100 Hz for 35 sampling points in 35 mm profiles (Note that the physical experiments were conducted prior to the introduction of any manufacturer's re-calibration and probe upgrade). The sampling profile of Profiler 1 was arranged in the vertical direction, and in the transverse direction for Profiler 2. The first point of each sampling profile was located 40 mm from the probe central emitter. Figure 2c shows dimensioned sketches of the two Profilers and the arrangement of their sampling profiles.

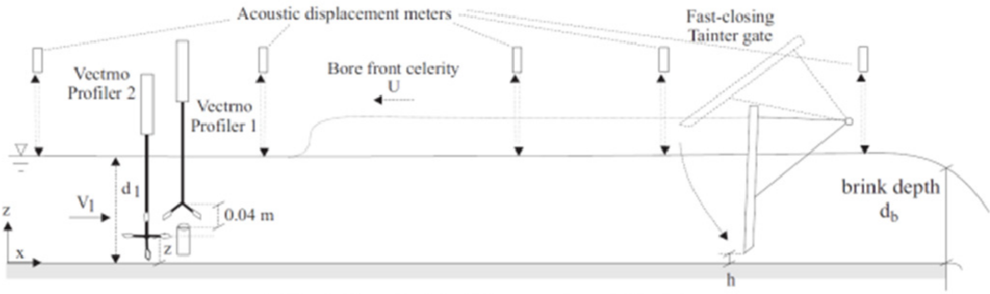

(a) Definition sketch of the experimental facility

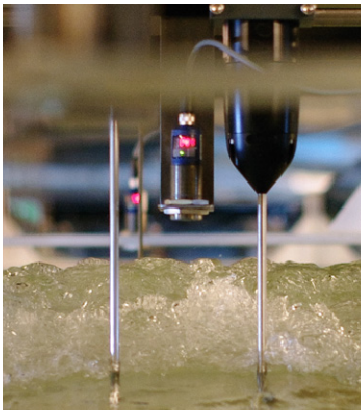

(b) Mounting of the ADMs (pointed by red arrow) looking downstream at an incoming bore

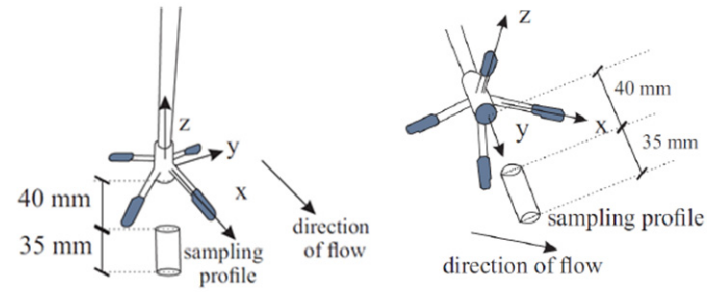

(c) Coordinated sketch of Profiler 1 (left) and 2 (right).

Figure 2. Definition sketch of the experimental facility.

The two Profilers, 1 and 2, were mounted at x = 8.5 m and 8.425 m respectively. The velocity range was set to ± 1 to ± 1.5 m/s, and the sampling frequency was 100 Hz. Figure 3 shows the setup of the two Profilers during unsteady turbulent velocity measurements. At the lowest vertical elevation, the sampling profile of Profiler 1 covers z = 1 – 35 mm with z = 0 at the channel bed. Whereas the sampling profile of Profiler 2 was arranged to be orthogonal to that of Profiler 1, located at z = 30 mm, which was the lowest possible elevation with this setup. During the present study, the relative distance between the two Profilers' sampling profiles remained constant longitudinally, transversely and vertically. This setup was tested and chosen based upon a series of systematic experiments to ensure minimum interactions between instruments and adequate correlations between two sets of velocity signals. Both Profilers were synchronised together with all 10 ADMs. The synchronization between instruments was within ± 1ms.

The steady flow data of both Profiler signals were post-processed by the MATLAB program VTMT version 1.1, designed and written by Becker (2014). In steady flows, the post-processing included removing data with averaged correlation values less than 60% and averaged signal to noise ratio less than 5 dB. The phase-space thresholding technique developed by Goring and Nikora (2002) was applied to remove spurious points. In unsteady flows, the above post-processing technique was not applicable (Nikora, 2004; Person. Comm.; Chanson, 2008; 2010; Koch and Chanson, 2009) and raw data was used directly for analysis.

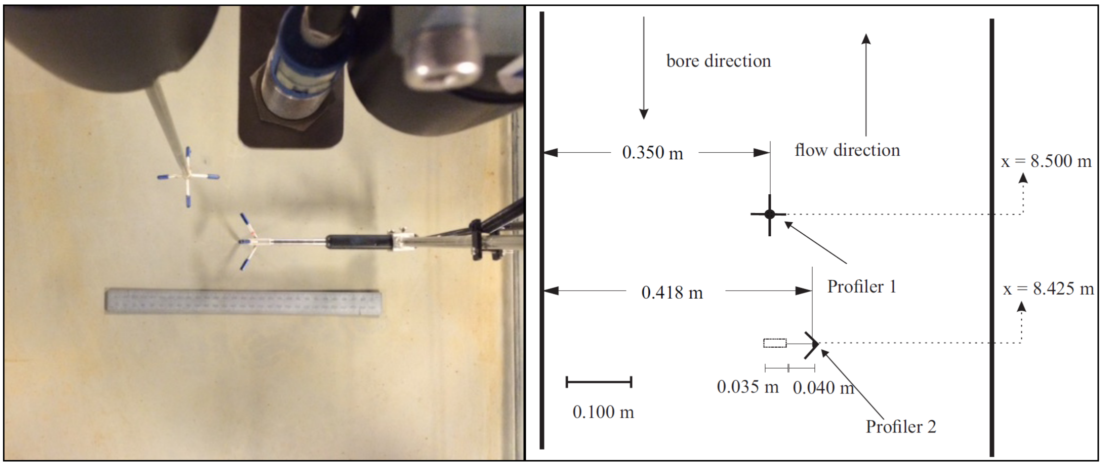

Figure 3. Photograph and dimensioned sketch of the profilers setup viewed in elevation.

2.2 Experimental flow conditions

Since the propagation of tidal bores is a highly unsteady turbulent process, a time-averaging technique would not be meaningful. Hence, ensemble-averaged measurements were necessary, where experiments were repeated 25 times for each controlled flow condition and the results were ensemble-averaged. Table 1 summarises the experimental flow conditions for ensemble-averaged measurements conducted with an array of two Profilers. In Table 1, S_o is the bed slope, Q is the initially steady water discharge, d_1 is the initial water depth at x = 8.5 m before the bore arrival, h is the gate opening after the rapid closure, y is the distance measured from the right side wall, B is the channel width which equals to 0.7 m, throughout and U was the bore celerity.

Table 1. Experimental flow conditions for velocity measurements using an array of two profilers.

	o	Q (m^3/s)	d_1 (m)	h (m)	z/d_1 Profiler 1	z/d_1 Profiler 2	y/B Profiler 1	y/B Profiler 2	U (m/s)	Fr_1
Present		0.101	0.174	0	0.01-0.20	0.17	0.5	0.46-0.51	1.15	1.52
Study		0.101	0.176	0	0.09-0.28	0.26	0.5	0.46-0.51	1.11	1.50
		0.101	0.176	0	0.23-0.43	0.40	0.5	0.46-0.51	1.18	1.55

3 VELOCITY MEASUREMENTS IN THE INITIALLY STEADY FLOW

3.1 Presentation

A Nortek^{TM} Vectrino II profiling velocimeter is a relatively newly developed instrument which is more and more broadly in the laboratory and field. Compared to traditional Nortek^{TM} Vectrino+ acoustic Doppler velocimeter (ADV), the advantage of a Vectrino II Profiler is its ability to simultaneously measure the instantaneous velocity in a profile, containing up to 35 sampling points with a minimum size of 1 mm. The performance of a Vetcrino II Profiler in steady and unsteady flows were previously documented by Craig et al. (2011), Zedel and Hay (2011), MacVicar et al. (2014), Dilling and MacVicar (2017), Leng and Chanson (2017a; 2017b). Leng and Chanson (2017b) found satisfactory performances of the Vectrino II Profiler in highly-fluctuating turbulent steady and unsteady flows, and was relatively accurate in estimating the time-averaged instantaneous velocity at high frequency (up to 100 Hz). Issues with the Profiler included erroneous points (weak spots) at certain positions beneath the flow, where velocity data were not meaningful. Other issues included wrong estimation of velocity variances and Reynolds stresses except at the sample "sweet spot". Overall, previous experimental results for application of a Vectrino II Profiler in turbulent flows were encouraging, while careful post-processing and validation were required.

Steady flow measurements were herein performed under controlled flow conditions to test the performance and data quality of the newly introduced Profiler 2. The same methodology was used to check and validate the performance of Profiler 1, and was documented in Leng and Chanson (2017b). Steady flow experiments were conducted using Profiler 2 at a range of vertical elevations (z/d_1 = 0.17 – 0.86) and transverse locations (y/B = 0.22 to 1.00) under the same flow conditions as in Table 1. The results were compared to previous measurements using ADV - an instrument which has been carefully validated against Pitot tube and proven to be accurate in steady and unsteady turbulent flows (Koch and Chanson, 2005; Leng and Chanson, 2017b). Figure 4 shows the comparison between the Profiler 2 results (y/B = 0.48 – 0.52) and previous ADV measurements (Leng and Chanson, 2016a) in steady flows. The ADV data was collected under the same flow conditions at about the same elevations and on the channel centerline. Note that the ADV data was sampled at 200 Hz for 60 s, whereas Profiler 2 was sampled at 100 Hz for 90 s.

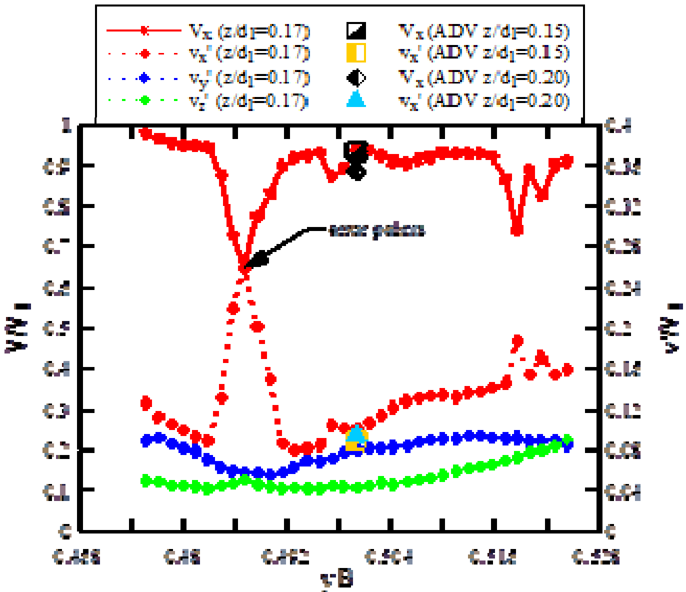

Figure 4. Transverse profile of time-averaged longitudinal velocity, velocity fluctuations with comparison to ADV data (Leng and Chanson, 2016a); ADV data measured at a point on the channel centerline.

3.2 Results

For the tested range of vertical elevations, the Profiler 2 gave good estimation of time-averaged velocity for a majority of sampling points in a transverse profile. The velocity magnitudes agreed well with previous centerline ADV data at similar vertical elevations. A few outliers were observed as marked in Figure 4. These error points were also observed in past studies by Zedel and Hay (2011), MacVicar et al. (2014), Dilling and MacVicar (2017), Leng and Chanson (2017a; 2017b). The number and proportion of these outliers were small, usually less than 5 points for a 35-point sampling profile, and thus can be easily removed before further analysis.

Previous studies highlighted inaccurate estimation of root-mean-square (RMS) of the velocity data using a Vectrino II Profiler (Zedel and Hay, 2011; MacVicar et al., 2014; Dilling and MacVicar, 2017; Leng and Chanson, 2017a; 2017b). The present study found spurious shapes and values in terms of the velocity RMS v' especially for the longitudinal component (Fig. 4). Only a small portion of the transverse profile was associated with meaningful values of velocity RMS close to the ADV data (y/B = 0.48 – 0.50). A few outliers were highlighted between y/B = 0.48 – 0.49 (~ 5 points). The transverse and vertical velocity components were associated with better quality data, however with an unreasonable curvy shape of the profile.

Overall, for the experimental range of vertical and transverse locations, Profiler 2 demonstrated good approximations of time-averaged velocity for the majority of sampling profile, and reasonable velocity RMS at the sampling “sweet spot” (typically at the middle or 1/3 of the sampling profile). The error points, where time-averaged velocity was not well estimated, occurred at different numbers and locations as the sampling location varied. It would be hard to predict the occurrence of these points. However, for a fixed location, the presence of error points were consistent, i.e. always at the same point in a profile with repeating experiments. This important feature enabled fast quality control to be carried out. Namely a wide range of transverse and vertical locations needs to be experimented first to know the number and location of error points, then a location with least number of error points can be selected for further experiments. Herein, the vertical and transverse ranges for ensemble-averaged experiments in Table 1 were selected based upon these steady flow results.

4 ENSEMBLE-AVERAGED MEASUREMENTS USING AN ARRAY OF TWO PROFILERS

4.1 Ensemble-averaged velocity characteristics

Typical ensemble-averaged time-variations of the longitudinal, transverse and vertical velocity components measured by the array of two Profilers are shown in Figure 5. The results of Profiler 1 show data at different vertical elevations in a sampling profile, whereas the results of Profiler 2 show data at different transverse locations. The ensemble-median free-surface elevation is shown in Figure 5 with black diamond symbols to indicate the arrival of the bore. The dimensionless time equals to 0 at the instance of gate closure.

  / ISSN 1562-6865 (Online) - ISSN 1063-7710 (Print)

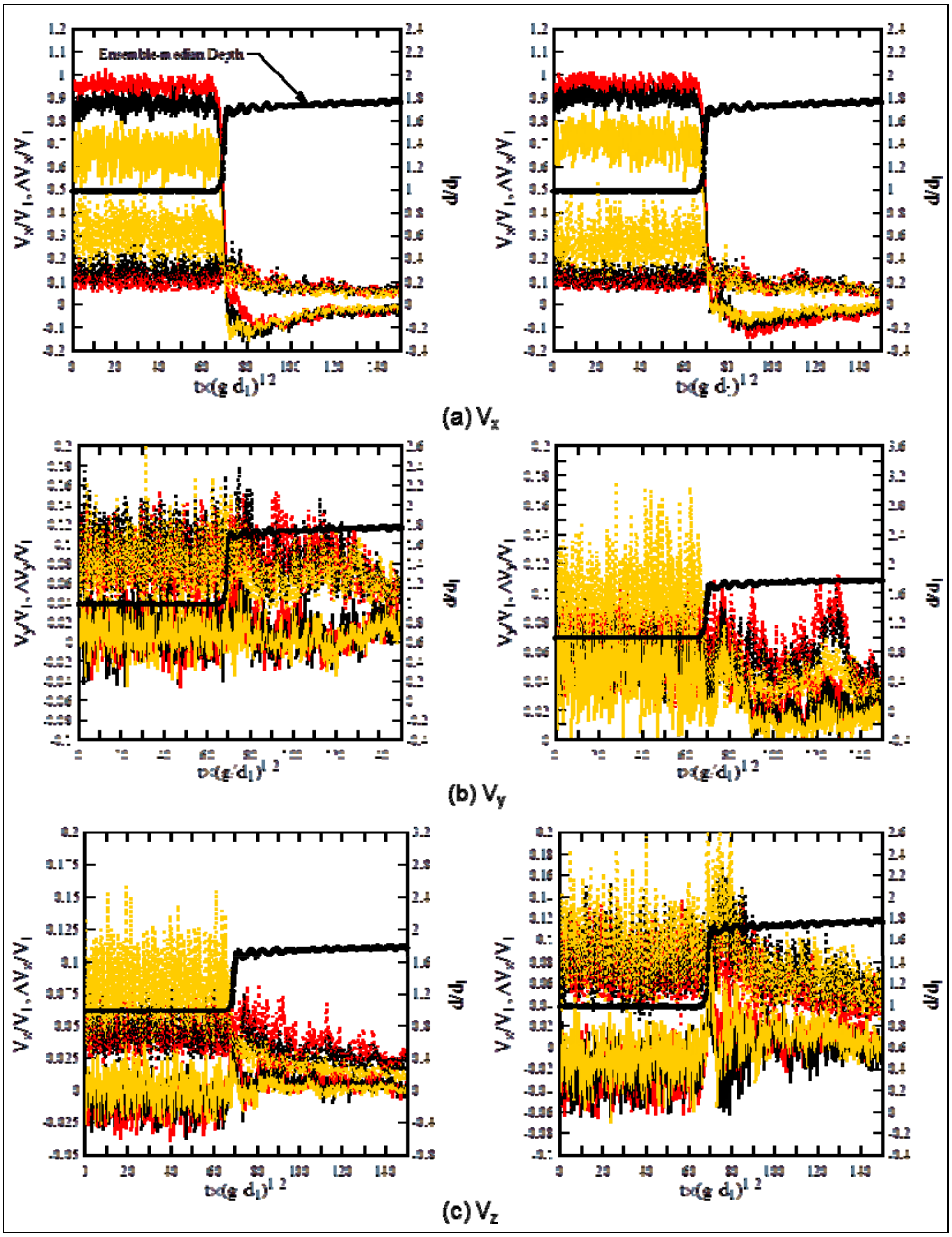

Figure 5. Ensemble-averaged time-variations of the longitudinal V_x, transverse V_y and vertical V_z velocity components measured by Profiler 1 (left) at z/d_1 = 0.17 (red), 0.09 (black) and 0.03 (yellow), and Profiler 2 (right) at y/B = 0.47 (red), 0.48 (black) and 0.50 (yellow); ensemble-median velocity marked by solid lines, velocity fluctuations $\Delta V = (V_{75}-V_{25})$ marked by dotted lines; ensemble-median depth denoted by black rounded symbols.

The velocity data in the initially steady flow prior to the bore arrival highlight clearly the presence of a bottom boundary layer, where the velocity magnitudes increase with higher vertical elevations (Fig. 5). On the other hand, the data of Profiler 2 show decreasing velocity magnitudes with increasing transverse distance from the right side wall in steady flow, indicating the sidewall boundary layer.

Overall, the ensemble-average longitudinal velocity measured by both Profilers shows simultaneous deceleration associated with the rapid increase in water depth, indicating the arrival of the bore. A recirculation velocity is often observed at low vertical elevations (z/d_1 < 0.5 - 0.6) marked by the negative transient longitudinal velocity at the end of declaration during the propagation of breaking bores (Chanson and Toi, 2015; Leng and Chanson, 2016a). Present study highlights longitudinal recirculation velocity measured by both Profilers up to a vertical elevation of z/d_1 = 0.4. This finding is consistent with past studies.

The velocity fluctuations are characterized by the difference between the third and first quartiles (V_{75}-V_{25}), marked by dotted lines in Figure 5. For a dataset with Gaussian distribution, this difference (V_{75}-V_{25}) would be equal to 1.3 of the standard deviation (Spiegel, 1972). The longitudinal velocity fluctuations are associated with sharp increases recorded by both Profilers as the bore passed, except at the end points of a sampling Profiler (z/d_1 = 0.03 and y/B = 0.50), highlighted by the yellow dotted lines. Past experiments documented issues with Profilers in estimating velocity variances at the end points of a sampling profile (Craig et al., 2011; Zedel and Hay, 2011; MacVicar et al., 2014). At the other locations within the profile, the longitudinal velocity fluctuations reach a maxima shortly after the arrival of the bore. This maximum velocity fluctuation and its time lag relative to the bore arrival were previously observed in both ADV and Profiler 1 measurements (Leng and Chanson, 2016a; 2017b). The velocity fluctuations and the associated time lags in the longitudinal directions are very close to past measurements using an ADV or Profiler 1.

The ensemble-averaged transverse velocity measured by both Profilers fluctuates drastically as the tidal bore passes. The data measured by Profiler 2 show an abrupt increase and then decrease shortly after the arrival of the bore. The steady flow transverse velocity shows larger fluctuations and mean values, highlighted by the Profiler 2 data, as compared to Profiler 1 data. The larger mean values could be a result of slight tilt of the probe head due to direct flow impact on the receivers. The comparatively large fluctuations may be caused by some reflection of the acoustic signal on the channel bed, as the receiver associated with the transverse and vertical velocity components was placed very close to the bed. The transverse velocity fluctuations measured by Profiler 1 are larger than the velocity magnitudes, and are comparable to the velocity magnitudes measured by Profiler 2. Some very large oscillations in transverse velocity fluctuations are highlighted at the later stage of the early flood tide phase after the bore passage, with amplitudes twice as large as the velocity magnitudes (Fig. 5, dotted lines). This could be associated with some transverse recirculation and mixing, linked with some large-scale vortical structures.

The vertical velocity components show a rapid acceleration and deceleration associated with the bore arrival, as measured by both Profilers. The data of Profiler 2 is associated with larger fluctuations at all locations, possibly caused by the acoustic reflection near the bed. The vertical acceleration measured by Profiler 2 seems to be more abrupt and sharp. The fluctuations in the early flood tide flow after the bore passage are higher in the measurements of Profiler 2 compared to those of Profiler 1. Both Profilers measured vertical velocity fluctuations twice the magnitudes of the vertical velocity. With Profiler 2, all locations show large increase in fluctuations associated with the passage of the bore. Peak fluctuations are reached shortly after the bore passage.

4.2 Discussion

The ensemble-averaged velocity characteristics measured by the two Profilers at almost the same location were compared (z/d_1 = 0.17, y/B = 0.50 with Δx = 0.075 m). Figure 6 shows one set of the results. The steady longitudinal velocity before the bore arrival shows smaller velocity magnitude measured by Profiler 2, which is 20% lower than that of Profiler 1. This could be caused by the interactions between the two instruments. During the rapidly-varied flow phase with the bore passage, the two Profilers show results which are almost identical, with the same deceleration gradient and almost the same recirculation velocity magnitudes at the end of deceleration. During the early flood tide phase immediately after the bore passage, the ensemble-averaged longitudinal velocity components measured by the two Profilers are very similar, with almost no difference in terms of the magnitudes and variations with time.

The ensemble-median transverse velocity shows some large fluctuations following the arrival of the bore. A peak in transverse velocity was observed for both Profiler measurements. The two peaks of the two instruments has a dimensionless time difference of 2.7, corresponding to a time difference of 0.36 s and a longitudinal distance of 0.41 m (local bore celerity = 1.14 m/s). Hence, this time lag is not caused by the difference in bore arrival times at the two instruments but by the transverse motion of the bore. This could be confirmed by the ensemble-averaged vertical velocity data of the two Profilers. Both Profilers show an abrupt acceleration and deceleration of the vertical velocity with the bore passage. The results of the two Profilers have almost overlapped during the acceleration then deceleration phase, highlighting a maximum vertical velocity nearly at the same time.

The velocity fluctuations show general trends of increase with the bore arrival in all directions measured by the two Profilers. Profiler 1 measurements highlight maximum velocity fluctuations occurred shortly after the bore arrival in the longitudinal, transverse and vertical directions for most of the data sets. Profiler 2 measurements are generally associated with larger velocity fluctuations in all directions compared to Profiler 1 measurements. Some data are associated with peaks in velocity fluctuations, and are more commonly observed in the transverse and vertical components.

To sum up, the array of measurements highlights rapid longitudinal deceleration, transient recirculation and large fluctuations in the transverse and vertical velocity components. The transverse velocity data highlight rapid transverse motion of the bore, possibly linked with large vortical structures near the fluctuating free-surface. The results are combined to show that the propagation of a tidal bore is a three-dimensional process, with turbulent properties rapidly-varied in all three directions.

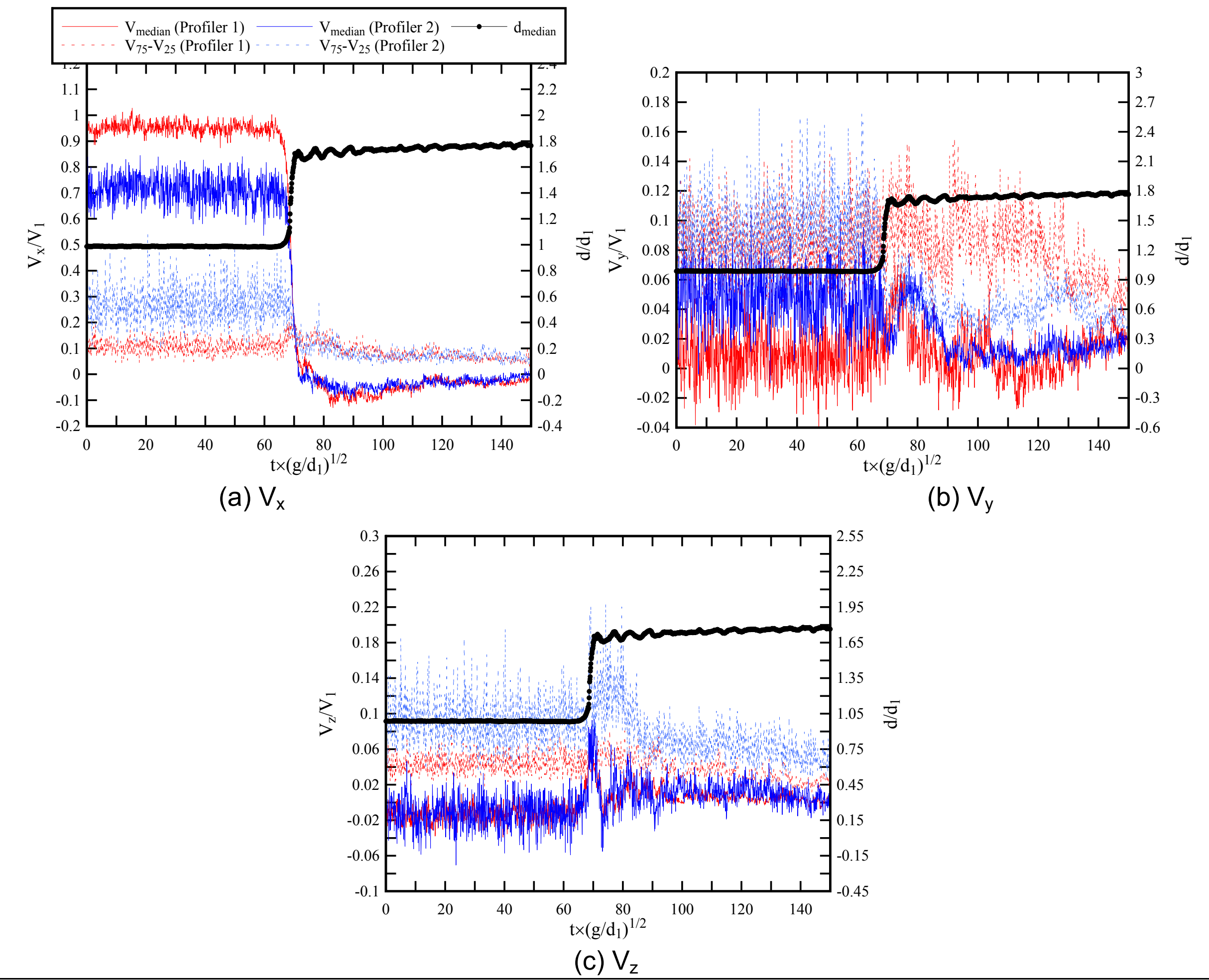

Figure 6. Ensemble-averaged time-variations of the longitudinal (a), transverse (b) and vertical (c) velocity components measured by Profiler 1 and 2 at z/d_1 = 0.17, y/B = 0.50, x = 8.5 m and 8.425 m respectively.

5 CONCLUSION

New experiments were conducted in a relatively large size facility to study the unsteady turbulent properties of tidal bores propagating in open channel flows using an array of two ADV Profilers. Two Nortek™ ADV Vectrino II Profilers were deployed to sample simultaneously at close range the turbulent velocity characteristics in vertical and transverse profiles. Ensemble-averaged measurements were performed, where experiments were repeated 25 times for each controlled flow condition and the results were ensemble-averaged. Present studies demonstrated that both Profilers gave satisfactory performances in highly unsteady turbulent flows when sampled simultaneously and close to each other. Some interactions existed between the two Profilers, causing an underestimation of ensemble-averaged velocity data by Profiler 2 in the initially steady flow. However the interactions did not affect the rapidly-decelerating flow phase and unsteady flow phase after the bore arrival.

The propagation of breaking bores was associated with a rapid longitudinal deceleration, transient recirculation and large velocity fluctuations in all directions. The vertical velocity increased then decreased with the sharp free-surface rise. The transverse velocity data in vertical and transverse profiles highlighted some differences, indicating transverse motions of bores and existence of large vortical structures. Overall, the results suggested that the propagation of tidal bore is a highly unsteady turbulent process, and a three-dimensional phenomenon. The process was associated with large fluctuations in all velocity components, formation of large vortical structures and intense turbulent mixing in the wake of breaking bores.

ACKNOWLEDGEMENTS

The authors acknowledge the technical contribution of Dr. Jan BECKER (Federal Waterways Engineering and Research Institute, Germany) in the data post processing program. The authors also acknowledge the technical assistance of Jason VAN DER GEVEL, Stewart MATTHEWS and Dr. Van Thuan NGUYEN (The University of Queensland). The financial support through the Australian Research Council (Grant DP120100481) is acknowledged.

DISCLOSURE STATEMENT

The authors have no conflict of interest nor any vested interests. This is not an industry sponsored study.

REFERENCES

Becker, J. (2014). *VTMT (Version 1.1). Computer Software.* Federal Waterways Engineering and Research Institute (BAW), Karlsruhe. *Retrieved from http://sdrv.ms/12eHgvw/.*

Chanson, H. (2008). Acoustic Doppler Velocimetry (ADV) in the Field and in Laboratory: Practical Experiences. *Proceedings of the International Meeting on Measurements and Hydraulics of Sewers IMMHS*, 8, 49-66.

Chanson, H. (2010). Unsteady Turbulence in Tidal Bores: Effects of Bed Roughness. *Journal of Waterway, Port, Coastal, and Ocean Engineering*, ASCE, 136(5), 247-256.

Chanson, H. (2011*). Tidal Bores, Aegir, Eagre, Mascaret, Pororoca: Theory and Observations*. World Scientific, Singapore, 220.

Chanson, H. & Toi, Y.H. (2015). Physical Modelling of Breaking Tidal Bores: Comparison with Prototype Data. *Journal of Hydraulic Research*, IAHR, 53(2), 264-273.

Craig, R.G. A., Loadman, C., Clement, B., Ruesello, P.J. & Siegel, E. (2011). Characterization and Testing of a New Bistatic Profiling Acoustic Doppler Velocimeter: The Vectrino-II. *Proc. IEEE/OES/CWTM 10th Working Conference on Current, Waves and Turbulence Measurement (CWTM),* Monterey, Canada, 246-252.

Dilling, S. & Macvicar, B. (2017). Cleaning High-Frequency Velocity Profile Data with Autoregressive Moving Average (ARMA) Models. *Flow Measurement and Instrumentation,* 54, 68-81.

Goring, D.G. & Nikora, V.I. (2002). Despiking Acoustic Doppler Velocimeter Data. *Journal of Hydraulic Engineering*, ASCE, 128(1), 117-126.

Hornung, H.G., Willert, C. & Turner, S. (1995). The Flow Field Downstream of a Hydraulic Jump. *Journal of Fluid Mechanics*, 287, 299-316.

Koch, C. & Chanson, H. (2005). *An Experimental Study of Tidal Bores and Positive Surges: Hydrodynamics and Turbulence of the Bore Front*, Report No. CH56/05, Dept. of Civil Engineering, The University of Queensland, Brisbane, Australia, July, 170.

Koch, C. & Chanson, H. (2008). Turbulent Mixing Beneath an Undular Bore Front. *Journal of Coastal Research*, 24(4), 999-1007.

Koch, C. & Chanson, H. (2009). Turbulence Measurements in Positive Surges and Bores. *Journal of Hydraulic Research*, IAHR, 47(1), 29-40.

Leng, X. & Chanson, H. (2017a). Integral Turbulent Scales in Unsteady Rapidly Varied Open Channel Flows. *Experimental Thermal and Fluid Science*, 81, 382–395.

Leng, X. & Chanson, H. (2017b). Unsteady Velocity Profiling in Bores and Positive Surges. *Flow Measurement and Instrumentation*, 54, 136-145.

Leng, X. & Chanson, H. (2016a). Coupling between Free-surface Fluctuations, Velocity Fluctuations and Turbulent Reynolds Stresses during the Upstream Propagation of Positive Surges, Bores and Compression Waves. *Environmental Fluid Mechanics*, 16(4), 695-719.

Leng, X. & Chanson, H. (2016b). Unsteady Turbulent Velocity Profiling in Open Channel Flows and Tidal Bores using a Vectrino Profiler. *Hydraulic Model Report No. CH101/15*, School of Civil Engineering, The University of Queensland, Brisbane, Australia, 118 pp.

Macvicar, B., Dilling, S., Lacey, J. & Hipel, K. (2014). A Quality Analysis of The Vectrino II Instrument Using A New Open-source MATLAB Toolbox and 2D ARMA Models to Detect and Replace Spikes. *Proceedings of the 7th International Conference on Fluvial Hydraulics (River Flow)*, Lausanne, Switzerland, 1951-1959.

Nikora, V. (2004). *Personnel Communication on the Suitability of ADV Despiking Techniques in Rapidly-Varied Unsteady Flows*, National Institute of Water and Atmospheric Research. Christchurch, New Zealand.

Nortek. (2012). *Vectrino Profiler: User Guide,* Nortek Scientific Acoustic Development Group Inc., User Manual.

Treske, A. (1994). Undular Bores (Favre-Waves) in Open Channels - Experimental Studies. *Journal of Hydraulic Research*, IAHR, 32(3), 355-370. Discussion: 33 (3), 274-278.

Spiegel, M.R. (1972). *Theory and Problems of Statistics*. *McGraw-Hill Inc.*, New York, USA, 359.

Zedel, L. & Hay, A. (2011). Turbulence Measurements in a Jet: Comparing the Vectrino and Vectrino II. *Proceedings of the IEEE/OES/CWTM 10th Working Conference on Current, Waves and Turbulence Measurements (CWTM)*, Monterey, Canada, 173-178.

HIGH SPATIO-TEMPORAL MEASUREMENTS OF EROSION RATES OF COHESIVE SEDIMENTS USING PHOTOGRAMMETRIC METHODS

MARKUS NOACK(1), GERHARD SCHMID(2), ALINE SCHAEFER RODRIGUES SILVA(3) & SILKE WIEPRECHT(4)

(1,2,3,4) Institute for Modelling Hydraulic and Environmental Systems, Department of Hydraulic Engineering and Water Resources Management, University of Stuttgart, Germany
markus.noack@iws.uni-stuttgart.de; gerhard.schmid@iws.uni-stuttgart.de; aline.schaefer@iws.uni-stuttgart.de; wieprecht@iws.uni-stuttgart.de

ABSTRACT

Knowledge about critical shear stress and erosion rates of cohesive sediments are fundamental to establish a sustainable sediment management in rivers worldwide. However, compared to non-cohesive sediments the incipient motion of cohesive sediments is more complex given the large number of interacting physical, chemical and biological parameters. This article describes a novel method to measure erosion rates in laboratory flumes using photogrammetric methods in a high spatio-temporal resolution. In addition, a Vectrino profiler is applied to account for changes in Reynolds shear stresses given the changing roughness of the sediment surfaces. The results show that the photogrammetric method allows for the detection of minimal erosion volumes of <10 mm³ on a surface of 8000 mm², while the Vectrino profiler proved to be a suitable device considering the influence of roughness on bed shear stresses.

Keywords: Cohesive sediments; critical shear stresses; erosion rates; photogrammetry.

1 INTRODUCTION

The investigation of critical shear stress and erosion rates of cohesive and mixed non-cohesive/cohesive sediments has a long history and is still a challenging research field given to the complex interactions among the involved physical, chemical and biological processes and parameters (e.g. Krone, 1999; Black et al., 2002; Gerbersdorf et al., 2005; Mostafa et al., 2008; Grabowski et al., 2011; Gerbersdorf and Wieprecht, 2015; Noack et al., 2016). In fact, the erosion of cohesive sediments is of high relevance for many hydraulic engineering issues such as sediment management in reservoirs and estuaries, riverbank stability, siltation of harbors and artificial waterways among others (e.g. Zhu et al., 2008). It is due to its complexity that no general analytical theory for the erosion of cohesive sediment has been developed yet. Consequently, field and laboratory experiment are required to investigate the erosion behavior of cohesive sediments (e.g. Black et al., 2002). In principal, the available measurement techniques can be subdivided into *in situ* devices and laboratory experiments. However, both obtained results are often difficult to interpret and compare because of the immense variations of specifically applied devices and the high spatial and temporal variability of field conditions (e.g. Amos et al., 1992; Debnath et al., 2007). In the last decades, different approaches to measure critical shear stress and erosion rates have been conducted using open flumes, closed tunnels or annular flumes (e.g. Aberle, 2008). In order to detect critical shear stresses, usually the discharge is increased in small increments until incipient motion is observed. Subsequently, the critical discharge is assigned to a critical shear stress based on a hydraulic calibration function (Q-τ-relation), which for example can be obtained by previous high-resolution LDA measurements. To derive the erosion rates in laboratory flumes, several methods have been developed. For the 'SEDflume', the erosion volume is recorded over time by the upward movement of a sediment core. Therefore, the operator continuously moves the sediment core in upward direction to level the sediment-water interface with the bottom of the flume (McNeil et al., 1996). Afterwards, the erosion rate is derived by dividing the erosion volume and time. Jacobs et al. (2011) use a sediment trap downstream of the sediment sample to record the erosion volume visually for each discharge step. Subsequently, the total mass is proportionally divided over the steps to obtain an erosion rate. Another commonly used method is the measurement of the suspended sediment flux assuming that the erosion rate is equivalent to the resuspension rate. But several studies have proven that for cohesive/non-cohesive mixtures, bed load is the dominating transport type during the erosion process (e.g. Mitchener and Torfs, 1996; Aberle et al., 2003; Debnath et al., 2007; Righetti and Lucarelli, 2007). However, the detection of erosion volumes has also its limitations. Usually, the monitoring of bed evolution over time implies a change in roughness because the erosion of aggregated sediments leads to a severe structuring of the sediment surface. Correspondingly, the bed shear stress is affected by the change of roughness. Other non-flume based methods are presented in Walder (2015). For example the jet erosion test (JET), (Hanson and Cook, 2004), in which a jet of water is directed normal to the sediment surface and is deflected radially outward resulting in a scouring process or the hole erosion test (HET, (Wan and Fell, 2004), which was developed for purposes of characterizing piping erosion.

At the hydraulic laboratory of the Institute for Modelling Hydraulic and Environmental Systems (IWS), University of Stuttgart, erosion volumes of cohesive sediments and non-cohesive/cohesive sediment mixtures have been investigated in the SETEG-fume (Kern et al., 1999; Noack et al., 2015) for more than 15 years. In the SETEG-flume, the erosion rates have been derived from measured erosion volumes over time using computer-assisted image analyses (SEDCIA, Sediment Erosion Rate Detection by Computerized Image Analysis, (Witt and Westrich, 2003), see also section 2).

In this study, we present significant advancements of the SETEG-flume by: (i) optimizing the monitoring of erosion volumes over time using a photogrammetric method; and (ii) a continuous recording of flow velocity measurements to calculate the Reynolds shear stress over time to account for the effect of changing roughness on bed shear stresses. This allows not only an improved spatio-temporal description of the erosion behavior of cohesive sediments but also the consideration of changing bed shear stress due to varying roughness.

2 METHODS

2.1 The erosion flume at the hydraulic laboratory of IWS (SETEG)

The SETEG-flume consists of a pressurized rectangular flume (length 8.32 m, width 0.145 m, height 0.10 m) which has a test section with an open bottom, through which cylindrical sediment cores (13.5 cm in diameter) can be inserted that are subsequently exposed to the flume’s flow . Thereby, the cores are inserted from below and moved up stepwise by a jack stepping motor, until the core surface is flush with the flume bottom. To detect the critical shear stress, the adjustable discharge is increased continuously until entrainment of sediment particles from the sediment surface can be observed. The resulting critical shear stress is then determined by a hydraulic calibration function (Q-τ-relation), which is obtained by previous high-resolution LDA measurements. For vertical profiles, the measurements are conducted at depth intervals of 1.0 to 5.0 cm. Figure 1 shows a schematic overview of the current SETEG-system.

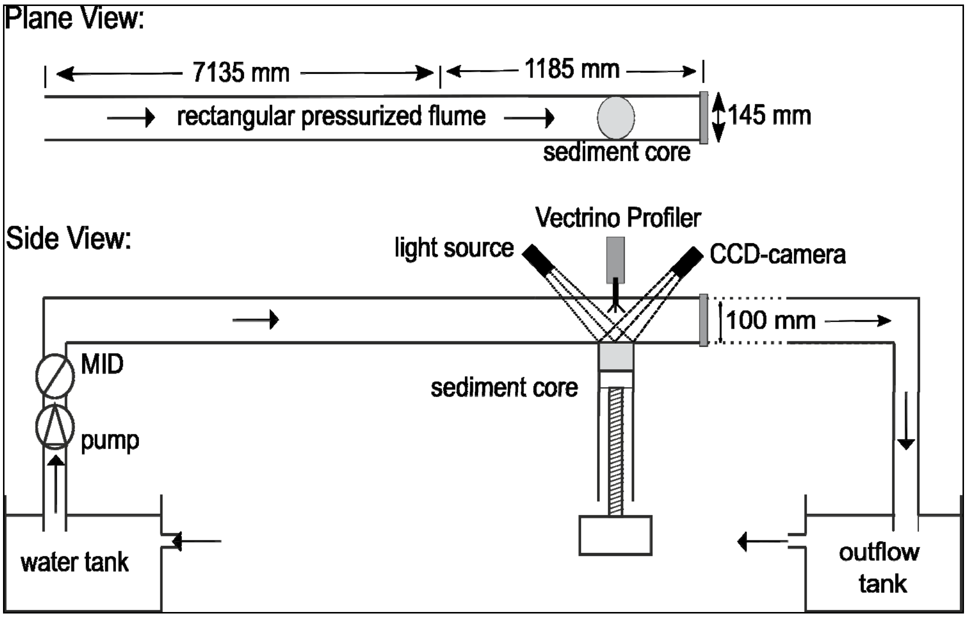

Figure 1. Schematic overview of the SETEG- system to measure depth-dependent critical shear stresses and erosion rates in the hydraulic laboratory of the IWS, University of Stuttgart.

2.2 Measuring of erosion rates

The former applied SEDCIA-method consists of a semiconductor laser (light source) that projects 30 laser lines onto the sediment surface. Those laser lines are continuously photographed by a CCD-camera during the erosion experiments. Using computer-assisted image-analyses of subsequent snapshots, the sediment surface is recalculated by a bilinear interpolation algorithm. Considering the time interval between the two photographs, the eroded volume is determined in relation to time. Hence, the system accounts for both suspended load and bed load in contrast to other approaches that estimate the erosion rate solely by the changes of the suspended load. However, the spatio-temporal resolution of the recordable erosion volumes is limited because of the minimal detectable erosion volume is approx. 40 mm³ on a surface area of 8000 mm². Another limitation is that the SEDCIA-system requires an adequate identification and numerical reproduction

  / ISSN 1562-6865 (Online) - ISSN 1063-7710 (Print)

of the line deviation after the erosion process. Missing parts and inaccurate line reproductions can lead to massive errors in erosion volume detection.

To improve the system, a novel photogrammetric method is developed at the IWS. For this purpose, the SETEG-flume is equipped with a new semiconductor laser as light source, which projects a pseudo-random pattern of 24.000 light points on the sediment surface (approx. 300 points/cm²). To measure erosion volumes, the displacement of each projected light point is analyzed for consecutive time-steps (images) using a dense optical flow algorithm from the OpenCV library (Open Source Computer Vision). The light source is placed above the sediment surface in flow direction in an angle of 35° to a vertical line, while the new CMOS-camera with a temporal resolution of 10 Hz situates is placed in an angle of 35° above the sediment surface in opposite flow direction. Directly above the sediment surface a Vectrino Profiler (NORTEK AS, see section 2.3) is mounted. The comparison of the bed elevations of successive time-steps provides information about the eroded volume and allows the calculation of erosion rates over time. In Figure 2, the different spatial resolution of the SEDCIA-method (A-C) and the new photogrammetric method becomes obvious.

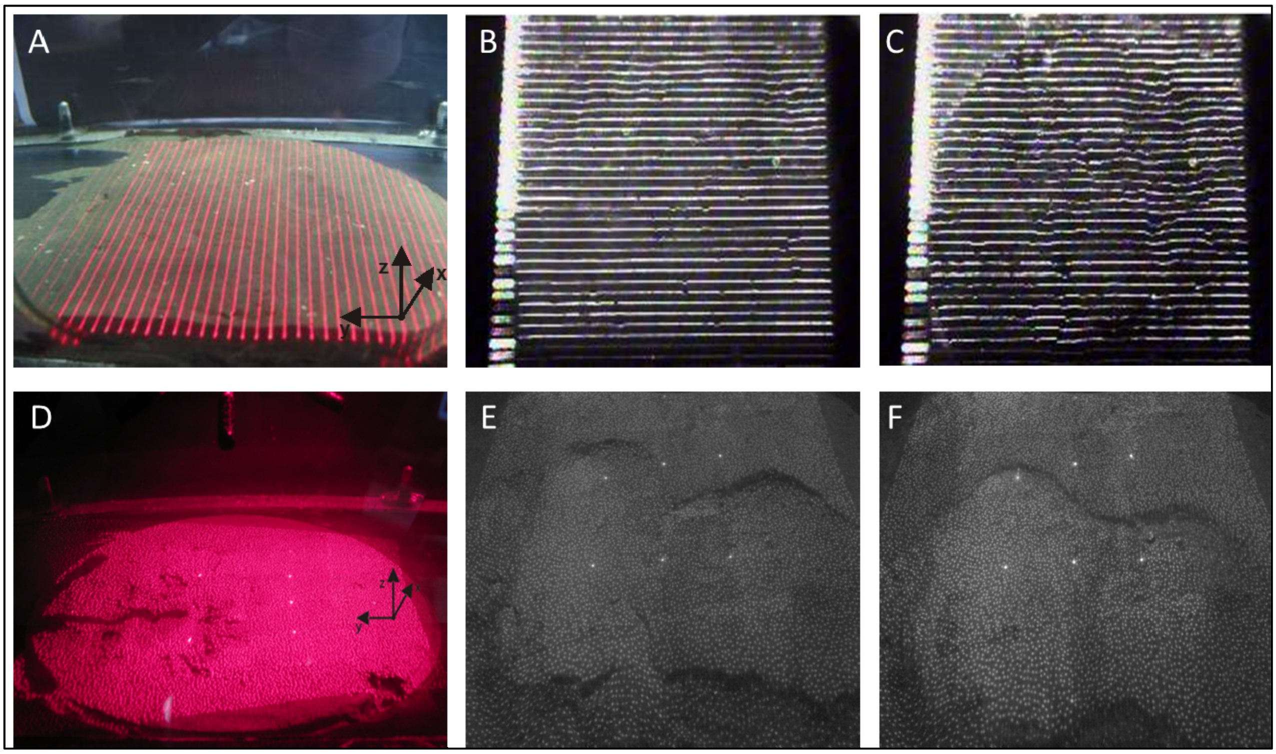

Figure 2. Comparison of the SEDCIA-system (A-C) with the new photogrammetric method (D-F) for the detection of erosion volumes. Figure A shows the projected laser line, while B and C represent images of the CCD camera for two different time steps illustrating the deviation of the parallel laser lines. Figure D depicts the plotted light pattern of the light source, while E and F show the movement of a dune on images of the CMOS-camera (Δt = 20s).

2.3 Measuring the influence of the changing of roughness on bed shear stresses

To measure the effect of an increasing roughness during the erosion process on bed shear stresses, a Vectrino Profiler from NORTEK AS is installed directly above the sediment surface. The Vectrino Profiler is able to measure 3D flow velocities up to 100 Hz with a vertical resolution of Δz = 1.0 mm. The basic measurement principle is coherent Doppler processing. To derive Reynolds shear stresses, a time series of the fluctuating velocity components u' (longitudinal direction) and w' (vertical direction) close to the sediment surface is used. The bed shear stress is then calculated by subtracting the mean values of the velocity components from their instantaneous values and then averaging their product. Because the temporal change of bed shear stress is of interest, the mean values are calculated for different time intervals (Δt = 5, 10, 30s) to investigate the roughness influence on the calculated bed shear stresses. Figure 3 depicts the Vectrino-Profiler above a rough sediment surface with projected light points.

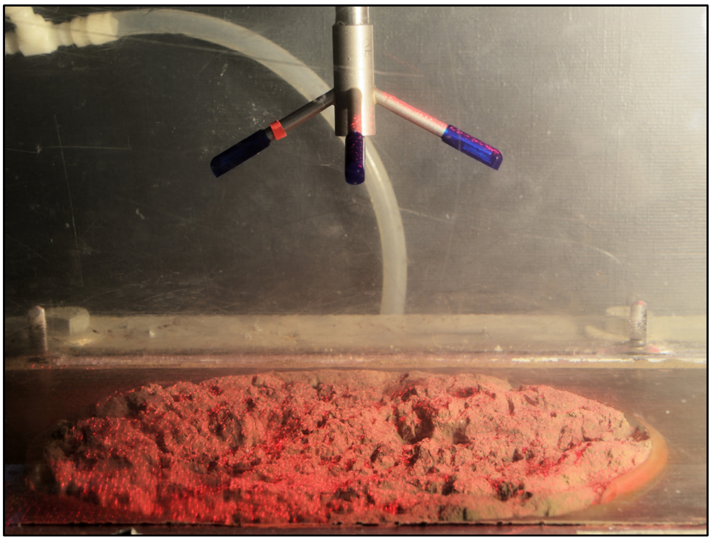

Figure 3. Vectrino-Profiler (NORTEK AS) above a rough sediment surface with projected light pattern from the semiconductor laser (light source).

3 Results and Discussion

3.1 Calibration and preliminary results of the photogrammetric method

Before applying the proposed method on natural sediment surfaces, an in-depth calibration is conducted to get an idea about the accuracy of the volume detection and to investigate minimal and maximal detection volumes. The angled mounting of both the camera and the light source leads to an optical distortion. This effect as well as the refraction indices of the penetrated media (air, water and glass) need to be considered by developing a calibration function. For this purpose, we use a round panel with the diameter of typical sediment cores (13.5 cm) including three areas with adjustable heights and known geometry to relate the results of the photogrammetric method to the known change of surface volumes. The height of the adjustable areas is controlled by screws to allow for the investigation of measurement accuracies for different predefined volumes. The inclination of the screws is 0.5; thus, a full rotation corresponds to a height increase of 0.5 mm. In total, 280 comparable measurements are conducted covering a range of 10 mm³ to 7500 mm³ resulting in a calibration function to transform the photogrammetric volumes with undefined units to metric units.

In Figure 4A, the panel with areas of adjustable heights as well as the projected light points are depicted, while Figure 4B shows the vertical shift of the light pattern to determine the volume change. Figure 4C plots the linear calibration function that relates the photogrammetric volume to the adjusted volumes.

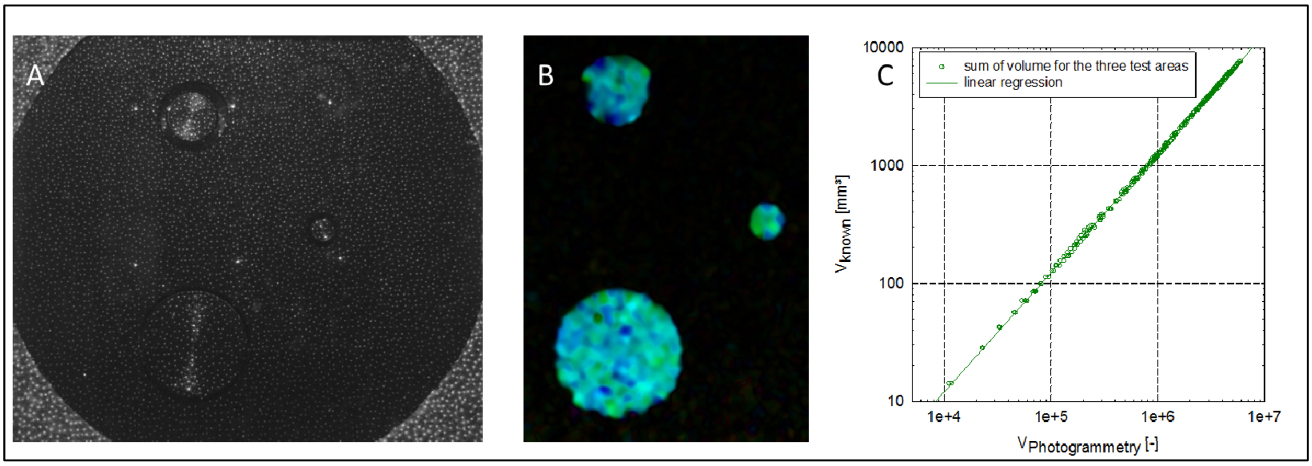

Figure 4. Figure A shows the panel with areas of known geometry and adjustable heights for calibration purposes, while Figure B shows exemplarily a vertical shift of the light points for these areas. Figure C plots the linear calibration function to relate the photogrammetric volume to the known volumes for a range of 10 mm³ to 7500 mm³.

Using the methods described above, Figure 4C outlines the linearity of the calibration curve over three orders of magnitude that proves the high accuracy of the photogrammetric method. The minimum detection limit is less than 10 mm³ for an observation area of about 8000 mm³.

On this basis, first experiments are conducted with real sediments to get an idea about the spatial and temporal erosion behavior using the newly photogrammetric method. Therefore, sandy sediment cores are inserted into the SETEG-flume and the erosion volumes are examined over a time period of 300 s and for five different flow rates (Q = 3, 4, 5, 6, 7 l/s). Figure 5A depicts the temporal resolution of erosion rates over time and Figure 5B represents the spatial resolution for one of these erosion experiments at a discharge of Q = 7 l/s. The blue and green colors indicate a negative vertical shift of the corresponding surface area (erosion) while the yellow and red colors indicate a positive vertical shift of the corresponding surface area (deposition).

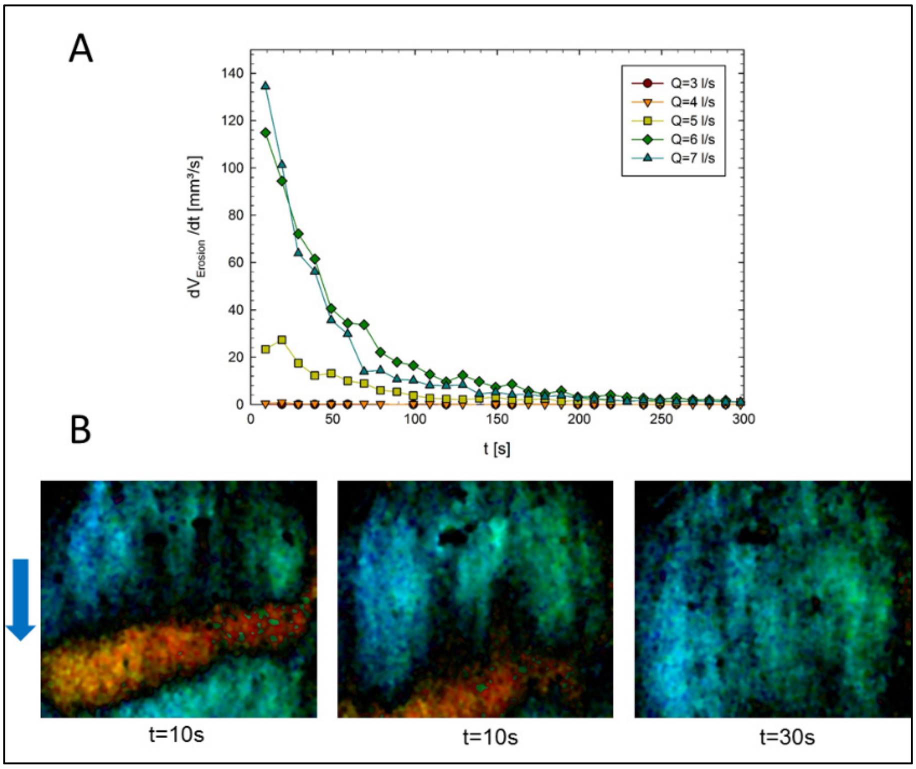

Figure 5. Temporal resolution of erosion volumes for different flow rates (Figure A) and spatial resolution of bed evolutions for three selected time-steps at a constant discharge (Figure B).

In Figure 5A, high erosion rates are indicated at the beginning, but then the bed shear stress exceeds the erosion threshold followed by a continuous decrease of eroded volumes over time until equilibrium conditions are reached. The maximal achievable temporal resolution is governed by the CMOS-camera and allows the assessment of erosion rates at time steps of 0.1 s (10 Hz). Analyzing different time-steps (different consecutive images) proves that, in consideration of the minimal detectable erosion volume, this temporal resolution is sufficient to resolve the erosion behavior (not shown here). Figure 5B shows the erosion and deposition in a spatial resolution of approx. 300 points/cm². Clearly, the formation of a dune is identified in Figure 5B that migrates downstream out of the ROI (region of interest). Compared to the previous method SECDIA the new method is much more robust and not as sensitive to measuring errors because it does not depend on a proper line reproduction after the erosion process. Moreover, in contrast to previous studies, that usually relate measured erosion rates to the entire sediment surface, the high spatio-temporal resolution of the photogrammetric method also allows the observation of incipient motion of single aggregates and thus enables a detailed investigation of the erosion progress.

However, areas with less light point density and even areas with no light points can occur in case of strong erosion events. This can exemplarily be seen in Figure 6B and is caused by the mounting angle of the light source as well as by the mounting angle of the camera, which result in shading effects. Therefore, it is important to notice that the sloped arrangements are necessary to provide sufficient space to place the Vectrino Profiler directly above the sediment surface. The removal of the Vectrino Profiler and centric mounting of the light source above the sediment surface would avoid most of the shading effects. Nevertheless, in this study, the angled mounting of the light source and camera is a compromise to allow the application of both the photogrammetric method as well as the Vectrino Profiler to account for the effect of changing roughness on bed shear stresses during the erosion process.

3.2 Effect of changing roughness on bed shear stress

The erosion process of cohesive sediments or non-cohesive/cohesive mixtures is not homogeneous over the entire surface but highly heterogeneous because of the resuspension of single aggregates as shown in Figure 6A (plane sediment surface at the beginning of the erosion experiment) and Figure 6B (structured surface after erosion). Consequently, the roughness of sediment surfaces is not constant over time but varies according to the structuring of the sediment surface.

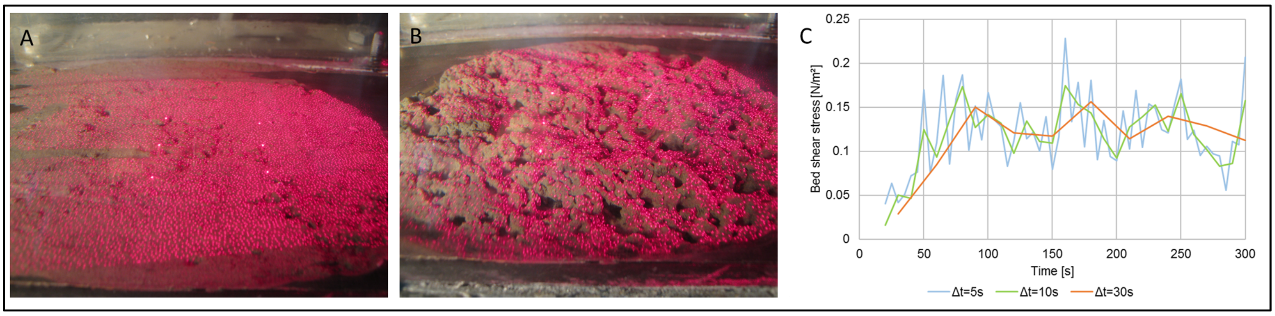

Figure 6. Sediment surface with projected light pattern at the beginning (A) and end during the erosion process (B). C represents exemplarily the measured time-dependent bed shear stresses.

In Figure 6C, the time-dependent Reynolds shear stresses close to the sediment surface are exemplarily shown indicating a constant increase of bed shear stresses until 80 s and a more or less constant trend for the remaining 220 s. The different colored lines represent different time intervals that are chosen to calculate the mean flow velocity which is required to derive Reynold shear stresses. As expected, the fluctuations are higher for the shorter time intervals ($\Delta t = 5$ s) compared to the longer time intervals ($\Delta t = 30$ s). The consideration of varying the roughness is highly relevant because the shear stress is commonly determined by a hydraulic calibration function (Q-τ-relation), which is most often obtained for well-defined surfaces with a constant roughness (e.g. Aberle et al., 2003). In case of varying roughness due to erosion, such calibration functions are not fully valid anymore. Moreover, erosion rates are plotted typically against the bed shear stress or excess shear stress. Measuring the bed shear stress simultaneously to the erosion process allows for an improved and more accurate presentation of such assessments.

However, the Vectrino Profiler allows only for point measurements in the x-y-plane, which represents a small detection area compared to the total observation area. Hence, the change in roughness can only be recorded at a specific point, which not necessarily allows conclusion on the effect of the entire sediment surface or at the exact location where erosion occurs. Nevertheless, the measurements provide helpful information of possible effects of changing roughness on bed shear stresses. Alternatively, the Reynolds shear stress could be measured with a high-frequent and non-intrusive PIV-system (particle image velocimetry) that would additionally allow investigating not only a certain area in the x-y-plane but a horizontal two-dimensional flow field encompassing the entire sediment surface.

4 CONCLUSIONS

In this study, a novel photogrammetric method to detect erosion rates of fine sediments is presented together with simultaneously measured high-frequent flow velocities to derive Reynolds shear stresses close to the sediment surface. The findings show that the photogrammetric method is a robust approach to measure erosion volumes accurately over several orders of magnitudes. In addition, the spatial resolution allows not only the derivation of erosion rates for the entire sediment surface but also for single aggregates that get eroded individually. In addition, the Vectrino Profiler proved to be a suitable device for the detection of Reynolds shear stresses close to the sediment surface. Hence, the time-dependent change of roughness and its subsequent effect on bed shear stresses during the erosion process can directly be considered for subsequent assessments (e.g. erosion rates in dependency of excess shear stress). The advancement of the measurement techniques for the SETEG-flume extend significantly its research possibilities because they allow high-detailed investigation and allow for gaining new knowledge on the phenomenon of erosion of cohesive sediments.

REFERENCES

Aberle, J. (2008). *Measurement Techniques for the Estimation of Cohesive Sediment Erosion, in: Rowiński, Hydraulic Methods for Catastrophes: Floods, Droughts, Environmental Disasters*. E-10. Publications of the Institute of Geophysics, Polish Academy of Sciences, 5–20.

Aberle, J., Nikora, V., McLean, S., Doscher, C., McEwan, I., Green, M., Goring, D. & Walsh, J. (2003). Straight Benthic Flow-through Flume for In Situ Measurement of Cohesive Sediment Dynamics. *Journal of Hydraulic Engineering,* 129, 63–67.

Amos, C.L., Grant, J., Daborn, G.R. & Black, K. (1992). Sea Carousel—A benthic, Annular Flume. Estuarine, *Coastal and Shelf Science*, 34, 557–577.
Black, K.S., Tolhurst, T.J., Paterson, D.M. & Hagerthey, S.E. (2002). Working with Natural Cohesive Sediments. *Journal of Hydraulic Engineering*, 128, 2–8.
Debnath, K., Nikora, V., Aberle, J., Westrich, B. & Muste, M. (2007). Erosion of Cohesive Sediments Resuspension, Bed Load, and Erosion Patterns from Field Experiments. *Journal of Hydraulic Engineering,* 133, 508–520.
Gerbersdorf, S.U., Jancke, T. & Westrich, B. (2005). Physico-Chemical and Biological Sediment Properties Determining Erosion Resistance of Contaminated Riverine Sediments – Temporal and Vertical Pattern at the Lauffen Reservoir/River Neckar, Germany. *Limnologica - Ecology and Management of Inland Waters,* 35, 132–144.
Gerbersdorf, S.U. & Wieprecht, S. (2015). Biostabilization of Cohesive Sediments: Revisiting the Role of Abiotic Conditions, Physiology and Diversity of Microbes, Polymeric Secretion, and Biofilm Architecture. *Geobiology*, 13, 68–97.
Grabowski, R.C., Droppo, I.G. & Wharton, G. (2011). Erodibility of Cohesive Sediment: The Importance of Sediment Properties. *Earth-Science Reviews*, 105, 101–120.
Hanson, G.J. & Cook, K.R. (2004). Apparatus, Test Procedures, and Analytical Methods to Measure Soil Erodibility In Situ. *Applied Engineering in Agriculture*, 20(4), 455-462.
Jacobs, W., Le Hir, P., Van Kesteren, W. & Cann, P. (2011). Erosion Threshold of Sand–Mud Mixtures. Continental Shelf Research, *Proceedings of the 9th International Conference on Nearshore and Estuarine Cohesive Sediment Transport Processes*, 14–25.
Kern, U., Haag, I., Schürlein, V., Holzwarth, M. & Westrich, B. (1999). Ein Strömungskanal zur Ermittlung der tiefenabhängigen Erosionsstabilität von Gewässersedimente. *WasserWirtschaft*, 89, 72–77. (in German)
Krone, R.B. (1999). Effects of Bed Structure on Erosion of Cohesive Sediments. *Journal of Hydraulic Engineering*, 125, 1297–1301.
McNeil, J., Taylor, C. & Lick, W. (1996). Measurements of Erosion of Undisturbed Bottom Sediments with Depth. *Journal of Hydraulic Engineering*, 122, 316–324.
Mitchener, H. & Torfs, H. (1996). Erosion of Mud/Sand Mixtures. *Coastal Engineering*, 29, 1–25.
Mostafa, T.S., Imran, J., Chaudhry, M.H. & Kahn, I.B. (2008). Erosion Resistance of Cohesive Soils. *Journal of Hydraulic Research,* 46, 777–787.
Noack, M., Gerbersdorf, S.U., Hillebrand, G. & Wieprecht, S. (2015). Combining Field and Laboratory Measurements to Determine the Erosion Risk of Cohesive Sediments Best. *Water,* 7, 5061–5077.
Noack, M., Hillebrand, G., Seidenkranz, U. & Wieprecht, S. (2016). Investigation on the Erosion Stability of Cohesive Sediment Deposits in the Weir Channel of the Barrage Iffezheim, River Rhine. *Hydrologie und Wasserbewirtschaftung*, 60, 164–175. (in German)
Righetti, M. & Lucarelli, C. (2007). May the Shields Theory be Extended to Cohesive and Adhesive Benthic Sediments? J*ournal of Geophysical Research (Oceans)*, 112(C5), 1-14.
Walder, J.S. (2015). Dimensionless Erosion Laws for Cohesive Sediment. *Journal of Hydraulic Engineering*, 142(2), 1-13.
Wan, C.F. & Fell, R. (2004). Investigation of Rate of Erosion of Soils in Embankment Dams. *Journal of Geotechnical and Geoenvironmental Engineering*, 130, 373–380.
Witt, O. & Westrich, B. (2003). Qunatification of Erosion Rates for Undistrubed Contaminated Cohesive Sediment Cores by Image Analysis. *Hydrobiologia,* 494, 271–276.
Zhu, Y., Lu, J., Liao, H., Wang, J., Fan, B. & Yao, S. (2008). Research on Cohesive Sediment Erosion by Flow: An Overview. *Science in China Series E: Technological Sciences,* 51(11), 2001-2012.

Proceedings of the 37th IAHR World Congress
August 13 – 18, 2017, Kuala Lumpur, Malaysia

STRUCTURE FROM MOTION IN HYDRAULIC LABORATORIES: TOPOGRAPHICAL SURVEYS USING SUBMERGED IMAGE ACQUISITION

MARKUS NOACK[(1)], RENÉ LORENZ[(2)], GERHARD SCHMID[(3)] & SILKE WIEPRECHT[(4)]

[(1,2,3,4)] Institute for Modelling Hydraulic and Environmental Systems, Department of Hydraulic Engineering and Water Resources Management, University of Stuttgart, Germany
markus.noack@iws.uni-stuttgart.de, rene0202@gmx.net, gerhard.schmid@iws.uni-stuttgart.de, wieprecht@iws.uni-stuttgart.de

ABSTRACT

In experimental research, photogrammetric methods have been successfully used for high-resolution topographic surveys. This study investigates the performance of the fully automated photogrammetric method ‘Structure from Motion’ with ‘Multi-View-Stereo’ (SfM-MVS) for sediment surfaces using dry and submerged image acquisitions. To evaluate the quality of the obtained SfM digital elevation models (DEMs), the DEMs were compared with data from laser profiling and stereo-photogrammetry. The results show that the quality of submerged image acquisition is sufficient to generate highly detailed DEMs of sediment surfaces. Comparing dry and submerged image acquisition yielded a mean absolute deviation of <1.0 mm. In conclusion, the achievable accuracy of topographical measurements for sediment surfaces demonstrated the high potential of SfM-MVS for many applications in hydraulic laboratories.

Keywords: Structure-from-Motion; photogrammetry; topographic surveys; hydraulic laboratory, sediments.

1 INTRODUCTION

High-resolution topographic surveys are fundamental in hydraulic and sedimentary research, both in field surveys and laboratory experiments. Particularly for sediment transport processes with associated assessments of bed level changes, bed roughness, bed forms or bed load transport, accurate digital elevation models (DEMs) allow for detailed investigations of the ongoing morphological processes. For field applications, conventional surveys include terrestrial methods such as total stations and terrestrial laser scanning (TLS) or remote sensing methods such as LiDAR (light detection and ranging). Conventional methods in hydraulic laboratories, on the other hand, comprise mainly the application of laser profilers or ultrasonic sensors that are mounted on automated transversals to measure a predefined rasterized area. Next to the conventional methods, aerial and close-range photogrammetry has emerged in the last decades and is a powerful alternative for three-dimensional topographic modelling (Smith et al., 2015; Eltner et al., 2016). The principal procedure of digital photogrammetry is reviewed in Lane (2000) and solves collinear equations which relate the 2D-coordinates of images to 3D-coordinates of the photographed object (Woodget et al., 2015). Therefore, the internal camera geometry, position and orientation or the exact location of several ground control points need to be known precisely (GCP, Smith et al., 2015).

Structure-from-Motion (SfM) coupled with Multi-View-Stereo (MVS) represents an emerging alternative photogrammetric method using non-metric and low-cost cameras. The general method of SfM-MVS is described in various publications (e.g. Snavely et al., 2007; Westoby et al., 2012; Micheletti et al., 2015) and its merits and limits are reviewed in Eltner et al. (2016). In contrast to conventional stereo-photogrammetric methods, SfM-MVS has a higher level of automation, at lower costs compared to other methods (Javernick et al., 2014). The principle of SfM is to capture images of an object from different positions to obtain overlapping images of the object. Afterwards, these images are processed to calculate the exact camera positions and to reconstruct subsequently a three-dimensional topographic model of this object. The increasing numbers of scientific publications that used SfM-MVS for topographic surveys confirms the rapidly extending SfM-MVS applications. Especially for topographic modelling in the field, SfM-MVS has been widely used and tested (Fonstad et al., 2013; Hugenholtz et al., 2013; Javernick et al., 2014; Mancini et al., 2013; Stumpf et al., 2015; Westoby et al., 2012; Woodget et al., 2015). This has also resulted in recommendations and guidelines for image acquisition and SfM-MVS post-processing (Smith et al., 2015). However, the number of SfM-MVS applications in hydraulic laboratories is significantly less (Kasprak et al., 2015; Wang et al., 2016; Ramos et al., 2016; Morgan et al., 2017) and to the authors knowledge, only the study of Morgan et al. (2017) provide detailed guidelines and recommendation of SfM-MVS applications in laboratories.

Although the quality of DEMs has been significantly increased with respect to spatial resolution and accuracy (Westoby et al., 2012), topographic 3D-modelling remains challenging regarding morphological issues due to inundation and high sediment mobility (Javernick et al., 2014). So far, the feasibility of SfM-MVS for submerged image acquisition and subsequent DEM generation has not been investigated. Woodget at al. (2015) studied the potential of SfM-MVS for submerged fluvial topography but used airborne image acquisition considering a refraction correction. Therefore, the objective of this study is to test SfM-MVS using submerged image acquisition for topographical surveys in hydraulic laboratories.

2 METHODS

Similar to traditional photogrammetry, SfM-MVS depends on overlapping images from multiple viewpoints but internal camera geometry, position and orientation are determined automatically through the identification of matching features in multiple images (Westoby et al., 2012).

In general, the SfM-MVS-technique consists of three main steps. The first step includes the feature detection. Within this step, identical features of multiple individual images, which are captured from multiple views of an object, are detected using the scale invariant feature transform (SIFT; Lowe, 1999). This algorithm identifies features in each image that are invariant to image scaling and rotations as well as to the 3D camera viewpoint. The second step is called the bundle adjustment (Snavely et al., 2007), which derives spatial relationships between the original camera positions and an arbitrary 3D-coordinate system resulting in three-dimensional locations of the previously identified featured points (sparse point cloud). This procedure is fully automated and allows the accurate reconstruction of scene geometry by optimizing geometric and viewing parameters. It does not require 3D location or the orientation of the camera because these parameters are automatically computed. This represents a major advantage of SfM over traditional photogrammetric approaches (Javernick et al., 2014). The last step includes the intensification of the sparse point cloud. In this step, the Clustering View for Multi-view Stereo (CMVS; Furukawa and Ponce, 2007) and Patch-based Multi-view-Stereo (PMVS2) are often applied. The first algorithm (CMVS) derives camera positions using the output of the sparse point cloud and decomposed overlapping images into subsets (clusters) of manageable sizes, while the second algorithm (PMVS2) reconstructs 3-Ddata from these individual clusters. This procedure results in a significantly increased point density (increase of two orders of magnitude) (Westoby et al., 2012).

For this study, an artificial sediment panel with a diameter of 219 mm (see Figure 1A) was created. The round panel consisted of attached particles with different particle sizes that were arranged annularly. The inner circle of sediments consisted of particles with a diameter between 1.0 mm and 1.8 mm, while the outer circle had particle sizes ranging from 5.0 mm to 10.0 mm. The particles between these two circles had diameters ranging from 2.5 mm to 5.6 mm. Figure 1B shows an example of a DEM created with VisualSfM. In contrast to laser-based measuring techniques, SfM-DEMs additionally include color information. In addition, several two-colored columns are mounted on the sediment panel which function as ground control points (GCP) to transform the laser profiling data into a metric scale and to subsequently transform the obtained SfM-DEMs to the this coordinate system as well.

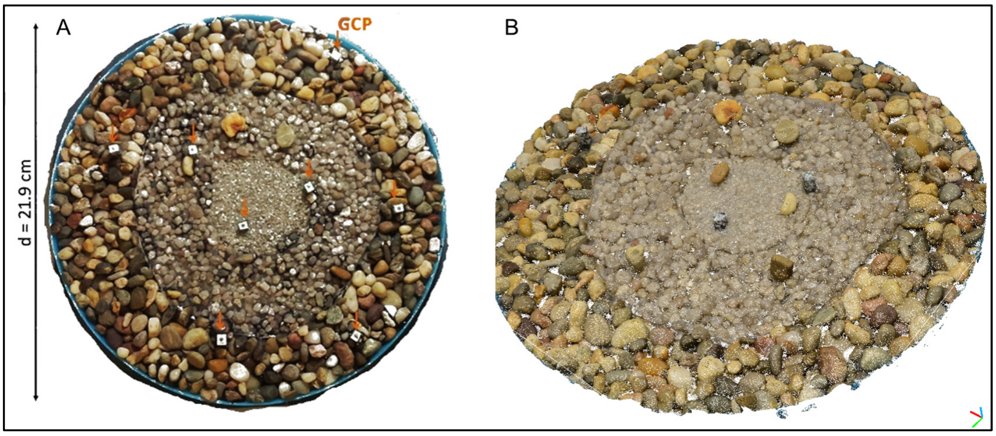

Figure 1. Image of the round sediment panel with three different particle sizes (between 1.0 mm and 10.0 mm) arranged annularly and additional ground control points (Figure A). Example of an unprocessed point cloud obtained by SfM-MVS using images from different camera positions (Figure B).

For this study, the freeware Visual SfM (University of Washington, Seattle) was used for the first two steps: feature detection and sparse point cloud generation. To generate the dense point cloud, the algorithms developed by Jancosek and Pajdla (2011) were applied. Their algorithms (CMPMVS) are particularly beneficial for weakly supported surfaces (e.g. smooth surfaces with low textures), while achieving the same or higher quality on other surfaces. For morphological purposes, this becomes important when working on a particle scale or when smooth and uniformly colored gravels are present.

To obtain reference data for the generated SfM-DEMs, both laser profiling (Pepperl+Fuchs GmbH) as well as stereo-photogrammetry (ENSENSO GmbH) was applied. The laser recorded the height of the sediment panel on an xy- grid with a horizontal resolution of 0.75 mm. This resulted in a raster data set of a total of 64,118 points.

To compare dry and submerged image acquisition, five Raspberry Pi computers with cameras of 5.0 MP resolution were used. In a previous study, the minimal requirements for image acquisition were experimentally investigated and it was found that five cameras, arranged as a ‘five on a dice’ with a 100% overlap, are sufficient to achieve high quality DEMs from sediment surfaces (Noack et al., 2016). The image capturing occured simultaneously, as controlled by a short Python script. All generated SfM-DEMs were compared to the laser profiling and stereo-photogrammetric data using the open source tool Cloud Compare (Version 2.62).

3 RESULTS AND DISCUSSION

Two criteria were used to compare the resulting DEMs generated with SfM-MVS. The first included the number of points obtained from SfM-algorithms, while the second criterion consisted of the distances which describe the closest distance between the mesh from laser data to the mesh generated with SfM. For the deviations of the mean of absolute error, the single standard deviation (68% of all values) and the doubled standard deviation (95% of all values) were calculated to estimate the accuracy of the generated DEMs (Table 1).

As a first result, the DEMs of the sediment panel that were generated with SfM-MVS using dry and submerged image acquisition were compared. Figure 2A illustrates the spatial distribution of deviations while Figure 2B depicts the frequency distribution of the deviations.

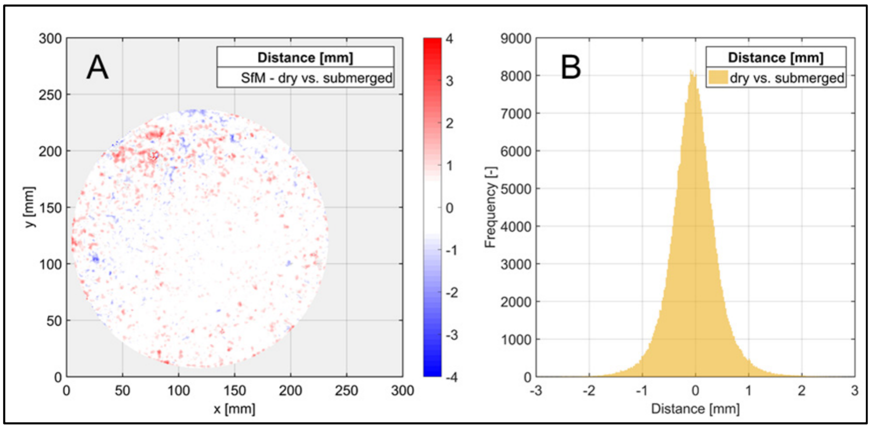

Figure 2. Spatial distribution of deviations between dry and submerged image acquisition using SfM-MVS (Figure A). Frequency distribution of deviations between dry and submerged image acquisition (Figure B).

The spatial distribution of deviations in Figure 2A indicates only minor discrepancies between the DEMs generated with dry and submerged image acquisitions. Only a minor trend towards positive deviations can be identified. The high symmetry and the narrow shape of the histogram in Figure 2B also represent good agreement of both image acquisition techniques. The mean absolute error is 0.33 mm while the standard deviation is 0.45 mm. 95% of all deviations (doubled standard deviation) are smaller than 0.90 mm (Table 1). Accordingly, the image quality of the submerged images is sufficiently high to produce a DEM with the same quality as for dry image acquisition. The DEM with dry image acquisition contains 314,749 points while the DEM with submerged image acquisition consists of 363,210 points. This corresponds to a point density of 837 per cm² for dry image acquisition and 966 points per cm² for submerged image acquisition, since the focal length of the lens and hence the reproduction scale depends on the refraction index of the ambient medium.

However, to ensure that the generated DEMs with SfM-MVS have no methodological error, the SfM-surfaces generated were compared to DEMs that were created with laser profiling and stereo-photogrammetry. Both laser profiling and stereo-photogrammetry were conducted only under dry conditions. Therefore, both image acquisitions for SfM-MVS (dry and submerged) have been compared to the ‘dry’ DEMs of laser profiling and stereo-photogrammetry.

In Figure 3A, the spatial distribution of deviations between the SfM-DEM with dry image acquisition and the laser profiling data is plotted while Figure 3B illustrates the deviations of SfM-DEM with submerged image acquisition to laser profiling data. Figure 3C depicts the frequency distributions of deviations to laser profiling data for both image acquisition techniques.

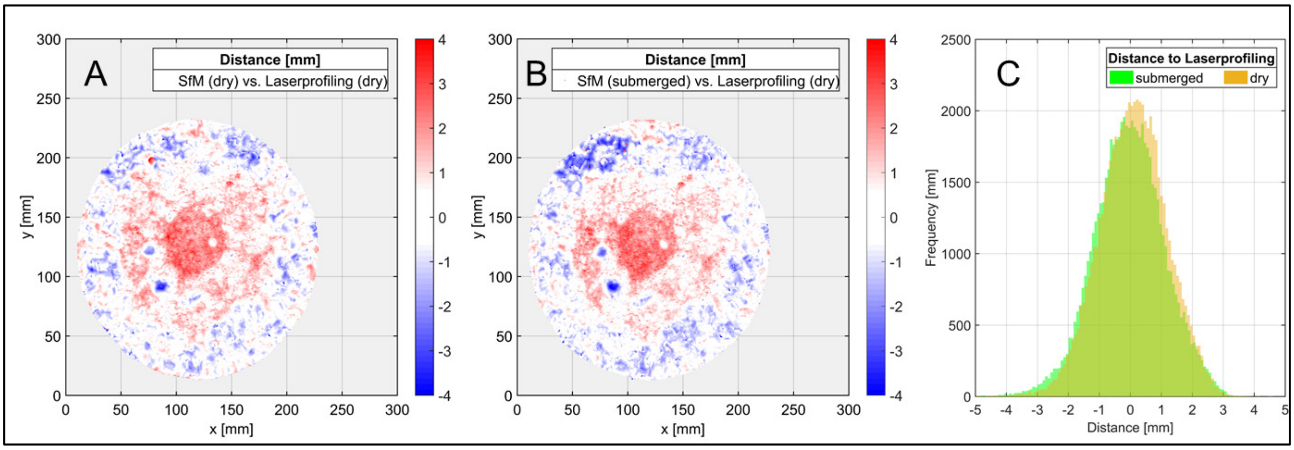

Figure 3. Spatial distribution of deviations between dry image acquisition for SfM-MVS and laser-profiling (dry) (Figure A). Spatial distribution of deviations between submerged image acquisition for SfM-MVS and laser profiling (dry) (Figure B). Frequency distributions of deviations between dry and submerged image acquisition in comparison to laser profiling (Figure C).

Comparing the spatial distribution of deviations for both image acquisition techniques to the data from laser profiling, a similar distribution of the deviations can be observed. However, compared to Figure 2, the deviations are significantly higher. The mean absolute error is 0.86 mm for the DEM with dry image acquisition while it is 0.89 mm for the DEM with submerged image acquisition. The doubled standard deviation is 2.15 mm for the DEM with dry image acquisition and 2.27 mm for the DEM with submerged image acquisition (Table 1). The relative deviation between both image acquisition techniques is, however, very low (0.03 mm for the mean absolute error).

It is important to note that the laser profiling data consist of fewer points (64,118) compared to the DEM of SfM-MVS (> 300,000) and that the laser measures only in the vertical direction. Moreover, the dimensions of the laser spot are 0.8 x 3.0 mm. This leads to problems on particle edges, when the laser spot covers partly more than one particle or a high elevation gradient. Naturally, this is more relevant for smaller particle sizes than for larger particle sizes. This is also the reason for the highest deviations at the inner circle of the sediment panel, which represents the smallest particle sizes. Therefore, it is not possible to state explicitly which method is more accurate, but it can be concluded that the deviations are not caused by the different image acquisition techniques. Given the higher point density and the possibility to use angled camera positions in the SfM-MVS technique, it can be assumed that the deviations are caused by limitations of the laser-based measuring technique itself.

To verify this assumption, the generated DEMs with SfM-MVS were additionally compared to a DEM that was generated using stereo-photogrammetric data. In Figure 4A, the spatial distribution of deviations between the SfM-DEM with dry image acquisition and the stereo-photogrammetric data is plotted while Figure 4B illustrates the deviations between the SfM-DEM with submerged image acquisition and the stereo-photogrammetric data. Figure 4C depicts the frequency distributions of deviations to stereo-photogrammetric data for both image acquisition techniques.

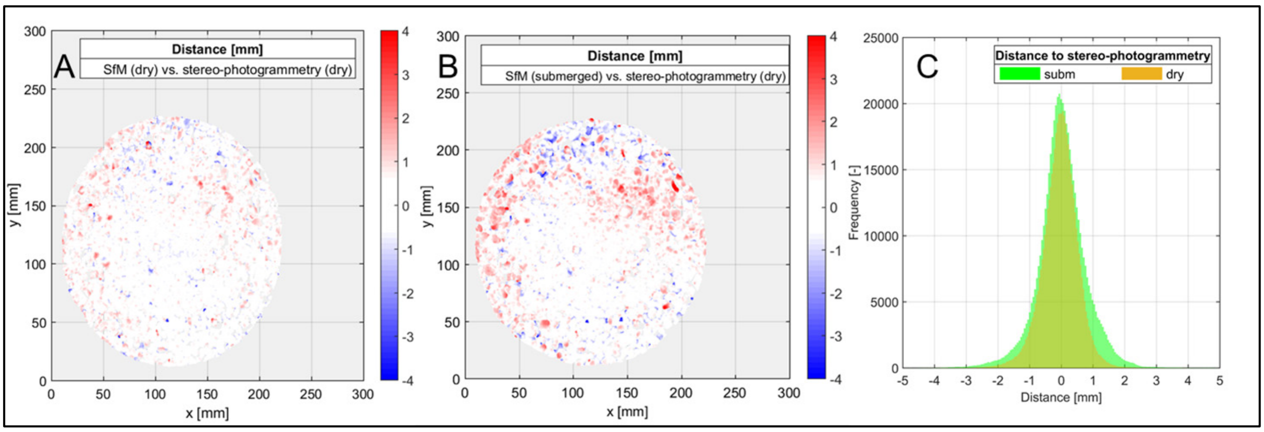

Figure 4. Spatial distribution of deviations between dry image acquisition for SfM-MVS and stereo-photogrammetry (dry) (Figure A). Spatial distribution of deviations between submerged image acquisition for SfM-MVS and stereo-photogrammetry (dry) (Figure B). Frequency distributions of deviations between dry and submerged image acquisition in comparison to stereo-photogrammetry (Figure C).

The visual comparison of the spatial distributions of deviations between SfM-MVS and stereo-photogrammetry shows two aspects (Figure 4A): First, the deviations are higher compared to Figure 2A and less compared to the laser profiling data (Figure 3A). Second, the deviations of the SfM-models with submerged image acquisition are higher compared to the DEM with dry image acquisition. The mean absolute error is 0.42 mm for the DEM with dry image acquisition, while it is 0.55 mm for the DEM with submerged image acquisition. The doubled standard deviation is 1.13 mm for the DEM with dry image acquisition and 1.52 mm for the DEM with submerged image acquisition (Table 1). Hence, the deviations are closer to the deviations obtained from comparing SfM-models with dry and submerged image acquisition. Moreover, the number of points (SfM-MVS: > 300,000; stereo-photogrammetry: > 530,000) are in a similar order of magnitude and are both considerably higher compared to the data from laser profiling (64,118). Therefore, this investigation supports the assumption that the higher deviations obtained from the comparison to laser profiling data is due to the limitations of DEM generation with laser profiling data (point density, vertical detection, dimensions of laser spot). The deviations for all conducted comparison between SfM-MVS and laser profiling as well as stereo-photogrammetry are summarized in Table 1.

Table 1. Overview of deviations of generated DEMs using SFM-MVS (dry and submerged image acquisitions), laser profiling and stereo-photogrammetry.

	SfM comparison	SfM vs. laser-profiling		SfM vs. stereo-photogrammetry	
	dry vs. submerged	dry	submerged	dry	submerged
mean absolute error (MAE) [mm]	0.33	0.86	0.89	0.42	0.55
standard deviation (68%) [mm]	0.45	1.07	1.13	0.57	0.76
doubled standard deviation (95%) [mm]	0.90	2.15	2.27	1.13	1.52

4 CONCLUSIONS

In this study, the effect of dry and submerged image acquisition on the accuracy of DEMs using the photogrammetric technique ‘structure from motion’ was investigated. Different SfM-DEMs were compared based on point numbers and their deviations to alternative measuring techniques such as laser profiling and stereo-photogrammetry.

The comparison of SfM-DEMs using dry and submerged image acquisition revealed only marginal differences (mean absolute error of 0.33 mm). This verifies that the image quality of submerged images is sufficient to produce high-resolution DEMs (in cases of low turbidity). The comparison to DEMs based on laser profiling showed higher deviations for both dry and submerged image acquisition. However, the mean absolute error is smaller than 1.0 mm. Moreover, the reliability of the laser profiling data is also limited by a lower spatial resolution and topographical features that are smaller than the diameter of the laser spot cannot be correctly recognized. The comparison to the DEMs based on stereo-photogrammetry indicates smaller deviations (mean absolute error of 0.45 mm and 0.55 mm) than the comparison to laser profiling data, which verifies the limitations of the laser profiling method.

The results of this study indicate that the high spatial resolution of DEMs generated with the SfM-MVS-technique may be used for many topographical surveys in hydraulic laboratories, such as the determination of sediment transport rates based on topographical measurements, transport of bed forms (dune migration) or for roughness determination.

REFERENCES

Eltner, A., Kaiser, A., Castillo, C., Rock, G., Neugirg, F. & Abellán, A. (2016). Image-Based Surface Reconstruction in Geomorphometry & Ndash; Merits, Limits and Developments. *Earth Surface Dynamics,* 4, 359-389.

Fonstad, M.A., Dietrich, J.T., Courville, B.C., Jensen, J.L. & Carbonneau, P.E. (2013). Topographic Structure from Motion: A New Development in Photogrammetric Measurement. *Earth Surface Process. Landforms,* 38, 421-430.

Furukawa, Y. & Ponce, J. (2007). Accurate, Dense, and Robust Multi-View Stereopsis, *IEEE Conference on Computer Vision and Pattern Recognition*, 2007. 1-8.

Hugenholtz, C.H., Whitehead, K., Brown, O.W., Barchyn, T.E., Moorman, B.J., LeClair, A., Riddell, K. & Hamilton, T. (2013). Geomorphological Mapping with a Small Unmanned Aircraft System (Suas): Feature Detection and Accuracy Assessment of a Photogrammetrically-Derived Digital Terrain Model. *Geomorphology,* 194, 16–24.

Jancosek, M. & Pajdla, T. (2011). Multi-View Reconstruction Preserving Weakly-Supported Surfaces, *Computer Vision and Pattern Recognition (CVPR)*, 3121–3128.

Javernick, L., Brasington, J. & Caruso, B. (2014). Modeling the Topography of Shallow Braided Rivers using Structure-from-Motion Photogrammetry. *Geomorphology,* 213, 166-182.

Kasprak, A., Wheaton, J.M., Ashmore, P.E., Hensleigh, J.W. & Peirce, S. (2015). The Relationship between Particle Travel Distance and Channel Morphology: Results from Physical Models of Braided Rivers. *Journal of Geophysical Research: Earth Surface*, 120(1), 55-74

Lane, S.N. (2000). The Measurement of River Channel Morphology Using Digital Photogrammetry. *The Photogrammetric Record*, 16, 937-961.

Mancini, F., Dubbini, M., Gattelli, M., Stecchi, F., Fabbri, S. & Gabbianelli, G. (2013). Using Unmanned Aerial Vehicles (UAV) for High-Resolution Reconstruction of Topography: The Structure from Motion Approach on Coastal Environments. *Remote Sensing*, 5, 6880–6898.

Micheletti, N., Chandler, J.H. & Lane, S.N. (2015). *Structure from Motion (SfM) Photogrammetry. In: Cook, S.J., Clarke, L.E. & Nield, J.M. (Eds) Geomorphological Techniques (Online Edition).* London, UK: British Society for Geomorphology.

Morgan, J.A., Brogan, D.J. & Nelson, P.A. (2017). Application of Structure-from-Motion Photogrammetry in Laboratory Flumes. *Geomorphology,* 276, 125-143.

Noack, M., Schmid, G., Thom, M. & Wieprecht, S. (2016). Testing “Structure-from-Motion” Photogrammetry for High-Resolution Topographic Surveys in Hydraulic Laboratories. *Conference Proceedings of 8th International Conference on Fluvial Hydraulics*, CRC Press, St. Louis, USA, 630-635.

Smith, M.W., Carrivick, J.L. & Quincey, D.J. (2015). Structure from Motion Photogrammetry in Physical Geography. P*rogress in Physical Geography*, 40, 247-275.

Snavely, N., Seitz, S.M. & Szeliski, R. (2007). Modeling the World from Internet Photo Collections. *International Journal of Computer Vision*, 80, 189–210.

Stumpf, A., Malet, J.-P., Allemand, P., Pierrot-Deseilligny, M. & Skupinski, G. (2015). Ground-Based Multi-View Photogrammetry for the Monitoring of Landslide Deformation and Erosion. *Geomorphology,* 231, 130-145.

Wang, C., Wang, Q., Meire, D., Ma, W., Wu, C., Meng, Z., Van de Koppel, J., Troch, P., Verhoeven, R., De Mulder, T. & Temmerman, S. (2016). Biogeomorphic Feedback between Plant Growth and Flooding Causes Alternative Stable States in an Experimental Floodplain. *Advances in Water Resources,* 93, 223-235.

Westoby, M.J., Brasington, J., Glasser, N.F., Hambrey, M.J. & Reynolds, J.M. (2012). “Structure-from-Motion” Photogrammetry: A low-cost, Effective Tool for Geoscience Applications. *Geomorphology,* 179, 300-314.

Woodget, A.S., Carbonneau, P.E., Visser, F. & Maddock, I.P. (2015). Quantifying Submerged Fluvial Topography using Hyperspatial Resolution UAS Imagery and Structure from Motion Photogrammetry: Submerged Fluvial Topography from UAS Imagery and Sfm. *Earth Surface Processes and Landforms,* 40, 47-64.

Proceedings of the 37th IAHR World Congress
August 13 – 18, 2017, Kuala Lumpur, Malaysia

A NOVEL HYDRO-ACOUSTIC SYSTEM FOR AUTOMATICALLY, PERMANENTLY COLLECTING REAL-TIME RIVER FLOW DATA

KIYOSI KAWANISI [1] & MOHAMAD BASEL AL SAWAF [2]

[1,2] Dept. of Civil and Environmental Engineering, Institute of Engineering, Hiroshima University, Higashi Hiroshima, Japan,
kiyosi@hiroshima-u.ac.jp; mbalsawaf@gmail.com

ABSTRACT

This study demonstrates the fluvial acoustic tomography system (FATS), a promising approach for measuring streamflow with high sampling rate for a long period. Unlike traditional point/transect measurements of discharge, FATS enables measurements of the depth- and range-averaged flow velocity along the ray path in a fraction of a second. FATS with an automatic data transfer function and internet connection allows one to automatically obtain real-time flow data. Streamflow measurements were performed on November 26, 2015, in a shallow gravel-bed river (depth: 0.8 m, width: 110 m under low-flow conditions). This paper presents a 258-day record of the flow. The mean water depth along the transmission line ranged from 0.8 to 3.7 m and the FATS streamflow estimate ranged from 15 to 580 m^3/s during the observation period. The FATS record showed temporal discharge changes at multiple time scales ranging from a few tens of minutes to the order of days. The continuous FATS estimates indicate that the streamflow does not change smoothly with the river stage. Although the “true” value of streamflow is not known, 77% of the relative differences between FATS and RC estimates are within ±10% under the flow condition $(50 \leq Q \leq 350\ \mathrm{m}^3/\mathrm{s})$.

Keywords: Streamflow; acoustic tomography; shallow flow; gravel-bed river; mountainous river.

1 INTRODUCTION

Acquiring continuous streamflow is crucial in hydrological studies, extreme event analyses, water resources management. In addition, the real-time knowledge of river discharge is an environmental, social, and economic asset. Therefore, various techniques and instruments have been developed to improve streamflow measurements.

The streamflow is commonly estimated using stage-discharge relations. The relation is called rating curve (RC). Because the RCs are liable to change depending on channel conditions such as cross-sectional shape, vegetation, and so on, the frequent direct discharge measurements that are expensive and pass through many hands, are needed to keep the accuracy of the discharge data.

Several hydro-acoustic instruments are available for the continuous measurement of water discharge, such as acoustic velocity meters (AVMs) (Laenen and Smith, 1983) and horizontal acoustic Doppler current profilers (H-ADCPs) (Le Coz et al., 2008). However, these also have many limitations (Kawanisi et al., 2012). These methods require several hydraulic parameters, which must be deduced from labor-intensive moving-boat ADCP measurements.

The purpose of this study is to demonstrate the feasibility of monitoring streamflow using new Fluvial Acoustic Tomography system (FATS) (Kawanisi et al., 2012; Kawanisi et al., 2010). The FATS is a promising system for permanent gauging river at a high sampling rate; flow data are collected at intervals of 30 s typically. An automatic data transfer function and internet connection make FATS more practical. It allows to automatically obtain real-time flow data and monitor the system’s conditions. The FATS is deployed in a shallow gravel-bed river (water depth 0.8 m, width 110 m under low-flow conditions). This paper presents a 258-day record of the flow data.

2 METHODOLOGY

2.1 Field site

The riverine surveys were carried out in a straight reach of the Gono River in Japan. The Gono River is a shallow gravel-bed river (depth: 0.8 m, width: 110 m under low-flow conditions). The catchment area is 3900 km^2. The bed slope around the observation site was 0.11%, and the Manning roughness estimated from the water surface profile was approximately 0.03. The grain size distribution at the observation site indicates an average median size (d50) of 27 mm and an average d90 of 115 mm. As shown in Figure 1, the main tributaries of the Gono River (the Saijo River and Basen River) meet the Gono River ~3.6-km upstream of the survey site. The Ozekiyama gauging station of “Ministry of Land, Infrastructure, Transport and Tourism, Japan" is located ~1.1 km upstream of the survey site. The minimum water depth around the transducer was mere 0.2 m under low flows.

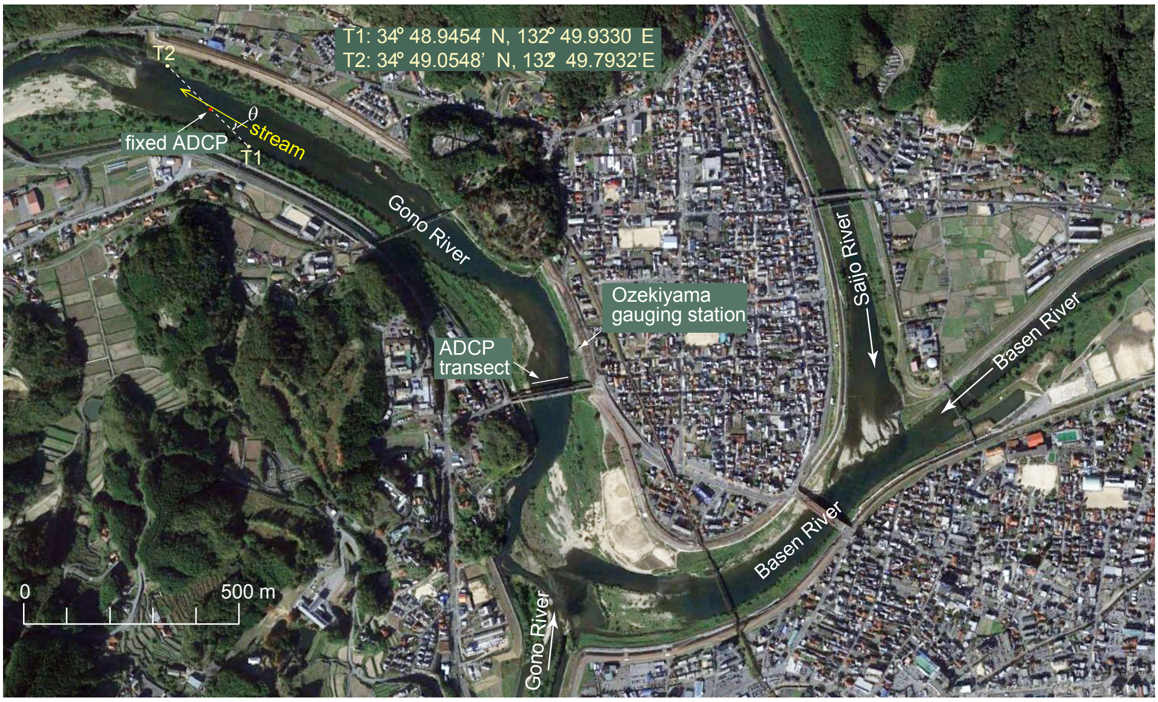

Figure 1. Gono River network and the deployments of the instruments.

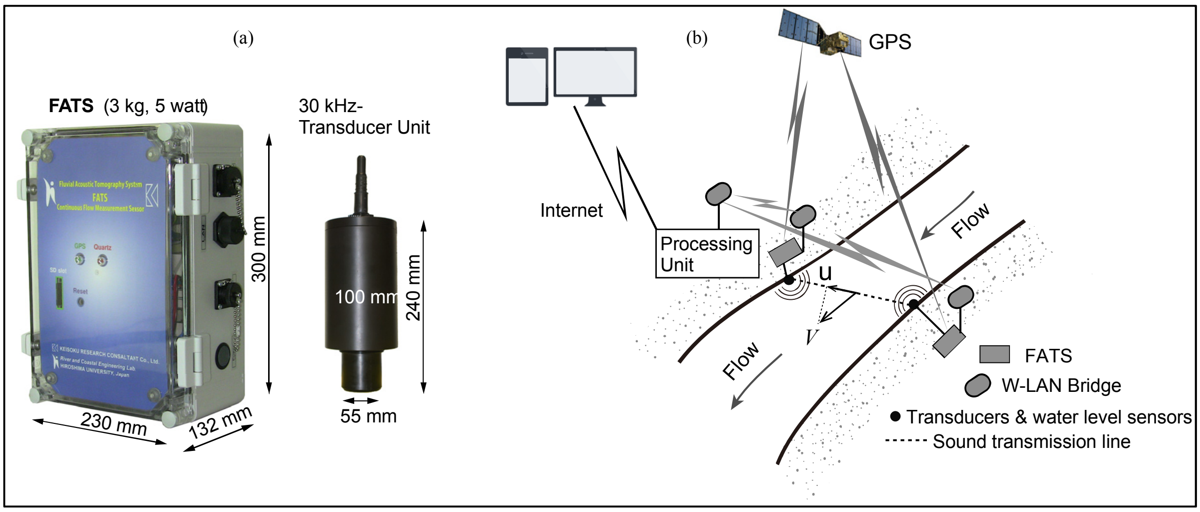

Figure 2. Fluvial acoustic tomography system (FATS) and schematic illustration of gauging station.

2.2 Fluvial acoustic tomography system (FATS) and its deployment

The FATS continuously measures reciprocal travel times in shallow waters using acoustic waves that are emitted from omnidirectional transducers in the range of 10–50 kHz. The phase of the transmitting signal is modulated by the M-sequence (maximum length sequence) (Simon et al., 1985). Although the range averaged velocity is measured using the "time-of-travel method" (Laenen and Smith, 1983), FATS utilizes the multi-ray throughout the cross section to estimate the cross-sectional averaged velocity (Kawanisi et al., 2012). The sound rays of FATS instantly cover the entire cross section of a river. As a result, FATS can gauge the instantaneous discharge continuously. FATS is small, lightweight and low power consumption (Figure 2a).

The cross-sectional average velocity and streamflow was continuously measured using the FATS during 258 days (26 Nov. 2015 to 10 August 2016). Two omnidirectional broadband transducers (T257, Neptune Sonar Ltd.) were installed diagonally across the river with a horizontal distance of 294 m between them (T1 and T2) as shown in Figure 1. Figure 3 presents a view from T1. In unidirectional flows, measuring only one component of the velocity would be adequate to estimate streamflow reliably. The acoustic pulses modulated by 9th order M-sequence were triggered by the 1 Hz timing pulse from the GPS and were transmitted simultaneously from both transducers every 30 s. The central frequency of the transducers was set to 30 kHz.

The water levels at both acoustic stations were also measured every 30 s using water level sensors with the internet connection.

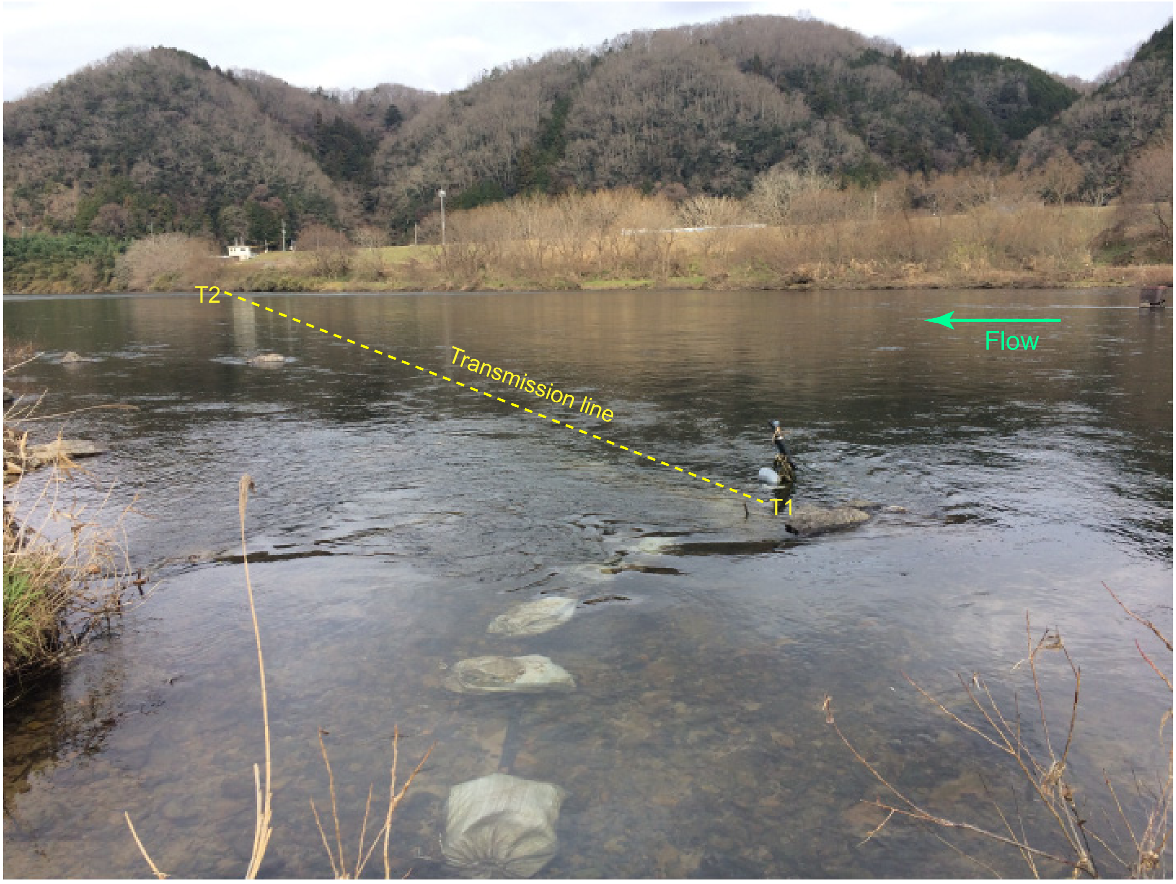

Figure 3. View from the left transducer T1.

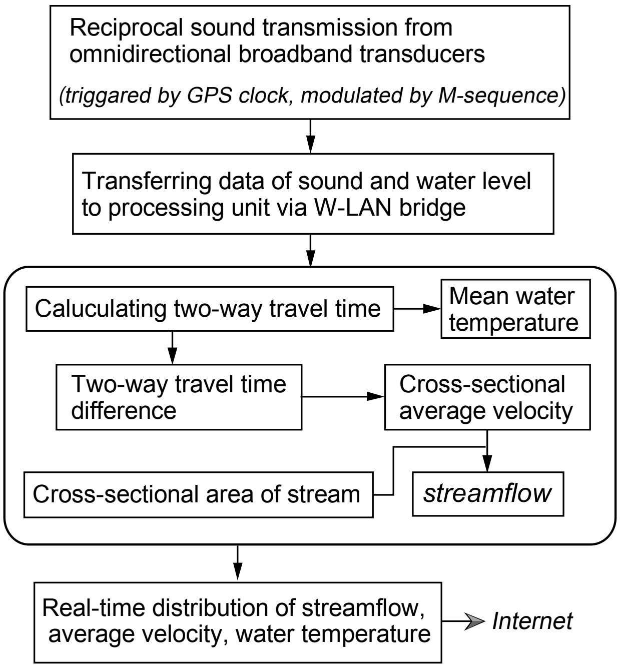

Figure 4. Flowchart of the data processing of FATS.

FAT systems are currently equipped with GPS receivers that provide two accurate timing signals. One timing pulse (1 Hz) is used to ensure that both systems run absolutely synchronously. Another signal of 10 MHz, which has excellent long-term frequency accuracy and stability, is used as the base clock of FATS for high-precision transmitting/receiving signal processing. Besides, an automatic data transfer function and internet connection are added for the automated real-time acquisition of flow data (Figure 2b). Water level sensors are also connected to the processing unit of FATS to estimate the cross-sectional area of stream. Thus, streamflow data can be automatically collected at a high temporal resolution (every several minutes) for long periods. Figure 4 shows the flowchart of the data processing.

FATS can deal with various hydrological issues and problems that can be considered a promising technology in the field of water resources. For example, a promising application of FATS is to deploy an array of acoustic stations using different M-sequence codes and to reconstruct a depth-averaged flow velocity distribution pattern using inversion schemes (Razaz et al., 2015).

2.3 ADCP campaigns

To obtain reference discharge data, 25 streamflow estimates were collected using a moving-boat ADCP during July 2015 to March 2016. The discharges ranged from 23.60 m^3/s to 726.55 m^3/s. Each streamflow was estimated from 2–4 transects at the Ozekiyama gauging station. The ADCP measurements were performed using a Teledyne RDI StreamPro ADCP (2457.6 kHz) or a WH-Monitor ADCP (1228.8 kHz). Either ADCP was selected depending on the water level at the Ozekiyama gauging station. Specifically, the WH-Monitor ADCP was used for the water levels exceeding 147.2 m above mean sea level (m a.s.l.) because it did not work in shallow water conditions owing to weak backscattering in clear water. The discharge at the water level of 147.2 m a.s.l. was around 100 m^3/s.

Each transect extended from the immediate left shore and ended 8 m from the right shore. The edge type was set to rectangular. The float speed was maintained at ~0.2 m/s. Consequently, a crossing took ~9 min. The relative velocity between the ADCP and the bottom of the stream was estimated by ADCP bottom tracking. The moving bed effects on the bottom tracking was not observed because of the large bed constituent material (Kawanisi et al., 2012).

The StreamPro ADCP was deployed in shallow water conditions at water mode 12; the cell depth was 0.1 m, and the depth of the first cell was 0.19 m. The WH-monitor ADCP was configured as follows: water mode 1, cell size = 0.25 m, and first cell depth = 0.68 m.

3 RESULTS

3.1 Bottom topography

In the present study, the bed level between both transducers was directly measured using an unmanned autonomous boat with a single-beam echo-sounder and a GPS on December 25, 2015. The vertical resolution of the echo-sounder was 0.01 m. The horizontal interval changed between 0.9 and 10 m along the transmission line; 68% of the interval was less than or equal to 2 m.

The soundings along the transmission line are shown by red dots in Figure 5. There is a thalweg around 200 m from the left transducer. This bottom topography was used to calculate the cross-section area of stream.

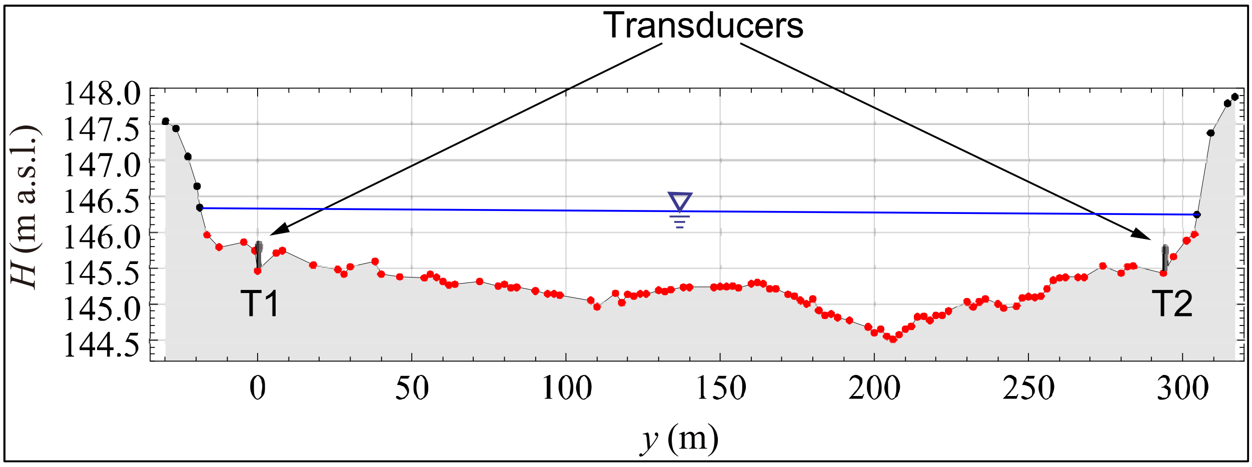

Figure 5. Oblique cross-section and deployment of the transducers.

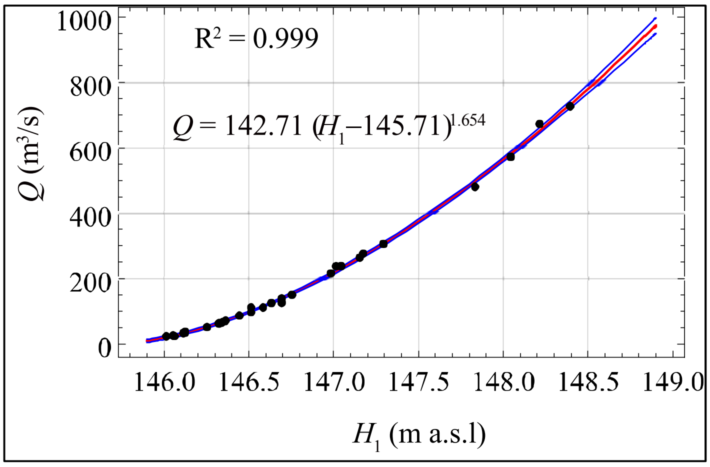

Figure 6. Rating curve established by moving-boat ADCP measurements.

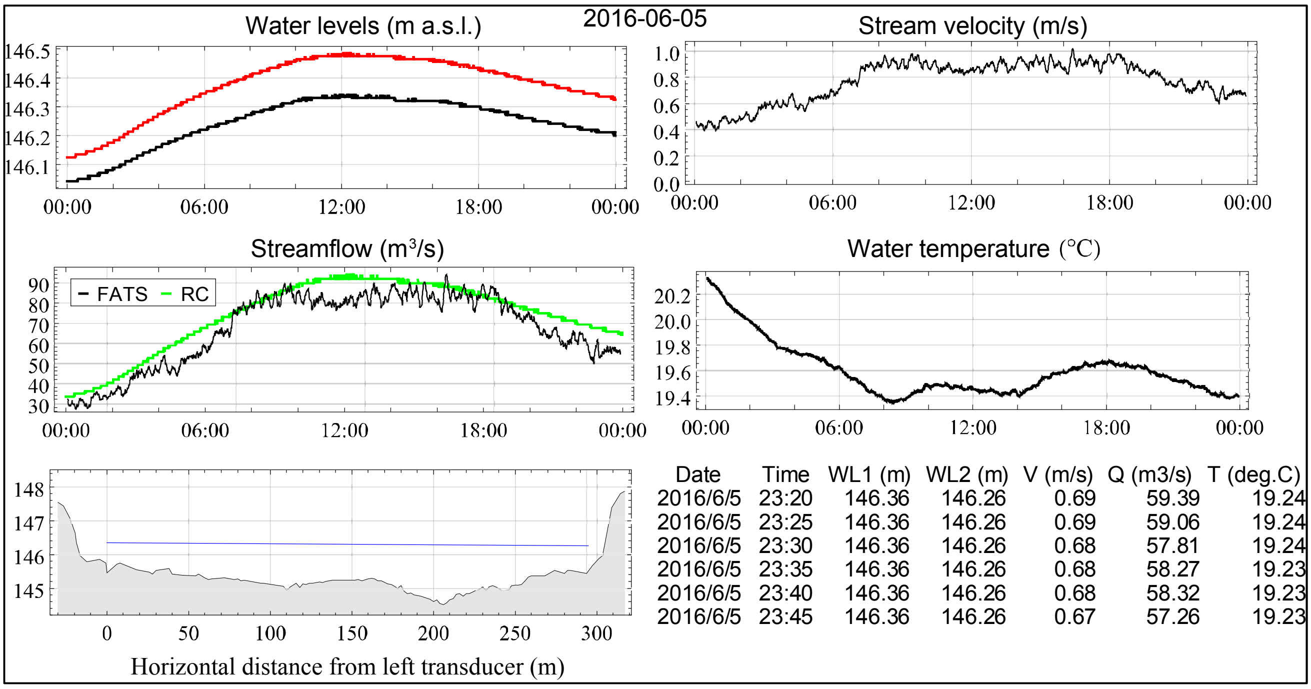

Figure 7. Real-time distribution of FATS estimates.

3.2 Rating curve

A rating curve (RC) expressed by Eq. [1] was established using streamflow estimates measured by moving-boat ADCPs. The results is shown in Figure 6. The RC is given as

$$Q = 142.706\left(H_1 - 145.708\right)^{1.6544} \qquad [1]$$

where H_1 is the water level at the left transducer (T1). The blue lines in Figure 6 show mean prediction bands of 95% confidence level. Although the determined coefficient of fitting is substantially high (R2 = 0.999), the relative residuals exceeded the ±10% band.

3.3 Real-time distribution of FATS estimates

FATS automatically estimate the real-time cross-sectional averaged velocity, water temperature and streamflow. These FATS estimate are concurrently displayed with the water levels by the processing unit.

Figure 7 shows a typical real-time distribution from the processing unit of FATS. The red and black lines in the top left plot denote the water levels at the locations of both transducers. The green line in the streamflow plot denotes the RC estimate using Eq. [1]. The time interval of each time series is 5 min. The plots are updated every ten minutes. The blue line shown in the bottom left plot denotes the latest water surface between the transducers (T1, T2).

As shown in the streamflow plots, the continuous FATS estimate reveals that the streamflow does not change smoothly with the river stage.

3.4 Temporal variations in FATS estimates

Fig. 8(a) and (b) show the water level at the location of the left transducer (T1) and the mean water depth (h_m) at the FATS observation site, respectively. A couple of spikes observed on March 25 and 26 were due to flushes of dams. The mean water depth ranges from 0.8 to 3.7 m during the observation period. The velocity resolution of FATS is improved with the acoustic path length and frequency (Kawanisi et al., 2012). In this study, a single measurement has the relatively low velocity resolution $(\approx 0.058\ \mathrm{m/s})$. Therefore, in this study, 20 samples were averaged. As a result, the uncertainty can be reduced to $0.058/\sqrt{20} = 0.012\ \mathrm{m/s}$. Because the measurement interval is 30 s, averaging 20 samples corresponds to an average of 10 min.

There are a few short missing periods in the FATS measurement. The missing interval on January 22–27 was caused by the interrupt of saving data on the memory card of FATS. Unfortunately, FATS was not able to measure the flood peak on June 23 because the flood flow damaged the cable of left transducer. The abeyance during 2–4 July was due to a failure of power supply.

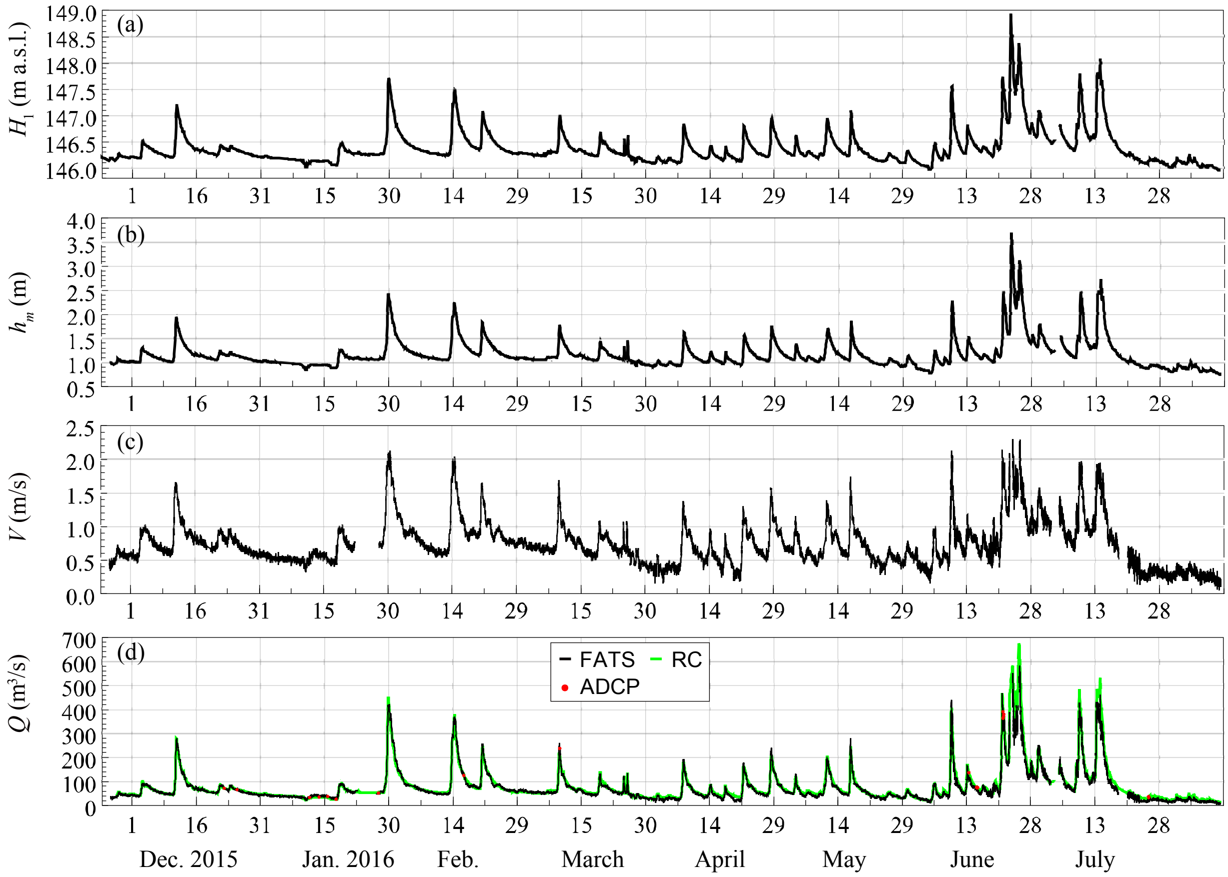

Figure 8. Temporal variations in (a) water level at T1, (b) mean water depth, (c) cross-sectional averaged velocity and (d) streamflows.

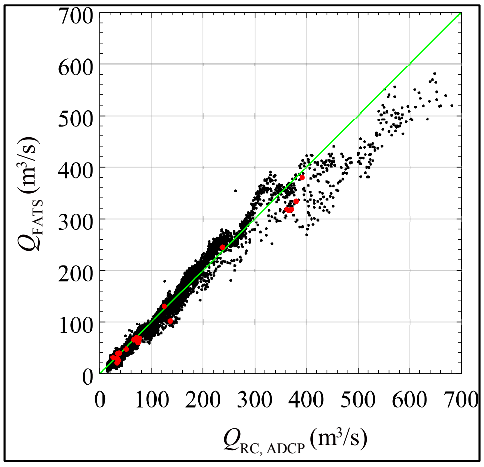

Figure 9. Comparison between FATS and RC/ADCP estimates.

The maximum stream velocity measured by FATS is 2.3 m/s (Figure 8c). Figure 8(d) shows the time history of streamflow estimates by FATS, the RC [1] and the moving-boat ADCP. The streamflow measured by FATS ranges from 15–580 m^3/s.

3.5 Comparison between FATS and RC/ADCP estimates

Figure 9 shows the relations between FATS and RC estimates and FATS and moving-boat ADCP estimates. For the high-flow condition $(Q > 350\ \mathrm{m^3/s})$, the ten-minute averaged estimates of FATS are somewhat smaller than the RC estimates. The underestimate is discussed in the next section.

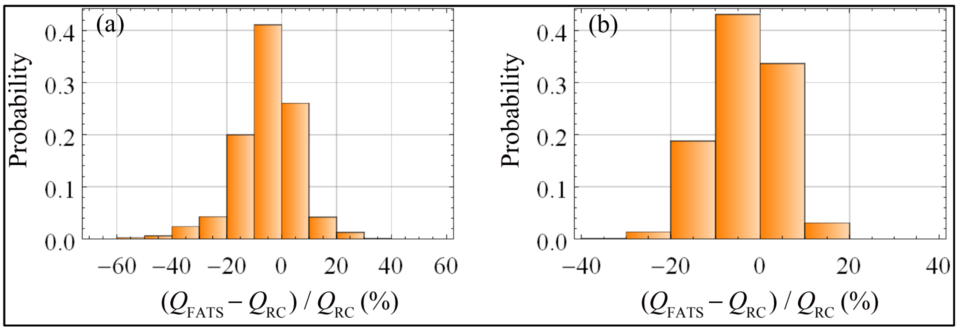

Figure 10. Probability of relative difference between FATS and RC estimates for (a) $Q \le 350\ \mathrm{m^3/s}$ and (b) $50 \le Q \le 350\ \mathrm{m^3/s}$.

Figure 10 shows the probability distributions of the relative differences between FATS and RC estimates. The probability distributions of the relative differences in Figure 10(a) and (b) are for $Q \le 350\ \mathrm{m^3/s}$ and $50 \le Q \le 350\ \mathrm{m^3/s}$, respectively. 77% of the relative differences between FATS and RC estimates are within ±10% under the flow condition $(50 \le Q \le 350\ \mathrm{m^3/s})$; 67% of the relative differences are within ±10% under the flow condition $(Q \le 350\ \mathrm{m^3/s})$.

4 DISCUSSIONS

Although the “true” value of discharge is not known, the reliability of FATS for measuring streamflow should be confirmed by the comparison between FATS and RC/ADCP. As shown in Figure 8(d), The FATS streamflows appear to fit in RC and ADCP estimates. The underestimate of FATS for the high-flow condition $(Q > 350\ \mathrm{m^3/s})$ is probably due to the unmeasured area between T1 and the left bank. Because the ground elevation was approximately 147.5 m a.s.l., the river water overflows the ground under high-flow conditions (see Figure 6).

Another cause for the difference between FATS and RC is short-wave streamflow irregularities that the RC method cannot capture. The streamflow does not change smoothly with the river stage. The boundary roughness in natural rivers can change according to the water level owing to the complex topography and heavy riverside vegetation. As a result, a smooth RC has limitations for the accurate streamflow estimation.

5 CONCLUSIONS

This study demonstrates the feasibility of a novel acoustic system (FATS) for long-term continuous monitoring of river flow. The FATS enabled us to automatically collect streamflow data with high temporal resolution (10-min intervals) for a long period. The cross-sectional average velocity and streamflow of FATS range, respectively, from 0.15 to 2.3 m/s and 15 to 600 m^3/s during the observation period (258 days); the mean water depth ranges from 0.8 to 3.7 m. The relative differences between the 10-minute averaged FATS estimates and the moving-boat ADCP estimates are within ±5% under the flow condition $(50 \le Q \le 250 \text{ m}^3/\text{s})$. 77% of the relative differences between FATS and RC estimates are within ±10% for the flow condition $(50 \le Q \le 350 \text{ m}^3/\text{s})$.

The underestimate of FATS for the high-flow condition $(Q > 350 \text{ m}^3/\text{s})$ is assumed to be due to the unmeasured area between the left transducer and the left bank. One of the causes for the difference between FATS and RC is short-wave streamflow irregularities that RC method cannot capture. The FATS measurement at a high frequency demonstrates that the streamflow changes at time scales of a few tens of minutes to days. Besides, the streamflow does not change smoothly with the river stage.

For effective management of water resources, it is essential to acquire reliable discharge estimates. The streamflow data with high temporal resolution provide new insights on streamflow fluctuations. Future studies should clear the fluctuations that do not directly link to the river stage.

ACKNOWLEDGEMENTS

This study was supported by JSPS KAKENHI grant numbers 24656296, 26289165, and FRIC grant number 27-2. The authors express their gratitude to Dr. Noriaki Gohda of Hiroshima University/Aqua Environmental Monitoring Limited Liability Partnership (AEM-LLP) for his unwavering technical support.

REFERENCES

Kawanisi K., Bahrainimotlagh M., Al Sawaf B.M. & Razaz M. (2016). High-Frequency Streamflow Acquisition and Bed Level/Flow Angle Estimates in a Mountainous River using Shallow-Water Acoustic Tomography, *Hydrological Processes,* 30(13), 2247–2254.

Kawanisi, K., Razaz, M., Ishikawa, K., Yano, J. & Soltaniasl, M. (2012). Continuous Measurements of Flow Rate in a Shallow Gravel-Bed River by a New Acoustic System. *Water Resources Research*, 48(5), 1-10.

Kawanisi, K., Razaz, M., Kaneko, A. & Watanabe, S. (2010). Long-Term Measurement of Stream Flow and Salinity in a Tidal River by the use of the Fluvial Acoustic Tomography System. *Journal of Hydrology*, 380(1), 74-81.

Le Coz, J., Pierrefeu, G. & Paquier, A. (2008). Evaluation of River Discharges Monitored by a Fixed Side-Looking Doppler Profiler. *Water resources research*, 44(4), 13.

Laenen A. & Smith W. (1983). *Acoustic Systems for the Measurement of Streamflow*, US Geological Survey Water Supply Paper 2213, 26.

Razaz, M., Kawanisi, K., Kaneko, A. & Nistor, I. (2015). Application of Acoustic Tomography to Reconstruct the Horizontal Flow Velocity Field in a Shallow River. *Water Resources Research*, 51(12), 9665-9678.

Simon M.K., Omura J.K. & Levitt B.K. (1985). *Spread Spectrum Communications Handbook*. 423, McGraw-Hill, New York.

Proceedings of the 37th IAHR World Congress
August 13 – 18, 2017, Kuala Lumpur, Malaysia

FIELD MEASUREMENTS OF THE ABSOLUTE PRESSURE DISTRIBUTION ACTING ON BED MATERIAL

RYOTA TSUBAKI(1), YUJI TODA(2) & MASAYA MIYAMOTO(3)

(1, 2, 3) Department of Civil Engineering, Nagoya University, Chikusa-ku, Nagoya 464-8603, Japan
rtsubaki@civil.nagoya-u.ac.jp; ytoda@cc.nagoya-u.ac.jp

ABSTRACT

To estimate the pressure distribution surrounding model cobble, two pressure sensors are embedded in a model cobble and placed in a river bed. A field measurement campaign within a cobble-bed river during an artificial flood is implemented and a time-series of pressure changes on the upstream and downstream side of the model cobble are analyzed in order to determine information regarding turbulent fluid forces acting on bed material during an artificial flood. Running average upstream pressure is higher than downstream pressure. The difference between upstream and downstream pressure is related to the form-drag acting on bed material. Fluctuations in upstream pressure are substantially larger as compared to downstream pressure, especially during high flow periods.

Keywords: Pressure measurements; bed materials; gravel bed rivers.

1 INTRODUCTION

Due to complexities of flow and bed forms, and variations in bed material size, estimations of water flow rates and sediment transport quantities in rivers having a complicated bathymetry have limited accuracy when determined using numerical models. As a result, direct measurements of flow and sediment transport in streams are quite useful and essential for: 1) estimating flow (e.g. Tsubaki et al., 2012), 2) accounting for sediment transport quantities (e.g. Muste et al., 2016), 3) predicting bed-form changes, and 4) assessing the ecological functions provided by rivers (e.g. Tsubaki et al., 2017).

In the past, to estimate fluid forces acting on bed roughness (e.g. in the context of the incipient motion of bed material), the time-averaged pressure distribution surrounding roughness elements was measured in experimental flumes (e.g. Chepil (1958) for even spaced hemispheres and Jyo et al. (1987) for packed spheres). Thanks to the development of accurate pressure sensors, measurements of pressure *fluctuations* surrounding bed materials in experimental flumes followed. Using a 30 mm cube as model bed material in an experimental flume, Hofland et al. (2005) measured fluctuating pressures and analyzed changes in fluctuation patterns depending on the exposure of a measurement cube relative to bed material. Celik et al. (2014) conducted a flume experiment to measure pressure fluctuations on a fully exposed sphere (with a diameter d = 12.7 mm) on a bed of close-packed spheres under a condition of Re_*=330—440. Amir et al. (2014) measured streamwise and vertical pressure differences on measurement spheres embedded in a close-packed sphere bed. At present, limited research is available regarding pressure measurements in actual rivers. One exception is the study of Smart and Habersack (2007) who measured near-bed uplift pressure fluctuations in New Zealand in gravel-bed rivers.

For this study, pressure sensors are embedded inside an artificial model cobble and then the model cobble is placed in a river bed in order to estimate the pressure distribution and fluctuation surrounding bed material. For proof of concept, we have used two pressure sensors. Field measurements are obtained in a cobble-bed river during an artificial flood controlled by a dam. To estimate turbulent fluid forces acting on the bed material during small floods, we have acquired time-series changes in pressure on both the upstream and downstream sides of the model cobble.

2 ABSOLUTE PRESSURE ACTING ON MODEL GRAVEL DURING FLUSHING FLOW

2.1 Field site

The field site was located in a reach of the Jyoge River, ~10 km downstream from the Haizuka Dam. Both the Jyoge River and the Haizuka Dam are located in mid-western Japan. Flushing flows were conducted in this reach during the spring of every year and mimicked the snowmelt flood that naturally occurred prior to dam construction. Figure 1 shows a map of the observational reach and the measurement point. The measurement point was located on a riffle. The peak flow rate during flushing flow was 100 m^3 s^{-1} and the local peak flow rate at the measurement point was slightly larger than 100 m^3 s^{-1}due to convergence of flow by the Honmura River. Water depth was estimated by a water level gauge fixed to the river bank. Bulk velocity was measured to 1.3 m s^{-1} using a rotational type current meter hung from the bridge 30 m upstream from the measurement point. Based on water depth and water surface slope, peak bed shear stress during the event was estimated as 33 Pa.

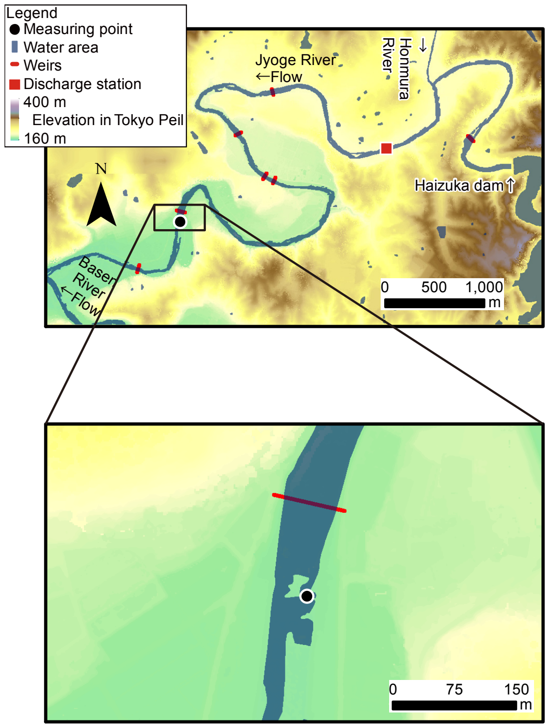

Figure 1. A map of the river reach measured during this study.

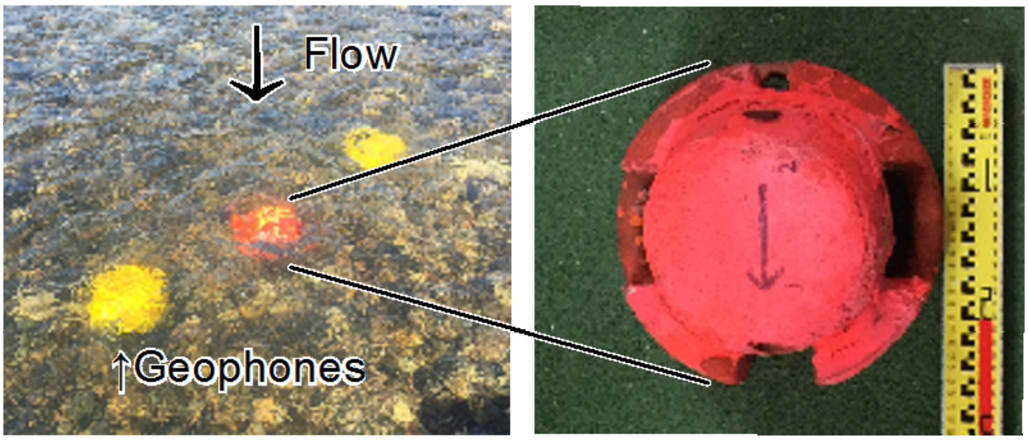

(a) Installation in the river bed (b) Close-up of a model cobble used to measure pressures fixed to an iron weight

Figure 2. Photos of the devices installed in the river.

2.2 Model cobble

The model cobble used in this study was made of concrete and had a diameter of 0.19 m and a thickness of 0.09 m. The model cobble was fixed onto a 20 kg iron weight (Figure 2b). Two water pressure loggers were housed inside the model cobble. The model cobble was then placed in the riffle (Figure 2a). One pressure logger was directed in the downstream direction and the other was oriented upstream. Readings obtained from the upstream- and downstream-directed pressure loggers are denoted here as P_{up} and P_{down}, respectively.

Logger type absolute pressure sensors (the S&DL mini-series of Oyo Co.) were employed. During field measurements, two 5 meter water depth range units were embedded inside the model cobble and one barometer was placed on the river bank. To record water level changes surrounding the measurement point, another 20m water depth logger was placed near the river bank. The accuracy of pressure measurements was 0.1% at full scale or, in other terms, 0.005 mH_2O or 49 Pa in water pressure accuracy for the 5 meter water loggers. Pressures were recorded at a one-second interval (1 Hz measurement). The pressure logger can memorize 40,000 samples during a measurement event, so loggers were capable of recording a pressure change for 11 hours at a one-second interval. Each pressure measurement was a snap-shot of approximately

5 milliseconds. To time synchronize the two 5 meter loggers, two loggers were moved up and down by hand at an approximate two-second interval prior to device installation on the river bed. Pressure waves recorded by two water level sensors were compared after completion of the field measurement and the time difference was adjusted in order to make the time difference between the two sensors less than 0.5 seconds.

2.3 Results obtained from the field survey

Figure 3 provides a time series change in pressures for both the upstream and downstream points for model cobble during the flushing flow event on 25 March 2016. During the event, the flow rate in this section changed from 5.0 m^3 s^{-1} to 101 m^3 s^{-1} during the rising phase and dropped to 5.0 m^3 s^{-1} during the descending phase of water release. As shown in Figure 3a, water depth above the model cobble changed with respect to the flow rate change. Prior to the flow rate increase, the pressure recorded by the two loggers was less than 0.1 mH_2O. Pressure at the upstream point was approximately 0.08 mH_2O and the downstream gauge displayed 0.06 mH_2O (Figure 3b). During the high flow period, as shown in Figure 3c, pressure at the upstream point was approximately 1.4 mH_2O and fluctuated in the range from 1.37 to 1.52 mH_2O. On average, downstream pressure was approximately 1.38 mH_2O and the deviation from average was small as compared to the upstream pressure fluctuation.

In Figure 4, a summary histogram is provided for the pressure difference, $\delta P = P_{up} - P_{down}$, obtained during the high flow phase.

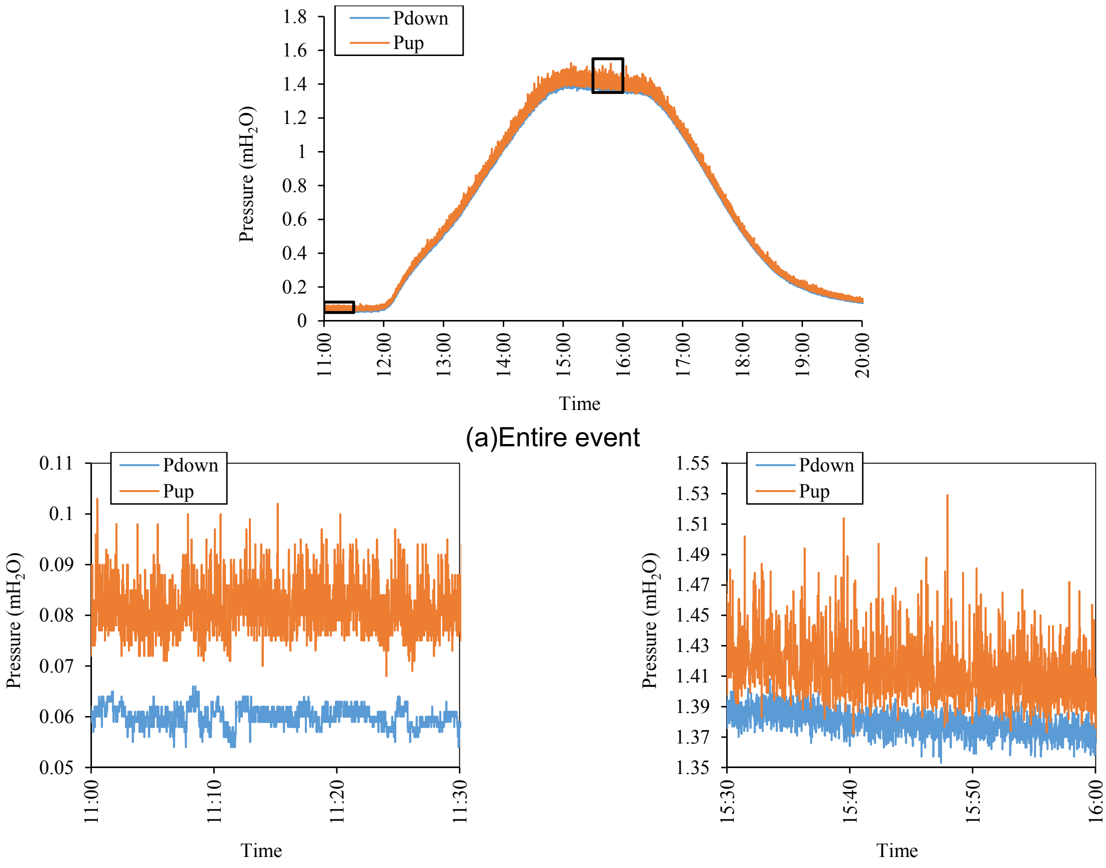

(b) A close-up of low flow (c) A close-up of high flow

Figure 3. A time series change of absolute pressures for both the upstream (P_{up}) and downstream (P_{down}) points.

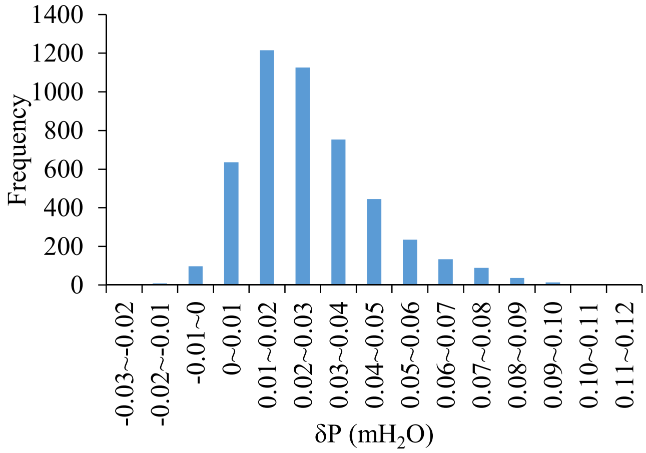

Figure 4. A histogram of the instantaneous pressure difference; $\delta P = P_{up} - P_{down}$.

3 DISCUSSION AND CONCLUSIONS

Schmeeckle et al. (2007) detected a negative drag force acting on a model cobble at some instants during their flume experiment. The result supported the adequacy of our result for instantaneous upstream pressure gradients at bed roughness. As shown in Figure 3b, the upstream pressure fluctuation relative to the pressure difference was limited to the low flow phase. The negative pressure difference was only observed during the high flow phase (Figures 3c and 4) when the upstream pressure fluctuation was quite large. The result suggests that flow during low flow is regulated by each roughness element on the bed. However, turbulent flow at high flow had a spatial scale larger than roughness element size and the magnitude of the pressure fluctuation increased. Small aquatic animals can migrate upstream during high flow if they can fully utilize this instantaneous upstream pressure and reverse flow.

ACKNOWLEDGEMENTS

This work is partially reported in Japanese in Tsubaki (2016). We thank the Miyoshi office of the River and National Highway, the administration office of Haizuka Dam, and the Chugoku Regional Development Bureau for providing fundamental data regarding flushing flows and the Jyoge River. We also thank Prof. Yoshihisa Kawahara and students at Hiroshima University, Japan for substantial contributions to this study. Our work is supported by: Grant-in-Aid for Young Scientists (B), No. 26820205; and Grant-in-Aid of the Japan Society for the Promotion of Science (JSPS) (C), Nos. 16K06609, 17K06574, and 17K06575.

REFERENCES

Amir, M., Nikora, V.I. & Stewart, M.T. (2014). Pressure Forces on Sediment Particles in Turbulent Open-Channel Flow: A Laboratory Study. *Journal of Fluid Mechanics*, 757, 458−497.

Celik, A.O., Diplas, P. & Dancey, C.L. (2014). Instantaneous Pressure Measurements on a Spherical Grain under Threshold Flow Conditions. *Journal of Fluid Mechanics*, 741, 60−97.

Chepil, W.S. (1958). The use of Evenly Spaced Hemispheres to Evaluate Aerodynamic Forces on a Soil Surface. *Eos, Transactions American Geophysical Union*, 39(3), 397−404.

Hofland, B., Battjes, J.A. & Booij, R. (2005). Measurement of Fluctuating Pressures on Coarse Bed Material. *Journal of Hydraulic Engineering*, 131(9), 770−781.

Jyo, M., Uematsu, R., Fujisaki S. & Kikkawa, H. (1987). Experimental Study on the Flow in the Vicinity of the Rough Boundary and on Aerodynamic Forces. *Proceedings of the Japanese Conference on Hydraulics*, JSCE, 31, 377−382.

Muste, M., Baranya, S., Tsubaki, R., Kim, D., Ho, H., Tsai, H. & Law, D. (2016). Acoustic Mapping Velocimetry. *Water Resources Research*, 52(5), 4132-4150.

Smart, G.M. & Habersack, H.M., (2007). Pressure Fluctuations and Gravel Entrainment in Rivers. *Journal of Hydraulic Research*, 45(5), 661−673.

Tsubaki, R., Kawahara, Y., Zhang, X. & Tsuboshita, K. (2017). A New Geophone Device for Understanding Environmental Impacts Caused by Gravel Bedload during Artificial Floods. *Water Resources Research*, 53(2), 1491-1508.

Tsubaki, R., Kawahara, Y., Muto, Y. & Fujita, I. (2012). New 3-D Flow Interpolation Method on Moving ADCP Data. *Water Resources Research*, 48(5), 1-15.

Tsubaki, R. (2016). On the Field Measurement of Pressure Acting on Bed Material in Cobble-Bed River during Small Flood. *Journal of Japan Society of Civil Engineers, Ser.* B1(Hydraulic Engineering), 72(4),in press, in Japanese.

Proceedings of the 37th IAHR World Congress
August 13 – 18, 2017, Kuala Lumpur, Malaysia

LATERAL VARIATION OF TURBULENCE IN DEVELOPING NARROW OPEN CHANNEL FLOW

MINAKSHEE MAHANANDA[1] & PRASHANTH REDDY HANMAIAHGARI[2]

[1,2] Dept. of Civil Eng., Indian Institute of Technology Kharagpur, Kharagpur, West Bengal, India,
minakshee.m@iitkgp.ac.i; hpr@civil.iitkgp.ernet.in

ABSTRACT

A detailed experimental investigation of lateral variation of turbulent characteristics is carried out in developing and fully developed flow over a fixed rough bed. Experiments are conducted in a rectangular flume with gravel bed and keeping flow aspect ratio below four. In this study, instantaneous 3-D velocities are measured using a Nortek Vectrino plus down-looking ADV. Raw velocity data has been filtered as prescribed in the recent literature. The characteristics of normalized flow velocity, turbulent intensities, Reynolds shear stresses and TKE distribution have been investigated. It is observed that the boundary layer thickness increases along the streamwise distance in the developing flow region and reaches maximum in fully developed flow. On contrary, boundary layer thickness decreases in the lateral direction from the centerline of the channel towards sidewalls in both developing and fully developed flows. Local shear velocities are estimated using the Reynolds shear stress distribution in the intermediate layer. Lateral variation of shear velocity shows decreasing trend in both developing and fully developed flow from the centerline towards sidewalls. Dip phenomenon is observed in both the vertical distribution of normalized streamwise velocity and Reynolds shear stress profiles along the lateral direction in the region adjacent to sidewalls in both the developing and fully developed flow.

Keywords: Turbulence; open channel flow; flow development; secondary currents; boundary layer.

1 INTRODUCTION

In order to address the hydraulic engineering problems such as fluid-sediment interactions, sediment erosion and deposition etc. which are directly linked to the hydrodynamic characteristics such as vertical distribution of time averaged velocities, effect of secondary currents, turbulent intensities, variation of Reynold shear stresses along streamwise and lateral direction and turbulent kinetic energy, it is essential to understand the flow characteristics in the developing and developed open channel flow. However, in nature, open channel flows are non-uniform/fully developed flows because of ever changing boundary conditions such as changes in discharge, changes in geometry, bed roughness, vicinity of hydraulic structures and etc. Flow becomes disturbed whenever there is a change in boundary condition because of imbalance of viscous, gravitational and inertial forces. Subsequently flow tries to attain fully a developed flow conditions, in the downstream direction.

The developing turbulent flow in open channel is a complex three-dimensional flow which is influenced by aspect ratio, bed roughness, flow parameters and downstream distance from the inlet. Therefore, comprehensive study of variation of turbulent characteristics of developing narrow open channel flow on rough surfaces, which are often encountered, hence it is of vital importance in hydraulic engineering.

It is well known that the classical log-law is applicable in the inner region of wall bounded turbulent flow (Cardoso et al., 1989; Nezu and Rodi, 1986). On the other hand, the log-law deviates from the experimental data in the outer region and the most reasonable formula to account the velocity together with deviation is the log-wake law where the wake function was introduced by Coles (1956). However, the classical log-wake law is not valid for narrow open channel where the value of aspect ratio, being defined by the ratio of width to height of the open channel, is less than 5. Moreover, it needs to be mentioned here that for wide open channel where the aspect ratio is greater than 5, the log-wake law is not valid near the sidewalls. Another important feature of narrow open channel flow is occurrence of the dip phenomenon, a century ago; researchers reported that in fully developed narrow open channel flow, the maximum velocity occurs below the free surface which is known as dip-phenomenon. In the last few decades, several experimental investigations proved the existence of dip-phenomenon in narrow open channel (Kirkgoz and Ardiclioglu, 1997; Sarma et al., 2000; Nezu, 2005; Yan et al., 2011). Recently, Auel et al. (2014) experimentally investigated the effect of Froude number and aspect ratio on the turbulence characteristics in supercritical open channel flow. Apart from the experimental study, available theoretical literature predicted the velocity distribution together with dip-phenomenon in narrow open channel (Yang et al., 2004; Absi, 2011). All the above-mentioned literature is focussed only on the fully developed flow condition. Literature on the developing flow is presented below.

Silberman (1980) analysed the boundary layer growth of the developing open channel flow by using Bernoulli and continuity equations. Antonia et al. (1990) verified that the achieved boundary layer for the experimental consideration behaves according to the criteria adopted to ensure fully developed turbulent boundary layer. Kirkgoz and Ardiclioglu (1997) experimentally studied the velocity profiles of developing and fully developed smooth open channel flow. Laser-Doppler anemometer was used to measure 3D velocities in developing and fully developed regions of subcritical smooth open channel flows. They suggested a reasonable agreement between the modified velocity-defect law and the experimental profile in the inner and outer regions with a profile parameter of 0.1 in the Coles's wake law. Ranga Raju et al. (2000) studied experimentally and numerically, the region of developing flow and the variation of the flow development length in smooth and rough rectangular channels of wind tunnel. Balachandar and Patel (2002) performed experiments to study the boundary layer growth on the rough surface and its interaction with the outer region and the free surface of flow. Balachandar and Patel (2002) used the turbulence intensity profile to provide an alternative definition of boundary layer thickness and found that the logarithmic law is valid in the near wall flow, however with a shift due to surface roughness. In addition, they revealed that outer layer profile is affected by the surface roughness which tends to increase the wake parameter and the free surface decreases the wake parameter.

Recently Marusic et al. (2010) reviewed the key issues and recent advances in high Reynolds number wall bounded turbulent flow. They also discussed on the important issue, i.e., evolution of turbulent boundary layer and the effect of upstream condition on the flow development length in pipe and channel. Kulandaivelu (2012) investigated experimentally the streamwise evolution of wall bounded turbulent flows in a wind tunnel. Kulandaivelu (2012) also investigated scaling of the streamwise broadband turbulence intensity and found that the logarithmic law of the wall provides universal behaviour in the inner region for the mean velocity profile distribution, which was also noted by Kirkgoz and Ardiclioglu (1997). Recently, Bonakdari et al. (2014) investigated the impact of relative roughness, Froude number and the Reynolds number on the establishment length using CFD analysis. They found that the effect of Froude number is negligible on the establishment length, whereas with increase in relative roughness decreases the establishment length. Bonakdari et al. (2014) also suggested a dimensionless establishment length which follows a linear relationship with Reynolds number. Marusic et al. (2015) also studied the streamwise evolution of turbulent boundary layers from the different tripping conditions.

It is well known that to perform an experimental or theoretical study in a narrow open channel flow, it is very important to know the characteristic length by which the flow would acquire a fully developed condition. From the literature survey, it is observed that streamwise evolution of developed flow in open channel and the understanding of the lateral variation of the turbulent hydrodynamics of developing open channel flow are not reached up to the desired level. In addition, the available knowledge on this topic is limited for the narrow open channel flow. To attempt the overlooked research problem, the aim of the study is to investigate the lateral variation of turbulence in developing and fully developed open channel flow over the fixed rough bed.

2 EXPERIMENTAL SET UP AND METHODOLOGY

Experiments were conducted in the Hydraulic and Water Resources Engineering Laboratory, IIT Kharagpur, India. The experiments were carried out in a rectangular flume of width 0.61 m, depth 0.71 m and length 7 m. To enable the visualization of flow, the rectangular flume is provided with glass sidewalls. The flume was provided with railings on both the sidewalls throughout the length and also provided with a carriage in order to take readings at different locations. Bed is cladded with uniform sand of median diameter 2.25 mm to simulate hydraulically rough surface. Overhead tank was used to supply the water to the flume. Two centrifugal pumps were used to recycle the water between underground sump and overhead tank. A honeycomb baffle wall was provided at the entrance of the channel in order to break larger eddies. The stream-wise bed slope and the depth of the flow were measured by using a point gauge provided with a Vernier scale with precision ± 0.1 mm. Velocity measurements were taken after 30 minutes of flow initiation in order to ensure the steady flow.

All the velocity measurements were taken by using a Nortek Vectrino Plus downlooking Acoustic Doppler Velocimeter (ADV) which was mounted on a point gauge fixed to the carriage to take velocity readings at different vertical depths, towards the sidewall and along the flow direction. Vectrino comprises of four downlooking probes and operates with an acoustic frequency of 10 MHz. Vectrino takes the measurement at a location 5 cm below the probe emitter. Hence the influence of the probes on the measuring data is minimal. The sampling rate considered in the experiments was 100 Hz and the sampling volume height was 6 mm diameter. The sampling duration was taken as 300 seconds, but near the side walls, depending on the level of turbulence, the sampling duration was taken between 360 and 600 seconds.

The noise in the raw Vectrino data were despiked by the Phase-space method (Goring and Nikora, 2002; Wahl, 2003) and the spikes were replaced by cubic interpolation method. To obtain good quality Vectrino data, the proposed SNR method of Chanson et al. (2008) was followed where the SNR value was maintained as greater than 20. After that, the data with Vectrino correlation signal value greater than 75% was used to analyze the turbulence characteristics of developing and developed flow in narrow open channel. A schematic diagram of the experimental set up is presented in Figure 1.

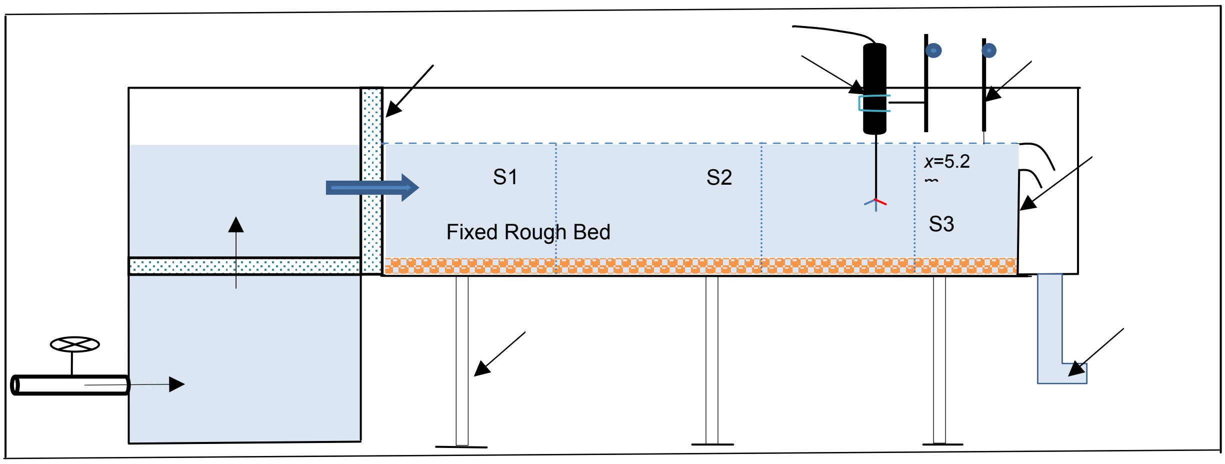

Figure 1. A schematic of experimental set up.

As the main motive of the present study is to investigate turbulence across the sections at three different streamwise locations in flow development region, the measurements were taken along the various cross sections in the developing flow region. In this study, the developing flow and fully developed flow regions were determined by measuring and comparing streamwise velocity profiles at different consecutive locations along the centerline of the channel. Hence, the region in which the consecutive velocity profiles are varying with streamwise distance is defined as developing flow region and the region at which the velocity profiles are independent of streamwise distance along the centerline of the channel is taken as fully developed flow region.

Three dimensional velocities were measured at three cross sections $(x = 2.2\ \mathrm{m}, x = 3.7\ \mathrm{m}\ \mathrm{and}\ x = 5.2\ \mathrm{m})$ along the developing region and these are represented as stations S1, S2 and S3 respectively. At each cross section, four verticals were chosen from the centerline of the flume towards the sidewall like as $y/0.5b = 0$, $0.25,\ 0.5,\ 0.75$.

A three-dimensional coordinate system is adopted to represent the direction i.e., x, y and z axes are representing the stream-wise, lateral and vertical directions respectively. The origin of the x-axis, y-axis and z-axis were located at the entrance of the channel $(x = 0)$, at the center line of the flume$(y/(0.5b) = 0)$ and at the bed level$(z/h = 0)$ respectively, where b is defined as flume width and h is defined as the depth of the flow. For a given streamwise station, four verticals were chosen for the data measurements as explained above. In this study at every vertical in x-y plane, velocity measurements were taken at 19 vertical locations $z = (0.3, 0.5, 0.7, 0.9, 1.5, 2, 2.5, 3, 4, 5, 6, 7, 8, 9, 10, 11, 12, 13, 14\ )\ \mathrm{cm}$.

Similarly, a three-dimensional coordinate system was used, where u, v and w are time averaged streamwise velocity, lateral and vertical velocity components, respectively, u', v' and w' are the fluctuations of corresponding velocity components. The flow velocities and all the turbulence quantities were normalized by local friction velocity (u_*). Vertical distance (z) of any location in the flow was normalized as z/h where h is defined as the total flow depth. As mentioned above,u/u_*, v/u_* and w/u_* are defined as the normalized time averaged velocities in streamwise, lateral and vertical directions, respectively; $\sqrt{(\overline{u'u'})}/u_*$, $\sqrt{(\overline{v'v'})}/u_*$ and $\sqrt{(\overline{w'w'})}/u_*$ are defined as the normalized streamwise turbulent intensity u'or u_{rms}/u_*, turbulence intensity in lateral direction v' or v_{rms}/u_* and vertical turbulent intensity w' or w_{rms}/u_*, respectively. Similarly normalized Reynolds stresses are denoted by $-\overline{u'w'}^+ = (\overline{-u'w'})/u_*^2$; $-\overline{u'v'}^+ = (\overline{-u'v'})/u_*^2$and $-\overline{v'w'}^+ = (\overline{-v'w'})/u_*^2$ and the turbulent kinetic energy k^+ is normalized as k/u_*^2. The boundary layer thickness (δ) is defined as vertical distance from the wall where the velocity is maximum. Flow condition has been given in Table 1 where U is defined as the depth average velocity at the centerline of the channel in fully developed flow station (S3). Reynolds roughness number is denoted by R_*.

Table 1. Flow parameters of the present study.

d_{50} **(mm)**	h **(m)**	b **(m)**	A_r	U **(m/s)**	R_e	Fr	d_{90} **(mm)**	R_*
2.25	0.2	0.61	3.05	0.322	64400	0.23	2.88	64.91

3 RESULTS AND DISCUSSIONS

3.1 Determination of friction velocity

Friction velocity (u_*) is a fundamental scaling parameter in wall bounded turbulent flows. Rowinski et al. (2005) discussed different methods for the determination of friction velocity in different fields of hydraulic research. It is very common to determine indirectly from the Clauser approach in hydraulically smooth and rough open channel turbulent flows. This involves fitting of experimental data in the inner region to the classical logarithmic law. Another method is extrapolation of Reynolds shear stress (RSS) distribution to the wall. However, the values of friction velocity obtained from the RSS distribution have been considered for the analysis in this present study.

Figure 2 shows the variation of friction velocity across the developing zone, fully developed flow zone and comparison with Run 6 (only the data at fully developed section considered here) of Kirkgoz and Ardicliogiu (1997). Kirkgoz and Ardicliogiu (1997) concluded that the friction velocity remains approximately constant in the streamwise direction in the turbulent boundary layer of open channel flow for the same flow conditions. In contrast, from Figure 2, it is found that the friction velocity decreases along the flow direction in the turbulent boundary layer for same flow conditions. However, the rate of decrease is very less near to the developed flow zone. It is also observed that at the fully developed zone, the friction velocity decreases across the section from the centerline of channel to the sidewall $y/0.5b < 0.5$ which is also contradicting the result of Run 6 of Kirkgoz and Ardicliogiu (1997). It is found that the friction velocities at fully developed section of present experiments and Kirkgoz and Ardicliogiu (1997) vary similarly for $y/0.5b \geq 0.5$.

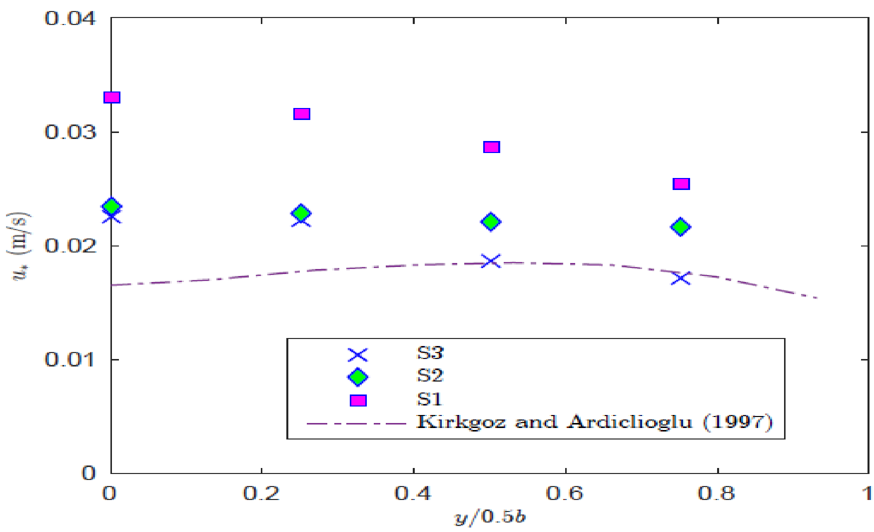

Figure 2. Variation of friction velocity across stations of developing and fully developed flow and comparison with Run 6 of Kirkgoz and Ardicliogiu (1997).

3.2 Mean velocity profile distribution

Figure 3 (a, b and c) depicts the vertical distribution of normalized time averaged streamwise velocity (u/u_*) and the lateral variation of velocity profile at two stations (S1 and S2) in the developing open channel flow and at another station (S3) in fully developed region.

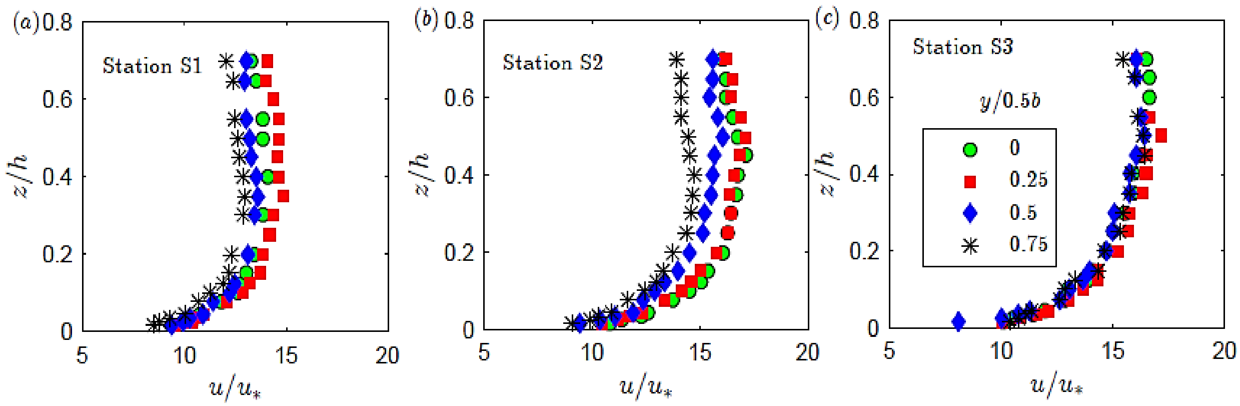

Figure 3. Vertical distribution of normalized streamwise velocity at developing stations (S1 and S2) and fully developed flow station (S3).

Figure 3 (a) shows that near to the inlet of the channel, at station S1, profiles of u/u^* are similar. With increasing lateral distance $(y/0.5b\ =\ 0.25, 0.5$ and 0.75) at CS1, it is observed that the location of maximum time averaged streamwise velocity is approaching boundary of inner layer. That means the boundary layer thickness in developing region, decreases towards the sidewall from the centerline of the channel which is also observed at sections S2 and S3 (shown in Figure 3 (b-c)). Figure 3 (b & c) show that with increasing streamwise distance (S2, x = 3.7 m; S3, x=5.2 m), the location of maximum value of u/u^* of midvertical is shifting away from the channel boundary. Along the streamwise distance, a developed flow phenomenon is observed at S3 and the developed flow characteristics is confirmed by taking the measurement at a downstream distance from station S3 (not shown here) and found that flow characteristics doesn't change with increase in streamwise distance. Hence, it is assumed that the length of the boundary layer development in the present study is around 5.2 m. By examining the profiles of velocities at S3 (Figure 3 c), it is found that the velocity data in the outer layer $(z/h\ > 0.6)$ signify the dip phenomena where the maximum streamwise velocity observed below the free surface of the open channel. Dip phenomenon is caused by the secondary currents in the flow.

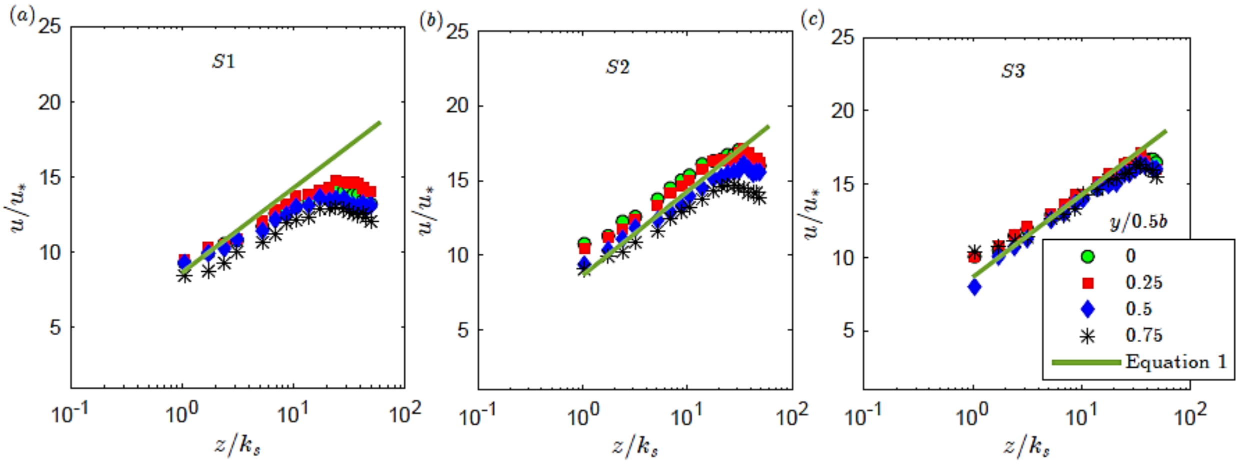

Figure 4. Normalized streamwise velocity profile (inner scaling) (a & b) for developing flow, (c) for fully developed flow region.

In addition, by observing the velocity data at all sections, it may be concluded that the peak magnitude of time averaged streamwise velocity decreases with increase in streamwise distance along the centerline of the flow and also decreases with increase in lateral distance from the centerline of the channel towards the sidewall due to the effect of no slip condition.

Figure 4 show the measured mean velocity profiles normalized with friction velocity and vertical normalization with Nikuradse Sand roughness (k_s). As mentioned above, u_* is estimated by extrapolating the local Reynolds shear stresses distribution to the wall in the intermediate region. In the present study, k_s is taken as equal to d_{90} of the channel bed sediment.

$$\frac{u}{u_*} = \frac{1}{\kappa}\ln\left(\frac{z}{k_s}\right) + B \qquad [1]$$

In this study, κ is the Von-Korman constant which is considered as 0.41 and $B = 8.659$. All profiles demonstrate that the velocity profiles have pronounced logarithmic behavior in the inner region at all measuring stations both in developing and fully developed stations.

3.3 Velocity defect distribution

The velocity defect distributions at station S3 (fully developed flow region) are shown in Figure 5. The velocity defect data of present study is compared with the velocity defect formula given by Kirkgoz and Ardiclioglu (1997) for smooth bed with $\kappa = 0.41$ and wake intensity $\Pi = 0.1$. It can be observed that the dip phenomenon is very prominently visible in the outer region that is due to the secondary currents in a narrow open channel flow.

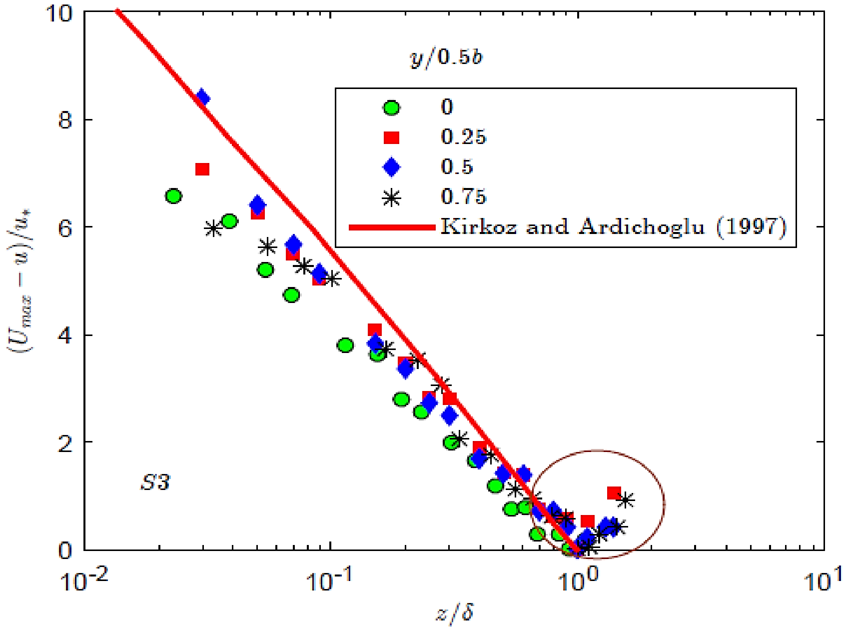

Figure 5. Velocity defect profile at fully developed flow station (S3).

3.4 Turbulence intensity

Figure 6 (a & b) shows that as the lateral distance increases from $y/0.5b = 0, 0.25$ and 0.5, u_{rms}/u_* increases, but profile at $y/0.5b = 0.75$ shows slightly different trend due to the sidewall effect on the turbulence. In the free surface layer, the magnitude of normalized streamwise turbulent intensity is found to be higher near to the sidewall (Figure 6 b) due to damping of vertical velocity by free surface layer.

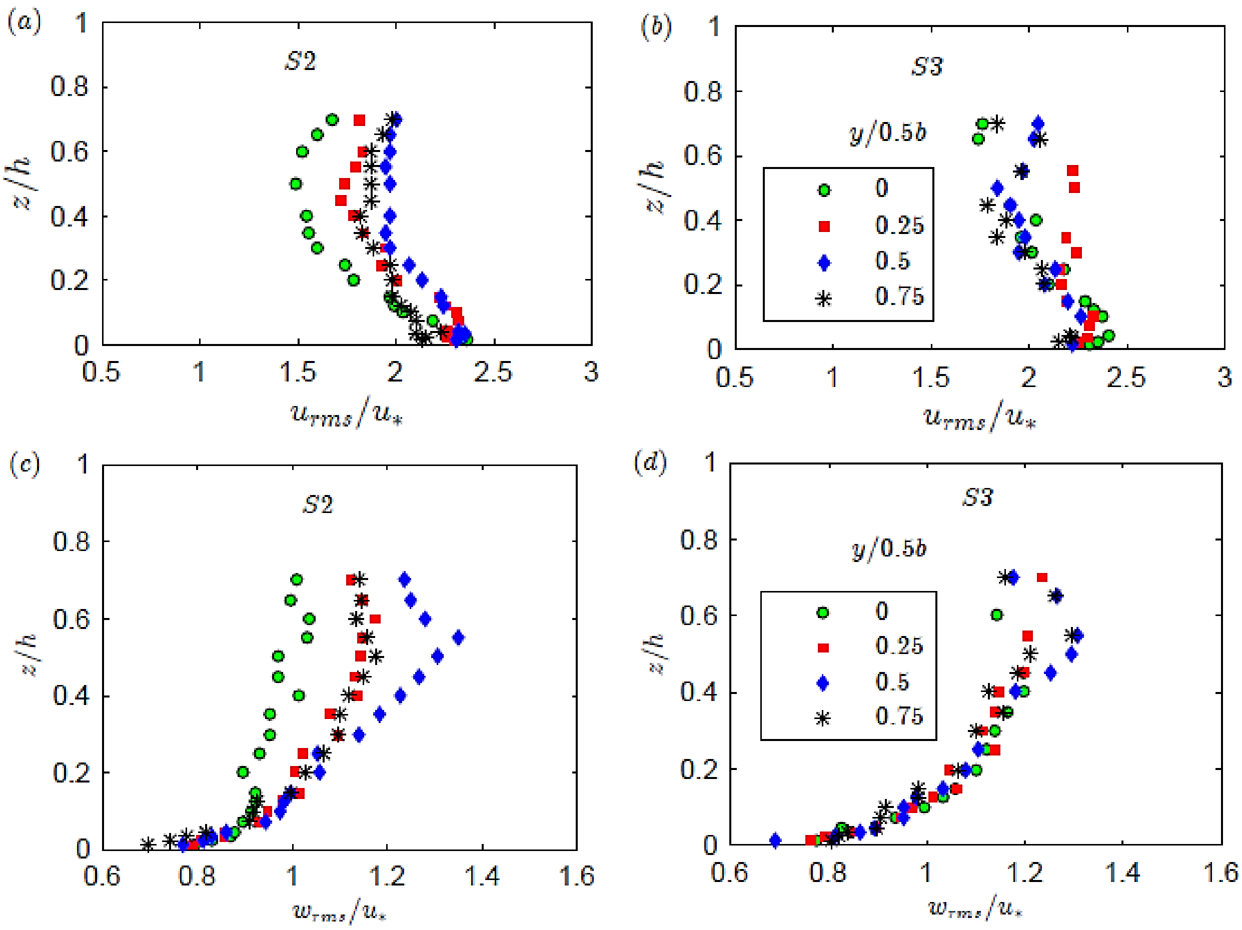

Figure 6. Lateral variation of streamwise turbulence intensity in (a) developing flow (S2), (b) fully developed flow (S3), c) developing flow (S2), (d) fully developed flow (S3).

An interesting phenomenon observed in Figure 6 (b) is that with increasing streamwise distance from the channel inlet, the increasing characteristics of u_{rms}/u_* from $0.4h$ above the bed decreases and becomes invariant of flow depth at lateral distance $y/0.5b = 0.25$. At midvertical of S3, the magnitude of streamwise turbulence intensity decreases with increasing vertical height from the channel bed which is similar to the trend found in the fully developed and hydraulically rough wide channel flow. However, in the outer region $z/h > 0.4$, the streamwise turbulent intensity profiles at $y/0.5b = 0.5$ and 0.75 of station S3 are showing increasing trend with increase in vertical height of flow, may be due to increase in shear at the corner region of sidewall and free surface. In addition, it may be concluded that the normalized streamwise turbulent intensity follows increasing trend along the lateral distance from the centreline of channel only up to $y/0.5b < 0.5$. By examining the experimental data, it is found that among the peak values of u_{rms}/u_* near the channel boundary are maximum at the midsection ($y/0.5b = 0$) along the channel. The location of peak value of u_{rms}/u_* is not changing along the streamwise distance which shows viscous sublayer thickness is constant along the flow development length.

Unlike the distribution of u_{rms}/u_*, the normalized vertical turbulent intensity w_{rms}/u_* exhibits a complete different behavior. Figure 6 (c & d) shows the vertical distribution of normalized vertical turbulent intensity. Moreover, at stations S2 and S3, the data trends of w_{rms}/u_* along all the lateral distances show an increasing tendency with z/h in the inner layer and decreasing in the free surface region ($z/h > 0.6$) because of suppression. On the other hand, at station S3, it is observed that the data trend of w_{rms}/u_* becomes invariant of lateral distance up to $z/h < 0.4$, similarly decreasing tendency is found in the free surface layer. The suppression of vertical turbulent intensities is caused by the free surface (Tominaga et al., 1989).

3.5 Reynolds shear stresses

Figure 7 (a and b) depicts the vertical distribution of normalized Reynolds shear stress ${\tau_{uw}}^+ = -\overline{u'w'}/u_*^2$ along the developing flow at two different stations S2 and S3.

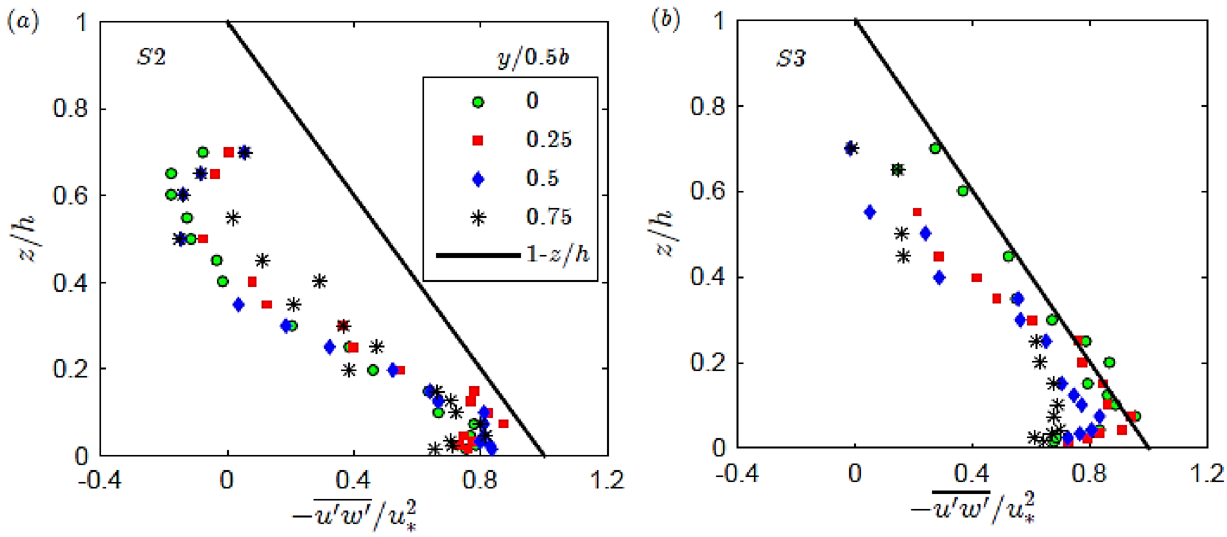

Figure 7. Lateral variations of RSS in (a) developing flow (S2), (b) fully developed flow (S3).

At station S2 (Figure 7 a) in the developing flow zone, it is observed that the values of ${\tau_{uw}}^+$ after reaching peak values near the channel bed, follow decreasing trend up to $0.6\,h$ and then increase with further increase in vertical height. At S2, ${\tau_{uw}}^+$ profiles are deviating from $1 - z/h$, above $z/h > 0.2$, which shows $1 - z/h$ is not applicable to approximate ${\tau_{uw}}^+$ in the developing flow region. The change of sign of ${\tau_{uw}}^+$ from positive to negative near the free surface signifies the existence of dip phenomena in narrow open channel flow. The negative values of normalized Reynolds shear stress are observed in the region where the velocity retardation takes place (Kironoto and Graf 1994). Nevertheless, the retardation region is decreasing with increase in streamwise distance. Vertical distribution of ${\tau_{uw}}^+$ at $y/0.5b = 0$ of station S3 ($x = 5.15m$) reasonably follows the linearly decreasing trend with increase in vertical height from the channel bed which shows the attainment of fully developed flow (Figure 7 (b)).

4 CONCLUSIONS

An experimental investigation of lateral variation of turbulence in developing and fully developed narrow open channel flow was carried out. A detailed study of the turbulence characteristics along the developing flow has been portrayed as follows. It is concluded that friction velocity decreases along the streamwise direction of flow. However, the decreasing rate is smaller near to the fully developed region as compared to the developing flow region. In addition, lateral variation of local shear velocities away from mid-section shows decreasing trend in both developing as well as fully developed flow. Boundary layer thickness decreases in the lateral direction from the centreline of channel, both in developing and fully developed flow. The classical log law is valid in the inner region of the developing flow. It is found that the normalized streamwise velocity profile and the defect profile shows dip phenomenon in the outer layer of the fully developed flow and developing flow, which confirms the existence of secondary current. Normalized streamwise turbulence intensity at centreline of the channel decreases along the streamwise direction in the developing flow; however, it increases along the lateral direction from the centreline of the channel towards the sidewall. In addition, the anisotropic turbulence is found in the region of developing flow. Reynolds shear stress decreases from the centerline of the channel towards the sidewall in the developing flow. From Reynolds shear stress profiles in the developing flow, it understood that flow retardation is taking place in the outer layer. In the developing flow region, normalized shear stress distribution is not following the linear distribution. However, shear stress along the centreline of the channel in the fully developed flow is following the linear distribution.

REFERENCES

Absi, R. (2011). An Ordinary Differential Equation for Velocity Distribution and Dip-Phenomenon in Open Channel Flows. *Journal of Hydraulic Research,* 49(1), 82–89.

Antonia, R.A., Bisset, D.K. & Browne, L.W.B. (1990). Effect of Reynolds Number on The Topology of The Organized Motion in a Turbulent Boundary Layer. *Journal of Fluid Mechanics,* 213, 267-286.

Auel, C., Albayrak, I. & Boes, R.M. (2014). Turbulence Characteristics in Supercritical Open Channel Flows: Effects of Froude Number and Aspect Ratio. *Journal of Hydraulic Engineering*, 140, 381–396.

Balachandar, R. & Patel, V. (2002). Flow Wall Boundary Layer on Plates in Open Channels. *Journal of Hydraulic Engineering*, 128(10), 947-951.

Bonakdari, H., Lipeme-Kouyi, G. & Asawa, G.L. (2014). Developing Turbulent Flows in Rectangular Channels: A Parametric Study. *J. Appl. Res. Water Wastewater*, 1(2), 53-58.

Cardoso, A.H., Graf, W.H. & Gust, G. (1989). Uniform Flow in a Smooth Open Channel. *Journal of Hydraulic Research*, 27(5), 603–616.

Chanson, H., Trevethan, M. & Aoki, S.I. (2008). Acoustic Doppler Velocimetry (ADV) in Small Estuary: Field Experience and Signal Post-Processing." *F. Measur. Instrum.,* 19(5), 307-313.

Coles, D. (1956). The Law of The Wake in The Turbulent Boundary Layer. *J. Fluid Mech.,* 1(2), 191–226.

Goring, D.G. & Nikora, V.I. (2002). Despiking Acoustic Doppler Velocimeter Data. *Journal of Hydraulic Engineering*, 128(1), 117-126.

Kirkgoz, M. S. & Ardiclioglu, M. (1997). Velocity Profiles of Developing and Developed Open Channel Flow. *Journal of Hydraulic Engineering,* 123(12), 1099-1105.

Kironoto, B. & Graf, W. H. (1994). Turbulence Characteristics in Rough Uniform Open Channel Flow. *Proceedings of the Institution of Civil Engineers – Water and Maritime Engineering*, 106(4), 333-344.

Kulandaivelu, V (2012). Evolution of Zero Pressure Gradient Turbulent Boundary Layers from Different Initial Conditions. *PhD thesis*, Dept. of Mechanical Engg., The University of Melbourne.

Marusic, I., McKeon, B. J., Monkewitz, P., Nagib, H. M., Smits, A. J. & Sreenivasan, K. R. (2010). Wall-bounded Turbulent Flows: Recent Advances and Key Issues. *Phys. Fluids 22*, 065103.

Marusic, I., Chauhan, K.A., Kulandaively, V. & Hutchins, H. (2015). Evolution of Zero Pressure Gradient Boundary Layers from Different Tripping Conditions. *Journal of Fluid Mechanics,* 783, 379-411.

Nezu, I. & Rodi, W. (1986) Open-Channel Flow Measurements with A Laser Doppler Anemometer. *Journal of Hydraulic Engineering,* 112(5), 335–355.

Nezu, I. (2005). Open Channel Flow Turbulence and Its Research Prospect in the 21st Century. *Journal of Hydraulic Engineering,* 131(4), 229–246.

Ranga Raju, K., Asawa, G. & Mishra, H. (2000). Flow Establishment Length in Rectangular Channels and Duct. *J. Hydraul. Eng.,* 126(7), 533-539.

Rowinski, P.M., Aberle, J. & Mazurczyk, A. (2005). Shear Velocity Estimation in Hydraulic Research. *Acta Geophysica Polonica*. 53(4), 567-583.

Sarma, K.V.N., Prasad, B.V.R. & Sarma, A.K. (2000). Detailed Study of Binary Law for Open Channels. *Journal of Hydraulic Engineering,* 126(3), 210–214.

Silberman, E. (1980). Boundary Layers in Developing Open Channel Flow. *Journal of Hydraulic Division*, 106, 1237-1241.

Tominaga, A., Nezu, I., Ezaki, K. & Nakagawa, H. (1989). Three-Dimensional Turbulent Structure in Straight Open Channel Flows. *Journal of Hydraulic Research*, 27(1), 149-173.

Wahl, T. L. (2003). Discussion of Despiking Acoustic Doppler Velocimeter Data by Derek G. Goring and Vladimir I. Nikora *Journal of Hydraulic Engineering,* 129(6), 484-487.

Yan, J., Tang, H.W., Xiao, Y., Li, K.J. & Tian, Z.J. (2011). Experimental Study on Influence of Boundary on Location of Maximum Velocity in Open Channel Flows. *Water Science and Engineering* 4(2), 185–191.

Yang, S.-Q., Tan, S.K. & Lim, S.Y. (2004). Velocity Distribution and Dip Phenomenon in Smooth Uniform Open Channel Flows. *Journal of Hydraulic Engineering,* 130(12), 1179-1186.

Proceedings of the 37th IAHR World Congress
August 13 – 18, 2017, Kuala Lumpur, Malaysia

RESEARCH ON DETECTION METHOD FOR LARGE-SCALE PARTICLE IMAGE VELOCIMETRY IN RIVER MODEL TEST

CHENG CHEN(1), YUNFENG XIA(2), ZIYANG LI(3) & XIN WANG(4)

(1,2,3,4) State Key Laboratory of Hydrology-Water Resources and Hydraulic Engineering,
Nanjing Hydraulic Research Institute, Nanjing, China,
cchen@nhri.cn

ABSTRACT

In the experimental study of large-scale river model in China, LSPIV (Large-Scale Particle Image Velocimetry) measurement technique for surface flow field has been applied widely. The measurement accuracy of LSPIV is affected by seeding particle, camera resolution, lens distortion, mounting height, time control precision of image acquisition, PIV algorithm, etc. In the process of the actual use of LSPIV measurement system, the size of the correlation window can also directly lead to measurement error. In order to analyze the LSPIV technique in river model test, it is necessary to research the detect method for the measurement accuracy. A new detection method for LSPIV in river model test is introduced in this paper. Water flow can be simulated by a uniform rotating platform with precisely controlled system. The measured data of LSPIV system has been compared with the true value of rotating platform to detect the accuracy of LSPIV system.

Keywords: Model test; flow measurement; particle image velocimetry; detection method; rotating platform.

1 INTRODUCTION

In the experimental study of large-scale river model in China, PIV (Particle Image Velocimetry) measurements for surface flow field have been applied widely. In order to research river hydrodynamic structure and provide scientific basis for project plan, velocity distribution information of surface flow field can be obtained by LSPIV (Large-Scale PIV) technique in river model test (Wang et al., 1996; Tian et al., 1998). The main differences between LSPIV and conventional PIV are as follows (Kantoush and Schleiss, 2009; Fox and Patrick, 2008): (a) Measuring field and tracer particles of LSPIV are much bigger than conventional PIV; (b) Cameras in LSPIV system are much more; (c) Measuring distance of LSPIV is much farther; (d) There are no special laser source system in LSPIV.

A typical LSPIV system mainly includes tracer particles, cameras, image acquisition control system and image processing system. The measurement accuracy of LSPIV system could be directly affected by following features of tracer particle, camera resolution, lens distortion, installation height, control accuracy of image acquisition time, PIV algorithm, etc. In addition, the size of correlation window in PIV cross-correlation algorithm will directly lead to the measurement error in actual use of LSPIV system (Wu et al., 2002). In order to research LSPIV technique and improve its performance, it is necessary to research the detection method for the measurement accuracy of LSPIV system.

At present, commonly used flow velocity meters include the propeller current meter and the ADV (Acoustic Doppler Velocimeter) are used to detect the measurement accuracy of LSPIV. However, surface flow velocity cannot be directly measured by the above flow velocity meters because they must be underwater and keep a certain distance from the surface during the measurement process, which will directly impact on the detection results. A new detection method for LSPIV is introduced in this paper.

2 DISTRIBUTED LSPIV SYSTEM

A distributed LSPIV system was developed for large-scale river model test. Million pixel high-definition intelligent integrated industrial cameras were used in this LSPIV system and connected with computer through wireless network (Figure 1). Advanced digital image processing algorithm was combined with the basic theory of fluid mechanics for synchronous data acquisition of large-scale flow field.

The image resolution of the intelligent integrated industrial camera is 4000×3000. The camera is equipped with infrared light automatic gain, adaptive light adjustment and automatic zoom (2.8mm to 12mm). There is a gigabit POE (Power Over Ethernet) interface in the camera. Image transmission and camera power supply can be completed at the same time by only a cable with a gigabit POE switch. The complexity of wiring in LSPIV system can be significantly reduced so that cameras are easy to add in the system.

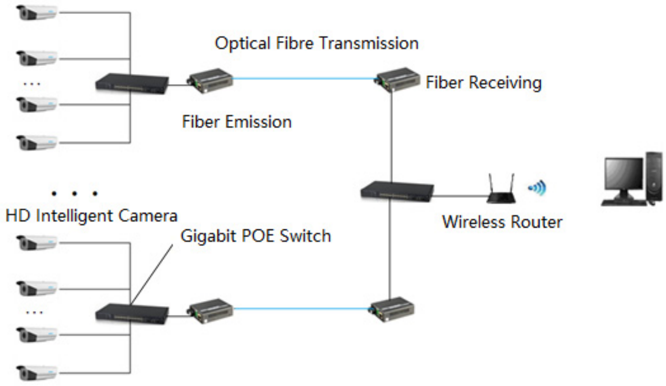

Figure 1. The composition of LSPIV system.

Image acquisition process is automatic without artificial adjustment. Particle distribution can be monitored by cameras in real-time. PIV cross-correlation algorithm and particle tracking algorithm are used in the data processing system of surface flow field. Measurement data can be directly exported in TXT, CAD, TECPLOT, BMP and other formats by the data processing system, and used to generate contour lines and streamlines of flow field, etc. (Figure 2).

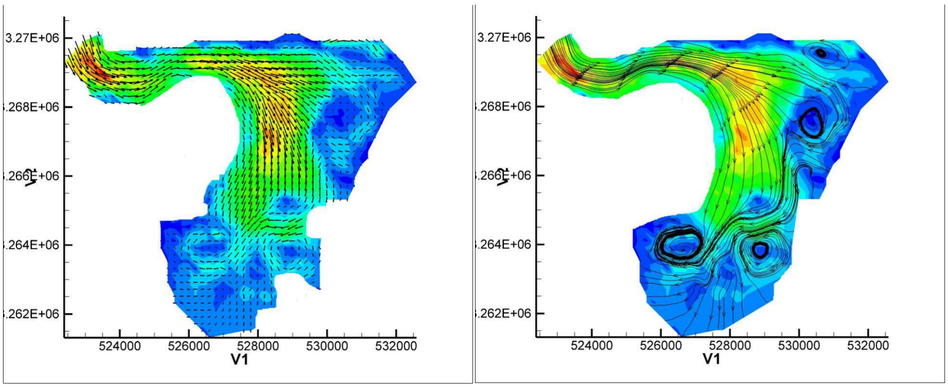

Figure 2. The measurement data of LSPIV system.

Real-time dynamic visualization of the streamline can be generated by particle recognition algorithm and saved as a video (Figure 3).

Figure 3. Streamline visualization.

3 DETECTION METHOD FOR LSPIV SYSTEM

Rotating flow usually exists in river model because of complex and changeable boundary. A uniform rotation platform was developed to simulate flow movement as close to the real situation in river model test. Particle image was randomly generated by computer and then printed on the rotating platform, which rotated at a constant angular velocity to simulate particle motion of the surface flow field in river model test. Since the particles on the rotating platform were accurately generated by computer, the coordinates of particles on the platform were accurately determined and the speed of any position on the rotating platform was accurately determined ($v = \omega \times \mathrm{r}$). The error was measured directly by comparing the measured data of the LSPIV system with the true value of the rotating platform.

The detection device for LSPIV mainly comprises circular rotating platform, stepping motor, controller, transmission mechanism (Figure 4). The circular rotating platform is a smooth aluminum rotating disk with a diameter of 30cm. The resolution of the stepping motor is 0.001 degrees and the maximum rotating speed is up to 50 degrees /s. The drive mode adopts the structure of worm gear and the transmission ratio is 90:1. The rotating shaft is made by precision machining with multiple process. The dial scale ring is a laser scribing ruler, which is convenient for the initial positioning and reading. Stepper motor is connected with worm by elastic coupling. The eccentric disturbance and noise was greatly reduced because of synchronous transmission and perfect depolarization. The controller is always working in one of four states: automatic state, manual state, program editing state and parameter setting state. When the controller is powered up, the controller is in manual state and the coordinate value is automatically cleared. Then the manual / automatic mode can be switched and the rotation speed, rotation time, rotation direction and other parameters can be set.

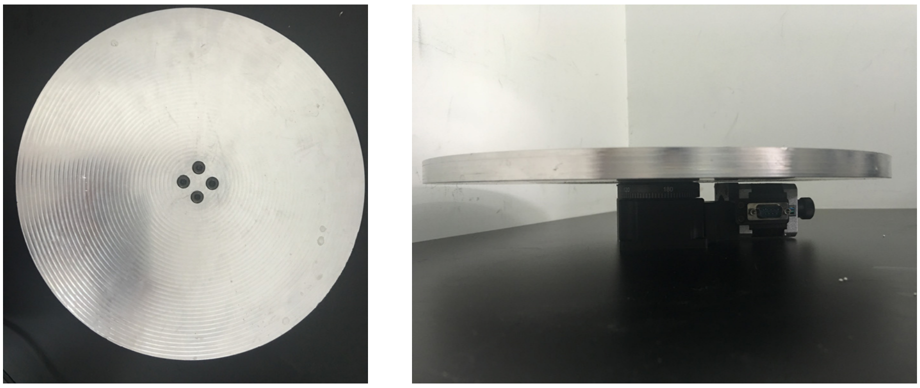

Figure 4. The detection device for LSPIV system.

In order to analyze the performance index of LSPIV system, the influence on the measurement results caused by camera resolution, lens distortion, image acquisition system and flow extraction algorithm was detected by uniform rotating detection platform. Rotating platform was placed in the center of the image shooting (P1), the rotating speed was respectively set as 1 degree/s、5 degrees/s、10 degrees/s、20 degrees/s、30 degrees/s. The LSPIV system was used to measure speed data of particles during the smooth operation of the platform. In order to detect the distortion correction performance of LSPIV system, the rotating platform was respectively placed at P2 and P3 (as shown in Figure 5) which were between the center and the edge of the image. In addition, the performance of LSPIV system at different heights can be detected.

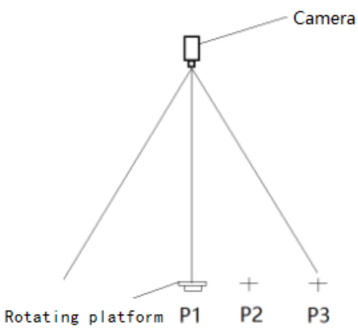

Figure 5. The detection positions of the rotating platform.

The measurement data of LSPIV system was analyzed and compared with the exact value of the rotating platform, the maximum measurement error is less than 5%. The measurement results can be intuitively detected through flow field contours (Figure 6).

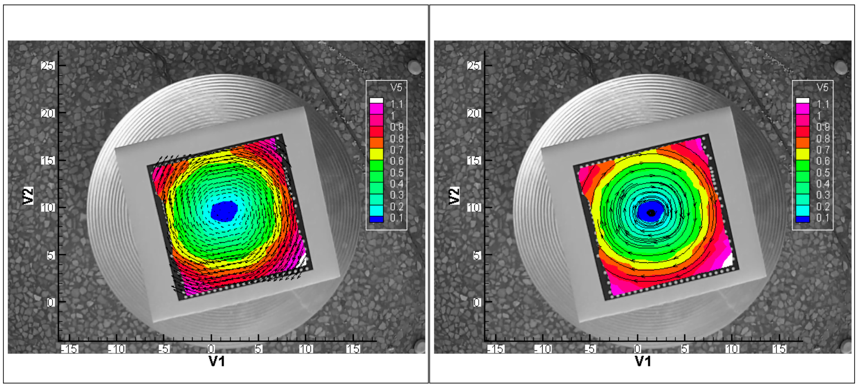

Figure 6. The detection results of LSPIV system.

In order to detect the accuracy of LSPIV system mounted on river model, a bigger detection device with a diameter of 100 cm was developed (Figure 7). The maximum rotating speed is up to 120 degrees/s.

Figure 7. The detection device with a diameter of 100 cm.

4 CONCLUSIONS

A new detection method for LSPIV system in river model test is introduced in this paper. Water flow can be simulated by a uniform rotating platform with precisely controlled system. The measured data of LSPIV system was compared with the true value of rotating platform to detect the accuracy of LSPIV system.

This detection method is based on the precondition of tracer particles completely follow water flow. The influence of tracer particle tracing on the measurement error is not considered in this paper. This study should be improved in future work.

ACKNOWLEDGEMENTS

This paper was supported by the National Key Scientific Instrument and Equipment Development Project (No.2011YQ070055), the National Natural Science Foundation of China (No.51309159, No.51479124), and the Fundamental Research Funds of Nanjing Hydraulic Research Institute (No. Y216004,No.Y215006,No. Y214002,Y716020)

REFERENCES

Fox, J.F. & Patrick, A.(2008). Large-Scale Eddies Measured with Large Scale Particle Image Velocimetry. *Flow Measurement and Instrumentation,* (19), 283-291.

Kantoush, S.A. & Schleiss A.J. (2009). Large-Scale PIV Surface Flow Measurements in Shallow Basins with Different Geometries. *Journal of Visualization,* 12(4), 361-373.

Tian, X.D., Chen, J.F., Li, Y.S., Li & Y.L. (1998). Application of Image Processing Technics to Velocity Field Measurement in Physical Model. *Journal of Tsinghua University (Sci&Tech),* 38(1), 103-106.

Wang, X.K., Pang, D.M., Wang, G.X. & An, F.L. (2003). Application of Image Processing Technics to Velocity Field Measurement in Physical Model. *Journal of Sediment Research,* (4), 21-26.

Wu, L.H., Yan, Z.M. &Tang H.W. (2002). Determination of The Correlation Window Sizes in Correlation Analysis if DPIV. *Advances in Water Science,* 13(5), 594-598.

Proceedings of the 37th IAHR World Congress
August 13 – 18, 2017, Kuala Lumpur, Malaysia

MEASUREMENT OF TWO-DIMENSIONAL WATER SURFACE PROFILE OF ROUGH WALL TURBULENCE BY SAMPLING MOIRE METHOD

KOJIRO TANI[1], ICHIRO FUJITA[2] & HIDETO YOSHIMURA[3]

[1,2,3] Graduate School of Engineering, Department of Civil Engineering, Kobe University, Kobe, Japan,
kojiro0531@gmail.com; ifujita@kobe-u.ac.jp; hideto_y_3@hotmail.com

ABSTRACT

The characteristics of water surface deformation is subject to various causes such as the sub-surface turbulence structure but detailed examination of the free-surface dynamics has not been fully understood yet. In order to examine the water surface features in a laboratory scale flow, a sampling moiré method was used to capture the two-dimensional deformation at a high sampling rate. The target flow is a shallow open-channel flow roughened by density packed glass marbles. For the shallow flow with a depth one and a half times the marble diameter, time-dependent water surface features were captured by varying the Froude number. The instantaneous water surface profiles were analyzed as a form of the space-time image expression to examine the advection feature of the surface pattern. Subsequently, in order to clarify the spatial and temporal behavior of water surface fluctuations, the frequency wavenumber spectra were calculated. According to the results, the effect of dispersive gravity waves travelling on the water surface is greater than non-dispersive waves advected by the turbulence in the hydraulic condition where the rough wall effects directly influence the free-surface dynamics. In addition, the intensity of water surface fluctuation is found to increase with the squared value of the Froude number, which can be estimated from a theoretical consideration.

Keywords: Water surface deformation, sampling moiré technique, Space-Time Image Velocimetry (STIV), image analysis.

1 INTRODUCTION

It is commonly observed in open-channel flow that water surface profile changes its feature significantly subject to various causes such as turbulence, wind, submerged or protruded objects and navigating boats. Among them, turbulence is the most fundamental source generating various scales of water surface features including very small-scale fluctuations. In a practical utilization of such water surface features, surface velocity distributions are measured by assuming that the advection speed of surface patterns agrees well with the water surface velocity in a large scale fully developed turbulence in the actual river flow conditions. This assumption was verified empirically by comparing with the other velocity measurement instrument such as an acoustic Doppler current profiler (ADCP) in actual river field measurements. Among the techniques to measure the advection speed of such surface feature, the space time image velocimetry (STIV) technique was developed by the authors with success to measure flood surface velocity distributions. However, paying attention to laboratory scale open-channel flows, there has been a limited number of researches tackling water surface phenomenon (Guo and Shen, 2013; Roy et al., 2004; Savelsberg et al., 2006; Horoshenkov et al., 2013). According to the previous laboratory scale experiments especially in shallow water conditions at relatively low Reynolds number, the above assumption sometimes seems to fail with a contradictory result much different from those observed in actual rivers.

In order to examine the water surface features experimentally, a two-dimensional water surface measurement technique, i.e. a sampling moiré method, was introduced to capture time-dependent two-dimensional profiles. A number of measurement techniques has been proposed to capture the free- surface deformations (Grant et al., 1990; Cobelli, 2009; Zhang, 1996; Tsubaki and Fujita, 2005), but the proposed method is considered one of the most accurate methods to detect small deformations based on the sampling moiré methods developed by Ri et al. (2010). From the time-dependent two-dimensional measurement results of water surface deformation, their advection feature was examined in detail.

2 EXPERIMENTAL SETUPS

The experiment was conducted using a straight open-channel with a length of 4m and a width of 20cm. The channel slope is variable and the channel walls are made of transparent acrylic plates on all sides. The channel bottom was densely packed in a staggered fashion by glass marbles with a diameter of 1.7cm. The relative water depth was kept constant at about 1.5 times the diameter. The hydraulic condition is shown in Table 1. The water depth H is measured from the virtual origin y_b, which is set 0.8 times the roughness height k. Three cases each in subcritical flow conditions with the same water depth were examined by varying the channel slope and input discharge to cover the range of the Froude number from 0.47 to 0.70. The water depth was kept very shallow so that the bed roughness condition would directly influence the water surface deformation and fluctuation.

Table 1. Hydraulic conditions.

CASE	Water depth H(cm)	Roughness height k(cm)	Froude number Fr(-)	Reynolds number Re(-)	Channel slope I(-)	Surface velocity U_s (cm/s)
Case 1			0.47	6374	0.006	28.8
Case 2	2.89	1.7	0.59	7965	0.009	42.7
Case 3			0.70	9558	0.012	51.1

The experimental setup for applying the sampling moiré method is shown in Figure 1. A lattice pattern was projected on the water surface so that direction of the pattern agrees with the flow direction. The lattice pattern was generated so that its image intensity has a cyclic sinusoidal distribution as indicated in Figure 2. In order to enhance the color difference of the lattice pattern, the water was colored white by mixing a white poster color dye. Then, the water surface fluctuation was capture by using a high-speed camera at a sampling rate of 100 frame per second with a spatial resolution of 1024 by 1024 pixels. About 100 seconds of data, i.e. about 10,000 sequential frames were obtained in one case. The target area was a square with a side of about 10 cm. The water surface velocity U_s in Table 1 was measured by the particle image velocimetry (PIV) technique by separately supplying fine charcoal power from the upstream location.

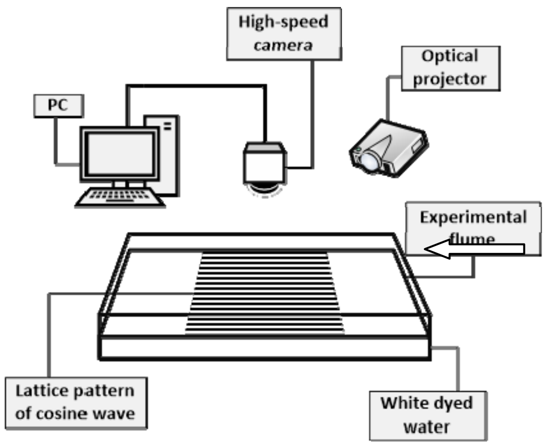

Figure 1. Experimental setup for water surface measurement.

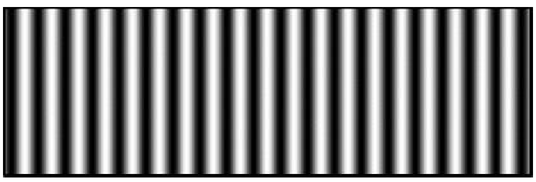

Figure 2. Lattice pattern used for surface measurement.

3 THE SAMPLING MOIRÉ METHOD

In a basic moiré method, small displacement of an object can be detected by superposing a lattice pattern before and after the deformation, i.e. the phase difference of moiré pattern appeared by the superposition is proportional to the amount of displacement. In this sense, the displacement of water level during a small-time interval Δh is directly related to the phase difference $\Delta\phi$ as:

$$\Delta h = m\Delta\phi, \tag{1}$$

where m is the coefficient of proportionality.

In the sampling moiré method, a phase modulation related to displacement information can be measured by using a single camera (Ri et al., 2010). The lattice pattern projected on the water surface has an image intensity distribution as:

$$I = a\cos\phi + b. \tag{2}$$

Here, a is an amplitude of image intensity and b is the background intensity. The variables a, b and can be determined from at least three images by shifting the phase difference. When one cycle of lattice pattern is divided into N, the image intensity distribution of I_n can be expressed by the following relation by shifting the phase step by step:

$$I_n = a\cos\left(\phi + n\frac{2\pi}{N}\right) + b. \qquad [3]$$

The phase distribution can then be obtained by the following relation:

$$\tan\phi = -\frac{\sum_{n=0}^{N} I_n \sin\left(n\frac{2\pi}{N}\right)}{\sum_{n=0}^{N} I_n \cos\left(n\frac{2\pi}{N}\right)} \qquad [4]$$

The above technique is basically called as a phase shift method usually applied for displace measurement of a static object, which is not applicable to water surface displacement with dynamic variation in time. Hence, in the sampling moiré method, a number of phase-shift images are generated by thinning out pixels at regular intervals, which are then used in the conventional phase shift method explained above. With this method, three-dimensional water surface deformation can be measured only by using a single high-speed camera.

4 EXPERIMENTAL RESULTS

Before the experiment, the measurement accuracy was examined by adding a small amount of water into a static container little by little to increase the water depth at a rate of 0.2mm per one filling, while measuring the surface by the sampling moiré method. The measured results are compared with the water level calculated from the added water volume for evaluating the measurement accuracy. The calibration plot is shown in Figure 3 demonstrating a favorable accuracy within a small range of 1mm.

Figure 4 provides instantaneous water surface deformations for the three cases indicated in Table 1. The area is the in the middle of the channel away from the side walls. In the present measurement system, about ten thousand instantaneous profiles that correspond to 100 seconds of sequential data were obtained. It is obvious that the water surface with smooth variation was obtained while reflecting a local change of surface level. Generally, the changes of local deformation seem to be arranged in a staggered manner which might be generated due to the effect of drag force acted on each glass marbles. The total pattern composed of the local deformations are advected in the downstream direction accompanying dispersive wave components that can travel in all directions.

In order to examine the advection feature of the surface deformations, a space-time image (STI) expression of surface variation for a search line in the streamwise direction was obtained and compared as provided in Figure 5 normalized by using the water depth H and the surface velocity U_s. The inclined lines in the figure corresponds to the advection trajectory by the surface velocity. It is interesting to note that patterns with speeds different from the advection can be seen in each case. It can be seen from the figure, that slower trajectory become more predominant for the larger Froude number indicating that the effect of dispersive gravity waves travelling in the downstream direction seems to be promoted in such a case.

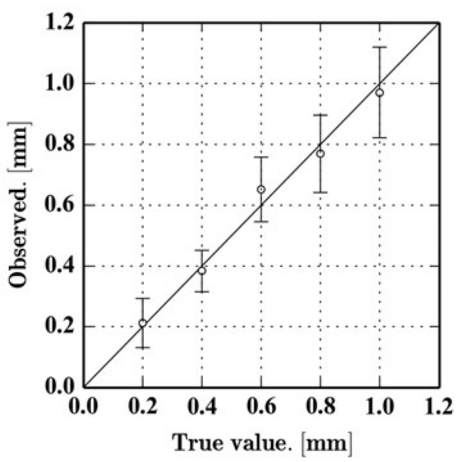

Figure 3. Evaluation of the sampling moiré method.

(a) Case1 (Fr=0.47) (b) Case2 (Fr=0.59) (c) Case3 (Fr=0.70)

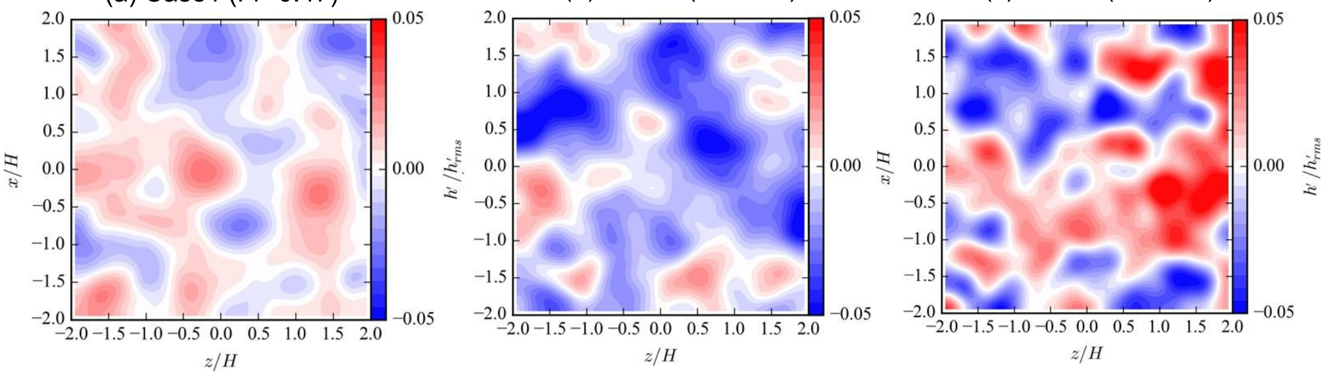

Figure 4. Instantaneous water surface deformation.

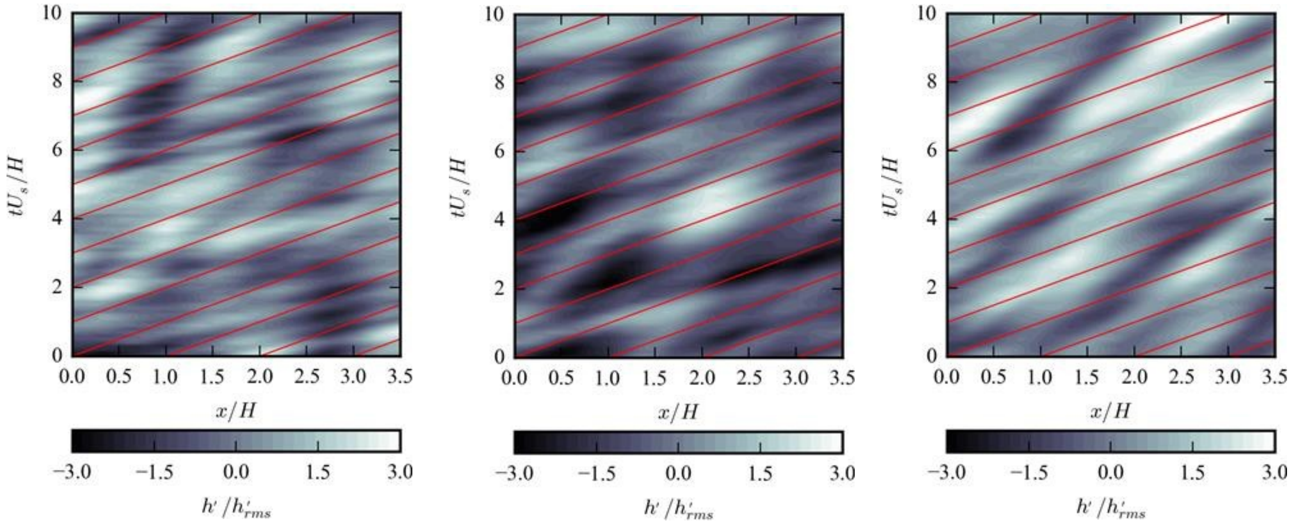

(a) Case1 (Fr=0.47) (b) Case2 (Fr=0.59) (c) Case3 (Fr=0.70)

Figure 5. Space-time image expression of water surface fluctuation.

In the subsequent analysis, the STI data was decomposed into a wavenumber frequency plane, indicating the water surface advection features caused either by wall turbulence or the dispersive gravity waves. The analyzed results are provided in Figure 6, in which the solid line corresponds to the advection by the free surface velocity *U*s, i.e.:

$$\sigma = U_s k_x \, , \qquad [5]$$

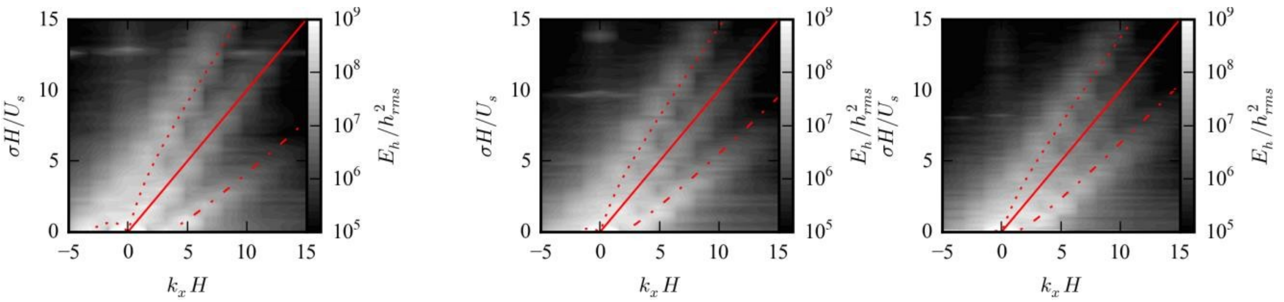

(a) Case1 (Fr=0.47) (b) Case2 (Fr=0.59) (c) Case3 (Fr=0.70)

Figure 6. Wavenumber frequency spectrum.

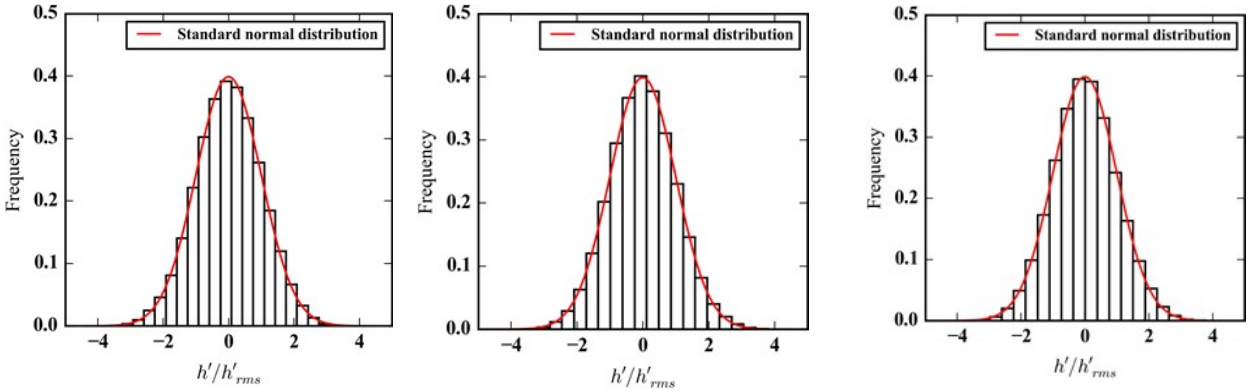

(a) Case1 (Fr=0.47) (b) Case2 (Fr=0.59) (c) Case3 (Fr=0.70)

Figure 7. Probability density function of water surface fluctuations.

in which σ is the angular frequency and k_x is the wave number in the streamwise direction. On the other hand, the broken line shows the proceeding wave speed and the dash-dotted line indicates the receding wave speed expressed by the following relations:

$$\sigma = \left[U_s \pm \sqrt{\frac{g}{k_x}\tanh\left(k_x H\right)} \right] k_x \quad [6]$$

Figure 6 clearly includes the three types of advections expressed by Eq. [5] and [6], but as has already discussed in terms of the STIs shown in Figure 5, the advection by the surface velocity in Figure 6(a) becomes relatively smaller than the other cases. Generally speaking, the effect of gravity waves travelling in the streamwise or upstream directions was comparable to or greater than the advection of wall turbulence moving with the surface velocity in very shallow hydraulic conditions, which is different from those observed in large scale turbulence.

In addition, the intensity of water surface fluctuation was examined by processing instantaneous surface data at all points within the measurement area. The obtained probability density distribution of water surface fluctuation agrees very closely with the standard normal distribution or the Gaussian distribution as shown in Figure 7. There is no dependence on the Froude number or other variables with respect to the distribution feature of water surface fluctuations. Finally, Figure 8 compares the total intensity of water surface fluctuations with those obtained for smooth wall data. As can be expected, the intensity for rough wall data is several times greater than those for a smooth wall. This is because the mechanism for generating surface fluctuations in a smooth wall might be different from that in rough walls in shallow water conditions, in which direct effect of roughness elements are predominant in the generation of surface deformation and fluctuation while in a smooth wall ejected vortices with a large vorticity that reach the water surface can influence the water surface deformation. It is interesting to note that the intensity increases with the squared value of the Froude number, which was also observed in a smooth wall simulation (Yokojima and Nakayama, 2002).

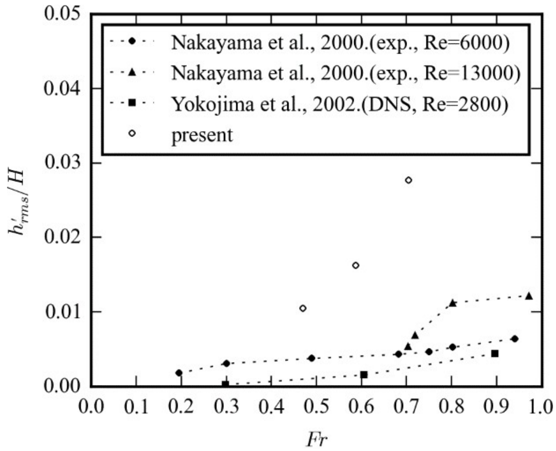

Figure 8. Intensity of water surface fluctuation.

5 CONCLUSIONS

The water surface deformations and fluctuations in shallow flow over a relatively large roughness were measured by a sampling moiré method with a reasonable accuracy. As the water depth is only 1.5 times the roughness element composed of glass marbles, the water surface is directly affected by the form drag or separated vortices from each roughness particles. Under such conditions, the effect of the Froude number was examined in view of the advection feature of surface variations and the intensity of fluctuation. It was found that the space-time image and the frequency-wavenumber expression of water surface variation that the advection due to dispersive gravity waves are predominant in such shallow water conditions with relatively large roughness. Moreover, the intensity of fluctuation increases with the square of the Froude number and the level of intensity is several times larger than that for smooth wall conditions. Further research regarding the effect of relative water depth is needed to fill the gap of the understandings between laboratory and field observation.

REFERENCES

Cobelli, P.J. (2009). Global Measurement of Water Waves by Fourier Transform Profilometry. *Experiments in Fluids,* 46, 1037–1047.

Grant, I., Stewart, N. & Padilla-Perez, I.A. (1990). Topographical Measurements of Water Waves Using the Projection Moire Method. Appl. Opt., 29, 3981–3983.

Guo, X. & Shen, L. (2013). Numerical Study of The Effect of Surface Waves on Turbulence Underneath. Part 1. Mean Flow and Turbulence Vorticity. *Journal of Fluid Mechanics*, 733, 558-587.

Horoshenkov, K.V., Nichols, A., Tait, S.J. & Maximov, G.A. (2013). The Pattern of Surface Waves in a Shallow Free Sur-Face Flow. *Journal of Geophysical Research, Earth Surface*, 118, 1864-1876.

Nakayama, A., Nakase, Y., Yokojima, S. & Fujita, I. (2000). Improvements of Two-Equation Turbulence Model with Surface Fluctuation Used as A Parameter for Calculation of Open-Channel Flows. *Journal of Applied Mechanics JSCE*, 50(4), 501–508 (in Japanese).

Ri, S., Fujigaki, M. & Morimoto, Y. (2010) Sampling Moiré Method for Accurate Small Deformation Distribution Measurement. *Experimental Mechanics*, 50(4), 501–508.

Roy, A.G., Buffin-Belanger, T., Lamarre, H. & Kirk-bride, A. (2004). Size, Shape and Dynamics of Large Scale Turbulent Flow Structures in a Gravel Bed River. *J. Fluid Mechanics*, 500, 1-27.

Savelsberg, R., Holten, A. & van de Water, W. (2006). Measurement of the Gradient Field of a Turbulent Free Surface*. Experiments in Fluids*, 41, 629–640.

Tsubaki, R. & Fujita, I. (2005). Stereoscopic Measurement of a Fluctuating Free Surface with Discontinuities. *Measurement Science and Technology*, 16, 1894–1902.

Yokojima, S. & Nakayama, A. (2002). Direct Numerical Simulation of Open-Channel Flow with Free-Surface Fluctuations. *Journal of JSCE*, 712, 57-72 (in Japanese).

Zhang, X. (1996). An Algorithm for Calculating Water Surface Elevations from Surface Gradient Image Data. *Experiments in Fluids*, 21, 43–48.

Proceedings of the 37th IAHR World Congress
August 13 – 18, 2017, Kuala Lumpur, Malaysia

THE ESTIMATION OF SPATIAL AND TEMPORAL DISTRIBUTION OF ACCIDENTALLY SPILLED POLLUTANT INTO RIVER

IL WON SEO[1] & DONGHAE BAEK[2]

[1,2] Dept. of Civil and Environmental Engineering, Seoul National University, Seoul, Republic of Korea
seoilwon@snu.ac.kr; wes1204@snu.ac.kr

ABSTRACT

The tracer test using fluorescent dye has been generally performed to understand the mixing behavior of pollutants accidently spilled into river. However the existing tracer test method requires a considerable amount of cost and labor, and it provides only concentration distribution in time at the fixed location of fluorometers. In this study, we developed the image processing techniques on the aerial images taken by digital camera which is mounted on the unmanned aerial vehicle (UAV) during performing the tracer test to overcome the limitation of conventional tracer test. The tracer tests were performed in the meandering channel which was artificially constructed but on large scale. The 20% of rhodamine WT was used as the tracer material. For acquisition of the aerial imageries, *DJI-Phantom3 professional*, which is the inexpensive and commercial UAV, was used and the images were taken by the normal digital camera, which has three optical bands. The images were sequentially taken as 4K resolution (3840×2160) and 30 frames per second during tracer test. The image data were converted to concentration data in all time applying the image processing technique. It showed the determination coefficient over 0.9 with the concentration data measured by fluorometers in water channel. The spatial distribution of concentration represents well the effect of advection and dispersion in meandering channel, especially the transient storage in vegetated area. It is expected that this experimental method can contribute to the spatial analysis of dye dispersion in open channel flow, and facilitates to reduce the cost and labor for tracer test.

Keywords: Pollutant mixing; Tracer Test; Fluorescent dye; UAV; Concentration fields.

1 INTRODUCTION

The tracer test using fluorescent dye has been generally performed to understand the mixing behavior of pollutants accidently spilled into river. However the existing tracer test method requires considerable amount of cost and labor, and it provides only concentration distribution in time at the fixed location of fluorometers. In this conventional tracer test, the mixing behavior has been analyzed by statistical approach based on frozen cloud approximation such as the analysis of the variance of time-concentration curves to determine the dispersion coefficients (Baek and Seo, 2010; Seo et al., 2016). Although the spatial distribution of pollutant concentration can be obtained using an interpolation or a kriging method, it is spatially inaccurate and limited due to the number of sensors installed in river. In this study, we have developed the image processing techniques on the imagery taken by the commercial digital camera which was mounted on the unmanned aerial vehicle (UAV) during performing the tracer test to overcome the limitation of conventional tracer test. The objectives of this study is to develop the tracer test method using the aerial digital image, and to obtain the temporal and spatial distribution of pollutant materials.

2 DESCRIPTION OF EXPERIMENT AND DATA COLLECTION

2.1 Experimental channel

The tracer test was performed in River Experimental Center established by *the Korean Institute of Civil Engineering and Building Technology* in Republic of Korea. The experimental channel was the meandering channel with 1.5 of sinuosity. The channel length in flow direction is 121 m, the average of channel width and depth are 4.91 m and 0.44 m respectively. And channel bed was covered by vegetation on the sand. Although it was a man-made channel artificially constructed, its geometric scale was closed to the small tributary in nature. The bed shape was similar to the meandering river which is naturally formed by sediment erosion and deposition.

The hydraulic data were measured by Acoustic Doppler Current Profiler (Sontek, RiverSurveyor S5) at six of cross sections. The averaged discharge was maintained as 0.96 m^3/s, and the cross-sectional mean velocity was measured as 0.45 m/s. The results of hydraulic data measurement are summarized in Table 1.

The 20% of rhodamine WT was used as tracer material. It have been widely used in tracer test because it is almost conservative and can be easily detected by fluorometers in the nature river. It absorbs the light that has a peak wavelength of approximately 540 nm and emits the light that has a peak wavelength of 580 nm. In this study, the 150 ml of rhodamine WT was injected into the experimental channel, and its concentration was measured by fluorometers (YSI, 600OMS) at three of cross-sections. The five fluorometers were uniformly installed in lateral direction at each cross-sections. The location of cross-sections for measurements of hydraulic and concentration data are described in Figure 1. And the temporal concentration data at each sections are expressed as concentration-time curves in Figure 2

Table 1. The measured hydraulic data at each cross-sections.

	Mean Velocity (m/s)	Width (m)	H (m)
I.P.	0.62	5.2	0.57
Sec. 1	0.64	5.2	0.46
Sec. 2	0.51	5.4	0.42
Sec. 3	0.64	5.0	0.36
Sec. 4	0.75	4.6	0.39
Sec. 5	0.57	4.6	0.48
Sec. 6	0.60	4.4	0.40
Average	0.62	4.91	0.44

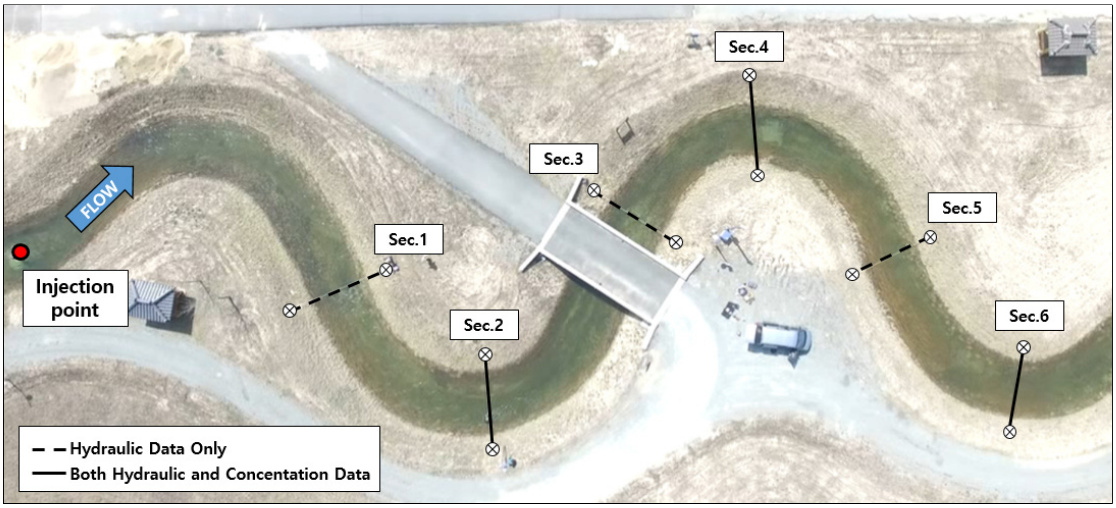

Figure 1. The aerial image on the experimental channel and the location of cross-section for measurements.

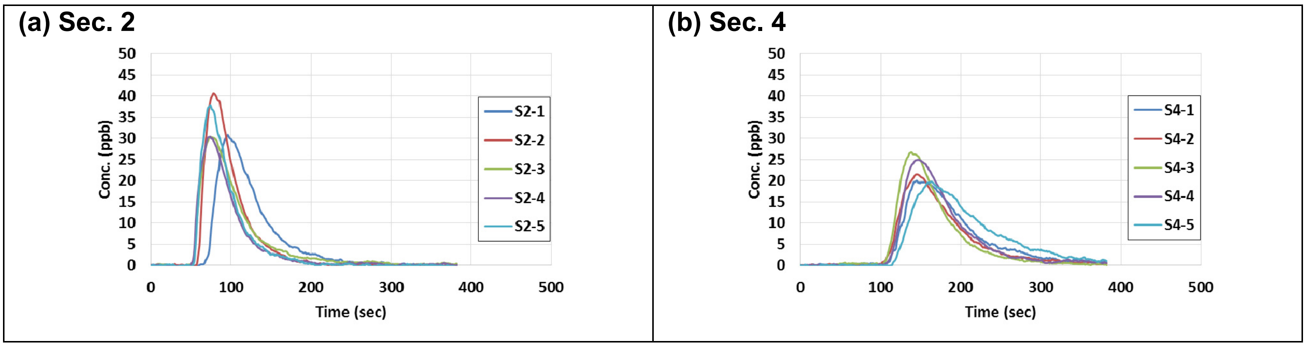

Figure 2. The result of concentration measurements.

2.2 Collection of image data

For acquisition of the aerial imageries, *DJI-Phantom3 professional*, which is the inexpensive and commercial UAV, was used, and the imageries were taken by the commercial digital camera, which has three-optical bands. The imageries were sequentially taken as 4K resolution (3840 × 2160) and 30 frames per second during tracer test. The setting of digital camera such as shutter speed and white balance were manually adjusted to prevent the pixel value changed automatically. And the all of imageries were normalized by the reference value. PTFE sheet was used as reference material. It is a kind of fluorocarbon solid, and widely used in the remote sensing field as a reference standard because it exhibits approximately the Lambertian reflectance over the UV-VIS-NIR region (Ball et al., 2013). It was installed near to experimental channel to be captured in all imageries.

The topographical survey was also performed to obtain the world coordinates on eight ground control points (GCPs). It was used for stabilizing the image sequence spatially and image registration.

3 IMAGE PROCESSING TECHNIQUE

3.1 Image registration

The captured scene in image sequences were unstable. It was displaced because the UAV was hovered around the experimental channel. The vibration due to the rotors of UAV and the wind effect make the scene displaced in short time. For stabilizing of scene in imagery, the pixel coordinates of each pixels were converted to world coordinates applying the projective transformation based on the coordinates of GCPs obtained from topographical survey. Then all images in sequence was fixed by its ground coordinates, and all pixels in each image were rescaled to a resolution of 5x5 cm in the world coordinates. The results showed that the root mean squared error of the coordinates of GCPs in images is less than 10 cm.

The unwanted pixels, which covered the water channel and cloud of dye such as bridge and equipment for measurements, were removed. Then it were filled by the cubic spline interpolation to recover the missing data in space. The procedures of the image processing were carried out by programming in MATLAB.

3.2 Conversion image data to concentration

The rhodamine WT, which was used in this study, is fluorescent dye. It is known that the fluorescence intensity is almost proportional to the concentration of material in the low concentration region. The fluorescent material absorbs the light of the certain wavelength, and emits the light in longer wavelength. Thus the fluorescence intensity depends on the amount of the absorbed light. Based on Lambert-beer's law, the equation [1] describes the fluorescence intensity in case of fluorescence dye is diluted with the water.

$$I(\lambda_F) = \phi\left[I_0(\lambda_A) - I_0(\lambda_A)\exp(-\alpha h)\right] \qquad [1]$$

where $I(\lambda_F)$ is the light intensity in the wavelength of fluorescence, $I_0(\lambda_A)$ is the light intensity in the wavelength of absorption before the light is transmitted into water, ϕ is the quantum yield which is the ratio between fluorescence and absorption of light, α is the attenuation coefficient in wavelength of absorption, h is water depth or thickness of water body.

The digital camera used in this study was the normal digital camera. It has three-optical bands which are Red, Green and Blue-band. The range of wavelength of light captured by each bands was unknown, and the overlapped ranges exist between each bands. It was hard to measure the light intensity in wavelength of florescence and absorption accurately. So the concentration data measured by fluorometers was compared to the digital number of each bands to figure out the relationship between the measured concentration and the digital number of each bands empirically. The digital number corresponding to each fluorometers were sequentially extracted from the pixel near to fluorometers in all images. The results of comparison are shown in Figure 3. The concentration of Rhodamine WT was positively correlated to the increment of digital value of Red-band and negatively correlated to the decrement of digital value of Green-band statistically. This tendency can be described as the range of wavelength of R-band that includes the fluorescence wavelength (580 nm), and the G-band that includes the absorption wavelength (540 nm).

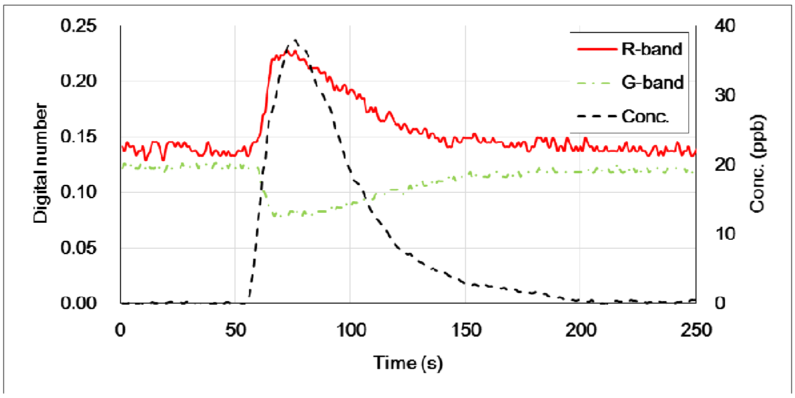

Figure 3. The time series data for digital number and concentration at center of sec. 2 (S2-3).

Based on the results of comparison, the ratio of the digital number of R-band to that of G-band was empirically introduced as the value of *Q*.

$$Q = \frac{R}{I - G} \qquad [2]$$

where I is the sunlight intensity just above water surface.

It is an analogy to the quantum yield of equation [1]. The denominator of equation [2] is the digital number corresponding to the amount of the absorbed sunlight which is transmitted into water column. The value of I is assumed as the digital number of pixel in the PTFE sheet installed near to water channel because it reflects the most of incident sunlight from its surface. The numerator of equation [2] is the digital number in wavelength of fluorescence. Figure 4 shows the relationship between the value of Q and the concentration of rhodamine WT. It shows that the value of Q is linearly increased with respect to concentration. The value of the y-intercept indicates its base. The value of base is affected by water depth at each pixel and the reflectance of bed material. Therefore it have different values at each pixel. It can be obtained from the image which is taken before rhodamine WT was injected into water channel.

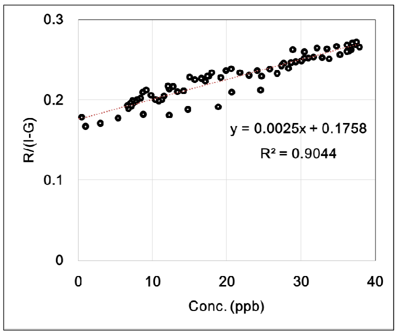

Figure 4. The relationship between the value of Q and concentration at the center of section 2.

The equation [3] is the relationship between the digital number and concentration considering the effect of the ambient light intensity. For the explicit calculation of concentration, it can be rearranged to equation [4].

$$\frac{R_{rho}}{I - G_{rho}} = aC + \frac{R_0}{I - G_0} \quad [3]$$

$$C = \frac{1}{a}\left[\frac{R_{rho}}{I - G_{rho}} - \frac{R_0}{I - G_0}\right] \quad [4]$$

where R_{rho} and G_{rho} are the digital number of R and G-band when rhodamine WT is injected into water channel, R_0 and G_0 are the digital number of R and G-band in water channel without rhodamine WT, C is the concentration of rhodamine WT, a is the coefficient of proportionality.

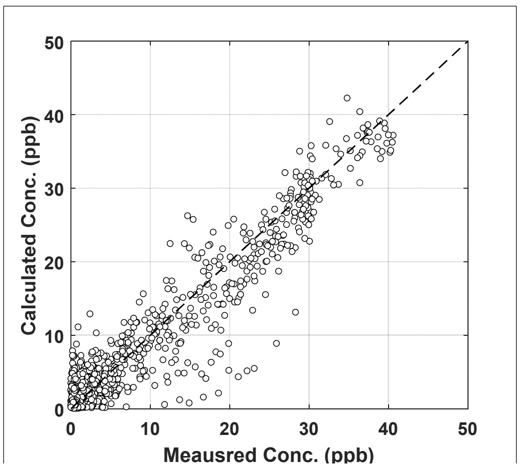

Figure 5. The comparison between the measured concentration and the results of the equation [4].

Figure 5 shows that the comparison between the measured concentration and the calculated concentration by the equation [4]. The optimum value for a was determined as the value of 0.0025, and it yields the value of R^2 as 0.90 for the date set from the five-fluorometers in the section 2.

4 VALIDATIONS AND RESULTS

4.1 Validation on the concentration-time curve

The equation [4] was applied to each pixel corresponding the location of fluorometers in all cross-sections, and compared to the concentration-time curves from measurements. Figure 6 shows the comparison between results measured by fluorometers and calculated by image processing. The solid line and square-shaped dot represent the concentrations measured by fluorometers and converted by images in time respectively.

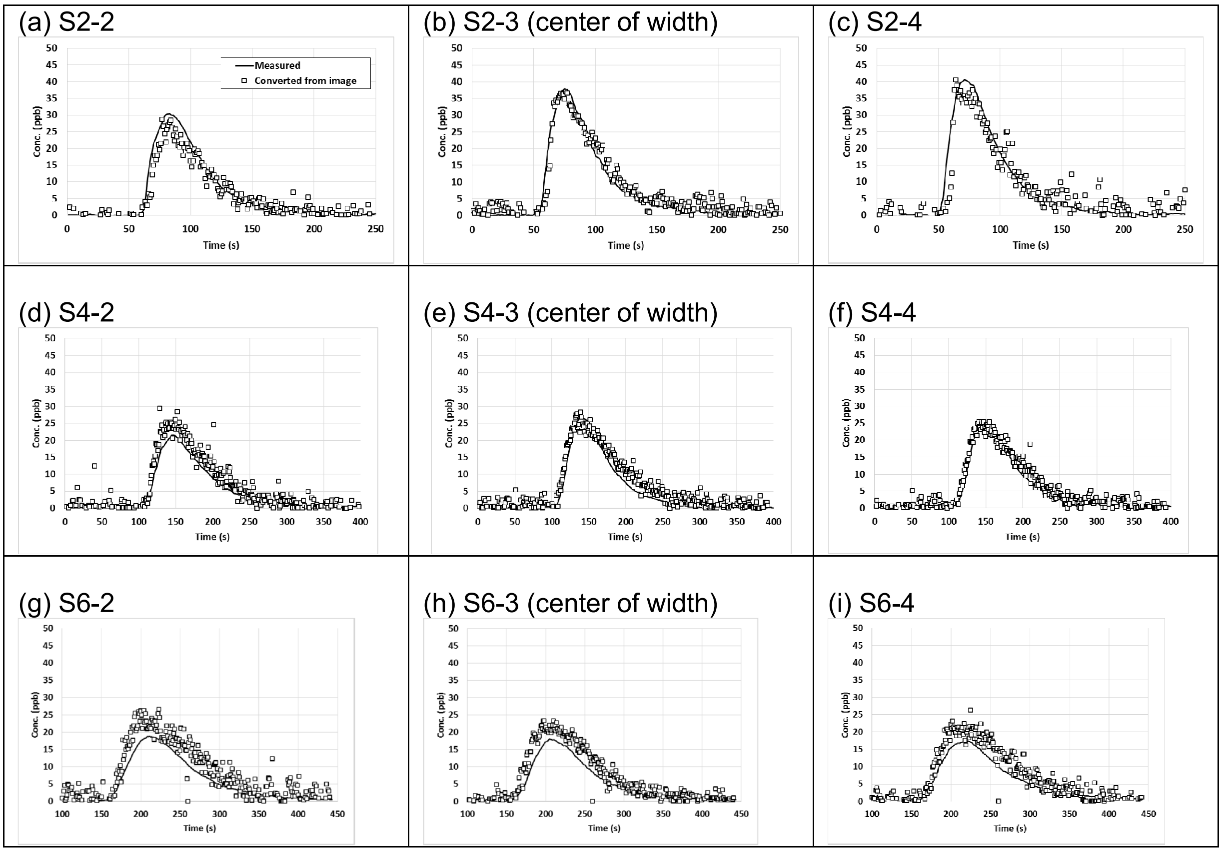

Figure 6. The results of concentration-time curve at each locations of fluorometers.

The concentration-time curves, which were converted from images using equation [4], show generally good agreement with the concentration measured by fluorometers at each cross sections. They were evaluated by the coefficient of determination, and were over the value of 0.9 for all of the concentration-time curves.

4.2 The spatial distribution of concentration

It is judged that the temporal and spatial concentration distribution were well estimated by image processing technique. All images were sequentially converted applying the equation [4]. Some pixels were converted into quite large value. It were induced by the error of coordinates in image registration, and the pixels in images has intrinsic noise itself. To remove the noise in space, the adaptive median filter was applied in reference to Hwang and Haddad (1995). The pixel values were determined as the median value in the searching window. Its advantages are that the size of window is changed adaptively, and is robust in removing the mixed impulses with high probability of occurrence while preserving sharpness. The filtered concentration fields are shown in Figure 7. The injected tracer was advected and dispersed by shear flow in meandering channel. Its maximum concentration was transported following the side of outer bank in the apex of curve. Especially the spatial distribution of concentration was formed as the v-shaped when the tracer clouds pass though the curved region shown in Figure 7 (b). It is due to the secondary flow which is the spiral motion perpendicular to the direction of the primary flow. And the low concentration remained in the vegetated bank of the channel. The tracer material was temporarily captured in the vegetated area, then it was slowly released over time. The effects of secondary flow and the transient storage in vegetated area caused the dispersion of tracer cloud increase.

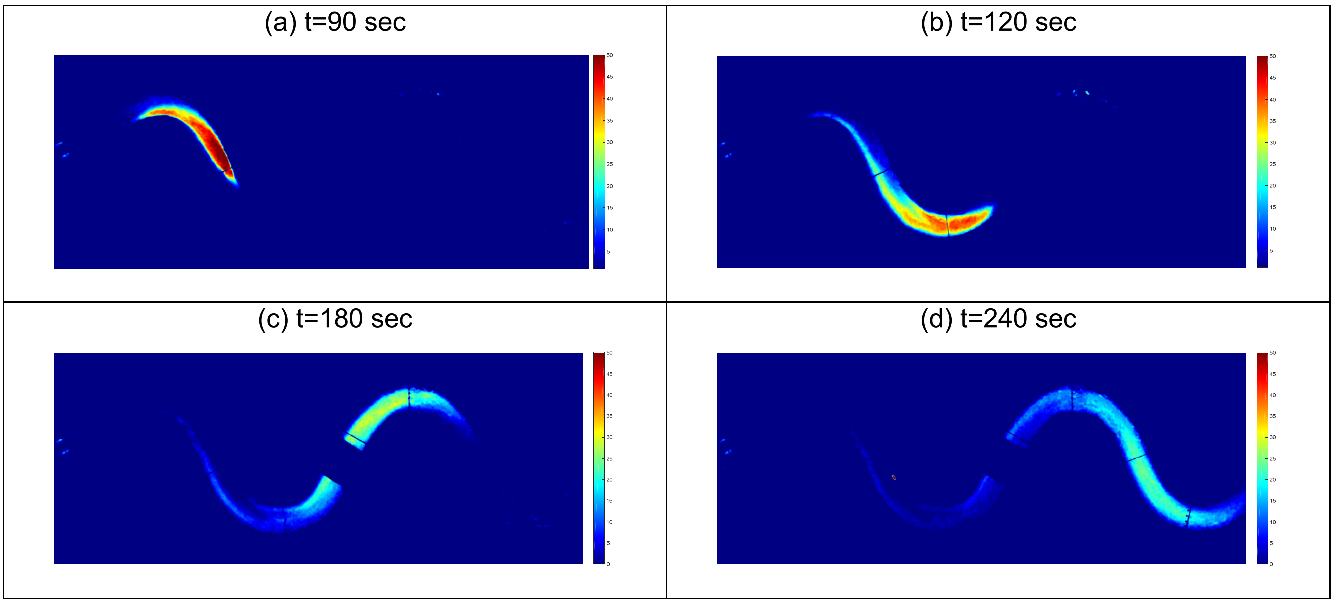

Figure 7. The spatial concentration distribution in time.

5 CONCLUSIONS

In this study, the temporal and spatial distribution of rhodamine WT was estimated by the image processing techniques using the characteristic of the fluorescence of rhodamine WT. The image data were collected by the commercial digital camera mounted in UAV. It was converted to concentration data applying the relationship between the pixel value in images and the concentration measured by fluorometers. The results for validation in time showed good agreement with the measured values showing the determination coefficient, R^2 to be over 0.9. Then it was applied to all pixel in space, and it produced the spatial concentration field at each time. The spatial concentration distribution of rhodamine WT showed the characteristics of advection and dispersion effects in meandering channel. It is expected that this experimental method can contribute to the spatial analysis of dye dispersion in open channel flow, and facilitates to reduce the cost and labor for tracer test efficiently.

ACKNOWLEDGEMENTS

This research is supported by a grant (11-TI-C06) from Advanced Water Management Research Program funded by Ministry of Land, Infrastructure and Transport of Korean government.

REFERENCES

Baek, K.O. & Seo, I.W. (2010). Routing Procedures for Observed Dispersion Coefficients in Two-Dimensional River Mixing. *Advances in Water Resources*, 33(12), 1551-1559.

Ball, C.P., Levick, A.P., Woolliams, E.R., Green, P.D., Dury, M.R., Winkler, R., Deadman, A.J., Fox, N.P. & King, M.D. (2013). Effect of Polytetrafluoroethylene (PTFE) Phase Transition at 19° C on the use of Spectralon as a Reference Standard for Reflectance. *Applied Optics*, 52(20), 4806-4812.

Hwang, H. & R.A. Haddad (1995). Adaptive Median Filters: New Algorithms and Results. *IEEE Transactions on image processing*, 4(4), 499-502.

Seo, I.W., Choi, H.J., Kim, Y.D. & Han, E.J. (2016). Analysis of Two-Dimensional Mixing in Natural Streams Based on Transient Tracer Tests. *Journal of Hydraulic Engineering*, 142(8), 1-16.

Proceedings of the 37th IAHR World Congress
August 13 – 18, 2017, Kuala Lumpur, Malaysia

EVALUATION OF SURFACE WATER QUALITY ASSESSMENT METHODS UNDER CLIMATE VARIABILITY

DONYA DEZFOOLI(1), KUMARS EBRAHIMI(2) & SHAHAB ARAGHINEJAD(3)

(1) MSc of Water Resources Engineering, University of Tehran, Karaj, IRAN
Donya.dezfooli@ut.ac.ir
(2,3) Associate Professor, Irrigation and Reclamation Engineering Department, University of Tehran, Karaj
EbrahimiK@ut.ac.ir; Araghinejad@ut.ac.ir

ABSTRACT

Climate variability could be defined as the climatic changes compared to the mean value. The increment of the greenhouse gases has deteriorated climate variability which in turn might exert a wide range of impacts on the quality and quantity of surface water resources. Therefore, not only it decreases available water resources, it also increases the cost of refinery and purification. This paper aims to analyze the impacts of climate variability on the quality of surface water resources and examine the methods used to assess the quality of surface water resources at Tale-Zang station, Dez River Iran. Two climate parameters namely precipitation and temperature were employed to analyze the climate variability. The Canadian Council of Ministers' Environment Water Quality Index (CCME-WQI) and Wilcox Diagram were applied to classify water quality. The results reveal that there is climate variability over the studied period which led to the emergence of dry and wet periods in the region. Furthermore, the results show that Wilcox diagram in incapable of explaining the quality status in terms of climate variability in most years of the studied period while CCME indicated that in most years, climate variability did not result in the emergence of critical values regarding the qualitative parameters under the study and the water quality was classified as good (80-95).

Keywords: CCME; climate variability; Dez river; surface water quality; wilcox diagram.

1 INTRODUCTION

Water is considered a critical element in human life; it is, therefore, necessary to seriously take quality and quantity of water resources into account. The ever-increasing population growth, urbanization and the increase in agricultural and industrial activities have led to water quality deterioration. On the other hand, the ever-increasing usage of green-house gases and fossil fuels has increased the earth temperature. Climate variability and change are among the principal consequences of the increase of greenhouse gases which might in turn affect the condition of water resources across the world. The increase in greenhouse gases has led to climate changes which in turn resulted in non-stationary climate variables; precipitation, temperature and solar radiation in particular (IPCC, 2001). Given that temperature is in a mutual interaction with other climate elements, it causes climate variability. The resulted phenomenon has a wide range of effects; however, it mainly affects the water resource and agriculture sections. Climate changes could be observed in various realms including plants growth period, the amount of agricultural water resources, severe frosts, floods, hurricanes, droughts and so on (Spinoni et al., 2014; Delpla et al., 2009).

Numerous studies have been carried out in this regard. For instance, Elshemy and Meon (2011) studied the effects of climate changes on the water quality indices of Aswan Dam. The effects of global climate change on NSFWQI and CCME-WQI were examined. The results revealed that the climate changes had slightly affected the indices that under the study. The study which carried out by El-Jabi et al. (2014) regarding the effects of climate change on the quality of surface water making use of WQI and CWQI methods was in line with the results obtained from the study conducted by Elshemy and Meon (2011). Laurent and Mazumder (2014) studied the effects of seasonal and inter-annual climate variability on the concentration of surface water fecal coliform in British Columbia. The results revealed that a positive correlation between the climate variability and the seasonal and intra-annual fecal coliform concentration could be observed at five percent of the stations under study. Mohammadi Ghaleni and Ebrahimi (2015) analyzed the effects of human activities and climate variability on the water resources of Saveh Plain, Iran. Making use of hydrometric and meteorological data, they analyzed the temporal and spatial variations in quality and quantity of surface and groundwater resources. Surface water quality assessment analysis revealed that electrical conductivity increased 957.34 µmho/cm in years subsequent to 1994 compared to that of years prior to 1994. Furthermore, Wilcox water quality classification decreased from C3-S1 to C4-S2.

Due to specific geographical conditions, Iran has not been protected from changes and problems have arisen from various climate conditions. Reduction of water resources in terms of quality and quantity has been one of the outstanding consequences in a way that many countries around the world, those in the Middle East in particular, are suffering from droughts and lack of high quality water that is in part due to changes occurred to the region's climate conditions. Therefore, this study generally aims to analyze the effects of climate variability on the methods of surface water quality assessment in the basin of Dez River located in Iran between the years 1969 to 2012.

2 MATERIALS AND METHODS

2.1 Study area

The great Karoon River watershed is comprised of Dez and Karoon rivers which are located on the heights of central Zagros Mountains. The coordinates are 48◦-00′ to 52◦-30′ eastern longitude and 30◦-00′ to 34◦-05′ northern latitude. The meteorological (precipitation and temperature) and water quality data regarding the period from 1969 to 2012 was provided by the Iran Water Resources Management Co. The geographical specifications of the region and the studied station are illustrated in Figure.1 and Table.1, respectively.

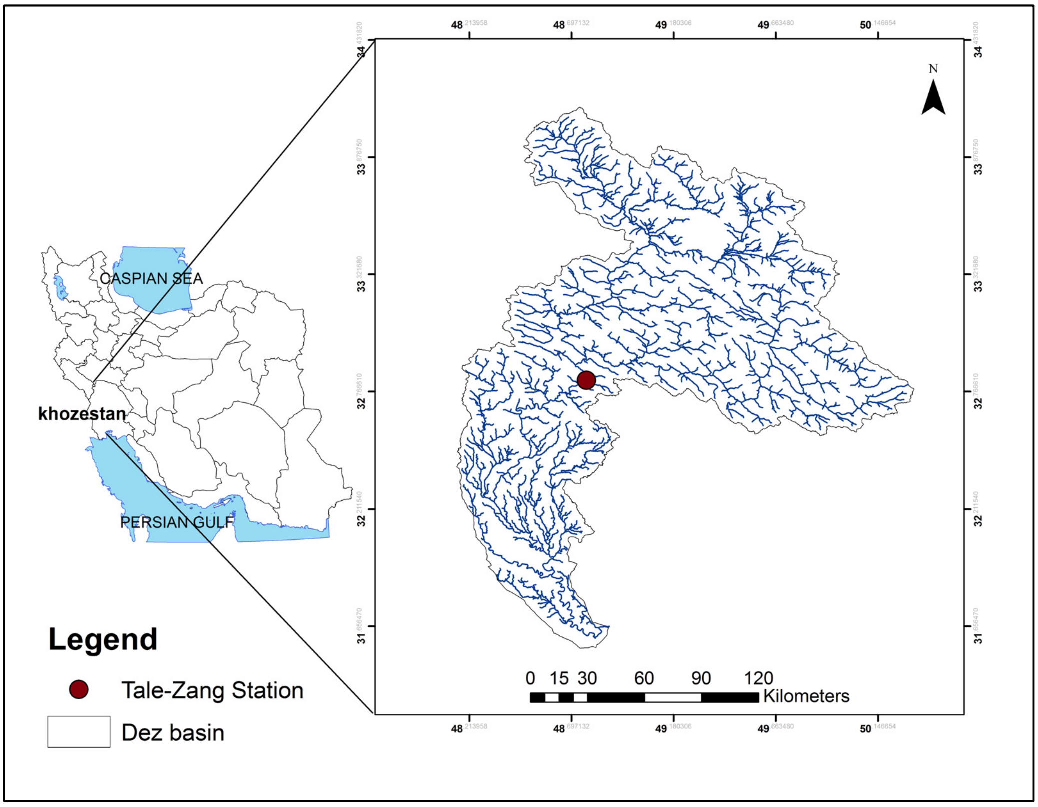

Figure 1. Location of the study area in the Dez Basin – IRAN.

Table 1. General characteristics of surveyed synoptic station in Dez Basin-IRAN.

Station	Longitude		Latitude		Elevation (m)	Long-term average precipitation(mm)
	Degree	Minute	Degree	Minute		
Tale-Zang	48	46	32	49	436	881.5

2.2 The standardized precipitation drought index

McKee et al. (1993) developed an index as the standardized precipitation index (SPI) in order to monitor the droughts in Colorado Province. The index is calculated through fitting precipitation data to the probability distribution function and then transforming the resulted probability into a standard normal distribution. SPI dependends solely on precipitation data and could be calculated on different monthly scales of 1, 3, 6, 9, 12, 24 and even 48. The seasonal SPI was used in this paper. Table 2 shows the drought categorization in terms of SPI (for more details see McKee et al., 1993).

In this paper, SPI drought index was used in order to analyze the climate variability in spring, fall and winter seasons. Given that the precipitation during summer equals to zero or is trivial, the analysis of SPI values would be void of meaning. Climate variability during this season was, therefore, analyzed through applying the climate parameter of temperature.

Table 2. Drought classification based on SPI (Mckee et al., 1993).

SPI Values	≤-2	-2 to -1.5	-1 to -1.49	-0.99 to 0.99	1 to 1.1.49	1.5 to 1.99	2 ≤
Drought Category	Extreme drought	Severe drought	Moderate drought	Normal	Moderateley wet	Severely wet	Extremely wet

2.3 Wilcox diagram

Regarding the agricultural section, the quality of water is as important as its quantity. Poor quality water could be regarded a restrictive factor in the agricultural section. Wilcox diagram is considered one the most prominent and oldest classifications in this regard. Agricultural water is classified based on electrical conductivity (EC) and Sodium Absorption Rate (SAR).

Table 3. Different water classification and types of quality based on Wilcox classification (Wilcox, 1955).

Water category	**Water quality for agriculture**
C1S1	Freshwater-Completely harmless
C1S2, C2S2, C2S1	A little salty- Almost Appropriate
C1S3, C2S3, C3S1, C3S2, C3S3	Passion- Applying the necessary measures
C1S4, C2S4, C3S4,C4S4, C4S3, C4S2, C4S1	Very salty- Harmful to agriculture

2.4 CCME-WQI

This index was developed by Canadian Council of Ministers of the Environment in 1990. Three different factors affecting the water quality are taken into account by this index. The index would be calculated based on three factors of F1, F2 and F3 (CCME, 2001). Table 3 shows water quality classification based on this index. The way, which CCME WQI is calculated, is as follows.

$$F_1 = \left(\frac{\text{Number of failded variables}}{\text{Total number of variables}}\right) \times 100 \quad [1]$$

$$F_2 = \left(\frac{\text{Number of failed tests}}{\text{Total number of tests}}\right) \times 100 \quad [2]$$

$$F_3 = \frac{nse}{0.01nse + 0.01} \rightarrow \begin{cases} nse = \dfrac{\sum_{i=1}^{n} excursion_i}{\text{Number of test}} \\ excursion = \dfrac{\text{Failed test value}_i}{\text{Objective}_j} - 1 \ (\text{Test value} < \text{Objective}) \\ excursion = \dfrac{\text{Objective}_j}{\text{Failed test value}} - 1 \ (\text{Test value} > \text{Objective}) \end{cases} \quad [3]$$

$$CCME = 100 \quad \left[\frac{\sqrt{F_1^2 + F_2^2 + F_3^2}}{1.732}\right] \quad [4]$$

Table 4. Categorization of CCME-WQI.

Index Value	**Category**
0-44	Poor
45-64	Marginal
65-79	Fair
80-94	Good
95-100	Excellent

3 RESULTS

3.1 Climate variability

Figure 2 shows the climate conditions during the four seasons over the period under study (1969-2012). In spring, SPI index showed that between the years 1969 and 1992, the climate condition was normal over almost all of the years. In the year 1969, 1971, 1972, 1976 and 1981, degrees of wet years were, however, observed. Furthermore, various degrees of droughts were observed over the period of study. The most severe ones occurred in 1978 and 2008. Figure 4-b shows the temperature variability over the years 1996 to 2012. As it could be observed in the figure, over the years from 1978 to 1996, the average temperature in summer was lower than the long-term temperature average at this station. Over the years from 1979 to 1993, the temperature has increased compared to the long-run average temperature. It could be generally said that over the years 2000 to 2012 (except the years 2002, 2005, 2008 and 2009), the temperature has increased (0.2 centigrade on average) compared to the observed long-run average temperature in this season. In fall, the most severe droughts were observed in 1969, 1990 and 1995. Over this season, some moderate and severe wet years were detected in 1971, 1972, 1992, 2000 and 2001. By considering SPI values, it was revealed that in winter, droughts of various degrees including moderate, severe and extreme ones were observed over the years 2007 to 2012. The climate condition in this season was normal over most of the studied years. Figure 4-d shows that there are wet years of various degrees including moderate, severe and extreme ones over the years 1973 to 1998.

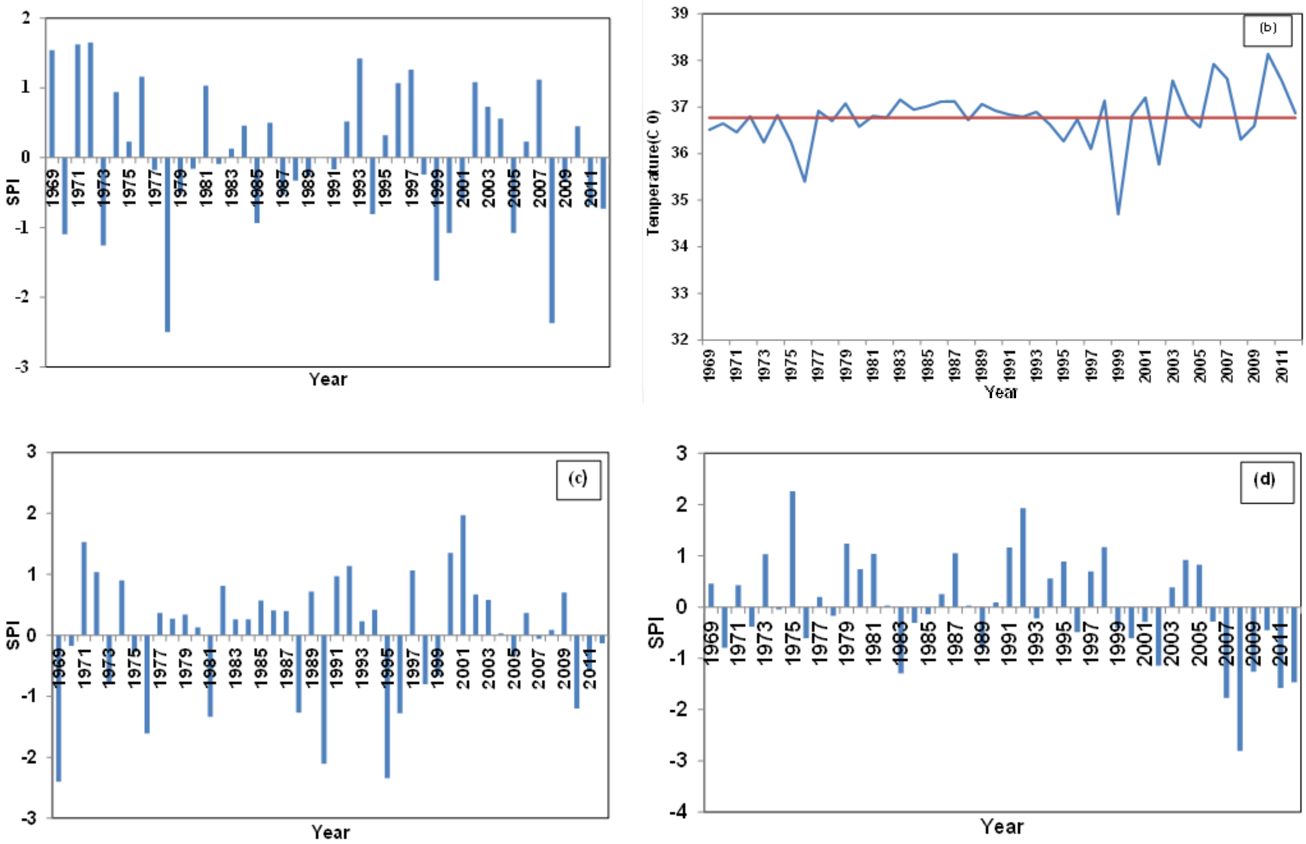

Figure 2. Climate variability at Tale-zang satation in Dez basin (a).Spring (b).Summer (c). Fall (d). Winter.

3.2 Wilcox diagrams

This section deals with the results obtained from the quality assessment of agricultural water in four different seasons over the studied period. Figure 3-a and 3-d show the Wilcox classification in spring and winter. As the diagram shows, EC and SAR parameters increase over the statistical studied period while the quality classification have not experienced any changes and remained at C2S1 (a little salty-almost appropriate). In summer, quality classification over all years was at C2S1 (a little salty-almost appropriate). However, in 2008, the quality classification was at C3S1 (passion–applying the necessary measures) with EC=767 µmho/cm and SAR=1.59. The values of EC and SAR increase a total of 154.47 µmho/cm and 0.6, respectively compared to the long-run average value which resulted in the change of water quality classification in this year. In the fall, the water quality was at C2S1 (a little salty-almost appropriate) over almost all of the years. The quality was classified at C3S1 (passion–applying the necessary measures) over some of the years. In general, the water quality classification has changed in some of the years in the season that was in part caused by climate variability.

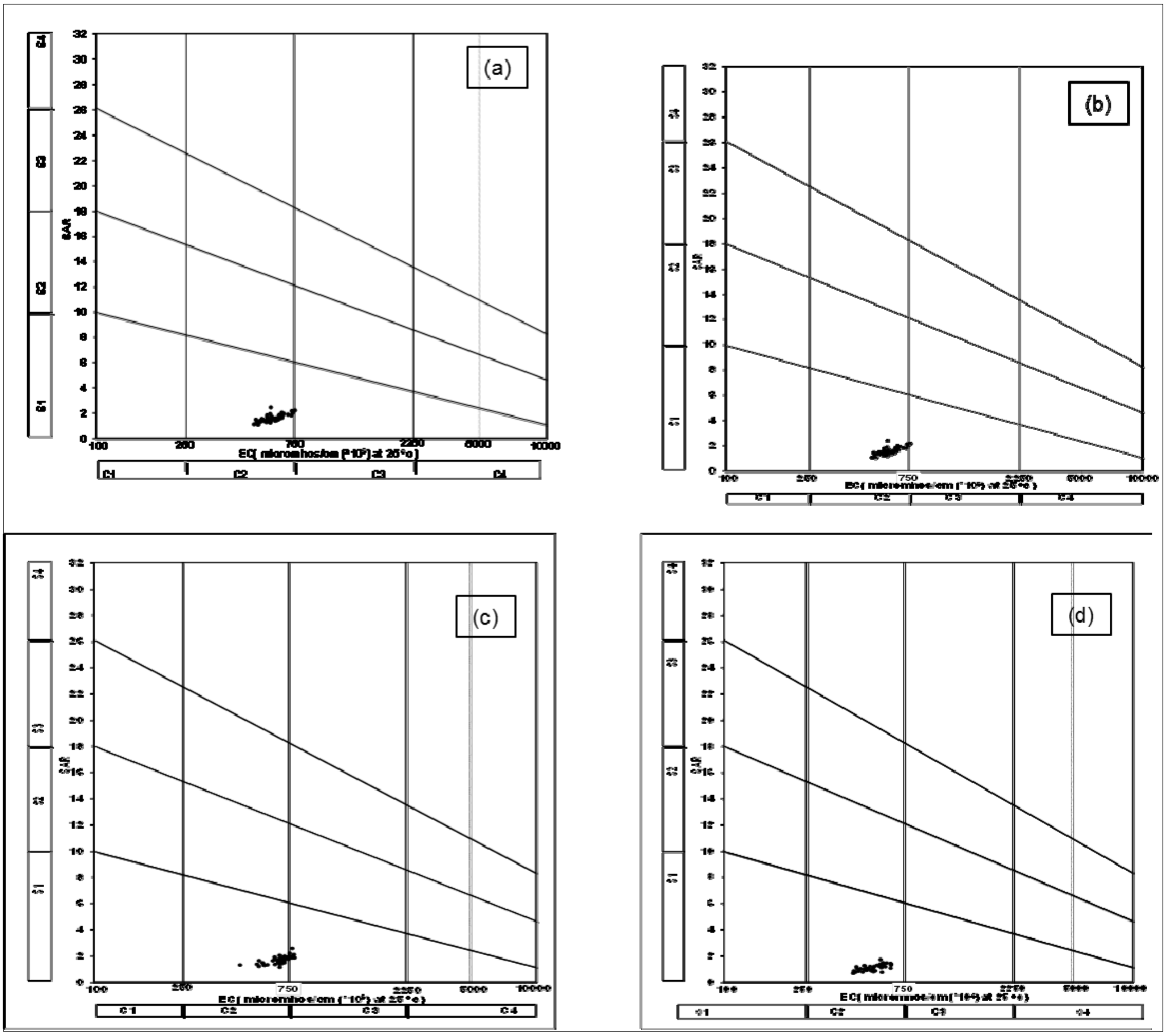

Figure 3. Wilcox classification (a). Spring (b). Summer (c). Fall (d). Winter.

3.3 CCME-WQI

This section deals with the results obtained from the water quality assessment in terms of CCME-WQI over the studied period. In spring, due to severe and moderate wet years in 1971, 1972 and 2002, the water quality was ranked as excellent at Tele-zang station in terms of this index, while over the other years it fell under the category of good, in range of 87.1 to 89.6, showing good water quality. The lowest value of the index was observed in 2011 due to high concentration of HCO3, Ca, EC and TDS parameters. In summer, the index changed in the range of 89 to 100 as well and the water quality was excellent in 1971, 1973 and 1974. In fall, the water quality classification degraded to the moderate category due to droughts occurred in 1990 and 1996. In case the CWQI values are compared to the climate variability occurred in fall over the period under study, it could be inferred that the climate variability occurred in this season have affected the final value obtained from the index in many years. In winter, the water quality fell under the category of good among all of the years. The highest value obtained from the index was 89.8 observed in 1971 and 1972 while the lowest one was 87.8 observed in 2011. The climate variability in this season increased or decreased the index value while not changing the water quality classification. For instance, droughts occurred in the years from 2007 to 2012 resulted in reduction of water quality index.

Generally, the analysis of index values in four seasons at Tele-zang station reveals that the water quality could be classified as good in most years, since in most years the only parameter that exceeded the permitted values set by the WHO standards was HCO3 while other parameters were in acceptable ranges.

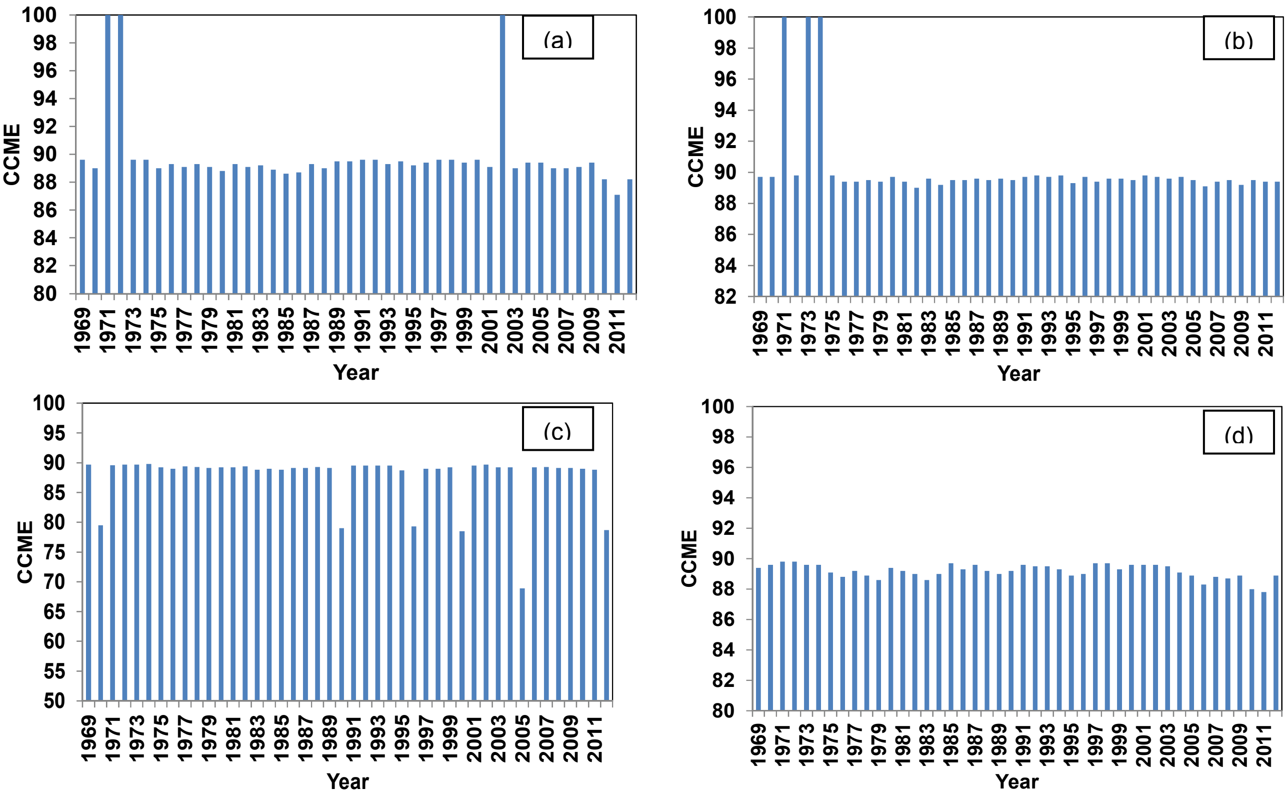

Figure 4. CCME-WQI classification (a). Spring (b). Summer (c). Fall (d). Winter.

4 CONCLUSIONS

The present study aimed to analyze the surface water quality assessment methods under climate variability. The meteorological and qualitative data regarding Tele-zang station were, therefore, studied over the period 1969 to 2012. Wilcox method and CCME-WQI were employed in the present study in order to examine the water quality. The results revealed that given its graphic nature, Wilcox diagram was incapable of defining the quality status and classifying the quality under the climate variability in most years and seasons under study. On the other hand, due to its mathematical structure, CCME index was somehow capable of revealing the changes within index values. The results obtained from the present study reveals that in most years the climate variability did not cause quality parameters of critical values exceeding the permitted standards (except bicarbonate). The water quality is, therefore, classified in the range of 80-94 (good).

ACKNOWLEDGEMENTS

I hereby would like to express my gratitude to University of Tehran that has provided all required facilities and relevant essays to do the present study.

REFERENCES

Canadian Council of Ministers of the Environment (CCME). (2001). *Canadian Water Quality Guidelines for the Protection of Aquatic life*: CCME Water Quality Index 1.0, Technical Report, Canadian Council of Ministers of the Environment Winnipeg MB, Canada.

Delpla, I., Jung, A.V., Baures, E., Clement, M. & Thomas, O. (2009). Impacts of Climate Change on Surface Water Quality in Relation to Drinking Water Production. *Environment International*, 35(8), 1225-1233.

El-Jabi, N., Caissie, D. & Turkkan, N. (2014). Water Quality Index Assessment under Climate Change. *Journal of Water Resource and Protection*, 6(6), 533.

Elshemy, M. & Meon, G. (2011). Climate Change Impacts on Water Quality Indices of the Southern Part of Aswan High Dam Reservoir. Lake Nubia. In *Fifteenth International Water Technology Conference*, *IWTC-*15(17).

Ghaleni, M.M. & Ebrahimi, K. (2015). Effects of Human Activities and Climate Variability on Water Resources in the Saveh Plain, Iran. *Environmental Monitoring and Assessment*, 187(2), 1-7.

Intergovernmental Panel on Climate Change (IPCC). (2001). *Climate change 2001: The scientific Basis*. Contribution of Working Group I to the Third Assessment Report of the Intergovernmental Panel on Climate Change. Cambridge University Press, Cambridge, UK and New York, NY, USA, 881.

McKee, T.B., Doesken, N.J. & Kleist, J. (1993). The Relationship of Drought Frequency and Duration to Time Scales. In *Proceedings of the 8th Conference on Applied Climatology,* 17(22), 179-183. Boston, MA: American Meteorological Society.

Spinoni, J., Naumann, G., Carrao, H., Barbosa, P. & Vogt, J. (2014). World Drought Frequency, Duration, and Severity for 1951–2010. *International Journal of Climatology*, 34(8), 2792-2804.

St Laurent, J. & Mazumder, A. (2014). Influence of Seasonal and Inter-Annual Hydro-Meteorological Variability on Surface Water Fecal Coliform Concentration under Varying Land-Use Composition. *Water Research*, 48, 170-178.

Wilcox, L. (1955). *Classification And Use Of Irrigation Waters*, Circular No. 969, Soil and Water Conservation Research Branch, Agricultural Research Service, and the Agricultural Experiment Stations of the 17 Western States and the Territory of Hawaii United States Department Of Agriculture Washington, D. C.

OPTICAL MEASUREMENT SYSTEM FOR WAVE PROFILES USING MODIFIED SUZUKI-SUMINO METHOD

KAZUHIDE DAN[(1)] & ATSUSHI KISHI[(2)]

[(1)] Department of Civil Engineering, National Institute of Technology, Akashi College, Akashi, Japan,
dan@akashi.ac.jp
[(2)] JFE ENGINEERING Corporation, Japan

ABSTRACT

When sunlight waves travel into the interface between water and air, a part of the sunlight waves refracts at this interface. The observed sunlight intensity profiles related to wave profiles were recorded at the observation board below the transparent acrylic test channel in experiment. It is possible to calculate the wave profile by applying modified Suzuki-Sumino's method to this recorded sunlight intensity profile. The relative errors which show the accuracy is introduced as the value of the difference between the calculated wave height and the measured wave height using the wave meter divided by the measured wave height. This accuracy of wave profile depends on the weather (fine or cloudy), the incident angle of the sunlight, the water depth, the wave steepness, the refractive index of the bottom, the incident wave length and the distance between the bottom and the observation board. It is confirmed that the relative error increases as the water depth increases and the refractive index increases and the brightness in the still water surface increases and the relative error decreases as the distance between the channel bottom and the observation board decreases.

Keywords: Optical wave profile measurement; sunlight intensity profile; Suzuki-Sumino's method.

1 INTRODUCTION

When the natural light waves travel into the interface between water and air, a part of the incident light wave refracts and diffracts at the interface. When these light waves travel to the horizontal observation plane located in water near the water surface, these waves make the light intensity profile, and the fringe pattern in brightness on this observation plane. It is possible to calculate the wave profile by applying modified Suzuki-Sumino's method to the fringe pattern in brightness recorded on this observation plane (Dan, 2002). The fringe pattern in brightness related to the water surface image can be recorded easily with the video camera at and below the bottom of the water. This technique can be used to measure the wave height in an observation plane simultaneously.

Wave gages for the experimental study, a servo-type wave gage, a resistance-type wave gage and a capacitance-type wave gage are quite standard. Wave gages for the field study, an ultrasonic-type wave gage and a pressure-type wave gage are suitable. These wave gages are capable of measuring the wave heights at an observation point. This method can be called as “wave measurement at a point”. It costs much and needs many wave gages in order to measure the wave surface elevation in an observation plane simultaneously. It is well known that the wave meter using the laser light sheet is useful in order to improve these problems. The wave surface elevation can be imaged by a laser-induced-fluorescence when the laser beam is scanned and illuminated on the interface between air and water. This is a nonintrusive-type wave measurement technique developed by using optical devices and process the laser-induced image without disturbing the wave field. This method can be called “wave measurement in an observation line”. Suzuki and Sumino (1993) developed the new wave measurement technique in an observation plane. This method is capable of calculating the wave surface elevation by using the refraction of the incident light waves at the interface between air and water. The incident light waves converge under the crest and diverge under the trough after the refraction in an observation plane near the wave surface. These images in this observation plane can be recorded on the videotape with a video camera at the sea bottom. Performing the Fourier and inverse Fourier transformation to the brightness profile in these recorded images is capable of calculating the wave surface elevation. When the natural light waves travel to the wave surface, it is possible to calculate the wave surface elevation in an observation plane in water near the wave surface by applying the modified Suzuki-Sumino's method to the brightness profile in this observation plane. By processing the recorded image data on the glass plate located at the bottom of the water, the wave height and the wave length are estimated in the case of regular waves (Dan et al., 1993). These methods are capable of measuring the wave profile simultaneously in an observation plane by processing the recorded image of the wave surface. These methods can be called as “simultaneous wave measurement in an observation plane”.

By making use of the refraction of the natural light waves at the wave surface the fringe pattern of bright and dark portions can also be recorded in the focused observation plane in water with the camera at the sea bottom. By applying Suzuki-Sumino's method to this recorded image, the wave profile in an observation plane can be calculated simultaneously (Dan, 2002). It is also possible to estimate the wave profile by using the relationship between the light intensity profile calculated according to Snell's law and Fresnel-Kirchhoff's formula in the observation plane in water and the wave steepness when the incident parallel light waves travel to the wave surface (Dan and Otsuki, 2000; Dan and Kawabata, 2001). Due to the loss of the light energy at the transparent bottom, the relative error of the wave profile in the case of the transparent bottom is greater than that in the case of the bottom of the ground glass (Dan et al., 2014).

2 OBSERVED IMAGES ON THE BOTTOM IN THE FIELD AND IN THE EXPERIMENTAL CASE

The fringe pattern in brightness on the bottom can be seen in many cases. For example, in the wave tank (Figure 1.), in the experimental water channel (Figure 2 and 5), in the coastline (Figure 3.), and in the riverside (Figure 4.).

Water waves generated in the wave tank.mp4

Figure 1. (Movie and picture) Observed wave images on the bottom of a wave tank.

Finger touch & knocking the wall.mp4

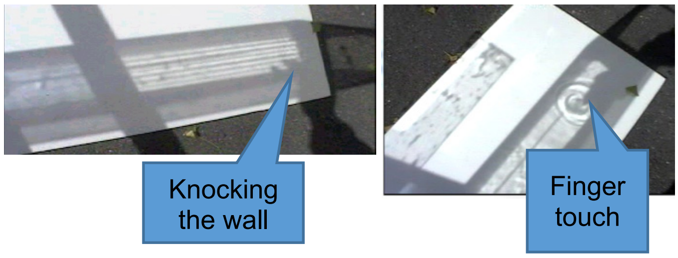

Figure 2. (Movie and picture) Observed wave images (finger touch and knocking the wall) on the bottom of a wave tank.

Wave breaking.mp4

Figure3. (Movie and picture) Observed wave images (scattering and wave breaking) in the seashore.

Sinusoidal waves in the riverside.mp4

Figure 4. (Movie and picture) Observed wave images in the riverside.

water wave motion and fringe pattern in brightness.mp4

Figure 5. (Movie and picture) Observed wave images (water wave motion and fringe pattern in brightness).

A camera can be located as in the following cases, ①over the sea, ②in the sea, ③below the bottom, ④ on the bottom, and ⑤below the transparent bottom, in Figure 6 in order to measure the wave motion using a camera.

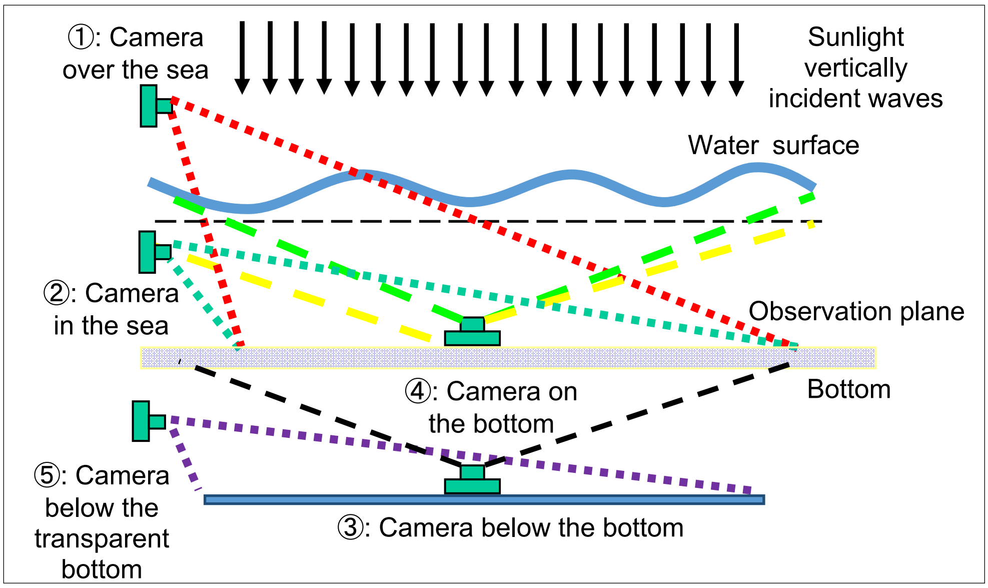

Figure 6. Camera's location of wave meters using a camera.

Figure 7 shows the observed images using a camera below the transparent bottom of the channel.

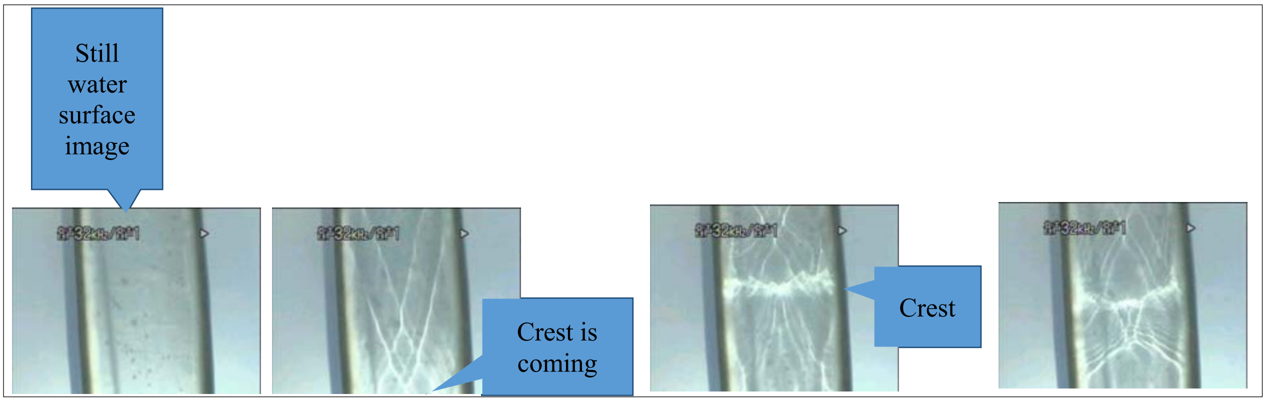

Figure 7. Recorded images of fringe patterns in brightness on the bottom of the channel.

3 ANALYTICAL APPROACH

3.1 One-dimensional approach

When the natural parallel light waves travel to a wave surface vertically in x-z plane, the refracted waves travel to the transparent acrylic bottom and these transmitted waves make the fringe pattern of brightness on the white observation plane (Figure 8). The water waves travel in x-direction. These water waves can be irregular waves.

When the incident light waves travel vertically at the point, x=x, the refracted light waves travel to the point on the observation plane, $x=x_1$ (Figure 8 and 9). x_1 is the coordinate axis on the upper surface of the transparent acrylic bottom and x_2 is the axis on the bottom and x_3 is the axis on the surface of the observation board (Figure 8).

Now it is assumed that the natural parallel light waves travel to the interface vertically (Fig. 8 and 9). The light waves traveling between x=x and $x=x+\Delta x$ refract at the interfaces and then these waves travel to the observation plane like in water between $x_1=x_1$ and $x_1=x_1+\Delta x_1$, in an acrylic plate between $x_2=x_2$ and $x_2=x_2+\Delta x_2$ and in air between $x_3=x_3$ and $x_3=x_3+\Delta x_3$ (Figure 9), where n_1, n_2 and n_3 are the indexes of refraction at the wave surface, at the upper surface of the transparent acrylic bottom and at the upper surface of the observation board respectively. α is an incident angle at the water surface, β is a refraction angle, γ is an incident angle, δ is an incident angle and ε is a refraction angle (Figure 9).

C(x) is the light intensity profile at the interface before the incidence, $B(x_1)$ is that on the observation plane, D is that on the lower surface of the transparent acrylic bottom and E is that on the observation board. As the distance between the point on the observation plane and the camera is not constant, the light intensity C recorded with a camera in the case of still water is also not constant. However, in this paper, it is assumed that C recorded with a camera in still water is constant.

There is a reflection of incident waves at the boundary and a dissipation of waves both in the air and in the water. It can be assumed that there is no dissipation energy both in the air and in the water. The energy balance is expressed as

$$k_3E(x_3)dx_3 = k_2D(x_2)dx_2 = k_1B(x_1)dx_1 = k_0C(x)dx = C(x)dx \qquad [1]$$

where k_0, k_1, k_2, k_3 are reduction coefficients due to the reflection at the boundaries 0, 1, 2, 3 respectively.

If there was no reflection at the boundaries, then $k_0=k_1=k_2=k_3=1$.

$$E(x_3)dx_3 = D(x_2)dx_2 = B(x_1)dx_1 = C(x)dx \qquad [2]$$

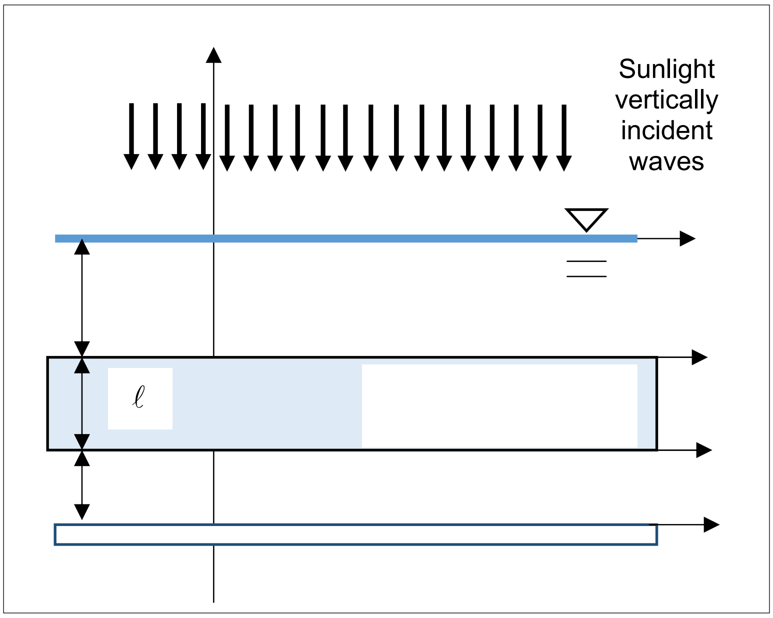

Figure 8. Coordinates system.

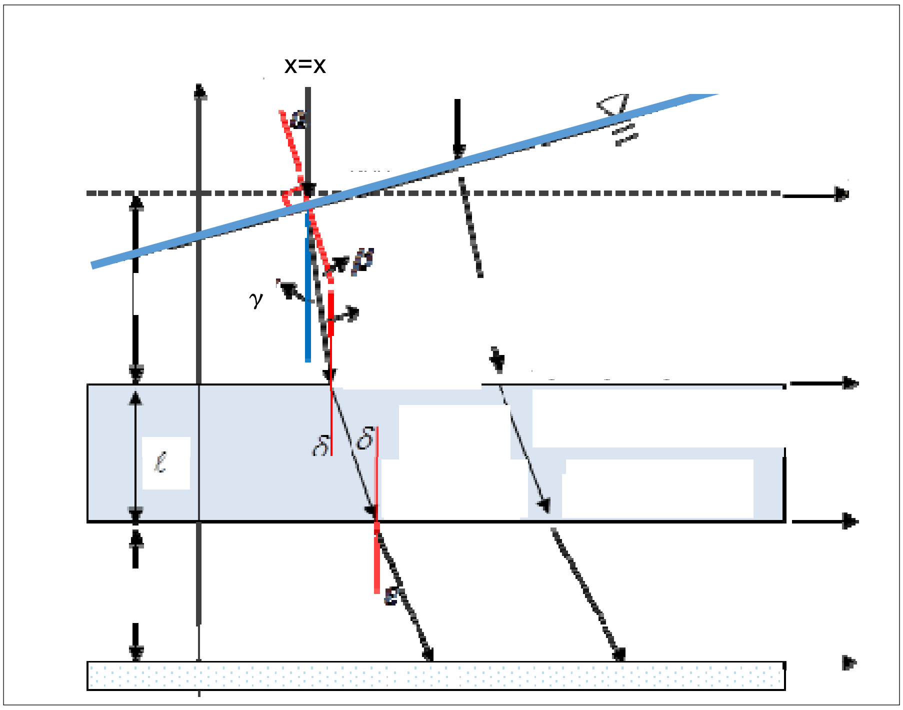

Figure 9. Rays tracing.

According to Snell's law and modified Suzuki-Sumino's method the following equations are derived.

$$\frac{d^2\zeta}{dx^2}=\frac{C(x)-B(x_1)}{B(x_1)h\left(1-\frac{1}{n_1}\right)} \quad [3]$$

$$\frac{d^2\zeta}{dx^2}=\frac{C(x)-D(x_2)}{D(x_2)\left(h+\frac{\ell}{n_2}\right)\left(1-\frac{1}{n_1}\right)} \quad [4]$$

$$\frac{d^2\zeta}{dx^2}=\frac{C(x)-E(x_3)}{E(x_3)\left(h+\frac{\ell}{n_2}+\frac{d}{n_2 n_3}\right)\left(1-\frac{1}{n_1}\right)} \quad [5]$$

Performing the Fourier transformation and the inverse Fourier transformation the wave surface $\zeta(x)$ is written as

$$\zeta(x)=\Im^{-1}\left[\frac{\Im\left[\frac{C-B}{Bh\left(1-\frac{1}{n_1}\right)}\right]}{\omega^2}\right] \quad [6]$$

$$\zeta(x)=\Im^{-1}\left[\frac{\Im\left[\frac{C-D}{D\left\{h\left(1-\frac{1}{n_1}\right)\left(h+\frac{\ell}{n_2}\right)\right\}}\right]}{\omega^2}\right] \quad [7]$$

$$\zeta(x)=\Im^{-1}\left[\frac{\Im\left[\frac{C-E}{E\left(1-\frac{1}{n_1}\right)\left(h+\frac{\ell}{n_2}+\frac{d}{n_2 n_3}\right)}\right]}{\omega^2}\right] \quad [8]$$

where $\Im$ is the Fourier transformation and $\Im^{-1}$ is the inverse Fourier transformation and h is the uniform water depth. ω is the spatial angular frequency expressed as

$$\omega = i2\pi f \quad [9]$$

where $i=\sqrt{-1}$ and f is the spatial frequency. B is the brightness profile along the x-axis in the observation plane and C is the brightness profile in still water in the observation plane. As there are no days in still water in ocean, it is assumed that C is nearly equal to the averaged brightness in the observation plane.

The water depth, h and the index of refraction, n_1, n_2, and n_3 can be constant. The brightness profile C is not always constant because the optical path between the camera and the point on the observation plane varies and the light absorption is not constant along this optical path.

3.2 Two-dimensional approach

The wave surface $\varsigma(x, y)$ is derived in the same way as Equations (5, 6 and 7) and is expressed as

$$\zeta = \Im^{-1}\left[\frac{\Im\left[\dfrac{C-E}{C\left(h+\dfrac{\ell}{n_2}+\dfrac{d}{n_2 n_3}\right)\left(1-\dfrac{1}{n_1}\right)}\right]}{\omega_x{}^2+\omega_y{}^2}\right] \quad [10]$$

where ω_x and ω_y are the spatial angular frequencies in x-direction and y-direction respectively and expressed as

$$\omega_x = i2\pi 2_x, \omega_y = i2\pi 2_y \quad [11]$$

where f_x and f_y are the spatial frequencies in x-direction and y-direction respectively.

Equation (9) shows that the wave surface elevation, ς increases when we estimate the water depth, h greater and ς decreases when we estimate the index of refraction in water n_{12} to be greater. When we estimate the light intensity C before the incidence on the wave surface to be greater, ς decreases and estimate C smaller, ς increases by the numerical simulation. The accuracy of the wave surface elevation depends on the accuracy of C considerably.

4 EXPERIMENTAL APPROACH

4.1 Experimental setup

The wave tank used is 5.40m long, 0.15m wide and 0.20m tall (Figure 10). Regular waves are produced using this tank. White observation plane is located in a horizontal plane and can be moved vertically at any position. The distance d between the bottom of the channel and the observation plane can be changed. (Figure 10).

Figure 10 (d) shows some examples of recorded images. The left image is the recorded intensity profile image in case of still water surface and the right is the image of the wave surface. Both images are recorded on the observation plane by a video camera.

4.2 Experimental cases

Table 1 shows the experimental cases. Cases A, B, C and D are shown. Experimental Case A is made under the following conditions that the water depth, h is 10cm. The water waves are regular waves. The wave period T is 0.29 sec, the wave length L is 15.6cm, the wave height H is 0.77cm and the wave steepness H/L is 0.05. Cases B, C and D are also made under the conditions as shown in Table 1.

Table 1. Experimental cases.

Cases / Wave properties	A	B	C	D
Water depth h [cm]	10	10	10	10
Wave period T [sec]	0.29	0.36	0.46	0.53
Wave length [cm]	15.6	23.7	35.3	47.9
Wave height [cm]	0.77	1.09	2.02	1.54
Wave steepness	0.05	0.05	0.06	0.03
Solar altitude [°]	65	75	65	73

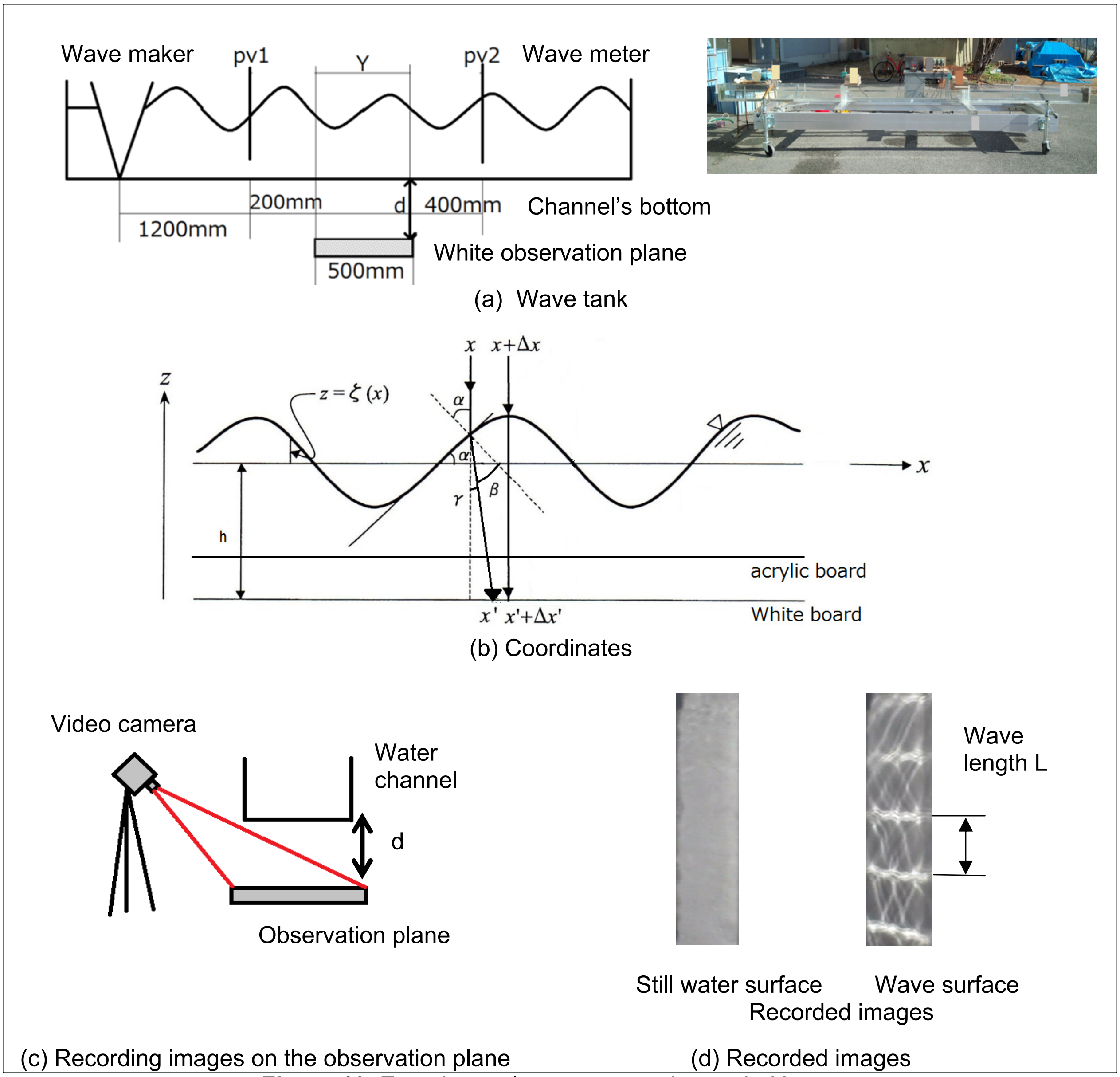

Figure 10. Experimental apparatus and recorded images.

5 WAVE ANALYSIS

The wave profile $\varsigma(x, y)$ calculated by using Equation (9) contains errors because of using image data of RGB intensity composed. In Equation (9), the waves are expressed as having one frequency. To decide the wave height correctly, it is analyzed by using the intensity profile data of a frequency. Sunlight waves contain many waves with different frequencies. Another reason why the errors occur is the reflection at all boundaries. The reflection loses the light wave energy and the residual energy travel to the observation board.

5.1 Results of two-dimensional wave analysis

Figure 11 shows calculated wave profiles by using the software “OriginPro 9.0” according to equation (9). The recorded image of still water surface of each case is shown at top left, the wave profile along the center of the water channel is shown at top right and the bottom shows a calculated wave profile of each case.

Table 2 shows the experimental results. Relative error is greater in case A than in case B and in case C. Relative error is 19.6% in case B and is the smallest among the three cases. This is because the observation plane is located around the point of rays crossing. In Cases A, B and C, the minimum relative errors can be found as d increases from 7cm to 49cm (Figure 12).

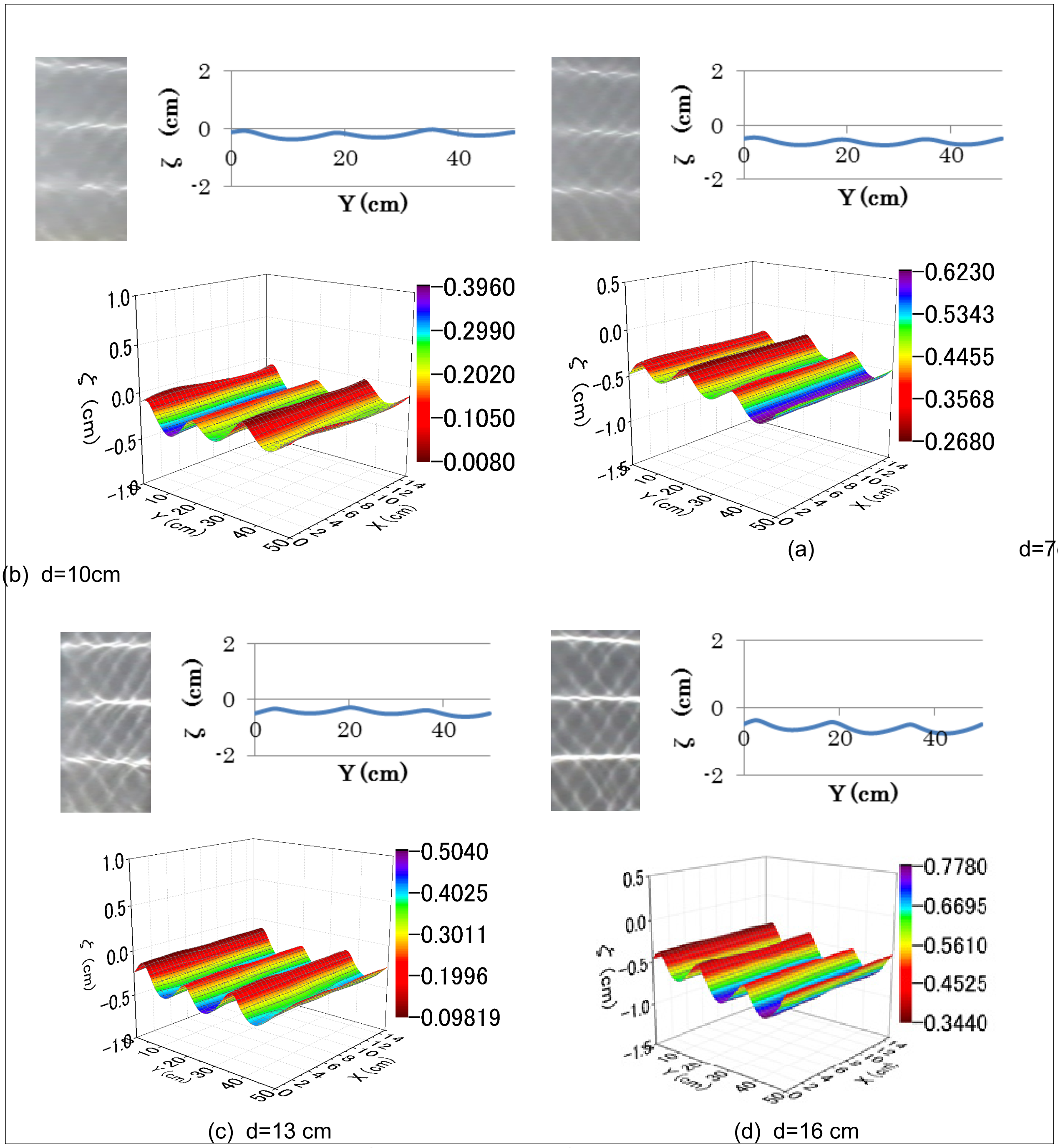

(a) d=7cm

(b) d=10cm

(c) d=13 cm

(d) d=16 cm

Figure 11. Calculated wave profile images depending on d.

Table 2. Experimental results (Relative errors as d increases from 7cm to 49cm).

d [cm]	CASE A		CASE B		CASE C		CASE D	
	Analyzed wave height [cm]	Relative error %	Analyzed wave height [cm]	Relative error %	Analyzed wave height [cm]	Relative error %	Analyzed wave height [cm]	Relative error %
7	0.17	78.4	0.64	41.1	1.19	41.1	1.44	6.2
10	0.24	69.4	0.74	32.4	1.23	39.1	1.19	22.8
13	0.24	68.7	0.88	19.6	1.18	41.7	1.11	28.1
16	0.33	56.6	0.75	31.5	1.22	39.4	0.62	59.6
19	0.31	59.9	0.76	30.2	1.12	44.3	0.94	38.9
22	0.26	66.7	0.50	54.0	1.19	40.9	0.79	48.6
25	0.21	72.7	0.47	56.6	1.28	36.6	0.93	39.4
28	0.23	69.7	0.60	45.2	1.39	31.0	0.59	61.6
31	0.23	70.1	0.54	50.5	1.29	35.9	0.41	73.7
34	0.17	77.3	0.57	47.3	1.52	24.6	0.37	75.7
37	0.17	78.1	0.61	44.2	1.56	22.8	0.39	75.0
40	0.17	77.6	0.50	54.6	1.40	30.5	0.33	78.5
43	0.17	78.0	0.50	54.6	1.45	28.0	0.37	76.2
46	0.23	70.6	0.55	49.5	1.31	35.2	0.33	78.8
49	0.21	72.4	0.48	56.0	1.29	36.0	0.37	76.2

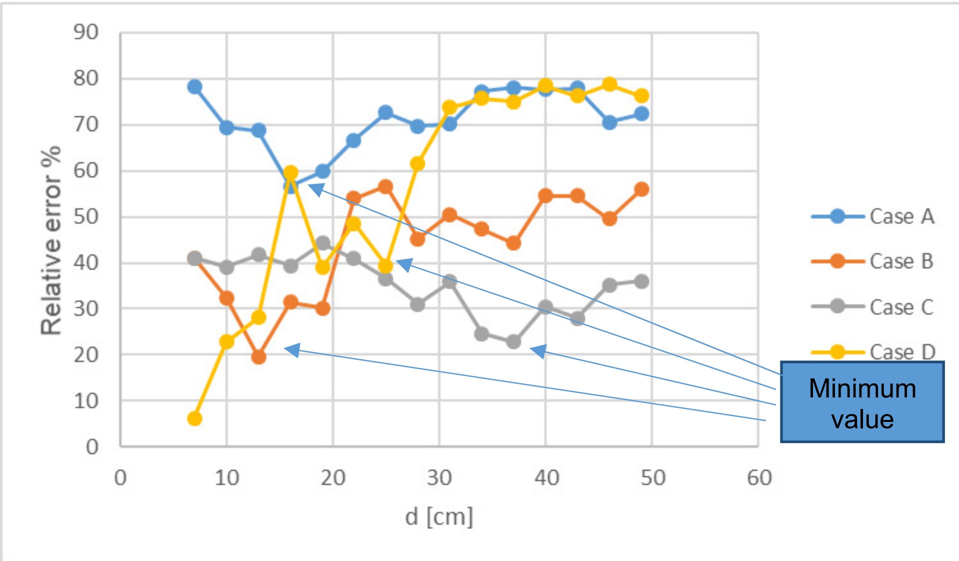

Figure 12. Relationship between d and the relative error.

5.2 Ray-crossing dependencies

This is because the natural sunlight meets near the point that the minimum relative error appears (Figure 12). The relative error is decreasing which is calculated by using the projected images recorded over the meeting point of sun's rays and next is increasing as d increases in Cases A, B and C. The equation (9) is available without the ray's crossing. Suzuki-Sumino's method can be applied to the projected images recorded over the crossing point. The relative error is almost 20% at best in Case B (d=13cm). The main reason of this is that the natural sun lights travel not vertically but obliquely. The other reasons are that a reflection factor changes at a water surface and at both ends of the bottom plate with various incident angles, the reflection energy is not the same on the boundary and equation (9) is derived at the condition of one frequency.

Fig.13 shows an example of ray-tracing. It is shown that rays meet together at some points. In Table 3, the crossing points of some vertical incident rays in the case of some water waves are shown.

Table 3. Ray-tracing's results.

Case	Wave length [cm]	Wave height [cm]	Wave steepness	Crossing point of rays
1	14.3	0.87	0.061	d=10cm
2	47.2	1.68	0.036	Over d=26cm

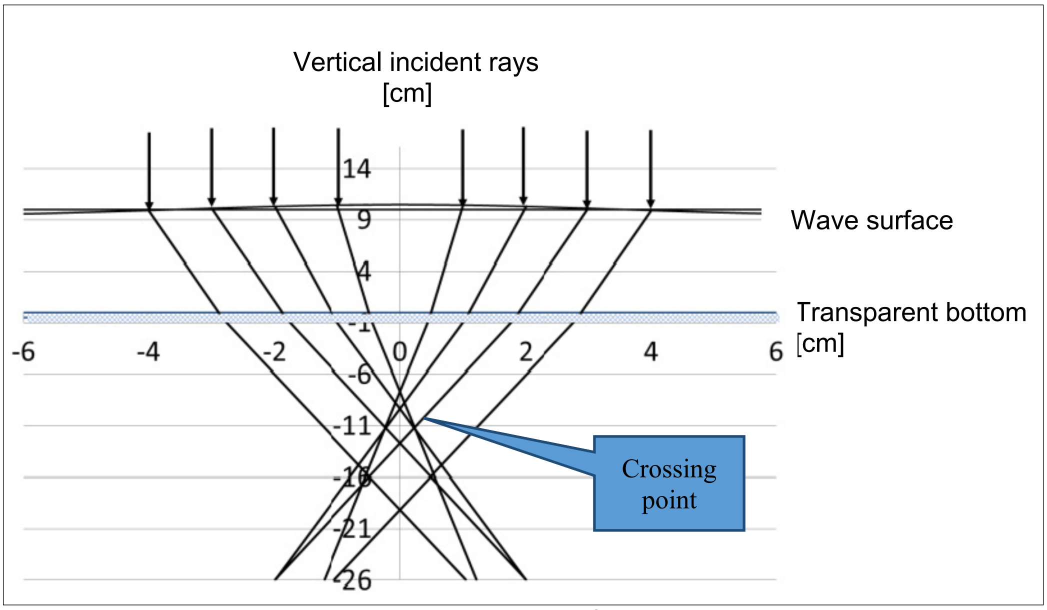

Figure 13. Ray-tracings in case of vertical incident rays.

5.3.1 Reflection dependencies

Eq. [10] is derived assuming that there is no reflection at the boundaries. By experiments, it is confirmed that k_3 is about 0.8 in the case of a glass plate, and thickness is 3mm using the laser beam of the wave length, 632.8nm. The reflection intensity of the light at the boundary also depends on the incident angle and materials. It is considered that the calculation due to this reflection influence will be carried both by experiments and the computer simulation.

6 CONCLUSIONS

There are reasons why inaccuracy happens. One of the main reasons is the intersection of natural lays. The other reason is to assume that there is no reflection at the boundaries. This is investigated by introducing the reduction factors, k0, k1, k2 and k3 in eq. [1].

It follows that the obvious limitations are necessary when using this method in order to measure the wave profile. The better cleared limitations should be shown in non-dimensional factors. There are imposed tasks to make clear the limitations on the lays-crossing, the reflection dependencies and light wave length dependency.

It is shown that the wave profile can be calculated by applying modified Suzuki-Sumino method to the projected images on the observation plane located below the transparent bottom of the water channel but including the errors. It is noticed that the observation plane should be located sufficiently shallow not to meet rays-crossing point. The reflection dependencies are to be confirmed in order to estimate the reflection error by experiments and simulations.

REFERENCES

Dan, K., Yagi, N. & Yano, M. (1993). Wave Height Measurement by Analyzing Image Data of the Water Surface Observed in Water (in Japanese). *Journal of the Visualization Society of Japan*, 13(1), 233-236.

Dan, K. & Otsuki, K. (2000). Numerical Calculation of the Image Intensity in a Horizontal Plane Located at the Sea Bottom by Using Fresnel-Kirchhoff's Formula (in Japanese), *Proceedings of 55th Annual Conference of Civil Engineers*, 210, 1-2.

Dan, K. (2001). Wave Profile and Brightness Observed at the Bottom of the Water (in Japanese). *Journal of the Visualization of Japan*, 21(1), 83-88.

Dan, K. (2002). Simultaneous Wave Height Measurement in an Observation Plane (in Japanese). *Kansai Chapter, Report of the Co-operative Research*, 50-59.

Dan, K. (2002). Wave Meter at the Sea Bottom Using a Camera, *Proceedings of 10th International Symposium on Flow Visualization*, E26 F1087, 1-13.

Dan, K., Kishi, A. & Nakamura, F. (2014). Experimental Results on the Accuracy of Wave Height Calculated by Applying Suzuki-Sumino's Method to the Projected Images Observed at and Below the Bottom of the Channel Changing the Distance Between the Bottom and the Observation Plane (in Japanese), *Memoirs of Akashi National College of Technology*, 56, 5-14.

Suzuki, T. & Sumino, K. (1993). A Technique to Measure Wave Height Using Projected Light Distribution on a Screen Near the Wave Surface (in Japanese). *Journal of the Visualization Society of Japan*, 13(1), 241-244.

DEVELOPMENT OF EVALUATION METHOD OF UPLIFT FORCES ON THE WAVE DISSIPATING CAISSON BY USING NUMERICAL SIMULATION

HIROMU IGARASHI (1), KAZUKI NAMIKI(2) & TARO ARIKAWA(3)

(1,2,3) Chuo University, Tokyo, Japan,
igarashi@civil.chuo-u.ac.jp; kaz_0501@civil.chuo-u.ac.jp; arikawa@civil.chuo-u.ac.jp

ABSTRACT

In order to solve phenomena such as breaking wave and overflow accurately, a numerical model, considering the influence of air is necessary. In this report, we calculated uplift pressure in wave chamber of slit caisson by using gas-liquid two-phase model based on the VOF method. The validity of this model was also verified by comparing with the results of small and middle-scale experiments. As a result, wave profile of the numerical results and the experimental results were almost matched.

Keywords: Multiphase flow; CADMAS-SURF/3D-2F; VOF method; slit caisson; air pressure.

1 INTRODUCTION

Wave dissipating slit caisson has a permeable wall and a wave chamber. These are effective to absorb wave energy. Therefore, it is not necessary to install wave-dissipating blocks in front of the caisson so that the caisson body is available to the quay. However, in the case of using it as the quay, the ceiling slab should be installed at the top of wave chamber. Then, as high waves act on the slit caisson, the ceiling slab may be subjected to severe uplift forces because the air in the wave chamber is enclosed and compressed.

With regard to such pressure, Tanimoto et al. (1980) has already shown the calculation model of uplift pressure considering the effect of air compression. However, in this model, there are parameters that must be given by experiments reproducing local wave and structural conditions. Therefore, its applicability to practice is low.

In order to reproduce this phenomenon accurately without using the above model, it is necessary to use gas-liquid two-phase model. In this report, we analyze uplift pressure on the ceiling slab by using CADMAS-SURF/3D-2F to examine the validity of this model.

2 CONCEPT OF CADMAS-SURF/3D-2F

2.1 Governing equation

The governing equation used in CADMAS-SURF/3D-2F consists of the continuity equation (Eq. [1]) and the Reynolds equations (Eq. [2]-[4]) based on a porous-body model.

$$\frac{\partial \gamma_x u}{\partial x} + \frac{\partial \gamma_y v}{\partial y} + \frac{\partial \gamma_z w}{\partial z} = \gamma_v S_\rho - \frac{1-F}{\rho_G}\dot{\rho}_G \quad [1]$$

$$\begin{aligned} \lambda_v \frac{\partial u}{\partial t} + \frac{\partial \lambda_x uu}{\partial x} + \frac{\partial \lambda_y vu}{\partial y} + \frac{\partial \lambda_z wu}{\partial z} &= -\frac{\gamma_v}{\bar{\rho}}\frac{\partial p}{\partial x} - u\frac{1-F}{\rho_G}\dot{\rho}_G \\ &+ \frac{\partial}{\partial x}\left\{\gamma_x \bar{\nu}_e \left(2\frac{\partial u}{\partial x}\right)\right\} + \frac{\partial}{\partial y}\left\{\gamma_y \bar{\nu}_e \left(\frac{\partial u}{\partial y} + \frac{\partial v}{\partial x}\right)\right\} + \frac{\partial}{\partial z}\left\{\gamma_z \bar{\nu}_e \left(\frac{\partial u}{\partial z} + \frac{\partial w}{\partial x}\right)\right\} - \gamma_v D_x u - R_x + \gamma_v S_u \end{aligned} \quad [2]$$

$$\begin{aligned} \lambda_v \frac{\partial v}{\partial t} + \frac{\partial \lambda_x uv}{\partial x} + \frac{\partial \lambda_y vv}{\partial y} + \frac{\partial \lambda_z wv}{\partial z} &= -\frac{\gamma_v}{\bar{\rho}}\frac{\partial p}{\partial y} - v\frac{1-F}{\rho_G}\dot{\rho}_G \\ &+ \frac{\partial}{\partial x}\left\{\gamma_x \bar{\nu}_e \left(\frac{\partial v}{\partial x} + \frac{\partial u}{\partial y}\right)\right\} + \frac{\partial}{\partial y}\left\{\gamma_y \bar{\nu}_e \left(2\frac{\partial v}{\partial y}\right)\right\} + \frac{\partial}{\partial z}\left\{\gamma_z \bar{\nu}_e \left(\frac{\partial v}{\partial z} + \frac{\partial w}{\partial y}\right)\right\} - \gamma_v D_y v - R_y + \gamma_v S_v \end{aligned} \quad [3]$$

$$\lambda_v \frac{\partial w}{\partial t} + \frac{\partial \lambda_x uw}{\partial x} + \frac{\partial \lambda_y vw}{\partial y} + \frac{\partial \lambda_z ww}{\partial z} = -\frac{\gamma_v}{\bar{\rho}}\frac{\partial p}{\partial z} - w\frac{1-F}{\rho_G}\dot{\rho}_G$$
$$+\frac{\partial}{\partial x}\left\{\gamma_x \bar{v}_e\left(\frac{\partial w}{\partial x} + \frac{\partial u}{\partial z}\right)\right\} + \frac{\partial}{\partial y}\left\{\gamma_y \bar{v}_e\left(\frac{\partial w}{\partial y} + \frac{\partial v}{\partial z}\right)\right\} + \frac{\partial}{\partial z}\left\{\gamma_z \bar{v}_e\left(2\frac{\partial w}{\partial z}\right)\right\} \quad [4]$$
$$-\gamma_v D_z w - R_z + \gamma_v S_w - \frac{\gamma_v \rho^* g}{\bar{\rho}}$$

where,

$$\dot{\rho} = \frac{D\rho_g}{Dt} \quad [5]$$

where t is the time, the x-, y-, and z-axes are in the Cartesian coordinate system, u, v, and w are the velocity components in the respective x-, y-, and z-axes, $\bar{\rho}$ is the mixed density, p is the pressure, $\bar{v}_e$ is the mixed viscosity, g is the gravitational acceleration, γ_v is the porosity, and γ_x, γ_y, and γ_z are the areal porosities in their respective directions. In addition, D_x, D_y, and D_z are the parameters used for the absorbing sponge zone in their respective directions, and S_ρ, S_u, S_v and S_w are wave generation source terms for the continuity equation, with the equations of motion in the respective directions of x, y, and z.

The coefficients λ_v, λ_x, λ_y, and λ_z are denoted as follows. The second term on the right hand sides of Eq [5], in which C_M is an inertia coefficient, expresses how the inertia forces are affected by the structure.

$$\left.\begin{aligned} \lambda_v &= \gamma_v + (1-\gamma_v)C_M \\ \lambda_x &= \gamma_x + (1-\gamma_x)C_M \\ \lambda_y &= \gamma_y + (1-\gamma_y)C_M \\ \lambda_z &= \gamma_z + (1-\gamma_z)C_M \end{aligned}\right\} \quad [6]$$

The resistance forces R_x, R_y, and R_z from the porous body are modeled as follows:

$$\left.\begin{aligned} R_x &= \frac{1}{2}\frac{C_D}{\Delta x}(1-\gamma_x)u\sqrt{u^2+v^2+w^2} \\ R_y &= \frac{1}{2}\frac{C_D}{\Delta y}(1-\gamma_y)v\sqrt{u^2+v^2+w^2} \\ R_z &= \frac{1}{2}\frac{C_D}{\Delta z}(1-\gamma_z)w\sqrt{u^2+v^2+w^2} \end{aligned}\right\} \quad [7]$$

where C_D is the drag coefficient, and Δx, Δy, and Δz are the mesh sizes in the x-, y-, and z-directions respectively.

$\bar{\rho}$ is expressed as follows by using the fractional volume of fluid of liquid phase, F, the density of liquid phase, ρ_f, and the density of gas phase, ρ_g:

$$\bar{\rho} = F\rho_f + (1-F)\rho_g \quad [8]$$

$\overline{\nu}_e$ is the summation of mixed molecular viscosity, $\overline{\nu}$ and eddy viscosity, ν_t

$$\overline{\nu}_e = \overline{\nu} + \nu_t = \{F\nu_f + (1-F)\nu_g\} + \nu_t \quad [9]$$

2.2 The free surface boundary

The VOF method was adopted to analyze the free surface boundary. Based on the porous body model, the advection equation of the VOF function F is expressed as follows:

$$\gamma_v \frac{\partial F}{\partial t} + \frac{\partial \gamma_x uF}{\partial x} + \frac{\partial \gamma_y vF}{\partial y} + \frac{\partial \gamma_z wF}{\partial z} = \gamma_v S_F \quad [10]$$

3 SMALL-SCALE EXPERIMENT

3.1 Summary of experiment

The wave flume used for the experiment is 18.35m in length, 0.30m in width, and 0.50m in height. The model of slit caisson is located in the wave flume. Waves were generated by wave generator which has wave absorbing function. Table 1 shows calculation conditions. Calculating area and detail of slit caisson are shown in Figure 1, and Figure 2 respectively.

Table 1. Calculation conditions.

Water depth [cm]		20, 24
Wave height [cm]		4.0, 6.0
Wave period [s]		1.0
Grid width [cm]	X	1.0
	Y	0.5
	Z	1.0
Number of meshes		4,351,500
Incident wave		Regular wave (Stokes 5th)

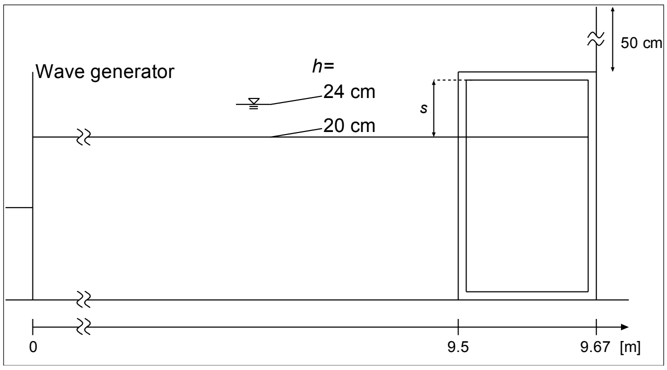

Figure 1. Calculating area.

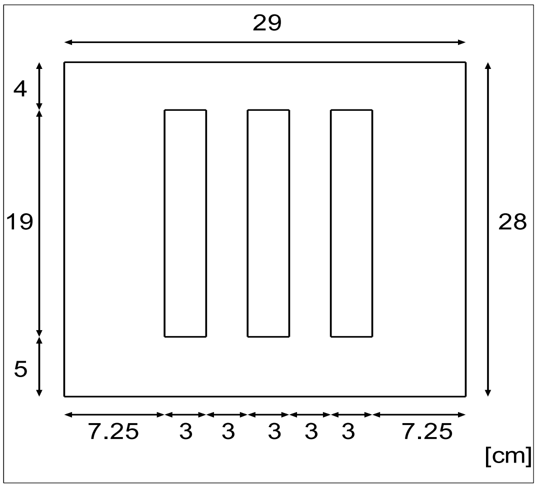

Figure 2. Detail of slit caisson.

3.2 Uplift pressure in the wave chamber

Figure 3 shows the numerical results and the experimental results of the time variation of the intensity of uplift pressure $p/w_0 H$, where p is the pressure relative to the atomospheric pressure, w_0 is unit weight of water, and H is each incident wave height.

In the case of 20cm in depth and 4.0cm in incident wave height, the water level did not rise over the top of slit so that air in the wave chamber was not enclosed. Therefore, the compression effect of air was low, and pressure hardly change. On the other hand, in the case of 20cm in depth and 6.0cm in incident wave height, the water level rose over the top of slit, therefore pressure in the wave chamber had risen by the compression effect of air.

Besides, in the case of 24cm in depth, that slit was filled with water from the beginning, and the acting time of uplift pressure was longer. The reason is that the time when air was enclosed was longer.

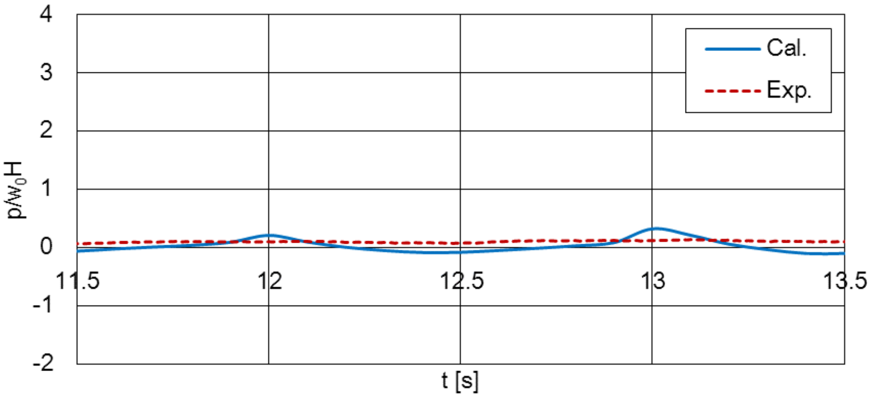

Time variation of uplift pressure in the wave chamber (h=20cm, H=4.0cm)

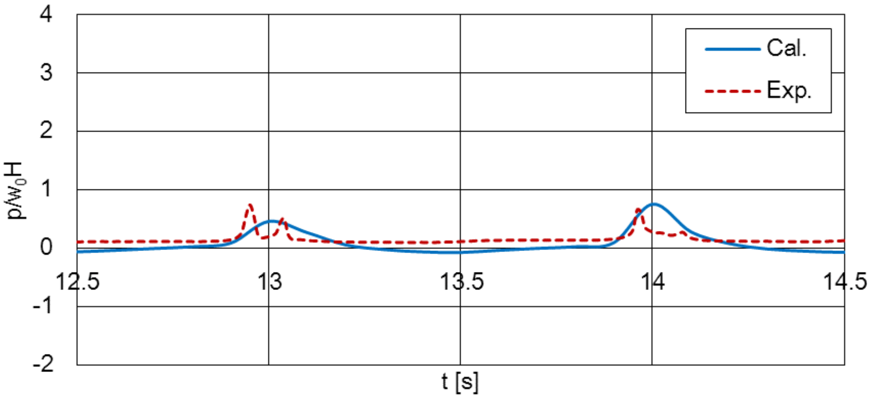

Time variation of uplift pressure in the wave chamber (h=20, H=6.0cm)

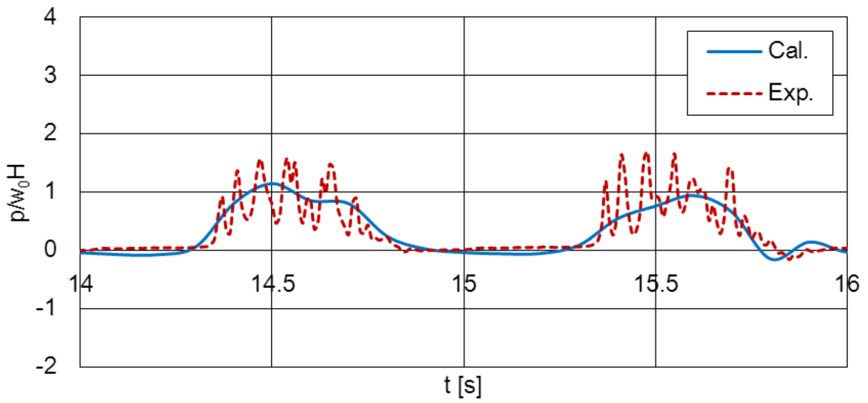

Time variation of uplift pressure in the wave chamber (h=24cm, H=4.0cm)

Figure 3. Time variation of the intensity of uplift pressure.

Figure 4 shows comparison with peak pressure. In Figure 4, the horizontal axis indicates the relative clearance s/H , and the vertical axis indicates the intensity of uplift pressure. The peak pressure is the average value of the maximum values of the uplift pressure of the each cases.

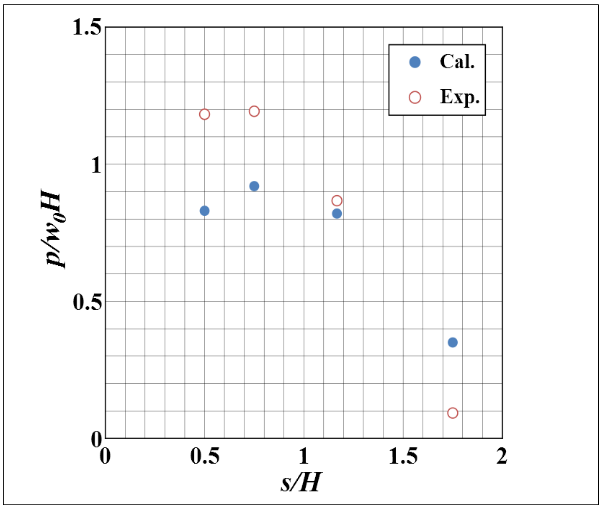

Figure 4. Comparison with peak pressure.

4 MIDDLE-SCALE EXPERIMENT

4.1 Summary of experiment

In this report, we comfirmed the validity of CADMAS-SURF/3D-2F by comparing with experimental results of Tanimoto et al. (1980). The wave flume used for the experiment is 160m in length, 1.0m in width, and 1.5m in height. Table 2 shows the calculation conditions. Calculating area and detail of slit caisson are shown in Figure 5, and Figure 6 respectively. The slit caisson used for the experiment has 9 slits. However, in the calculation, the caisson has 3 slits in order to reduce computation load. In Figure 5, Clearance, s indicates the distance from the bottom of the ceiling slab to the water surface.

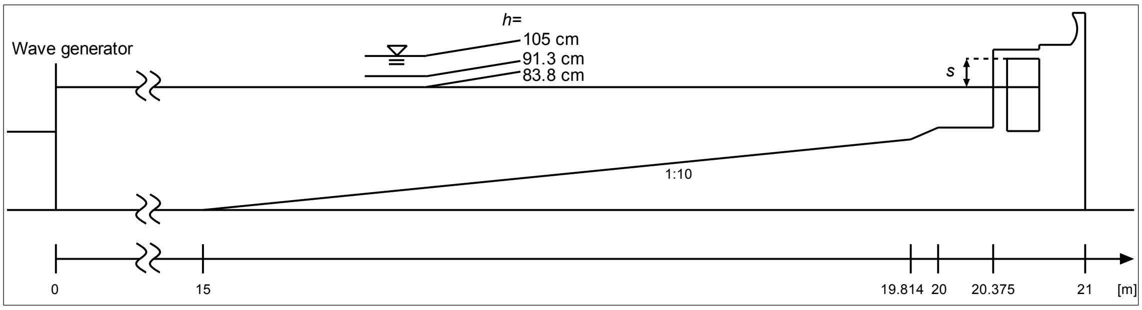

Figure 5. Calculation area.

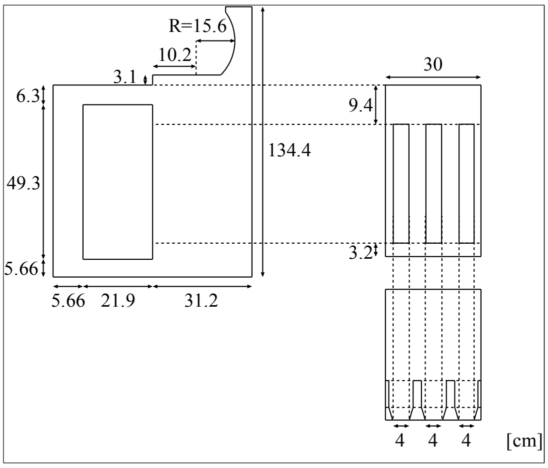

Figure 6. Detail of slit caisson.

Table 2. Calculation conditions.

Water depth [cm]		83.8, 91.3, 105
Wave height [cm]		10, 15, 20
Wave period [s]		2.0
Grid width [cm]	X	2.5
	Y	1.25
	Z	2.5
Number of meshes		2,419,200
Incident wave		Regular wave (SFM 19th)

4.2 Numerical results

Figure 7 shows snapshot of the numerical results.

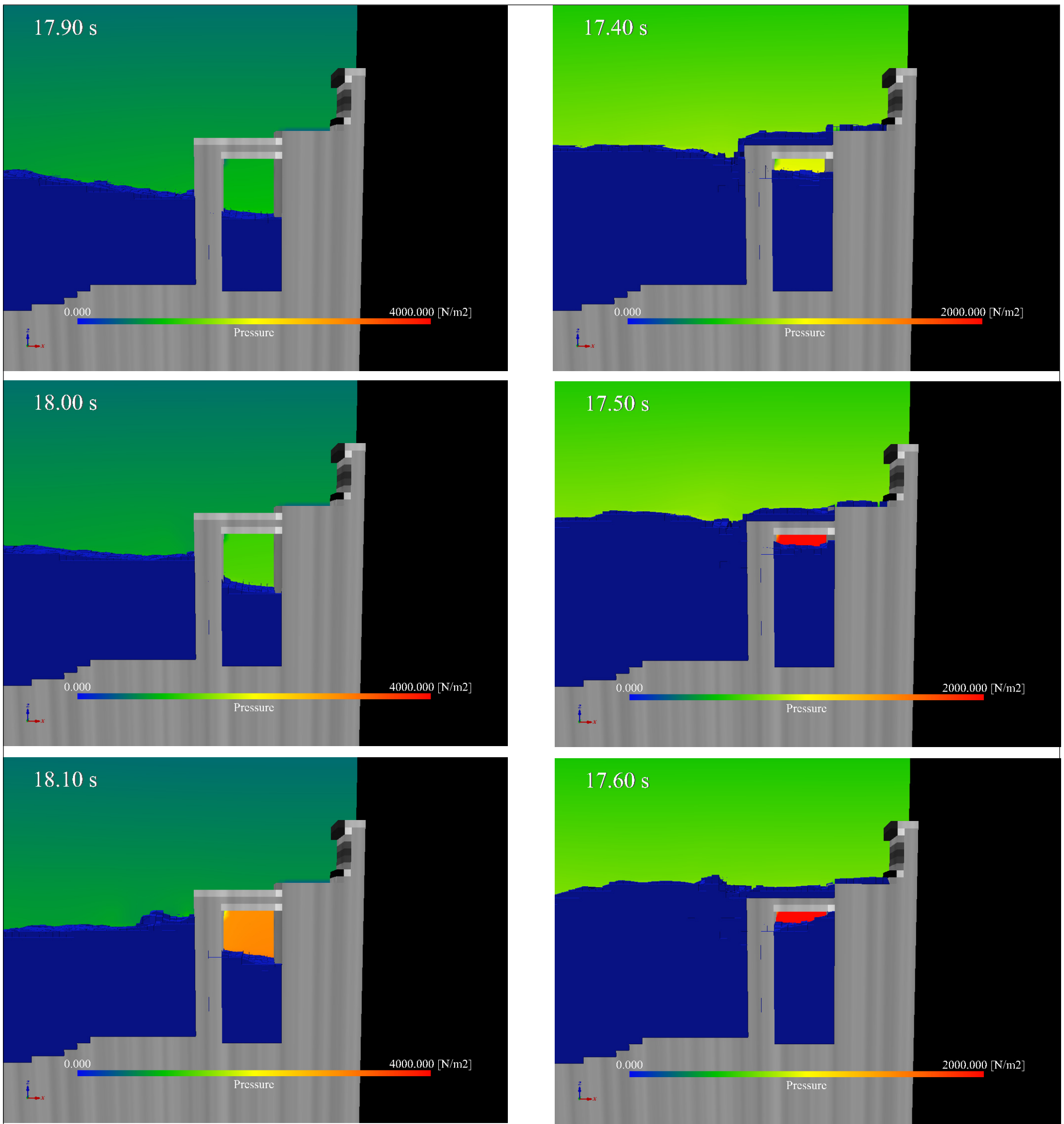

h=91.3cm, H=15cm h=105cm, H=15cm

Figure 7. Snapshot of the numerical results.

As in the past experiment, it is clear that the wave surface does not hit the ceiling slab directly and uplift pressure manifiest through air compression.

4.3 Level and pressure

Figure 8 shows the numerical results of time variation of uplift pressure and water level, η. Uplift pressure took a maximum value when water level in front of caisson was to be high and air was enclosed in the wave chamber. In the cases of 83.8cm and 91.3cm in depth, uplift pressure was impulsive. After peak pressure subjected, enclosed air escaped to the outside of the wave chamber, pressure in the wave chamber dropped, and water flowed and the water level rose. In the case of 105cm in depth, uplift pressure with a long acting time prevented from water level rising so that variation of water level was low as compared with other cases.

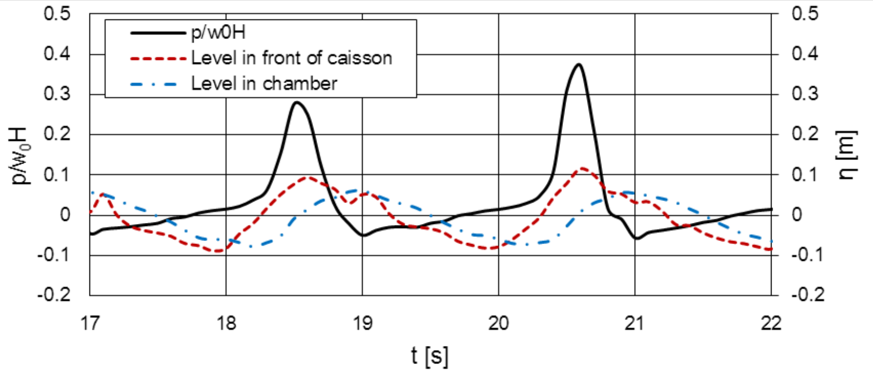

Time variation of uplift pressure and water level (h=83.8cm, H=10.0cm)

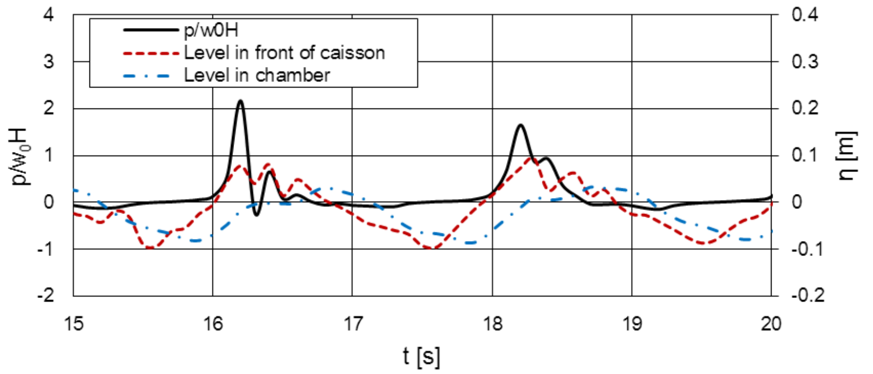

Time variation of uplift pressure and water level (h=91.3cm, H=10.0cm)

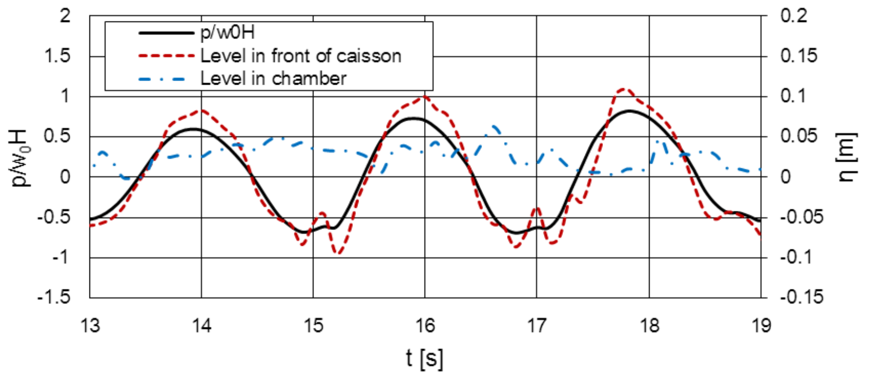

Time variation of uplift pressure and water level (h=105cm, H=10.0cm)

Figure 8. Time variation of uplift pressure and water level.

4.4 Uplift pressure in the wave chamber

Figure 9 shows the numerical results and the experimental results of time variation of uplift pressure in the wave chamber.

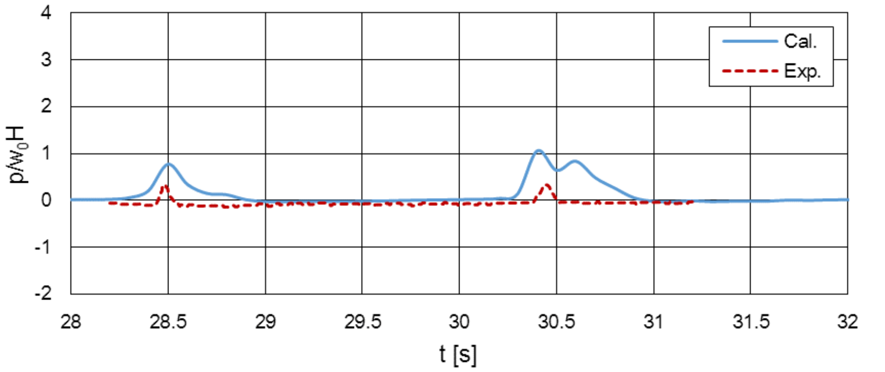

Time variation of uplift pressure in the wave chamber (h=83.8cm, H=15.0cm)

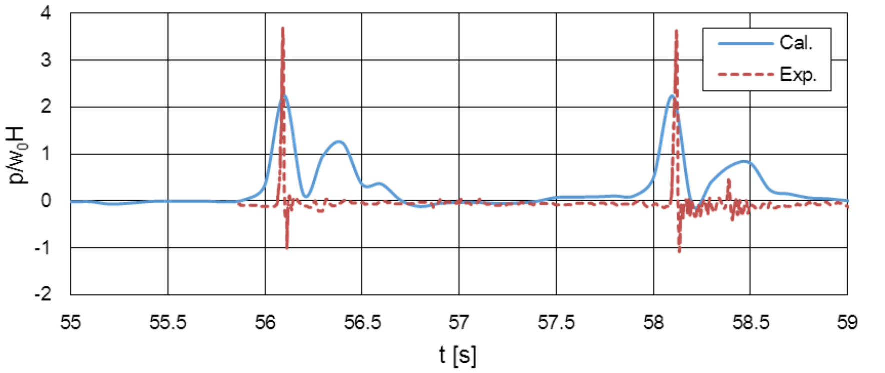

Time variation of uplift pressure in the wave chamber (h=91.3cm, H=15.0cm)

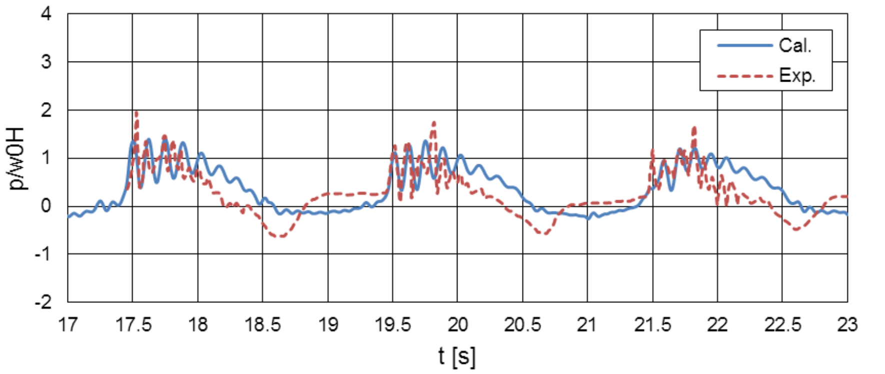

Time variation of uplift pressure in the wave chamber (h=105cm, H=15.0cm)

Figure 9. Time variation of uplift pressure in the wave chamber

Wave profile of the numerical results and the experimental results were almost matched. However, in the case of 91.3cm in depth, the peak pressure was lower than the experimental results. The reason why is that the time step size and the sampling interval were too large as compared with the acting time of the peak pressure in the experiment. Figure 10 shows comparison with peak pressure.

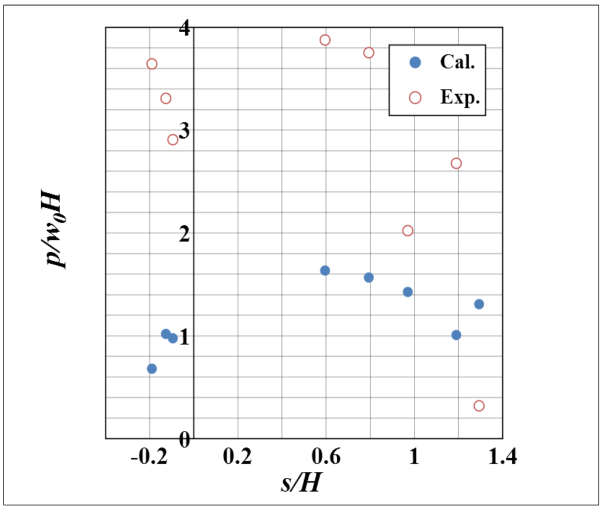

Figure 10. Comparison with peak pressure.

5 CONCLUSIONS

Conclusions are as follows:

(a) Uplift pressure on the wave dissipating slit caisson installed with the ceiling slab took a maximum value when water level in front of caisson was to be high and air was completely enclosed in the wave chamber;

(b) In any case, wave profile of the numerical results and the experimental results were almost matched;

(c) In order to obtain accurate numerical results, it is considered that it is necessary to set finer time step size and the sampling interval as compared with the acting time of pressure in the experiment.

REFERENCES

Tanimoto, K., Takahashi, S. & Muranaga, T. (1980). Uplift Forces on a Ceiling Slab of Wave Dissipating Caisson with a Permeable Front Wall. *Report of the Port and Harbour Research Institute*, 19(1), 1-31. (in Japanese).

POST PROCESSING OF ULTRASONIC RANGING SYSTEM AND ACOUSTIC DOPPLER VELOCIMETER DATA FOR MORPHOLOGICAL STUDIES

PASUPULETI LAXMI NARAYANA(1), PRAFUL VASHARAMBHAI TIMBADIYA(2) & PREM LAL PATEL(3)

(1,2,3) Sardar Vallabhbhai National Institute of Technology, Surat, India,
laxmiraagini@gmail.com; praful.timbadiya@gmail.com; premlalpatel1966@gmail.com

ABSTRACT

Post processing of the data, collected using Ultrasonic Ranging Systems (URS) and Acoustic Doppler velocimeter (ADV), is prerequisite before using it for further analysis of bed elevations and flow velocity respectively in alluvial channels. The data acquired from such systems include undesirable high frequency contents (noises), spikes, affecting the measurement accuracy of aforesaid variables. The present study aims to demonstrate the step wise procedure for post processing of URS and ADV data collected for measurement of bed level variation and three dimensional velocities (3D), respectively. The bed level and 3D velocity data are collected in a 15 m long recirculated tilting sediment transport flume at Advanced Hydraulics Laboratory, SVNIT-Surat, India. The channel is having 0.89 m width, 0.60 m depth and flow discharge is kept 44 liter per second. Here, low pass Butterworth filter is employed to remove the noises in the above mentioned variables. The low pass filter at Nyquist frequency does not create any effect on the main signal. The results reveal that computed spectra for three dimensional velocities from ADV data is nearer to theoretical spectra following -5/3 law. Also, the employed filter effectively removes all noises below Nyquist frequencies for URS data. In case of URS data, the maximum and minimum spike counts are 30% and 2%, respectively. It is observed that increase in the distance between blanking and maximum range reduces the spike count.

Keywords: Nyquist Frequency; noises, spikes; low pass Butterworth filter; theoretical spectra.

1 INTRODUCTION

The Ultrasonic Ranging System (URS) and Acoustic Doppler Velocimeter (ADV) are useful in measurement of bed levels and three dimensional (3D) velocities in flow field, respectively. The data acquired from the URS and ADV incudes high frequency contents (noises), spikes, which influence the measurement of variable under measurement. It is necessary to carry out post processing of data in order to remove high frequency contents (noises), spikes. Hence, it is important to filter out noise to obtain the correct results through measurements. Extensive research work has been carried out through experimentations using ADV since 1990. Voulgaris and Trowbridge (1998) carried out evaluation of the ADV data for turbulence measurements using laboratory experimental data of both ADV and LDV. The data was acquired at a sampling frequency of 25 Hz for a 6 min of time. Analytical equations were used to identify the noises in the signals. The method described to estimate the noise was by integrating over the whole range of frequencies. The calibration of this technique was done by spectral estimation which agreed with theoretical spectra. Venditti and Bennett (2000) have carried out spectral analysis of turbulent flow and suspended sediment transport over fixed dunes by laboratory measurements of turbulence fluctuations in velocity and sediment load concentrations. As for the velocity data sampled at 25Hz, the noise in the signals are filtered by Gaussian low pass filter at Nyquist frequency 12.5Hz to reduce aliasing effect, using cut-off frequency 12.5 Hz. Strom and Papanicolaou (2007) carried out ADV measurements around a cluster microform in a shallow mountain stream using 3D ADV. They encountered the problems while making the measurements very close to the bed (less than 3 cm). The data was taken with 10 MHz ADV at a sampling frequency of 25 Hz for 2 min. The spike detection and its replacement were based on signal to noise ratio and correlation coefficient scores. The SNR values less than 15 dB and COR less than 70% were considered to be spikes and they were replaced by their mean values. The reported critical SNR and COR values were $0 \leq SNRcr \leq 10$ and for $0 \leq CORcr \leq 50$, respectively. Since, Wahl (2000) claimed that COR scores with less than 70% were less in number, and hence proved to be good data. The raw signals of ADV data were entrained initially with the presence of spike and they were detected by phase space thresholding method (PSTM) proposed by Goring and Nikora (2000). The replacement of spike was computed by cubic interpolation technique on either side of 12 points with 10% of replacement of signals were carried out in their study. The power spectrum showed that the data fit with Kolmogorov's -5/3 law for all three directional velocity components. The calculations of power spectral density were applied for the data which were filtered by using low pass Gaussian filter with cutoff frequency at Nyquist frequency (f_n=12.5 Hz) and removed all noises, and spectrum showed that those data followed -5/3 law. Parsheh et al. (2010) estimated power spectra of ADV data contaminated with intermittent spikes. They presented with a powerful technique for detecting and removing spikes for ADV time series and mentioned that the technique recovered the low-frequency region with high energy content. Also, high frequency regions were not accurately reconstructed at last data points and verified by -5/3 slope region in the inertial sub range of spectra. The validation of their technique was carried out by comparing the spectral density of the reconstructed signal to the original data set. For spike detection, modified Phase-Space Thresholding technique was used for spectral analysis and replacement was carried out with last valid data points. They also tested their proposed technique by adding random spikes to clean data set and compared energy spectrum with intentionally contaminated data. Few studies on bed level measurements were documented using URS data. Singh et al. (2012) carried out the coupled dynamics of the co-evolution of gravel bed topography, flow turbulence and sediment transport by studying in an experimental channel by performing series of flume experiments. In their experimentation, the data on both velocity, and bed elevations were collected at different locations of the channel. The sampling frequency for the bed elevation studies was 0.20 Hz with a sonar transducers and velocity studies at 200Hz using ADV. The noise in the sediment transport sampling was removed by moving average window of 5 min. The noise in the bed elevation data and velocity data were removed by Gaussian filter. Sarkar and Mazumdar (2014) carried out the turbulence flow over the trough region formed by a pair of forward-facing bedforms shapes by conducting the experiments in a recirculated laboratory flume. The velocity data were sampled at 40Hz by using 16 MHz ADV. The noise in the ADV data was filtered by Butterworth low-pass filter with cut-off frequency at 10, 5, 2Hz. Sarkar et al. (2015) studied the space-time dynamics of bed forms due to turbulence around submerged bridge piers through experiments in a recirculated laboratory flume. Instantaneous bed elevations were sampled at 4Hz using 5 MHz Ultrasonic Ranging System. The velocity data were sampled at 40Hz using 16 MHz ADV. The noise in the ADV data was filtered by Butterworth low-pass filter, Nyquist frequency at 20Hz and cut-off frequency at 5Hz in order to reduce the aliasing effect in signals. In the present study, the instrumental set up for measurement of bed level and three dimensional velocities will be discussed. The work carried out using such instruments are reported and their noise removal techniques are presented. The bed levels have been measured in Advanced Hydraulics Laboratory, Sardar Vallabhbhai National Institute of Technology-Surat, India using URS and noise removal is also explained in detail. The three-dimensional velocities, measured in aforesaid laboratory flume using ADV and noise removal, are explained in the present study. The main purpose of the study is to understand the post processing of data collected using URS and ADV. It is important to study this in order to quantify the bed topography of morphological studies and measurements of three-dimensional point velocities of flow. The objectives of the present study are a) to collect the URS and ADV data in sediment transport flume available in Advanced Hydraulic Laboratory SVNIT-Surat, India, b) to post process the collected URS data in order to remove noise to get correct bed levels and c) to post process the collected ADV data in order to remove noise to get the correct three-dimensional point velocities.

2 EXPERIMENTATION

2.1 Instrumental set-up of URS

The URS is used to measure bed elevations in laboratory flume to study the variation in the fields of sediment transport, where other techniques like point gauges are impractical. URS is composed of 32 transducers, the acoustic operating frequency of this system is 5 MHz and transducer diameter of 1 cm. The closest measurement range of this system is 3 cm, while the farthest range is 110 cm (SeaTek URS 5 MHz Technical note, 2014). The data output starts with the 'starting' transducer and continue to scan in increasing order by the assigned 'increment' until the 'ending' transducer is reached. The number of 'bursts' or scans to record and the 'sample rate' were set. The sample rate should be entered as the number of Milliseconds between the beginnings of each scan. The maximum sample rate setting is 50 Milliseconds (20 Hz), which should be entered as 50. A sample rate of 1 second should be entered as 1000.

2.2 Instrumental set-up of ADV

The ADV is used to measure three dimensional velocities in flow field of laboratory flume experiments. The operating frequency of the system is 16 MHz with the principle of pulse-coherent technique. This system has sampling volumes at a distance of 5-7 cm, i.e., the minimum distance from transmitter to the target point and velocity ranges of 250, 100, 30, 10 and 3 cm/s (Son Tek/YSI Technical note, 2009). The three basic data on velocity, signal strength and correlation coefficient scores were collected. Ramagnoli et al. (2012) carried out the signal post processing technique and uncertainty analysis of ADV turbulence measurements on free hydraulic jumps using 16 MHz microADV at a sampling rate of 50Hz. The recorded signals showed signal strength less than 15 dB and COR values observed in between 45 to 95.

2.3 Experimental set-up

Experiments were conducted in a recirculating tilting sediment transport flume located in the Advanced Hydraulics Laboratory (AHL) SVNIT-Surat, Gujarat, India. The experimental channel had the dimensions of 15 m length, 0.89m width and 0.6m height (Patel et al., 2015). The flume walls were made of Perspex windows over a distance of 8 m providing clear view of flow. The plan and longitudinal section of the flume is shown in

Figure 1. The upstream section of the channel was divided into three sub-channels of equal dimensions, and a honeycomb cage was placed at each end of sub-channel to ensure smooth flow. The collections of sediments were done by using a sediment trap placed at downstream section of flume.

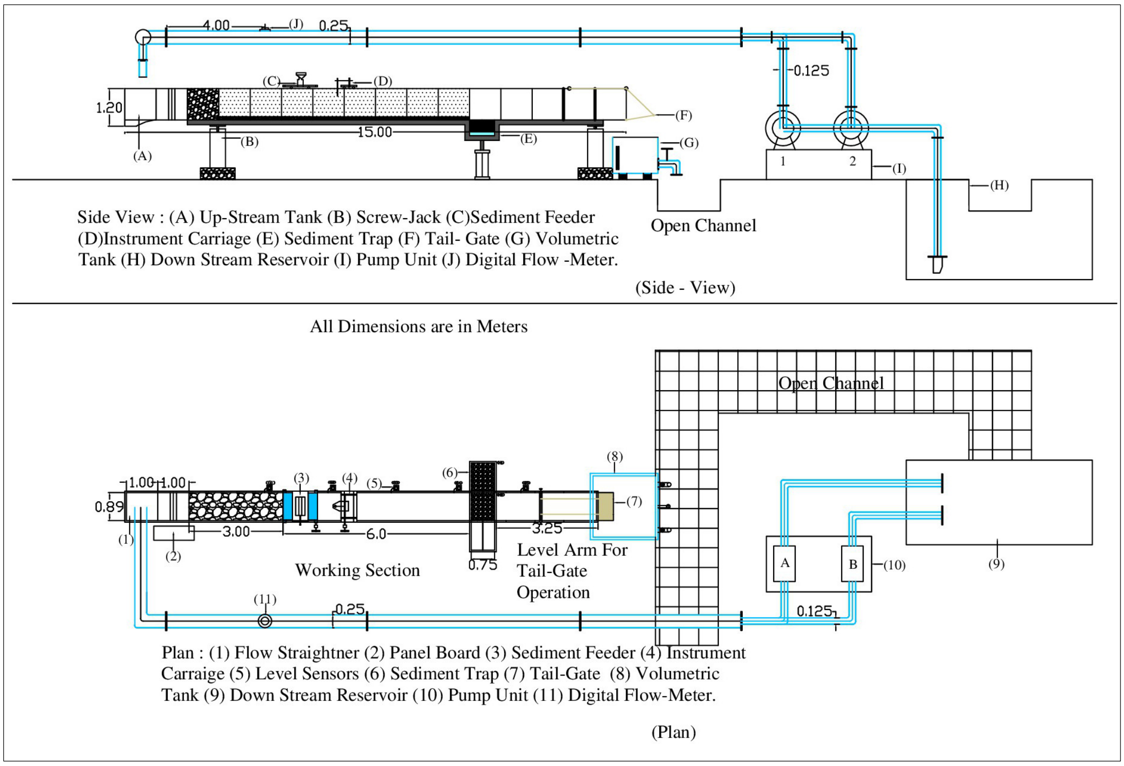

Figure 1. Schematic diagram of Experimental set-up.

The system was mounted in an aluminum trolley placed at working sections. The instrumental set-up shown in Photograph (1a) shows the placement of transducers, while photograph (1b) shows the channel with its allied data acquisition system. Photograph (1c) shows the down looking SonTek ADV which is mounted on Trolley and its allied data acquisition system is shown in Photograph (1d).

(a) **(b)**

(c) **(d)**

Photograph 1. (a) Placement of URS transducers mounted on aluminum trolley; (b) Data acquisition system for URS; (c) Down looking SonTek ADV which mounted on Trolley; (d) Data acquisition system for ADV.

3 METHODOLOGY

3.1 Method for post processing of URS data

The flow chart for Post Processing of URS data is shown in Figure 2. Different ranges of data were collected at sampling frequency, $(f_s = 4Hz)$ by using Ultrasonic Ranging System. Despiking involved two steps, in which, the first step was detecting the spike, the outliers of the data set were considered as spikes and detected by plotting simple scatterplots using MATLAB tool. Second step was replacing the spike, in which, the excluded signals were replaced with Not a Number (NAN). Since the data set was in uneven series, to make it even, the process, so called interpolation had been carried out. In general, interpolations like linear, spline, cubic were used to make even series. When acquiring the data from any electrical set-up, the noise was also included along with our time domain signals. The presence of this noise at high frequencies creates an undesirable condition called aliasing effect. To reduce this effect, one should filter the data with the help of low pass filter. In the present case, Butterworth low pass filter was employed to remove high frequency contents at Nyquist frequency, (f_n=2Hz). Step by step procedure is described below:-

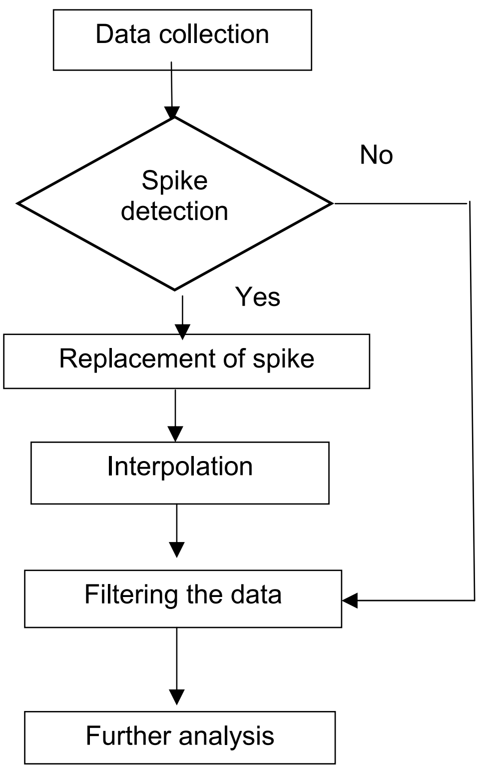

Figure 2. Flow chart for Post Processing of URS data.

I. Collection of data by using ultrasonic ranging system;
II. Detecting the spikes of an existing data;
III. Replacement of spikes;
IV. Make the uneven series to even series by cubic or spline interpolation;
V. Filtering the data to remove the high frequency contents in the signals.

3.2 Method for post processing of ADV data

The flow chart of Post Processing of ADV data is shown in Figure 3.

The ADV collects three basic data i.e., velocity in three directions, signal to noise ratio (SNR) and correlation coefficient scores. In general, strength of signal is represented as SNR. An SNR value of 0 dB means that there is no difference between the acoustic energy being detected by the ADV and the background noise level. For low sample rate data collection, i.e. 1-2Hz, SNR as low as 4 dB allows for accurate velocity measurements. For higher rates, i.e. more than 25Hz, SNR should be higher than 15 dB. Correlation coefficient scores represent the quality of the data; a typical threshold for data acceptance should be 70% or higher, Velasco and Huhta (2010). The sample data was collected at a rate of 40Hz.and the presence of this noise at high frequencies created an undesirable condition called aliasing effect. To reduce this effect, one has to filter the data with the help of low pass filter. In the present case, Butterworth low pass filter was employed to remove high frequency contents at Nyquist frequency, $(f_n = 20Hz)$.The spectral characteristics of the vertical, horizontal and transverse flows were measured by ADV and examined in this study. The calculated spectra was compared to Kolmogorov's -5/3 law. The procedure to calculate power spectra is given below:

1) Make data an evenly spaced series of instantaneous velocity data by interpolation at the place of rejected spikes using MATLAB (8.01, 2013);
2) Make ensembles which is a power of 2 for a de-trended data series;
3) Calculate power spectral density (PSD) for each ensemble separately with existing window by using aforesaid MATLAB code;
4) Take average of all ensembles at each frequency. Plot it to check Kolmogorov's -5/3 law for data.

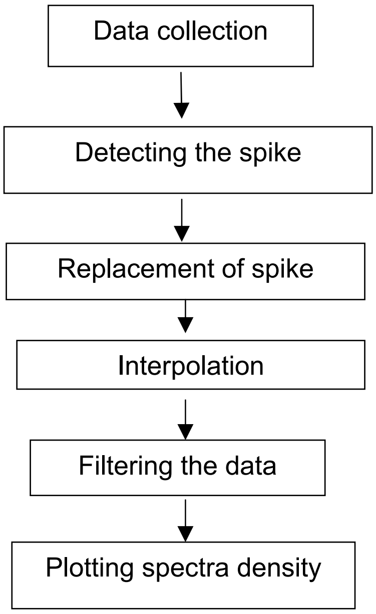

Figure 3. Flow chart for Post Processing of ADV data.

4 POST PROCESSING OF URS DATA

The different ranges of data were collected at sampling frequency of 4 Hz using URS in between blanking distance 6 to 8 cm and maximum range 12 to 15 cm. Post Processing was carried out for the corresponding range measurements and following plots with results are shown below.

4.1 Detecting the spike

The spike detection was carried out, as mentioned in Section 3.1. The outliers of corresponding ranges are shown in Figure 4 (a) and (b), respectively. The distance between blanking and maximum range for the data in Figure 4 (a) and (b) was kept at 9 and 4, respectively.

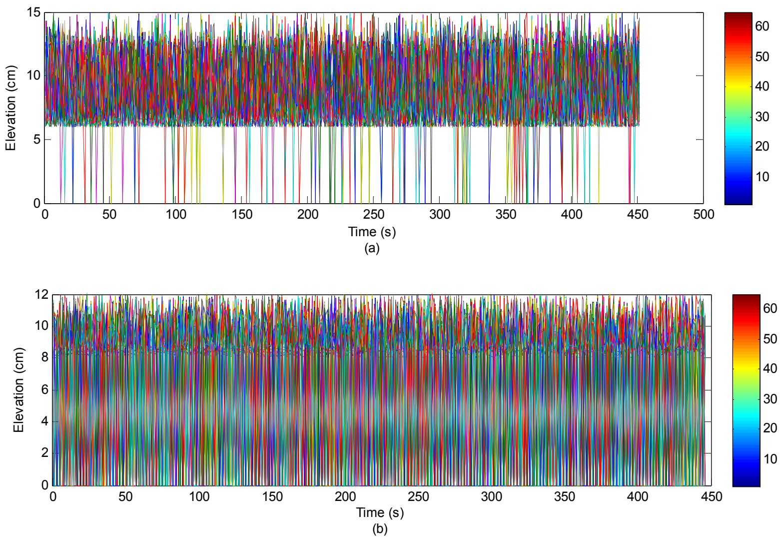

Figure 4. Detection of minimum and maximum spikes.

More spikes were detected when the distance of blanking and maximum range was closer. Among them, one of the data set has more distance between blanking and range reading is shown in Figure 4 (a), which depicts lesser spikes observed in our investigation.

4.2 Replacement and Interpolation of spike

The spike replacement had been carried out, as mentioned in Section 3.1. The plot of replaced spikes of corresponding ranges are shown in Figure 5.

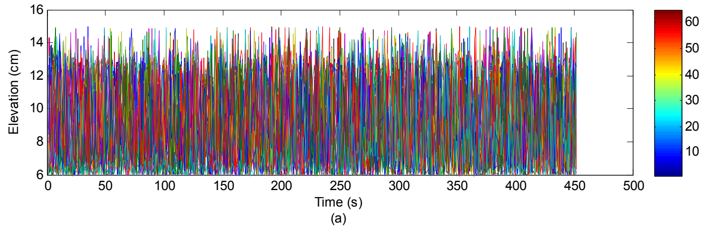

Figure 5. Spikes replacement.

The replaced spike had to be interpolated to make even data series and it was carried out, as per mentioned in Section 2.1. The plot of interpolated spikes of corresponding ranges is shown in Figure 6.

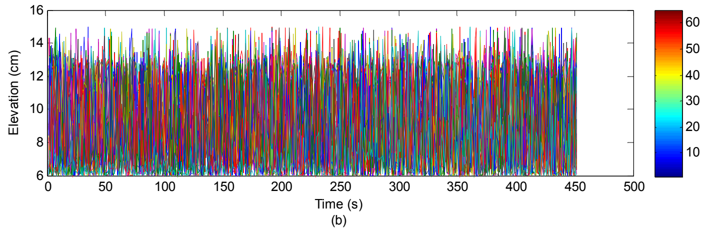

Figure 6. Cubic interpolation.

4.3 Filtering the data

The filtering of data had been carried out, as mentioned in Section 3.1. Filtered and unfiltered plots of corresponding ranges are shown in Figure 7 (a) and (b), respectively.

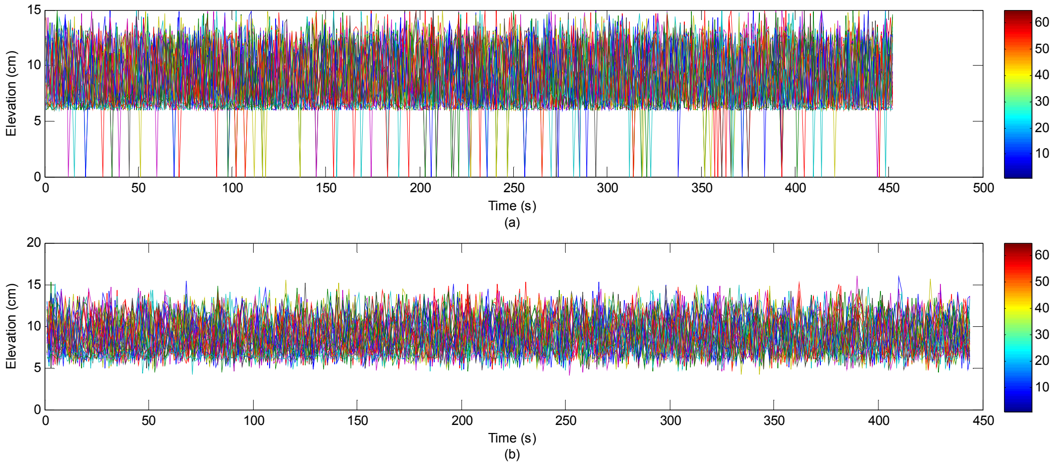

Figure 7. Unfiltered and filtered signals, respectively.

5 POST PROCESSING OF ADV DATA

Instantaneous three-dimensional velocity data were collected using 16 MHz ADV along flume centerline with sampling frequency of 40 Hz in 4 min of time. Post processing of corresponding measurements was carried out and described below.

5.1 Plotting the power spectral density

The procedure for plotting the spectral density is mentioned in Section 3.2. Spectral analysis of horizontal, transverse and vertical velocity–time series, corresponding plots with five ensembles of computed Power Spectral Density of respective velocity components are shown in Figures 8 and 9, respectively.

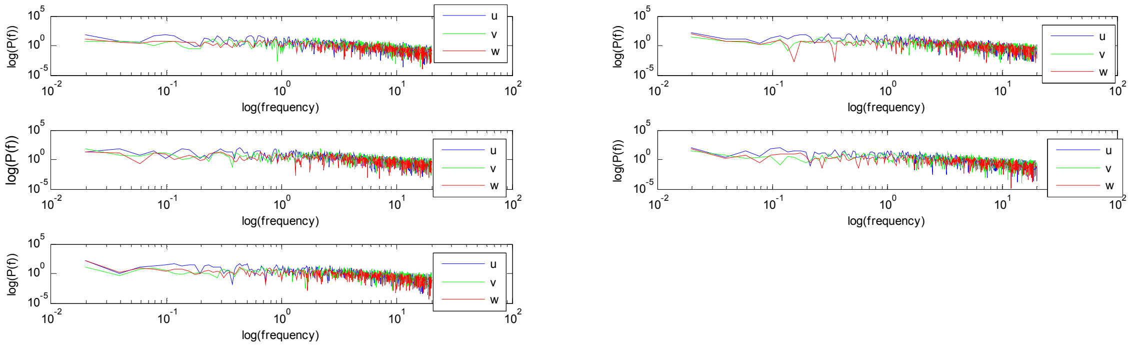

Figure 8. Power Spectral Densities of an unfiltered velocity-time series*****.
*Blue line indicates stream wise spectra, green line indicates cross-stream spectra and red line indicates wall-normal spectra.

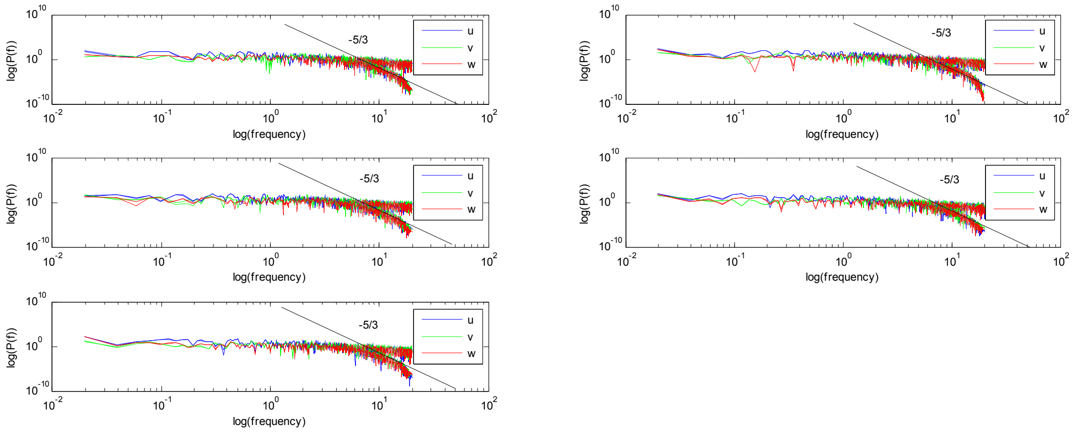

Figure 9. Power Spectral Densities of a filtered velocity-time series*.
*Blue line indicates stream wise spectra, green line indicates cross-stream spectra and red line indicates wall-normal spectra.

6 RESULTS AND DISCUSSIONS

A total of four data sets were acquired using URS and velocity data at different points along depth of flow were measured using ADV. In case of URS data, the maximum and minimum spike counts were 30% and 2%, respectively as shown in Figure 4 (a) and (b). It is observed that by increasing the distance between blanking and maximum range, it reduces the spike count. The presence of spikes leads to inaccurate results. On the other hand, simply removing them will result in discontinuity in the series. More than 3000 data points were detected as spikes as shown in Figure 4 (b), which were then replaced using cubic interpolation technique and shown in Figure 6. To remove the noise in even series, low pass Butterworth filter was employed at cut off frequency, $f_c = 1.5\ Hz$. The filter effectively removed the noise below the Nyquist frequency, $f_n = 2.0\ Hz$. The filtered and unfiltered plots of Maximum range readings are shown in Figure 7 (a and b).

The power spectra of the unfiltered and filtered data are shown in Figure 8 and 9, respectively for three dimensional velocities i.e., u, v and w. The filtered signals, between 6 to10 Hz, are followed by a -5/3 slope which indicates that the data in this range would be useful to utilize in the turbulence modelling.

7 CONCLUSIONS

I. The bed levels measured in a laboratory flume using 5 MHz URS at sampling frequency ($f_s = 4\ Hz$), and, step wise procedure for post processing of data have been explained;
II. The replacement of spikes has been carried out using cubic interpolation technique;
III. Butterworth low pass filter has been employed to remove high frequency contents at Nyquist frequency, ($f_n = 2Hz$). The filter effectively removes all noises below the Nyquist frequency;
IV. The three-dimensional velocities measured in laboratory flume using 16 MHz ADV at sampling frequency ($f_s = 40Hz$), and step wise procedure for post processing have been explained;
V. Replacement of spikes and filtering of the noise in ADV data have been carried out similar to those done in bed levels;
VI. The calculation of power spectral density of three dimensional velocities has been reported. The corresponding plots and the results show that the computed spectra for three dimensional velocities computed from ADV data is close to the theoretical spectra.

ACKNOWLEDGEMENTS

The authors would like to acknowledge the necessary infrastructural support provided by Centre of Excellence (CoE) on "Water Resources and Flood Management", TEQIP-II, Ministry of Human Resources Development (MHRD), Government of India, for conducting the study reported in the paper.

We appreciate the cooperation and efforts of all authors in producing the Proceedings. This will be a great congress following the tradition of our sponsoring organizations.

REFERENCES

Goring, D.G. & Nikora, V.I. (2000). Despiking Acoustic Doppler Velocimeter Data. *Journal of Hydraulic Engineering,* 128(1), 117-126

Patel, S.B., Patel, P.L. & Porey, P.D. (2015). Fractional Bed Load Transport Model for Non-Uniform Unimodel and Bimodal Sediments, *Journal of Hydro-environment Research*, 9(1), 104-119.

Parsheh, M., Sotiropoulos, F. & Porté-Agel, F. (2010). Estimation of Power Spectra of Acoustic-Doppler Velocimetry Data Contaminated with Intermittent Spikes. *Journal of Hydraulic Engineering,* 136(6), 368-378.

Romagnoli, M., García, C.M. & Lopardo, R.A. (2012). Signal Post Processing Technique and Uncertainty Analysis of ADV Turbulence Measurements on Free Hydraulic Jumps. *Journal of Hydraulic Engineering,* 138(4), 353-357.

SeaTek. (2014). 5 MHz Ultrasonic Ranging System, *SeaTek Technical note*.

Strom, K.B. & Papanicolaou, A.N. (2007). ADV Measurements Around a Cluster Microform in a Shallow Mountain Stream. *Journal of Hydraulic Engineering,* 133(12), 1379-1389.

Singh, A., Porté-Agel, F. & Foufoula-Georgiou, E. (2010). On the Influence of Gravel Bed Dynamics on Velocity Power Spectra. *Water resources research,* 46(W04509), 1-10

Singh, A., Foufoula-Georgiou, E., Porté-Agel, F. & Wilcock, P.R. (2012). Coupled Dynamics of The Co-Evolution of Gravel Bed Topography, Flow Turbulence and Sediment Transport in an Experimental Channel. *Journal of Geophysical Research: Earth Surface,* 117(F04016), 1-20

Sarkar, K. & Mazumder, B.S. (2014). Turbulent Flow Over the Trough Region Formed by a Pair of Forward-Facing Bedform Shapes. *European Journal of Mechanics-B/Fluids,* 46, 126-143.

Sarkar, K., Chakraborty, C. & Mazumder, B.S. (2015). Space-Time Dynamicso of Bed Forms due to Turbulence Around Submerged Bridge Piers. *Stochastic Environmental Research and Risk Assessment,* 29(3), 995-1017.

Velasco, D.W. & Huhta, C.A. (2010). Experimental Verification of Acoustic Doppler Velocimeter (ADV) Performance in Fine-Grained, High Sediment Concentration Fluids. *SonTek/YSI Application Note*, 1-19.

Voulgaris, G. & Trowbridge, J.H. (1998). Evaluation of the Acoustic Doppler Velocimeter (ADV) for Turbulence Measurements. *Journal of atmospheric and oceanic technology*, 15(1), 272-289.

Venditti, J.G. & Bennett, S.J. (2000). Spectral Analysis of Turbulent Flow and Suspended Sediment Transport over Fixed Dunes. *Journal of Geophysical Research: Oceans,* 105(C9), 22035-22047.

Wahl, T.L. (2000). Analyzing ADV Data using WinADV. *Building Partnerships*, *Water Resources*, 1-10.

Proceedings of the 37th IAHR World Congress
August 13 – 18, 2017, Kuala Lumpur, Malaysia

STUDY ON TSUNAMI ACTION FORM TO INFLUENCE THE SLIDE OF THE FUEL TANK BASED ON NUMERICAL COMPUTATION

YUKI OHKI(1), NAOKI YOSHIDA(2) & TARO ARIKAWA(3)

(1,2,3) Chuo University, Tokyo, Japan,
yukioki@civil.chuo-u.ac.jp; naoki-y@civil.chuo-u.ac.jp; ariakwa@civil.chuo-u.ac.jp

ABSTRACT

During tsunami disaster, fire occurs because of outflow of fuel due to damage and drifting of fuel tank. Convolt Tank is the fuel tank which unified oil wall and storage tanks-proof. It is required to examine the stability of Convolt tank by using physical experiment and numerical experiment, and the safety of fuel tank against tsunami can be evaluated. We have generated three solitary waves and examined wave pressure based on the result in physical experiment. As a result, in physical experiment, tank slid in most cases. CADMAS-STR/3D (Arikawa et al., 2009) was used as the numerical simulators. This simulator is formed from fluid analysis and structure analysis. By using this coupling method, sliding phenomena was able to be reproduced, and pressure effect on sliding tank can be evaluated.

Keywords: Convolt tank; CADMAS-STR/3D; sliding; fuel tank; tsunami.

1 INTRODUCTION

As a result of the tsunami whose scale was far beyond assumptions, generated by the March 11, 2011, Tohoku district Pacific Offing Earthquake, Japan suffered catastrophic damage. Fuel storage facilities were damaged by the tsunami and the earthquakes. Oil leaks from tanks due to the damage of the facilities, and it was the factor of fire that occurred in the city area. It may be said that the earthquake and the tsunami resistance of the fuel tank are needed to reduce damage of tsunami. Convolt type ground tank that is not the general type but the Oil-proof tsunami integrated type is suggested. Figure 1 shows a snap shot of Convolt Tank. In this study, I assumed the tsunami of the Nankai-trough earthquake scale and performed the experiment about the safe evaluation for the tank against tsunami. Furthermore, using calculation system CADMAS-STR/3D which enabled coupling analysis of the fluid and structure, I performed the reproducible examination of the slide phenomenon of tank at the time of tsunami action.

Figure 1. Snap shot of Convolt tank.

2 METHOD OF PHYSICAL EXPERIMENT

The experiment used a section water tank. The water tank is 0.30m in width, 0.50m in height, and 18.35m in total length. Experiment summary is shown in Figure 2. The tank model of 1/25 scale was installed in the position of 0.10m from a slope. Filling rate of oil in tank was reproduced by changing the weight in tank model, with 0.78kg as empty model, and 2.22kg as full model.

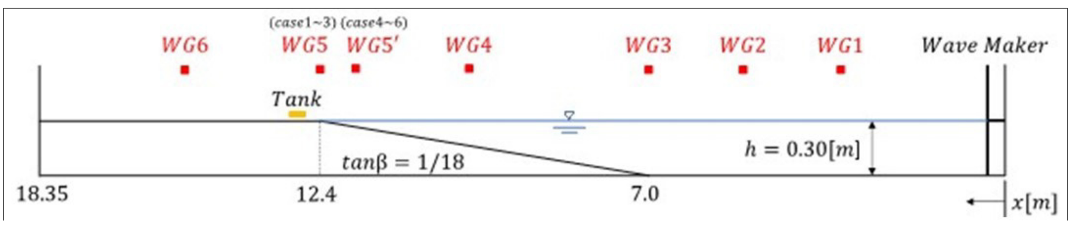

Figure 2. Experiment setup.

Figure 3 shows the positions of pressure gauges. Pressure gauges were set up with two in the front side, and three on the base. Three solitary waves were triggered and tested in case01~06 shown in Table 1. In case01~03, the contents were reproduced in an empty state and in case04~06, the contents were reproduced in a filled-up state and all the cases were tested.

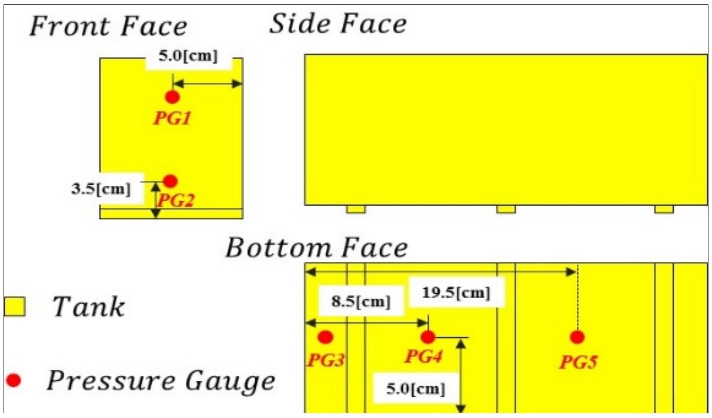

Figure 3. Position of pressure gauges at tank.

Table 1. Slide in each experiment case.

case	Wave Height[cm]	Condition of Tank	Slide
1	5	empty	○
2	7.5	empty	○
3	10	empty	○
4	5	full	×
5	7.5	full	○
6	10	full	○

3 METHOD OF NUMERICAL EXPERIMENT

3.1 CADMAS-SURF/3D

CADMAS-SURF/3D is a three-dimensional wave tank model under development, which has recently been applied to some studies of wave-structure interaction. The basic equation uses consecutive expressions and exercise equations and uses the VOF method by the limited volume method as free surface processing.

3.1.1 Basic equation

$$\frac{\partial \gamma_x u}{\partial \mathrm{x}} + \frac{\partial \gamma_y v}{\partial y} + \frac{\partial \gamma_z w}{\partial z} = S_p \quad [1]$$

$$\lambda_v \frac{\partial u}{\partial \mathrm{t}} + \frac{\partial \lambda_x uu}{\partial x} + \frac{\partial \lambda_y uv}{\partial y} + \frac{\partial \lambda_z uw}{\partial z} = -\frac{1}{\rho}\frac{\partial P}{\partial x} + \frac{\partial}{\partial x}\left\{\gamma_x \nu_e \left(2\frac{\partial u}{\partial x}\right)\right\} + \frac{\partial}{\partial y}\left\{\gamma_y \nu_e \left(\frac{\partial u}{\partial y} + \frac{\partial v}{\partial x}\right)\right\} + \frac{\partial}{\partial z}\left\{\gamma_z \nu_e \left(\frac{\partial u}{\partial z} + \frac{\partial w}{\partial x}\right)\right\} + S_u \quad [2]$$

$$\lambda_v \frac{\partial v}{\partial \mathrm{t}} + \frac{\partial \lambda_x vu}{\partial x} + \frac{\partial \lambda_y vv}{\partial y} + \frac{\partial \lambda_z vw}{\partial z} = -\frac{1}{\rho}\frac{\partial P}{\partial y} + \frac{\partial}{\partial x}\left\{\gamma_x \nu_e \left(\frac{\partial v}{\partial x} + \frac{\partial u}{\partial y}\right)\right\} + \frac{\partial}{\partial y}\left\{\gamma_y \nu_e \left(2\frac{\partial v}{\partial y}\right)\right\} + \frac{\partial}{\partial z}\left\{\gamma_z \nu_e \left(\frac{\partial v}{\partial z} + \frac{\partial w}{\partial y}\right)\right\} + S_v \quad [3]$$

$$\lambda_v \frac{\partial w}{\partial \mathrm{t}} + \frac{\partial \lambda_x wu}{\partial x} + \frac{\partial \lambda_y wv}{\partial y} + \frac{\partial \lambda_z ww}{\partial z} = -\frac{1}{\rho}\frac{\partial P}{\partial x} + \frac{\partial}{\partial x}\left\{\gamma_x \nu_e \left(\frac{\partial w}{\partial x} + \frac{\partial u}{\partial z}\right)\right\} + \frac{\partial}{\partial y}\left\{\gamma_y \nu_e \left(\frac{\partial w}{\partial y} + \frac{\partial v}{\partial z}\right)\right\} + \frac{\partial}{\partial z}\left\{\gamma_z \nu_e \left(2\frac{\partial w}{\partial z}\right)\right\} + S_w - \gamma_v g \quad [4]$$

where

$$\begin{cases} \lambda_v = \gamma_v + (1-\gamma_v)C_M \\ \lambda_x = \gamma_x + (1-\gamma_x)C_M \\ \lambda_y = \gamma_y + (1-\gamma_y)C_M \\ \lambda_z = \gamma_z + (1-\gamma_z)C_M \end{cases} \quad [5]$$

3.1.2 Free surface analysis model

Volume of Fluid method which could analyze a complicated surface shape is adapted as a free surface analysis model

$$\gamma_v \frac{\partial \mathrm{F}}{\partial \mathrm{t}} + \frac{\partial \gamma_x uF}{\partial x} + \frac{\partial \gamma_y vF}{\partial y} + \frac{\partial \gamma_z wF}{\partial z} = S_F \quad [6]$$

We made the disintegration of the advection equation mentioned above by the donor lye septa method which increases improvement. With the VOF method which increases improvement for free surface analysis; using the studio guard mesh spatial; break up, and become disintegration by technique.

I performed wave-making by matrix data about wave-making of the soliton and it is shown as follows

$$\gamma_v \eta_{(x,t)} = Hsech^2\{k(x-Ct)\} \quad [7]$$

Velocity in each point in time and quantity of water level change were calculated and velocity provided on an analysis domain boundary surface was given based on the wave-making water level change quantity.

3.2 CADMAS-STR/3D

CADMAS-STR3D (Arikawa et al., 20109 is the structure-fluid calculation system which enables coupling with Femap which is CADMAS-SURF3D and the structural calculation system. It calculates displacement caused by pressure calculated in the CADMAS side, as shown in Figure 4, and enables structural calculation and coupling analysis of the fluid calculation by data changing of both sides.

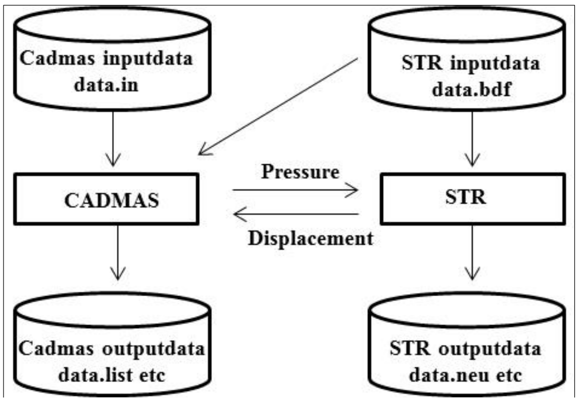

Figure 4. Scheme of coupling analysis for CADMAS-STR/3D.

The fluid side expresses that the obstacle not to completely bury a cell in although we use a structure lattice by porosity. The porosity changes in terms of time. A continuous exercise equation is just as we showed it by a summary of CADMAS-SURF/3D. When assuming acceleration of gravity, u displacement in stress tensor, ρ in σ in density of the structure, g, the exercise equation in the structure is

$$\nabla \cdot \sigma + \rho g = \rho \ddot{u} \quad [8]$$

Effective stress level σ` in the ground is

$$\dot{\sigma} = \sigma + pI \quad [9]$$

Structure analyzes these double equations as a rule equation.

3.3 Contact analysis

Figure 5 shows the image of the contact analysis in CADMAS-STR/3D.

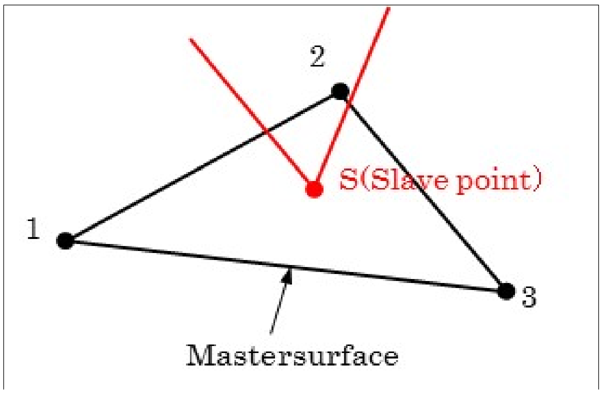

Figure 5. Image of the contact analysis in CADMAS-STR/3D.

CADMAS-STR/3D has a contact analysis function. I repeated it about the position of the node point of contact that each structure expenses were sober and indicated master slave relations, penetrated from a supposition of surface, calculated it and judged contact. The MPC condition that a master should meet, for example, in the case of a triangular aspect about a MPC condition of the plane maintenance is

$$U_S \cdot n = L_1 U_1 \cdot n + L_2 U_2 \cdot n + L_3 U_3 \cdot n \qquad [10]$$

where

$$\begin{cases} L_i: Area\ of\ slave\ point\ S\ coordinate\ in\ triangle\ 123 \\ n: Normal\ vector\ of\ triangle\ 123 \end{cases} \qquad [11]$$

3.4 Analysis condition

Figure 6 shows the analysis model of Convolt tank. Mesh divisions are 1.0cm in each section. Contact surface is defined at the bottom of structure colored in Figure 6.

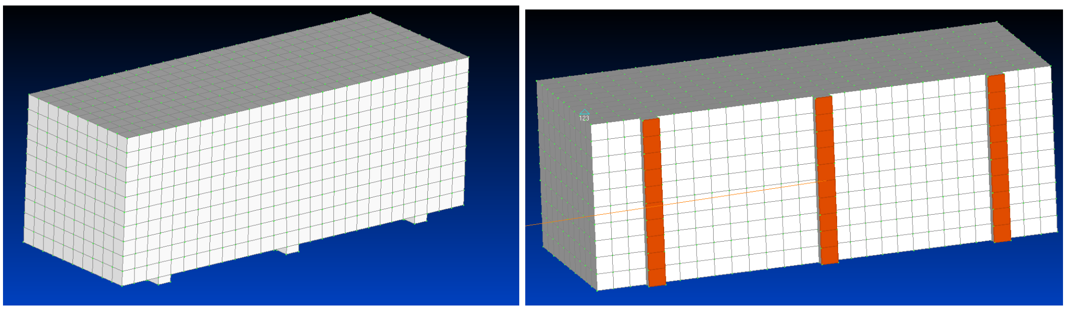

Figure 6. Analysis model of Convolt tank.

Table 2 shows the material property in this study. Density was defined in two ways, 2246 for full and 746 for empty model. Coefficient of static friction and dynamic friction coefficient were decided by physical experiment.

Table 2. Material property.

Material Property			
density[kg/m3]		Young's Modulus	Poisson Ratio
empty	full		
746	2200	3.00E+10	0.33
Coefficient of static friction	Dynamic friction coefficient		
0.2	0.4		

4 COMPARISON OF WAVE PRESSURE IN THE STATE OF NOT SLIDING

Figure 7 shows the comparison of wave profiles at WG1 in the calculation and the experiment in Case 4. The peak of the wave height and the wave profiles are in good agreement, and the calculated value accords with experimental value about WG1.

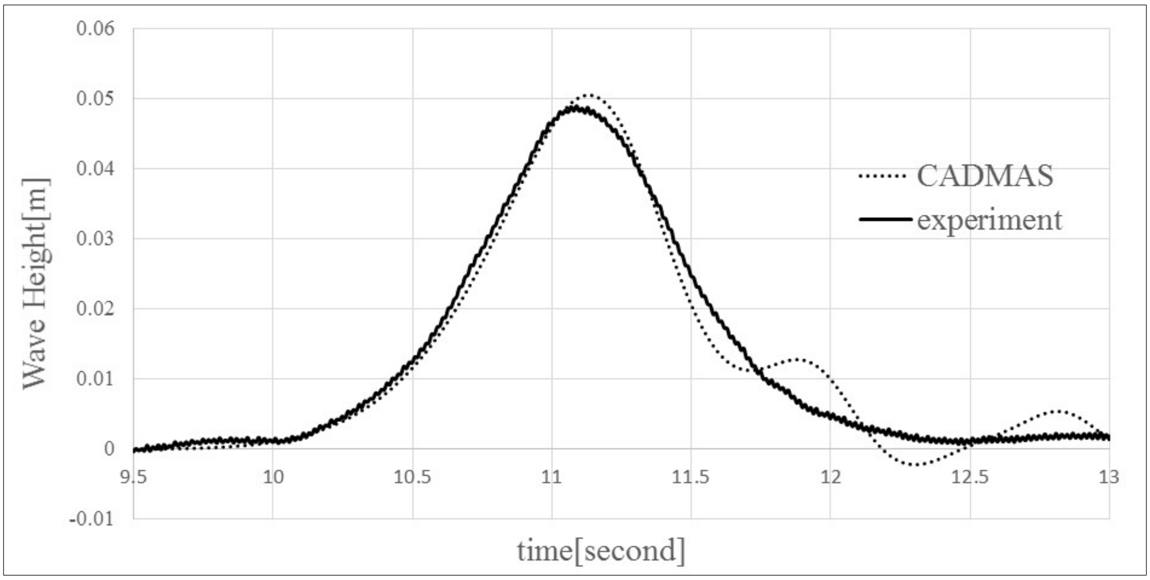

Figure 7. Comparison of wave profiles at WG1 in the calculation and the experiment in Case 4.

Figure 8 shows the comparison of wave pressure at PG2 in the calculation and the experiment in Case 4. The peak of the wave pressure is in accord between calculation and experiment results. Wave profiles after the peak are almost different. However, the wave profiles as a whole are almost in accord between the calculation and the experiment results, and the calculated value accords with experimental value about PG2.

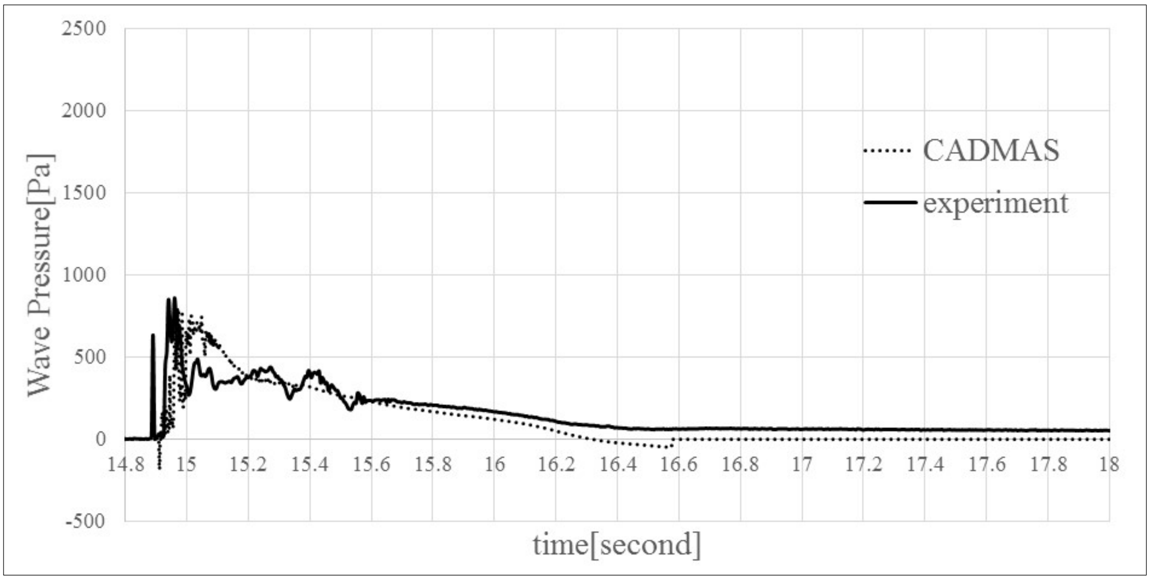

Figure 8. Comparison of wave pressure at PG2 in the calculation and the experiment in Case 4.

Figure 9 shows the comparison of wave pressure at PG3 in the calculation and the experiment in Case 4. Wave profiles and the peak are in accord between calculation and experiment results. Peak time is different between calculation and experiment. In case 4, calculation and experiment results are in good agreement in PG2 and PG3. It may be able to confirm reproducibility of not sliding phenomenon by CADMAS-STR/3D.

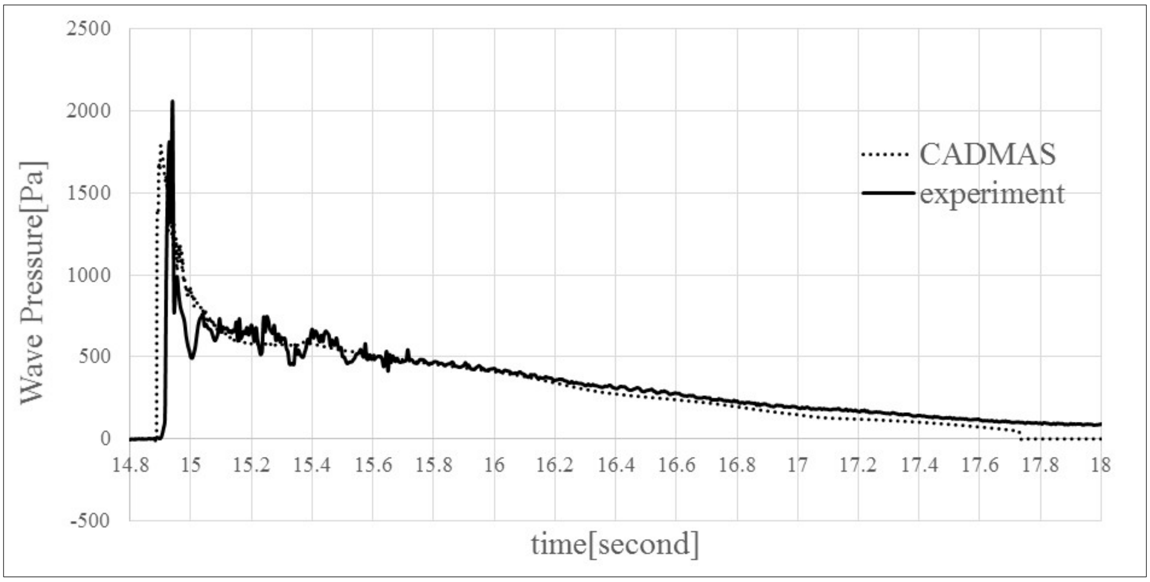

Figure 9. Comparison of wave pressure at PG3 in the calculation and the experiment in Case 4.

5 COMPARISON OF WAVE PRESSURE IN THE STATE OF SLIDING

Figure 10 shows the comparison of wave profiles at WG1 in the calculation and the experiment in Case 6. Maximum wave height is in accord between calculation and experiment results. Wave profiles after the peak are almost different. However, the wave profiles as a whole are almost in accord between the calculation and the experiment results, and the calculated value accords with experimental value about WG1.

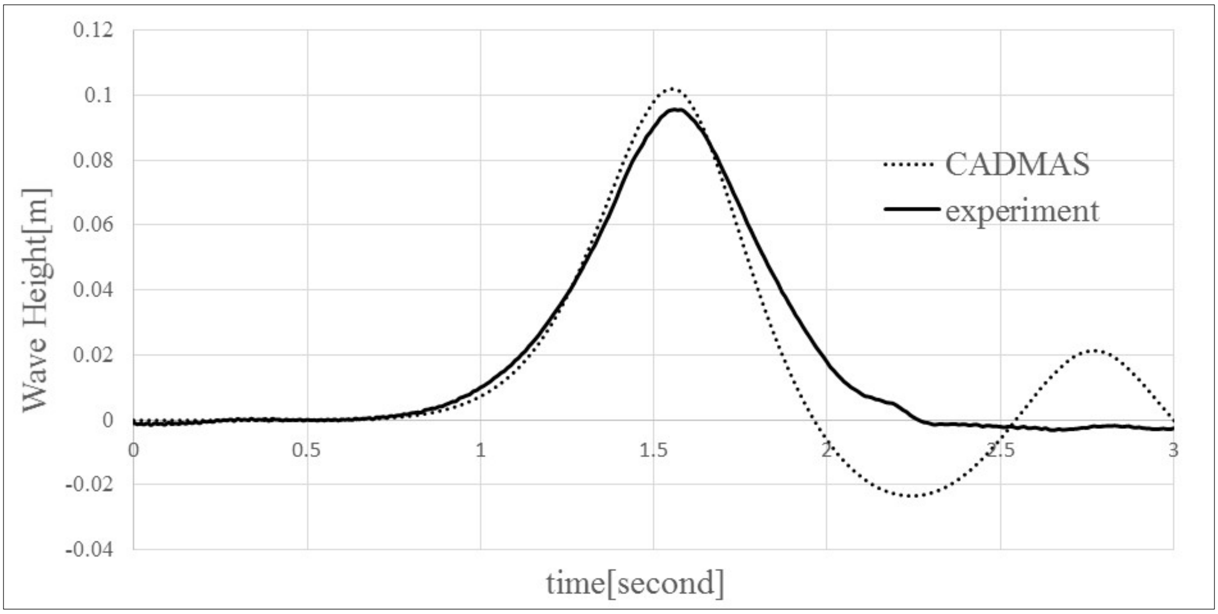

Figure 10. Comparison of wave profiles at WG1 in the calculation and the experiment in Case 6.

Figure 11 shows the comparison of wave pressure at PG2 in the calculation and the experiment in Case 6. The time of leading edge of wave pressures are in good agreement between calculation and experiment results. However, each peak of pressures is almost different from each other.

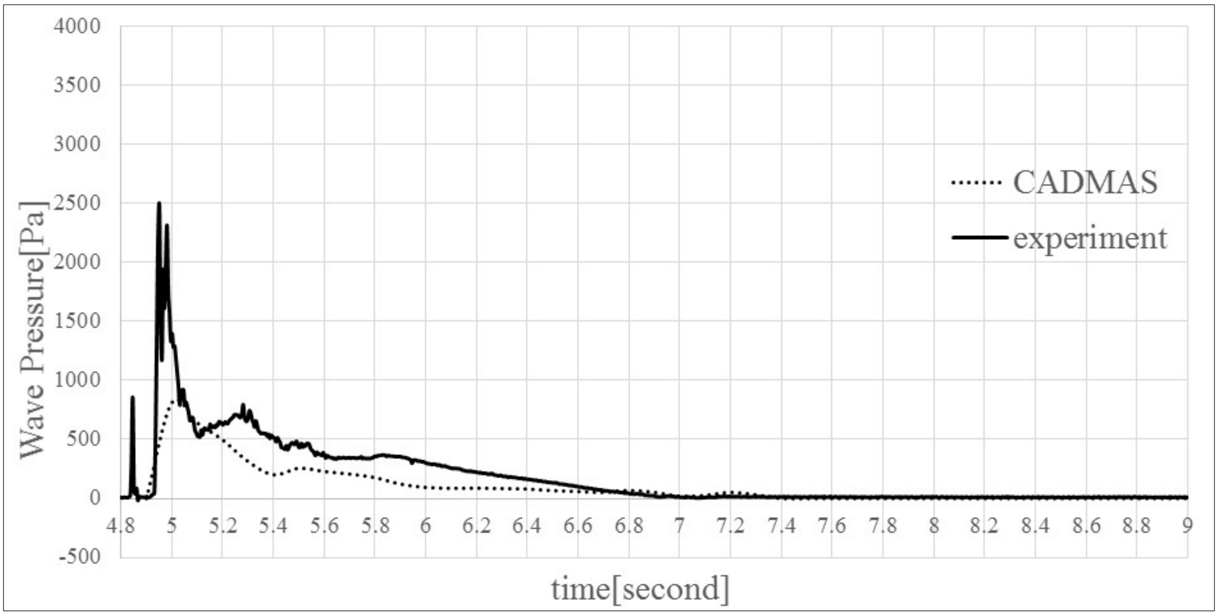

Figure 11. Comparison of wave pressure at PG2 in the calculation and the experiment in Case 6.

Figure 12 shows the comparison of wave pressure at PG3 in calculation and experiment in Case 6. The time of leading edge of wave pressures are in good agreement between calculation and experiment results. However, each peak of pressures is almost different from each other.

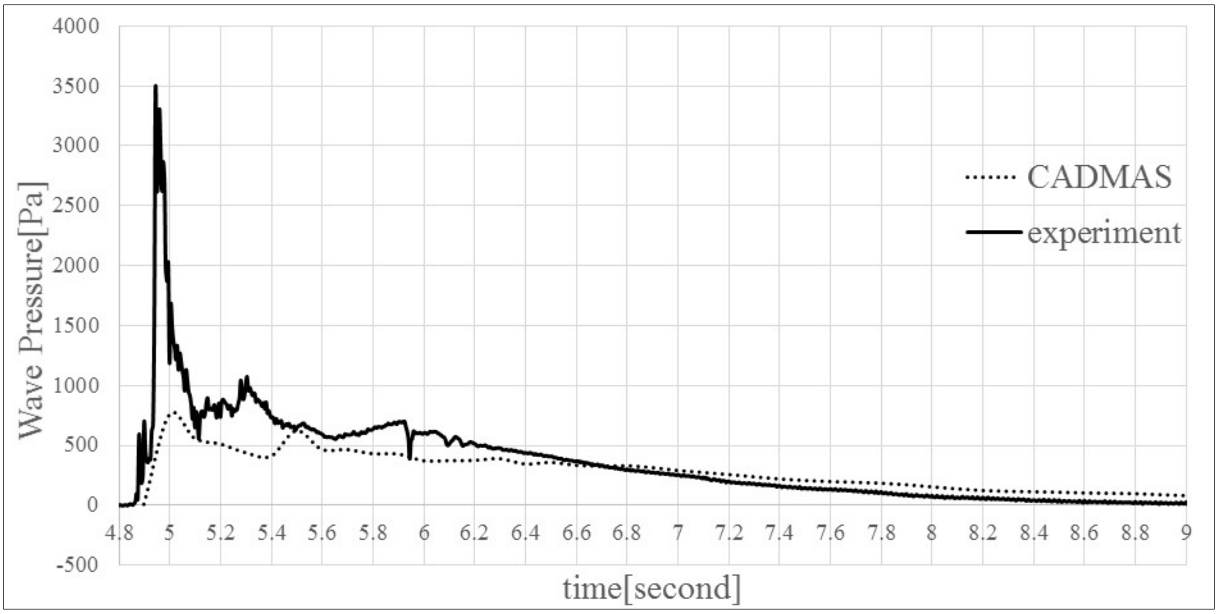

Figure 12. Comparison of wave pressure at PG3 in the calculation and the experiment in Case 6.

Figure 13 shows the comparison of snap shots at physical experiment and calculation in case 6. It is a comparison of the points in time when a wave leader arrived at the tank, but the spatial distributions almost accords with each other.

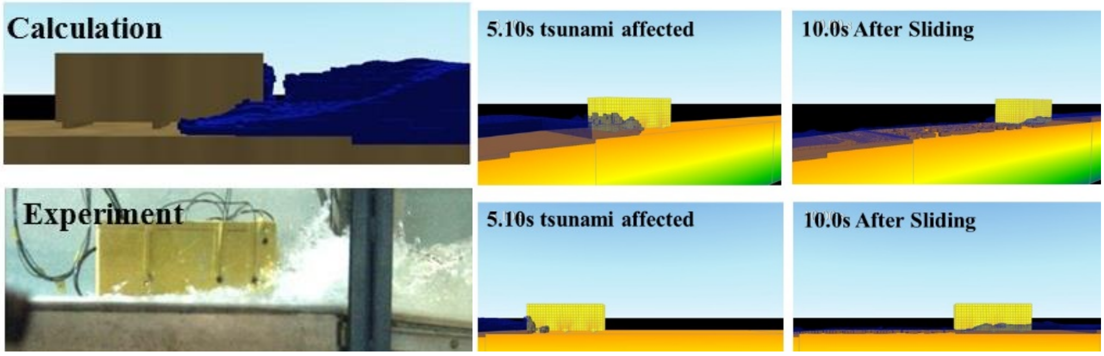

Figure 13. Comparison of snap shot of at physical experiment and calculation.

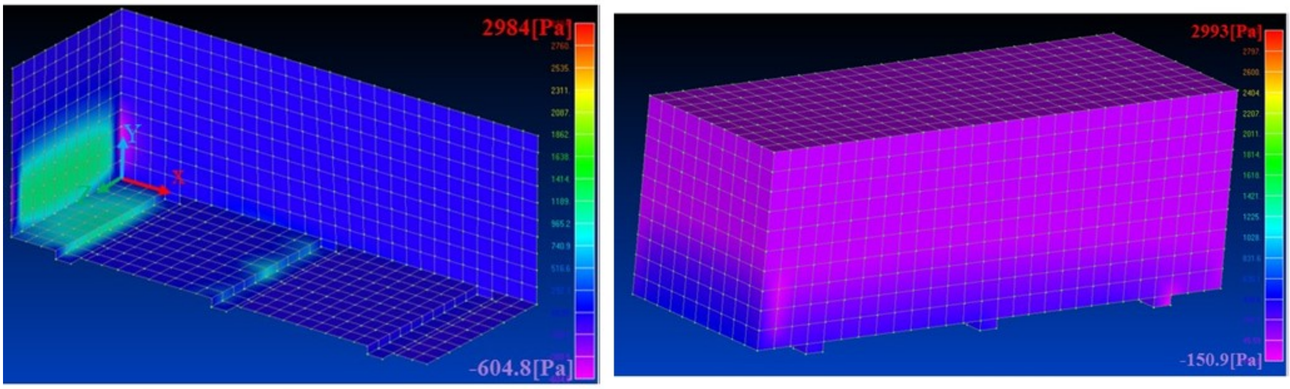

Figure 14. Contour figures of surface pressure that is affected by tsunami STEP 60 TIME 5.10[s] STEP 170 TIME 5.60[s].

Figure 15 shows the comparison of snap shots of total pressure, pressure gauge2, and pressure gauge3. Sliding may occur when a peak appears in wave pressure.

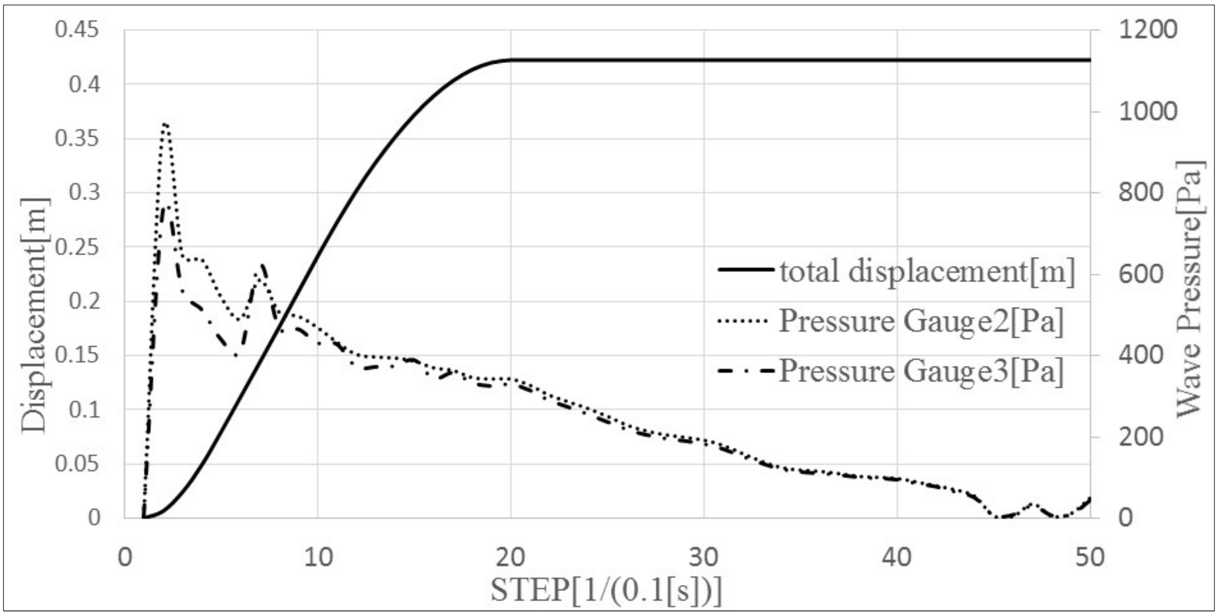

Figure 15. Comparison of snap shot of total pressure, pressure gauge2 and pressure gauge3.

Figure 16 shows the contour figures of wave height around tank. The slide is understood as a result of the shock wave pressure, the drifting occurred because of the flow. The tank did slide by the horizontal power of the flow of the water without considering the buoyancy that acts on the tank base foot part, and drifting produced it.

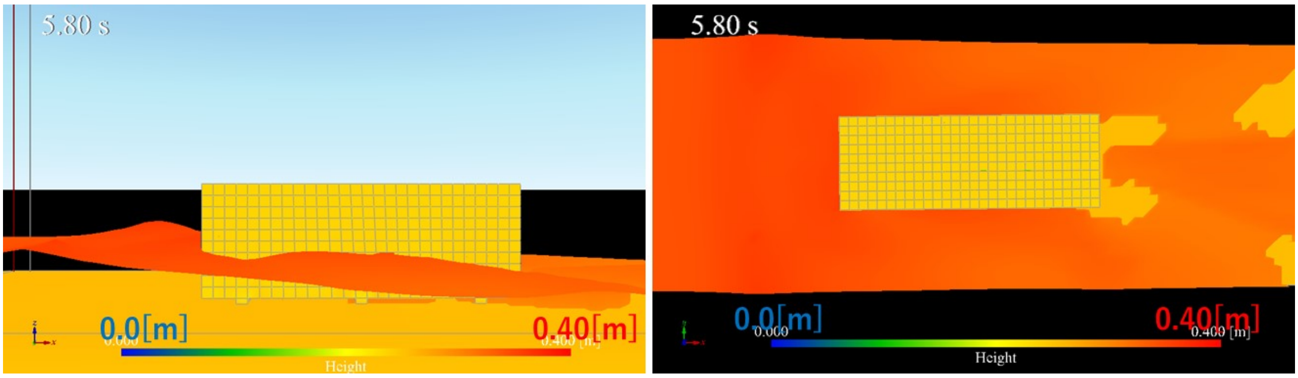

Figure 16. Contour figures of wave height around tank TIME 5.60[s].

6 CONCLUSIONS

I could put it in CADMAS-STR/3D which enables coupling analysis with fluid analysis and the structure analysis and performed tank slide analysis. I performed the comparison with the calculation result in CADMAS-STR/3D in case6 which case4 and the slide that slide did not produce in the model experiment in the section waterway produced.

Incident wave height, maximum wave height, wave profile are in good agreement, and, the calculated values accord with experimental values.

About the comparison between laboratory finding and numerical computation result in Case4, the calculated value accords with the laboratory finding about wave height well, and the calculated value agrees with the laboratory finding on wave pressure observation at point PG2 installed in the front part of tank model in terms of maximum wave pressure and wave patterns.

About the comparison between laboratory finding and numerical computation result in Case6, the calculated value accords with the laboratory finding about wave height well. However, about the wave pressures, observation at point PG2 installed in the front part of tank, do not accord between the laboratory finding and the calculated value, wave pattern almost agrees on the wave pressure maximum.

Since a laboratory finding caused slide at the time of the initial biggest wave pressure action, as for the back-water pressure, it was thought as action wave pressure at the time of the drifting after the slide.

It may occur by two reasons. Firstly, the difference of buoyancy under the tank between physical experiment and numerical experiment has problem. In CADMAS-STR/3D, buoyancy only occur in the surface of structure. It will not occur in the contact surface. Under the influence of Convolt type of tank, the buoyancy may occur in case fluid get into the bottom of tank. However, buoyancy will not occur in contact surface in calculation. So, it is supposed that this result cannot reproduce Yang pressure to occur by fluid analysis. Figure 17 shows the image of buoyancy of CADMAS-STR/3D.

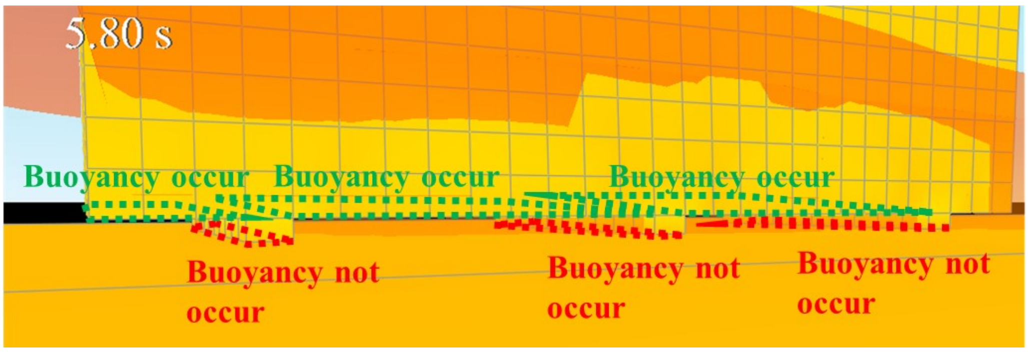

Figure 17. Image of buoyancy of CADMAS-STR/3D.

Secondly, structural features of tank model have problem. In real scale, tank is filled with fuel of liquid. It may cause inertial force due to the vibration of fuel inside the tank. In physical experiment, weight as fuel are moving when tsunami attacked. Weight are moved to the back of the tank by tsunami, vertical force is increased there. So, the tank will be risen instead of sliding. Therefore, wave pressure may increase by long sliding time.

  / ISSN 1562-6865 (Online) - ISSN 1063-7710 (Print)

As a feature problem, we must measure the time of sliding in physical experiment. The mechanism of sliding may be clarified by comparing numerical experiment.

CADMAS-STR/3D was able to confirm what dynamic wave pressure to produce when a structure moved could reproduce.

REFERENCES

Arikawa, T., Yamano, T. & Akiyama, M. (2007). Advanced Deformation Method for Breaking Waves by using CADMAS-SURF/3D, In *Proceedings of Coastal Engineering*, Japan Society of Civil Engineers, 54, 71-75.

Arikawa, T., Hamaguchi, K., Kitagawa, K. & Suzuki, T. (2009). Development of Numerical Wave Tank Coupled with Structure Analysis Based on FEM. *Journal of Japan Society of Civil Engineers, Ser. B2 (Coastal Engineering)*, 65(1), 866-870

Takabatake, D., Kihara, N. & Tanaka, N. (2013). Numerical Study for the Hydrodynamic Pressure on the Front of Onshore Structures by Tsunami, In *Proceedings of Coastal Engineering*, Japan Society of Civil Engineers, 69(2), 851-855.

Proceedings of the 37th IAHR World Congress
August 13 – 18, 2017, Kuala Lumpur, Malaysia

USING REMOTELY SENSED DATA TO ESTIMATE RIVER CHARACTERISTICS, INCLUDING WATER-SURFACE VELOCITY AND DISCHARGE

JONATHAN M. NELSON[1], PAUL J. KINZEL[2], CARL J. LEGLEITER[3], RICHARD R. MCDONALD[4], BRANDON T. OVERSTREET[5] & JEFFREY S. CONAWAY[6]

[1,2,3,4] U.S. Geological Survey, Geomorphology and Sediment Transport Laboratory, Golden, United States of America,
jmn@usgs.gov; pjkinzel@usgs.gov; cjl@usgs.gov
[5] U.S. Geological Survey, Oregon Water Science Center, Portland, United States of America,
boverstreet@usgs.gov
[6] U.S. Geological Survey, Alaska Science Center, Anchorage, United States of America,
jconaway@usgs.gov

ABSTRACT

This paper describes a project combining field studies and analyses directed at providing an assessment of the accuracy of remotely sensed methods for determining river characteristics such as velocity and discharge. In particular, we describe a remote sensing method for surface velocities using mid-wave thermal camera videography combined with image analysis. One of the critical problems in this work is determining a method for relating remotely measured water-surface velocities to vertically averaged velocities through a velocity index. We explore three similarity profiles that allow a relationship between surface and vertically averaged velocity to be found either using empirical results or simple roughness-to-depth ratios. To test the approaches, we compare them in a situation where vertical structure is known over most of the flow depth through ADCP measurements. By determining best-fit profiles through the ADCP profiles, average values of the velocity index are found for the cross-sections where measurements are made. By comparing these to the predicted velocity indices from the three similarity profiles, we find that, although the differences between the various similarity profiles are substantial, they are smaller than those differences associated with local nonuniformity and nonhydrostatic flow. Nevertheless, the velocity indices are accurate to about +/-5%, meaning that remotely sensed vertically averaged velocities can be computed to well within the current accuracy standard for such values when used for river gauging.

Keywords: Rivers; remote sensing; discharge, floods; geomorphology.

1 INTRODUCTION

As part of an ongoing U.S. Geological Survey effort to complement conventional river gauging methods with remotely sensed measurement techniques, during 2016 we measured a variety of remotely sensed data sets at sites on seven U.S. rivers including the Deschutes River, the Niobrara River, the Knik River, the Matenuska River, Montana Creek, the Chena River, and the Kenai River. At each of the seven sites, both remote sensing data collection and conventional ground-based techniques were applied to evaluate the applicability and accuracy of remote-sensing methods, particularly as they relate to water-surface velocity, depth and discharge measurements. Thus, the primary goal of the measurement program was to test measurement and analysis methods for obtaining river depth and water-surface velocity measurements from remotely sensed information by comparing them to the same quantities measured using conventional methods.

Much of this comparison is complete. Kinzel et al. (2017, this volume) compared water-surface velocities collected with radar and infrared videography to Acoustic Doppler Current Profiler (ADCP) velocity data extrapolated to the water surface for a subset of the field sites. Legleiter et al. (submitted) used the ADCP extrapolation to determine vertically averaged velocities from the water-surface velocity estimates from infrared imagery; they then combined those with depth estimates found through correlation of depth with hyperspectral information using the method described by Legleiter (2009). Using the estimated vertically averaged velocity with the estimated depth provides a straightforward computation of discharge which compares well to conventionally measured values. The results of these comparisons are encouraging where remotely sensed velocities agree well with extrapolated ADCP measurements, and depths can be inferred accurately from hyperspectral data provided the river is relatively clear and a calibration data set is available. However, our ultimate goal is to provide discharge estimates without on-the-ground calibration information through ADCP or depth measurements. With this in mind, use of ADCP data to determine ratios between vertically averaged and surface flows or use of measured depth to calibrate hyperspectral information is not entirely satisfactory.

To deal with the depth estimation issue for situations where calibration data are unavailable or the water column is too deep or turbid to permit optical returns for bathymetric LiDAR or multi/hyperspectral scans, various investigators have explored methods to extract depth only from surface-based information. For example, Johnson and Cowen (2016) estimated water depths by correlating them with length scales determined from water-surface turbulence. Nonlinear data assimilation techniques incorporating three-dimensional fluid flow models can be used to infer depths such that errors between measured and predicted surface velocities (or other data) are minimized by the computed depth distribution. Nelson et al. (2012) used a simplified form of the vertically averaged equations of motion to develop a mathematical relationship between local depth and detailed fields of measured water-surface velocity and elevation. While these methods are still in development, it may be possible to determine depths from water-surface information, possibly using a hybrid method that incorporates all the above ideas.

Unfortunately, the determination of ratios between local surface velocity and vertically averaged velocities is not well treated by any these methods with the possible exception of doing inversions with a fully nonhydrostatic three-dimensional flow model. Even using the best available three-dimensional computational models suitable for use on rivers where nonhydrostatic effects are locally important yield results for this ratio that are at least somewhat dependent on the choice of turbulence closures and methods for addressing free-surface dynamics. Given the potential roles of turbulence-driven secondary flows in altering local vertical structure, especially near banks, even most common turbulence closures used in river flow calculations (such as k-Ɛ turbulence closures) cannot be expected to work well, as such flows cannot be generated in models with isotropic diffusivities. Using turbulence-resolving models is appealing, but impractical in riverine flows. Thus, it appears that this part of the problem must still be dealt with in some semi-empirical manner, such as assuming a single value of the vertically averaged to surface velocity ratio for all conditions (e.g., 0.85, Muste et al., 2008) or using well-developed velocity profiles from steady, uniform flows to provide information about the ratio of vertically averaged to surface velocities.

In this short paper, we specifically focus on this problem in the context of two Alaskan rivers, the Chena and the Knik. We begin by briefly describing the method used to collect surface velocity with examples, and then use that data along with three well-known vertical structure functions for velocity in order relate surface velocities to vertically averaged ones using simple relations. We then examine the vertical structure functions and the results they predict in the context of measured vertical velocity profiles measured using ADCP methods. This leads to conclusions about the applicability of using similarity vertical structure functions to relate surface velocities to vertically averaged velocities and helps to clarify where these relations can produce bias or other errors in discharge estimates.

2 MEASUREMENT METHODS

We visited seven field sites: one in Nebraska on the Niobrara, one in Oregon on the Deschutes, and 5 locations in Alaska on the Chena, Knik, Matanuska, Salcha Rivers and Montana Creek. At each site, a variety of ground data and remote sensing data were collected; the sites were also chosen for their proximity to active USGS gauges. In all cases, water-surface velocities were measured using non-contact thermal infrared videography methods (described in more detail below). On the Niobrara and Deschutes, these surface velocities were measured using manned aircraft, while on the Alaska rivers, the surface velocities were measured using a stationary infrared camera and radar from a transect of bridge locations. For the purposes of this paper, which concentrates on the problem of determining discharge with only measurements of surface velocity, data analysis suggested that the dwell time (period of data collection at a specific location on the water surface) for the aerial data sets was too short (typically under 10s) for accurate discharge computation, so data from the Niobrara and Deschutes, while valuable for ongoing modeling calculation, are excluded from the analysis presented here. For the Alaska rivers where surface velocities were detected remotely from stationary bridge locations, collecting longer time series was straightforward. For information on the location and characteristics of the study reaches, the reader is referred to Figure 1 and Table 1 in Kinzel et al. (2017, this volume). In addition to the remotely sensed measurements of surface velocity at these sites, discharge, bed elevation, water column velocities and water temperature were measured with an ADCP.

To measure water-surface velocity fields remotely, both radar and infrared videography techniques were employed. The radar measurements were straightforward, but the lack of simple directional resolution and poor data returns from regions of relatively low velocities (and smooth water surfaces) were problematic. The infrared video technique was tested both from stationary viewpoints (bridges) and aircraft; in both cases, good directional resolution of the water-surface velocity field was straightforward and a single video could yield large areas of surface velocity highly resolved in both a temporal and spatial sense. This paper concentrates on the infrared camera surface velocities although much of the reasoning on relating local surface velocities to vertically averaged velocities apply directly to radar measurements of surface velocity. Kinzel et al. (2017, this volume) compares the radar and infrared video surface velocity measurements in more detail

The method of using thermal infrared videography to measure surface velocities is described by Dugan et al. (2012). In general terms, a thermal infrared camera yields imagery of the water surface that has thermal structures differentiated by small temperature differences that can be tracked using simple particle-image velocimetry or other correlation techniques. The variability and structure in these images, which essentially show temperature on a very thin boundary layer at the water surface, is dependent on the flow Reynolds number and the water-air temperature difference. Figure 1a shows a single frame of a video series of imagery of a water-surface in a flume with a Reynolds number of about 104 with a field of view 0.3m wide; Figure 1b shows the same thermal imagery for a short reach of the South Platte River near Denver with a Reynolds number of about 106 and a field of view of about 10m. In both cases (and in cases shown below for the Alaskan rivers), a Flir SC8340 cooled mid-wavelength (3 to 5 micron) camera was employed with a sensitivity of 25 milliKelvins and a resolution of 1280 x 720 pixels.

As shown in Figure 2, the camera was mounted on a conventional camera stand base with a cantilevered mounting arm that allowed extension of the camera beyond the bridge railing, typically by 50cm or so depending on the details of the bridge structure. We also tilted the camera normal to the cross-section slightly (77 degrees from the vertical) to look further away from the bridge itself than allowed by a vertical view. Infrared video was collected at a number of stations across the bridges in order to provide 10-20 measurement locations. Generally, these were evenly spaced, but in situations where piers intruded in the field of view or the bridge superstructure would not allow a certain camera placement, the location was adjusted and recorded. Videos were collected for 60s at 10 frames/sec. Although the maximum camera speed is 47 frame/sec for a full field of view, we believe that 10 frames/sec provided adequate temporal resolution, while maintaining reasonable file sizes for processing. Depending on the size of the river (height of the bridge above the river), the field of view varied over a wide range (about 2 to 10m) but in all cases, most of the surface was recorded, although not contemporaneously as is typical using aerial platforms at high elevation, where the field of view encompasses the entire river width.

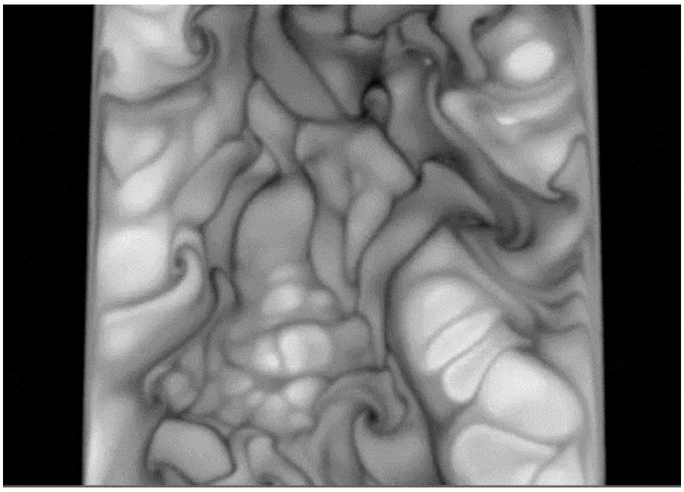

a.

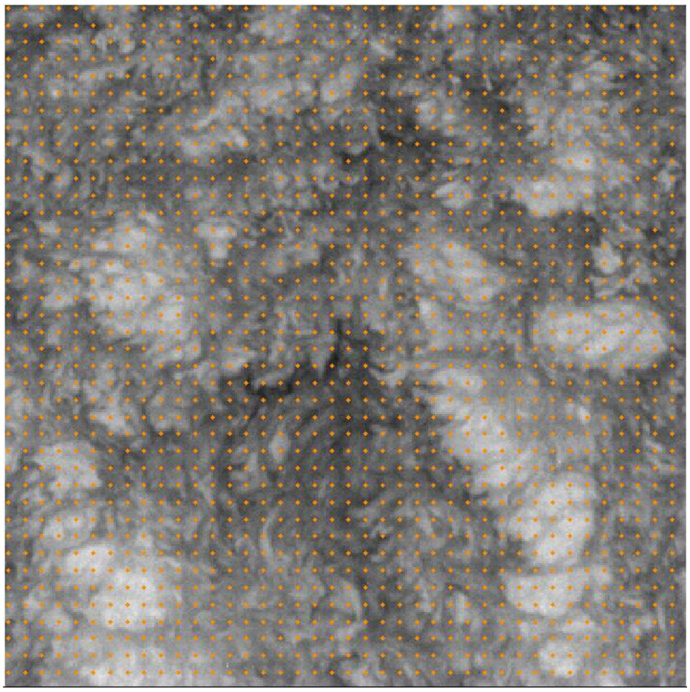

b.

Figure 1. Mid-wavelength thermal imagery of (a) laboratory flume flow with Re~10^4 and (b) river flow with Re~10^6.

  / ISSN 1562-6865 (Online) - ISSN 1063-7710 (Print)

In addition to measuring surface velocities, we used ADCP measurements to measure velocity and depth at a cross-section coincident with that used for the infrared video measurements. The idea behind this was to both compare the ADCP and remotely sensed velocity measurements (see Kinzel et al., 2017, this volume) and to compare discharges using different measurement methodologies (Legleiter et al., submitted). Given that ADCPs have a significant unmeasured region both near the water surface and near the river bed; part of both of these objectives was related to determining appropriate relations between surface and either vertically averaged or otherwise below-surface velocities, the subject of this short paper. All of the field measurements described here and discussed in more detail below can be found on the USGS Science Base (Legleiter et al., 2017a; 2017b).

Figure 2. Picture of the deployment apparatus and the cooled, mid-wavelength infrared camera as deployed on the Matenuska River. All the Alaskan sites used the same arrangement for stationary measurements.

3 FIELD DATA AND PROCESSING

3.1 Remotely sensed water-surface velocities from infrared video

For the purposes of this paper, the basic field data are the infrared video and the ADCP velocity measurements along with stationing information. The infrared video was processed using standard particle image velocimetry (PIV) techniques, primarily using the PIVview software package (PivTec, 2015). We also checked all results by verifying results using the public-domain software PIVLab (PIVlab.blogspot.com) and found essentially the same results for the cases we compared. A typical example showing results from a single 60s video is shown in Figure 3. As can be seen in the figure, processing windows and areas were chosen to exclude overlap at the frame edges. We also focused on a single cross-sectional transect, as our interest here is comparison to the ADCP and computation of discharge, rather than a full field of vector velocity values; this also greatly speeds the computational PIV process. The image shows pixel displacements averaged over a full 60s video; these displacements are turned into surface velocities using measured camera heights and lens characteristics (also measured carefully, rather than assumed from lens specifications) along with known frame rates. By performing this same computation at each location along the transect determined by the bridge locations, it was possible to create velocity maps such as the one shown in Figure 4, which shows a single imagery picture and the 60s velocity averages for each measurement location along the bridge on the Chena River. This profile shows relatively smooth variation in velocities along the transect, but careful inspection shows some mismatch in the velocity vectors across adjacent panels, suggesting that the 60s averaging time probably should have been somewhat longer, an observation that supports our own concerns based on known time variability. However, given the additional processing and data storage requirements of collecting substantially longer time series, we believe the choice of 60s was acceptable. This highlights the issue that arises in obtaining sufficient dwell time from fixed-wing aircraft, as mentioned above, where aircraft motion and high minimum speeds make obtaining long time series difficult without specialized active camera mounts. Clearly, the other way to deal with this issue is to use drones or helicopters with hovering capability.

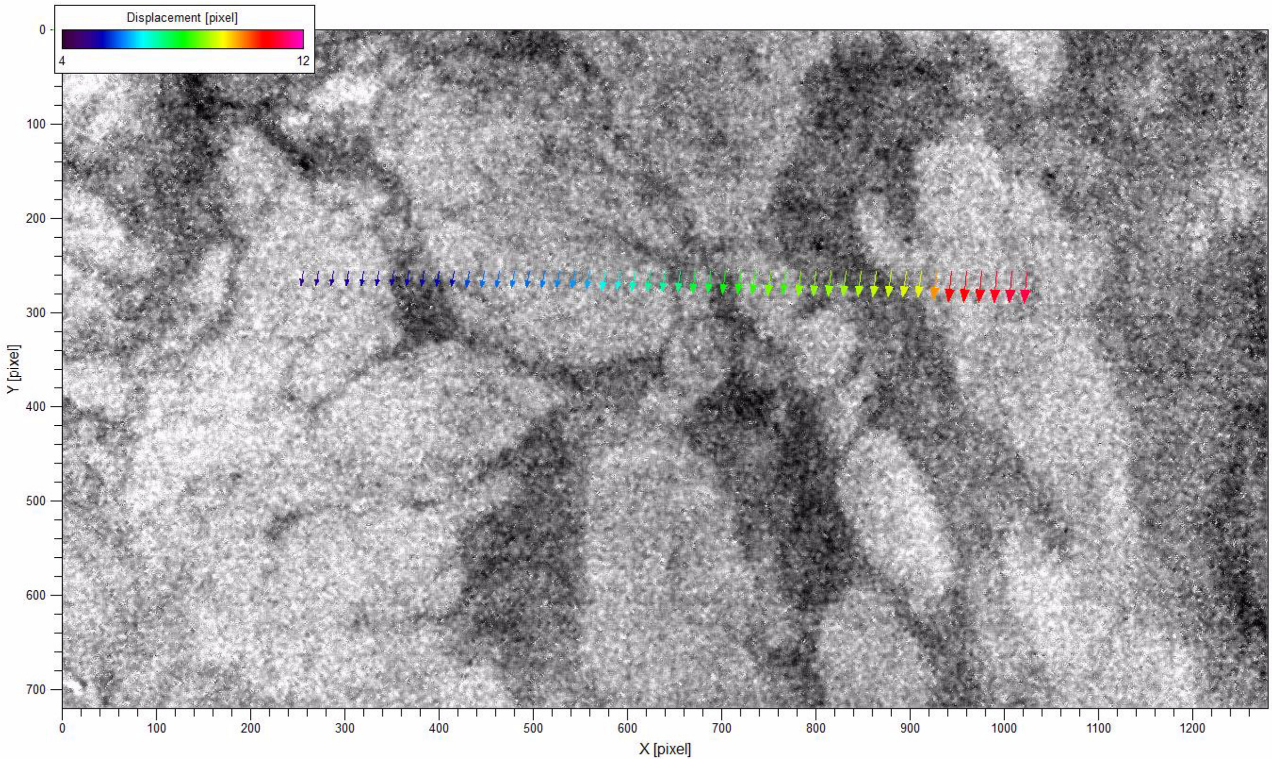

Figure 3. Single frame of thermal imagery from the Chena River overlain by time-averaged pixel displacement vectors determined from PIV analysis of 60s of similar imagery.

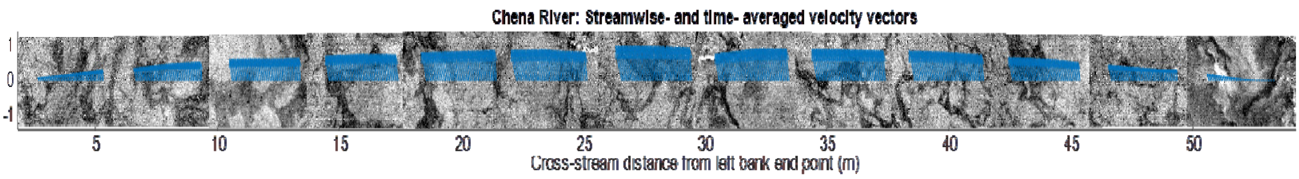

Figure 4. Montage of single infrared video frames and 60s-time averaged velocity fields across the Chena River.

3.2 Acoustic doppler current profiler data

The raw ADCP data were processed using the WinRiver software (Kinzel et al., 2017, this volume). In addition to computing mean heading and rotating measured velocities into cross-transect and transect-parallel components, this software provides several options for estimating velocity in the unsampled zones near the bed and surface in order to compute discharge. For reasons that will become clearer below, we chose to extrapolate the measurements by fitting a power law velocity profile, which is a common technique for extrapolating the unsampled zones in ADCP data. In the default mode, WinRiver uses a 1/6 power for these fits, but allows the user to specify a different power if desired, as will be discussed in more detail below.

4 ANALYSIS

Relating the surface velocities to vertical averages or even relating the incomplete ADCP profiles to vertical averages requires some additional assumptions. As noted above, here we consider similarity profiles as a potential solution for this missing information, despite the fact that nonhydrostatic effects in the form of sharp bed-induced accelerations or decelerations or strong secondary flows can produce local changes in vertical structure. Nelson et al. (2016) explored a simple method for treating along streamline acceleration or decelerations (with bedforms primarily in mind). For the rivers studied here, small scale bedforms are absent or minimal, so these data provides an opportunity to analyze how well similarity methods can work, where they may break down, and the errors associated with the assumption.

There are a few common vertical structures used in the analysis of free surface turbulent flows. In the engineering literature, the most common choice is a power law profile, given by the following simple equation:

$$u(z) = Az^m \qquad [1]$$

where u is velocity, A is an empirical coefficient, and m is an exponent equal to 1/6 for consistency with Mannings roughness formulation, but may vary. For this simple profile, if the depth is denoted by h, the vertically average velocity is given by the equation below:

$$< u >= \frac{1}{h}\int_0^h u(z)dz = \frac{A}{m+1}h^m \qquad [2]$$

This expression can be used to develop a nondimensional velocity structure defined as follows:

$$\frac{u(z)}{< u >} = (m+1)\left[\frac{z}{h}\right]^m \qquad [3]$$

The ratio of the vertically averaged velocity to the surface velocity, k, which can be found by evaluating Eq. [1] at the surface and dividing Eq. [2] by the result, is given by:

$$k_{power} = \frac{1}{m+1} \qquad [4]$$

In this case, for the Manning's power of 1/6, the value of k is 0.857, which is very close to the empirically determined value of 0.85 mentioned above.

In the literature on geophysical boundary layers and turbulence in general, velocity structure for steady uniform flows generally proceed from dimensional arguments yielding turbulent diffusivity near a boundary. In a constant stress layer, these arguments yield an effective diffusivity due to turbulent fluctuations characterized by the distance from the boundary and the local shear velocity, u_*, where u_* is the square root of ratio of boundary shear stress to the fluid density. For depth-limited or ducted steady, uniform boundary layers, this can be generalized to a parabolic eddy viscosity as follows:

$$K_v = \kappa u_* z(1 - z/h) \qquad [5]$$

where κ is von Karman's constant (≈ 0.4). Using this relation with the linear stress profile with zero surface stress in a simple boundary layer yields the well-known logarithmic velocity profile below:

$$u(z) = \frac{u_*}{\kappa}\ln\frac{z}{z_0} \qquad [6]$$

where z_0 is the roughness length, which can be related to the physical roughness of the bed in terms of protrusion or grain size. Proceeding as in equation one and two, by integrating this equation over the depth (from z_0 to h, since u goes to zero at z_0), we find that the vertically averaged velocity is given as follows:

$$< u >= \frac{u_*}{\kappa}\left[\ln\left(\frac{h}{z_0}\right) - 1 + \left(\frac{z_0}{h}\right)\right] \qquad [7]$$

Normalizing the velocity profile using the vertically averaged value yields the following nondimensional profile:

$$\frac{u(z)}{< u >} = \frac{\ln(z/z_0)}{\left[\ln(h/z_0) - 1 + z_0/h\right]} \qquad [8]$$

Dividing Eq. [7] by Eq. [6] evaluated at the water surface, we can again compute the k value:

$$k_{\log} = \frac{\ln(h/z_0) - 1 + z_0/h}{\ln(h/z_0)} \qquad [9]$$

For the logarithmic profile, the ratio of the vertically averaged to surface velocity depends only on the ratio of roughness length to the depth of the flow. Generally, the third term on the right-hand side of Eq. [9] is very small and is often ignored. Comparing Eq. [4] and [9], it is easy to show that an m of 1/6 corresponds to an h/z_0 of about 10^3. The final boundary layer profile to be considered here is the one described by Rattray and Mitsuda (1974). Considering measured profiles, they inferred that the best-fit eddy viscosity for a steady, uniform turbulent boundary layer was not Eq. [2] throughout the flow depth. They suggested that the following choice gave the best fit to measured data.

$$K_v = \kappa u_* z(1 - z/h) \quad \text{for } z/h<0.2 \qquad [10]$$

$$K_v = \frac{\kappa u_* h}{\beta} \quad \text{for } z/h>0.2$$

The empirical constant β was determined to be 6.25. With this choice of eddy viscosity, the velocity profile has two parts, one of which is logarithmic and one of which is parabolic, as follows:

$$u(z) = \frac{u_*}{\kappa} \ln\frac{z}{z_0} \quad \text{for z/h< 0.2} \qquad [11]$$

$$u(z) = \beta\frac{u_*}{\kappa}\left[\frac{z}{h} - \frac{1}{2}\left(\frac{z}{h}\right)^2 + \frac{1}{\beta}\ln\left(\frac{0.2h}{z_0}\right) - 0.18\right] \text{for } z/h>0.2 \qquad [12]$$

Integrating Eq. [11] and [12] over the flow depth and using β=6.25 yield the vertically averaged velocity, as follows:

$$<u> = \frac{u_*}{\kappa}\left[\ln\left(\frac{0.2h}{z_0}\right) + 0.85 + \frac{z_0}{h}\right] \qquad [13]$$

This yields a two-part nondimensional profile as follows:

$$\frac{u(z)}{<u>} = \frac{\ln(z/z_0)}{\left[\ln(0.2h/z_0) + 0.85 + z_0/h\right]} \quad \text{for } z/h<0.2 \qquad [14]$$

$$\frac{u(z)}{<u>} = \frac{6.25(\mathrm{z/h}) - 3.125(\mathrm{z/h})^2 + \ln(0.2\mathrm{h}/z_0) - 1.125}{\left[\ln(0.2h/z_0) + 0.85 + z_0/h\right]} \text{ for } z/h>0.2 \qquad [15]$$

Dividing Eq. [13] by Eq. [12] evaluated at the water surface yields k, as follows:

$$k_{\log para} = \frac{\ln(0.2h/z_0) + 0.85 + z_0/h}{\ln(0.2h/z_0) + 2.0} \qquad [16]$$

Eq. [4], [9], and [16] give the information required to turn measured surface velocities into vertically averaged velocities, but they do so subject to the assumption that effects that can change vertical structure are small and that a uniform boundary layer profile is close enough to reality to use as an approximation. The vertical structures described by the three profiles described above do not differ greatly, nor do the ratios in Eq. [9] and [16] depend strongly on the depth to roughness ratio. Figure 5 shows a plot of the three profiles for the case where m is given the standard value of 1/6 and the depth to roughness ratio in Eq. [9] and [16] are approximately adjusted to give the same k value (0.86). For Eq. [9], this corresponds to a depth to roughness of about 1000 and in Eq. [16] this corresponds to a depth to roughness ratio of about 2000. Note that the lower roughness required in Eq. [16] occurs because Eq. [12] always has no shear at the water surface, unlike the power law or logarithmic profiles, so a lower roughness is required to give the same relation between the vertically averaged and surface velocity. The three profiles differ by at most about 4% and typically much less. Figure 6 shows the variability of the three k values over a wide range of depth to roughness ratios.

Noting that WinRiver software defaults to a power law value of 1/6 and noting that the measured structure of ADCP profiles could be used to improve this value, Mueller (2013) developed a simple software program Extrap to fit normalized ADCP profiles to find the best fit value of m (and hence *k*, through Eq. [4]) for a given transect. However, this method cannot be used for determining *k* when ADCP data (or other profile data) is not available. Thus, estimate of *k* must be made using only depth to roughness estimates, which is at most what is likely to be available when estimating k for discharge estimates using remotely sensed data.

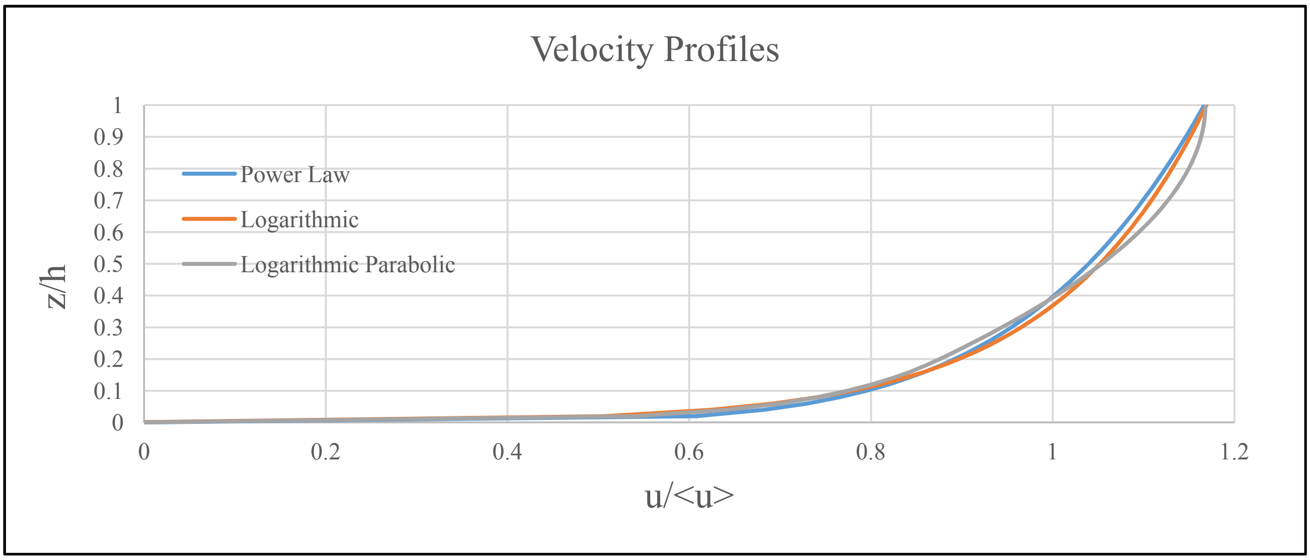

Figure 5. Normalized velocity structure versus normalized depth for the three similarity profiles discussed in the text.

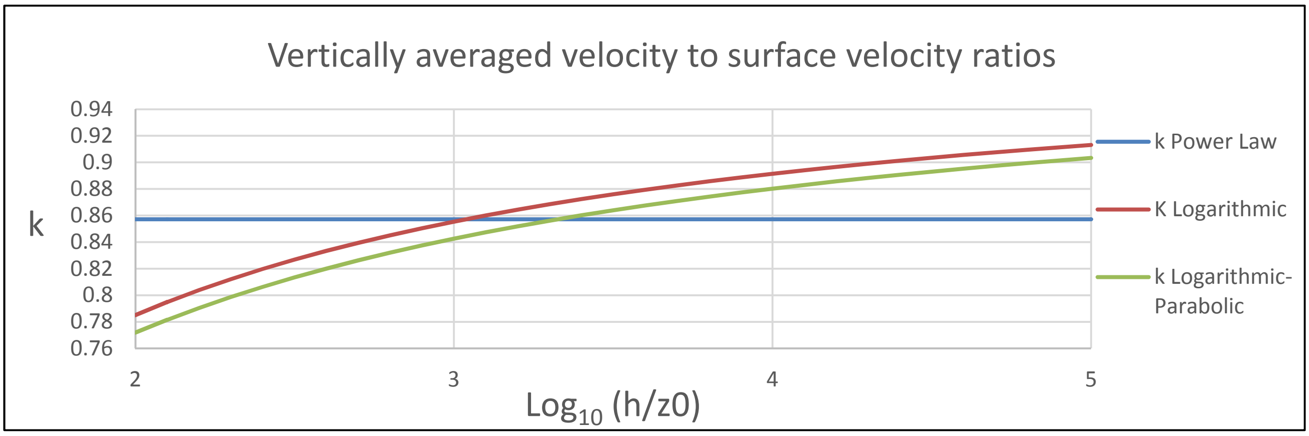

Figure 6. Values of *k*, the ratio between vertically averaged and surface velocities for *m*=1/6 for the power law profile, and a range of h/z_0 ratios for the logarithmic and logarithmic-parabolic profiles.

To evaluate the best choice for k when using surface velocities determined from remote sensing, the most feasible method is to estimate roughness and depth. Since k only depends on this ratio in a logarithmic fashion, even crude estimates should be suitable. To evaluate this, we estimated z0 and average depth using grain size observations and the cross-sectional data. Unfortunately, it was difficult or impossible to do synoptic grain size data collection at most of these sites. All the reaches were mixed coarse sand and fine to medium gravel on observed bar surfaces. We estimated the 84th percentile grain size for the reaches to be 1cm. Using the relation of 0.1D84 (Whiting and Dietrich, 1990) for the roughness length, we used 0.001m for the roughness length at all reaches. In addition, we used Extrap (Mueller, 2013) to find the best fit power law to the measured ADCP data, and then inserted that value into WinRiver to determine the best possible ADCP-derived estimate of discharge. Finally, we estimated the k values from the three simple profiles described above, using 1/6 for the standard power law profile (yielding k=0.86). This information is presented in Table 1.

For the three profile choices, the k value for the logarithmic result was the closest to the best fit value at two of the sites (Knik and Matenuska), while the logarithmic-parabolic k was best at the other three. The power law gave a very good mean, but was not the closest to the best-fit k at any site. In order to understand why the value was very poorly predicted at some sites, we looked at the detailed velocity structure at those sites. The worst-case fit was for the Knik, where even the best value of k from the log profile was low by about 5%. Figure 7 shows the cross-sectional ADCP data.

Table 1. Table showing best-fit discharge, the *k* from those best fits, average depth, estimated roughness length, and *k* values for the three simple profiles.

	Chena R.	Knik R.	Matanuska R.	Montana Cr.	Salcha R.
ADCP Q (m^3/s)	94.9	345	177	17.6	86.3
k, best fit ADCP profiles	0.819	0.927	0.890	0.837	0.833
Avg. Depth (m)	1.9	2.8	1.5	0.8	1.3
Z_0(m)	0.001	0.001	0.001	0.001	0.001
k (Power Law)	0.857	0.857	0.857	0.857	0.857
k (Logarithmic)	0.867	0.874	0.864	0.851	0.861
k(Log-Parabolic)	0.855	0.861	0.851	0.837	0.848

.

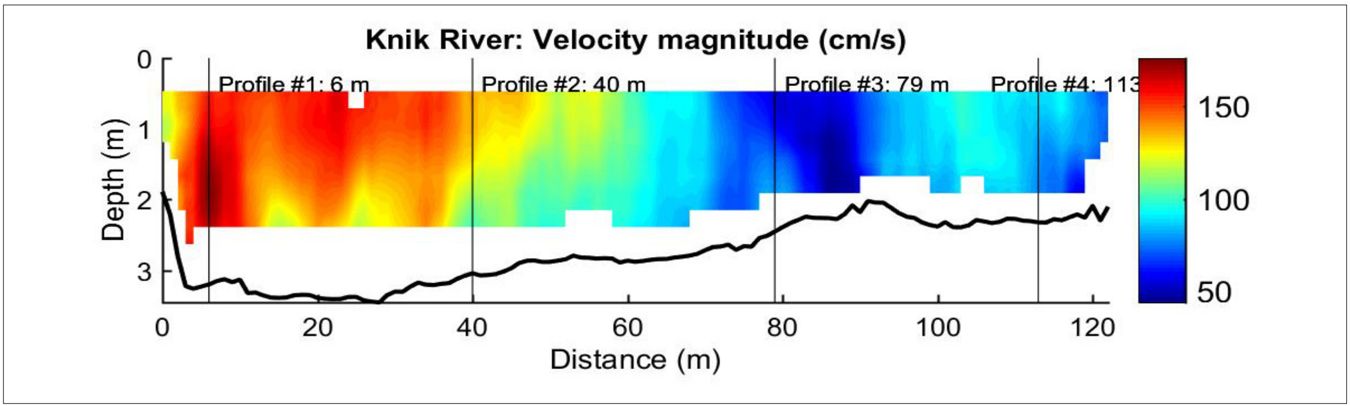

Figure 7. Cross-section of the ADCP velocity data at the Knik River site.

In Figure 7, the velocity maximum occurred below the surface near the left bank (distance of 6m in Figure 7). Figure 8 shows laterally averaged vertical profiles in this region and three others (as marked in Figure 7). In this case, the local *k* value may be greater than one, so it is not surprising that there is a large discrepancy for all of the three profile methods. This effect is associated with nonhydrostatic flow because of the nearly direct impact of the high-velocity core with an angled wing wall which directs flow into the narrowed bridge opening immediately downstream. This explains why the best-fit k value (0.927) was higher than that predicted with any of the three methodologies. The same sort of effect can be seen around a cross-stream distance of 79m, while profiles number 2 and 4 showed more "normal" behavior. Depression of the high-velocity region below the surface of the flow is common near steep banks, steeper lateral slopes, or as a result of secondary flows. None of the similarity vertical profiles can capture this effect, as they have velocity increasing toward the surface. This effect can be treated in discharge estimates only by using measured vertical profiles or a complete hydrodynamic modeling treatment.

5 DISCUSSIONS AND CONCLUSIONS

In this paper, we explore methods for extrapolating surface velocities to estimate vertically averaged velocities for discharge measurements. Although further corroboration should be carried out, it appears that using logarithmic or logarithmic-parabolic profiles generally gives the best relations in this regard, but still has substantial errors in estimating vertically averaged velocities relative to those developed using best fits to vertical velocity structure. Nevertheless, even for the worst-case scenarios, the errors incurred for local vertically averaged velocities are about 5% or less, with a clear central tendency. Notably, issues arising because of nonhydrostatic flows dwarf the differences found between using different similarity profiles. This suggests that mean velocities can be measured using remote sensing (and infrared videography in particular) with accuracy comparable to conventional velocity measurements for discharge measurement. To improve this technology, a more spatially complete view of the problem needs to be developed, so that both the depth and discharge can be computed from remotely sensed information in a manner that allows inclusion of spatial accelerations and nonhydrostatic effects.

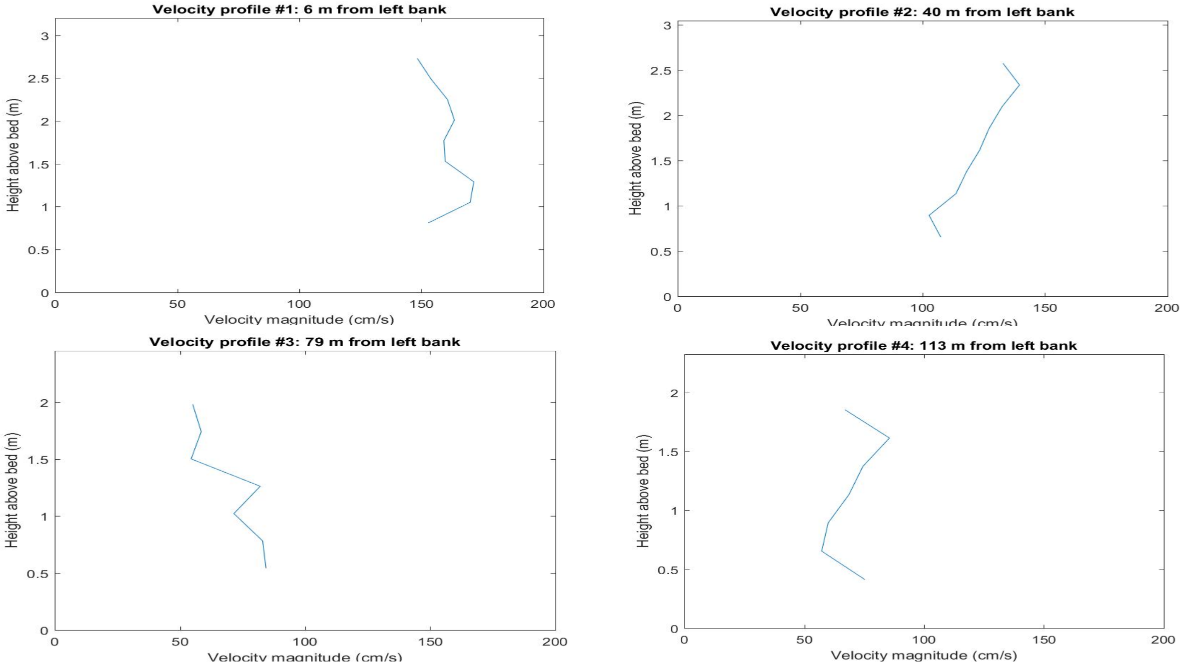

Figure 8. Vertical profiles of streamwise velocity at the 4 locations shown in Figure 7.

6 DISCLAIMER

Any use of trade, firm or product name is for descriptive purposes only and does not imply endorsement by the United States Government.

ACKNOWLEDGEMENTS

The authors would like to thank Robin Beebee, Heather Best, Karenth Dworsky (USGS Alaska Science Center) and John Fulton (USGS Colorado Water Science Center) for their assistance with the field program.

REFERENCES

Dugan, J.P., Anderson, S.P., Piotrowski, C.C. & Zuckerman, S.B. (2012). Airborne Infrared Remote Sensing of Riverine Currents*, IEEE Trans. on Geoscience and Remote Sensing*, doi:10.1109/TGRS.2013.2277815.

Johnson, E.D. & Cowen, E.A. (2016). Remote Monitoring of Volumetric Discharge Employing Bathymetry Determined from Surface Turbulence Metrics, *Water Resources Research*, 52 (3), 2178-2193.

Kinzel, P.J., Legleiter, C.J., Nelson, J.M. & Conaway, J.S. (2017). Remote Measurement of Surface-Water Velocity Using Infrared Videography and PIV: A Proof-Of-Concept for Alaskan Rivers, *Proceedings of the 37th IAHR World Congress*. (Submitted)

Legleiter, C.J., Roberts, D.A. & Lawrence, R.L. (2009). Spectrally based Remote Sensing of River Bathymetry. *Earth Surface Processes & Landforms*, 34(8), 1039-1059.

Legleiter, C.J., Kinzel, P.J. & Nelson, J.M. (Submitted). Remote Measurement of River Discharge Using Thermal PIV and Various Sources of Bathymetric Information. *Journal of Hydrology.*

Legleiter, C. J., Kinzel, P. J., Nelson & J. M. (2017a). *ADCP Data from Rivers in Alaska*, U.S. Geological Survey, September 18-20, 2016. doi: 10.5066/F7J964K7.

Legleiter, C. J., Kinzel, P. J. & Nelson, J. M. (2017b). Thermal Image Time Series from Rivers in Alaska, Geological Survey, September 18-20, 2016. U.S. doi: 10.5066/F7ST7N0J.

Mueller, D. S. (2013). extrap: Software to assist the selection of extrapolation methods for moving-boat ADCP streamflow measurements. *Computers & Geosciences*, 54, 211-218.

Muste, M.I., Fujita, I. & Hauet, A. (2008). Large-Scale Particle Image Velocimetry for Measurements in Riverine Environments, *Water Resources Research*, 44, W00D19. doi:10.1029/2008WR006950.

Nelson, J.M., McDonald, R.R., Kinzel, P.J. & Shimizu, Y. (2012) Using Computational Modeling of River Flow with Remotely Sensed Data to Infer Channel Bathymetry, *River Flow 2016*, 8.

Nelson, J. M., Kinzel, P. J., McDonald, R. R. & Schmeeckle, M. W. (2016). Noncontact Methods for Measuring Water-Surface Elevations and Velocities in Rivers: Implications for Depth and Discharge Extraction. In *River Flow 2016*, 637-645. CRC Press.

PivTec. (2015). *PIVview 2C/3C User Manual Version 3.6*¸ Göttingen, Germany, 93.

Rattray, M. & Mitsuda, E. (1974) Theoretical Analysis of Conditions in a Salt Wedge. *Estuarine and Coastal Marine Science*, 2, 375-394.

Whiting, P.J., Dietrich & W.E. (1990) Boundary Shear Stress and Roughness Over Mobile Alluvial Beds. *Journal of Hydraulic Engineering*, 116, 1495-1511.

Proceedings of the 37th IAHR World Congress
August 13 – 18, 2017, Kuala Lumpur, Malaysia

JET EROSION TEST FOR SOIL ERODIBILITY CHARACTERIZATION: ASSESSMENT OF THE UNDERLYING PHYSICS

EDDY J. LANGENDOEN[(1)] & JORGE D. ABAD[(2)]

[(1)] U.S. Department of Agriculture, Agricultural Research Service, Oxford, MS, USA,
eddy.langendoen@ars.usda.gov
[(2)] Department of Environmental Engineering, University of Engineering and Technology, Lima, Peru,
jabadc@utec.edu.pe

ABSTRACT

With the increasing social, political and natural pressures being placed on earthen embankments, such as levees and dams, an accurate characterization of the erodibility of fine-grained, cohesive soils is critical. Besides, eroding upland and stream bank soils in agricultural and urban environments are the primary sources of elevated fine-grain sediment concentration in U.S. stream systems. U.S. government agencies are increasingly using jet erosion test devices to measure the typical soil erodibility parameters, namely critical shear stress and soil detachment coefficient, for management and risk assessment of earthen resources. Recent experimental findings showed that the equations used to analyze the jet erosion test measurement can introduce errors up to 300%. However, assumptions made to analyze the experimental results are debatable. This paper summarizes the current state of knowledge on jet erosion tests, identifies gaps in knowledge to be addressed, and introduces the effort of the Agricultural Research Service of the U.S. Department of Agriculture to improve the equations used in the jet erosion test analysis through a numerical assessment.

Keywords: Erosion; Cohesive materials; Jet erosion test; Computer modeling.

1 INTRODUCTION

Fine-grained, suspended sediments are leading pollutants of water bodies (streams, lakes, reservoirs, etc.) in the United States of America (U.S. Environmental Protection Agency, 2014). Farmland and stream banks are the main sources of the fine-grained sediments. Hence, the U.S. Department of Agriculture (USDA) has recently emphasized the development of physically- and process-based prediction technology to improve the assessment of sheet and rill, gully, and stream bank erosion processes, and the impact of best management practices to control these types of erosion.

The erosion rate of fine-grained sediments is typically calculated using an excess-shear stress equation (e.g., Ariathurai and Arulanandan, 1978):

$$E=K_d(\tau-\tau_c) \quad [1]$$

where E is erosion rate (typically volumetric or mass based), τ_c is critical shear stress that needs to be exceeded for erosion to commence, and K_d is detachment coefficient (volumetric or mass based) that indicates the rate at which particles or aggregates are entrained. The critical shear stress and detachment coefficient will be hereafter referred to as the soil erodibility parameters. Unfortunately, unlike soil erosion prediction technology such as RUSLE (Renard et al., 1991), no national database exists that tabulates the critical shear stress and detachment coefficient for each soil series. Moreover, it may not be feasible to develop such a database as these parameters can greatly vary for a given soil with, among others, soil water content, land management practices, application of soil amendments, and are therefore strongly site- and time-specific.

Specialized, standardized submerged jet erosion test (JET) devices were developed by USDA to determine critical shear stress and detachment coefficient in the field or in the laboratory (Al-Madhhachi et al., 2013; Hanson and Cook, 2004; 1997; Hanson, 1990). JET testers are portable, cost effective and time efficient, and are therefore widely used both inside and outside the United States and by USDA to develop databases of soil erodibility parameters (e.g., Simon et al., 2010) and simulations of land and river management practices (e.g., Langendoen et al., 2009), and assess the risk of failure of levees and earthen dams (e.g., (Robbins and Wibowo, 2012; Courivaud et al., 2009).

The USDA-developed JET testers have a submergence tank with a diameter of either 0.3 m (12 in) or 0.1 m (4 in). The JET test device with a 0.3 m-diameter submergence tank is known as the 'standard' JET test device, whereas that with the 0.1 m-diameter submergence tank is known as the 'mini' JET test device. The nozzle diameters are respectively 6.4 mm (0.25 in) for the standard JET tester and 3.2 mm (0.125 in) for the mini JET tester. Note that the ASTM standard for the standard JET test device (ASTM International, 2007) was withdrawn in 2016.

The derivation of the soil erodibility parameters using the JET test device is based on the theory of unconfined impinging jets (Beltaos and Rajaratnam, 1974). However, recent experimental studies have indicated that the shear stresses acting on the impinged surface for confined submerged jets, which is the case for the JET test device, could be much larger (>300%) than those under unconfined conditions (Ghaneeizad et al., 2014). Likewise, the location of the maximum boundary shear stress was found to be much closer to the stagnation point. This could have significant implications on erosion estimates and the design of soil and water conservation measures. In the experiments of (Ghaneeizad et al., 2014), the submergence tank was a box with a square plan-view area of 0.67 x 0.67 m^2. It is worth noting that these observed 'increased' shear stresses were based on indirect measurements. They were estimated from measured turbulent kinetic energy because it is difficult to directly measure the shear stresses acting on the impinged surface. Haehnel and Dade (2008) showed that there does not exist a direct relationship between turbulent kinetic energy and mean-flow-based boundary shear stress. Moreover, Al-Madhhachi et al. (2013) showed that the soil erodibility parameters derived using standard and mini JET testers were different, which could be related to the different size of the JET tester submergence tanks, i.e. different magnitudes of jet confinement.

Weidner (2012) performed numerical simulations using the ANSYS FLUENT 13.0 computer model (Ansys, 2011) of a submerged impinging jet on both a flat plat and a series of scour holes within a cylindrical 0.3 m-diameter submergence tank (standard JET test device). Weidner's simulations showed that, in contrast to the observations of Ghaneeizad et al. (2014), the simulated boundary shear stresses and wall-jet velocity distributions were very similar to those measured by Beltaos and Rajaratnam (1974).

Given the uncertainty in soil erodibility parameters measured with JET devices and the increasing use of these devices for management and risk assessment of natural resources and protection measures, a thorough analysis of impinging jet hydrodynamics on an erodible soil surface is needed. This paper summarizes the current state of knowledge on jet erosion tests, identifies gaps in knowledge to be addressed, and introduces the effort of the Agricultural Research Service of the U.S. Department of Agriculture to improve the equations used in the JET analysis through a numerical assessment.

2 IMPINGING JET HYDRODYNAMICS

Hanson and Cook (1997) developed the methodology to derive the soil erodibility parameters using a submerged JET test device. The methodology is based on determining the maximum shear stress exerted by a submerged impinging circular jet on an erodible soil surface and measuring the time evolution of the depth of the scour hole formed by the impinging jet. The JET operation produces a series of paired E and τ values, which are used to derive τ_c and K_d using various procedures (e.g., Cossette et al., 2012; Simon et al., 2010; Hanson and Cook, 2004). The procedure relies on observations from experimental studies of the hydrodynamics of both non-submerged and submerged impinging circular jets.

A schematic of an impinging jet is shown in Figure 1. Typically, three regions are identified (Poreh and Cermak, 1959): a free jet region comprised of a zone with flow establishment (containing the potential core) and a zone of established flow, an impingement region, and a wall jet region. When the impingement height H exceeds the length of the potential core H_p, the centerline velocity in the established zone of the free jet is given as:

$$\frac{U}{U_0}=C_d\frac{d}{y} \qquad [2]$$

where U is the centerline velocity of the free jet, U_0 is the centerline velocity at the nozzle, C_d is the diffusion coefficient, d is nozzle diameter, and y is the distance to the nozzle. Hanson and Cook (1997) relate the maximum shear stress (τ_m) in the impingement region to the maximum velocity (U_m) in this region as:

$$\tau_m=\rho C_f U_m^2 \qquad [3]$$

where C_f is a friction coefficient and ρ is fluid density. Combining Eq. (2) and (3) yields:

$$\tau_m=\rho C_f\left(\frac{C_d U_0 d}{H}\right)^2 \qquad [4]$$

Hanson et al. (1990) used a flush mounted hot-film anemometer to measure the shear stress along the bottom of a 0.61 m cylindrical plexiglass tank impinged by a submerged circular jet of different strengths (d = 0.13 mm, H = 0.215 m, and U_0 varied between 1.8 and 6.5 m/s). They determined C_d = 6.3 and C_f = 0.00416, yielding $C_f C_d^2$ = 0.165, which is similar to the value (0.16) found by Beltaos and Rajaratnam (1974) using a

Preston tube for a study of an unconfined impinging air jet (d = 6.4 and 23.4 mm, H varied between 0.4 and 0.5 m, and U_0 varied between 46.6 and 89.3 m/s).

Beltaos and Rajaratnam (1974) found this maximum to occur in the impingement region at a distance $\lambda = r/H$ = 0.14 from the stagnation point. A similar distance was also found by Haehnel and Dade (2008) using a Preston tube for an unconfined air jet (d = 7.7 mm, H = 1.19 m, and U_0 varied between 140 and 150 m/s). However, for submerged conditions, Hanson et al. (1990) found the maximum shear stress to occur at $\lambda \approx$ 0.07. Using particle image velocimetry (PIV), Ghaneeizad et al. (2014) were unable to adequately resolve Reynolds stresses near the boundary (for experimental details see Section 4), and therefore, resorted to derive boundary shear stress from the turbulent kinetic energy at the boundary (k) as τ = 0.2k, which peaked at λ = 0.06. Using this approach, they found the coefficient in the maximum shear stress relation (4) $C_f C_d^2$ = 0.38, which is 240% larger than that found by Hanson and Cook (1997).

The approach of relating boundary shear stress to turbulent kinetic energy in the wall jet region of an impinging jet was proposed by Haehnel and Dade (2008), who, like Ghaneeizad et al. (2014), found that k peaked in the region λ = 0.06 to 0.07. The objective of the Haehnel and Dade (2008) experiment was to study the physics of particle entrainment from a packed bed due to an impinging turbulent jet. Interestingly, they found that the peak in particle entrainment occurred at the same location as the peak in k. Haehnel and Dade (2008) further concluded that the entrainment rate did not correlate well with the surface shear stress computed from the average flow, but did correlate well to a surface shear stress based on the turbulent fluctuations in the flow.

The more recent observations challenge the basis of the approach developed by Hanson and Cook (1997) to derive the soil erodibility parameters. A numerical model of submerged impinging jet dynamics could therefore assist in exploring these challenges.

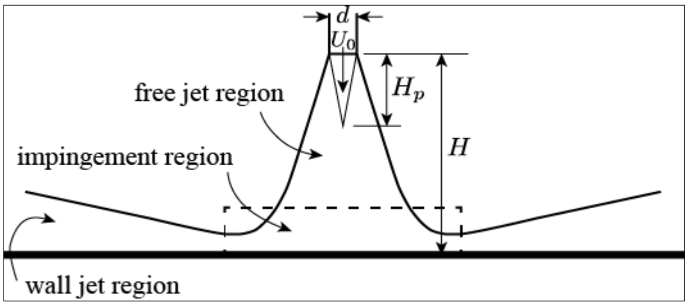

Figure 1. Schematic of a jet impinging on a flat plate, where d is nozzle diameter, U_0 is the flow velocity at the nozzle, H_p is potential core length, H is impingement height, and r is radial distance from the stagnation point.

3 NUMERICAL MODELING OF IMPINGING JETS

Zuckerman and Lior (2006) describe the physics of an impinging turbulent jet that need to be simulated by a computational fluid dynamics (CFD) model, and compare the performance of various turbulence models. Practically, the hydrodynamics of impinging jets can be studied using: (1) Large Eddy Simulation (LES) models that resolve temporally the turbulent fluid motions down to a length scale given by the grid spacing; or (2) Reynolds-Averaged Navier Stokes (RANS) models that simulate the time-averaged turbulent fluid motions. Of the three regions with distinct flow physics (see Figure 1), the impingement region exhibits the greatest complexity because of strong pressure strain stresses, unsteadiness, and strong curvatures. Such physics are difficult to capture with wall functions that are typically used in the simpler turbulence models.

Table 1. CFD turbulence model performance for simulating the hydrodynamics of impinging jets (adapted from Zuckerman and Lior, 2006).

Turbulence model	Computational cost	Ability
k-ϵ	Low	Poor
k-ω	Low to moderate	Fair
Reynolds stress model	Moderate to high	Fair
Shear stress transport	Low to moderate	Fair to good
$\bar{v}^2$-f	Moderate	Excellent
Large eddy simulation	High	Good to excellent

Zuckerman and Lior (2006) recommended using the $\bar{v}^2$-f and Shear Stress Transport (SST) turbulence models in case of RANS models, see Table 1. The SST model combines the k-ω model near the wall and the k-ϵ model away from the wall (Menter, 1993), which improves predictions of turbulence in adverse pressure gradients. The normal velocity relaxation, or $\bar{v}^2$-f, model is an extension of the k-ϵ model that includes the effects of near-wall anisotropy and non-local pressure strains (Durbin, 1991). The $\overline{v}^2$-f model uses two additional equations for the variables $\overline{v}^2$ (wall-normal Reynolds stress) and f (representing the redistribution of turbulent energy from the streamwise component to the wall-normal component by pressure strain). However, these two RANS models provide time-averaged turbulence metrics (e.g., Reynolds shear stresses and turbulent kinetic energy); they cannot simulate the large temporal fluctuations in these metrics. To simulate the complete range of boundary shear stresses, an LES model is required.

4 JET TEST SIMULATION

We will assess the submerged impinging jet hydrodynamics of both standard and mini JET testers using $\overline{v}^2$-f and LES turbulence models. The selected models will be rigorously validated against readily available experimental data, for example: (1) European Research Community On Flow, Turbulence And Combustion (ERCOFTAC) Test Case 25 “Normally-Impinging Jet from a Circular Nozzle” (ERCOFTAC, 1993) of unconfined jets; and (2) the submerged, confined impinging jet study of Ghaneeizad et al. (2014).

Herein, we present some very early results of a numerical simulation of the flow field in an impinging jet using the three-dimensional and non-hydrostatic CFD model FLOW-3D (Flow3d, 2015). FLOW-3D solves the transient Navier-Stokes equations and uses different turbulence closure models such as k-ϵ and LES. The model was used in different hydrodynamic applications: 1) flow over bedforms and submerged bodies (Catano et al., 2013), 2) flow around instream structures (Abad et al., 2008), and 3) flow around submerged acoustic instruments (Muller et al., 2007). Herein, since we are interested on solving the instantaneous flow structure of the impinging jet, an LES model was used in combination with a Smagorinsky sub-grid scale model for unresolved eddies.

Ghaneeizad et al. (2014) performed an experimental study of confined submerged jet hydrodynamics using a box-shaped, plexiglas submergence tank of size 0.67 x 0.67 x 0.4 m (or 4.24H x 4.24H x 2.53H, where the impingement height H = 0.158 m). The nozzle diameter used was the same as that for the standard JET device, namely 6.4 mm. Two experimental runs were conducted with differing heads: 0.735 m and 1.487 m. The corresponding water velocity U_0 at the nozzle was 3.67 and $5.27 m/s, respectively. Here, results are presented corresponding to U_0 = 3.67 m/s.

A particle image velocimetry (PIV) system was used to measure the two-dimensional velocity field focusing on the plane passing the jet centerline (Fig. 1), and was measured in five separate zones: (1) the near-field of the free jet region, (2) the far-field of the free jet region, (3) the impingement region, (4) the near-field of the wall jet region, and (5) the far-field of the wall jet region.

Using FLOW-3D, four blocks of 5,066,141 cells (block 1, 2,153,628 cells; block 2, 2,275,008 cells; block 3, 472,305 cells; and block 4, 165,200 cells) with different resolutions (with a finer mesh of 1 x 1 mm along the free and wall jet regions) were used to represent the experimental tank. The boundary conditions were: solid impermeable wall that represents the edges of the tank, a symmetry condition at the free surface, and a nozzle discharge of 104x10^{-6} m^3/s. Figure 2 shows a plot of the instantaneous velocity vector field. As can be observed, the ambient water is entrained into the jet's high velocity region, thereby dissipating the jet's energy and mean centerline velocity (cf. Eq. (2)). Figure 3 presents a plot of the instantaneous flow field in and around the impingement region near the bottom of the tank showing various vortical structures and strong flow curvature.

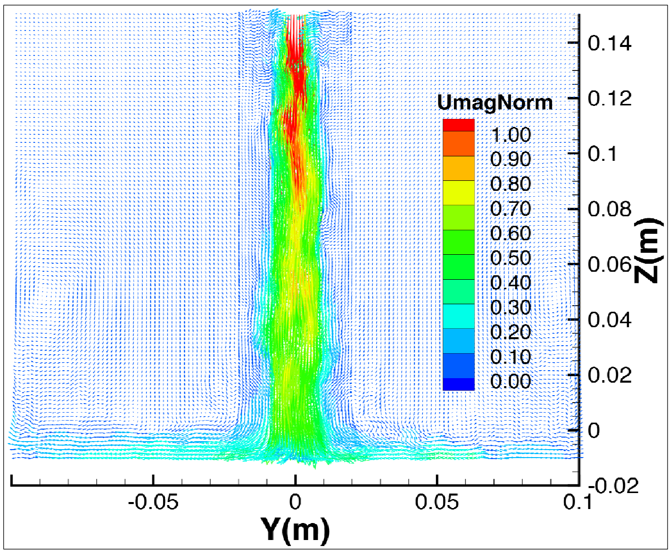

Figure 2. Vector plot of instantaneous flow field of the impinging jet study of Ghaneeizad et al. (2014). Vectors are colored according to the normalized velocity magnitude (using the flow velocity at the nozzle).

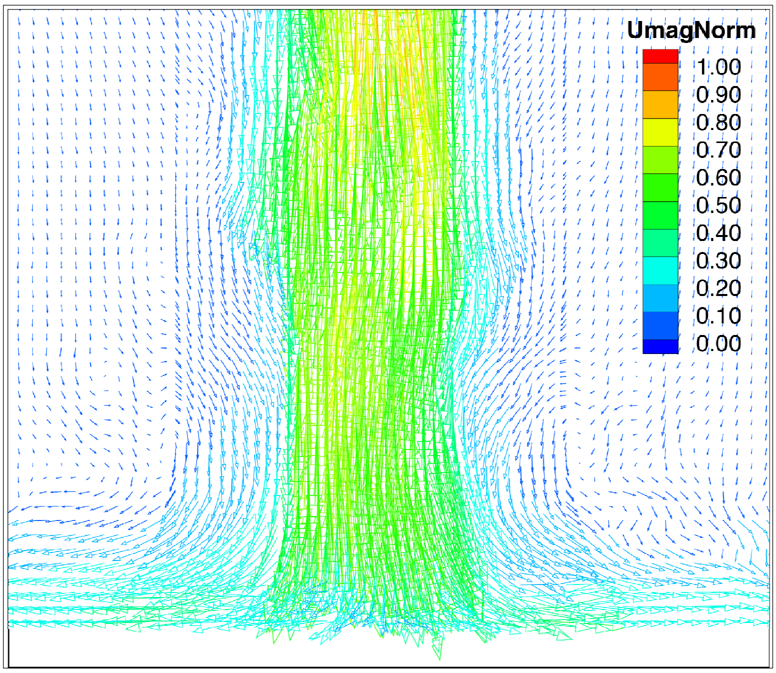

Figure 3. Vector plot of the instantaneous flow field in and around the impingement region of Figure 2, showing vortical structures and strong flow curvature.

5 SUMMARY

JET devices are increasingly being used by U.S. government agencies to characterize the erodibility of fine-grained, cohesive soils in order to assess, among others, the integrity of levees and earthen embankments, and sediment loadings into stream systems. The peer-reviewed literature on JET devices and impinging jet hydrodynamics show not only deficiencies in the basic concepts of the JET data analysis, but also in the experimental methods used to investigate these deficiencies. A rigorous numerical assessment of the hydrodynamics of submerged impinging jets has been initiated to evaluate the performance of the standard and mini JET devices developed by the USDA.

REFERENCES

Abad, J.D., Rhoads, B.L., Guneralp, I & Garcia, M.H. (2008). Flow structure at Different Stages in a Meander-Bend with Bendway Weirs. *Journal of Hydraulic Engineering*, 138(8), 1052-1053.

Al-Madhhachi, A.-S. T., Hanson, G.J., Fox, G.A., Tyagi, A.K. & Bulut, R. (2013). Measuring Soil Erodibility using a Laboratory “Mini” Jet. *Transactions of the ASABE*, 56(3), 901-910.

ANSYS (2011). Ansys Fluent. http://www.ansys.com/Products/Fluids/ANSYS-Fluent, [Accessed: January 16, 2017].

Ariathurai, R. & Arulanandan, K. (1978). Erosion Rates of Cohesive Soils. *Journal of the Hydraulics Division* 104(2), 279-283.

ASTM International (2007). *Standard Test Method for Erodibility Determination of Soil in the Field or in the Laboratory by the Jet Index Method (Withdrawn 2016)*. ASTM D5852-00(2007) e1. ASTM International, West Conshohocken, PA.

Beltaos, S. & Rajaratnam, N. (1974). Impinging Circular Turbulent Jets. *Journal of the Hydraulics Division*, 100(10), 1313-1328.

Catano, Y., Landry, B., Abad, J.D. & Garcia, M.H. (2013). Experimental and Numerical Study of the Flow Structure around Two Partially Buried Objects on a Deformed Bed. *Journal of Hydraulic Engineering*, 139(3), 269-283.

Cossette, D., Mazurek, K.A. & Rennie, C.D. (2012). Critical Shear Stress from Varied Method of Analysis of a Submerged Circular Turbulent Impinging Jet Test for Determining Erosion Resistance of Cohesive Soils. *6th International Conference on Scour and Erosion*, Paris, France, 22-29.

Courivaud, J.R., Fry, J.J., Bonelli, S., Benahmed, N., Regazzoni, P.L. & D., Marot (2009). Measuring the Erodibility of Soil Materials Constituting Earth Embankments: A Key Input for Dams and Levees Safety Assessment. *Hydro 2009*, Lyon, France, 9 pp.

Durbin, P.A. (1991). Near-Wall Turbulence Closure Modeling without “Damping Functions”. *Theoretical and Computational Fluid Dynamics*, 3(1), 1-13.

ERCOFTAC (1993). Normally-Impinging Jet from a Circular Nozzle. http://cfd.mace.manchester.ac.uk/ercoftac, [Accessed: January 26, 2017].

Ghaneeizad, S.M., Atkinson, J.F. & Bennett, S.J. (2014). Effect of Flow Confinement on the Hydrodynamics of Circular Impinging Jets: Implications for Erosion Assessment. *Environmental Fluid Mechanics*, 15(1), 1-25.

Haehnel, R. & Dade, W.B. (2008). Physics of Particle Entrainment under the Influence of an Impinging Jet. *Proceedings of the 26th Army Science Conference*, Orlando, FL, 8 pp.

Hanson, G.J. (1990). Surface Erodibility of Earthen Channels at High Stresses Part II - Developing an in Situ Testing Device. *Transactions of the ASAE*, 33(1), 132-137.

Hanson, G.J. & Cook, K.R. (1997). Development of Excess Shear Stress Parameters for Circulating Jet Testing. *1997 ASAE Annual International Meeting*, Minneapolis, MN, 22 pp.

Hanson, G.J. & Cook, K.R. (2004). Apparatus, Test Procedures, and Analytical Methods to Measure Soil Erodibility in Situ. *Applied Engineering in Agriculture*, 20(4), 455-462.

Hanson, G.J., Robinson, K.M. & Temple, D.M. (1990). Pressure and Stress Distributions Due to a Submerged Impinging Jet. *Proceedings of the 1990 National Conference on Hydraulic Engineering*, San Diego, CA, 525-530.

Langendoen, E.J., Wells, R.R., Thomas, R.E., Simon, A. & Bingner, R.L. (2009). Modeling the Evolution of Incised Streams. III: Model Application. *Journal of Hydraulic Engineering*, 135(6), 476-486.

Menter, F.R. (1993). Zonal Two Equation Κ-Ω Turbulence Models for Aerodynamic Flows. *23rd Fluid Dynamics, Plasmadynamics, and Lasers Conference*, Orlando, FL. American Institute of Aeronautics and Astronautics, 2906.

Muller, D., Abad, J.D., Garcia, C., Gatner, J.W. & Garcia, M.H. (2007). Errors in Acoustic Doppler Velocity Measurements Caused by Flow Disturbance. *Journal of Hydraulic Engineering*, 133(12), 1411-1420.

Poreh, M. & Cermak, J.E. (1959). Flow Characteristics of a Circular Submerged Jet Impinging Normally on a Smooth Boundary. *Proceedings of the Sixth Midwestern Conference on Fluid Mechanics*, Austin, TX, 198-212.

Renard, K.G., Foster, G.R., Weesies, G.A. & Porter J.P. (1991). Rusle: Revised Universal Soil Loss Equation. *Journal of Soil and Water Conservation*, 46(1), 30-33.

Robbins, B.A. & Wibowo, J.L. (2012). Field Jet Erosion Tests of Treated Clay Levee Embankments. *6th International Conference on Scour and Erosion*, Paris, France, 1239-1246.

Simon, A., Thomas, R.E. & Klimetz, L. (2010). Comparison and Experiences with Field Techniques to Measure Critical Shear Stress and Erodibility of Cohesive Deposits. *Joint Federal Interagency Conference 2010*, Las Vegas, NV, 13 pp.

U.S. Environmental Protection Agency (2014). National Summary of State Information. http://ofmpub.epa.gov/tmdl_waters10/attains_nation_cy.control. [Accessed: January 16, 2017].

Weidner, K.L. (2012). Evaluation of the Jet Test Method for Determiningt the Erosional Properties of Cohesive Soils: a Numerical Approach. *MSc thesis*. Virginia Polytechnic Institute and State University, Blacksburg, VA.

Zuckerman, N. & Lior, N. (2006). *Jet Impingement Heat Transfer: Physics, Correlations, and Numerical Modeling*. Advances in Heat Transfer Volume 39, Ed. G.A. Greene, J.P. Hartnett, A. Bar-Cohen and Y.I. Cho, Elsevier/Academic Press, London, U.K., 565–631.

THE KINECT SENSOR AS A TOOL FOR REMOTE FLOW CHARACTERISATION

YUN-HANG CHO[(1)], MATTEO RUBINATO[(2)] & ANDY NICHOLS[(3)]

[(1,2,3)] Pennine Water Group, Department of Civil and Structural Engineering, University of Sheffield, Sheffield, UK
yun-hang.cho@sheffield.ac.uk

ABSTRACT

Recent research has shown a practical interest in the dynamics of water surfaces (Fujita et al., 2011; Nichols, 2013; Horoshenkov et al., 2013). However, the ability to robustly measure the three-dimensional shape or water surfaces, particularly in the field, is still challenging. One technology that shows promise is the Microsoft Kinect sensor. An examination of low-cost 3D flow surface measurements was presented by Nichols and Rubinato (2016), who showed the potential for the sensors to measure opaque flow surfaces, with some limited examination of clear water flows. However, many flows involve clear water without an opaque surface, and the ability of Kinect sensors to measure in these conditions is unknown. This paper presents an initial study into the potential for Kinect sensors to be used for mapping clear water surfaces.

Keywords: Water surface fluctuation; Kinect sensor; Open-channel flow; Free-surface dynamics; Clear water.

1 INTRODUCTION

In shallow flows, the dynamic fluctuations in free surface elevations are of practical importance in fields such as sound propagation, gas evasion, and flow monitoring (Horoshenkov et al., 2013). Several techniques exist for measuring water surface position (Boon and Brubaker, 2008; Tsubaki et al., 2005; Takamasa et al., 2000; Nichols, 2013; Lommer and Levinsen, 2002; Rubinato, 2013), but these techniques are limited in their spatial resolution, and generally only measure in one or two dimensions.

Nichols and Rubinato (2016) presented an initial examination of low-cost 3D flow surface measurements using a Microsoft Kinect sensor (Figure 1, right). Until then, Kinect sensors had never been used to measure turbulence-generated water surface roughness, and never for measuring clear, un-seeded water surfaces. Nichols and Rubinato (2016) showed that the Kinect is able to measure gravity waves in opaque flow, and may have potential in clear water flows via the principle of refraction. The application to clear water is of practical importance since many flows do not exhibit the opaque surface generally required for optical mapping. This paper presents an examination of the Kinect water surface sensing approach for clear water flows.

2 METHODOLOGY

Testing was undertaken in a flume within the University of Sheffield 'Diamond' fluids laboratory. The flume (Figure 1) has an experimental length of 12.5 m, a width of 0.309 m and a maximum depth of 0.450 m. For this set of tests, the slope was fixed at 0.001 with the measurement section 3.50-4.00 m from the upstream end of the flume. The flume was instrumented with a Microsoft Kinect V1 sensor and a conductance-based wave monitor. A range of free-surface conditions were established via a reciprocal wave generator and by flow turbulence.

Figure 1. Experimental flume.

2.1 Free-surface conditions

Initial tests involved a set of 45 gravity wave conditions imposed on still water at depths of 30, 66, 105, 123 and 141 mm (Figure 2). For each depth, nine gravity wave conditions were established using a reciprocal wave generator, using three different frequencies (0, 1, 1.5 Hz) and three wave generator stroke lengths (70 mm, 135 mm and 200 mm). A scaled beach was used at the opposite end of the flume to avoid the reflection of waves from the wall (Figure 3, left).

Five steady uniform flows were then established over a smooth boundary to generate different free-surface patterns via the inherent flow turbulence. The flow depths matched those used for gravity waves, and as a result, the mean flow velocity varied from 0.32 to 0.64 m/s. Bulk flow conditions are given in Table 1, and images of the five flows are shown in Figure 2. It can be seen that the turbulence generated surface pattern is very subtle.

Table 1. Flow conditions.

Water depth (m)	Velocity (m/s)	Flow rate (l/s)	Reynolds number	Froude number	Weber number
0.030	0.32	2.94	9600	0.59	42
0.066	0.48	9.83	31600	0.60	208
0.105	0.60	19.60	62900	0.59	519
0.123	0.63	23.83	77300	0.57	670
0.141	0.64	28.00	90100	0.54	793

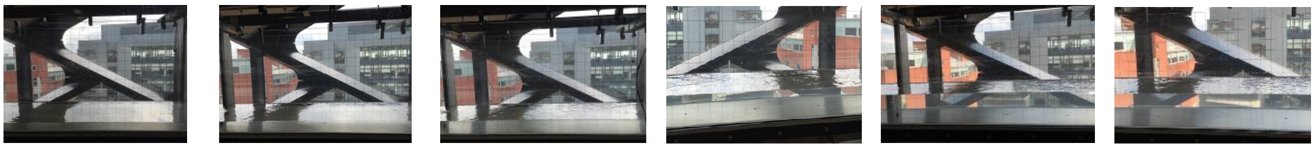

Figure 2. Steady flow conditions.

2.2 Wave Probe Data

In order to validate the Kinect data, a conductance-based wave probe (Figure 3-Right) was installed to measure depth data at a small area. The probe was placed in the middle of the flume (150 mm from the side edge of the flume) and 50mm within the downstream edge of the measurement area. This ensured any secondary patterns (wake effect) generated by the wave probe did not affect the free-surface in the measurement area.

Figure 3. (Left) – Beached bed, (Centre) – Kinect mounted above flume, (Right) – Conductance wave probe.

2.3 Kinect Data

A chequered board grid was used to characterize the spatial lens distortion, and to derive a transformation that would convert pixel coordinates into spatial coordinates. Details of this process can be found in (Nichols & Rubinato, 2016). The Kinect data were pre-processed to remove obviously anomalous data points and any slight trends. To achieve this, data was detrended over time, and a median filter was then applied to each frame, with a window size of 29 x 29 mm.

Using the known position of the wave probe, windows of data were extracted from each frame of collected Kinect data, covering a small patch (26 mm x 26 mm) around the position of the wave probe. These windows were then averaged to produce a single depth reading for each recorded time frame. The resulting time series vector was then compared against the wave probe data collected at the same location.

3 RESULTS & DISCUSSION

3.1 Time series comparison

Figure 4 shows the time averaged depth recorded by Kinect compared with that recorded by the conductance wave probe. The mean depth is underestimated by the Kinect sensor, due to a refractive effect, but shows a clear linear relationship with the true depth. Based on this, a linear recalibration function was determined, to transform the water depth observed by the Kinect sensor into a true water depth. This function was then applied across all the data prior to further analysis.

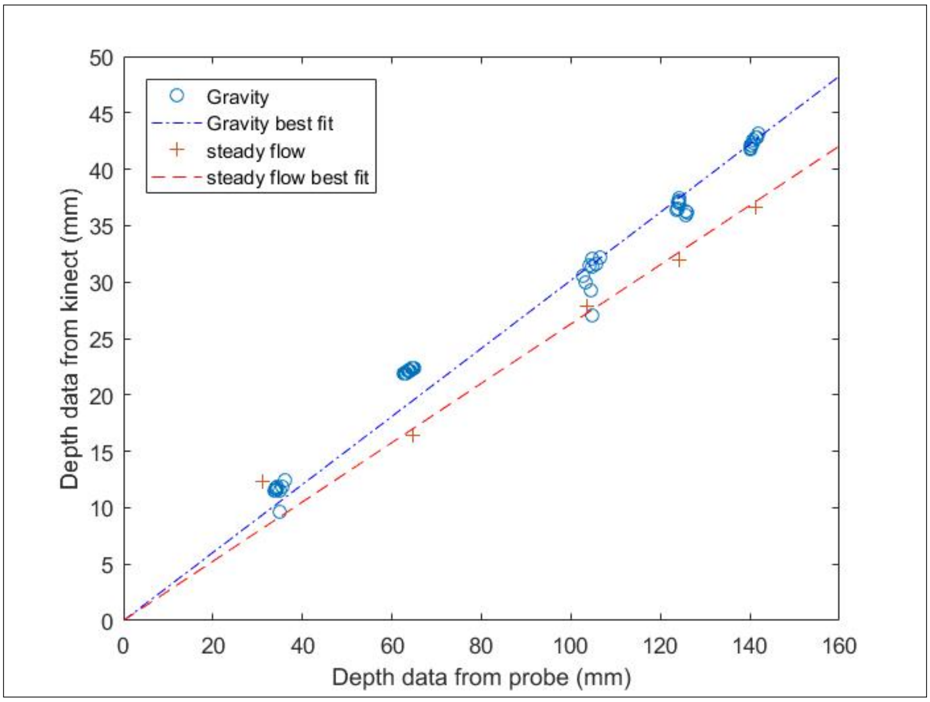

Figure 4. Mean depth recorded by Kinect vs mean depth from wave probe.

Figure 5 (left) shows an example of the resulting signal recorded by the Kinect sensor for an arbitrary gravity wave, and the corresponding measurement from the wave probe at the location of the wave probe. A phase difference is expected since the data recordings from the two systems were only synchronized to within 1 s. It can be seen that in general a wave pattern is detected, though with significant distortions and differences from the wave probe data.

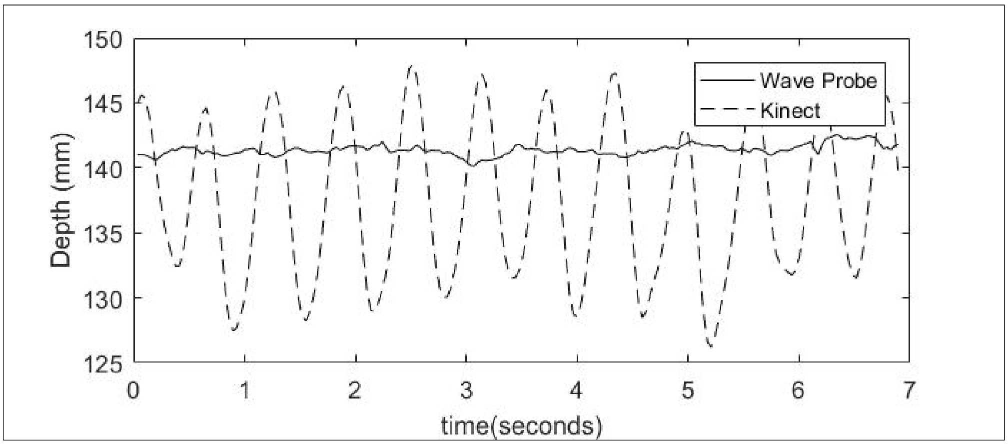

Figure 5 (Left) – Kinect signal at 1.5Hz, 200mm stroke, 141mm depth.

For the flowing water conditions, time series data from the wave probe is compared against data from the Kinect in Figure 6. Four observations can be drawn from this:

(i) The difference in mean depth seems to be captured by the Kinect sensor;

(ii) The wave height generally seems to increase with increasing flow depth, for both the wave probe and Kinect data;
(iii) There is perhaps a similarity in the frequency content of the recorded signals;
(iv) The signals of wave probe and Kinect sensor do not, otherwise, appear very similar.

These observations are examined further in the following sections through an examination of the statistical and spectral properties of the time series captured by the two measurement methods.

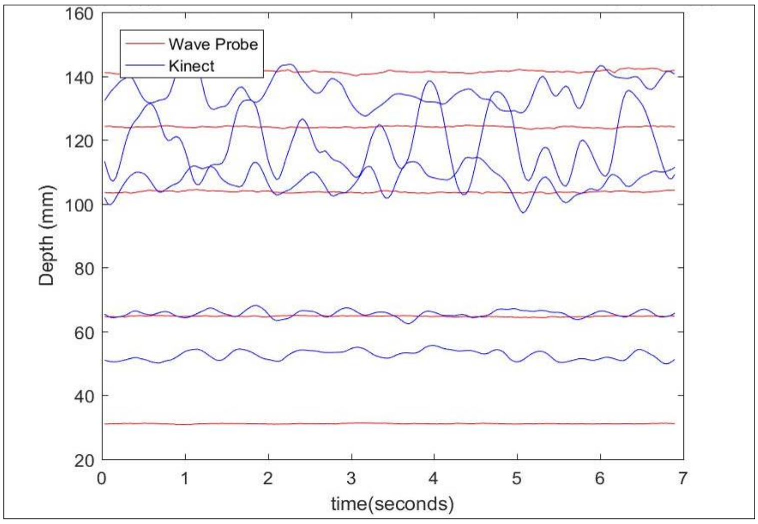

Figure 6. Flow depth measured by Kinect vs wave probe.

3.2 Statistical Comparison

In order to determine whether the Kinect sensor could be used to infer free-surface properties, and specifically what properties it may be sensitive to, a statistical approach is used here. Figure 7 shows the measured recalibrated depth (right) and root-mean-square wave height (left) recorded by the Kinect sensor and by the wave probe; for both gravity waves and turbulence-generated waves. The results show that the Kinect data consistently overestimates the wave amplitude, most probably due to ambiguity in the way the infra-red light is refracted, which will depend on the complex distribution of local surface gradient over time. A subset of points appears to lie close to the 1:1 line, and further study is needed to determine the conditions under which more precise amplitude measurement can be achieved. In contrast, the mean depth detected by the Kinect is now very close to the detected value from the wave probe. This is true for both the gravity waves and turbulence generated waves.

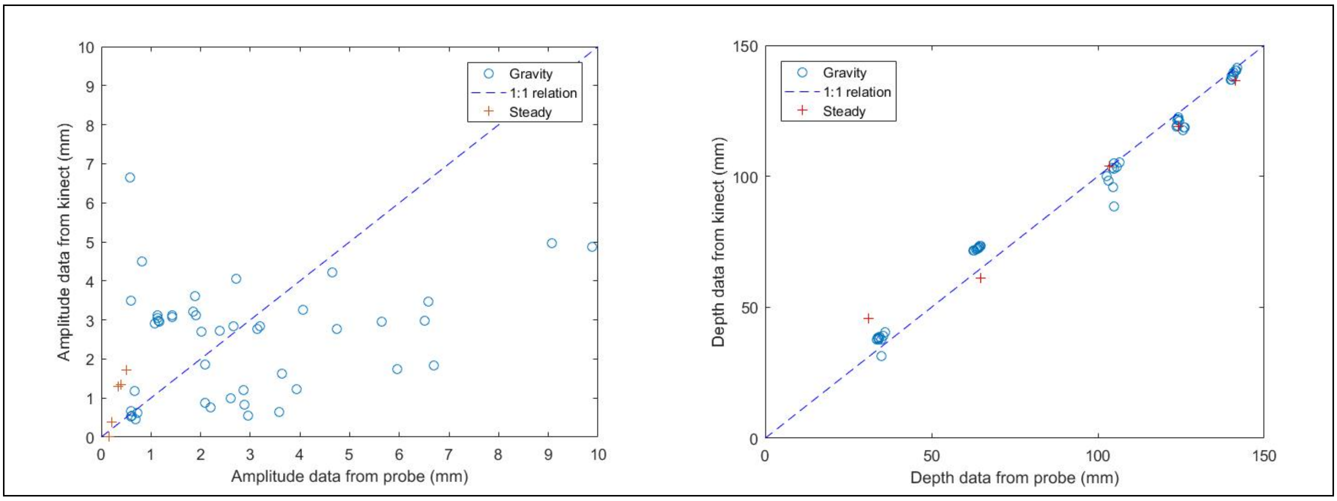

Figure 7. (Left) - Wave amplitude detected by Kinect vs wave probe, (Right) – Mean flow depth detected by Kinect vs wave probe.

3.3 Spectral Comparison

Figure 8 shows the dominant frequency component of the Kinect signal versus that of the wave probe signal for gravity waves. These were determined from the maximum amplitude in the Fourier spectrum of the signals. Overall, most of the Kinect frequency readings appear to be similar to the wave probe, with the rest outliers. These may be due to noise in the frequency spectrum as has previously been noted for opaque flows. Ignoring outliers, the frequency relation with the wave probe is almost 1:1, suggesting that the Kinect sensor accurately detects the wave frequency for the majority of cases.

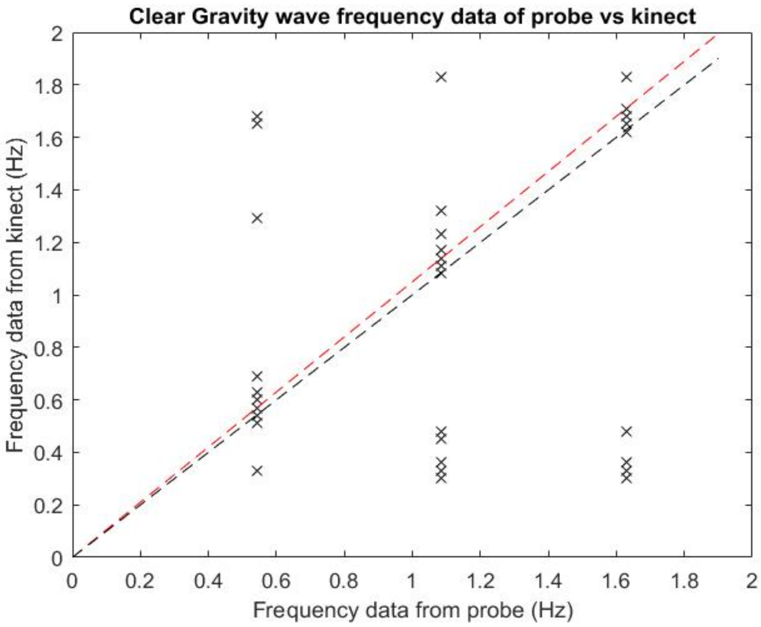

Figure 8. Maximum frequency response detected by Kinect vs wave probe.

A Fourier transform was used to investigate the frequency spectra of the Kinect and wave probe data for the five steady turbulent flow conditions. These spectra were calculated after normalising the wave heights, and are shown in Figure 9. Three observations are of note:

(i) Both devices show a decay in wave amplitude as the frequency component increases, consistent with a traditional turbulent energy cascade, and a similar spectral gradient;

(ii) Both devices show a general increase in spectral content as the flow depth is increased, consistent with larger waves formed by more energetic flows;

(iii) Generally, the spectra match better for higher flow depths and hence larger surface features, and particularly for low frequency components versus the higher frequency components.

Figure 10 shows the autocorrelation of the Kinect and wave probe data on the same axes. The autocorrelation identifies dominant length scales in the data, assuming the variables are a stochastic process with a random probability function which can be predicted statistically. It can be seen that the wave probe is more sensitive at lower depths with higher sensitivity to minor fluctuations. However, for most depths, the Kinect and wave probe autocorrelations show a similar trend, particularly for larger length scales.

The spectra and autocorrelation data suggest that the Kinect sensor could be detecting the dominant large length scale features on the free-surface, (even if they do not correlate directly in the time domain), but struggles with smaller, higher-frequency components of the surface roughness.

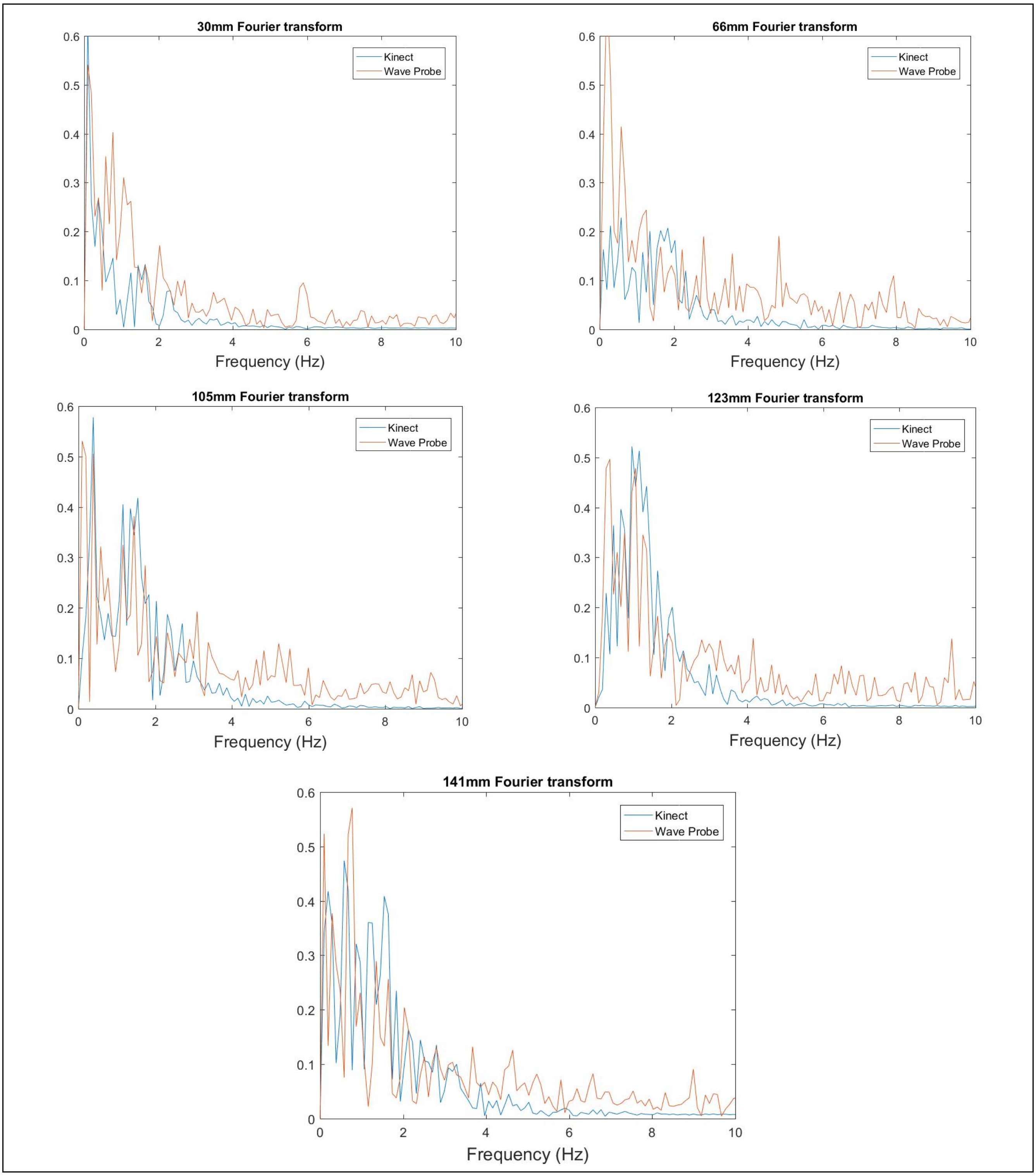

Figure 9. Fourier transform of steady flows.

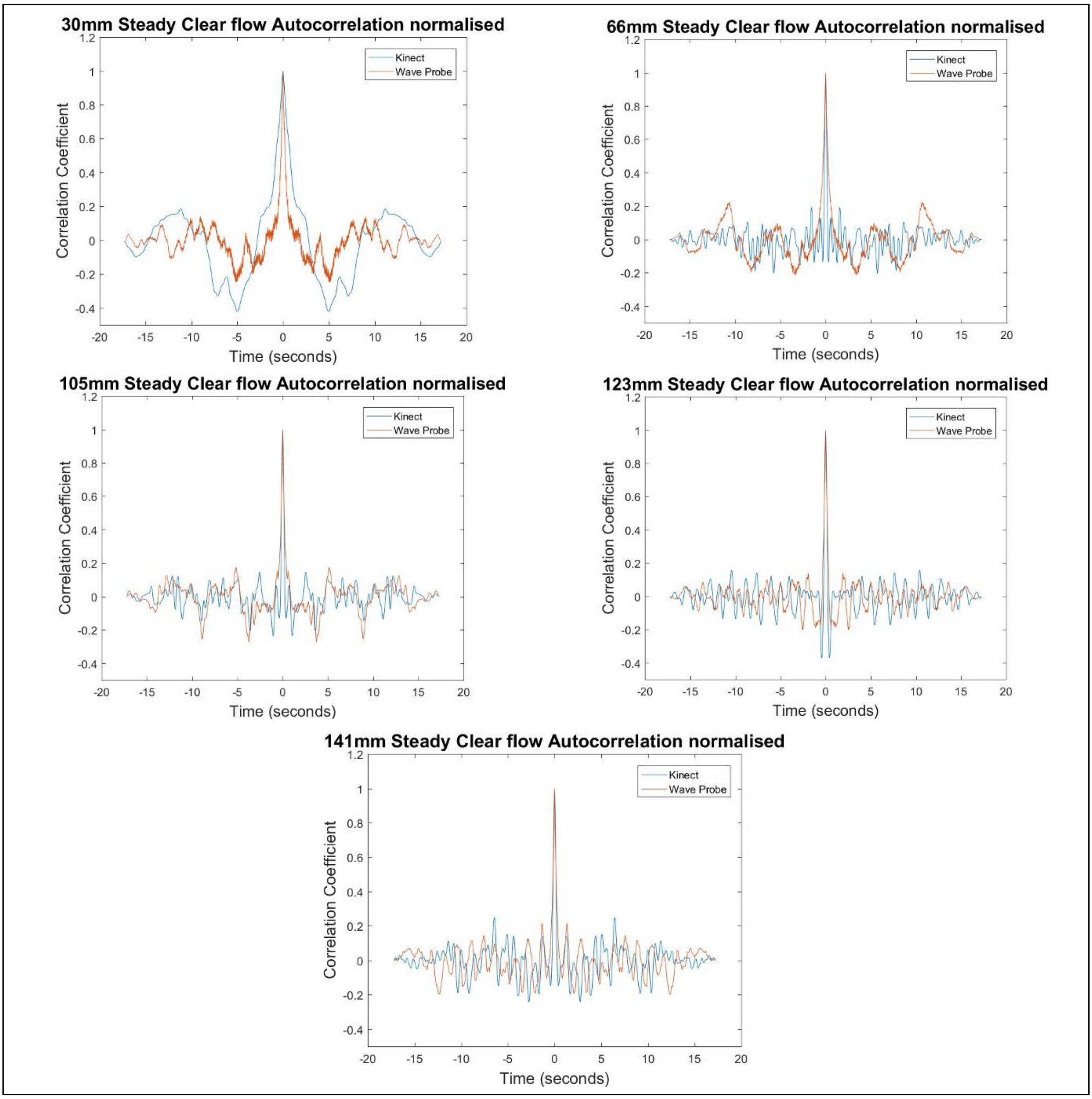

Figure 10. Autocorrelation of steady flows.

4 CONCLUSIONS

The data recorded from the Kinect shows potential and suggests that the sensor is able to accurately detect average flow depth in both clear gravity wave and clear flow conditions, after applying a suitable calibration. The wave amplitudes from the Kinect V1 appear to be ambiguous, perhaps due to complex refractive effects, so cannot accurately be used. The spectral content and dominant length scales within the Kinect data are shown to be similar to those within the wave probe data, and display similar trends, suggesting that the Kinect 3D free-surface sensing approach has potential for characterising large, dominant length scales. A newer, second generation sensor is now available and is able to measure depth more accurately. The next step in testing is to examine the applicability of Kinect V2 sensors for detecting small features in free-surface patterns, with clear or opaque water surfaces.

The results of this study and related ongoing work could provide a new method for characterising rough water surfaces, giving new insights to the fields of 3D sound scattering, greenhouse gas evasion, and remote flow monitoring.

ACKNOWLEDGEMENTS

This research has been supported by the EPSRC Pennine Water Group Platform Grant (EP/I029346/1), The University of Sheffield's Early Career Researcher Scheme, and the A*STAR research attachment programme.

REFERENCES

Boon, J.D. & Brubaker, J.M. (2008). Acoustic-Microwave Water Level Sensor Comparisons In An Estuarine Environment. In: *Oceans International Conference*, Quebec City, Canada. Marine Technology Society/IEEE, 1-5.

Fujita, I., Furutani, Y. & T. Okanishi. (2011). Advection Features of Water Surface Profile in Turbulent Open-Channel Flow with Hemisphere Roughness Elements. *Visualation of Mechanical. Processes: an International Journal,* 1(4).

Horoshenkov, K.V., Nichols, A., Tait, S.J. & G.A. Maximov. (2013). The Pattern of Surface Waves in a Shallow Free-Surface Flow. *Journal of Geophysical Research: Earth Surface* 118(3), 1864-1876.

Lommer, M. & Levinsen, M.T. (2002). Using Laser-Induced fluorescence in the Study of Surface Water Turbulence. *J. Fluorescence.* 12(1), 45-50.

Nichols A. (2013). Free-Surface Dynamics in Shallow Turbulent Flows. *PhD Thesis*, University of Bradford.

Nichols A. & Rubinato M. (2016). Remote Sensing of Environmental Processes via Low-Cost 3D Free-Surface Mapping. *4th IHAR Europe Congress*, Liege, Belgium.

Rubinato, M., Shucksmith, J. & Saul A.J. (2013). Comparison between Infoworks Results and a Physical Model of an Urban Drainage System, *Water Science and Technology*, 68(2), 372–379.

Takamasa, T. & T. Hazuku. (2000). Measuring Inter-Facial Waves on Film Flowing Down a Vertical Plate Wall in the Entry Region using Laser Focus Displacement Meters. *International Journal of Heat and Mass Transfer*, 43(15), 2807–2819.

Tsubaki, R., & I. Fujita. (2005). Stereoscopic Measurement of a Fluctuating Free-Surface with Discontinuities. *Measurement Science and Technology* 16(10), 1894–1902.

Proceedings of the 37th IAHR World Congress
August 13 – 18, 2017, Kuala Lumpur, Malaysia

REMOTE MEASUREMENT OF SURFACE-WATER VELOCITY USING INFRARED VIDEOGRAPHY AND PIV: A PROOF-OF-CONCEPT FOR ALASKAN RIVERS

PAUL KINZEL[(1)], CARL LEGLEITER[(2)], JONATHAN NELSON[(3)] & JEFFREY CONAWAY[(4)]

[(1,2,3)] U.S. Geological Survey, Geomorphology and Sediment Transport Laboratory, Golden, United States of America,
pkinzel@usgs.gov; cjl@usgs.gov; jmn@usgs.gov
[(4)] U.S. Geological Survey, Alaska Science Center, Anchorage, United States of America,
jconaway@usgs.gov

ABSTRACT

Thermal cameras with high sensitivity to medium and long wavelengths can resolve features at the surface of flowing water arising from turbulent mixing. Images acquired by these cameras can be processed with particle image velocimetry (PIV) to compute surface velocities based on the displacement of thermal features as they advect with the flow. We conducted a series of field measurements to test this methodology for remote sensing of surface velocities in rivers. We positioned an infrared video camera at multiple stations across bridges that spanned five rivers in Alaska. Simultaneous non-contact measurements of surface velocity were collected with a radar gun. *In situ* velocity profiles were collected with Acoustic Doppler Current Profilers (ADCP). Infrared image time series were collected at a frequency of 10Hz for a one-minute duration at a number of stations spaced across each bridge. Commercial PIV software used a cross-correlation algorithm to calculate pixel displacements between successive frames, which were then scaled to produce surface velocities. A blanking distance below the ADCP prevents a direct measurement of the surface velocity. However, we estimated surface velocity from the ADCP measurements using a program that normalizes each ADCP transect and combines those normalized transects to compute a mean measurement profile. The program can fit a power law to the profile and in so doing provides a velocity index, the ratio between the depth-averaged and surface velocity. For the rivers in this study, the velocity index ranged from 0.82 – 0.92. Average radar and extrapolated ADCP surface velocities were in good agreement with average infrared PIV calculations.

Keywords: Infrared imaging; particle image velocimetry; remote sensing; river discharge; surface water hydraulics.

1 INTRODUCTION

The development of innovative techniques to measure river discharge has been an active area of research for the U.S. Geological Survey (USGS) which currently operates over 8,000 continuous streamgages in the United States. In 1996, the USGS-sponsored Hydro 21 committee was formed to investigate and identify non-contact technologies that could be incorporated into the USGS hydrologic data network. The effort resulted in a number of publications focused on the application of radar technology to measure surface velocity, cross-sectional channel area, and compute discharge (Spicer et al., 1997; Costa et al., 2000; Melcher et al., 2002). Passive optical methods such as Large-Scale Particle Image Velocimetry (LSPIV) also have been used to measure surface velocity and estimate discharge (Fujita and Komura, 1994; Creutin et al., 2003; Muste et al., 2008; Sun et al., 2010). LSPIV typically uses time series of images from conventional cameras to track the motion of artificial or natural tracers (e.g. foam, debris, surface texture). An alternative approach involves using infrared cameras to detect the advection of thermal features at the surface of laboratory, coastal, and riverine flows (Helmle, 2005; Chickadel et al., 2009; Kinzel et al., 2012; Puleo et al., 2012; Dugan et al., 2014; Nelson et al. 2016a; 2106b). However, for any surface velocity measurement to be used for discharge computation it must: (1) rely on the use of an empirical or theoretical relationship to transform the surface velocity to a depth-averaged velocity; and (2) have either some a priori knowledge of the channel bathymetry, or employ an alternative, or preferably companion, means to obtain depth information for calculating cross-sectional area. The focus of this paper is not to describe a complete technique for gaging rivers but rather to describe the approach, equipment, and processing we used to compute surface velocity from infrared image sequences collected from bridges spanning five Alaskan rivers and compare the resulting velocities to those measured using both non-contact and *in situ* techniques.

Alaska is the largest state in the United States with an area of 1,718,000 km^2. The Alaska Department of Fish and Game (2017) states that Alaska has more than 40% of the surface water resources in the United States including 3 million lakes and approximately 12,000 rivers. Of the 20 largest rivers in the United States, ranked by average discharge at the mouth, seven are located in Alaska (Kammerer, 1990). The USGS presently operates 102 streamgaging stations that are distributed throughout the state (USGS, 2017). To put this number of gages in perspective, there is an average of approximately one USGS streamgage per 17,000

km^2 in Alaska compared to an average of about one USGS streamgage per 1,000 km^2 in the conterminous United States (http://dx.doi.org/10.5066/F7P55KJN). As many of the gaging stations in Alaska are remote, considerable effort is necessary to collect periodic measurements and maintain the stations. Thus, developing remote sensing methods for measuring surface velocity and ultimately streamflow in this vast geographic area is valuable for a number of reasons. Such a capacity could potentially augment and economize the current USGS Alaskan hydrologic network, reduce or eliminate the risk to personnel during extreme events, and provide a better understanding of water fluxes in currently ungaged watersheds.

2 STUDY SITES

We visited five study sites located between Anchorage and Fairbanks, Alaska: the Chena, Knik, Matanuska, and Salcha Rivers and Montana Creek, (Figure 1). Each site was spanned by a bridge in close proximity to a USGS streamgage. These sites were selected to encompass a range of widths, depths, and discharges (Table 1). Discharge, width, average depth, and water temperature were measured with an ADCP.

We collected velocity measurements at the study sites between September 18 and 20, 2016. The mean daily air temperature was approximately 10° C. The days were relatively calm so we do not believe wind substantially affected our surface-velocity measurements. With the exception of the Salcha River, we collected measurements from pedestrian bridges or former bridge sites to avoid vehicular traffic and optimize safety.

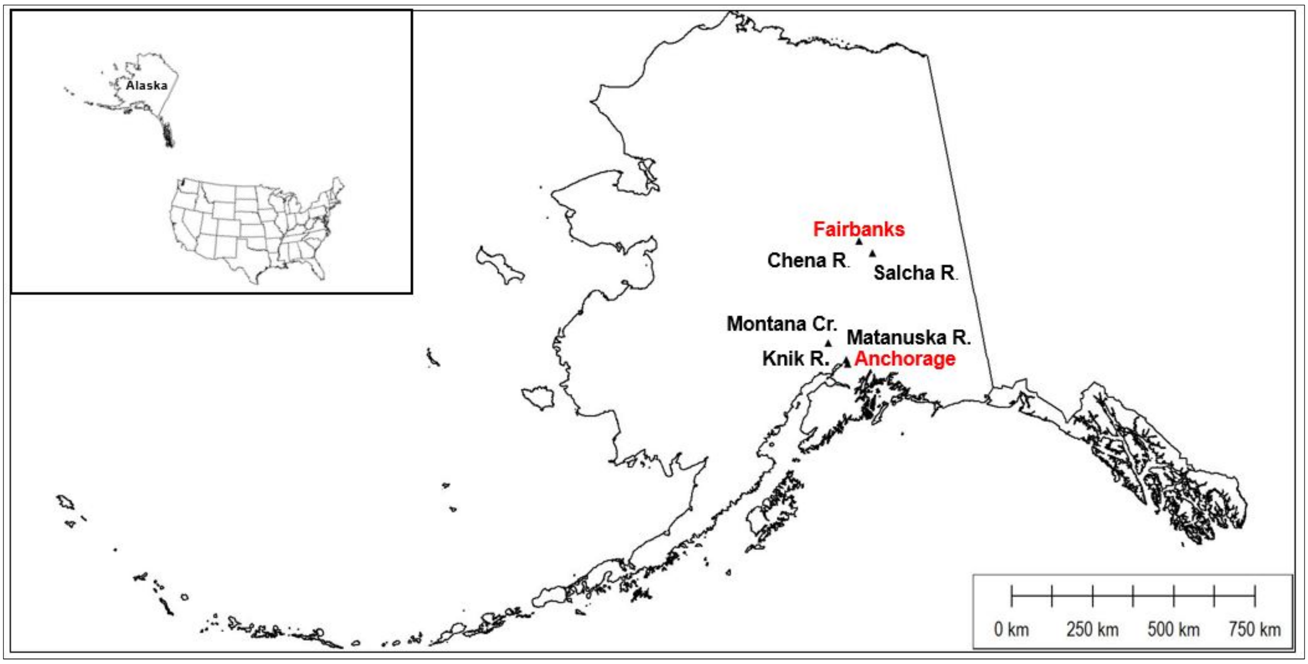

Figure 1.Map showing the location of study sites.

Table 1. Site characteristics at the time of infrared video collection.

	CHENA R.	KNIK R.	MATANUSKA R.	MONTANA CR.	SALCHA R.
Q (cms)	96	338	175	17	87
Width (m)	54	123	92	24	90
Avg. Depth (m)	1.9	2.8	1.5	0.8	1.3
Water Temperature (°C)	5.6	3.7	6.1	10.4	6.3

3 FIELD METHODS

3.1 Infrared Video Collection

Time series of infrared images were collected with a FLIR SC8340 medium wavelength infrared camera. The camera has an Indium Antimonide (InSb) detector sensitive in the 3 to 5 micron wavelength, a resolution of 1280 x 720 pixels, a sensitivity or Noise Equivalent Temperature Difference (NETD) of < 25 milli-Kelvin, and can capture up to 47 frames per second. The camera was operated from a laptop computer using FLIR's ResearchIR™ software, which allowed us to specify the dimensions of the captured image, frame rate, and duration of acquisition. The software also provides the user real-time output from the camera through a Gigabit Ethernet connection. We modified the appearance of the imagery in the ResearchIR™ software by adjusting the range of temperatures displayed to ensure that the imagery was captured with adequate sensitivity to identify signal and that the thermal signal of interest could be distinguished from background and instrumental noise. For our application, we did not require the accurate absolute water temperature but rather only sufficient contrast in the amount of radiation emitted from the water surface to detect the motion of thermal features.

The camera was positioned over the bridge railings with a jib crane, tripod, and dolly (Figure 2). Counter weights on the jib crane balanced the weight of the camera and improved the stability of the assembly. Additionally, we attached safety straps from the camera and dolly to the bridge railing. We generally moved the camera in fixed increments across each bridge to collect data from a number of equally spaced measuring stations. However, in some cases obstructions along the rail forced us to alter the positioning. The camera was inclined at approximately 77° to prevent portions of the bridge from appearing in the images and to reduce the amount of near-field thermal energy reflected into the detector, which we had observed to produce artifacts when acquiring imagery in the laboratory. A 25-mm focal length lens mounted to the camera body provided a field of view of 41.2° x 24.8°. To measure the distance from the camera lens to the water surface at each station we lowered a weight attached to the end of a graduated fiberglass tape. We used these distance measurements to compute the horizontal and vertical dimensions of the field of view for that station. Imagery was collected at 10 frames per second for one minute at each station and saved to the laptop computer in FLIR's ats file format.

Figure 2.Photograph showing infrared camera positioned on a bridge over the Salcha River.

3.2 ADCP and Radar Data Collection

At each site we made coincident measurements of river discharge, velocity, temperature, and bathymetry using ADCPs (Turnipseed and Sauer, 2010). For the Knik River and Montana Creek a remote controlled ADCP boat with GPS was used. At the Matanuska River, a crane and winch was used to lower an ADCP trimaran at each station. For the Chena and Salcha Rivers, the ADCP was towed behind a kayak. In addition, a Stalker Pro II SVR™ handheld radar gun was used to measure surface velocity parallel to the streamlines at each station across each bridge. The radar gun operates in the 34.7 GHz (Ka band) range, has a beam width of 12° +/- 1°, and can measure between 0.2 m/s and 18 m/s with an accuracy of +/- 0.1 m/s. The radar gun automatically compensates for tilt of the sensor when collecting a velocity measurement.

4 VELOCITY COMPUTATIONS

4.1 Image Processing

The raw FLIR ats video file collected for each station was exported from ResearchIR™ as a time series of images. Each image was de-trended in MATLAB™ (Mathworks, 2016) by subtracting the time-averaged mean of the image time series. The images were smoothed with a Wiener filter and a uniform contrast stretch applied. The resulting images were scaled between 0 and 1 and exported from MATLAB™ as *.jpg files. This process removed vertical and horizontal lines present in the images that spanned a relatively small range of temperatures, 2-3 degrees Celsius.

4.2 Particle Image Velocimetry

Particle Image Velocimetry (PIV) has been used for decades to compute the displacement of individual particles or tracers in both laboratory and field studies. For a comprehensive discussion and treatment of the technique, the reader is referred to Raffel et al. (2007). In our application, the thermal features are not particles *per say*, but cross-correlation algorithms used in PIV software can detect the advection of these features from one frame to the next and thus compute their displacement. We selected a commercial PIV software, PIVview™ (PivTech GmbH, 2015), to measure the movement of thermal features in the processed image sequences. As a check of our PIVview computations, a freely available PIV software, PIVlab, was used and produced similar results (Thielicke and Stamhuis, 2014). Selection of the interrogation window in PIV is important because this parameter sets the spatial dimensions over which the cross correlation is computed. Since the images were 1280 by 720 pixels, we selected a window size of 512 by 512 pixels. For the bridge heights in this study, this window size was large enough to capture the surface features we observed. The step size parameter defines the spatial dimensions of the sampling. In other words, the step values produce the mesh size or resolution of the velocity vectors resulting from the PIV calculations. We selected a step size of one half the window size in the vertical, 256 pixels, to produce a single vector in the stream-wise direction and a step size of 16 pixels in the horizontal to produce 49 pixel displacement vectors in the cross-stream direction (Figure 3). Once the displacement in pixels between successive frames was calculated for all 599 image pairs in the sequence, the result time was averaged to provide a mean displacement. To convert pixel displacements to velocity we used the frame rate and the pixel dimensions determined from the field of view of the camera lens and the distance to the water surface at each station. Although the camera was slightly inclined from vertical, we verified in the laboratory that this small difference produced a small effect on the scaling at these distances. Therefore, the results reported herein do not account for perspective distortion. The velocities for each station were averaged across the bridge to provide a single mean surface-velocity measurement for each river (Table 2).

4.3 ADCP Processing

In cases where a GPS was integrated with the ADCP (Knik River and Montana Creek), we were able to average multiple passes and determine a depth-averaged velocity that corresponded with the location of our infrared video and radar collection stations. For the Matanuska River, the ADCP was lowered by a crane at each station and a velocity profile was sampled explicitly. The ADCP used on the Chena and Salcha Rivers was towed behind a kayak and we had to use the bottom track feature of the ADCP to average passes and calculate a depth-averaged velocity for each station. However, since ADCPs do not sample at the water surface, in order to compare these measurements with infrared PIV, we had to use a method to compute surface velocity from the ADCP ensembles. We used the USGS program extrap (Mueller, 2013) developed for moving-boat ADCP measurements that processes multiple passes to determine a normalized profile and automatically selects an appropriate extrapolation method. The output permits the user to visualize the computed fit and adjust it if necessary. In this study, we used extrap to fit a power function to the normalized ADCP profile to relate depth-averaged velocity and the surface velocity (Figure 4). The ratio of depth-averaged velocity (U_d) to the surface velocity (U_s) is the velocity index (k) (Table 2).

Table 2. Mean velocity for each measurement type and velocity index (k).

	Chena R.	**Knik R.**	**Matanuska R.**	**Montana Creek**	**Salcha R.**
$PIV_{surface}$ (m/s)	0.96	1.04	1.42	0.97	0.79
$Radar_{surface}$ (m/s)	0.92	0.98	1.3	0.98	0.85
$ADCP_{surface}$ (m/s)	0.95	1.15	1.49	0.98	0.81
$ADCP_{depth\ avg.}$ (m/s)	0.78	1.06	1.33	0.82	0.67
Velocity Index	0.82	0.92	0.89	0.84	0.83

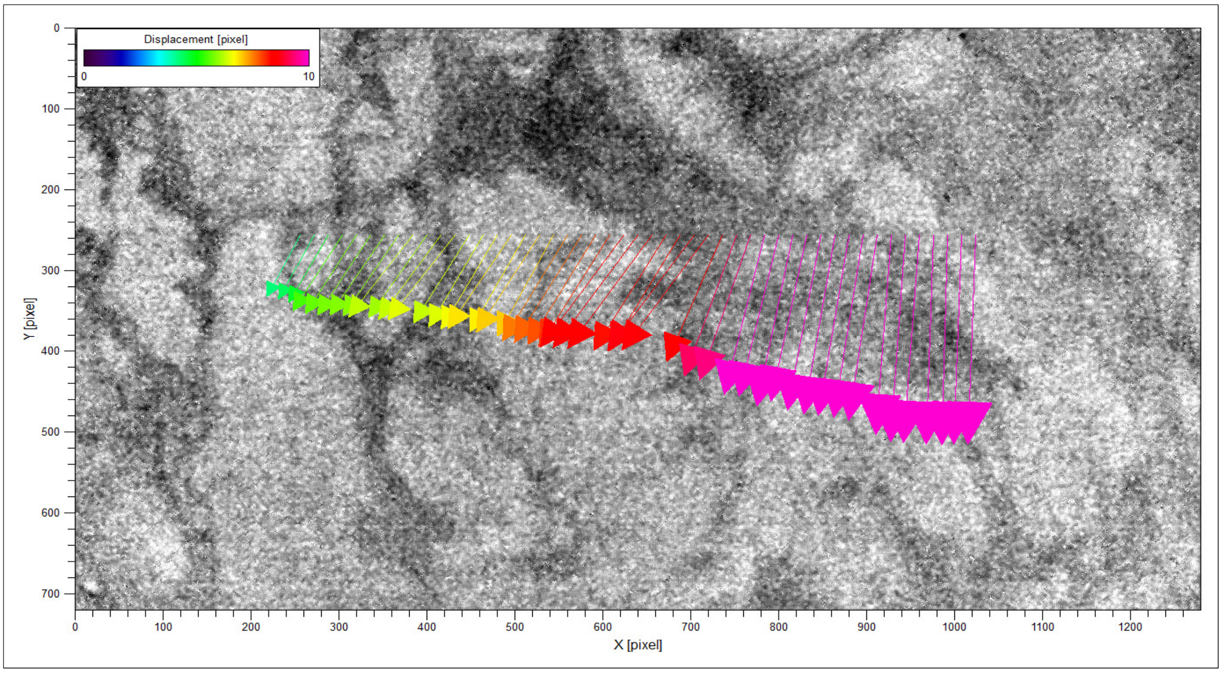

Figure 3. Infrared image overlain with vectors showing the magnitude and direction of pixel displacement at the Chena River station 4 meters from the right bank. For emphasis, the vector length is exaggerated by a factor of 20.

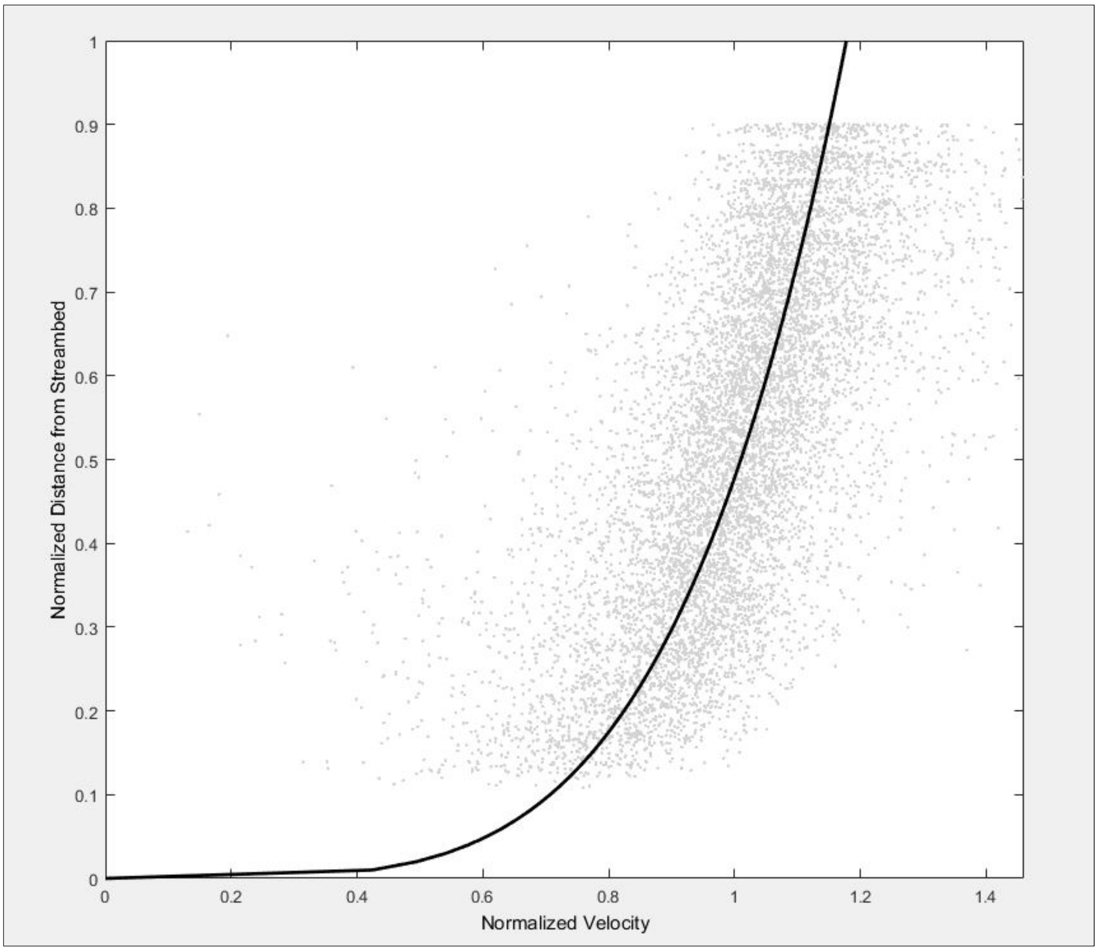

Figure 4. Screen capture of the extrap program output applied to Chena River ADCP velocity measurements. Gray dots are the cell values and the black line is the automatic fit generated by the program. The fit is a power law with an exponent of 0.22.

5 DISCUSSION

Non-contact methods to measure surface velocity with an active sensor (radar) and a passive sensor (infrared PIV) yielded similar values when comparing individual stations across the channel (Figure 5) and averaged velocities (Table 2). However, at stations near the river banks the radar gun reported slightly higher velocities whereas those in the center of the channel tended to be lower than the corresponding PIV velocity. These differences may be due to calibration of the instrument and/ or its inherently limited accuracy (+/- 0.1 m/s). A closer examination of stations near the river banks revealed that gradients in surface velocity can be resolved with the infrared PIV methodology (Figure 3). These gradients arise from shear along the banks. These locations may not have been sampled effectively by the radar due to its narrow beam width. Alternatively, the near bank velocities might have been below the radar gun's lower limit of detection (0.2 m/s).

ADCPs have become an established and pervasive technology for streamflow measurement by the USGS, with established protocols for field deployment, quality control, data processing, and reporting. The versatility of ADCPs is demonstrated in this study, as we collected data from a variety of floating or motorized platforms and from bridges where necessary. For comparison to infrared PIV one could argue that a preferable *in situ* instrument would be an electromagnetic current meter as used by Puleo et al. (2012), or a series of acoustic Doppler velocimeter (ADV) point measurements. For this proof of concept experiment, we used ADCPs as they are a common instrument for streamgaging in Alaska. It would also have been considerably more challenging to collect point measurements either from bridge decks or boats. Although beyond the scope of this paper, ADCPs provided a measurement of channel bathymetry and thus cross-sectional area that could be incorporated with the infrared PIV-derived surface velocity and velocity index to estimate river discharge.

As mentioned previously, ADCPs cannot measure the surface velocity directly and also have difficulties measuring near the river bottom because of side-lobe interference. Additionally, shallow depths prevent valid measurements at the banks. Thus, the contribution of the top and bottom portions of the velocity profile to the flow, in addition of that near the banks, must be accounted for in the ADCP software. Typically, the distance from the ADCP to the bank is measured and the discharge in those cells is computed by selecting an appropriate method. To compute the top and bottom contributions to the total discharge, a variety of methods can be used. For the purposes of this paper, we will focus on the top contribution to the velocity profile and discharge. The flow disturbance from the instrument and a time delay between when the ADCP transducer generates an acoustic signal and when that signal can be received results in a blanking distance. To account for the flow in this region the velocity profile can be extrapolated in ADCP software using a constant, power, or 3-point slope method (Teledyne RDI Instruments, 2015).

The extrap program offers an automatic procedure to determine, based on the data, an appropriate method for this kind of extrapolation. For the Chena River ADCP measurements, the extrap best fit was determined to be a power law with an exponent of 0.221. The normalized plot shown in Figure 4 represents the normalized velocity profile fit with a power law. The surface velocity (U_s) is 1.22 times the depth-averaged velocity (U_d). This provides a velocity index of $k = U_d/U_s = 1/1.22 = 0.82$. Figure 6 compares the infrared PIV surface velocity to the surface velocity extrapolated from the depth-averaged velocity measured by the ADCP. In the center of the channel, the ADCP velocity index exceeds the infrared PIV measurements. These results may indicate that a power law may not provide the best method to extrapolate the surface velocity. While one velocity index was used across all stations herein, alternatively velocity profiles collected at each station to produce a station specific velocity index may provide better agreement across a section.

A velocity index of 0.85 is often used for open channels (Costa et al., 2000; Creutin et al., 2003; Muste et al., 2008) but bed and bank roughness can influence the velocity profile. Wind shear at the water surface also can affect the shape of the profile near the surface (Mueller, 2013). The extrap power law velocity profile fits computed velocity index values that ranged from 0.82 to 0.92. The lowest index was found on the Chena River, 0.82. Both the Salcha River and Montana Creek were best fit with a standard 1/6 power law. The Knik River produced the highest velocity index (0.92). While this would not seem surprising considering both the thermal PIV surface velocity and the depth-averaged velocity were nearly identical, this site does represent the most deviation from the accepted 0.85 value of k. Velocity indexes of this magnitude (0.9 to 1.05) were determined for in-channel flows on the Blackwater River, however, this is a small (5.75-m width, 0.75-m depth) sinuous river (Sun et al., 2010). To investigate if this measurement was an anomaly, we used extrap to process the last 5 water years of direct discharge measurements from the Knik River streamgage collected between 5/1/12 and 10/3/16 (Figure 7). These 30 measurements had a mean velocity index of 0.88, a minimum of 0.84, and a maximum of 0.95. They were collected at discharges ranging from 66 to 1500 m^3/s. The velocity index showed a very weak positive correlation with discharge and little statistical significance, 0.47 correlation coefficient.

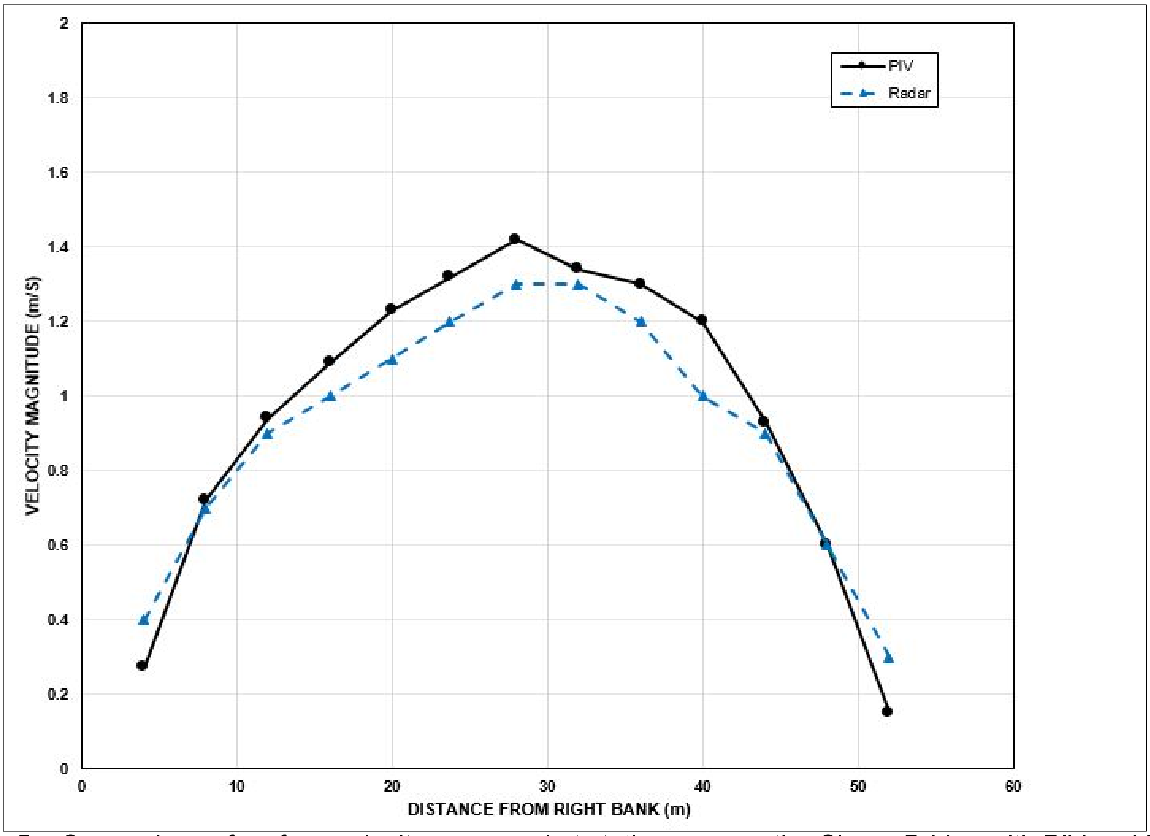

Figure 5. Comparison of surface velocity measured at stations across the Chena Bridge with PIV and Radar.

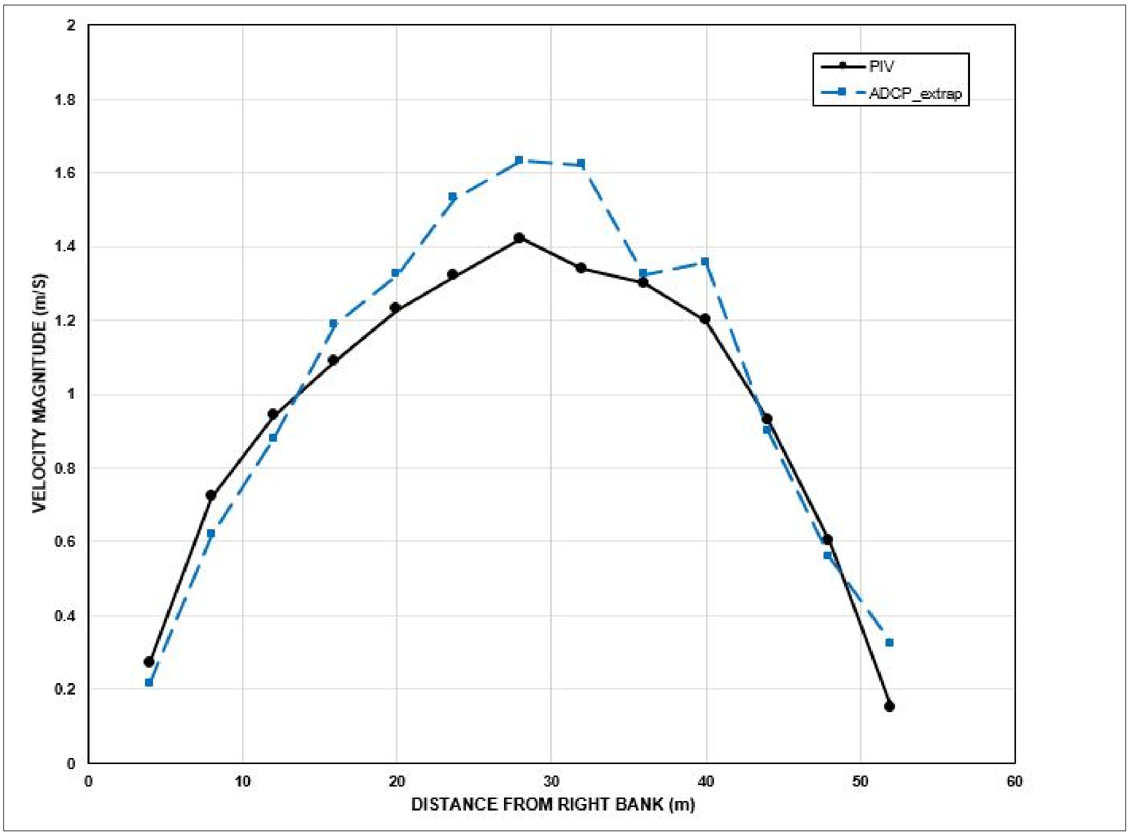

Figure 6. Comparison of surface velocity measured at stations across the Chena Bridge with PIV and surface velocity from an ADCP using automatic extrapolation from the extrap program and k = 0.82.

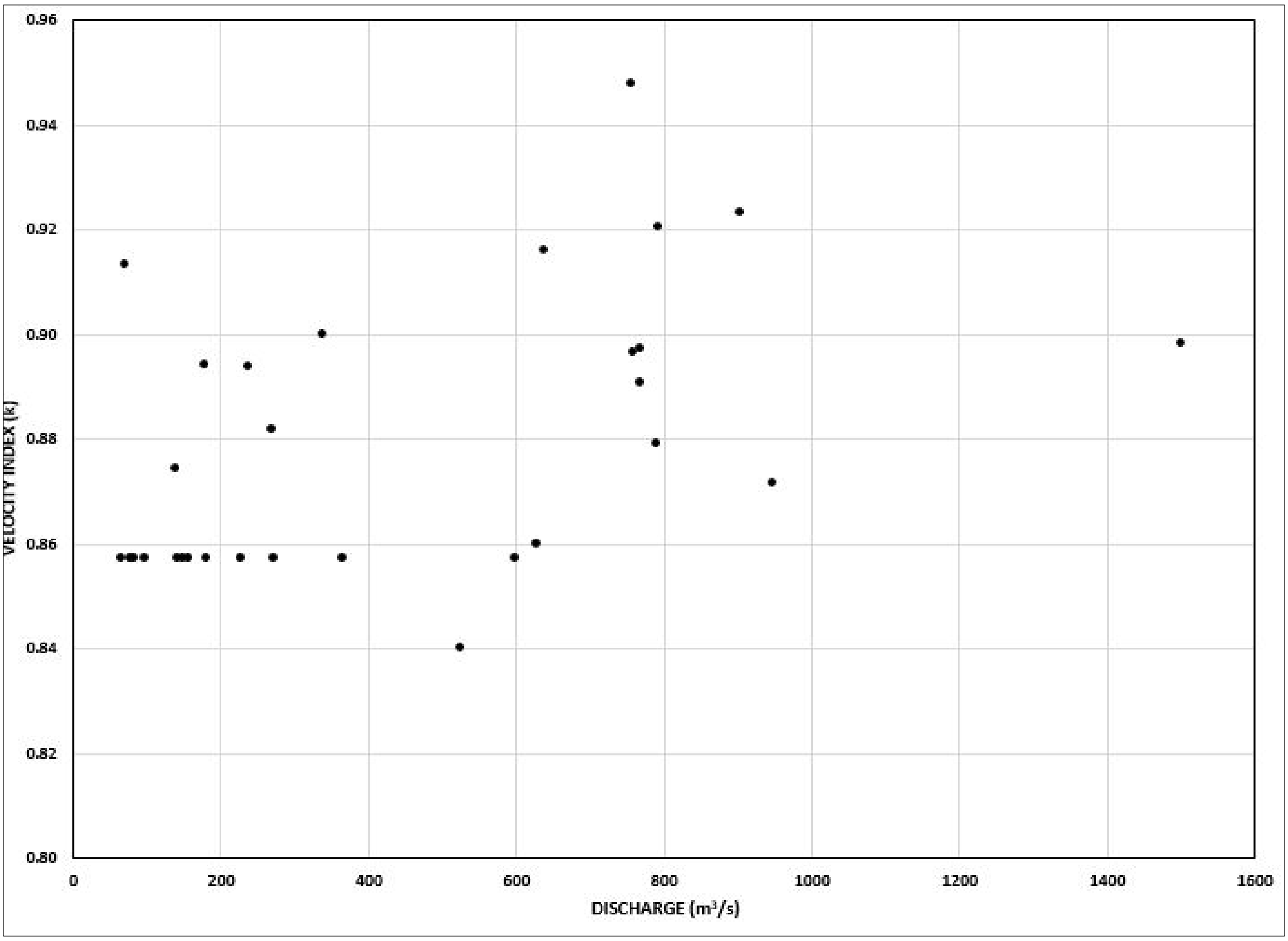

Figure 7. ADCP discharge measurements and associated k values computed with the extrap program for the Knik River collected between 5/1/12 and 10/3/16.

6 CONCLUSIONS

In this paper we describe a methodology used to collect thermal imagery and compute remote measurements of surface velocity using PIV for five rivers in Alaska. In all the rivers, the average radar surface velocity was similar to the value determined with PIV (within 10%). The extrap software program was used to automatically extrapolate a normalized ADCP velocity profile to a surface velocity. We found these surface-velocity extrapolations also to be within 10% of surface velocities measured with thermal PIV. The velocity index determined from ADCP measurements varied among sites (0.82 - 0.92). As a first attempt to quantify the variation of velocity indices at a single streamgage, we extrapolated a time series of 30 ADCP measurements collected at the Knik River and obtained velocity indices ranging from 0.84 to 0.95. An analysis of this type could provide a statistical justification for selecting a particular velocity index and also quantify potential error bounds. Further research to determine the best method for determining the velocity index is warranted, as k is a critical parameter for transforming a surface velocity collected either from radar, LSPIV, or infrared PIV to a depth-averaged value necessary for computing an accurate discharge.

When used in conjunction with PIV, infrared imaging provides a detailed depiction of surface velocity and has the advantage of being able to be collected during the day or night without the need for tracers. Moreover, infrared PIV might provide a mean to compute turbulent length scales and infer bottom structure. If deployed on a larger scale, infrared PIV could also be used to identify lateral separation zones in rivers that can influence sediment storage and aquatic habitat. If accurately calibrated, thermal images can quantify surface temperature which might be of ecological importance or used to identify locations of riparian seeps. The field effort described herein was performed as a proof of concept and a first step toward deploying the methodology from manned and unmanned aerial platforms. This proof-of-concept experiment also demonstrated a potential component of a complete methodology for computing river discharge using only remote sensing methods.

7 DISCLAIMER

Any use of trade, firm or product name is for descriptive purposes only and does not imply endorsement by the United States Government.

ACKNOWLEDGMENTS

The authors would like to thank Robin Beebee, Heather Best, and Karenth Dworsky (USGS Alaska Science Center) for assistance with ADCP measurements collected at the field sites. John Fulton (USGS Colorado Water Science Center) kindly allowed us to borrow his radar gun for this experiment. Funding for this project was provided by the USGS Water Mission Area.

REFERENCES

Alaska Department of Fish & Game. (2017). *http://www.adfg.alaska.gov/index.cfm?adfg=rivers.main* (Accessed March 31, 2017).

Chickadel, C., Horner-Devine, A.R., Talke, S.A. & Jessup, A.T. (2009). Vertical Boil Propagation from a Submerged Estuarine Sill. *Geophysical Research Letters*, 36, 1-6.

Costa, J. E., Spicer, K.R., Cheng, R.T., Haeni, F.P., Melcher, N. B., Thurman, E. M., Plant, W. J. & Keller, W.C. (2000). Measuring Stream Discharge by Non-Contact Methods: A Proof-of-Concept Experiment. *Geophysical Research Letters*, 27(4), 553– 556.

Creutin, J.D., Muste, M., Bradley, A.A., Kim, S.C. & Kruger A. (2003). River Gauging using PIV Technique: Proof of Concept Experiment on the Iowa River. *Journal of Hydrology*, 277 (3-4), 182-194.

Dugan, J.P., Anderson, S.P., Piotrowski, C.C. & Zuckerman, S.B. (2014). Airborne Infrared Remote Sensing of Riverine Currents. *IEEE Transactions on Geoscience and Remote Sensing*, 52(7), 3895-3907.

Fujita, I. & Komura, S. (1994). Application of Video Image Analysis for Measurement of Riverine Surface Flows. *Proceedings in Hydraulic Engineering, JSCE,* 38, 733-738. (In Japanese).

Helmle, C.S. (2005). A Quantitative Thermal Imaging Technique to Extract a Cross-Stream Velocity Profile from a Flowing Body of Water, *M.S. thesis*, Cornell Univ., Ithaca, N.Y. 69.

Kammerer, J.C. (1990). *Largest Rivers in the United States*, USGS Open-File Report 87-242. 2.

Kinzel, P.J., Legleiter, C.J., Overstreet, B., Hooper, B., Vierra, K., Nelson, J.M. & Zuckerman, S. (2012). Comparison of Acoustic and Remotely Sensed Bathymetry and Flow Velocity at a River Channel Confluence. *ASCE Hydraulic Methods and Experimental Methods Conference*, Snowbird Utah, 7.

Mathworks (2016). *MATLAB,Version 2016a*, Natick, Massachusetts.

Melcher, N.B., Costa, J.E., Haeni, F.P., Cheng, R.T., Thurman, E.M., Buursink, M., Spicer, K.R., Hayes, E., Plant, W.J., Keller, W.C. & Hayes, K. (2002). River Discharge Measurements by using Helicopter-Mounted Radar. *Geophysical Research Letter*, 29(22), 1-4.

Mueller, D.S. (2013). extrap: Software to Assist the Selection of Extrapolation Methods for Moving-Boat ADCP Streamflow Measurements. *Computers & Geosciences*, 54, 211–218.

Muste, M.I., Fujita, I. & Hauet, A. (2008). Large-Scale Particle Image Velocimetry for Measurements in Riverine Environments. *Water Resources Research*, 44(4), 1-14.

Nelson, J.M., Kinzel, P.J., McDonald, R.R. & Schmeeckle, M.W. (2016a). *Noncontact Methods for Measuring Water-Surface Elevations and Velocities in Rivers: Implications for Depth and Discharge Extraction, in Riverflow 2016*, Constantinescu, Garcia, and Hanes, eds., Taylor and Francis, London, 637-645.

Nelson, J.M., Kinzel, P.J., Schmeeckle, M.W., McDonald, R.R. & Minear, J.T. (2016b). Field and Laboratory Measurements of Water-Surface Elevation and Velocity using Remote Sensing. *Proceedings IAHR Meeting*, Colombo, Sri Lanka, 8 pp.

PivTec GmbH (2015). *PIVview 2C/3C User Manual Version 3.6¸* Göttingen, Germany, 1-93.

Puleo, J.A., McKenna, T.E., Holland, K.T. & Calantoni, J. (2012). Quantifying Riverine Surface Currents from Time Sequences of Thermal Infrared Imagery. *Water Resources Research*, 48(1), 1-20.

Raffel, M., Willert, C., Wereley, S. & Kompenhans, J. (2007). *Particle Image Velocimetry a Practical Guide*, Springer-Verlag Berlin Heidelberg, 2nd ed., 1-448.

Spicer, K.R., Costa, J.E. & Placzek, G. (1997). Measuring Flood Discharge in Unstable Stream Channels using Ground-Penetrating Radar. *Geology*, 25(5), 423-426.

Sun, X., Shiono, K., Chandler, J.H., Rameshwaran, P., Sellin, R.H. & Fujita, I. (2010). Discharge Estimation in a Small Irregular River using LSPIV. *Water Management*, 163(5), 247-254.

Teledyne RDI Instruments, (2015). *WinRiver II Software User's Guide*, Teledyne RD Instruments, 1-304.

Thielicke, W. & Stamhuis, E.J. (2014). PIVlab – Towards User-friendly, Affordable and Accurate Digital Particle Image Velocimetry in MATLAB. *Journal of Open Research Software*, 2(1):e30.

Turnipseed, D.P. & Sauer, V.B. (2010). *Discharge Measurements at Gaging Stations*, U.S. Geological Survey Techniques and Methods, book 3, Chap. A8, 1-87.

USGS (2017*). Distribution of Stream Gaging Stations*, United States Geological Survey. *http://waterdata.usgs.gov/ak/nwis/current/?type=flow* (Accessed March 31, 2017).

EXPERIMENTAL INVESTIGATION ON CORRELATION BETWEEN THE BREAKDOWN VOLTAGE OF CAPACITANCE AND THE SIZE OF A SPARK-INDUCED CAVITATION BUBBLE

YILAN LI[1]

[1] State Key Laboratory of Hydraulics and Mountain River Engineering, Sichuan University, Chengdu,China
christina_caffrey@163.com

ABSTRACT

In the study of cavitation bubble and the judgment of whether cavitation occurs on the solid boundary, relative distance that bubbles away from the boundary (compared to the radius) matters. It also has an important role to play when the research is related to two-bubble system. Sparked-induced cavitation bubble is one of the most widely used methods to generate cavitation bubble. However, so far the size of bubble produced by electric spark is undecided and uncontrolled. Therefore, it is of great significance to try to find a way to control the size of cavitation bubble. First and foremost, it is imperative to find the factors that affect its size. This paper investigates the relation between the breakdown voltage of capacitance and the size of cavitation bubble via high-speed photography. We changed breakdown voltage by adjusting the air-spherical gap. The biggest radius of spark-induced cavitation bubble (R_C) was used to clarify the size of the bubble. The results shows linear functional relation between the breakdown voltage of capacitance and maximum radius of the bubble to a certain extent and beyond a certain voltage value, the relation no longer follows the function we just concluded.

Keywords: Cavitation bubble; spark-induced; maximum radius; breakdown voltage.

1 INTRODUCTION

The research into the collapse behavior of cavitation bubbles is of great importance. It can be employed to analyze a lot of industrial areas like erosion, vibration and noise in turbo machineries and hydraulic systems as undesirable influences, while the upside of cavitation bubbles is mainly in cilinical areas like surface cleaning, droplet ejector, clinical therapy and drug/gene delivery. About 100 years ago, Lord Rayleigh started the theoretical research in bubble dynamics. Later, Rayleigh-Plesset equation is put forward to estimate the dynamics of a single cavitation bubble. Due to the limitation of technology, it is difficult to observe the details of bubble collapsed. With the appearance of high-speed camera, we are able to observe more details of bubble dynamics.

One of the most significant discovery is a liquid jet towards the surface caused by a single oscillating bubble near a rigid surface. Further studies on more complex systems have been carried out, such as two-bubble system, bubble-air bubble-boundary system and so on. Fong et al. did some research on the interaction of two similarly sized bubbles in a free field. However, considering to describe the interaction between two differently sized bubbles in a free field, it was Chew et al. who investigated it. Bai et al. studied the influence of air bubble and the influence of boundary combined. In all of these research, the size of bubble or relative distance plays an important part. Therefore, it is of great significance to find a way to control the size of bubbles. And it is useful and valuable to investigate the factors affecting bubble size. In this article, we discuss the correlation between cavitation bubble size and breakdown voltage of capacitance.

2 STUDY METHODS

The laboratory experiments have been conducted at the State Key Laboratory of Hydraulics and Mountain River Engineering in Sichuan University (China). As shown in Figure 1, the experimental device is composed of electric spark cavitation bubble generation system, illumination system, voltage collection system and high-speed camera recording system.

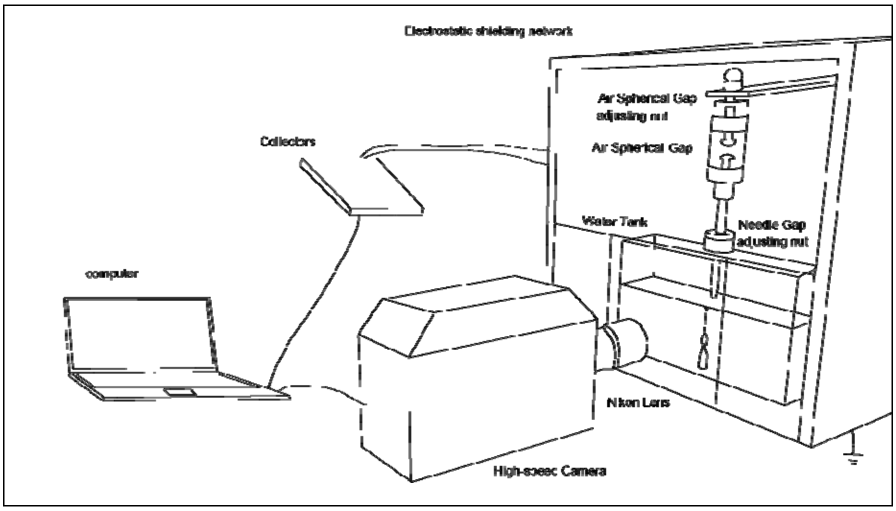

Figure 1. Sketch of experimental apparatus consisting of electric spark cavitation bubble generation system, illumination system, voltage collection system and high-speed camera recording system.

Among them, the electric spark cavitation bubble system used is a device invented by State Key Laboratory of Hydraulics and Mountain River Engineering in Sichuan University: An Experiment Device Generating Electric Spark (application number: 201610310914.7). Its circuit principle is shown in Figure 2, and the parameter of electric components is labeled. The basic principle to conduct cavitation bubble is instant short circuit and capacitance discharge simultaneously.

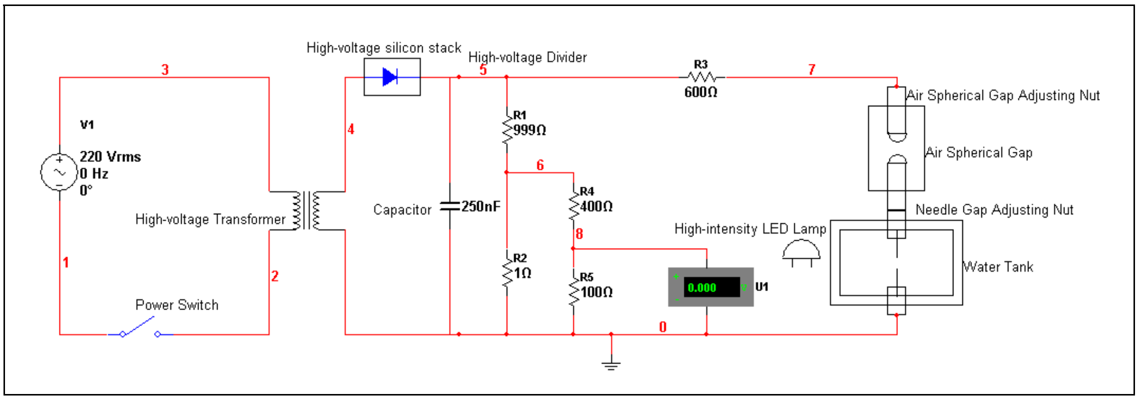

Figure 2. Electric circuit of An Experiment Device Generating Electric Spark.

Water tank filled with deionized water (400mm×200mm×80mm) is where cavitation bubbles occur and are observed. Because of the short exposure time and high speed in taking photographs, a high-intensity LED lamp is needed to provide light when taking photographs. The voltage collection system is a collector (USB3202) provided by art-control, whose main parameter is listed in Table1. In this experiment, we only use two channels to collect the voltages across the capacitance to get the breakdown voltage and voltage after discharging. A software in the computer was provided to display the voltage data and waveform collected. The collector was used at 50,000sps, the total number of samples was 100,000, and the range of the voltage was ±5V. Last but not least, the high-speed camera recording system consists of a high-speed camera (Photron FASTCAM SA-Z) and a micro-lens (Nikkor Lens 17-35mm f/2.8D IF-ED). The record rate and shutter speed of high-speed camera were set at 100000fps and 1/119149s, respectively.

Table1. Main parameters of collector.

Model of collector	USB3202
Maximum sampling frequency	250Ksps
AD accuracy	16-bit
Input Channels	8 channels (RSE, NRSE) 4 channels (DIFF)
AD Cache	4K point FIFO
AD range	± 10V, ± 5V, 0 ~ 10V, 0 ~ 5V

Since the collecting time of both high-speed camera and collectors are extremely short, it is significant to make sure that the collection process and generating spark-induced cavitation bubble process happens almost simulataneously. To avoid capacitance charging incompletely before discharging, generating on bubble once is necessary. During the experiment, the change of breakdown voltage follows the change of air spherical gap. And we repeated the experiment five times before adjusting the gap. Air spherical gap was changed by turning adjusting nut every quarter of a circle each turn. As its pitch is 1mm, the air spherical gap reduces 0.25mm each time. Our experiment focused on the correlation between breakdown voltage and the maximum radius of cavitation bubble. Therefore, the accurate length of the gap is irrelevant. Room temperature was maintained at 298.15K±2K under atmospheric pressure of p=101.5kPa, while doing experiments. The magnification factor and focal length were stable while doing experiments. Consequently, the unit length of each picture were unchanged, too. After setting all the parameters, we took a picture with a transparent ruler putting on the flat surface while taking the photographs afterwards. So, we can calculate using the length that each pixel represented and get all other lengths through the number of pixels.

3 CORRELATION BETWEEN BREAKDOWN VOLTAGE AND MAXIMUM RADIUS OF CAVITATION BUBBLE

3.1 Determination of the maximum radius

Cavitation bubbles generated under different breakdown voltage are presented in Fig.3. Under each voltage, we pick up only some photos among all the photos being taken in the whole process to see the process of generating cavitation bubble and its collapse. The very photo used as the maximum radius is not deliberately shown in the photos. The three cavitation bubbles were generated under the breakdown voltage of 21.83988kV, 17.50366kV, 9.755kV, and their maximum radius are 5.528356×10^{-2}m, 4.944463×10^{-2}m, 3.391553×10^{-2}m, respectively.

The way to get maximum radius is to choose the biggest bubble from the picture and to use the average diameter of major axes and minor axes as final maximum diameter in case that not all bubbles are perfectly round(Fig.3). Maximum radius is easily obtained.

$$Rc = \overline{D_C}/2 \qquad [1]$$

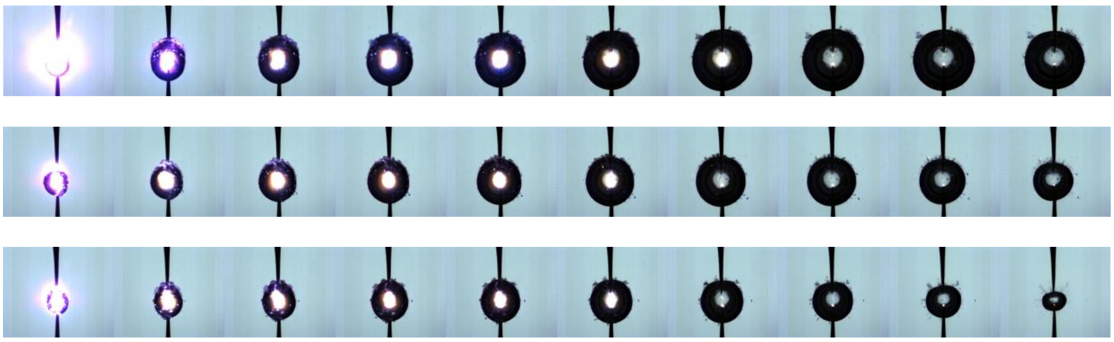

Figure3. The process of bubbles evolving under different voltage((a), (b), (c) are bubbles generated respectively under the breakdown voltage of 21.83988kV, 17.50366kV, 9.755kV; their maximum radius are 5.528356×10^{-2}m, 4.944463×10^{-2}m, 3.391553×10^{-2}m).

3.2 Determination of breakdown voltage

As depicted in Figure 4, the discharging process of capacitance is extremely short, but the time range of charging process varies. Moreover, the data collected by collectors is inevitably affected by electromagnetic noise causing apparent fluctuation. To unify the criterion and avoid the influence of electromagnetic noise, we choose the right voltage before the radius approaches zero and is approximate to the former ones as the start point(suppose it is No.j statistical point), and averages the former 20 statistic as the final breakdown voltage.

$$U = \sum_{j-19}^{j} U_i \Big/ 20 \qquad [2]$$

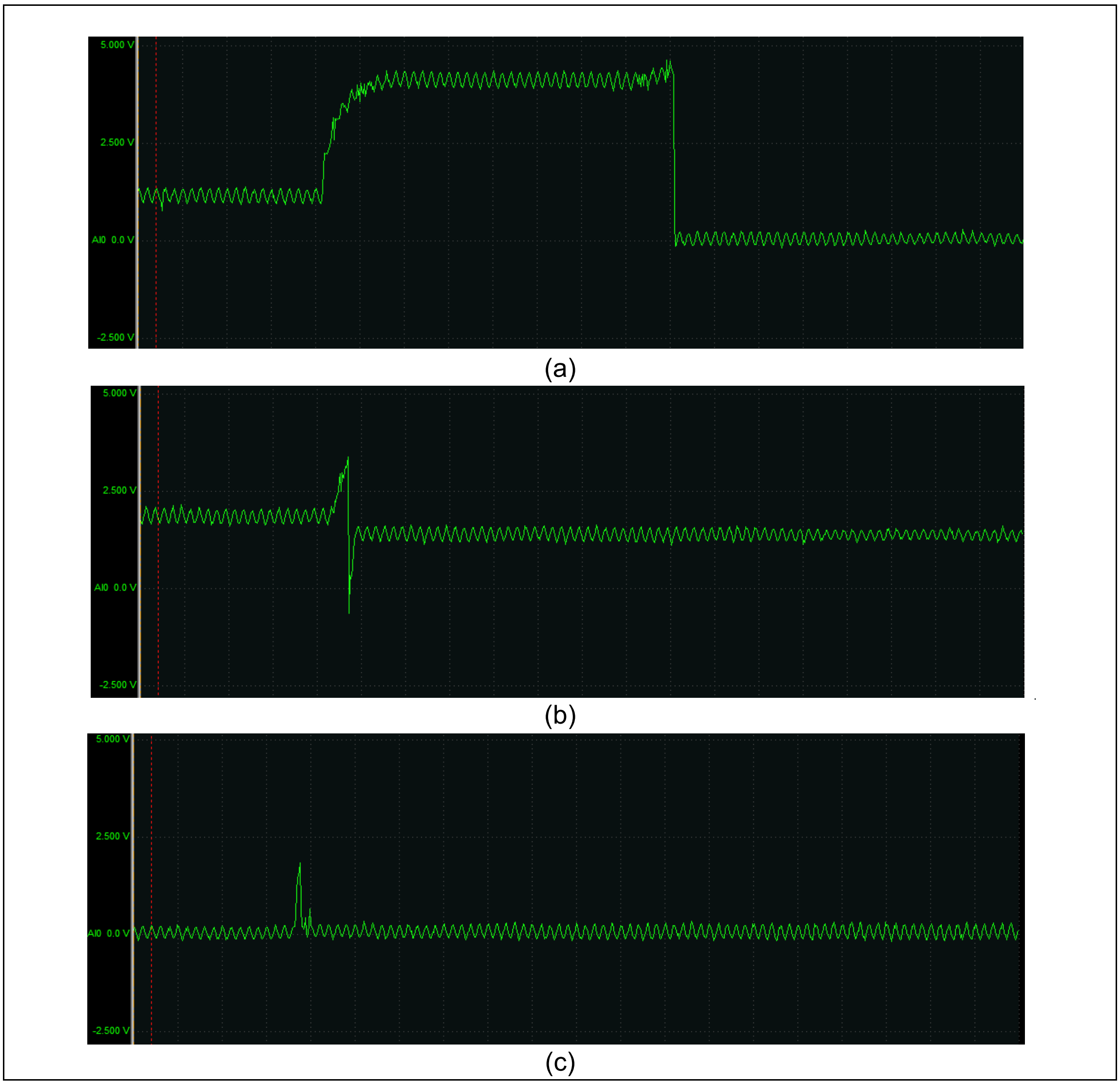

Figure 4. The waveform of capacitance charging and discharging under different voltage((a), (b), (c) are discharging respectively under the breakdown voltage of 21.83988kV, 17.50366kV, 9.755kV; the original waveform is too long to be performed in paper, the X-axis shrinks 100 times laterally in the picture).

4 RESULTS AND DISCUSSIONS

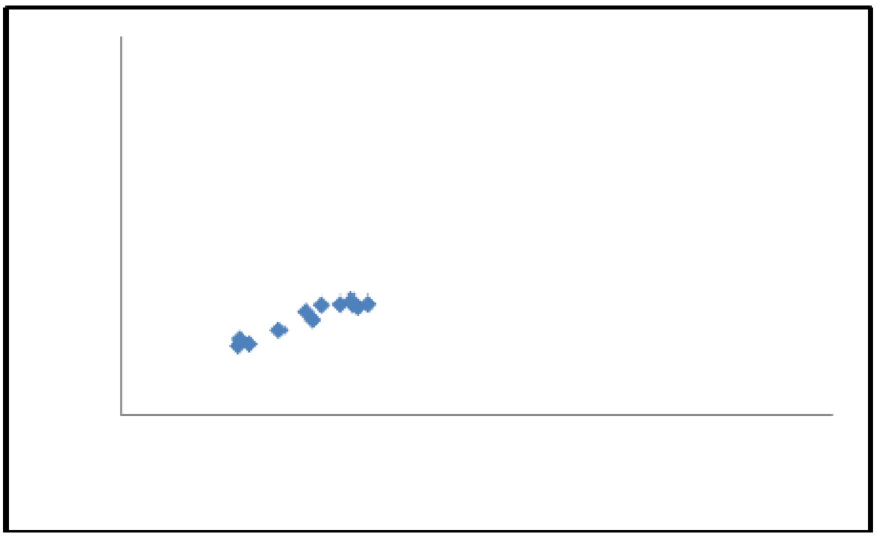

Figure 5. The bubble radius-breakdown voltage relation (R_c represent the maximum radius of cavitation bubble, U represent the breakdown voltage of capacitance.).

As shown in Fig.5 above, below 17kV, the relationship between breakdown voltage and the maximum radius is approximately linear, and the linear fitting function is

$$y=5.5799x-11.164 \quad [3]$$

From the function, it is apparent that Rc rises as U increases. We may also deduct that coefficient of primary term(λ) reflect how sensible Rc is as U changes. However, there are more influences that could affect the coefficient, like the parameter of electric components. And the x-axis interception of the linear fitting function(β) might lead to the conjecture that there is a minimum size of cavitation bubble, which is the limit of bubble size. Of course there is no way that breakdown voltage can get to zero, but there is still a chance that can make it small enough to see the trend.

However, when breakdown voltage went beyond 17kV(we may call it limited voltage), the radius oscillates as breakdown voltage increases. The linear functional regulation no longer applies when the relationship of breakdown voltage and maximum radius becomes unstable and erratic. At that time, breakdown voltage is no longer in the domain of bubble size. Possibly, the limit of radius is limited by other factors, for example the needle gap.

Further research could focus on studying other factors that I have mentioned. And it would be wonderful if the spark-induced bubble size is under control in the future.

5 CONCLUSIONS

The relation between breakdown voltage of capacitance and maximum radius of cavitation bubble was investigated using high-speed camera. Here are the conclusions, that were discovered:

i. Breakdown voltage is a factor of the size of cavitation voltage. Normally, maximum radius increases as breakdown voltage increases, but it does not increase uninhibitedly.
ii. In certain circumstances being set in this experiment, when breakdown voltage is smaller than 17kV(limited voltage), the relation between breakdown voltage and maximum size of cavitation bubble is approximately linear, the linear fitting function is $y=5.5799x-11.164$. When the breakdown voltage is more than 17kV(limited voltage), the relationship is unstable and erratic.

Acknowledgment

The author would like to extend great appreciation to the State Key Laboratory of hydraulics and mountain river engineering for the help in the use of spark-induced cavitation bubble system and high-speed photography system and providing foundation support. The funding of this research is provided by the National Basic Research Program of China (973 Program, Grant No. 2013CB035905), and the National Natural Science Foundation of China (Grant No. 51409180).

REFERENCES

Bai, L., Xu, W. & Zhang, F. (2010). Interaction of a Cavitation Bubble and an Air Bubble with a Rigid Boundary, *Journal of Hydrodynamics*, 22(4), 503-512.

Blake, J.R., Taib, B.B. & Doherty, G. (1986). Transient Cavities near Boundaries: Part 1, Rigid Boundary. *Journal of Fluid Mechanics*, 170, 479–497.

Chew, L.W., Klaseboer, E., Ohl, S.W. & Khoo, B.C. (2011). Interaction of Two Differently Sized Oscillating Bubbles in a Free Field. *Physical Review E,* 84(6), 1-11.

Fong, S.W., Adhikari, ED., Klaseboer, E. & Khoo, B.C. (2009). Interactions of Multiple Spark Generated Bubbles with Phase Differences. *Experiments in Fluids,* 46, 705–724.

Franc, J.P. & Michel, J.M. (2004). *Fundamentals of Cavitation.* Kluwer Academic Publishers, Dordrecht, 76, 306 p.

Lauterborn, W. & Kurz, T. (2010). *Physics of Bubble Oscillations*, Reports on Progress in Physics, 73(10), 88 pp.

Lauterborn, W.(1982). Cavitation Bubble Dynamics – New Tools for an Intricate Problem, *Applied Scientific Research,* 38, 165–178.

Lew, K.S.F., Klaseboer, E. & Khoo, B.C. (2007). A Collapsing Bubble-Induced Micropump: An Experimental Study, *Sensors and Actuators A: Physical,* 133(1),161–172.

Prosperetti, A. (2004) Bubbles, *Physics of Fluids*, 16(6), 1852–1865.

Rayleigh, L. (1917). On the Pressure Developed in a Liquid during the Collapse of a Spherical Cavity, *Philosophical Magazine*, 34, 94–98.

Tomita, Y., Shima, A. & Sato, K. (1990). Dynamic Behavior of 2-Laser-Induced Bubbles in Water, *Applied Physics Letters*, 57, 234–236.

Xu, C.M., Zou, J.J., Ruan, X.D. & Fu, X. (2014). Particle Removal by a Single Cavitation Bubble, *Science in China – Physics, Mechanical and Astronomy,* 57, 668–673.

Proceedings of the 37th IAHR World Congress
August 13 – 18, 2017, Kuala Lumpur, Malaysia

RAINFALL SIMULATOR AS A NONPOINT SOURCE POLLUTION RESEARCH TOOL ON TROPICAL URBAN SEALED SURFACES

MAHADI LAWAN YAKUBU[1], ZULKIFLI YUSOP[2] , MUTTAQA UBA ZANGO[3] & ABUBAKAR ABDULKARIM[4]

[1,3,4] Department of Civil Engineering, Faculty of Engineering, Kano University of Science and Technology, Wudil, Kano, Nigeria
mahadilawan@gmail.com, muttaqaubaz@yahoo.com, engineerabu01@gmail.com
[2] Institute of Environmental and Water Resources Management, Universiti Teknologi Malaysia, 81310 Skudai, Johor, Malaysia,
zulyusop@utm.my

ABSTRACT

Rainfall simulator (RS) is a specially made device that aims to replicate natural rainfall dynamics. It has been widely used in the investigation of processes associated with rainfall events, from soil erosion, soil infiltration, to recently urban wet weather processes involving nonpoint source pollution. There are few commercial suppliers of rainfall simulators, which are often too expensive. So, most researchers often fabricate their own in line with their research objectives. An RS is intended to investigate the influence of rainfall runoff in a wet-weather nonpoint source pollution on impervious urban surfaces was developed, and calibrated to ensure spatial and temporal variation of rain intensity, kinetic energy, and variation of drop size diameter, capable of replicating storms found in the tropics as closely as possible. The RS consisted of four interrelated components, the RS frame, the water system, the robotic system, and the plot. 783 measurements were carried out to evaluate the performance of the RS. The RS can remarkably achieve rain uniformity of 89%, 2.51±0.13 mm median raindrop diameter of the natural event, over 80% terminal velocity, and up to 87% kinetic energy.

Keywords: Nonpoint Source Pollution (NPS); Rain Uniformity; Raindrop Diameter; Simulator; Terminal Velocity.

1 INTRODUCTION

The success of RS lies in its ability to replicate natural rainfall as closely as possible. There is currently a dearth of comprehensive literature on temporal and spatial characteristics of simulated rainfall. Some researchers reported with the assumption that their RS was spatially and temporally uniform (e .g. Vahabi and Nikkami, 2008; Kim et al., 2010; Dunkerley, 2012; Wildhaber et al., 2012), others did not mentioned the intensity at which they operated their RS (e.g. Blanquies et al., 2003; Kim et al., 2006) or the nozzle operated pressure (Wildhaber et al., 2012) while others are silent on the RS Kinetic energy (KE) (e.g. Blanquies et al., 2003; Vahabi and Nikkami, 2008; Kim et al., 2010; Sangüesa et al., 2010; Dunkerley, 2012) and very few reported how they calculated the KE (e.g. Júnior and Siqueira, 2011; Wildhaber et al., 2012; Feng et al., 2013). This lack of comprehensive reporting has an underpinning implication of limiting knowledge in RS development. The objective of this study is to disclose a comprehensive calibration report of RS, which was conceived based on a typical tropical region's rainfall parameters.

The outstanding advantages of using RS as a research tool are the control of rainfall variables, which are innate in nature and the elimination of the need to wait for natural rainfall. Thus, it makes data collection faster and easier. RS was employed since 1930s in the study of geomorphological and pedological processes (e.g. Guevara-Escobar et al., 2007; Resso et al., 2007; Scherrer et al., 2007; Aksoy et al., 2012). However, the employment of RSs to investigate the effect of a hydrological process as they interrelate with nonpoint source (NPS) pollution on an impervious surface is only gaining attention in recent times. Among the few conducted studies that focused in the study of urban NPS on impervious surfaces were Tiefenthaler and Schiff (2003), Egodawatta et al. (2007), Brodie and Dunn (2010), Kim et al. (2010), and Júnior and Siqueira (2011). All these RSs were operated at constant intensities, and were not designed to model the sporadic fluctuation of drop size diameter within a rain intensity. Sporadic fluctuation of intensity with the drop diameter is one of the inherent characteristics of natural rainfall. And any successful rain simulation should take this into consideration. This study took further steps to widen the drop size distribution within particular rain intensity.

Operated pressure is the most important feature of pressure type RS. The pumping pressure, the type of nozzle, and the spatiality of the nozzles influence the simulated raindrop diameter, the drop size distribution, the intensity, and the KE of the RS (Corona et al., 2013). However, there are inconsistencies in the variation of pressure with other rain parameters in the literature. While others stipulate rain intensity increases with pressure (Pall et al., 1983; Júnior and Siqueira, 2011), others posit that it decreases with increase pressure (Cerdà et al., 1997; Pérez-Latorre et al., 2010). In another instance, Cerdà et al. (1997), Esteves et al. (2000), and Sangüesa et al. (2010) posit that D_{50} of the simulated rain increases with increasing pressure while others postulate otherwise (Júnior and Siqueira, 2011; Aksoy et al., 2012). These inconsistencies were mainly due to privation of RS comprehensive calibration reporting.

2 METHODOLOGY

2.1 Construction

The RS was intended to investigate the influence of rainfall runoff in a wet weather NPS pollution on impervious urban surfaces. It was designed to ensure spatial and temporal variation of rain intensity, KE and variation of drop size diameter. It is also capable to replicate storms found in the tropical regions based on the authors of this study's detailed characterisation of the rainfall dynamics of Skudai, Johor, Malaysia (Yakubu et al. 2014a; Yakubu et al. 2014b).

The RS consisted of four parts, the structural frame, water reticulation, the plot, and the robotic systems. Fig. 1 shows the illustration of the RS. The structural frame ensures the stability of the RS as a whole, the catch trays were made as an expandable unit both horizontally and vertically to match the rain spray line. The catch trays can recycle about half of the applied water in the system, thereby making the simulator efficient in water consumption. The reticulation system consisted of 32 mm diameter suction pipe and 25 mm diameter outlet pipe connected to a regulated flow meter. The flow meter measured the amount of water through the water system at any given pressure. The RS consisted of two Veejet 80100 nozzles spaced 1.0 m apart on an oscillating boom attached to robotic arm powered from a DC power source and regulated by a microcontroller. The flow and pressure can be regulated from a flow meter while a fast close-off valve could be used to initialise or terminates water flow in the system.

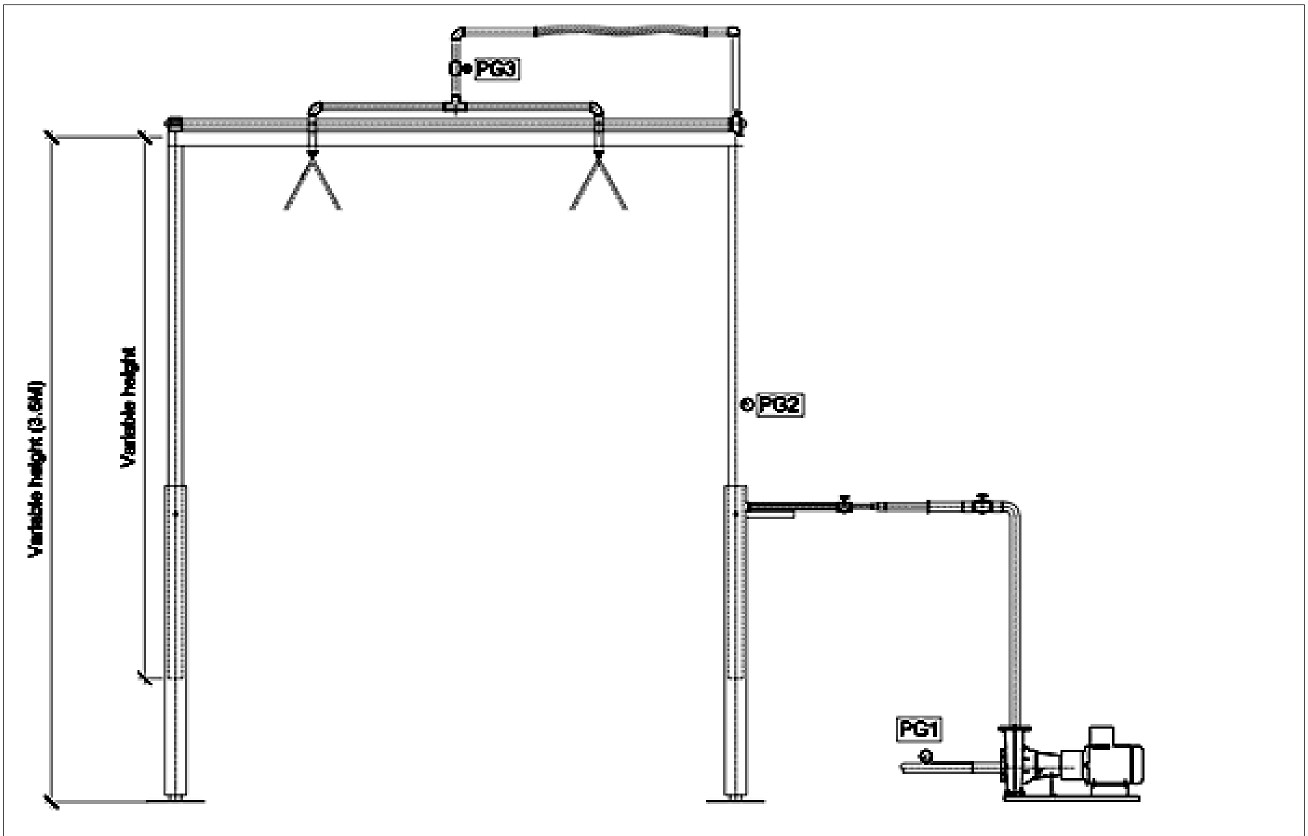

Figure 1. Illustration of the Rainfall Simulator.

To establish the influence of pressure, three pressure gauges were installed. The suction pressure was monitored using a pressure gauge (PG1) as shown in Fig 1. The nozzle pressure was monitored using pressure gauge (PG3), and the third pressure gauge (PG2) was installed halfway between the two pressure gauges at a height of 1.5 m above ground level. The frame of the simulator covered 3m2 (1.5 x 2.0 m), and the stands were made from light weight circular steel tubes with differentl diameters such that can conveniently be collapsed and secured. A pedal was provided to firmly secure the whole structure to the ground to avoid accidental sway of the RS. The structural frame, except the top frame that houses the nozzles, can be dismantled and coupled easily.

2.2 Measurement

The flour pellet method was used in this study to measure the drop diameter of the RS. The measurement of the drop diameter, its evaluation, and the mathematical steps followed to calculate the D_{50}, and the KEmm were consistent with the natural drop diameter's measurement and was reported elsewhere (Yakubu et al., 2014a). The number and weights of each particle class were obtained and converted into the corresponding diameter based on the Hudson (1963) calibration curve. Volumetric D_{50} were obtained from the plot of percent cumulative volume of the drop diameters for different pressures.

Using cups arranged on a grid was the most widely used method to calibrate RS intensity and its uniformity over the plot area (de Lima and Singh, 2003; Clarke and Walsh, 2007). The measurements were done similar to Esteves et al. (2000), and Fister et al. (2012) but using ninety cylindrical-like shaped containers and exposed to a continuous simulated rain for five minutes at different pressures. The spatial distribution of the rain depth is shown in Fig. 2. The rainfall intensity for each simulation run was calculated by converting the rain depth in each container into a rain intensity.

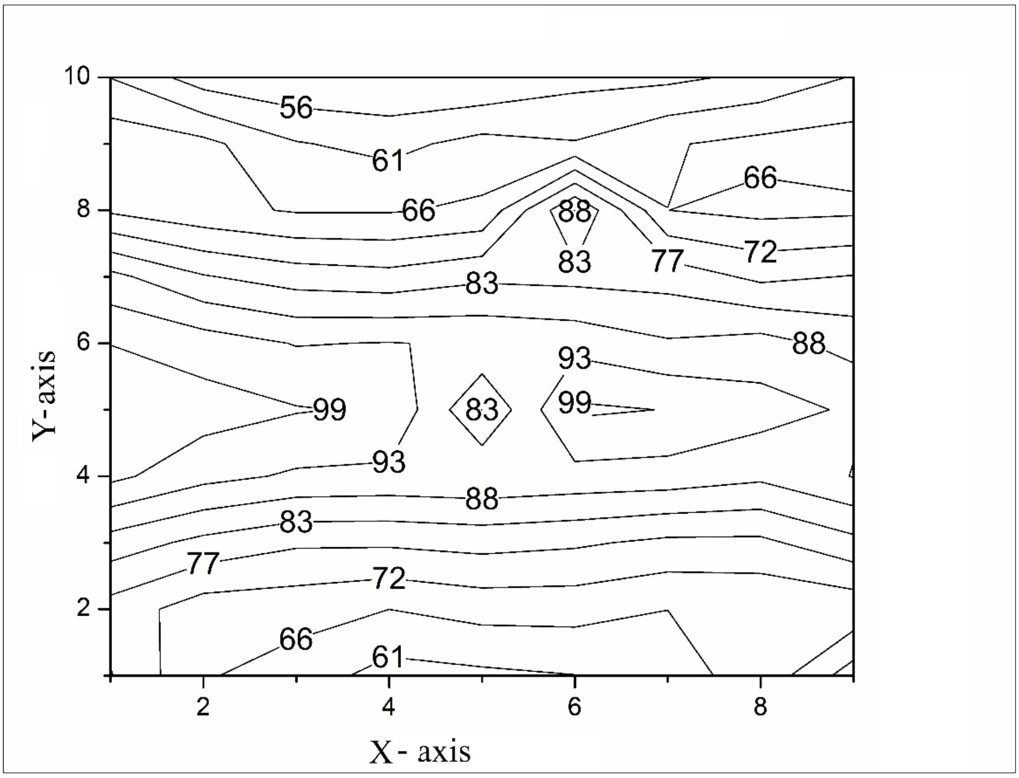

Figure 2. The contour for the chosen combination of nozzles (scale X 1:20cm; Y 1:16cm).

The spatiality of the rainfall was measured using the similarity of the intensity divergence formula (Eq.[1]) introduced by the Christiansen (1942).

$$Cu = \left(1 - \frac{\sum_{i=1}^{n}|x_i|}{n\bar{x}}\right)x100 \qquad [1]$$

$\bar{x}$ is the mean value of the intensity, x_i is the deviation of the intensity value from the mean, and n is the number of intensity measured.

3 RESULT AND DISCUSSIONS

3.1 Construction

RS are designed to mimic rain parameters of their rain characteristics study (Dimoyiannis et al. 2001, Clark et al. 2007). The RS in this study was designed to replicate the rainfall characteristics of the study area as closely as possible, but flexible to be adopted to other studies.

The nozzle pressure can be selected with a high degree of accuracy from the monitoring of either P2, or the FV. The contradictory reporting of the effect of pressure on the intensity in the literature could be due to the lack of precise reporting of the referral pressure reading, the suction, or the pumping pressure. In addition

  / ISSN 1562-6865 (Online) - ISSN 1063-7710 (Print)

to the P2, P3 and FV readings, the suction pressure (P1) was also monitored to establish their relationships. From Fig. 3, the intensity, which is a function of the flow rate in this case, increases with increasing pumping pressure (P2), while it increases with the decline suction pressure (P1). This could mean those researchers that inferred rain intensity decreases with increasing pressure (e.g. Cerdà et al., 1997; Pérez-Latorre et al., 2010) referred to the suction pressure. This brought to fore the need for comprehensive reporting of the RSs calibration, and the need to draw a standard calibration report for all RSs.

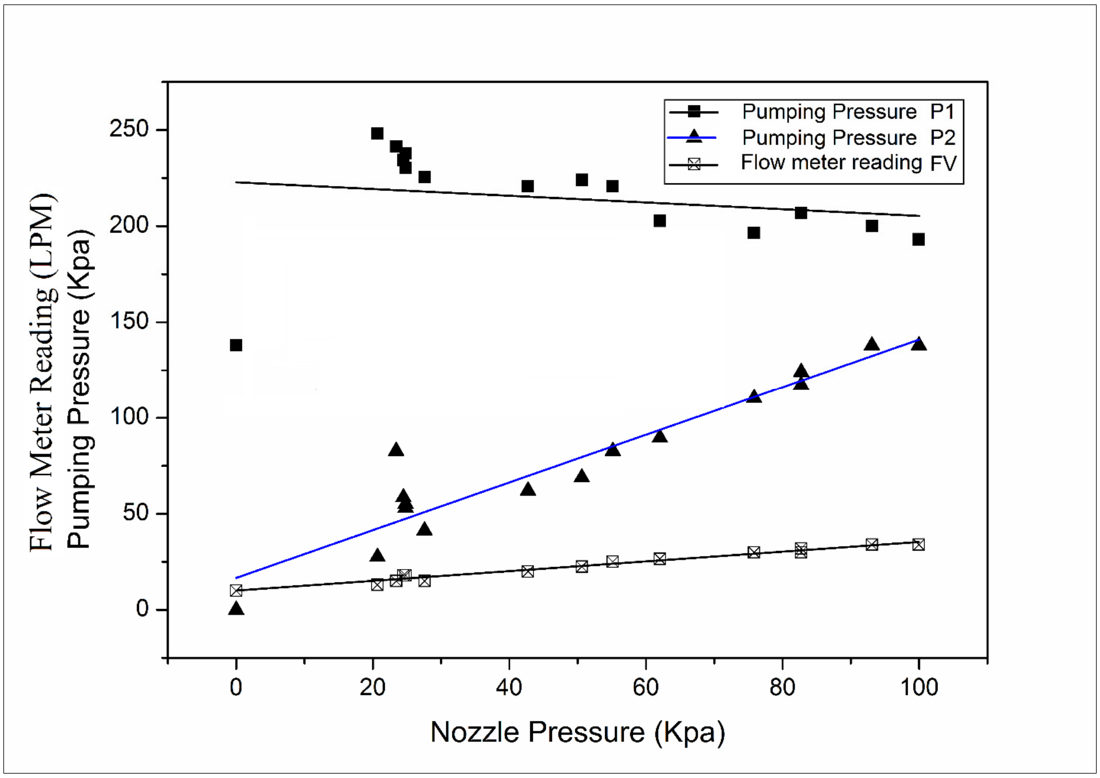

Figure 3. Relationship between monitored pressures in the RS system.

3.2 Rainfall intensity and rain uniformity

The spatiality of the intensity was measured in the Cartesian planes of the RS. Measurements were carried out for the intensity and their corresponding averaged intensity, and uniformity. The results are tabulated in Table 1.

Table 1: corresponding Intensity and uniformity of the RS.

Pressure (kPa)	Intensity	Uniformity
93	199	85
60	162	87
41	154	87
18	146	83
18-41 [b]	132	89

The spatial distribution of the intensity was not the same all over the plot. The RS was found to have consistently recorded higher uniformity along the intersection zones, and lower along boom oscillation. This was expected, because of the V-shape nature of the nozzles. The result of the descriptive analysis on the uniformity on both axes and the average over the entire plot area from the measurements is presented in Table 2.

Table 2: descriptive uniformity of the RS.

	Mean	S.D	Variance	Mode	Median	Min.	Max.
X-Cu	91	5.76	33.21	92	93	78	97
Y-Cu	79	4.92	24.20	81	81	68	83
Average Cu (%)	86	3.26	10.64	87	87	80	89

[b] Sporadic intensity.

On average, the RS achieved a uniformity of 91±5.76% along the X-grid, and 79±4.92% along the Y-grid. The overall average uniformity of the RS was found to be 86±3.26%. An RS uniformity greater than 80% is considered satisfactory for small plot, while 70% is acceptable for larger plot sizes (Esteves et al., 2000). Therefore, the uniformity of the RS was considered adequate for rain simulation.

Result from Table 3 shows that the more frequent the nozzles were temporally oscillated the lower the rain intensity, but the lesser the uniformity of the rain. The RS gave an intensity up to 214 mm h^{-1} at 93 kPa when oscillated at 0.08 Hz, and a minimum of 87 mm h^{-1} at the same pressure setting, but at 0.2 Hz temporal frequency. Delaying the nozzle at the catch tray would give as low as 33 mm h^{-1} at 41kPa.

Table 3: Intensity and uniformity at different frequency operated at 93kPa.

Intensity (mm h^{-1})	Uniformity (%)	Temporal frequency (Hz)
214	87	0.08
210	88	0.10
207	88	0.10
197	86	0.12
193	78	0.12
188	79	0.18
166	87	0.20

3.3 Simulated raindrops

The D_{50} values obtain for the RS is presented in Table 4, the drop diameter increases with decreasing pressure. The D_{50} at the vacillating intensity was not measured but was taken as an average of the D_{50} at 18 and 41 kPa.

Table 4: Median drop diameter at different operating pressure.

Pressure (kPa)	D50(mm)
93	2.41
60	2.38
41	2.43
18	2.64
18-41	2.54

For field investigation, the median drop diameters that corresponded to 18, 41, and 60 kPa were chosen for simulation. These diameters were simulated at the oscillation speed that corresponds to the frequency of 0.18 Hz.

The simulated D_{50} of the RS compared with the natural rainfall of the region was 2.51±0.13mm, and the ranges of drop diameters were from 0.73 to 6.53mm compared with the natural drop diameters of the study area of 1.2 to 7.0mm (Yakubu *et al.* 2014a). Both the drop diameter and its distributions of the RS were considered satisfactory to replicate the rain characteristics of the study area.

Table 5 outlines the terminal velocities of the RS using the derived formulation in this studies Eq. [2], and was compared with the terminal velocity of the natural raindrops calculated from Uplinger (1981) exponential formula Eq. [3], which was a close approximation of Gunn and Kinzer (1949).

$$v_{\mathrm{T}} = 4.0325\,\sqrt{d^{0.87603}} \qquad [2]$$

$$v_T = 4.854\,D\exp(-0.195D) \qquad [3]$$

D is the drop diameter (mm)

Table 5: Terminal velocities the RS using the derived formulation, and the terminal velocity of natural raindrop.

Drop diameter	v_T according to Eq. [2]	v_T according to Eq. [3]	v_T Similarity (%)
2.64	6.17	7.66	80.54
2.43	5.95	7.34	81.05
2.38	5.90	7.26	81.21
2.41	5.93	7.31	81.09

The RS achieved a terminal velocity similarity with natural rainfall of over 80%; this is considered satisfactory to replicate the natural rainfall's energy content. However, achieving terminal velocity in isolation with the fall height is not sufficient to make a conclusion of the RS's terminal velocity. Blanquies et al. (2003); and also Lynch and Lommatsch (2011) reported that drop from natural rainfall reach the receiving surface at terminal velocity, and noted that there was linear correlation between fall distance and drop size distribution. For this reason, the RS was evaluated at a varying height, to determine the appropriate height at which the RS could be fixed to ensure the achievement of responsive terminal velocity as in natural rainfall.

Unlike natural rainfall where drops fall under the influences of gravity (with zero velocity), the raindrops in the RS have an exit velocity which needs to be countered by the drag forces as they approach the plot surface. The RS's raindrops journey as they exited the nozzle towards the plot area was evaluated according to Eq. [4] and Eq. [5] proposed by Aksoy et al. (2012).

$$v_{exit} = 19 - \frac{50}{11} D_{50} \quad [4]$$

$$V_f(h) = \sqrt{\frac{g - \exp(-2kh)(g - k v_{exit}^2)}{k}} \quad [5]$$

where v_{exit} is the spraying velocity given in Eq. [3] as a function of median drop diameter. The fall velocity V_f at any given height $(h)$of the simulator is presented in Fig. 4.

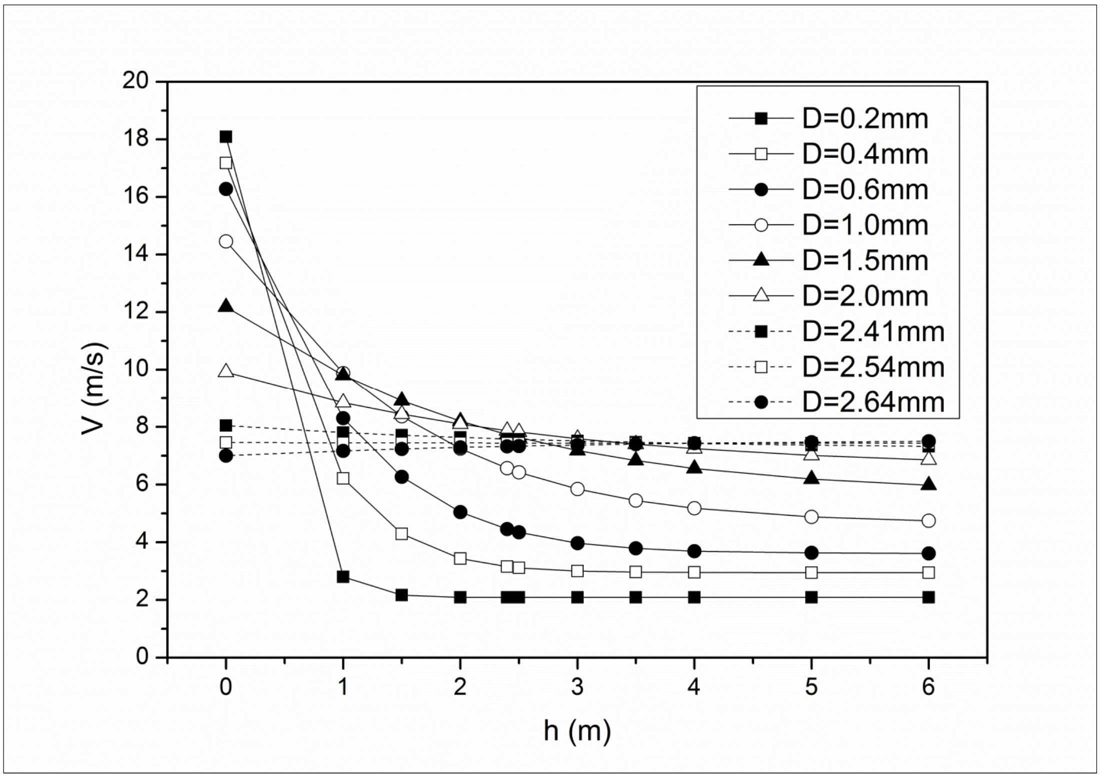

Figure 4. The velocity of fall at a given fall height for different simulated raindrop.

From Fig. 4, the smaller drops ≤ 4.0 mm reached their terminal velocities at about 2.5 m. This represents the natural falling raindrop quite well, where the smaller raindrops attain terminal velocity at a faster rate than the larger drops because they encountered a lesser force (Valette *et al.* 2012). Raindrops between 0.6 mm and 2.0 mm reached their terminal velocities at about 3.5 m, while drops >2.0 mm exited the nozzles almost at their terminal velocities. Considering the range of drop diameters simulated by RS in this study (0.73 to a maximum of 6.53 mm) a 2.5 m was adjudged sufficient for 90% of the drops to have fall at terminal velocity. Generally, a height of at least 2.0 m would be adequate for the simulated raindrops to fall at terminal velocity. Most researchers involved with rainfall simulator operated their RS from an average nozzle height of 2.34±0.30 (Cerdà et al., 1997; Blanquies et al., 2003; Herngren et al., 2004; Júnior and Siqueira, 2011; Aksoy et al., 2012; Iserloh et al., 2012).

3.4 Evaluation of kinetic energy

Kinetic energy is the energy possessed by a moving body, and the kinetic energy of rainfall is the sum total of the individual kinetic energies of rain drops. The kinetic energy of the RS was calculated as half the product of the estimated terminal velocities and the raindrop masses. The calculated kinetic energy content of the simulated RS was done similar with the obtained natural rainfall' KEmm of the study area and have been reported elsewhere (Yakubu *et al.* 2014a). The calculated KEmm (Eq. [6]) of the RS is presented in Table. 6, and compared with the KEmm of the region based on its natural appraisal according to Eq. [7].

$$\text{KEmm} = \frac{300\pi\rho D^3 v_T{}^2}{RtA_s} \qquad [6]$$

$$\mathrm{KEmm} = 50.94[1 - \mathrm{Exp}\,(-0.05\, I)] \qquad [7]$$

I is the rain intensity (mm h^{-1}), duration of sampling (*t* in seconds), and sample surface area (A_s in m^2)

Table. 6: Similarity of natural, and simulated KEmm.

D_{50}(mm)	I (mm h^{-1})	KEmm (simulated)	KEmm (natural)	KEmm Similarity (%)
2.64	145	42.00	50.90	83
2.43	154	33.28	50.92	65
2.38	162	44.40	50.92	87
2.41	217	69.81	50.94	73

The simulated KEmm of the region satisfactorily compares with the natural KEmm. The highest similarity value between the simulated rain and the natural rainfall was 87% corresponding to 2.38 mm D_{50}, while the lowest similarity was at 154 mm h^{-1} intensity. Overall, the RS can simulate KEmm satisfactorily similar with the natural rainfall by more than 75%. This was considered adequate for simulation of the rainfall events of similar characteristics.

4 CONCLUSION

The RS developed in this study was shown to satisfactorily replicate a natural rainfall event. The evaluation of the RS was consistently done from the first principle. The ability of the RS to replicate a natural rain event was adjudged from typical natural rainfall parameters. The RS can achieve a rain uniformity of 86%, between 2.41 and 2.64 mm median raindrop diameter of the natural event, over 80% terminal velocity, and up to 87% of kinetic energy. The RS can be conveniently used in the urban wet weather process involving impervious surfaces, and could easily be adopted in other processes that may need isolation of rainfall parameters.

ACKNOWLEDGEMENTS

The authors wish to acknowledge the Research Management Centre of Universiti Teknologi Malaysia (UTM) for facilitating this research under Research University Grant (vote no. Q.J130000.2509.01H72). This study was also supported by the Asian Core Program of the Japanese Society for the Promotion of Science (JSPS), the Ministry of Higher Education (MOHE) in Malaysia, and Nineteen Consult Ltd, Nigeria.

REFERENCES

Aksoy, H., Unal, N.E., Cokgor, S., Gedikli, A., Yoon, J., Koca, K., Inci, S.B. & Eris, E. (2012). A Rainfall Simulator for Laboratory-Scale Assessment of Rainfall-Runoff-Sediment Transport Processes over a Two-Dimensional Flume. *Catena*, 98, 63-72.

Blanquies, J., Scharff, M. & Hallock, B. (2003). The Design and Construction of a Rainfall Simulator. *International Erosion Control Association (IECA), 34th Annual Conference and Expo*, Las Vegas, Nevada, 1-10.

Brodie, I.M. & Dunn, P.K. (2010). Commonality of Rainfall Variables Influencing Suspended Solids Concentrations in Storm Runoff from Three Different Urban Impervious Surfaces. *Journal of Hydrology*, 387(3–4), 202-211.

Cerdà, A., Ibáñez, S. & Calvo, A. (1997). Design and Operation of a Small and Portable Rainfall Simulator for Rugged Terrain. *Soil Technology*, 11(2), 163-170.

Christiansen, J.E. (1942). *Irrigation by Sprinkling*. California agricultural experiment station bulletin 670. University of California, Berkeley, CA, 4275.
Clark, S.E., Burian, S., Pitt, R. & Field, R. (2007). Urban Wet-Weather Flows. *Water Environment Research*, 79(10), 1166-1227.
Clarke, M.A. & Walsh, R.P. (2007). A Portable Rainfall Simulator for Field Assessment of Splash and Slopewash in Remote Locations. *Earth Surface Processes and Landforms*, 32(13), 2052-2069.
Corona, R., Wilson, T., D'adderio, L.P., Porcù, F., Montaldo, N. & Albertson, J., (2013). On the Estimation of Surface Runoff through a New Plot Scale Rainfall Simulator in Sardinia, Italy. *Procedia Environmental Sciences*, 19, 875-884.
De Lima, J.L.M.P. & Singh, V.P. (2003). Laboratory Experiments on the Influence of Storm Movement on Overland Flow. *Physics and Chemistry of the Earth*, Parts A/B/C, 28 (6–7), 277-282.
Dimoyiannis, D.G., Valmis, S. & Vyrlas, P. (2001). A Rainfall Simulation Study of Erosion of Some Calcareous Soils. *7th International Conference on Environmental Science and Technology*. Ermoupolis, Syros island, Greece.
Dunkerley, D. (2012). Effects of Rainfall Intensity Fluctuations on Infiltration and Runoff: Rainfall Simulation on Dryland Soils, Fowlers Gap, Australia. *Hydrological Processes*, 26(15), 2211-2224.
Egodawatta, P., Thomas, E. & Goonetilleke, A. (2007). Mathematical Interpretation of Pollutant Wash-Off from Urban Road Surfaces using Simulated Rainfall. *Water Research*, 41(13), 3025-3031.
Esteves, M., Planchon, O., Lapetite, J.M., Silvera, N. & Cadet, P. (2000). The `Emire' Large Rainfall Simulator: Design and Field Testing. *Earth Surface Processes and Landforms*, 25 (Special issue), 681-690.
Feng, G., Sharratt, B. & Vaddella, V. (2013). Windblown Soil Crust Formation under Light Rainfall in a Semiarid Region. *Soil and Tillage Research*, 128, 91-96.
Fister, W., Iserloh, T., Ries, J.B. & Schmidt, R.G. (2012). A Portable Wind and Rainfall Simulator for in Situ Soil Erosion Measurements. *Catena*, 91, 72-84.
Guevara-Escobar, A., Gonzalez-Sosa, E., Ramos-Salinas, M. & Hernandez-Delgado, G.D. (2007). Experimental Analysis of Drainage and Water Storage of Litter Layers. *Hydrology Earth System and Sceince*, 11(5), 1703–1716.
Gunn, R. & Kinzer, G.D. (1949). The Terminal Velocity of fall for Water Droplets in Stagnant Air. *Journal of Meteorology*, 6(4), 243-248.
Herngren, L., Goonetilleke, A. & Ayoko, G. (2004). Investigation of Urban Water Quality using Artificial Rainfall. *Proceedings of the Water Environment Federation*, 2004(4), 1169-1184.
Hudson, N., (1963). Raindrop Size Distribution in High Intensity Storms. *Rhodesian Journal of Agricultural Research*, 1(1), 6-11.
Iserloh, T., Fister, W., Seeger, M., Willger, H. & Ries, J.B. (2012). A Small Portable Rainfall Simulator for Reproducible Experiments on Soil Erosion. *Soil and Tillage Research*, 124, 131-137.
Júnior, S.F.S. & Siqueira, E.Q. (2011). Development and Calibration of a Rainfall Simulator for Urban Hydrology Research. *12th International Conference on Urban Drainage*. Porto Alegre/Brazil, 11-16.
Kim, L.-H., Zoh, K.-D., Jeong, S.-M., Kayhanian, M. & Stenstrom, M.K. (2006). Estimating Pollutant Mass Accumulation on Highways during Dry Periods. *Journal of Environmental Engineering*, 132(9), 985-993.
Kim, S.C., Davis, J.G., Truman, C.C., Ascough Ii, J.C. & Carlson, K. (2010). Simulated Rainfall Study for Transport of Veterinary Antibiotics - Mass Balance Analysis. *Journal of Hazardous Materials*, 175(1-3), 836-843.
Lynch, B. & Lommatsch, G. (2011). *Modeling the velocity of a raindrop*, 1-13. Available at: http://home2.fvcc.edu/~dhicketh/DiffEqns/Spring11projects/Ben_Lynch_Gavin_Lommatsch/DiffEqProject/DiffEqProjectGavinBen.pdf [Accessed 28 October 2016].
Pall, R., Dickinson, W.T., Beals, D. & Mcgirr, R., (1983). Development and Calibration of a Rainfall Simulator. *Canadian Agricultural Engineering*, 25(2), 181-187.
Pérez-Latorre, F.J., De Castro, L. & Delgado, A. (2010). A Comparison of Two Variable Intensity Rainfall Simulators for Runoff Studies. *Soil and Tillage Research*, 107(1), 11-16.
Resso, R., Rulli, M.C. & Bocchiola, D. (2007). Transient Ctachment Hydrology after Wildfires in Mediterranean Basin: Runoff, Sediment and Woddy Debris. *Hydrology Earth System and Sceince*, 11(1), 125-140.
Sangüesa, C., Arumí, J., Pizarro, R. & Link, O. (2010). A Rainfall Simulator Forthe in Situ Study of Superficial Runoff and Soil Erosion. *Chilean Journal of Agricultural Research*, 70(1), 178 - 182.
Scherrer, S., Naef, F., Faeh, A.O. & Cordery, I. (2007). Formation of Runoff at the Hillslope Scale during Intense Precipitation. *Hydrology Earth System and Sceince*, 11(2), 907–922.
Tiefenthaler, L.L. & Schiff, K.C.,(2003). Effects of Rainfall Intensity and Duration on First Flush of Stormwater Pollutants. *Southern California Coastal Water Research Project Annual Report*, 209-215.

Uplinger, W. (1981). A New Formula for Raindrop Terminal Velocity. *Conference on Radar Meteorology*, 20 th, Boston, MA. 389-391.
Vahabi, J. & Nikkami, D. (2008). Assessing Dominant Factors Affecting Soil Erosion using a Portable Rainfall Simulator. *International Journal of Sediment Research*, 23(4), 376-386.
Valette, G., Prévost, S., Léonard, J. & Lucas, L. (2012). A Virtual Discrete Rainfall Simulator. *Environmental Modelling & Software*, 29(1), 51-60.
Wildhaber, S.Y., Bänninger, D., Burri, K. & Alewell, C. (2012). Evaluation and Application of a Portable Rainfall Simulator on Subalpine Grassland. *Catena*, 91, 56-62.
Yakubu, M.L. & Yusop, Z. (2014). Carbon Matrix as a Surrogate Measure for Polycyclic Aromatic Hydrocarbon Pollution in Road Sediments. *Journal Technology*, 69(2), 111-115.
Yakubu, M.L., Yusop, Z. and Fulazzaky, M.A. (2016). The Influence of Rain Intensity on Raindrop Diameter and the Kinetics of Tropical Rainfall: Case Study of Skudai, Malaysia. *Hydrological Sciences Journal*, 61(5), 944-951.
Yakubu, M.L., Yusop, Z. & Yusof, F. (2014b). The Modelled Raindrop Size Distribution of Skudai, Peninsular Malaysia, using Exponential and Lognormal Distributions. *The Scientific World Journal*, 2014, 1-7.

STUDY OF PRESSURE DISTRIBUTION AND VOLUME FRACTION OF AIR AND WATER ACROSS THE CHANNELS OF OXIDATION DITCH

NOOR AIDA SAAD(1), HAMIDI ABDUL AZIZ(2), MOHD ZULKIFLY ABDULLAH(3) & MOHAMED ZUBAIR(4)

(1)River Engineering and Urban Drainage Research Centre (REDAC), Universiti Sains Malaysia,
aidasaad@usm.my
(2)School of Civil Engineering, Universiti Sains Malaysia
cehamidi@usm.my
(3) School of Aerospace Engineering, Universiti Sains Malaysia,
mezul@usm.my
(4)Department of Aerospace Engineering, Faculty of Engineering,
mzuber@upm.edu.my

ABSTRACT

Orbal Biological System (OBS) has been designed to provide an optimized approach of the biological treatment process. The unique OBS aeration discs are claimed to provide high oxygen transfer and mixing efficiency. High power usage by aerators has commonly been a major issue for Extended Aeration (EA) biological system. In order to provide a better understanding of the OBS, as one type of a modified oxidation ditch, the research aims to develop a Computational Fluid Dynamics (CFD) model to visualize the water and air distribution throughout the oxidation ditch. The research aims to develop a model that can represent a full-scale OBS that may contribute to a better understanding of the unit process by assessing the current operational performance which is related to aeration shafts of the OBS. A 3D multiphase and an open channel CFD-based model have been developed to simulate the hydrodynamics in an OBS. Open channel flow modelling which takes into consideration the influence of atmospheric air provides the data of the volume fractions of water and air. The developed 3D two phases CFD model has shown a good representation of the real OBS. Variations of volume fractions are supporting the reality of the occurrence of anoxic and aerobic conditions throughout the OBS. It can also be observed that due to the mixers, the air composition is extended to at least half (50%) of the tank's depth. The volume fractions of the air are higher at the surface level compared to the bottom of OBS. This also demonstrates that the oxygen due to the mixing is facilitated by the mixers and they are effective in increasing the composition or volume fraction of oxygen throughout the ditch. These important findings are made possible due to the developed advanced CFD model which incorporating the open channel flow system.

Keywords: Orbal biological system (OBS); computational fluid dynamics (CFD); oxidation ditch; aeration devices; biological treatment.

1 INTRODUCTION

The Orbal Biological System (OBS) is one of the modified oxidation ditches that apply a sequence of concentric channels inside a single biological reactor. Oxidation Ditch (OD) is better than other biological treatment system because of its unique mixing performance (Wu et al., 2012). OBS has been designed to provide an optimized approach of the biological treatment process. The most important feature of OBS is its aeration devices. The unique OBS aeration discs are claimed to provide high oxygen transfer and mixing efficiency. Making dissolved oxygen (DO) transfer from gas to liquid phase is a very energy intensive activity in the treatment plant, as well as crucial for the treatment results (Amand, 2011). The system is designed to provide an extensive operational flexibility especially in terms of the ability to manipulate oxygen transfer rates. There are many advantages of this system claimed by its manufacturer. However, WWTPs that are currently applying the system faced some significant problems related to its operational system. High power usage by aerators has commonly been a major issue for EA biological system such as Orbal and also other multichannel ditches.

It is well known that full-scale bioreactors do not provide an entirely uniform environment. A system such as OBS, intense oxygen transfer occurs in one portion of the bioreactor, limited oxygen transfer occurs throughout the rest of the bioreactor and mixed liquor is recycled between the aerated and non-aerated zones (Daigger and Littleton, 2014). Anoxic and aerobic condition is developed and maintained in zones up-stream and downstream of the rotor. Due to the structural design of the OBS that has great potential to promote optimal treatment processes, it is very crucial to study its operating system. Due to this reason, the study was conducted to understand the complicated process of OBS. The research aims to develop a model that can represent a full-scale OBS that may contribute to a better understanding of the unit process by assessing the current operational performance which is related to aerations shafts of the OBS.

Currently, CFD application is well established not just among the researchers in the developed countries, but also in the developing countries. Many case studies from China (Xie et al., 2014; Lei and Ni, 2014; Guo et al., 2013; Xie et al., 2011; Yang et al., 2011; Yang et al., 2010; Luo et al., 2005) involve the application of CFD for the optimization of the biological treatment plant. These papers were established to stimulate the hydrodynamics and processes occurred in an OD. Although the CFD modelling of biological treatment systems has taken place for over 15 years now (Karpinska and Bridgeman, 2016), there are number of concerns which are still unresolved and which, if successfully be surmounted, would improve model reliability and stability.

2 METHODOLOGY

A 3D multiphase and an open channel CFD-based model were developed to simulate the hydrodynamics in an Orbal Biological System. Five major steps of CFD simulation are shown in Figure 1.

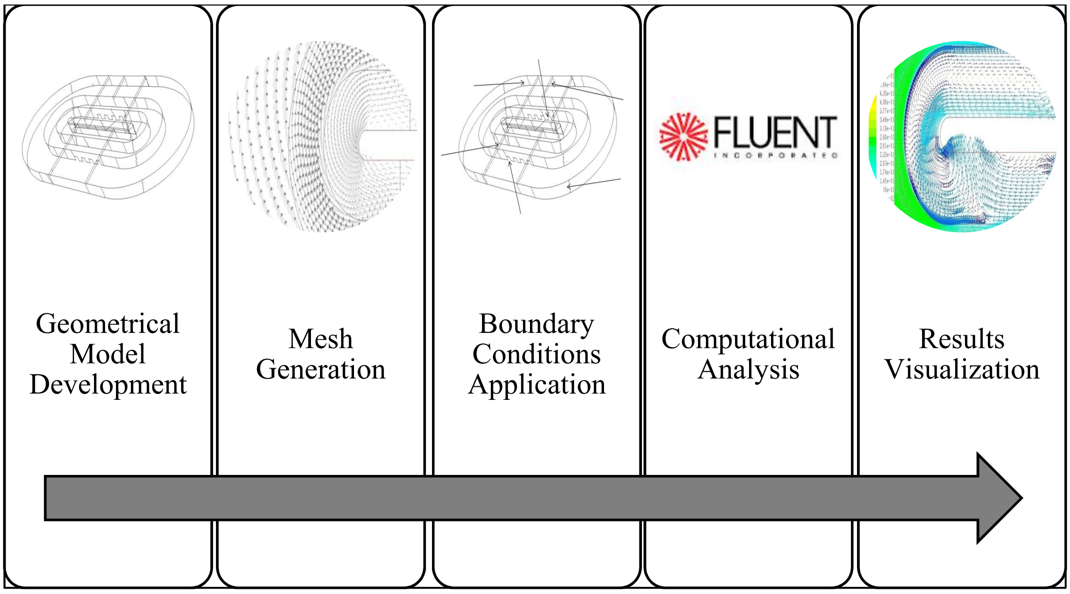

Figure 1. Five major steps of CFD simulation.

In 3D CFD model, the boundary condition of the inlet was applied as a mass flow inlet. This type of boundary condition was applied because it allows the total pressure to differ in response to the interior solution. Aeration shafts were represented by fan model with the definition of the pressure drop values. The pressure drop values were calculated using the parameters of the power input, area of the disc, the density of the fluid and the average flow velocity throughout the ditch. The fan model is actually predicting the amount of flow through the fan. Side walls and bottom walls of OBS were defined as a non-slip wall. The effluent was defined as outflow since the exit flow velocity and pressure are not known due to the complexity of the flow inside the ditch. The penstocks between the channels were presented as interface. The interface was used to unite two faces of different volumes. The details of the geometrical layout and boundary condition of 3D model are given in Table 1 and Figure 2.

Table 1. 3D model boundary condition.

Name	Type
Influent	Mass-flow-inlet (mass flow rate is 580 kg/s)
Outer, middle and inner channel	Fluid (water liquid, air)
Aeration shafts	Fan
Penstocks between channels	Interface
Effluent	Outflow

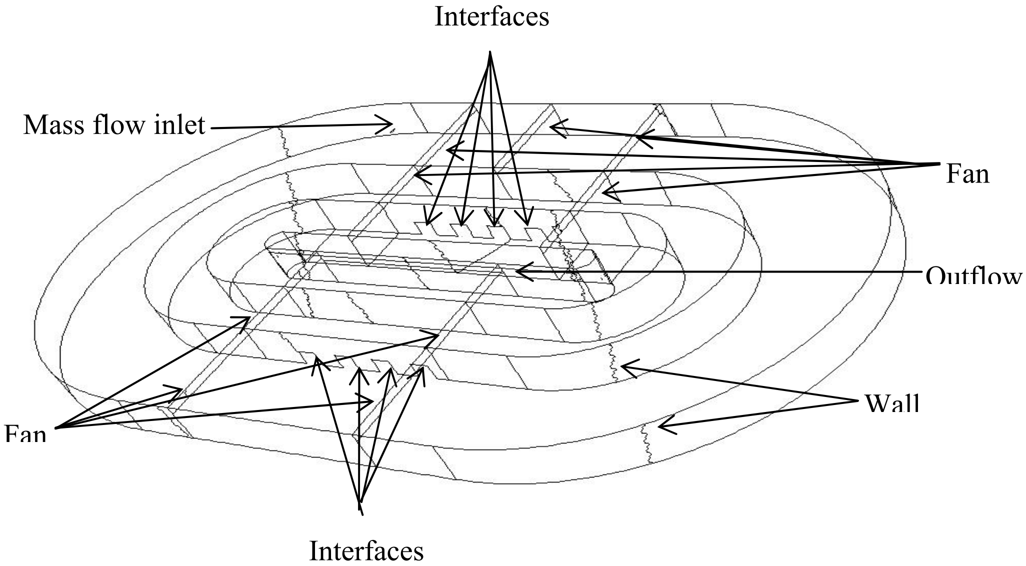

Figure 2. Boundary conditions of 3D model.

Solver settings of the 3D model simulation are summarized in Table 2. The segregated solver of Fluent 15.1 was used with the default parameter settings applied. All simulations were performed using Intel Core 2 Quad CPU2.5 GHz processor and 8 GB installed memory (RAM). Each run took more than 72 hr of CPU time to reach steady condition.

The default values of standard k-epsilon turbulence model were used in the simulation. K-epsilon turbulence model is suitable for turbulent flows. Based on the Fluent's user guide, k-epsilon turbulence model is considered as the simplest 'complete model', which allows the turbulent velocity and length, scales to be independently determined. Derivation of the standard k-epsilon are based on model transport equations for the turbulence kinetic energy (k) and its dissipation rate (ε).

Table 2. 3D model case setup.

Models	
Space	3D
Time	Unsteady
Viscous	Standard k-epsilon turbulence model
Wall Treatment	Standard Wall Functions
Coupled Dispersed Phase	Enabled
Solver settings	
Flow Equation	Solved
Volume Fraction Equation	Solved
Turbulence Equation	Solved

Sampling and water quality analyses were conducted for the purpose of calibrating and validating the models. Onsite sampling works were performed at Bayan Baru Wastewater Treatment Plant. Samples were collected for 20 days at six points (S1-S6 as described in Figure 3) which were identified within the channels to give an indication of the incoming (upstream) and outgoing (downstream) values for each channel. The sampling points were 1m from the channel walls (horizontally) and 0.4m below the water surface (vertically). During actual ditch operation, the water near the aeration disks is affected by a centrifugal force, causing the water surface to be uneven. However, this unevenness is negligible when compared to more than 4m water depth in the channel (Guo et al., 2013). For the pupose of the model validation, velocity values of same six points were obtained from the CFD results and compared to results of in situ measurements.

Onsite measurements were performed in order to get the idea of the values of some parameters, which were considered significant to the research, either for the purpose of analyzing or for the purpose of monitoring. The velocity values were obtained using current meter. Other parameters such as dissolved oxygen (DO), temperature, pH, conductivity, salinity and total dissolved solid were used for monitoring purposes.

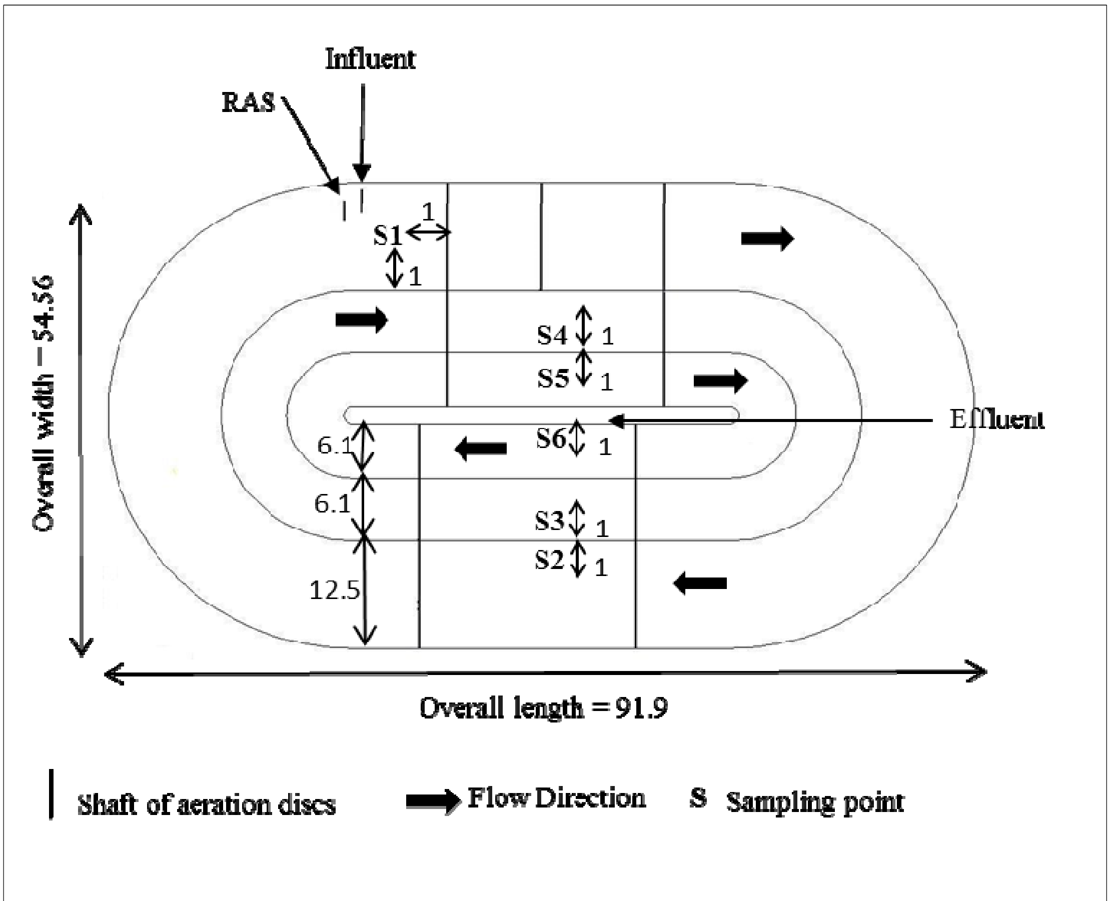

Figure Error! No text of specified style in document.**.** Plan view sketch (unit: m) of the OBS and sampling points at 4.4m depth of water level.

3 RESULTS AND DISCUSSION

Figure 4 and Figure 5 describe the distribution of two phases (air and water) involved in this study. The sectional contours obtained at the centre of the OBS show the distribution of air and its influence on the water due to the aeration discs. This was not possible using the simplified 2D model. The 3D model is able to provide more detailed information on the effects of the aeration devices as the mixers inside the OBS. Variation of volume fractions are in fact supporting the reality of the occurrence of anoxic and aerobic conditions throughout the OBS. The volume fractions have indicated the real conditions of OBS as an open channel system.

Figure 4 describes the fraction of water in the OBS. The distribution is represented in the array of colors with blue representing less or zero volume of water and red indicating the maximum portion of the composition to be water. Thus, it can be inferred from this figure that water composition is maximum at the bottom of the tank as expected, whilst it is lowest on the top of the tank. This is because the top portion of the tank is exposed to atmospheric air on account of the open channel flow modelling. This was possible only with 3D CFD model. The 2D model would fail to account this fundamental notion of mixing of air which was the purpose which the oxidation ditch was built for. Most works found in literature assume a 3D channel without the open channel system. This renders the flow to be identical to that of the inside of a closed duct and therefore would not accurately capture the realistic flow assumption of OBS.

Secondly, it can also be observed that due to the mixers, the air composition is extended to at least half of the tank's depth as can be inferred from Figure 5. Based on Figure 5, it can be seen that the volume fractions of the air are higher at the surface level compared to the bottom of OBS. This also demonstrates that the oxygen mixing is facilitated by the mixers and the mixers are effective in increasing the composition or volume fraction of oxygen throughout the ditch. The figure shows that oxygen penetration is almost negligible at the bottom of the OBS. These important findings are made possible due to the advanced CFD model developed incorporating the open channel flow system.

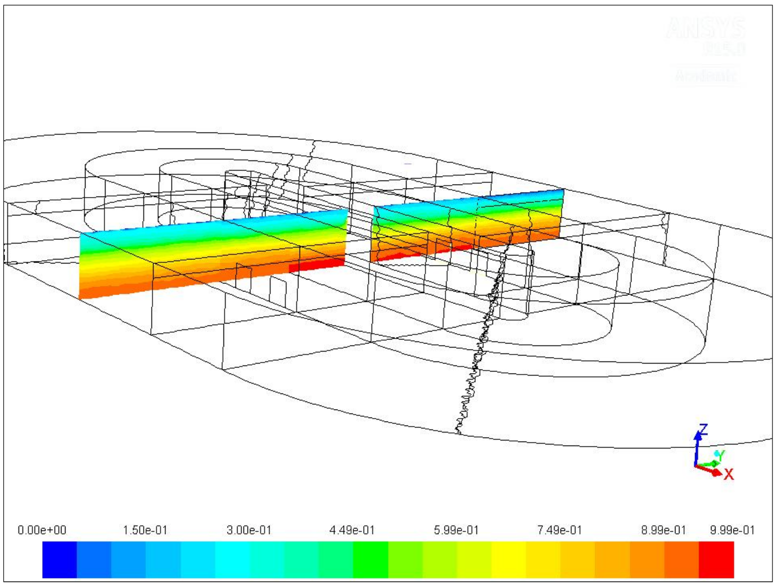

Figure 4. Contours of volume fraction of water.

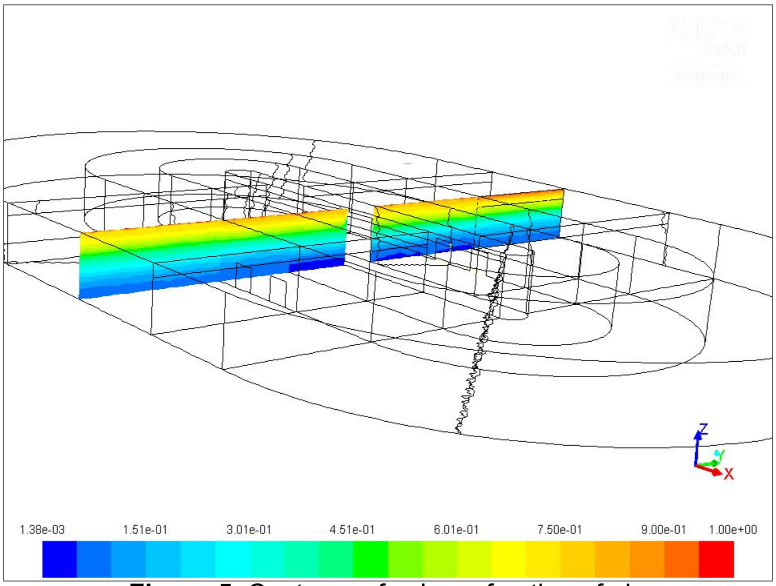

Figure 5. Contours of volume fraction of air.

4 CONCLUSIONS

The study shows that CFD application has the ability to provide a better look inside the OBS including the aspects of flow representation, flow distribution for different operating conditions and distribution of hydraulic residence time throughout the whole system. The developed 3D two phases CFD model has shown a good representation of the real OBS. The flow pattern given by this model indicates the right flow pattern and velocity distribution of the system. Velocity profiles given by 3D CFD model is well matched the velocity values obtained through in-situ measurements. The developed 3D model was able to provide more detailed information on the effects of the aeration devices as the mixers inside the OBS.

REFERENCES

Amand, L. (2011). Control of Aeration Systems in Activated Sludge Processes- A Review. *IVL Sweedish Environmental Research Institute,* 1-19.

Daigger, G.T. & Littleton, H.X. (2014). Simultaneous Biological Nutrient Removal: A State-of-the-Art Review. *Water Environment Research,* 86, 245-257.

Guo, X., Zhou, X., Chen, Q. & Liu, J. (2013). Flow Field and Dissolve Oxygen Distributions in the Outer Channel of the Orbal Oxidation Ditch by Monitor and CFD Simulation. *Journal of Environmental Sciences,* 25, 645-651.

Karpinska, A.M. & Bridgeman, J. (2016). CFD-Aided Modelling of Activated Sludge Systems - A critical Review. *Water Research,* 88, 861-879.

Lei, L. & Ni, J. (2014). Three-Dimensional Three-Phase Model for Simulation of Hydrodynamics, Oxygen Mass Transfer, Carbon Oxidation, Nitrification and Denitification in an Oxidation Ditch. *Water Research,* 53, 200-214.

Luo, L., Li, W.-M., Deng, Y.-S. & Wand, T. (2005). Numerical Simulation of a Combined Oxidation Ditch Flow using 3D k- & Epsilon; Turbulence Model. *Journal of Environmental Sciences,* 17, 808-812.

Wu, S.Y., Zhou, D.Q. & Zheng, Y. (2012). Energy Configuration Optimization of Submerged Propeller in Oxidation Ditch based on CFD. *26th IAHR Symposium on Hydraulic Machinery and Systems 2012.* IOP Publishing.

Xie, H., Yand, J., Hu, Y., Zhang, H., Yand, Y., Zhang, K., Zhu, X., Li, Y. & Yang, C. (2014). Simulation of Flow Field and Sludge Settling in a Full-Scale Oxidation. *Chemical Engineering Science,* 109, 296-305.

Xie, W.-M., Zhang, R., Li, W.-W., Ni, B.-J., Fang, F., Sheng, G.-P., Yu, H.-Q., Song, J., Le, D.-Z., Bi, X.-J., Liu, C.-Q. & Yang, M. (2011). Simulation and Optimization of a Full-Scale Carrousel Oxidation Ditch Plant for Municipal Wastewater Treatment. *Biochemical Engineering Journal,* 56, 9-16.

Yang, Y., Wu, Y.Y., Yang, X., Zhang, K. & Yang, J.K. (2010). Flow Field Prediction in Full-Scale Carrousel Oxidation Ditch by using Computational Fluid Dynamics. *Water Science Technology,* 62, 256-265

Yang, Y., Yang, J., Zuo, J., Li, Y., He, S., Yang, X. & Zhang, K. (2011). Study on Two Operating Conditions of a Full-Scale Oxidation Ditch for Optimization of Energy Consumption and Effluent Quality by using CFD Model. *Water Research,* 45, 3439-3452.

